NOAA ATLAS No. 12

Interseasonal and Interannual Variability: 1986 to 1993

Camp Springs, MD 20746
February 1995

U.S. DEPARTMENT OF COMMERCE
National Oceanic and Atmospheric Administration
National Weather Service

NOAA ATLAS No. 12

Interseasonal and Interannual Variability: 1986 to 1993

Gerald D. Bell and Michael S. Halpert

Climate Analysis Center
National Meteorological Center
National Weather Service

Camp Springs, MD 20746
February 1995

U.S. DEPARTMENT OF COMMERCE
Ronald H. Brown, Secretary
National Oceanic and Atmospheric Administration
Dr. D. James Baker, Under Secretary
National Weather Service
Dr. Elbert W. Friday, Jr., Assistant Administrator

TABLE OF CONTENTS

Interseasonal and Interannual Variability: 1986 to 1993

1. INTRODUCTION

This atlas documents the interseasonal and interannual variability in both the tropics and extratropics for the 8-year period from January 1986 through November 1993. The atlas is designed to serve three primary purposes:

1. Document the seasonal evolution of the major Pacific warm episodes (1986/87, 1991-1993), termed El Nino/ Southern Oscillation (ENSO) events, and cold episode (1988-89) that occurred since the 1982/83 ENSO (Arkin et al. 1983).
2. Document the seasonal extratropical atmospheric circulation, surface temperature and precipitation anomalies in both hemispheres during the above period.
3. Document the primary modes of low-frequency variability (termed teleconnection patterns) of the atmospheric circulation in the Northern Hemisphere extratropics, and their evolution during the above period.

2. DATA and ANALYSIS

Seasonal mean and anomaly fields are displayed in mercator and polar-stereographic projection, and in height-longitude and depth-longitude sections. Monthly anomaly fields are displayed in time-longitude sections only. The fields shown are sea-surface temperature and anomaly, sub-surface ocean temperature anomaly, Outgoing Longwave Radiation (OLR) anomaly, lower and upper-tropospheric wind anomaly, geopotential height and anomaly, storm track anomaly, surface temperature anomaly, precipitation percentiles of normal, and Northern Hemisphere teleconnection patterns and their time series.

a. Sea- Surface Temperature and Anomaly, (pp. 32-49):

Sea-surface temperatures are derived from an ocean-data assimilation system (ODAS)

developed at the Coupled Model Project/NMC (Smith and Chelliah 1994). A blended SST analysis (Reynolds and Marsico 1993) is used to produce the seasonal mean and anomaly fields shown in this atlas. The blended SST analysis has been used routinely at the Climate Analysis Center/NMC to monitor the state of the El Nino-Southern Oscillation (ENSO) on an operational basis (Climate Diagnostics Bulletin, ENSO Advisory).

Sea-surface temperatures are displayed in one format:

(1) Equatorial time-longitude sections spanning the Pacific Ocean (pp. 32-36).

Sea-surface temperature anomalies (°C) are displayed in three formats:

(1) Time series of anomalies in the Nino regions (p. 28) and along ship tracks 1 and 6 (p. 29).

(2) Seasonal maps between 50°S and 50°N (pp. 37-45).

(3) Equatorial time-longitude sections spanning the Pacific Ocean (pp. 46-49).

b. Sub-surface Ocean Temperature Anomaly, (pp. 50-66):

Ocean observing networks were greatly expanded over the tropical Pacific during the 1980's. These networks now include the TOGA-TAO array of moored buoys (Hayes et al. 1991), a network of sea-level monitoring stations in the tropical Pacific, sea-level variations from the Topex/Poseidon satellite, and SSTs from a combination of satellite and in situ observations (Reynolds and Smith 1994).

These data are incorporated into ocean GCMs and assimilated into near-real-time gridded fields of the subsurface ocean velocity, temperature and salinity (Leetmaa and Ji 1989, Ji et al. 1994). These gridded fields are displayed routinely in the Climate Diagnostics Bulletin, and have become an important part of the climate monitoring program, particularly with regard to monitoring the ENSO cycle and higher frequency phenomena such as oceanic Kelvin wave activity. The assimilated sub-surface ocean temperatures are monthly averaged on a 1°x1.5° latitude-longitude grid between 35°S and 45°N. The data are archived on 27 vertical levels to a maximum depth of 430 meters (m). The vertical resolution is 10 m in the

upper 100 m of the ocean, and increases to 85 m at maximum depth.

The 20°C isotherm is at the center of the oceanic thermocline in the tropical Pacific. Thus, this isotherm is used to monitor interseasonal and interannual variations in the structure and position of the oceanic thermocline, and the corresponding changes in sub-surface ocean temperature. An anomalously shallow (deep) thermocline is associated with a decreased (increased) depth of the 20°C isotherm, and with anomalously cold (warm) ocean temperatures.

The **sub-surface thermocline** structure is displayed in two formats:

(1) Seasonal maps of the anomalous depth of the 20°C isotherm spanning the Pacific Ocean (pp. 50-58).

(2) Equatorial depth-longitude sections of anomalous ocean temperature (°C) over the Pacific Ocean (pp. 58-66).

c. Outgoing Longwave Radiation Anomaly, (pp. 67-79):

Outgoing longwave radiation (OLR) values are directly related to cloud top temperatures, and are used as a proxy for deep convection in the tropics. For example, deep convection is associated with high and cold cloud tops, and is identified by low values of OLR (generally < 240 Wm^{-2}). Enhanced/ above-normal convection is indicated by negative OLR anomalies, while suppressed/ below-normal convection is indicated by positive OLR anomalies. OLR anomalies of ± 10 Wm^{-2} are generally considered near normal.

Global OLR values are obtained from the NOAA series of polar orbiting satellites. These measurements are currently obtained from the NOAA-11 AVHRR IR window channel by NESDIS/SRL, and are archived on 2.5°x2.5° latitude-longitude global grids at the Climate Analysis Center.

OLR anomalies are displayed in three formats:

(1) Time series of anomalies centered at the dateline (p. 30).

(2) Seasonal maps between 50°S and 50°N (pp. 67-75).

(3) Equatorial time-longitude sections spanning the Pacific Ocean (pp. 76-79).

d. Atmospheric Circulation: Tropics and Extratropics, (pp. 80-196):

The Climate Diagnostics Data Base (CDDB) has been archived at the National Meteorological Center (NMC) since October 1978, and contains gridded analyses of upper air fields at standard pressure levels. This archive is derived from the NMC Global Data Assimilation System (GDAS) (Dey 1989). All analyses are stored on 2.5°x2.5° latitude-longitude grids at the Climate Analysis Center, and are derived from twice-daily (0000 UTC and 1200 UTC) observations. The following atmospheric circulation fields were extracted from the CDDB: 200-mb vector wind anomaly, 850-mb vector wind anomaly, 200-mb geopotential height anomaly, 500-mb geopotential height and anomaly, and sea-level pressure anomaly.

Prior to June 1991, the GDAS data were subjected to normal mode initialization procedures (Kanamitsu 1989). However, numerous changes to the NMC analysis and assimilation system occurred during the 1978-91 period (Dey 1989). These analysis changes are sometimes apparent in the data (Janowiak et al. 1987), and uninformed users may infer anomalies in general circulation features that are nothing more than artifacts of these analysis changes.

For example, a complete revision of the objective analysis scheme of the NMC global spectral Medium Range Forecast Model (MRF) was implemented on 25 June 1991. The new objective analysis is still based on optimal interpolation equations, but is solved globally directly in the model's coordinate system (spectral space in the horizontal and sigma coordinates in the vertical). This system is referred to as Spectral Statistical Interpolation (SSI). In this new system, heights are determined from the temperature field, rather than from direct measurements of height. These new fields are smoother and have less noise, particularly in the tropics, compared to the previous analysis system. Thus, the height anomaly fields after June 1991 in the tropics should be interpreted with caution.

The circulation data is displayed as follows:

200-mb and 850-mb seasonal-mean vector wind anomalies (ms^{-1}) are displayed in four formats:

(1) Time series of anomalies over the equatorial Pacific (pp. 30, 31).

(2) Seasonal maps overlayed with anomalous OLR between 50°S and 50°N (pp. 80-88, 97-105).

(3) Equatorial time-longitude sections of the zonal wind anomaly over: (a) the Pacific Ocean (pp. 88-92, 124-127), and (b) the entire equatorial strip (pp. 93-96, 110-113).

(4) Equatorial height-longitude sections of zonal wind anomaly (pp. 114-122).

200-mb geopotential height anomalies are displayed in three formats:

(1) Equatorial time-longitude sections of height anomalies over: (a) the Pacific Ocean (pp. 123-127), and (b) the entire equatorial strip (pp. 128-131).

(2) Time-latitude sections from 75°S to 75°N over the Pacific Ocean (pp. 132-135).

(3) Equatorial height-longitude sections (pp. 136-144).

Sea-level pressure anomalies are displayed in three formats:

(1) Time series of the Southern Oscillation Index and of Tahiti and Darwin sea-level pressure anomalies (p. 27).

(1) Seasonal maps between 50°S and 50°N (pp. 145-153).

(2) Equatorial time-longitude section over: (a) the Pacific Ocean (pp. 154-157), and (b) the entire equatorial strip (pp. 158-161).

500-mb temperature and geopotential height anomalies are displayed in two formats:

(1) *Temperatures*: Equatorial time-longitude sections over: (a) the Pacific Ocean (pp. 162-166), and (b) the entire equatorial strip (pp. 167-170).

(2) *Heights and Anomalies*: Seasonal maps for each hemisphere independently (pp. 171-187).

Anomalous variance of the high-pass filtered 700-mb heights are displayed for the Northern Hemisphere only in one format:

(1) Seasonal maps of 700-mb heights overlayed with normalized anomalies of high-frequency variance (pp. 188-196).

This analysis documents the interannual and interseasonal variability of the primary storm tracks which accompany the observed seasonal-mean circulation. The high-pass filtered fields were derived from once-daily (0000 UTC) 700-mb height data archived at the National Meteorological Center (Barnston and Livezey 1987).

e. Surface Temperature and Precipitation, (pp. 197-230):

The seasonal mean surface temperature anomalies and precipitation percentiles were obtained from the Climate Anomaly and Monitoring System (CAMS), which has been developed and archived at the Climate Analysis Center (Ropelewski et al. 1985). This archive is based on real-time integrated synoptic reports and data summaries prepared by the stations and transmitted over the Global Telecommunications System (GTS). Between 7400 and 7500 stations around the world report monthly, and anomalies are calculated using the 1961-1990 base period means at each station.

The **seasonal mean surface temperature anomalies and precipitation percentiles** are displayed seasonally for each hemisphere separately (pp. 214-130).

f. Northern Hemisphere Teleconnection Patterns, (pp. 231-254):

One diagnostic procedure used to identify teleconnection patterns is the Rotated Principal Component Analysis --RPCA (Barnston and Livezey 1987- BL). This procedure isolates the primary teleconnection patterns for all months and allows for time series of the amplitudes of the patterns to be constructed. In this atlas, we have redone the BL study by applying the RPCA technique to monthly mean 700-mb height anomalies between January 1964- July 1994. In this analysis, ten patterns (or eigenvectors-- 10 Varimax spatial rotations) are determined for each calendar month by using all of the height anomaly fields for the

three-month period centered on that month: [i.e., The July patterns are calculated based on the June through August anomaly fields]. Thus, the analysis accounts for variability in the structure and amplitude of the teleconnection patterns associated with the annual cycle of the extratropical atmospheric circulation.

Time series' showing standardized amplitudes of selected Northern Hemisphere teleconnection patterns were then constructed as follows: For each month in the data record, the observed amplitudes of the ten teleconnection patterns corresponding to that calendar month are calculated using a Least-Squares regression analysis. In this analysis, the amplitudes are determined simultaneously such that the combined sum of their products with the corresponding pattern eigenvectors explains the maximum spatial structure of the observed height anomaly field during the month. For each pattern, the amplitudes were then assembled into a continuous time series, and standardized (mean equal to zero and variance equal to 1.0) for each calendar month independently.

The **teleconnection patterns** are displayed in three formats:

(1) Table: Summary of the first ten rotated principal components or modes (teleconnection patterns) for each month (p. 232).

(2) Polar stereographic analyses showing the prominent teleconnection patterns for each season (pp. 233-254).

(3) Standardized time series showing the amplitudes of each teleconnection pattern for all months in which the pattern represents a prominent mode of low-frequency variability (pp. 233-254).

3. TROPICAL PACIFIC/ ENSO

Three distinct periods of extreme phases of the Southern Oscillation (SO) were observed between December-February (DJF) 1985/86 - 1993 (p. 27), as measured by the Tahiti-Darwin Southern Oscillation Index (SOI). During DJF 1985/86 a somewhat innocuous pattern of slightly above- (below-) normal SSTs was observed in the western (eastern) equatorial Pacific (p. 38). These conditions were accompanied by enhanced upwelling and cooler than normal sub-surface ocean temperatures in the eastern equatorial Pacific, and by decreased upwelling and warmer than normal sub-surface ocean temperatures in the western equatorial Pacific (pp. 51, 59). Additionally, low-level equatorial easterlies were enhanced over much of the central and eastern Pacific at this time (pp. 31, 98, 106 109), and below- (above-) normal SLP (pp. 146, 154, 157) and convection (pp. 68, 76, 79) were noted west (east) of the dateline.

During the next two seasons, the area of negative SST anomalies east of the dateline disappeared (p. 38), and the area of anomalously large thermocline depths shifted eastward from the western to the east-central equatorial Pacific (p. 51). This evolution was accompanied by a weakening of the equatorial easterlies over the central and east-central Pacific (pp. 98-106).

Anomalous warming of the surface and sub-surface ocean temperatures east of the dateline continued during September-November (SON) 1986, with large positive SST anomalies covering much of the eastern tropical and subtropical Pacific (pp. 38, 46, 49). During this season, thermocline depths along the equator increased everywhere east of the dateline (p. 51), and ocean temperature anomalies at 100 m depth exceeded 3°C between 150°W and 100°W (p. 59). A further reduction in the strength of the low-level equatorial easterlies was also noted (pp. 31, 98, 106), as a pattern of above (below) normal SLP became established over the western (eastern) equatorial Pacific (pp. 146, 154, 157). This evolution was accompanied by a dramatic increase in the strength of the westerly wind anomalies at 200 mb between 150°E and the west coast of South America (pp. 30, 81, 115), and by a corresponding decrease in the strength of the equatorial Walker circulation throughout the region. Additionally, a pronounced eastward migration of the region of enhanced equatorial

convection had occurred by this time, with above-normal convective activity (pp. 30, 68, 76, 79) now evident over the area of warmest SSTs between 150°E and 175°W (pp. 33, 38).

Mature warm episode conditions then developed during DJF 1986/87, and subsequently persisted through July 1987 (Kousky and Leetma 1989). During this period, SST anomalies continued to increase in the east-central equatorial Pacific, and anomalies of 1-2°C also began to appear along the Peruvian coast (pp. 28, 29, 39, 46). By March-May (MAM) 1987, positive SST anomalies greater than 1°C occupied the entire tropical Pacific east of the dateline. SST anomalies continued to strengthen during the following season, and by June-August (JJA) 1987 positive anomalies greater than 2°C covered much of the equatorial Pacific east of 160°W. Throughout this period, sub-surface ocean temperatures down to the depth of the 20°C isotherm remained 2-3°C above normal east of the dateline (p. 60).

This evolution was accompanied by a dramatic intensification of convective activity near the dateline during DJF 1986/87 (pp. 30, 69, 76), and with the subsequent eastward expansion of enhanced convection to the South American Coast during MAM 1987. During JJA 1987, convective activity remained above-normal over a large area centered on the dateline, but returned to normal over much of the eastern equatorial Pacific. These conditions were accompanied by low-level westerly wind anomalies of 3-6 ms^{-1} along the equator near the dateline (pp. 99, 106), and by enhanced easterlies in the upper troposphere over large portions of the central and east-central equatorial Pacific (pp. 82, 89). Again, this overall circulation was indicative of a reduced strength of the equatorial Walker circulation (p. 116).

During SON 1987, a large area of above-normal SSTs persisted east of the dateline. However, enhanced convection at this time was confined to the vicinity of the dateline and the equator, and to the region north of the equator in the vicinity of the Intertropical Convergence Zone (ITCZ). These conditions were consistent with the demise of mature warm episode conditions, and with a continued return toward more normal conditions in the tropical Pacific.

This overall evolution illustrates the strong coupling that exists between ENSO and the annual cycle of SSTs in the east-central and eastern equatorial Pacific (Wang 1994). In these regions, SSTs reach their climatological maximum during MAM, and decrease to their

climatological minimum during SON. Thus, although SST anomalies were actually larger in these regions during SON 1987 than during MAM 1987, the overall sea surface temperature in the former (latter) season was below (above) that required to support sustained convection (approximately 28.5°C) (p. 33). Thus mature ENSO conditions were clearly favored during the Northern Hemisphere spring season relative to the fall season.

A shift to cold-episode conditions and positive values of the SOI (p. 27) then occurred during March-August 1988 (Janowiak 1988, Ropelewski 1988). During this period below-normal SSTs developed and intensified from the dateline eastward to the South American coast, with anomalies more than 3°C below-normal covering large portions of the region (pp. 40, 47). These conditions were accompanied by an anomalously shallow thermocline across much of the equatorial Pacific (pp. 53, 61), and with reduced convective activity over much of the central and east-central equatorial Pacific (pp. 30, 70, 77). Additionally, this area was dominated by westerly wind anomalies in the upper troposphere (pp. 30, 83, 90) and by enhanced easterlies in the lower troposphere (pp. 31, 100, 107), indicating an enhanced strength of the Walker circulation during the period (p. 117).

Mature cold episode conditions developed during the next two seasons as the region of significantly reduced convection became focused in the vicinity of the dateline (pp. 30, 70-71, 77), and flanking cyclonic circulation centers became established in the upper troposphere (pp. 83-84). These features were accompanied by westerly wind anomalies in excess of 10-15 ms^{-1} at 200 mb over the east-central equatorial Pacific (pp. 83-84, 90, 117-118), and by easterly wind anomalies exceeding 3 ms^{-1} at 850 mb (pp. 100-101).

Cold episode conditions weakened considerably during March-August 1989 as SSTs east of the dateline returned steadily back toward normal (pp. 41, 47). During the next year near-normal SSTs and OLR was observed over large portions of the equatorial Pacific. However, by JJA 1990, an area of above-normal SSTs exceeding 1°C had again begun to develop slightly west of the dateline (pp. 28, 42, 47). This feature then expanded during the next several seasons (pp. 43, 48), indicating the re-emergence of weak warm episode conditions (Bell and Halpert 1993, Halpert and Bell 1993).

The 1991-1993 period was then dominated by warm episode conditions in the tropical

Pacific (pp. 27-31), marking one of the longest periods of continuous warm episode conditions on record. During this event, two distinct periods of mature ENSO conditions were observed. This marks only the third time this century that mature ENSO conditions have been observed in two consecutive DJF and MAM periods. The previous two periods of prolonged warm episode conditions occurred during 1939-1941 and 1911-1913.

During the first five months of 1991, a pattern of above- (below-) normal sea level pressure (SLP) strengthened over the western (eastern) equatorial Pacific (pp. 151, 156). This evolution was accompanied by weaker than normal low-level easterlies over the east-central and eastern equatorial Pacific (pp. 103, 108), and by positive SST anomalies east of the dateline (pp. 43, 48-49). During JJA 1991, these conditions intensified as the equatorial easterlies further weakened over the east-central and eastern Pacific (Halpert and Bell 1993). Mature ENSO conditions then developed during November 1991(Janowiak 1993) as convective activity near the dateline intensified (pp. 73, 78) [OLR index values plummeted (p. 30)], easterly wind anomalies intensified at 200 mb (pp. 30, 86, 91) and the low-level equatorial easterlies weakened further throughout the Pacific (pp. 31, 103, 108).

These mature ENSO conditions strengthened during December 1991-February 1992 (Kousky 1993) and persisted until the end of May 1992 (Wang 1993). During this 6-month period, the SOI dropped below -3.0 (p. 27) and OLR index values decreased below -2.0 (p. 30). Moreover, SST indices exceeded 1.0 throughout the equatorial Pacific east of the dateline (p. 28), and the low-level wind indices reached their lowest values since the 1986/87 ENSO (p. 31). During March-May 1992, enhanced convection was observed along the equator from 150°E eastward to the South American coast (p. 74), a distance covering more than 14,000 km.

During July-October 1992, convection returned to normal over the central and east-central equatorial Pacific, and the region of above-normal SST's retreated westward to the dateline (Mo and Wang 1994, Chelliah 1994). However, a large area of above-normal SST's remained east of the dateline in both the subtropical North and South Pacific during this period (pp. 44, 48-49). Additionally, below- (above-) normal SLP persisted over the eastern (western) equatorial Pacific (pp. 152, 156-157), and the equatorial easterlies at 850 hPa

remained anomalously weak (pp. 104, 108-109). Thus, although *mature* warm episode conditions had ended during this period, weak warm episode conditions continued throughout the tropical Pacific.

During December-February (DJF) 1992/93, mature warm episode conditions redeveloped, as the region of above-normal SST's expanded to cover much of the tropical and subtropical Pacific east of the dateline (pp. 45, 48-49), and a broad area of enhanced convection became re-established in the vicinity of the dateline (pp. 75, 78-79). These conditions were again accompanied by strong easterly anomalies at 200 mb (pp. 88, 91-92), by a reduced strength of the low-level equatorial easterlies over large portions of the Pacific (pp. 105, 108-109), and by large negative values of the SOI (p. 27).

These conditions reached peak intensity during March-May 1993, and by the end of the season the area of SST anomalies exceeding 1°C above-normal again extended eastward from the dateline to the west coast of South America. During June-August, these conditions weakened considerably (Janowiak et al. 1994), and by August SSTs in the eastern equatorial Pacific had cooled to slightly below-normal levels. In addition, convection in the near-equatorial mid-Pacific diminished toward the end of the JJA season, while the strength of the 200 mb westerly winds increased. Each of these features is consistent with the demise of mature ENSO conditions. However, persistent positive SST anomalies greater than 1°C remained in the central equatorial Pacific through the end of 1993.

Each of these extreme phases of the ENSO cycle were accompanied by pronounced meridional shifts in the location of the extratropical jet stream over the Pacific sector of both hemispheres (pp. 132-135). In particular, each ENSO event was accompanied by below-normal 200-mb heights in the middle latitudes of both hemispheres, while the 1988/89 Pacific cold event was dominated by positive height anomalies at these latitudes. These conditions are consistent with an equatorward shift of the jet stream in both hemispheres during the warm episodes, and with a poleward contraction of the jet stream in both hemispheres during the cold episode.

Extremes in the Southern Oscillation are also associated with large variations in the global pattern of surface temperature and precipitation, as documented by Ropelewski and

Halpert (1986, 1987) and Halpert and Ropelewski (1992). During the eight-year period discussed here, a consistent precipitation-SO relationship was observed along the gulf coast of the United States. In particular, precipitation (pp. 215-222) was above normal in this region during the winters of 1986/87, 1991/92, and 1992/93, and below normal during DJF 1988/89. These conditions are consistent with the expected wintertime response to mature warm and cold episode conditions, respectively. The strength of the Indian monsoon also tends to be weaker than normal during the northern summer following the period of mature ENSO conditions. Consistent with this observation, India experienced relatively poor monsoons during JJA 1987 and JJA 1992.

In the Southern Hemisphere, northern Australia and large portions of Indonesia experienced excess precipitation (pp. 223-230) during the December - May period in association with the 1988/89 cold episode, and drier-than-normal conditions during the same period of 1986/87, 1991/92, and 1992/93. These conditions are consistent with the patterns of anomalous convection typically observed during extreme phases of the SO. Southern Africa also experienced abnormally dry conditions in association with the long-lived 1991-93 warm episode.

Prominent SO-temperature relationships (Halpert and Ropelewski 1992) were also observed during the eight-year study period. Over northwestern North America, temperatures (pp. 198-205) averaged well-above normal during the winters of 1986/87, 1991/92, and 1992/93, and below normal during the 1988/89 cold episode. Along the west coast of South America, temperatures (pp. 206-213) were above-normal during the first half of 1987 and 1992 in association with the above-normal SSTs and a negative phase of the SO. In contrast, temperatures were below normal in this region from December 1988 - May 1989 in association with the below-normal SSTs and a positive phase of the SO. In southern Africa, above-normal temperatures were observed during December - May 1986/87 and 1991/92, while below-normal temperatures were observed from September 1988 through February 1989.

4. NORTHERN HEMISPHERE TELECONNECTION PATTERNS

Thirteen distinct teleconnection patterns can be identified in the Northern Hemisphere extratropics throughout the year (pp. 232, 233-256), and many of these patterns have appeared previously in the meteorological literature. This analysis provides a basis for identifying the primary circulation features and teleconnection patterns observed in the seasonal mean 500-hPa circulation charts (pp. 172-179). The nomenclature of both Wallace and Gutzler (1981-WG) and BL has been retained where appropriate.

Three prominent teleconnection patterns are observed over the North Atlantic (p. 232): the North Atlantic Oscillation (NAO), which exists in all months; the East Atlantic Pattern (Ea), which exists from September to April; and the East Atlantic Jet (EA-Jet) pattern, which exists from April to August. Six prominent patterns are found over the North Pacific/ North American sector: the West Pacific pattern (WP), which exists in all months; the East Pacific pattern (EP), which exists in all months except August and September; the North Pacific pattern (NP), which exists from March to July; the Pacific/North American pattern (PNA), which exists in all months except June and July; the Tropical/ Northern Hemisphere pattern (TNH), which exists from November to January; and the Pacific Transition pattern (PT), which exists from May-August. Four patterns are found over the Eurasian sector: the East Atlantic/Western Russia pattern (EATL/WRUS), which exists from September to May; the Scandinavia pattern (SCAND), which exists in all seasons except June and July; the Polar/ Eurasia pattern, which exists from December-February; and the Asian Summer pattern, which exists from June to August. The East Atlantic/Western Russia pattern and the Scandinavia pattern are referred to by BL as the Eurasia-2 and Eurasia-1 patterns, respectively.

a. North Atlantic Oscillation (NAO), (pp. 233-234):

One of the most prominent teleconnection patterns in all seasons is the North Atlantic Oscillation (NAO). This pattern exhibits little structural variation from month-to-month, and consists of a north-south dipole of anomalies, with one center located over Greenland and the other of opposite sign spanning the central latitudes of the North Atlantic between 35°N and 40°N. The positive phase of the NAO reflects negative height anomalies over Greenland and

positive height anomalies over the central North Atlantic, and is associated with an intensification of the jet stream over much of the high latitudes of the North Atlantic. The NAO is well-documented by BL and Bell and Basist (1994), and combines parts of the East-Atlantic and West Atlantic patterns originally identified by WG for the winter season.

The NAO exhibits considerable interseasonal and interannual variability, and prolonged periods (several months) of both positive and negative phases of the pattern are common. For the period covered by this atlas, the most persistent positive phase of the NAO was observed throughout 1989 and during the first four months of 1990. The accompanying pattern of surface temperature anomalies during winter and spring 1989 and 1990 indicated much above-normal temperatures over large portions of Europe, Scandinavia and Siberia. In addition, enhanced storm activity (pp. 192-193) and above-normal precipitation (pp. 219-220) covered much of Scandinavia and western Russia during this period, while below-normal storm activity and below-normal precipitation covered large porions of southern Europe and the Mediterranean Sea.

b. East Atlantic (EA), (pp. 235-236):

The East Atlantic pattern is the second of three prominent modes of low-frequency variability over the North Atlantic, appearing in all months except May-August. The pattern is structurally similar to the NAO, and consists of a north-south dipole of anomaly centers which span the entire North Atlantic Ocean from east to west. However, the anomaly centers in the EA pattern are displaced southeastward to the approximate nodal lines of the NAO pattern. For this reason, the EA pattern is often mistaken as simply a slightly 'southward-shifted' NAO pattern. This EA pattern is similar to that shown in the BL study, but is distinctly different from the EA pattern originally defined by WG.

A positive phase of the EA pattern reflects enhanced westerlies near 40°N across the Atlantic basin, and a negative phase of the pattern reflects reduced westerlies in the middle latitudes across much of the basin. In contrast, the primary wind anomalies associated with the NAO are observed between 50°N-60°N.

The strongest and most persistent positive phase of the EA pattern occurred from

December 1989-March 1990, and coincides with the strong positive phase of the NAO described in section 4a. This period was dominated by a pronounced zonal wave-1 pattern in the middle and high latitudes (p. 176), with above-normal 500-hPa heights over the North Pacific and below-normal heights over the eastern half of Canada and the central and high latitudes of the North Atlantic. Farther east a highly amplified ridge was observed throughout southern Europe. Over the western and central North Atlantic, this circulation was accompanied by a much stronger-than-normal Icelandic Low, and with a pronounced southward shift of the North Atlantic jet stream to approximately 40°N.

No pronounced negative phases of the EA pattern were observed during the 1986-1993 period, although the complete time series does indicate the prevalence of a negative index values during the 6-year period between mid-1966 and mid-1972.

c. East Atlantic Jet (EA-Jet), (pp. 237-238):

The East Atlantic Jet pattern is the third primary mode of low frequency variability found over the North Atlantic, appearing between April and August. This pattern also consists of a north-south dipole of anomaly centers, with one main center located over the high latitudes of the eastern North Atlantic and Scandinavia, and the other center located over Northern Africa and the Mediterranean Sea. A positive phase of the EA-Jet pattern reflects an intensification of westerlies over the central latitudes of the eastern North Atlantic and over much of Europe, while a negative phase reflects a strong split-flow configuration over these regions, sometimes in association with long-lived blocking anticyclones in the vicinity of Greenland and Great Britain. This pattern is not discussed in the WG and BL studies.

The time series of the EA-jet pattern exhibits considerable interdecadal variability. For example, the 1971-1978 period is dominated by the negative phase of the pattern, while the 1985-1993 period is dominated by the positive phase of the pattern. In fact, from 1986-1993 the positive phase of the pattern was observed nearly 70% of the time.

d. West Pacific (WP), (pp. 239-240):

The WP pattern is a primary mode of low-frequency variability in all months, and has

been previously described by both BL and WG. During winter and spring, the pattern consists of a north-south dipole of anomalies, with one center located over the Kamchatka Peninsula and another broad center of opposite sign covering portions of southeastern Asia and the low latitudes of the extreme western North Pacific. Therefore, strong positive or negative phases of this pattern reflect pronounced latitudinal variations in the location and intensity of the entrance region of the Pacific jet steam.

In the summer and fall, the WP pattern becomes increasingly wave-like, and a third prominent center appears over Alaska and the Beaufort Sea, with a sign opposite to the center over the western North Pacific. This wave structure is most evident in the Fall, when it extends downstream along a quasi great-circle route into the western United States.

The time series of the WP pattern indicates considerable intermonthly and interannual variability, and persistence of a particular phase of the pattern is relatively common. During the period covered by this atlas, the most persistent positive phase of the WP pattern was observed from September 1986-June 1987, while the most persistent negative phase was observed from March-December 1989. The former period spanned the 1986-87 ENSO event, while the latter period included the 1988-89 Pacific cold event.

e. East Pacific (EP), (pp. 241-242):

The EP pattern is evident in all months except August and September, and reflects a north-south dipole of height anomalies over the eastern North Pacific. The northern center is located in the vicinity of Alaska and the west coast of Canada, while the southern center is of opposite sign and is found near, or east of, Hawaii. During strong positive phases of the EP pattern, a deeper than normal trough is located in the vicinity of the Gulf of Alaska/ western North America, and positive height anomalies are observed farther south. This phase of the pattern is associated with a pronounced northeastward extension of the Pacific jet stream toward western North America, and with enhanced westerlies over the Pacific Northwest States, northern California, and sometimes southwestern British Columbia.

In contrast, strong negative phases of the EP pattern are associated with a pronounced split-flow configuration over the eastern North Pacific, and with reduced westerlies throughout

the region. This circulation is accompanied by a confinement of the climatological mean Pacific trough to the western North Pacific, and possibly with a blocking flow configuration farther east.

The most persistent positive phase of the EP-Jet pattern occurred from 1973-1975, and the most persistent negative phase of the pattern occurred from early 1992 through mid-1993. This latter period was dominated by warm episode conditions in the equatorial Pacific, and by two distinct periods of mature ENSO conditions. During this period, the subtropical jet stream was generally stronger than normal and displaced well east of its climatological -mean position toward the southwestern United States. These conditions contributed to an end of prolonged drought conditions in California (Bell and Basist 1994), and brought abundant precipitation to the southwestern United States, particularly during the 1992/93 winter. These conditions were also associated with generally above-normal precipitation over the central United States during the year preceding the onset of the Midwest floods of June-July 1993 (Bell and Janowiak 1994). This enhanced precipitation then contributed to above-normal soil moisture levels throughout the Midwest during the period, and to near-saturated soil conditions just prior to the onset of the floods.

f. North Pacific (NP), (pp. 243-244):

The North Pacific pattern is prominent from March through July. This pattern consists of a primary anomaly center which spans the central latitudes of the western and central North Pacific, and weaker anomaly region of opposite sign which spans eastern Siberia, Alaska and the intermountain region of North America. Overall, pronounced positive phases of the NP pattern are associated with a southward shift and intensification of the Pacific jet stream from eastern Asia to the eastern North Pacific, followed downstream by an enhanced anticyclonic circulation over western North America, and by an enhanced cyclonic circulation over the southeastern United States. Pronounced negative phases of the NP pattern are associated with circulation anomalies of opposite sign in these regions.

Bell and Janowiak (1994) recently noted that a positive phase of the NP pattern reflects one of the preferred responses of the extratropical atmospheric circulation to ENSO

during the Northern Hemisphere spring. This response was particularly evident during the 1992 and 1993 spring seasons, when a prolonged positive phase of the NP pattern dominated the circulation.

Bell and Janowiak also note that the atmospheric circulation during the several month period prior to the onset of the Midwest floods of June-July 1993 was dominated by the most pronounced and persistent positive phase of the NP pattern in the historical record. Their study concluded that these conditions were *indirectly* important to the onset and overall magnitude of the floods, since they fostered an anomalously intense storm track over the midlatitudes of the North Pacific. Dramatic changes in this storm track during June then ultimately initiated the Midwest floods.

g. Pacific/ North America (PNA), (pp. 245-246):

The PNA pattern is one of the most prominent modes of low-frequency variability in the Northern Hemisphere extratropics, appearing in all months except June and July. The PNA pattern reflects a quadripole pattern of height anomalies, with anomalies of similar sign located south of the Aleutian Islands and over the southeastern United States. Anomalies with sign opposite to the Aleutian center are located in the vicinity of Hawaii, and over the intermountain region of North America (central Canada) during the winter and fall (spring).

The spatial scale of the PNA pattern is most expansive in Winter. During this period, the Aleutian center spans most of the northern latitudes of the North Pacific. In Spring, the Aleutian center contracts and becomes confined primarily to the Gulf of Alaska. However, the subtropical center near Hawaii reaches maximum amplitude during the spring. The PNA pattern then disappears during June and July, but reappears in the late summer and fall. During this period, the midlatitude centers become dominant and appear as a wave pattern emanating from the eastern North Pacific. The subtropical center near Hawaii is weakest during this period.

The time series of the PNA pattern also indicates substantial interseasonal, interannual and interdecadal variability. For example, a negative phase of the pattern dominated the period from 1964-1967, while a positive phase of the pattern tended to dominate from 1976-

1988. A negative phase of the PNA then dominated during the 1989-1990 period, followed by a prolonged positive phase from fall 1991- early spring 1993.

h. East Atlantic/ West Russia (EATL/WRUS), (pp. 247-248):

The East Atlantic/ West Russia (EATL/WRUS) pattern is one of two prominent modes (see also Scandinavia pattern, pp. 249-250) that affects Eurasia during most of the year. This pattern is prominent in all months except June-August, and has been referred to as the Eurasia-2 pattern by BL. In Winter, two main anomaly centers, located over the Caspian Sea and western Europe, comprise the East Atlantic/ West Russia pattern. A three-celled pattern is then evident in the spring and fall seasons, with two main anomaly centers of opposite sign located over western/ north-western Russia and over northwestern Europe. The third center, having same sign as the Russia center, is located off the Portuguese coast in spring, but exhibits a pronounced retrogression toward Newfoundland in the fall.

The most pronounced and persistent negative phases of the East Atlantic/ West Russia pattern tend to occur in winter and early spring, with particularly large negative phases noted during the winters and early springs of 1969/70, 1976/77 and 1978/79. Pronounced positive phases of the pattern are less common, with the most prominent positive phase evident during late winter/ early spring of 1992/93. During the 1992/93 winter, negative height anomalies were observed throughout western and southwestern Russia, and positive height anomalies were observed throughout Europe and the eastern North Atlantic (p. 179). These conditions were accompanied by warmer (p. 205) and wetter (p. 222) than normal conditions over large portions of Scandinavia and northwestern Russia, and by much colder and drier than normal conditions over the eastern Mediterranean Sea and the Middle East. During MAM 1993, the area of negative anomalies over western Russia persisted, the positive anomaly center over northwestern Europe became consolidated, and a negative anomaly center became established over the eastern North Atlantic. These conditions brought a continuation of warmer (colder) than normal conditions to Scandinavia (eastern Mediterranean Sea sector), and drier than normal conditions to much of Europe.

i. Scandinavia (SCAND), (pp. 249-250):

The Scandinavia pattern (SCAND) consists of a primary circulation center which spans Scandinavia and large portions of the Arctic Ocean north of Siberia. Two additional weaker centers with opposite sign to the Scandinavia center are located over western Europe and over the Mongolia/ western China sector. The Scandinavia pattern is a prominent mode of low frequency variability in all months except June and July, and has been previously referred to as the Eurasia-1 pattern by BL. The positive phase of this pattern is associated with positive height anomalies, sometimes reflecting major blocking anticyclones, over Scandinavia and western Russia, while the negative phase of the pattern is associated with negative height anomalies over these regions.

The time series for the Scandinavia pattern also exhibits relatively large interseasonal, interannual and interdecadal variability. For example, a negative phase of the pattern dominated the circulation from early 1964 through mid-1968 and from mid-1986 through early 1993. Negative phases of the pattern have also been prominent during winter 1988/89, spring 1990, and winter/spring 1991/92. In contrast, positive phases of the pattern were observed during much of 1972, 1976 and 1984.

j. Polar/ Eurasia, (pp. 251-252):

The Polar/ Eurasian pattern appears only in the winter, and is the most prominent mode of low-frequency variability during December and February. The pattern consists of one main anomaly center over the polar region, and separate centers of opposite sign to the polar anomaly over Europe and northeastern China. Thus, the pattern reflects major changes in the strength of the circumpolar circulation, and reveals the accompanying systematic changes which occur in the midlatitude circulation over large portions of Europe and Asia.

The polar/Eurasian pattern exhibits strong intradecadal and interdecadal variability, with several consecutive winters of a positive phase of the pattern often followed by several winters having a negative phase of the pattern. For example, the winters from 1964/65 through 1969/70 were dominated by a negative phase of the pattern, followed by a five-year period from 1971/72 through 1975/76 dominated by a positive phase of the pattern. A

negative phase then returned for much of the decade between 1976/77 and 1985/86, followed by a prolonged positive phase of the pattern from 1988/89 through 1992/93. These prolonged positive phases of the pattern reflected below-normal heights throughout the polar region and an enhanced circumpolar vortex, in combination with above-normal heights over much of Europe and eastern Asia. In contrast, the prolonged negative phases of the pattern reflected above-normal heights throughout the polar region and a weaker than normal polar vortex, in combination with below-normal heights over much of Europe and eastern Asia.

k. Tropical/ Northern Hemisphere (TNH), (pp. 251, 253):

The tropical Northern Hemisphere pattern was classified for the first time by Mo and Livezey (1986), and appears as a prominent mode from November-February. The pattern consists of one primary anomaly center over the Gulf of Alaska and a separate primary anomaly center of opposite sign over the Hudson Bay. A weaker area of anomalies having similar sign to the Gulf of Alaska anomaly extends across Mexico and the extreme southeastern United States. Pronounced negative phases of the TNH pattern are generally observed during December and January when Pacific warm (ENSO) episode conditions are present (Barnston et al. 1991). In contrast, positive phases of the TNH pattern tend to accompany Pacific cold events. An example is the very persistent positive phase of the TNH pattern during 1988/89 -1990/91, which developed in apparent association with a strong 1988/89 Pacific cold event.

l. Asian Summer, (pp. 254-255):

The Asian Summer pattern is a prominent mode from June-August. The pattern is a monopole pattern, and is dominated by anomalies of the same sign throughout southern Asia and northeastern Africa. A Positive phase of the pattern is indicated by above-normal heights throughout southern Asia and northeastern Africa. The Asian Summer pattern exhibits considerable interannual and interdecadal variability, with a pattern of one sign observed for several consecutive years, followed by a pattern of the opposite sign observed for several consecutive years. For example, a positive phase of the pattern dominated the summertime

circulation from 1987-1990. This period was preceded by a three-year period (1984-1964) in which the negative phase of the pattern was prominent.

m. Pacific Transition (PT), (pp. 254, 256):

The Pacific Transition pattern is prominent between May-August. The mode consists of a wave-like pattern of height anomalies, which extends from the Gulf of Alaska eastward to the Labrador Sea, and is aligned along the 40°N latitude circle. The prominent centers of action have a similar sign, and are located over the intermountain region of the United States and over the Labrador Sea. Relatively weak anomaly centers with signs opposite to the above are located over the Gulf of Alaska and over the eastern United States.

Two of the most pronounced negative phases of the PT pattern in the historical record occurred during July 1992 and July 1993. During each of these periods, well below-normal 500-mb heights were observed over the northwestern United States (pp. 178-179), in association with a substantially reduced strength of the climatological mean ridge, which is located over this region in Summer. Below-normal heights were also observed over the Canadian Maritime Provinces and over the central North Pacific during these months, while above-normal heights were observed over the Gulf of Alaska. During July 1993, these extremely anomalous conditions were associated with a continuation of record flooding throughout the Midwest United States.

5. REFERENCES

Arkin, P. A., J. D. Kopman and R. W. Reynolds, 1983: 1982-1983 El Nino/ Southern Oscillation event quick look atlas. NOAA/NWS/ Climate Analysis Center, Camp Springs, MD., 20746.

Barnston, A. G., and R. E. Livezey, 1987: Classification, seasonality and persistence of low-frequency atmospheric circulation patterns. *Mon. Wea. Rev.*, **115**, 1083-1126.

Barnston, A. G., R. E. Livezey, and M. S. Halpert 1991: Modulation of Southern Oscillation-Northern Hemisphere mid-winter climate relationships by the QBO. *J. Climate*, **4**, 203-217.

Bell, G. D., and A. N. Basist, 1994: Seasonal Climate Summary: The global climate of

December 1992 - February 1993, Part I: Warm ENSO conditions continue in the tropical Pacific, California drought abates. *J. Climate*, **7**, 1581-1605.

Bell, G. D. and M. S. Halpert, 1993: Seasonal Climate Summary: The global climate of March-May 1991: Anomalous low-frequency fluctuations dominate the midlatitudes: ENSO becomes established in the tropics. *J. Climate*, **6**, 1413-1433.

Bell, G. D., and J. E. Janowiak, 1994: Atmospheric circulation associated with the Midwest floods of 1993. To appear in *Bull. Amer. Met. Soc.*, May 1995.

Chelliah, M. C., 1992: Seasonal Climate Summary: The global climate of September-November 1992: Weak warm ENSO episode conditions linger in the tropical Pacific. *J. Climate*, **7**, 1565-1580.

Cressman, G. P., 1959: An operational objective analysis system. *Mon. Wea. Rev.*, **87**, 367-374.

Dey, C.H., 1989: The evolution of objective analysis methodology at the National Meteorological Center. *Wea. and Forecast.*, **4**, 297-312.

Duchon, C. E., 1979: Lanczos filtering in two dimensions. *J. Appl. Meteor.*, **18**, 1016-1022.

Halpert, M. S., and G. D. Bell, 1993: Seasonal Climate Summary: The global climate of June-August 1991: Weak tropical Pacific warm episode conditions continue. *J. Climate*, **6**, 1434-1456.

Halpert, M. S., and C. F. Ropelewski, 1992: Surface temperature patterns associated with the Southern Oscillation. *J. Climate*, **5**, 577-593.

Hayes, S.P., L.J. Mangum, J. Picaut, A. Sumi, and K. Takeuchi, 1991: TOGA-TAO: A moored array for real-time measurements in the tropical Pacific Ocean. *Bull. Amer. Meteor. Soc.*, **72**, 339-347.

Janowiak, J. E., 1988: Seasonal Climate Summary. The global climate for March-May 1988:The end of the 1986-87 Pacific warm episode and the onset of widespread drought in the United States. *J. Climate*, **1**, 1019-1040.

Janowiak, J. E., 1993: Seasonal Climate Summary. The global climate of September-November 1991:Warm (ENSO) episode conditions strengthen. *J. Climate*, **6**, 1616-1638.

Janowiak, J. E., G. D. Bell, and R. Tinker, 1993: Seasonal Climate Summary. The global climate of June-August 1993: The great Midwest U.S. flood. Submitted to *J. Climate*.

Janowiak, J. E., V.E. Kousky, and P.A. Arkin, 1987: The effects of changes in observation and data assimilation systems on CAC climate data sets. Proceedings of the Twelfth Annual Climate Diagnostics Workshop, Salt Lake City, UT, October 12-16, 1987, pp. 292-298.

Ji, M., A. Leetmaa, and J. Derber, 1994: An ocean analysis system for climate studies. Submitted to *Mon. Wea. Rev.*

Kalnay, E., M. Kanamitsu, R. Kistler, W. Collins, D. Deaven, L. Gandin, S. Saha, G. White, J. Woollen, M. Chelliah, J. Janowiak, K.C. Mo, X. Wang, A. Leetmaa, R. Reynolds, R. Jenne, E. Kung, and D. Salstein, 1993: *The NMC/NCAR CDAS/Reanalysis Project.* NMC Office Note 401. Unpublished manuscript available from NOAA/NMC, Washington, DC, 20233.

Kanamitsu, M., 1989: Description of the NMC global data assimilation and forecast system. *Wea. and Forecast.*, **4**, 335-342.

Kousky, V. E., 1993: Seasonal Climate Summary. The global climate of December 1991-February 1992: Mature phase warm (ENSO) episode conditions develop. *J. Climate,* **6**, 1639-1655.

Kousky, V.E., and A. Leetmaa, 1989: The 1986-87 Pacific warm episode: Evolution of oceanic an atmospheric anomaly fields. *J. Climate*, **2**, 254-267.

Leetmaa, A., and M. Ji., 1989: Operational hindcasting of the tropical Pacific. *Dyn. Atmos. Oceans*, **13**, 465-490.

Mo, K. C., and R. E. Livezey, 1976: Tropical-extratropical geopotential height teleconnections during the Northern Hemisphere winter. *Mon. Wea. Rev.*, **114**, 2488-2515.

Mo, K. C., and X. Wang, 1994: The global climate of June- August 1992: Warm ENSO episode decays and colder than normal conditions dominate the Northern Hemisphere. *J. Climate,* **7**, 335-357.

Rasmusson, E.M., and T. H. Carpenter, 1982: Variations in tropical sea surface temperature and surface wind fields associated with the Southern Oscillation/El Niño. *Mon. Wea. Rev.*, **110**, 354-384.

Reynolds, R. W., and D. C. Marsico, 1993: An improved real-time global sea surface temperature analysis. *J. Climate*, **6**, 114-119.

Reynolds, R.W., and T.M. Smith, 1994: Improved global sea surface temperature analyses using optimum interpolation. *J. Climate*, **7**, 929-948.

Ropelewski, C. F., 1988: The global climate of June- August 1988: A swing to the positive phase of the Southern Oscillation; Drought in the United States, and abundant rain in monsoon areas. *J. Climate,* **1**, 1153-1174.

Ropelewski, C. F., and M. S. Halpert, 1986: North American precipitation and temperature patterns associated with the El Nino/ Southern Oscillation. *Mon. Wea. Rev.*, **115**, 2352-2362.

Ropelewski, C. F., and M. S. Halpert, 1987: Global and regional scale precipitation patterns associated with the El Nino/ Southern Oscillation. *Mon. Wea. Rev.*, **114**, 1606-1626.

Ropelewski, C. F., J. E. Janowiak and M. S. Halpert, 1985: The analysis and display of real time surface climate data. *Mon. Wea. Rev.*, **113**, 1101-1106.

Smith, T. M., and M. Chelliah, 1994: Atlas of the Tropical Pacific Ocean Annual Cycle. NOAA Atlas No. 13., Available from Climate Analysis Center Rm. 605, Camp Springs, MD., 20746, 55 pp.

Wallace, J. M., and D. S. Gutzler, 1981: Teleconnections in the geopotential height field during the Northern Hemisphere winter. *Mon. Wea. Rev.*, **109**, 784-812.

Wang, X., 1993: The global climate for March-May 1992: Mature phase warm episode continues in the tropical Pacific. *J. Climate*, **12**, 2465-2485.

Wang, X., 1994: The coupling of the annual cycle and ENSO over the tropical Pacific. *J. Atmos. Sci.*, **51**, 1115-1136.

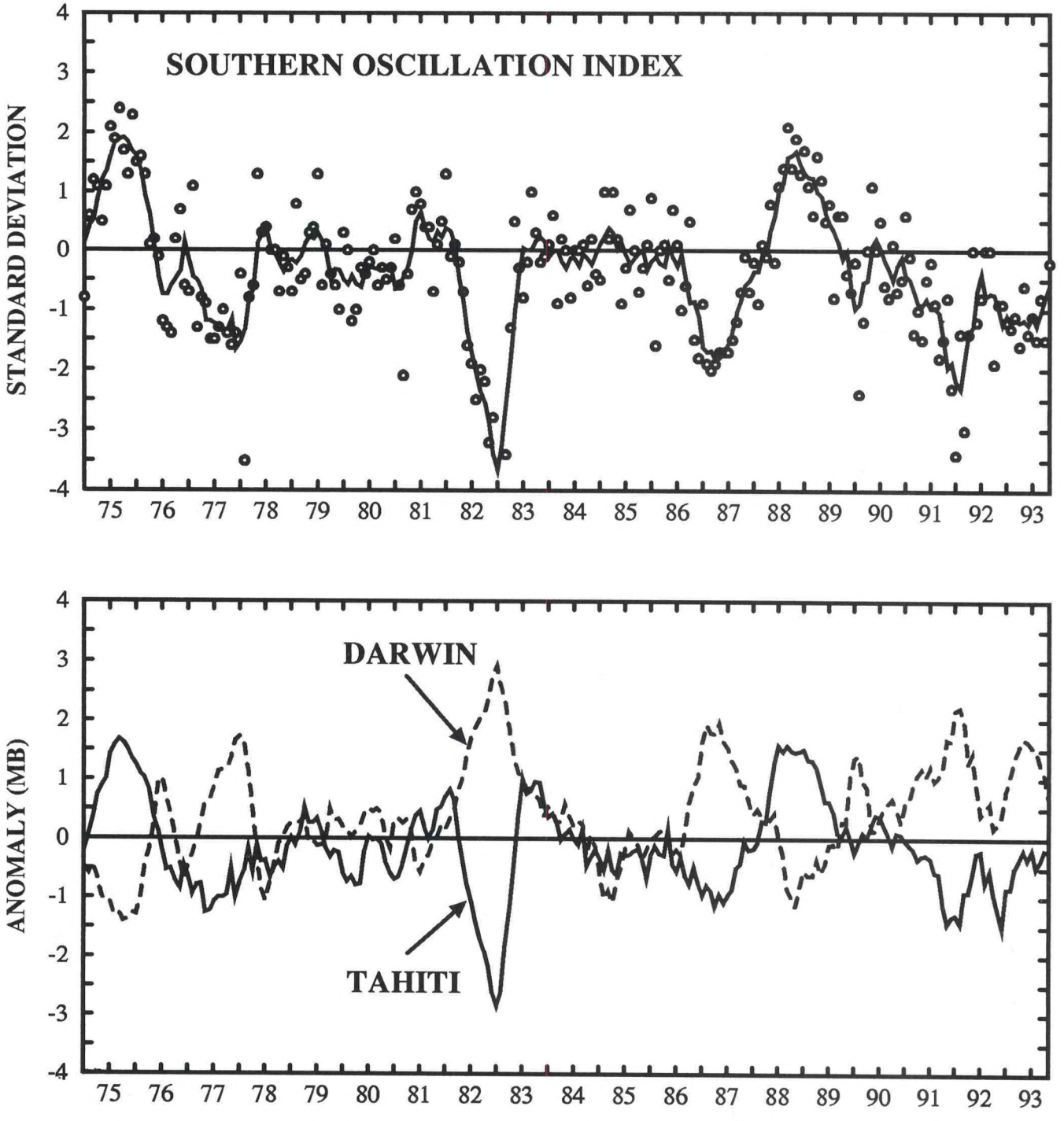

Top: Southern Oscillation Index (SOI): Five-month running mean of the difference between the standardized sea-level pressure anomalies at Tahiti and Darwin (Tahiti-darwin). Values are standardized by the mean annual standard deviation. Open circles indicate individual monthly means. The x-axis labels are centered on July.

Bottom: Five-month running mean of the sea-level pressure anomalies at Tahiti (solid) and Darwin (dashed). Anomalies are computed as departures from the 1951-1980 base period monthly means. The x-axis labels are centered on July.

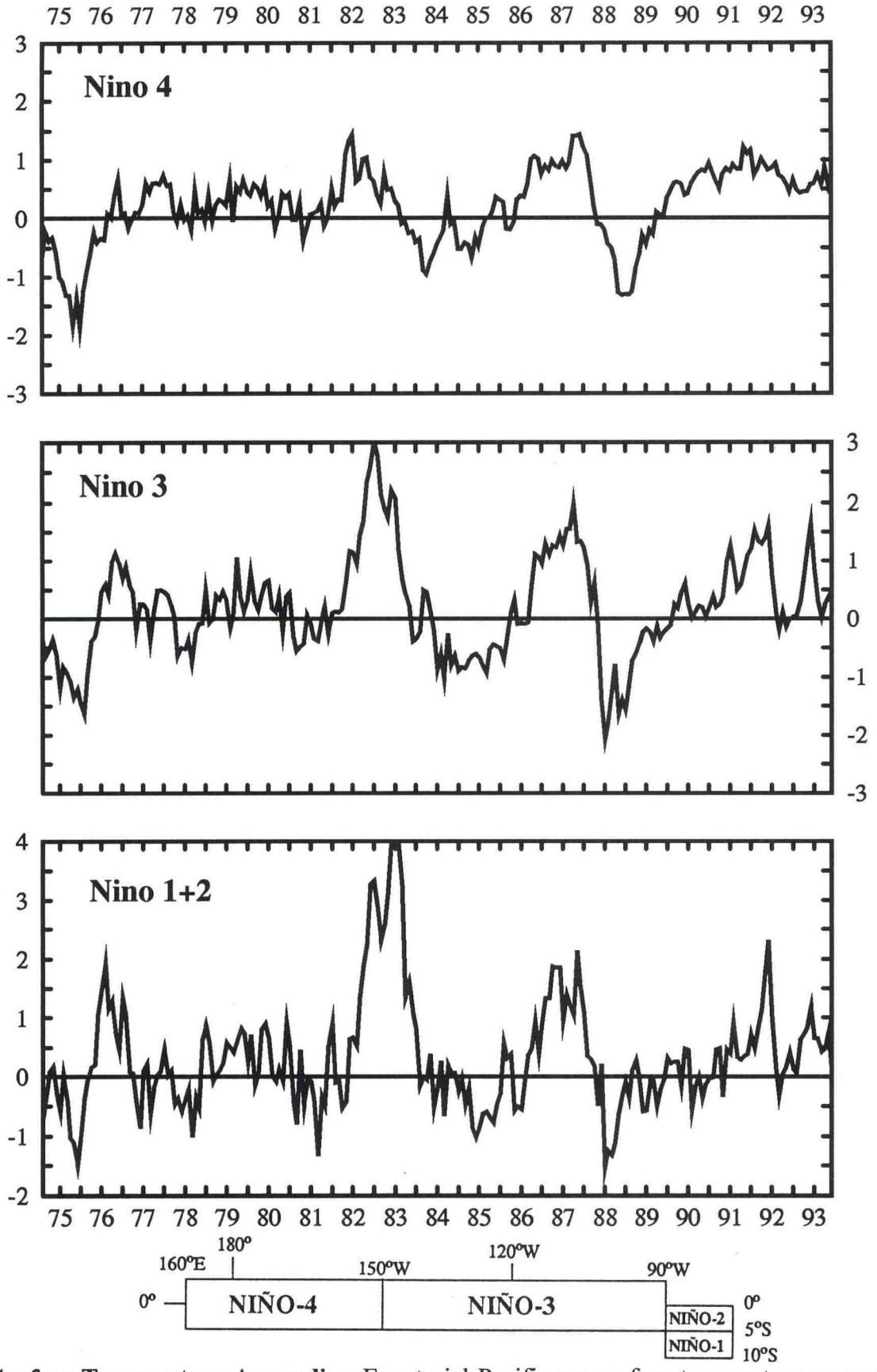

Sea-Surface Temperature Anomalies: Equatorial Pacific sea surface temperature anomalies (°C) for the areas indicated in the bottom schematic. Anomalies are with respect to the COADS/ICE climatology (Reynolds 1988, *J. Climate*, **1**, 75-86).

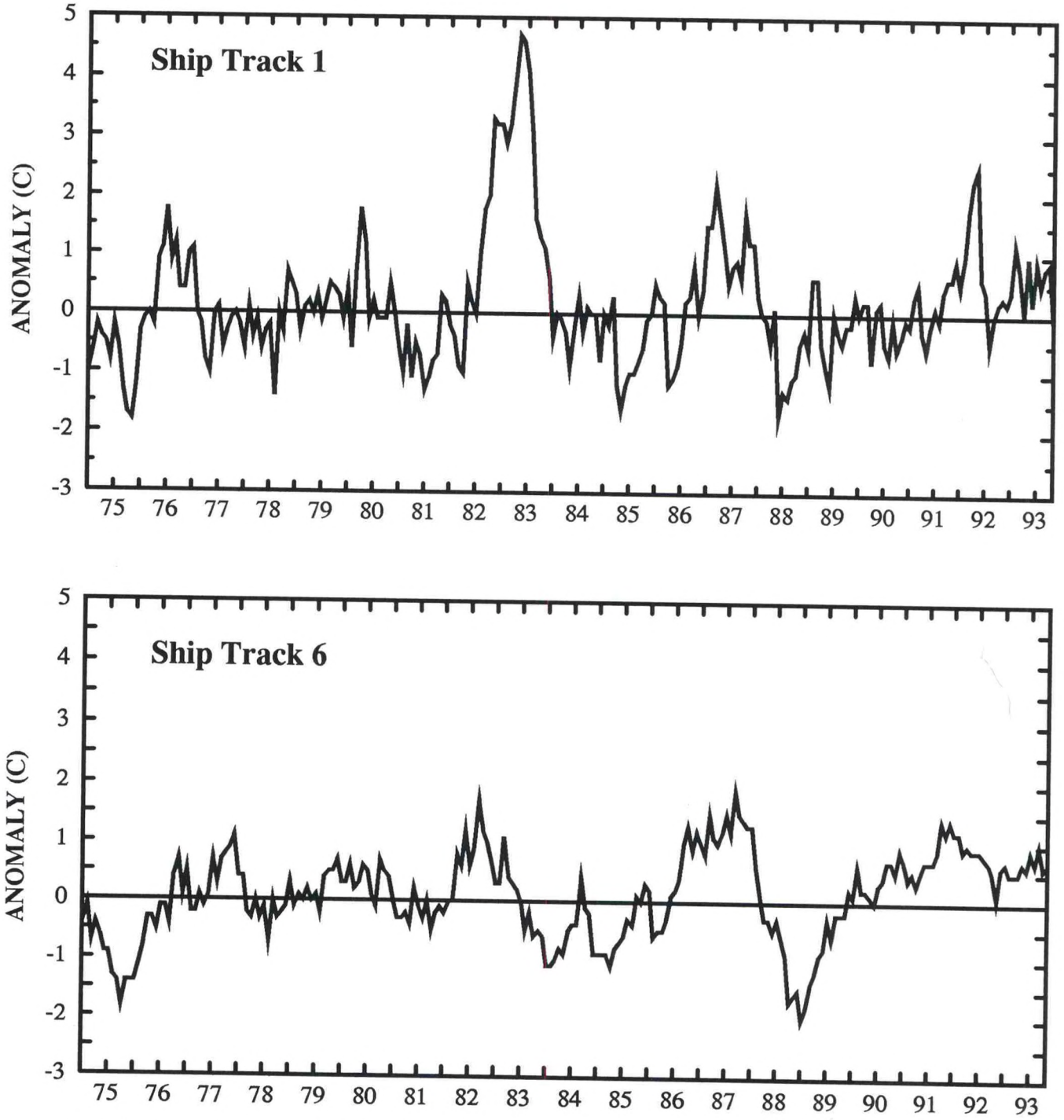

Sea-Surface Temperature Anomalies: Sea surface temperature anomalies (°C) for ship track-1 (top) and ship track-6 (bottom). The x-axis labels are centered on July. Ship track 1 extends north of 20°S along the South American west coast, and then northward to 7°N along the central American west coast. Ship track 6 lies along a nearly straight line from the Fiji Islands (19°S, 178°E) northeastward to Hawaii (20°N, 155°W) and crosses the equator at approximately 170°W.

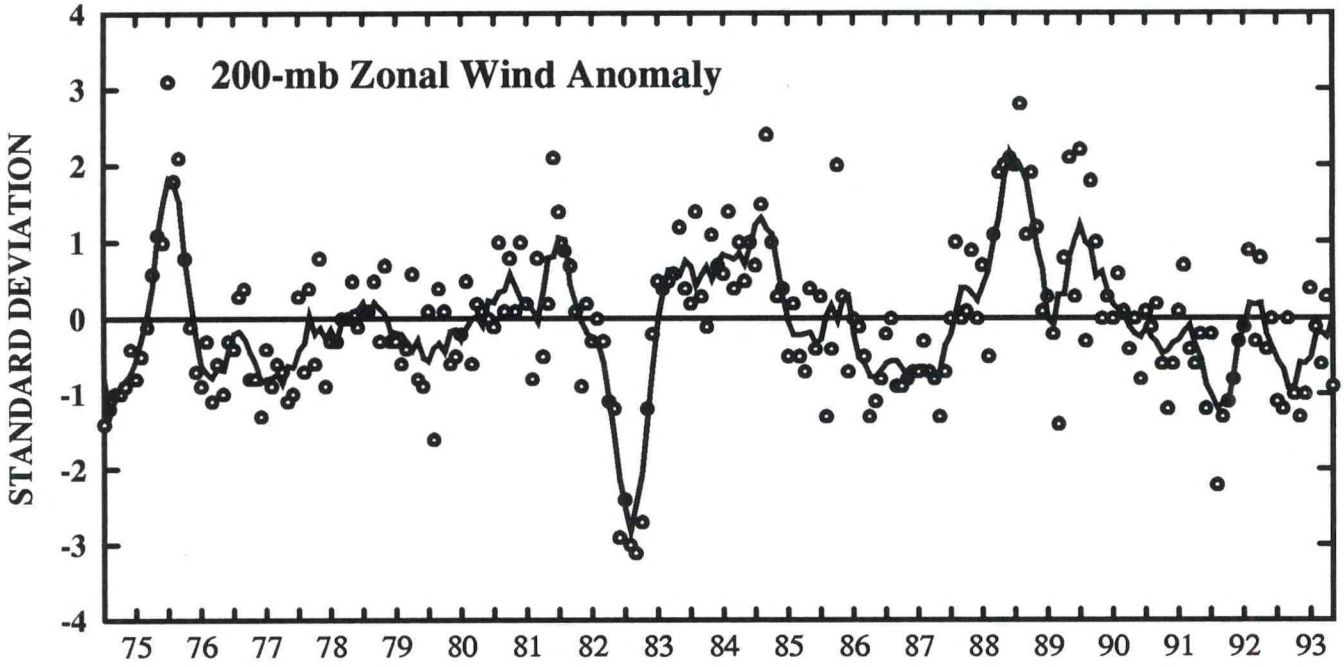

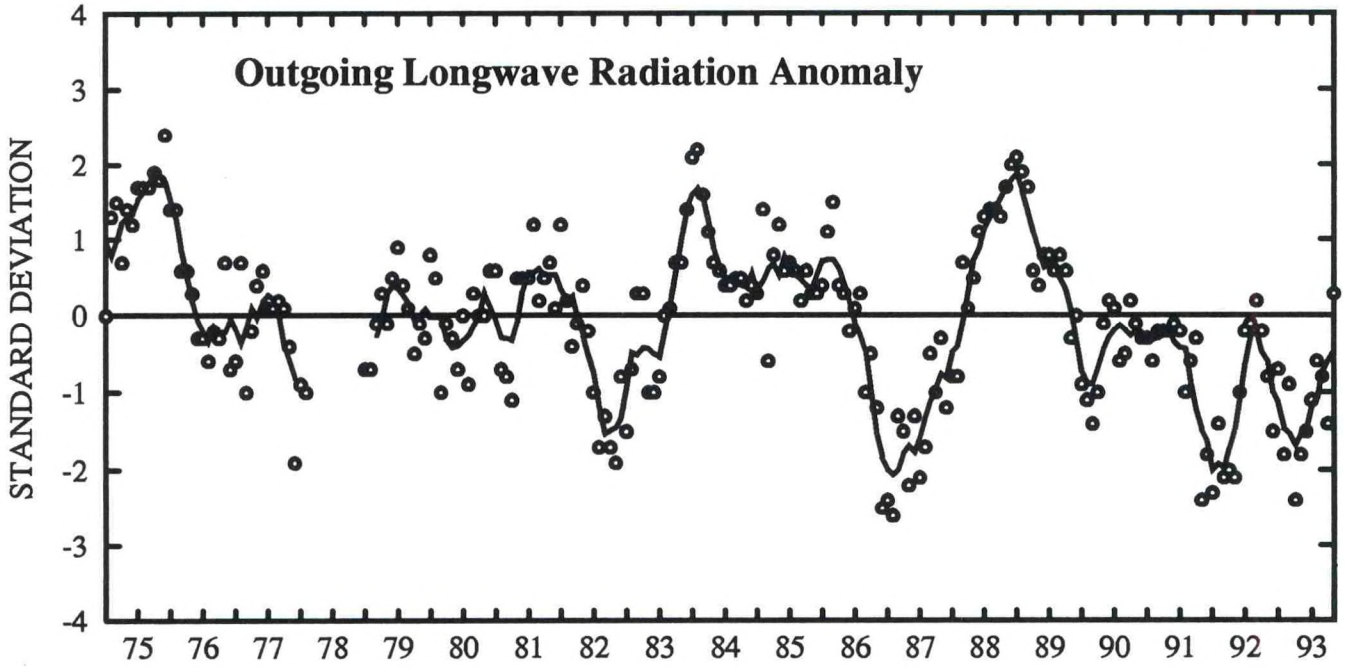

Top: Five-month running mean of the standardized monthly 200-mb zonal wind anomalies averages over the area 5°N-5°S, 165°W-110°W. Values are standardized by the mean annual standard deviation. Circles indicate individual monthly means. The x-axis labels are centered on July.

Bottom: As above, except for standardized monthly outgoing longwave radiation anomalies over the area 5°N-5°S, 160°E-160°W.

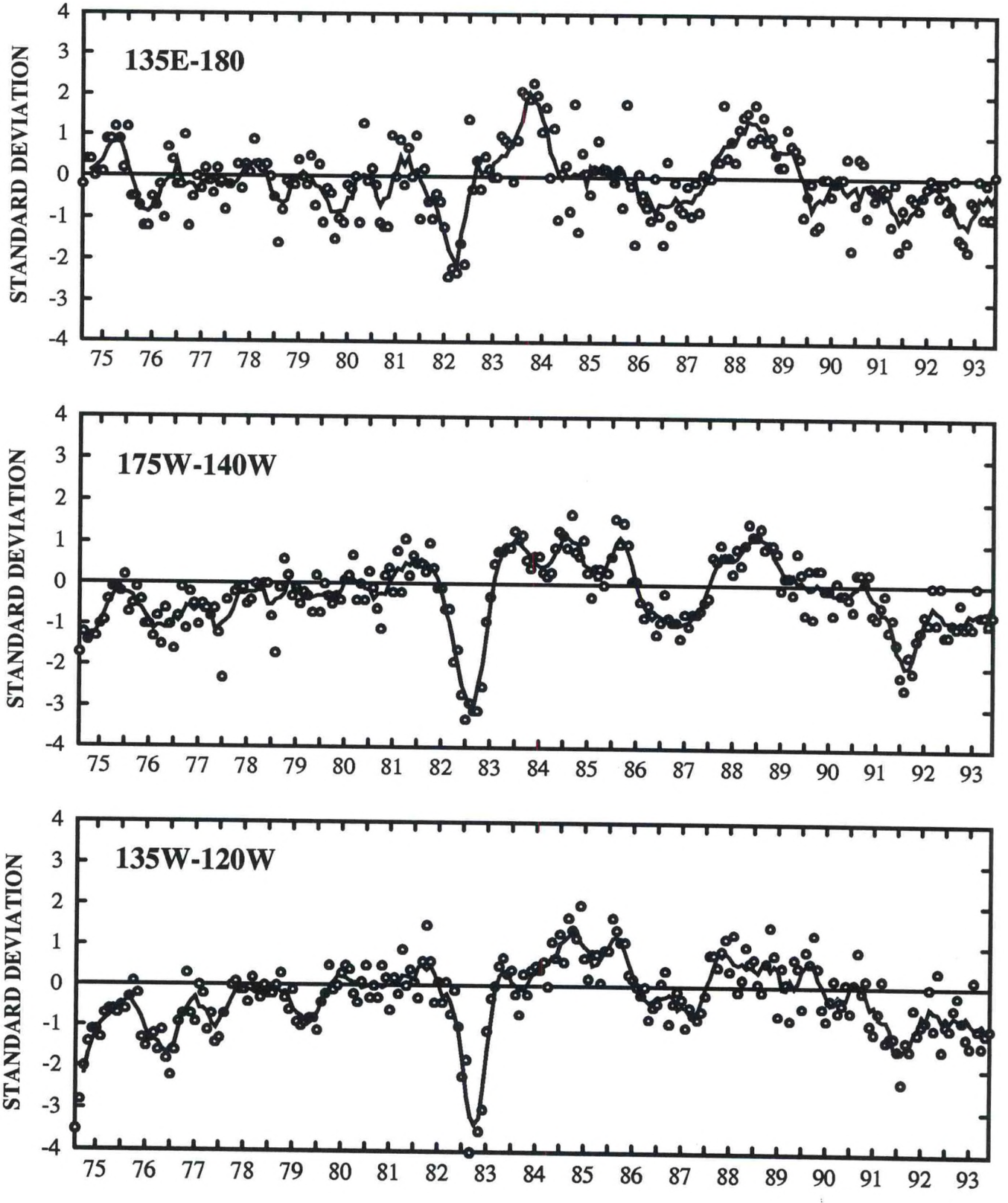

850-mb Zonal Wind Anomalies: Five-month running mean of the standardized monthly 850-mb zonal wind anomalies in the latitude belt 5°N-5°S between 135°E-180 (top) 175°W-140°W (middle) and 135°E-120°W (bottom). Circles indicate individual monthly means. The x-axis labels are centered on July. Positive (negative) values indicate easterly (westerly) anomalies.

SEA-SURFACE TEMPERATURE (SST)

Time-Longitude Section (pp. 33-36): Monthly-mean SST (°C) along the equator in the Pacific Ocean between 120°E and 80°W. Contour interval is 1°C, and values greater than 28°C are shaded. Shading interval is 1°C, with values greater than 30°C having the darkest shading.

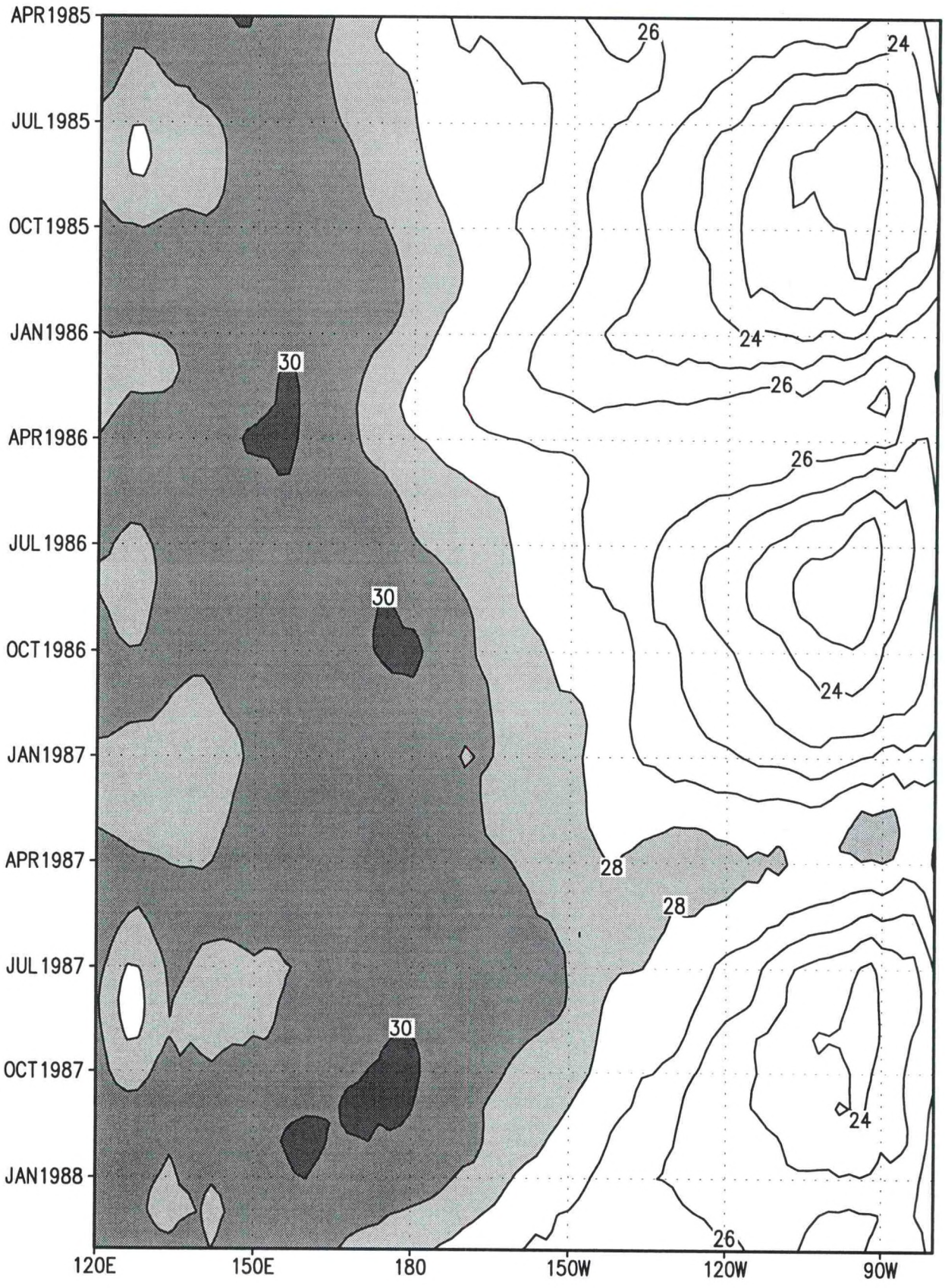

Sea-Surface Temperature (°C)

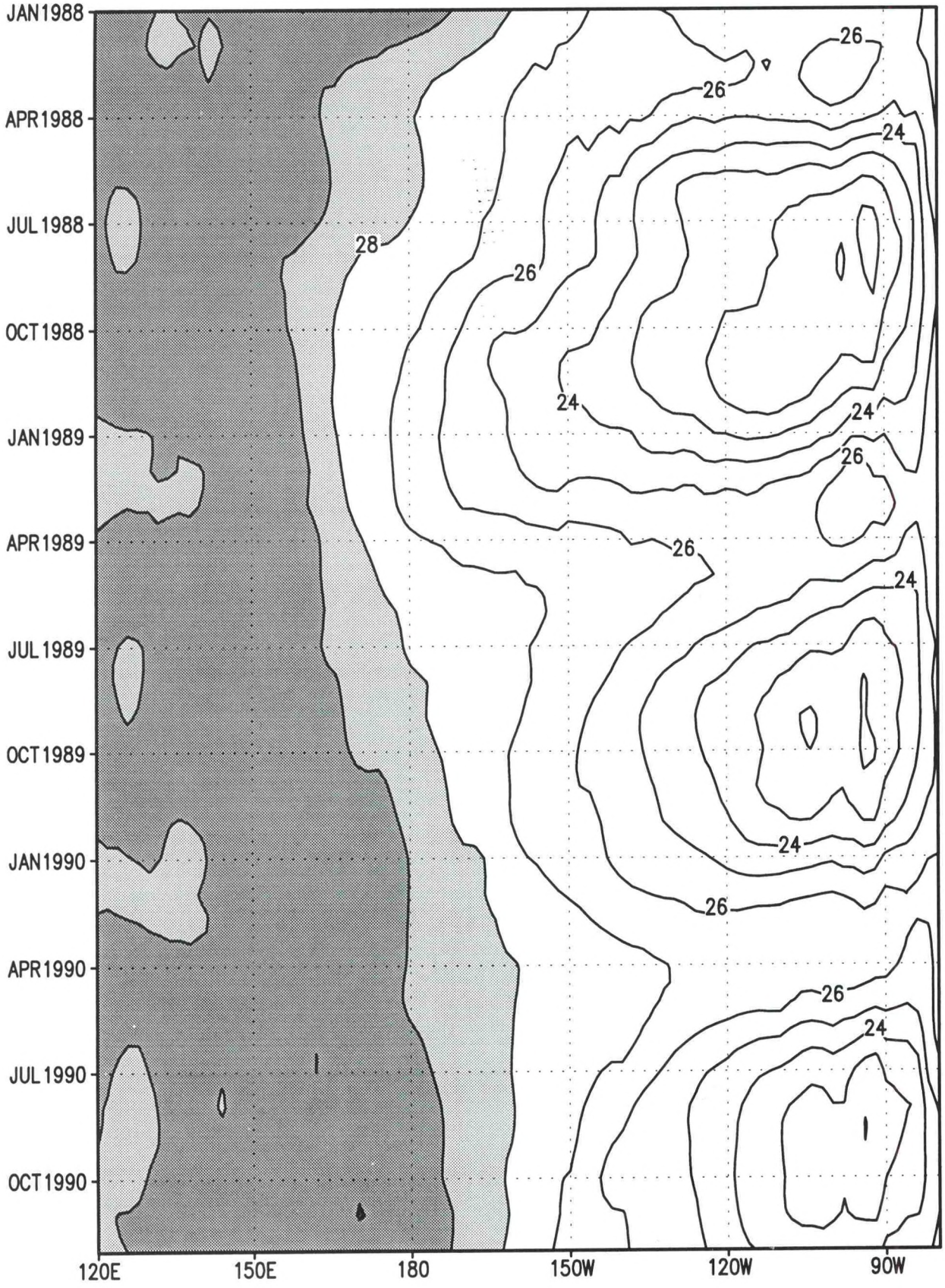

Sea-Surface Temperature (°C)

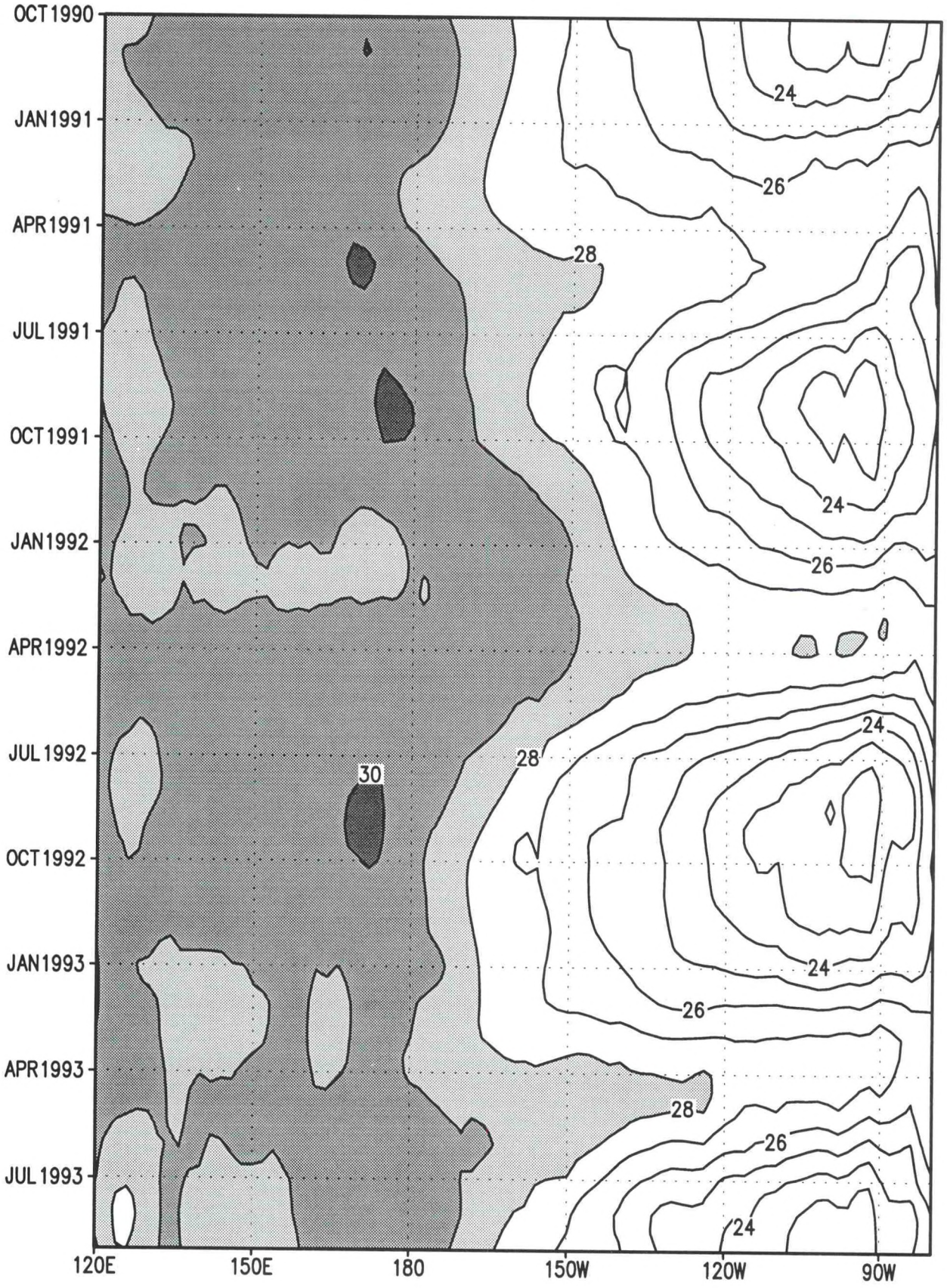

Sea-Surface Temperature (°C)

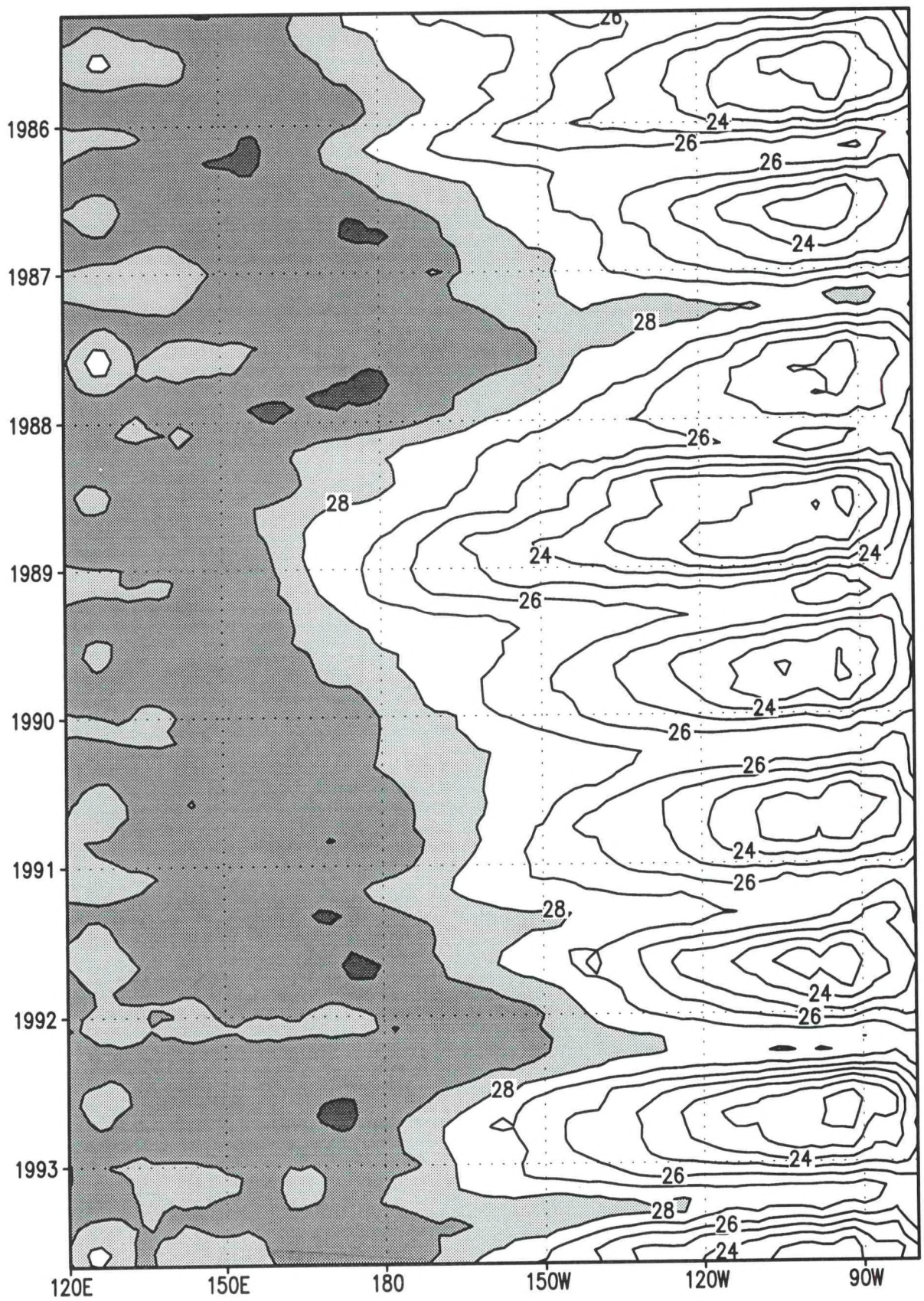

Sea-Surface Temperature (°C)

SEA-SURFACE TEMPERATURE (SST) ANOMALY

Seasonal Maps (pp. 38-45): Seasonal-mean SST anomalies (°C) for all longitudes from 50°N to 50°S. Contour interval is 1°C, and positive anomalies greater than 1°C are shaded dark with solid contours. Negative anomalies below -1°C are shaded light with dashed contours. Contours are also drawn at 0.5°C and -0.5°C, and zero contour is shown thick solid.

Time-Longitude Section (pp. 46-49): Monthly-mean SST anomalies (°C) along the equator in the Pacific Ocean between 120°E and 80°W. Positive anomalies greater than 1°C are shaded dark with solid contours. Negative anomalies below -1°C are shaded light with dashed contours. Contours are also drawn at 0.5°C and -0.5°C, and zero contour is shown thick solid.

DJF 1985/86

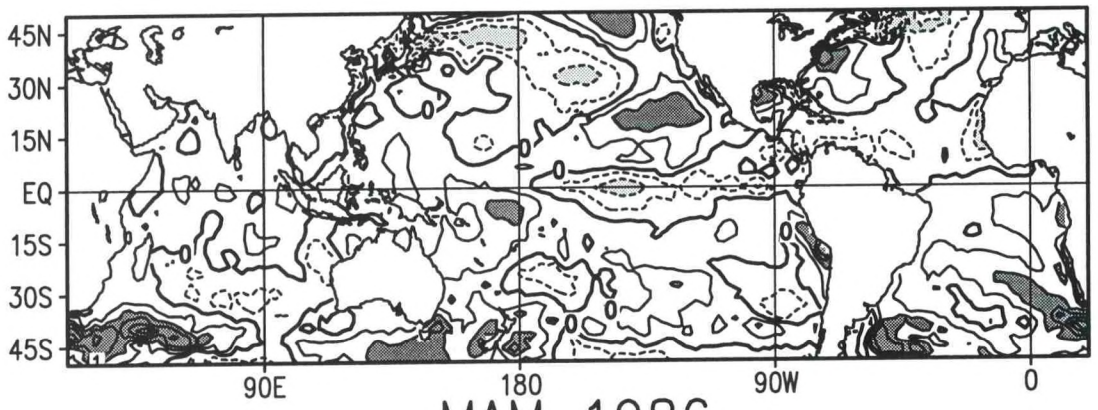

MAM 1986

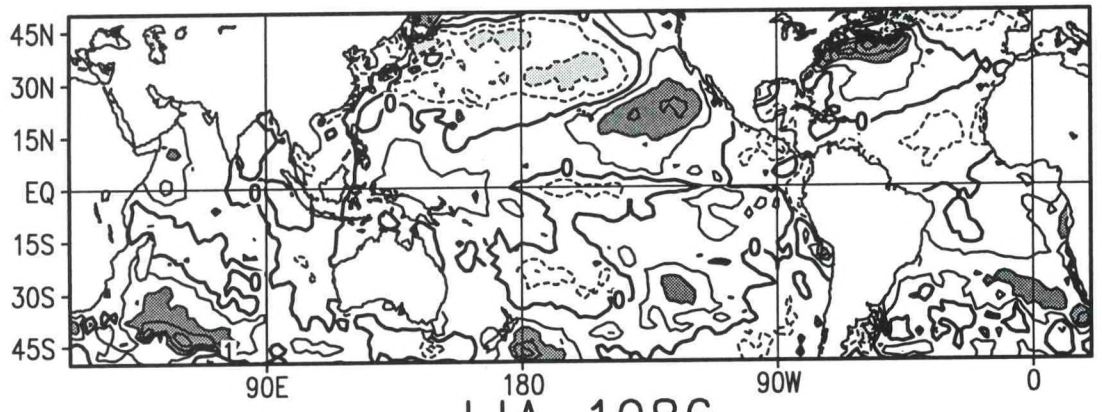

JJA 1986

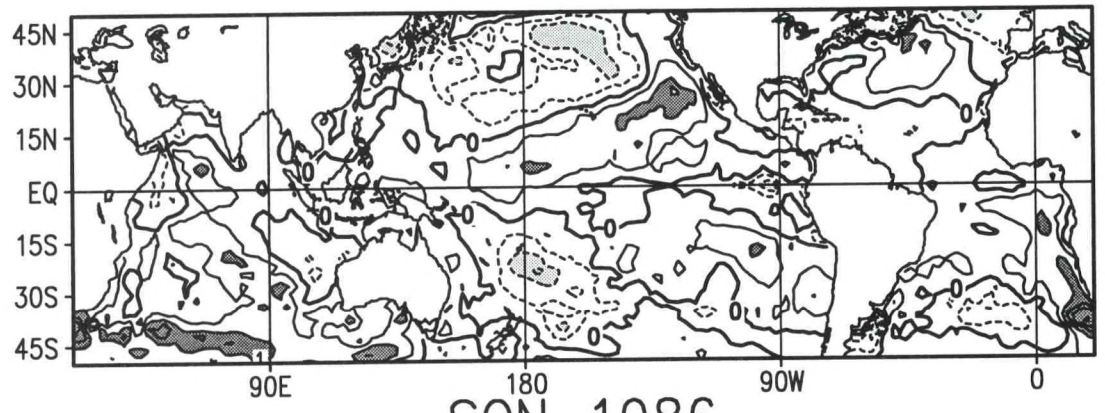

SON 1986

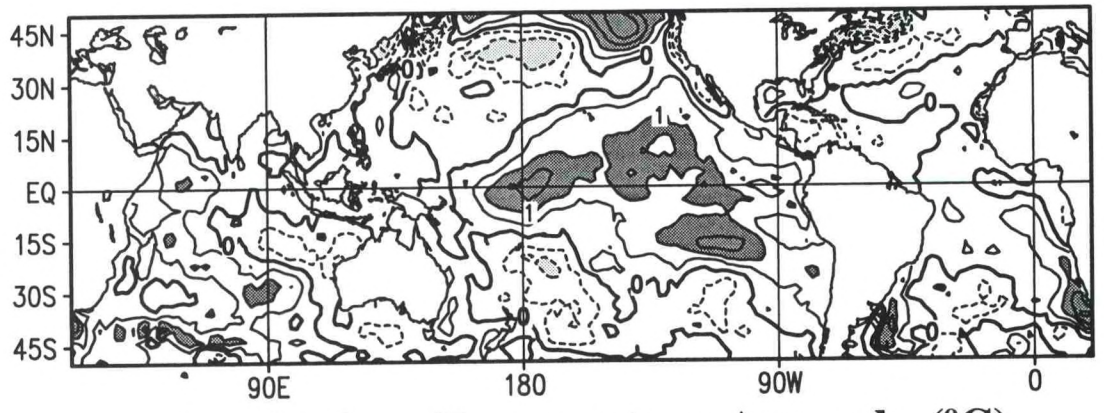

Sea-Surface Temperature Anomaly (°C)

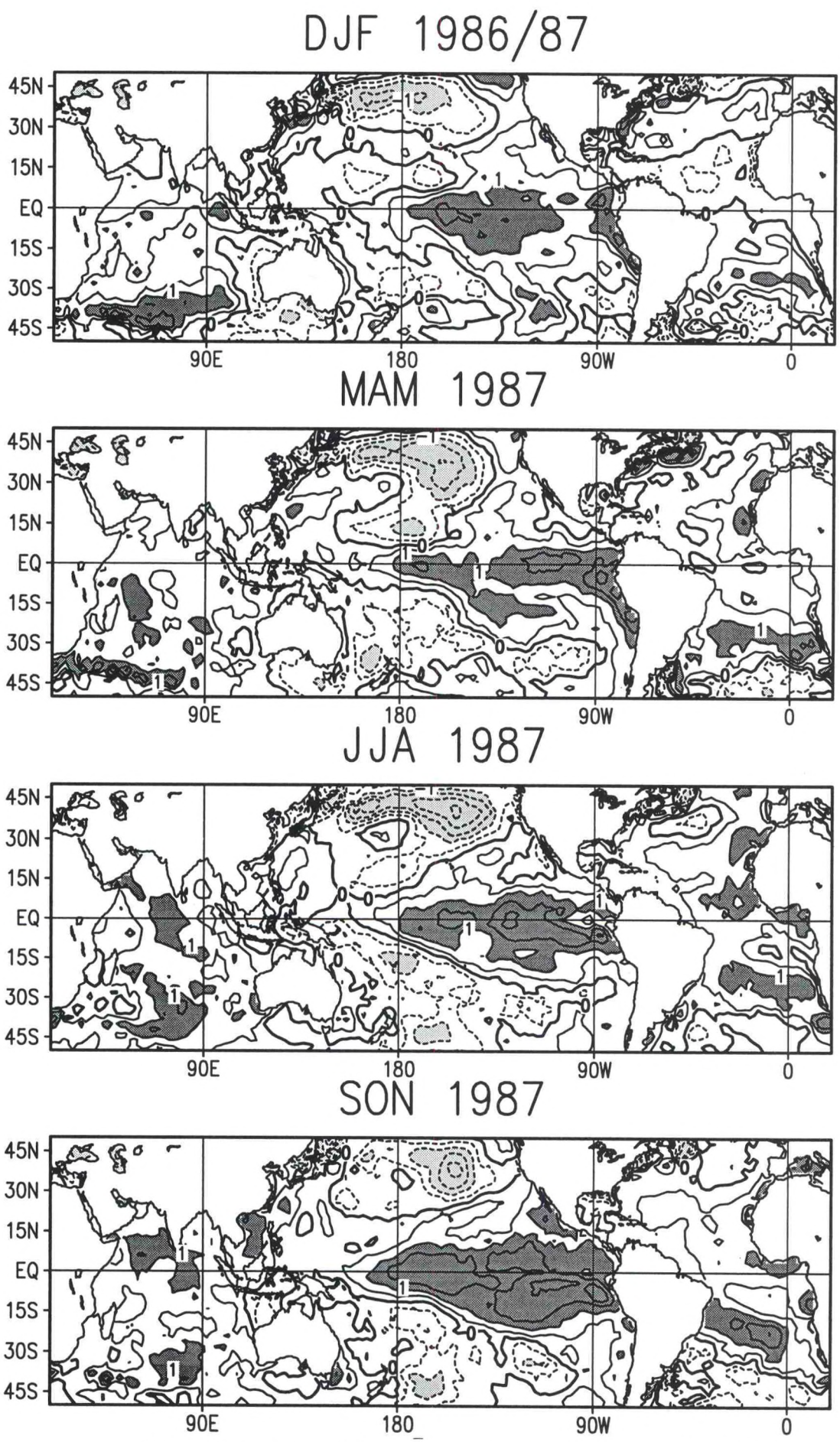

Sea-Surface Temperature Anomaly (°C)

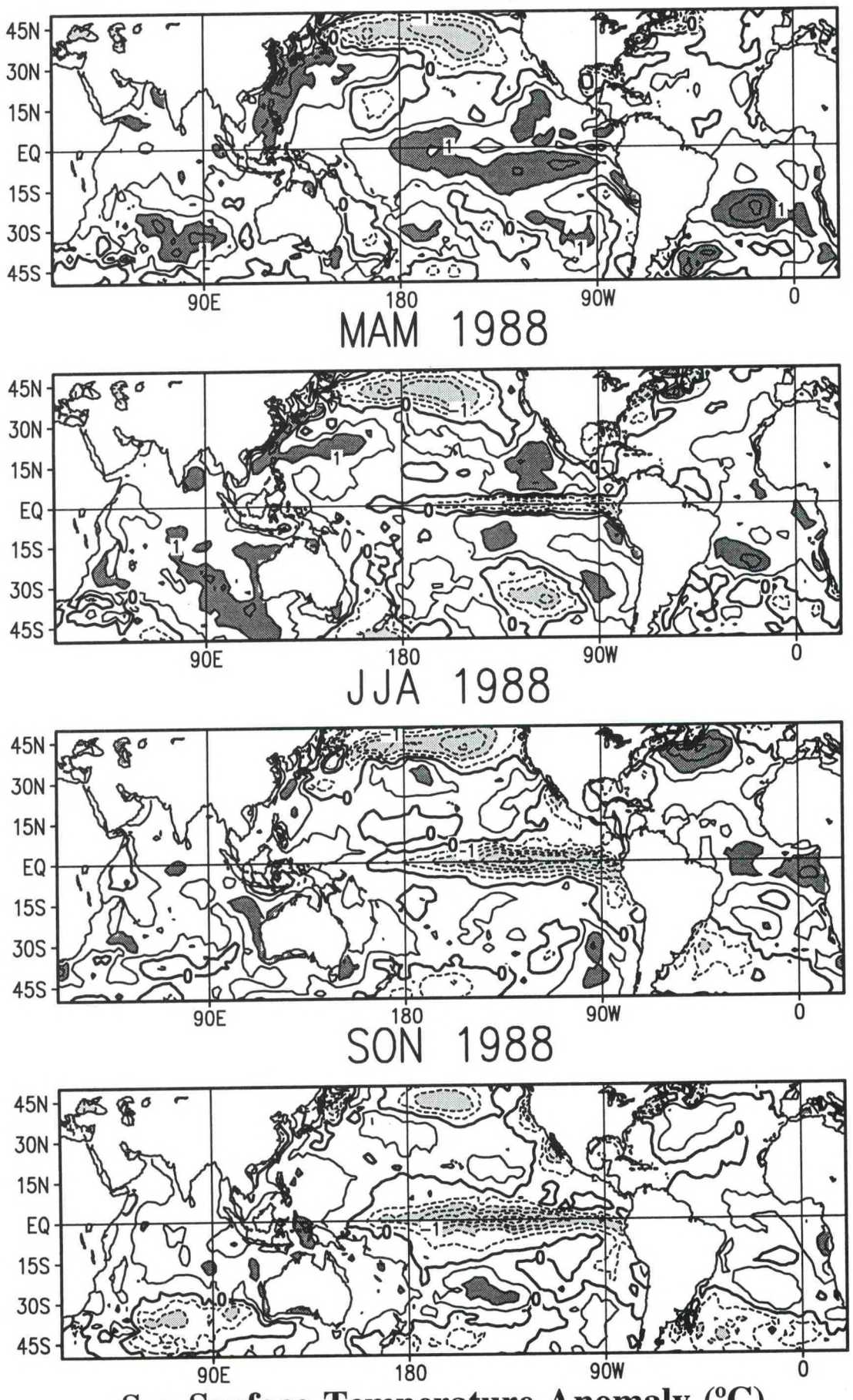

Sea-Surface Temperature Anomaly (°C)

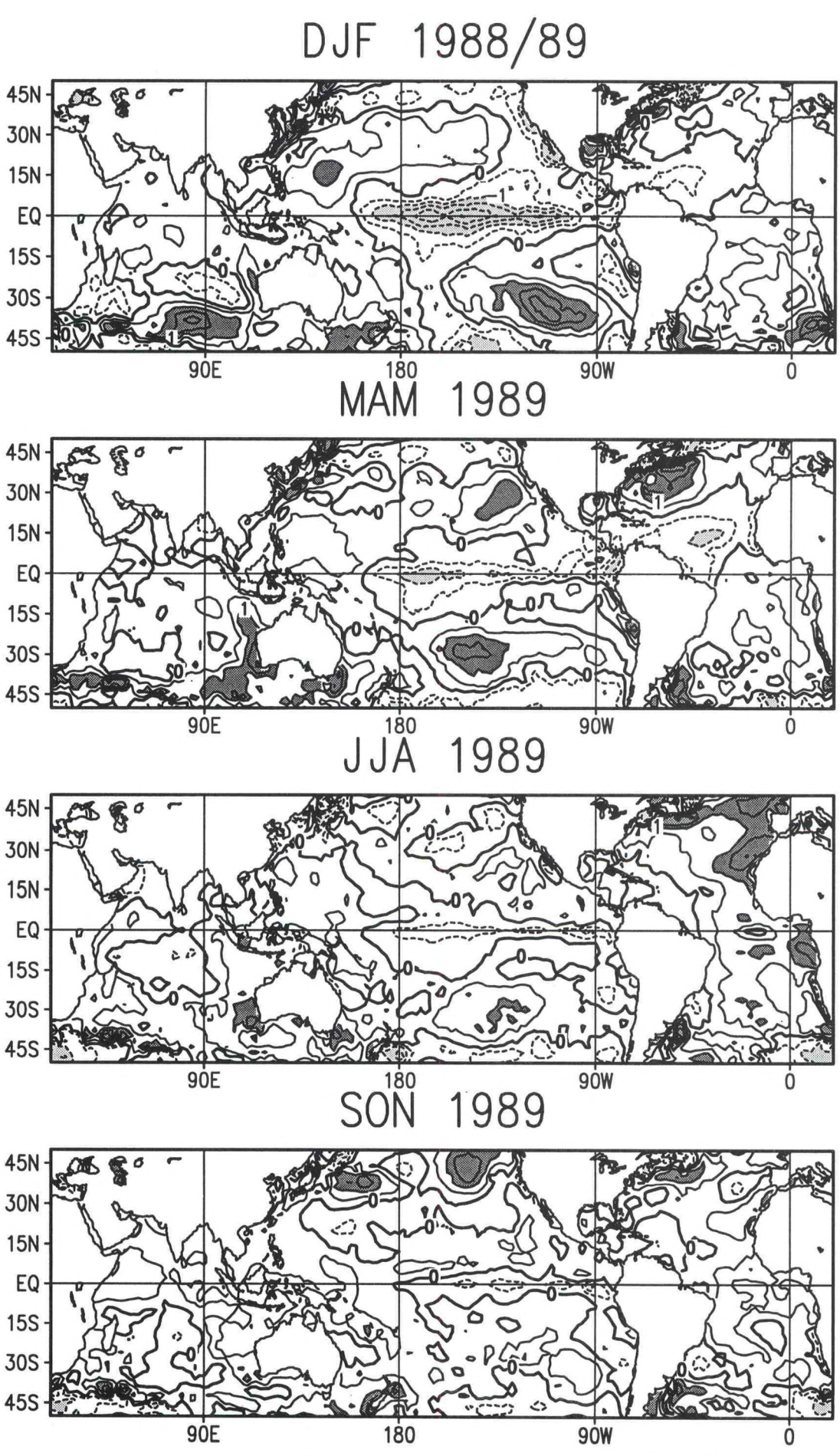

Sea-Surface Temperature Anomaly (°C)

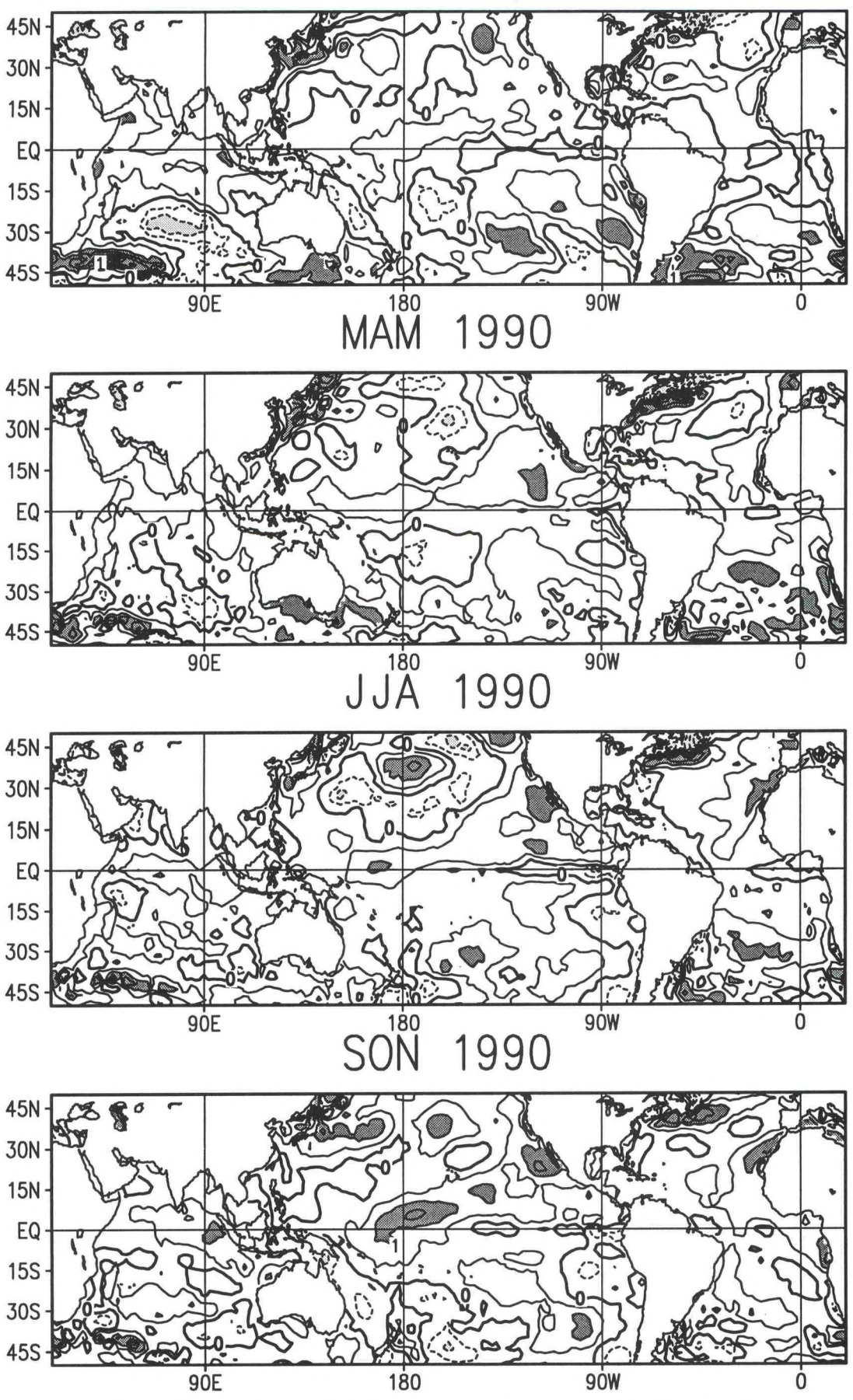

Sea-Surface Temperature Anomaly (°C)

DJF 1990/91

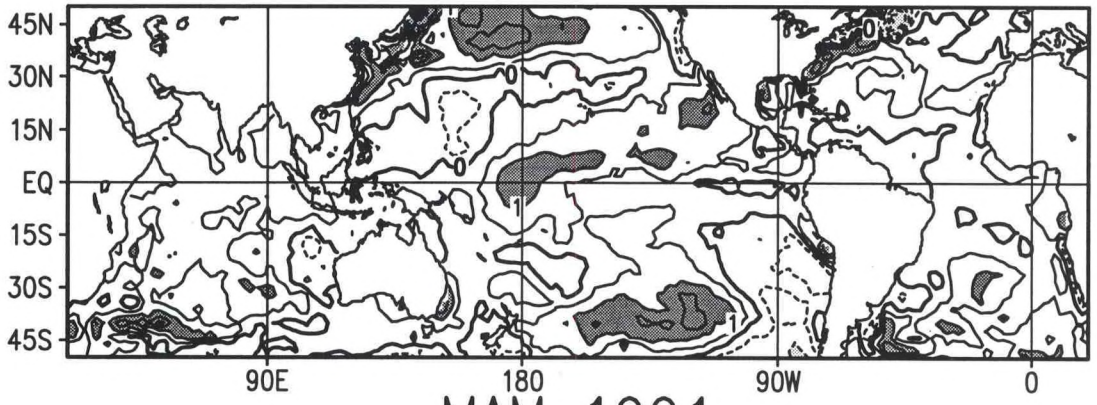

MAM 1991

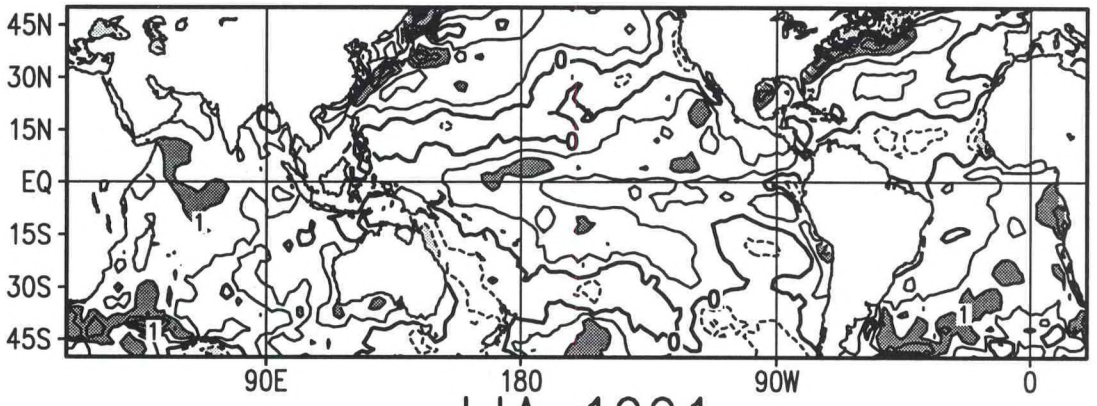

JJA 1991

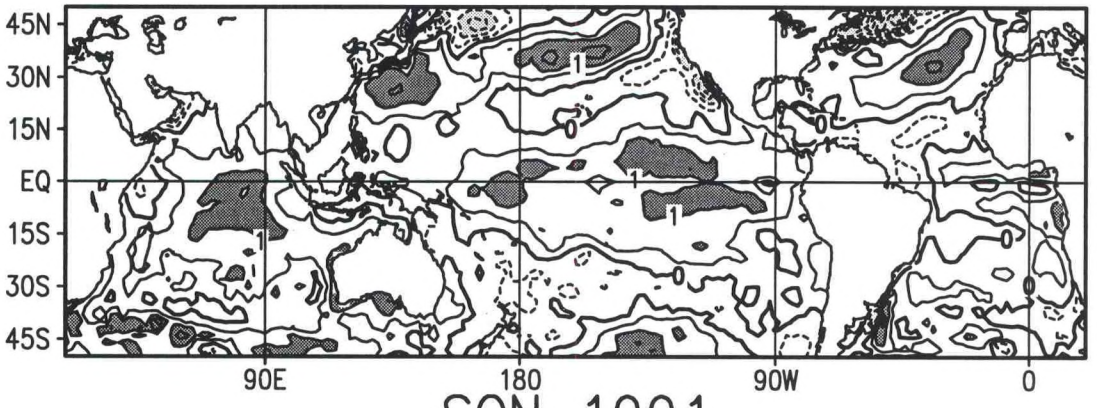

SON 1991

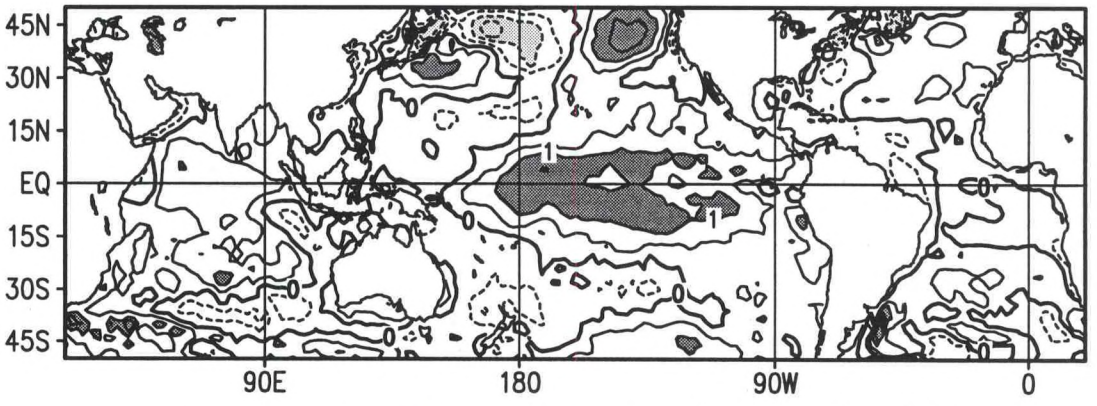

Sea-Surface Temperature Anomaly (°C)

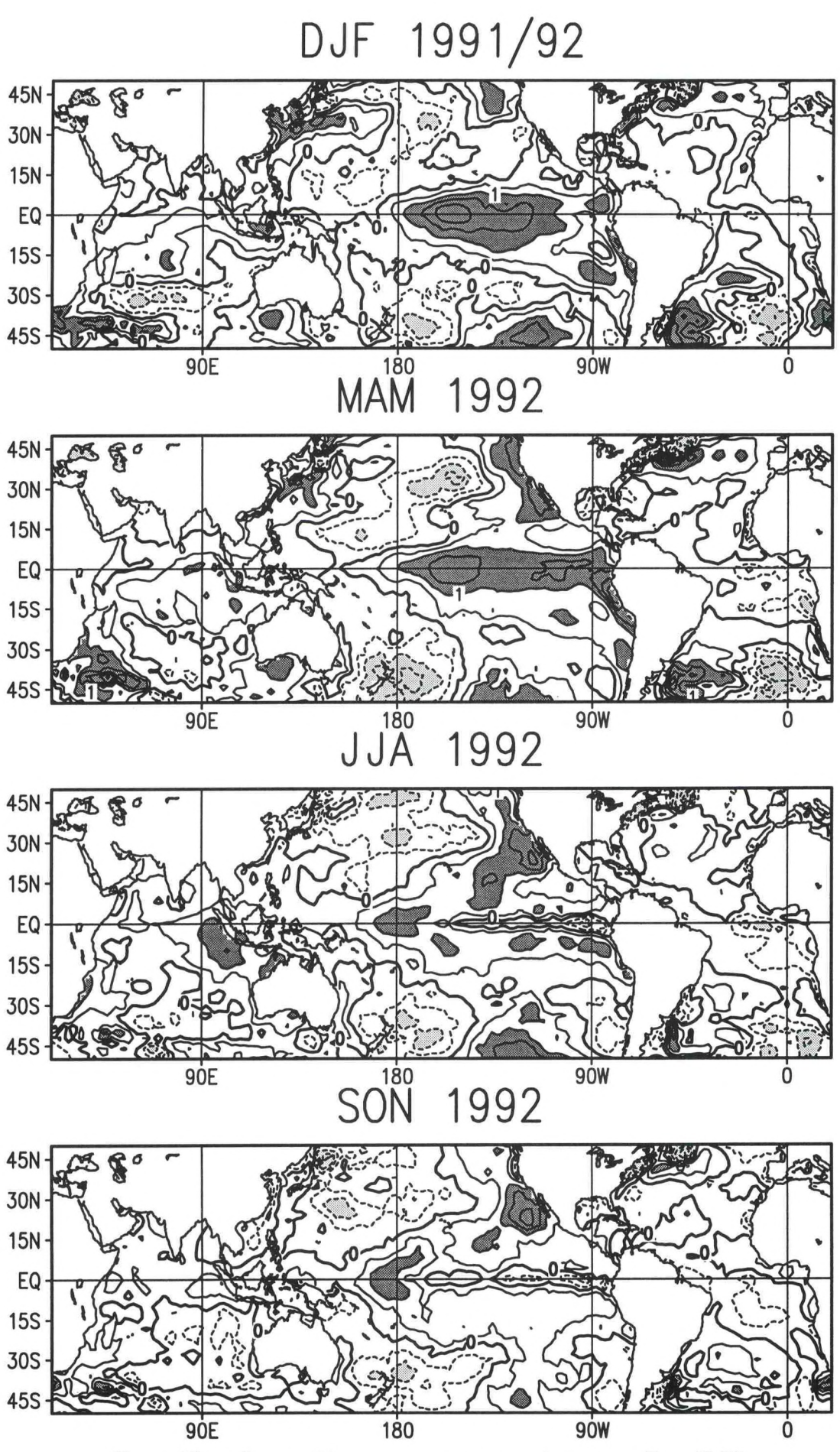

Sea-Surface Temperature Anomaly (°C)

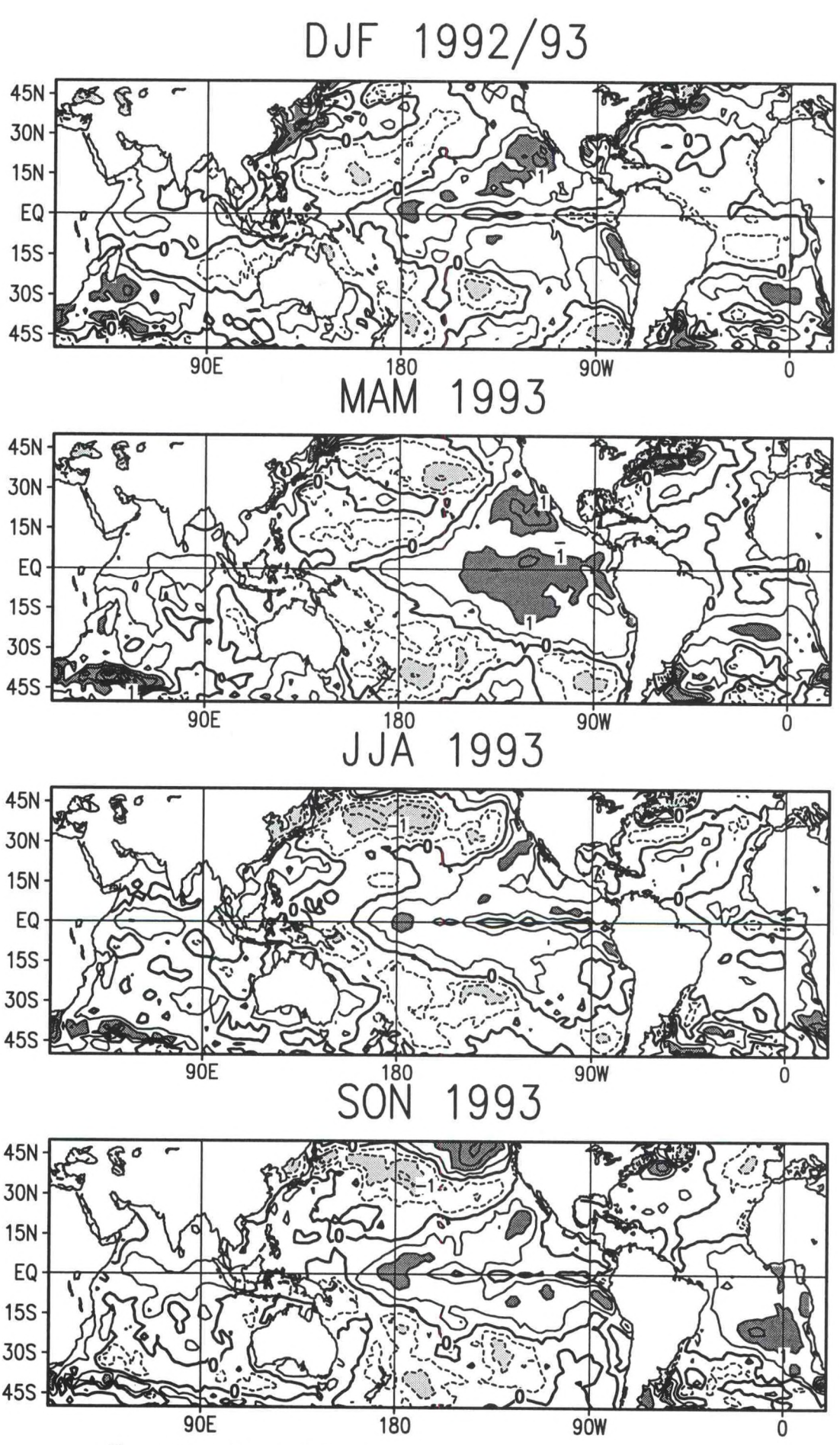

Sea-Surface Temperature Anomaly (°C)

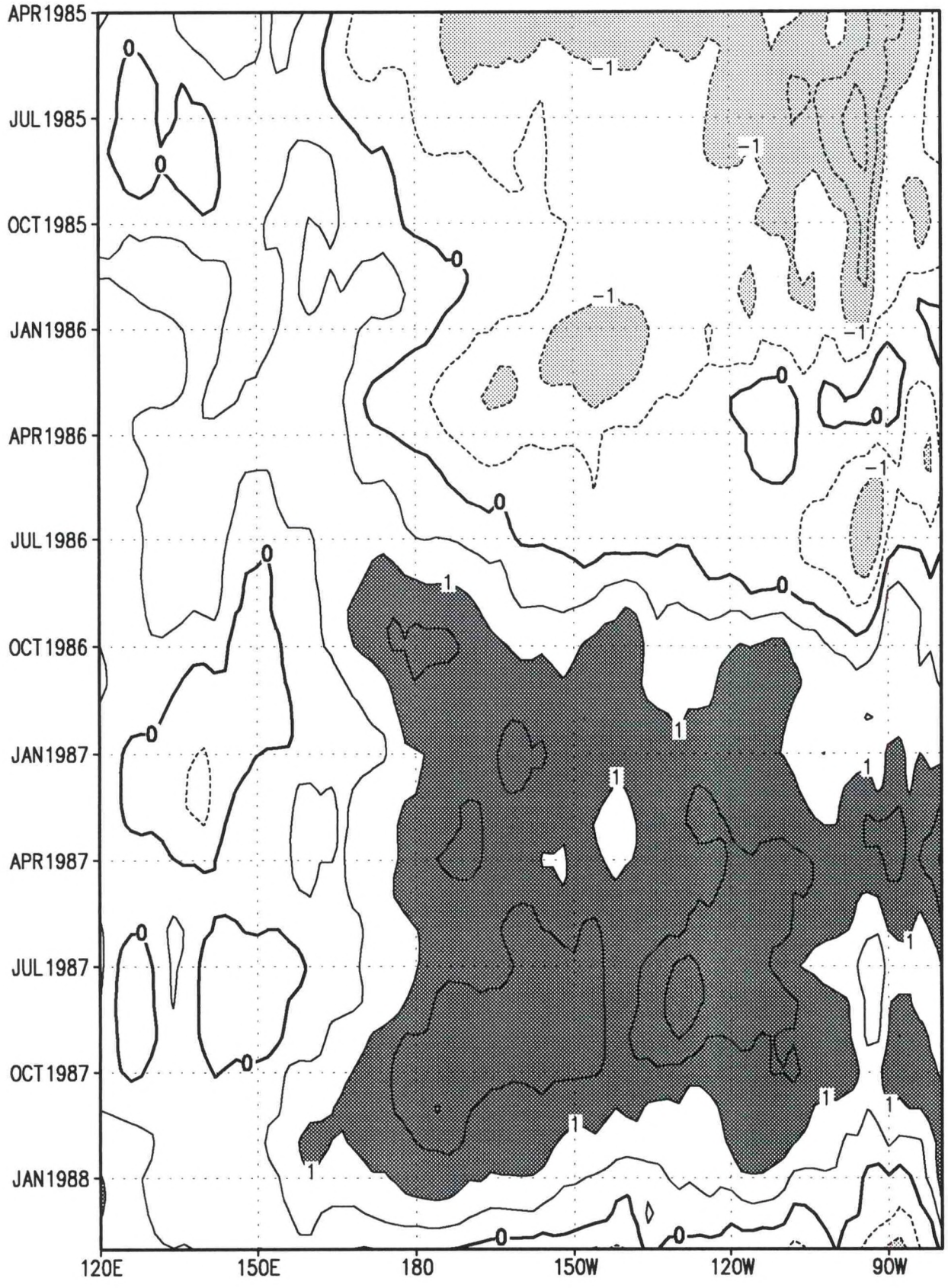

Sea-Surface Temperature Anomaly (°C)

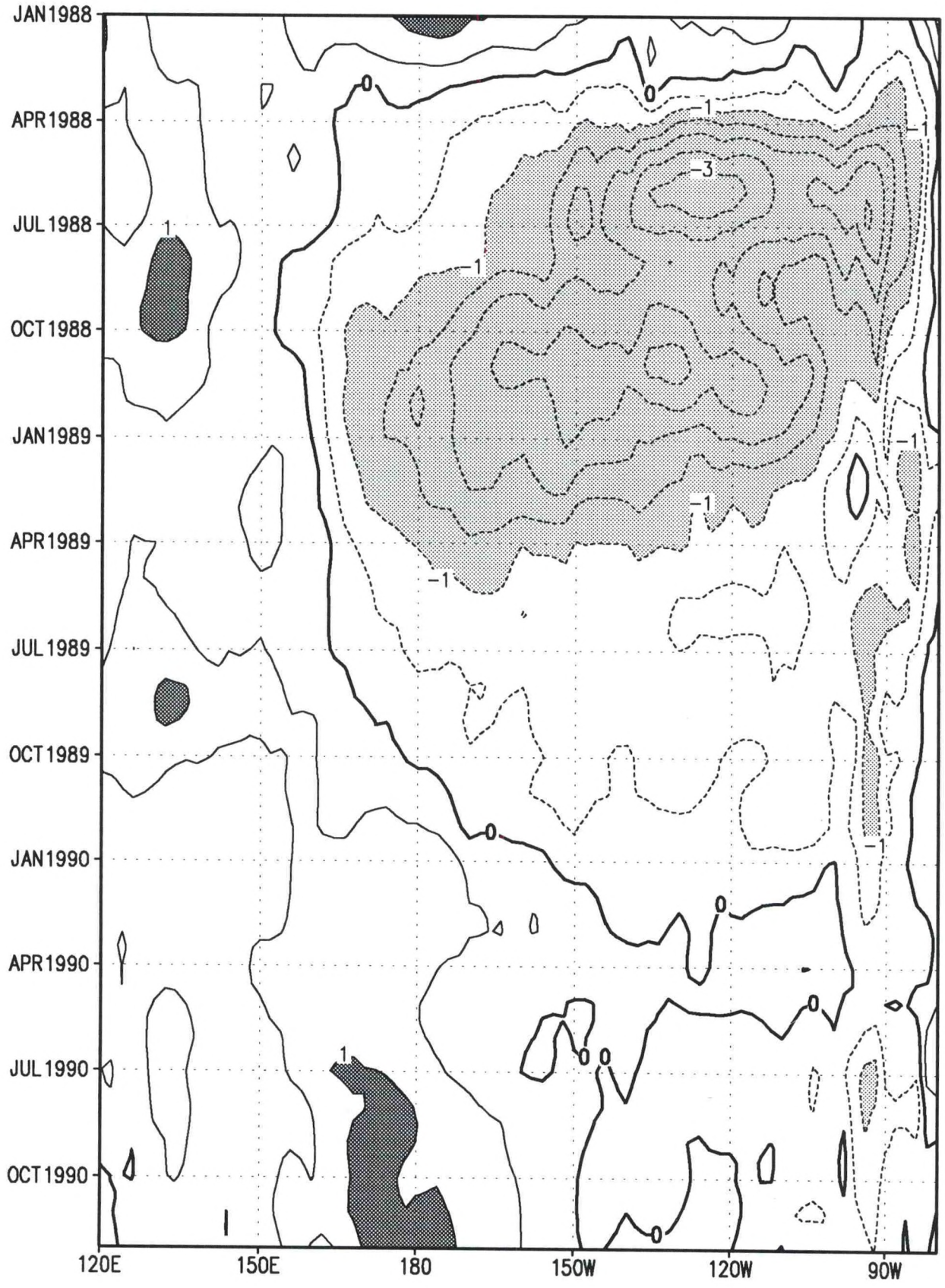

Sea-Surface Temperature Anomaly (°C)

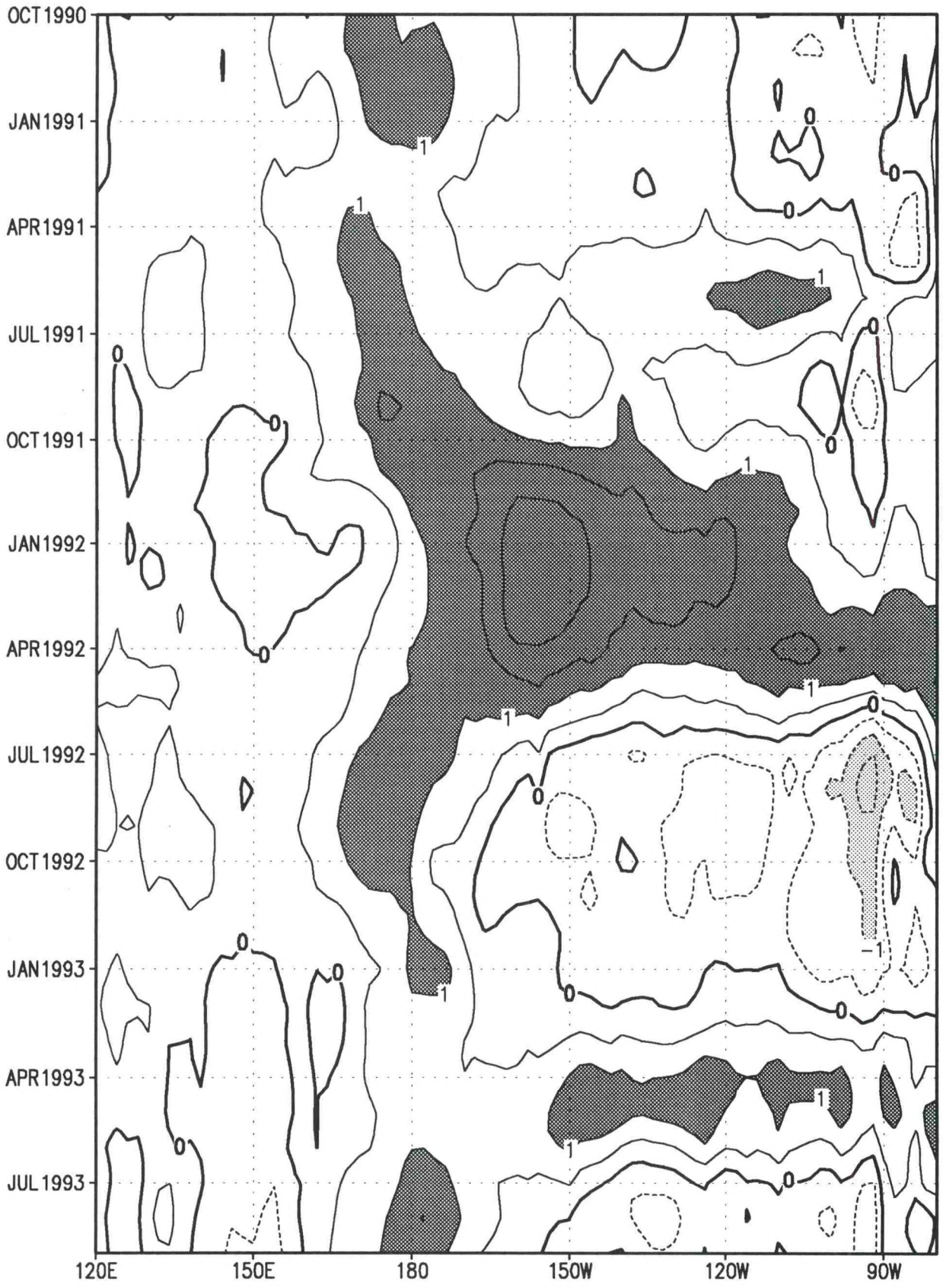

Sea-Surface Temperature Anomaly (°C)

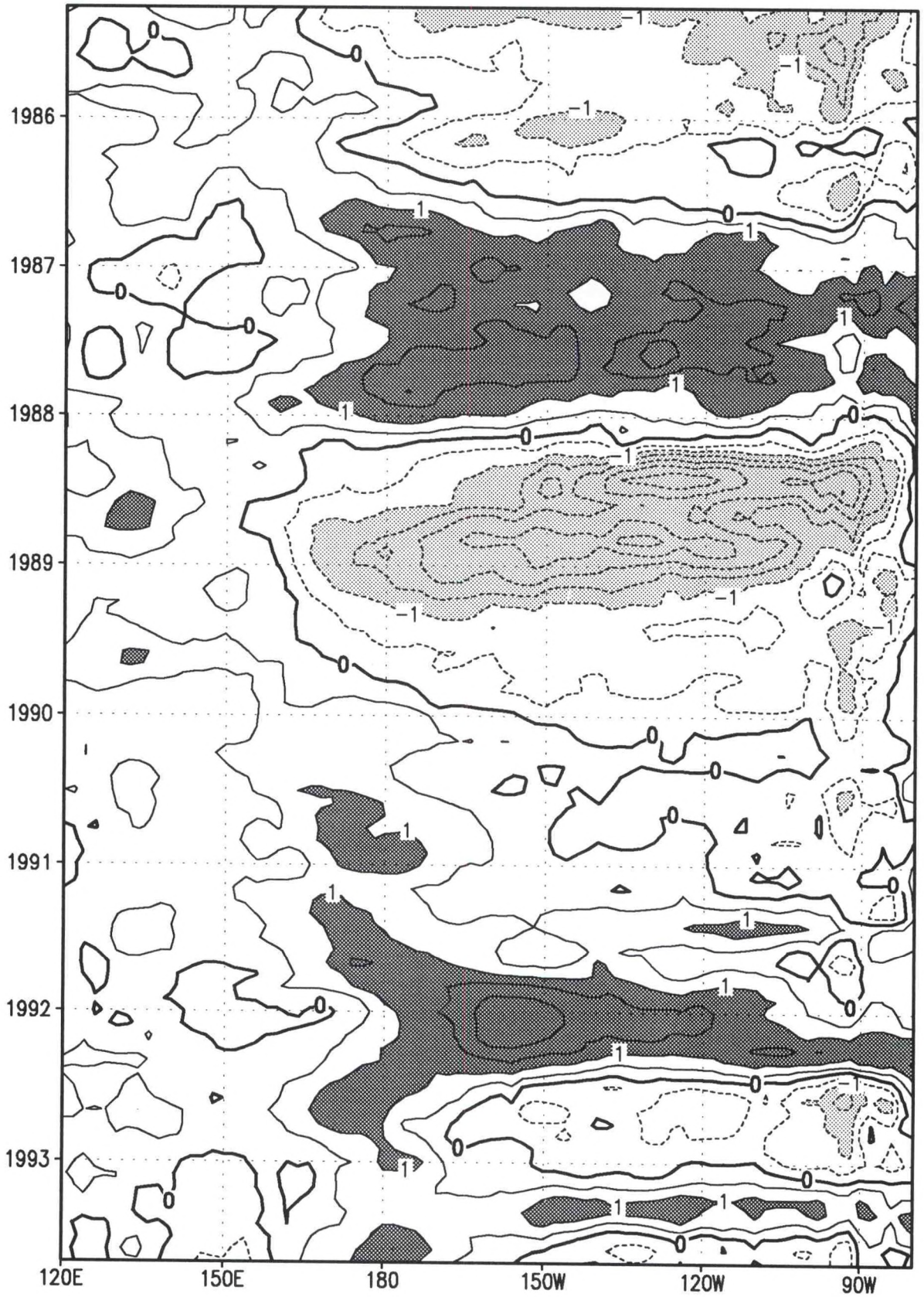

Sea-Surface Temperature Anomaly (°C)

OCEAN TEMPERATURE ANOMALY

Seasonal Maps (pp. 51-58): Anomalous seasonal-mean depth of the 20°C isotherm (m) over the Pacific sector from 20°N to 20°S. Positive anomalies (increased depth) greater than 10 m are shaded dark with solid contours. Negative anomalies (decreased depth) below -10 m are shaded light with dashed contours. Zero contour is shown thick solid.

Depth-Longitude Section (pp. 59-66): Seasonal-mean ocean temperature anomalies (°C) along the equator over the Pacific sector between 120°E and 80°W. Positive anomalies (increased depth) greater than 1°C are shaded dark with solid contours. Zero contour is shown thin solid. The 20°C isotherm is shown by thick solid contour. Vertical axis is ocean depth (m) and horizontal axis is longitude.

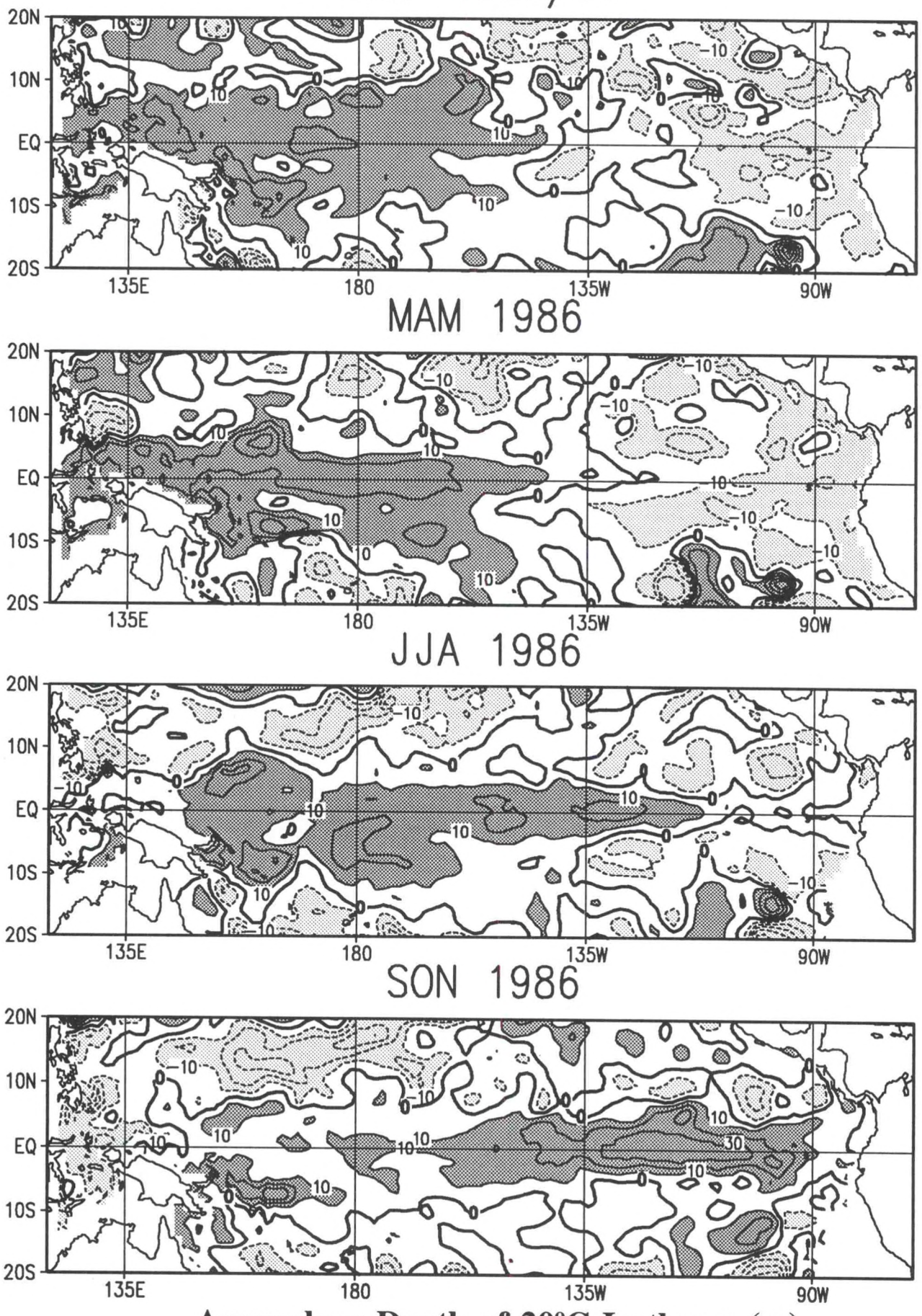

Anomalous Depth of 20°C Isotherm (m)

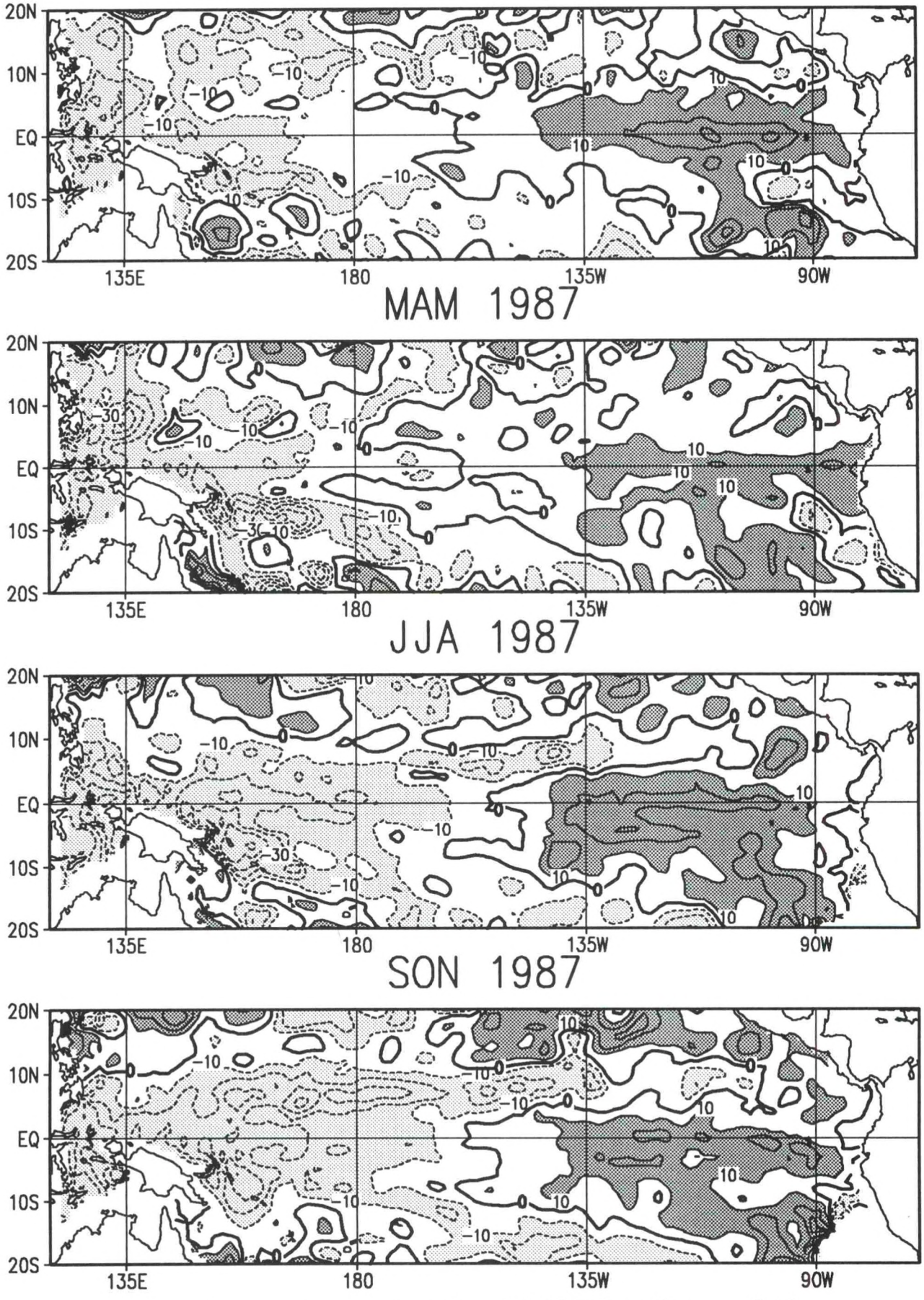

Anomalous Depth of 20°C Isotherm (m)

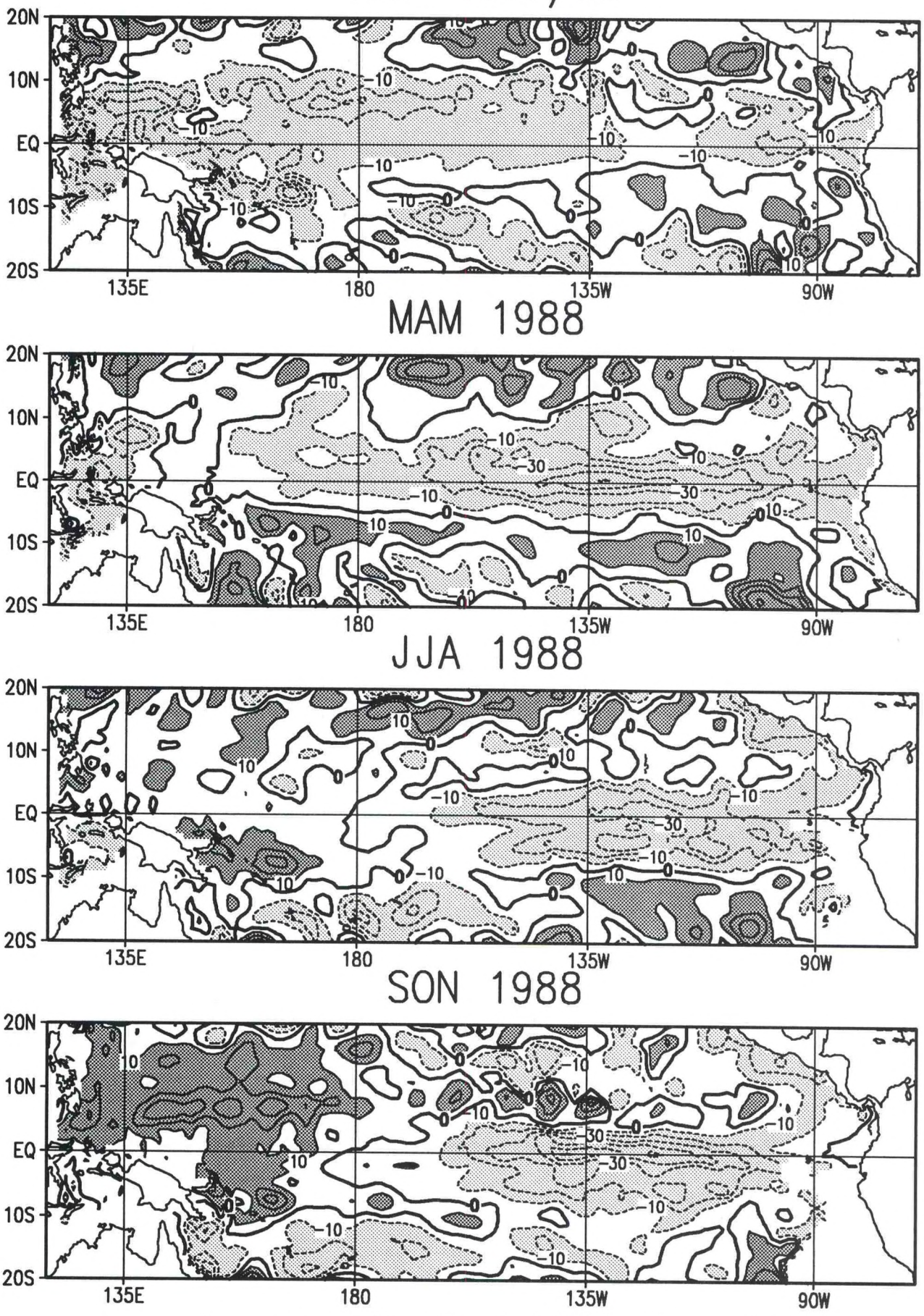

Anomalous Depth of 20°C Isotherm (m)

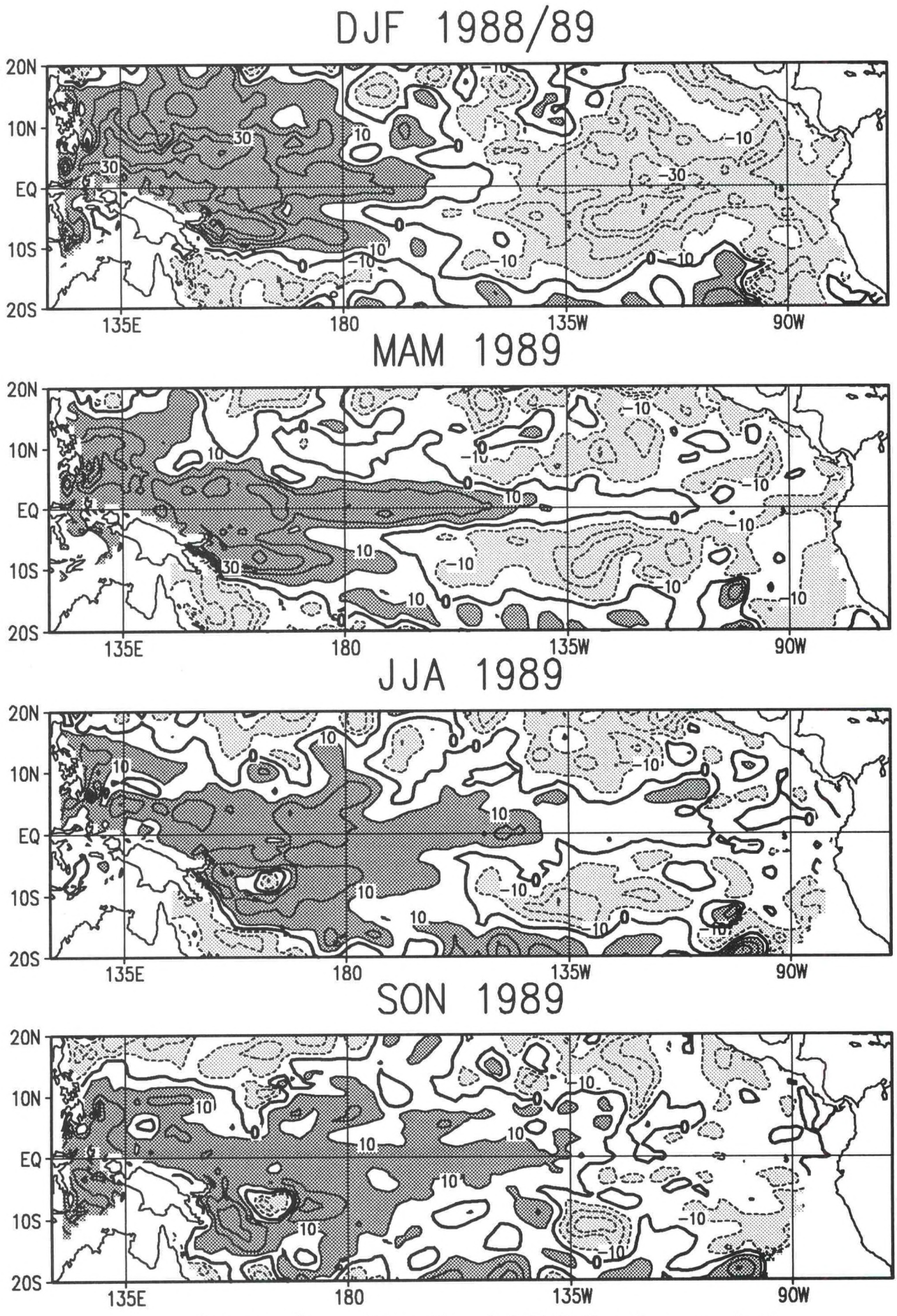

Anomalous Depth of 20°C Isotherm (m)

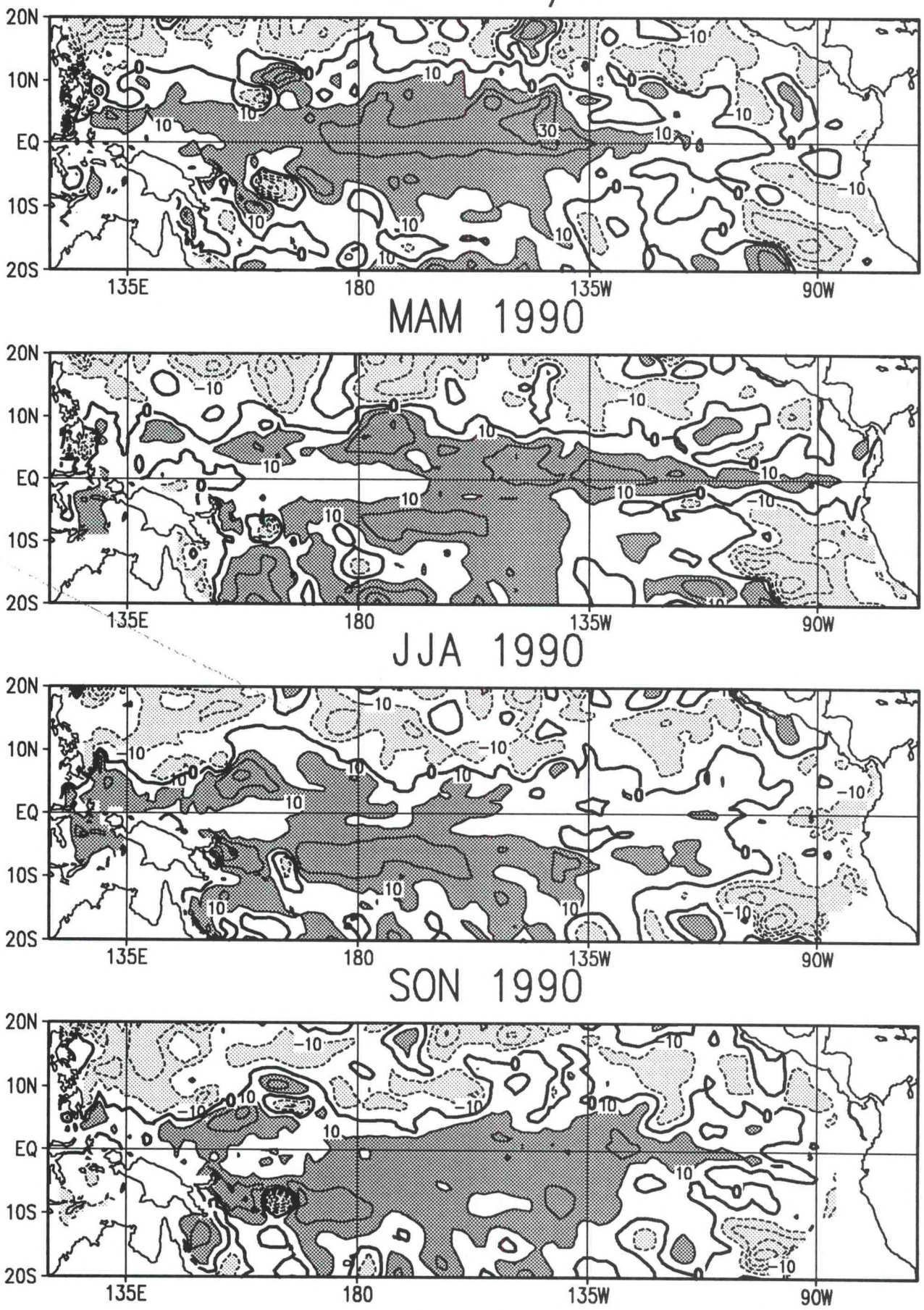

Anomalous Depth of 20°C Isotherm (m)

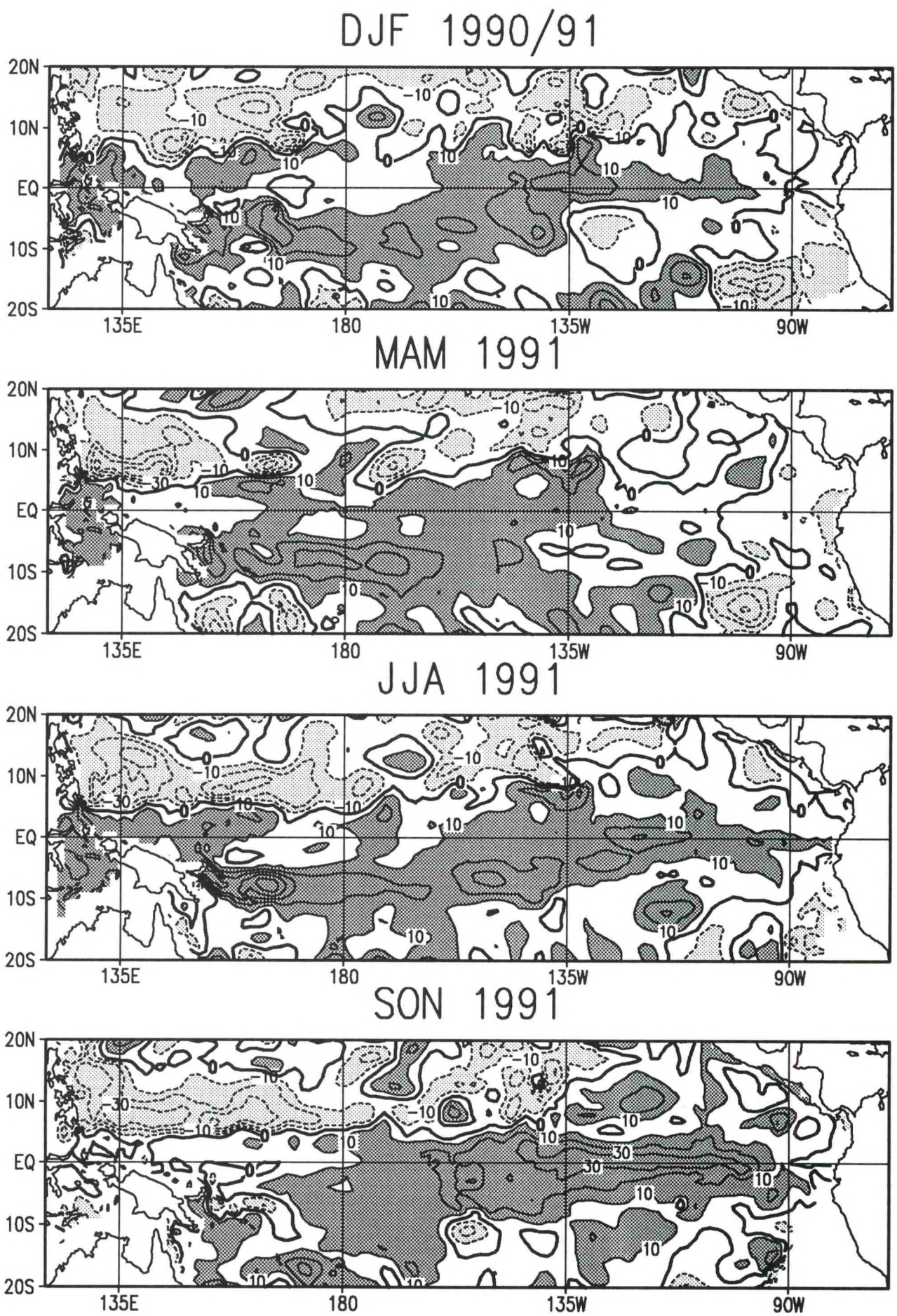

Anomalous Depth of 20°C Isotherm (m)

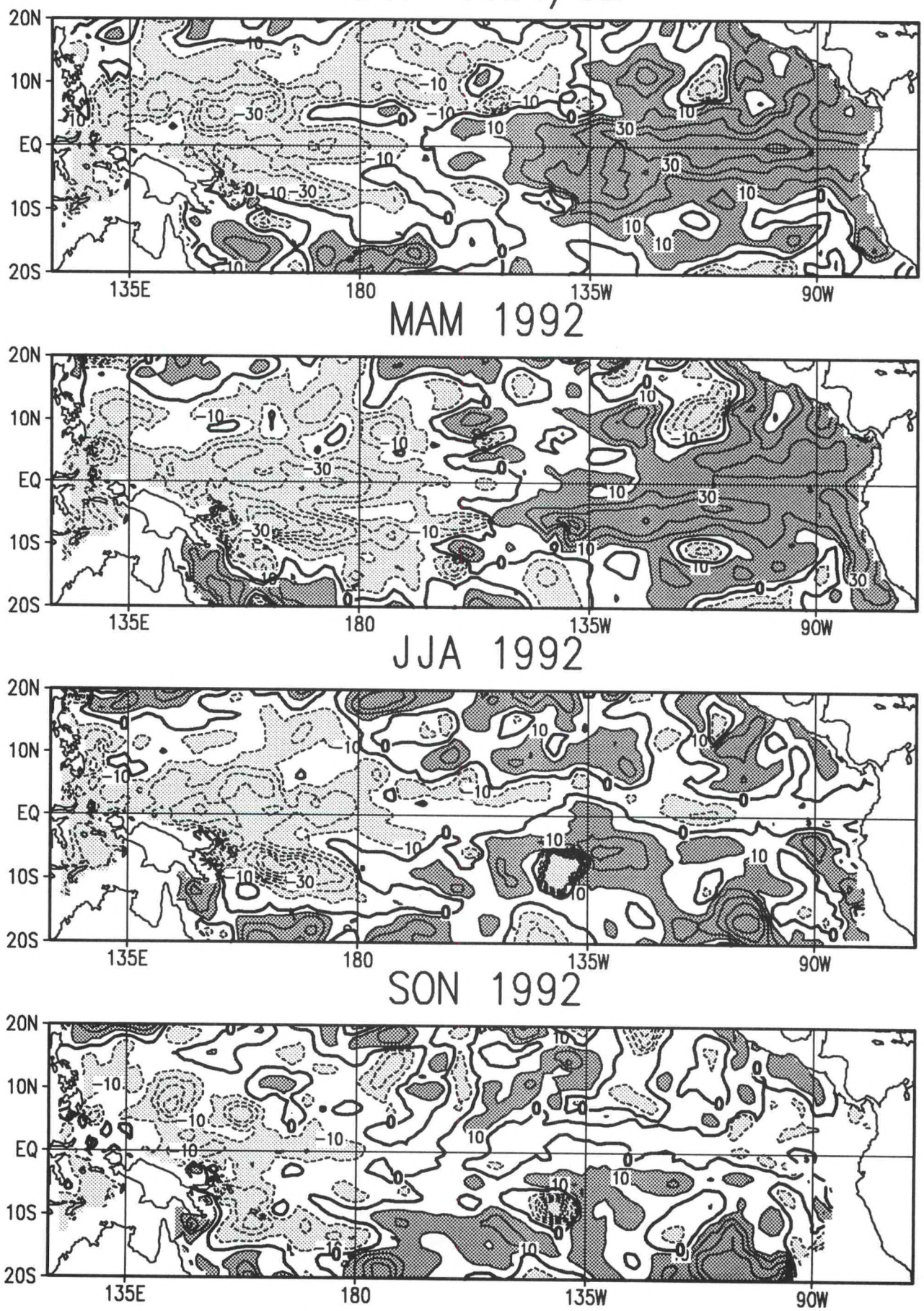

Anomalous Depth of 20°C Isotherm (m)

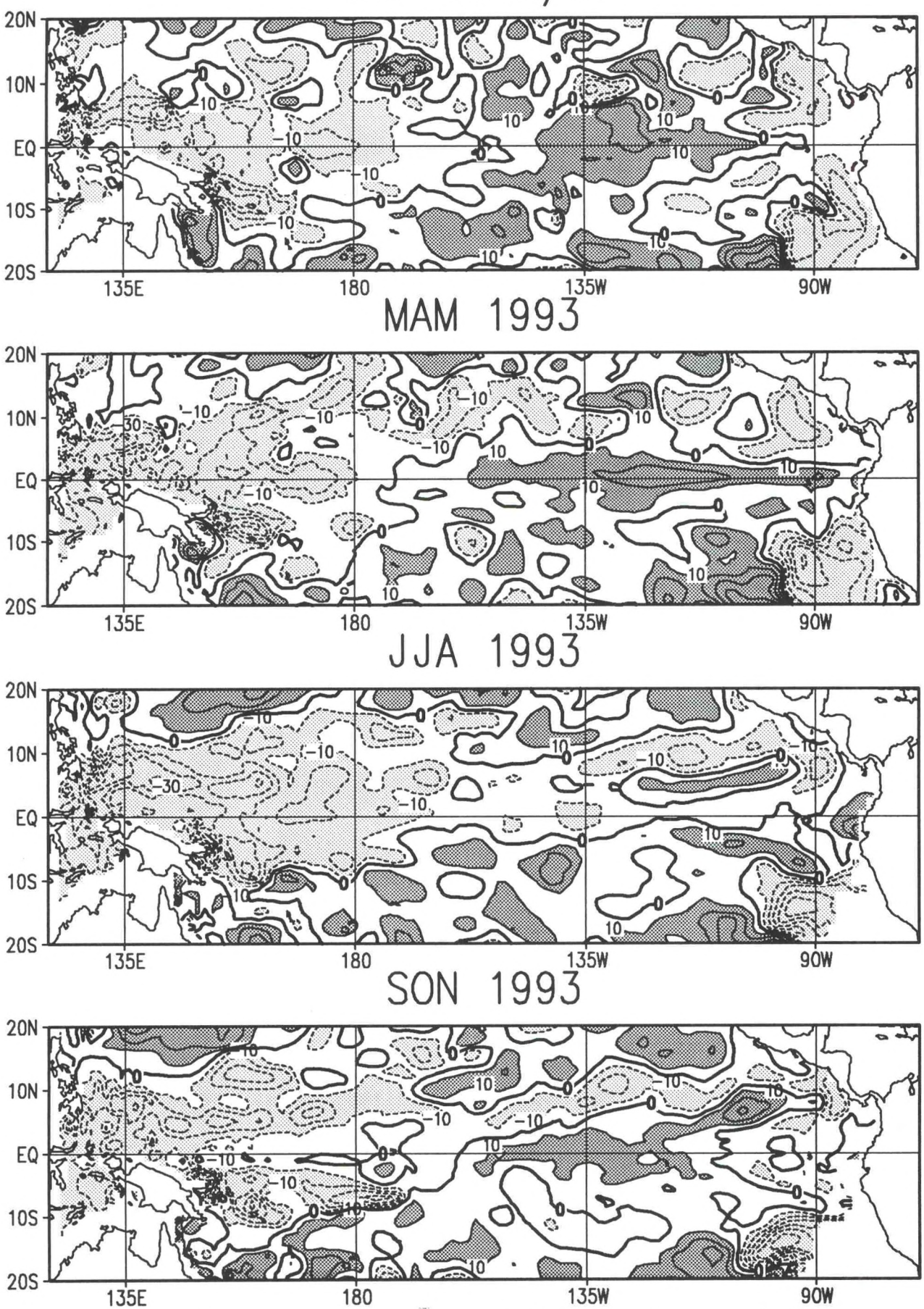

Anomalous Depth of 20°C Isotherm (m)

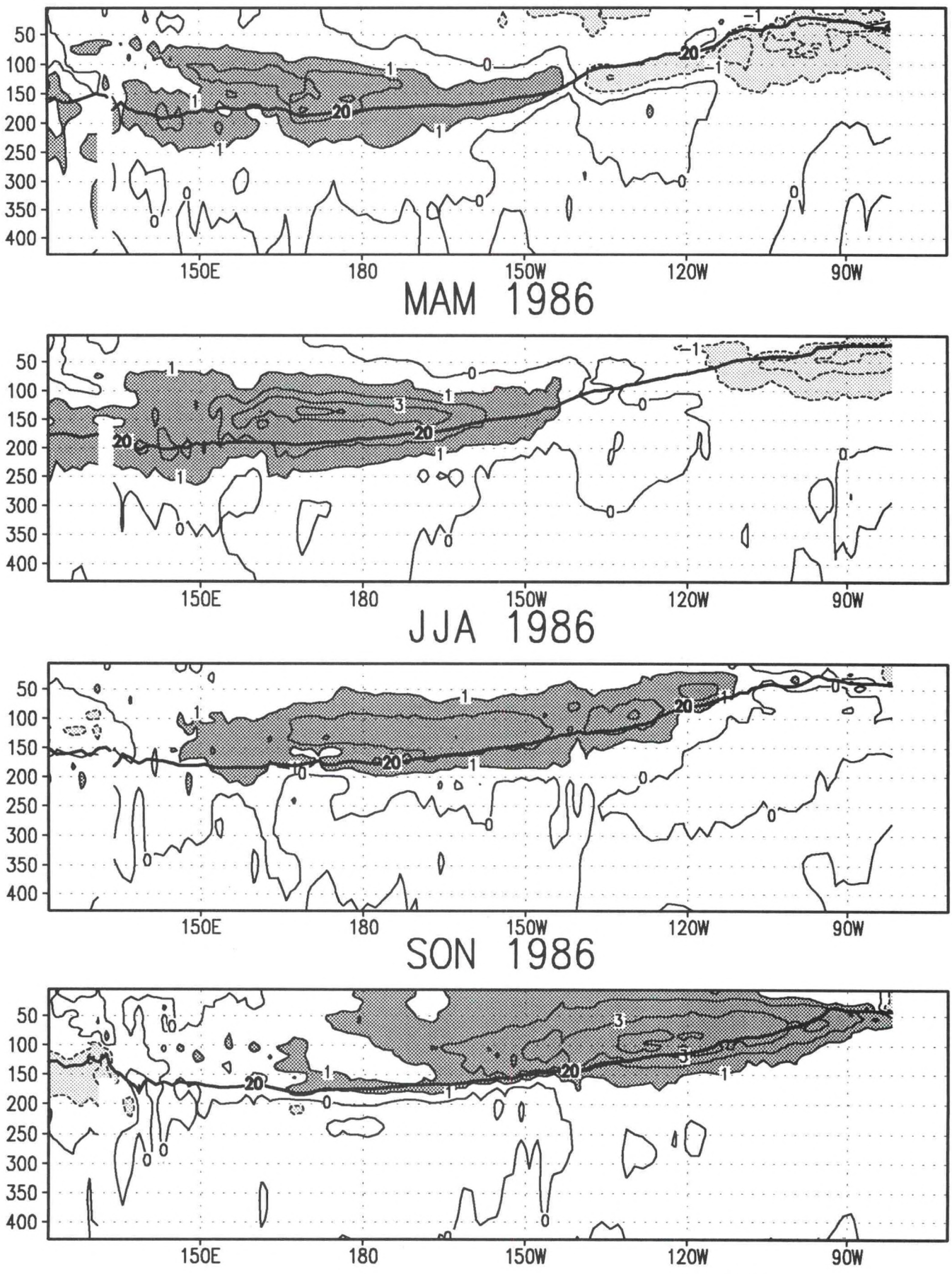

Ocean Temperature Anomaly (°C)

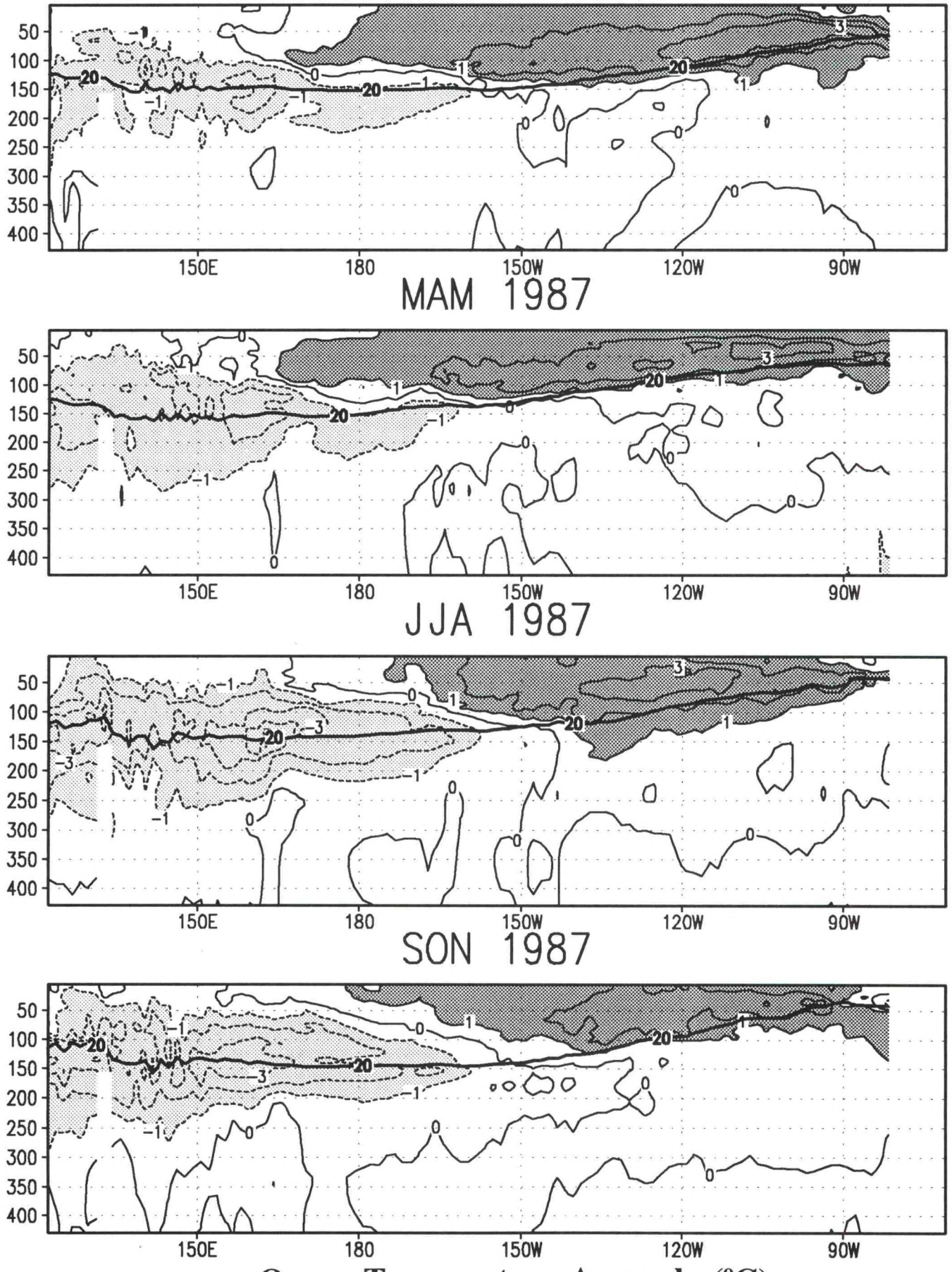

Ocean Temperature Anomaly (°C)

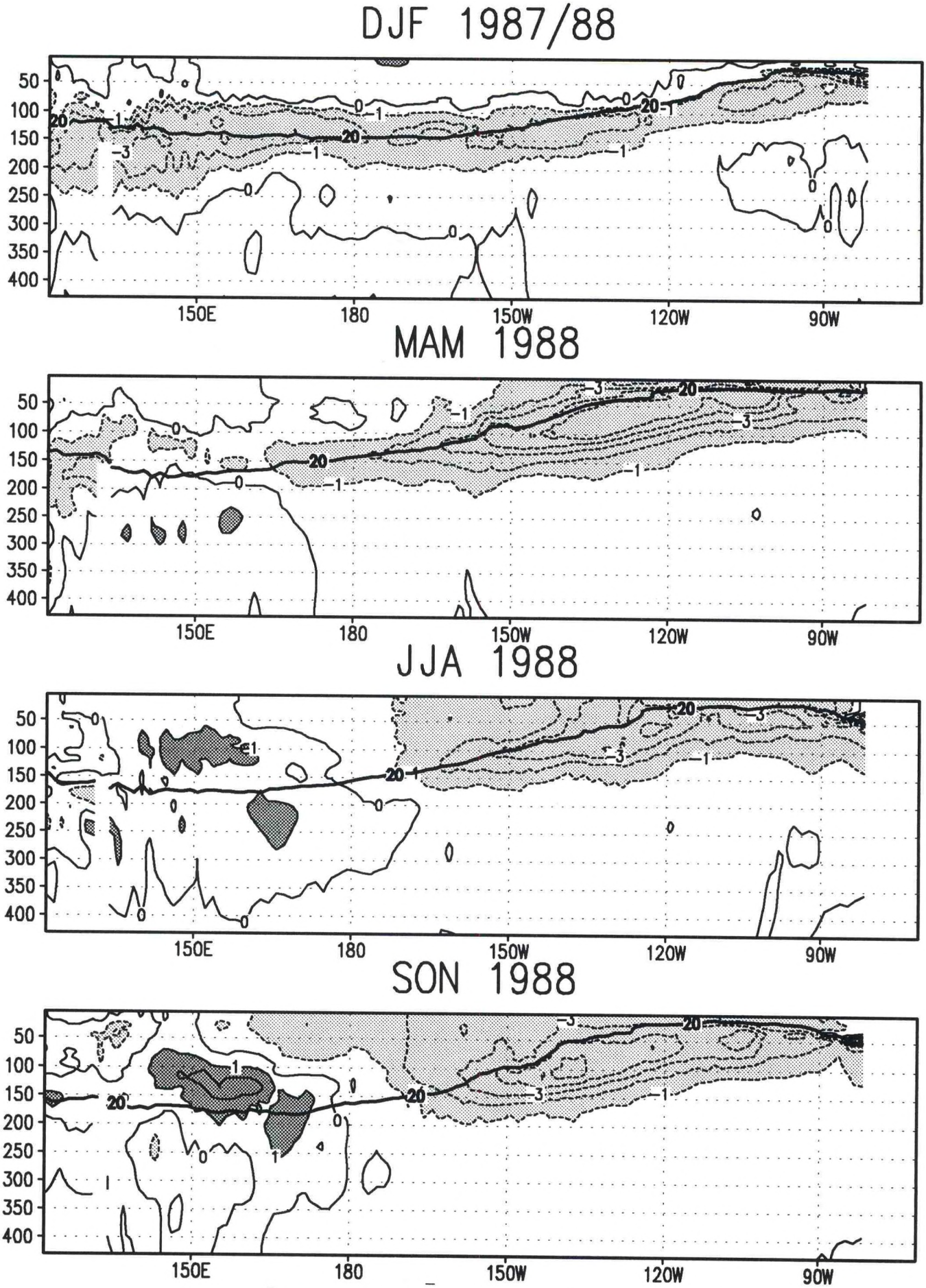

Ocean Temperature Anomaly (°C)

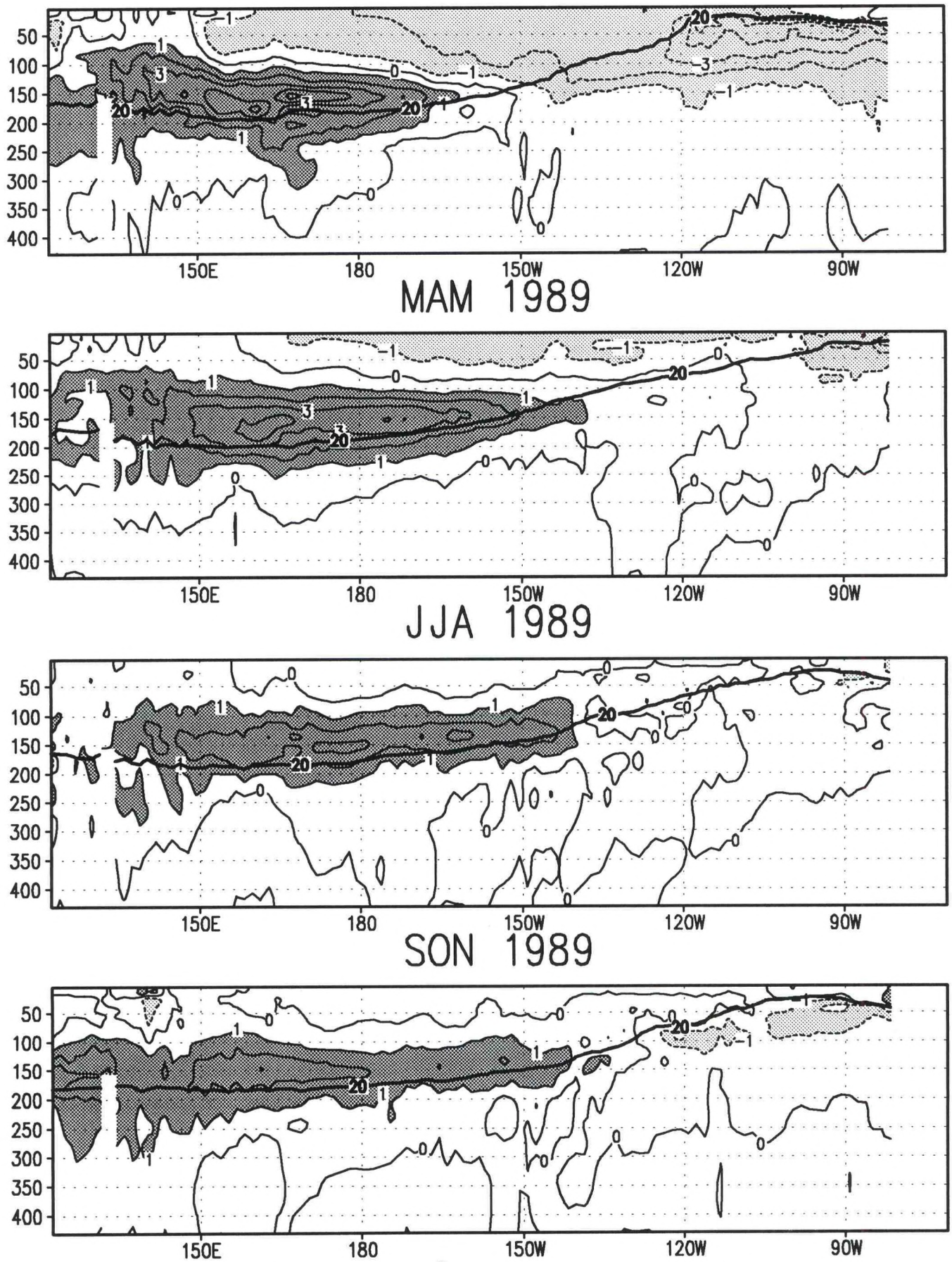

Ocean Temperature Anomaly (°C)

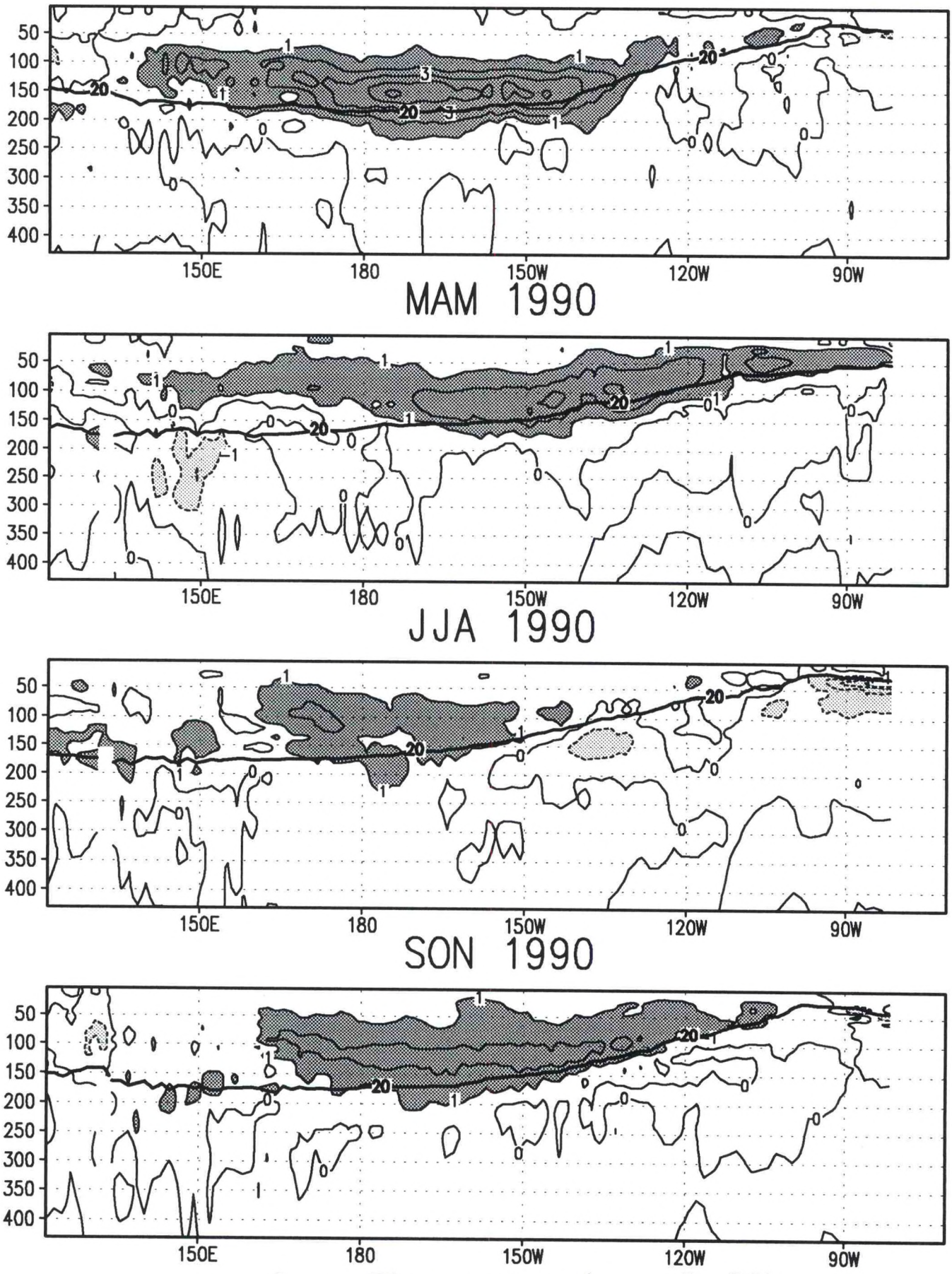

Ocean Temperature Anomaly (°C)

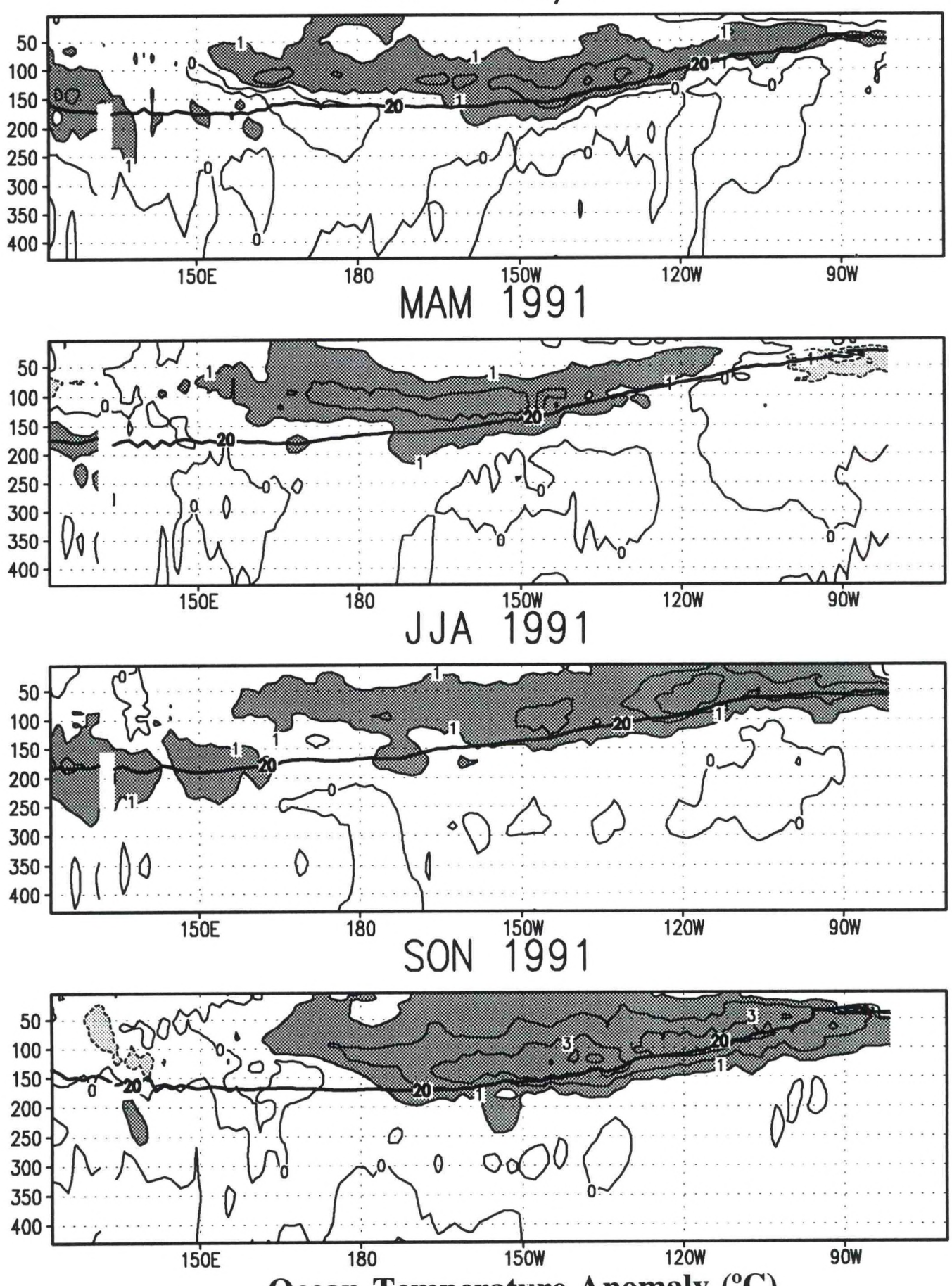

Ocean Temperature Anomaly (°C)

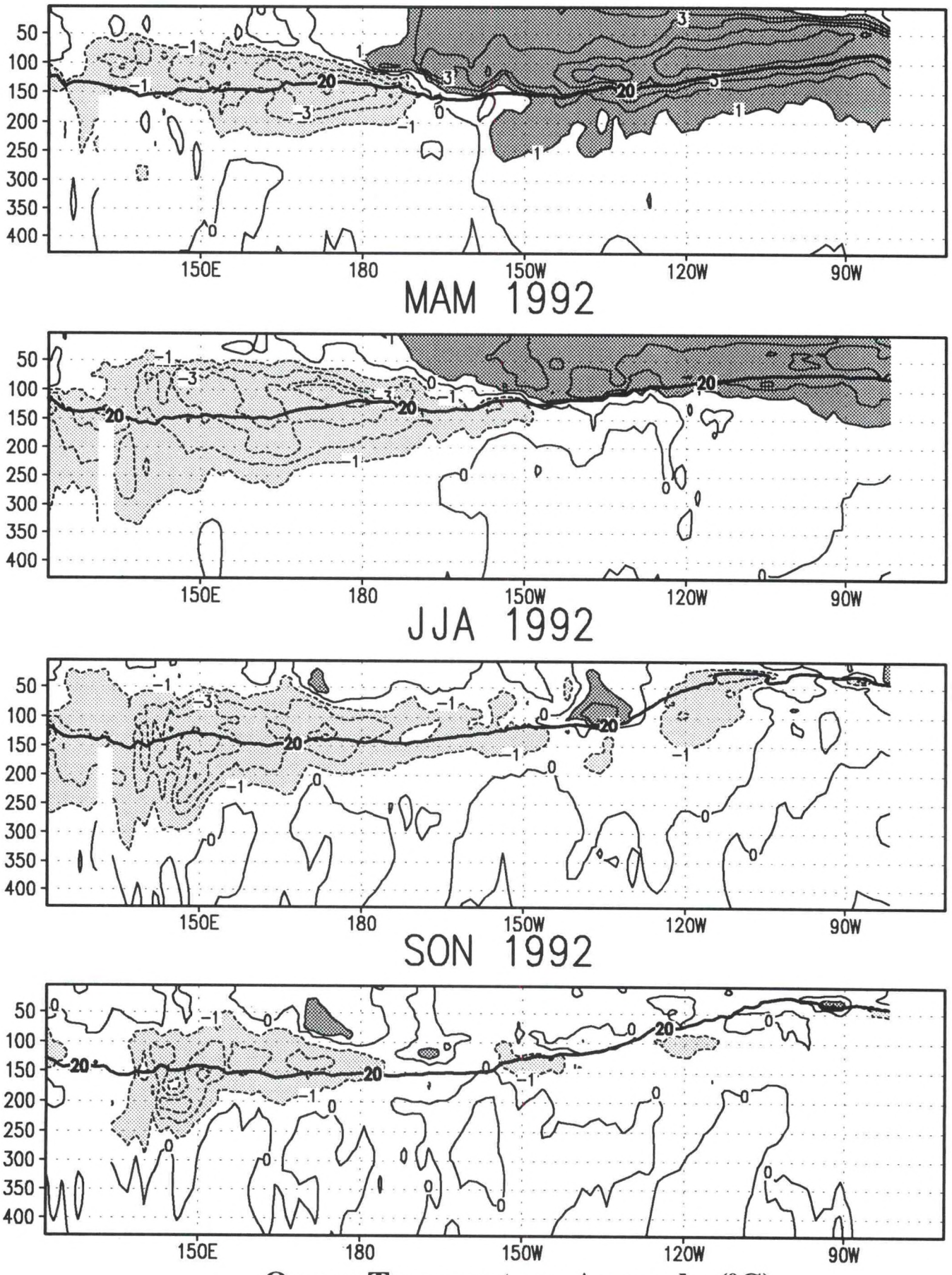

Ocean Temperature Anomaly (°C)

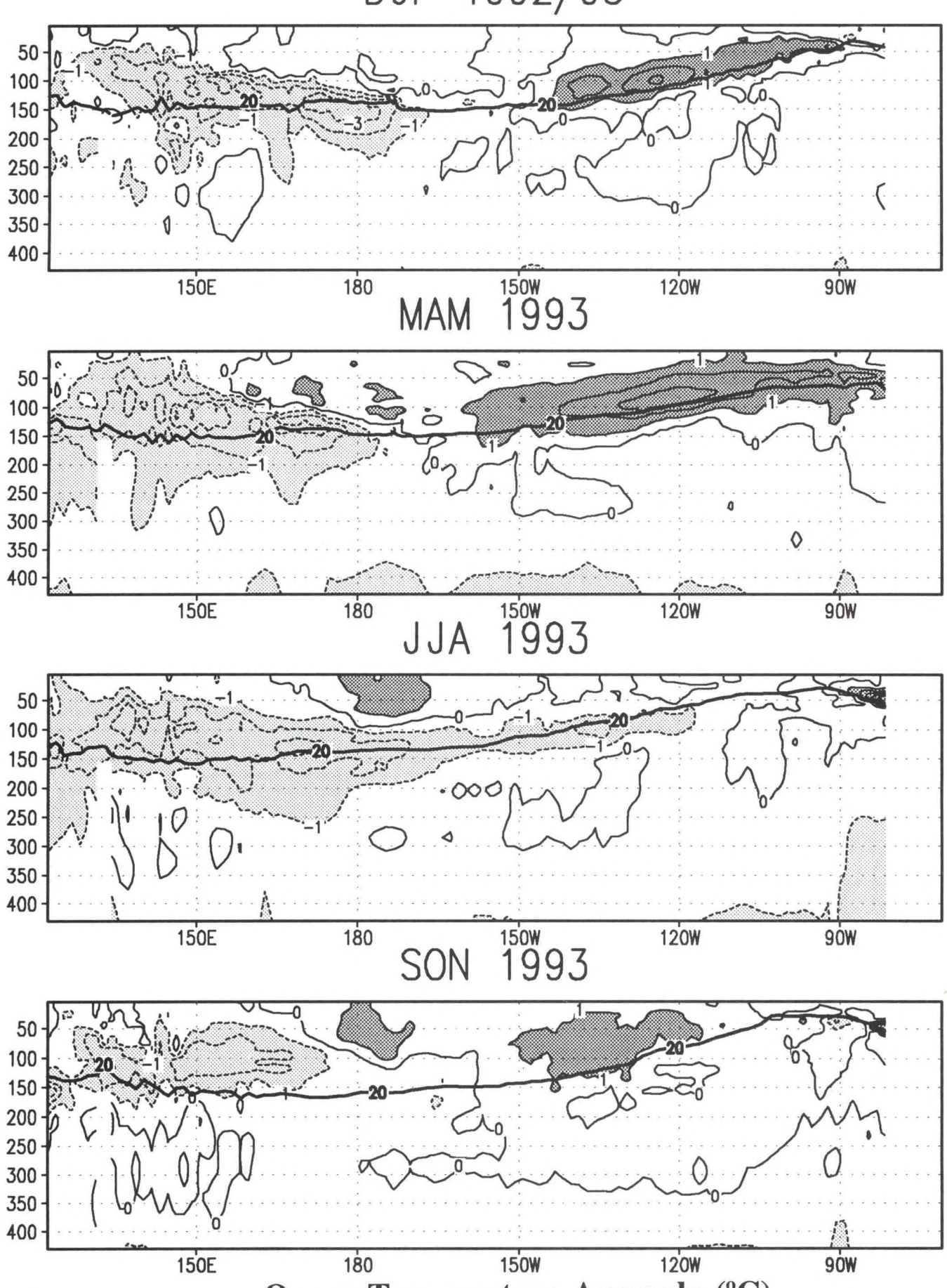

Ocean Temperature Anomaly (°C)

OUTGOING LONGWAVE RADIATION (OLR) ANOMALY

Seasonal Maps (pp. 68-75): Seasonal-mean OLR anomalies (W/m^2) for all longitudes from 50°N to 50°S. Positive anomalies greater than 10 W/m^2, indicative of reduced convective activity in the tropics and subtropics, are shaded light with solid contours. Negative anomalies below -10 W/m^2, indicative of enhanced convective activity in the tropics and subtropics, are shaded dark with dashed contours. Zero contour is shown thick solid.

Time-Longitude Section (pp. 76-79): Monthly-mean OLR anomalies (W/m^2) along the equator over the Pacific Ocean between 120°E and 80°W. Contour interval is 15 W/m^2. Positive anomalies greater than 15 W/m^2 are shaded light with solid contours. Negative anomalies below -15 W/m^2 are shaded dark with dashed contours. Zero contour is shown thick solid.

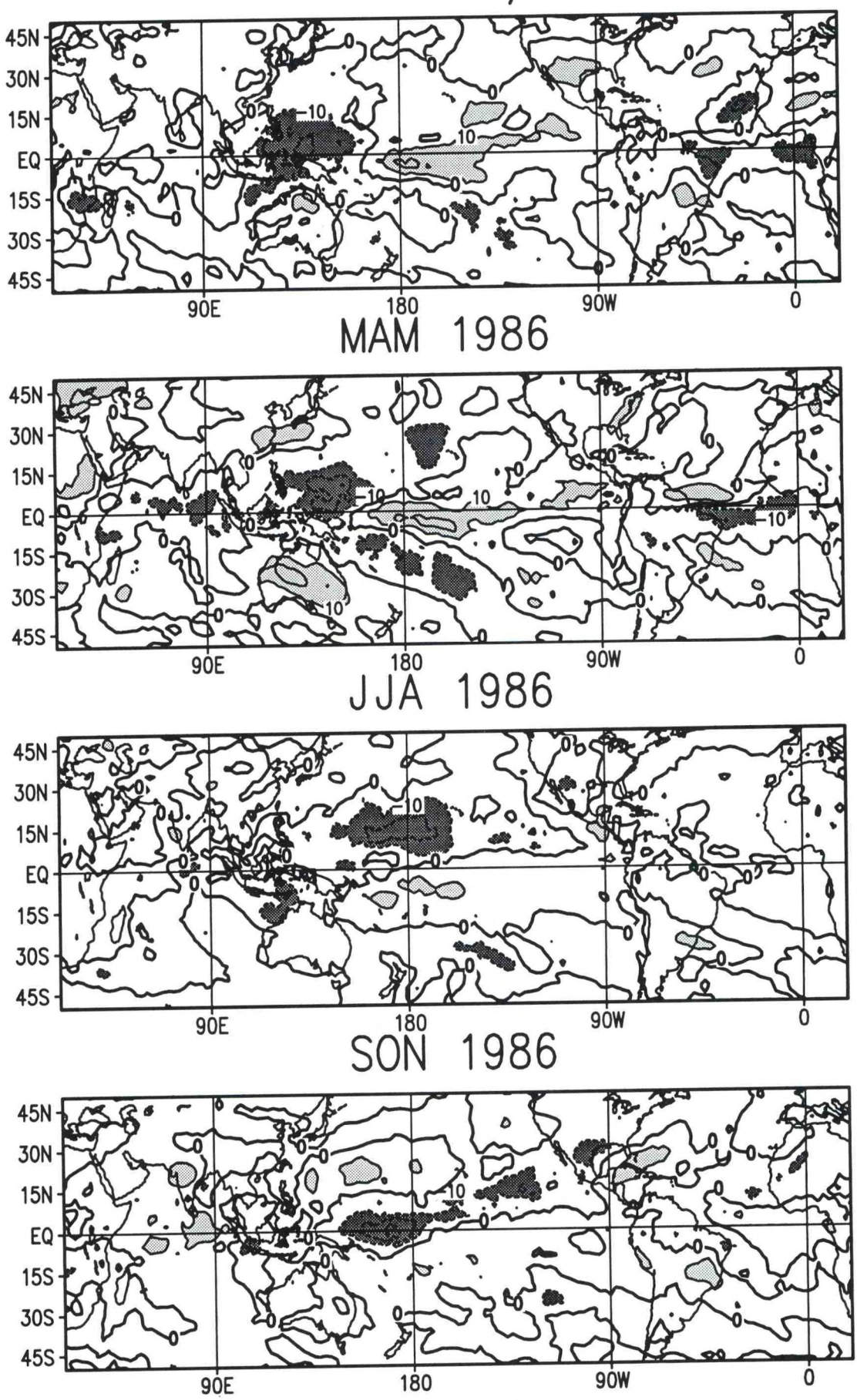

Outgoing Longwave Radiation Anomaly (W m^{-2})

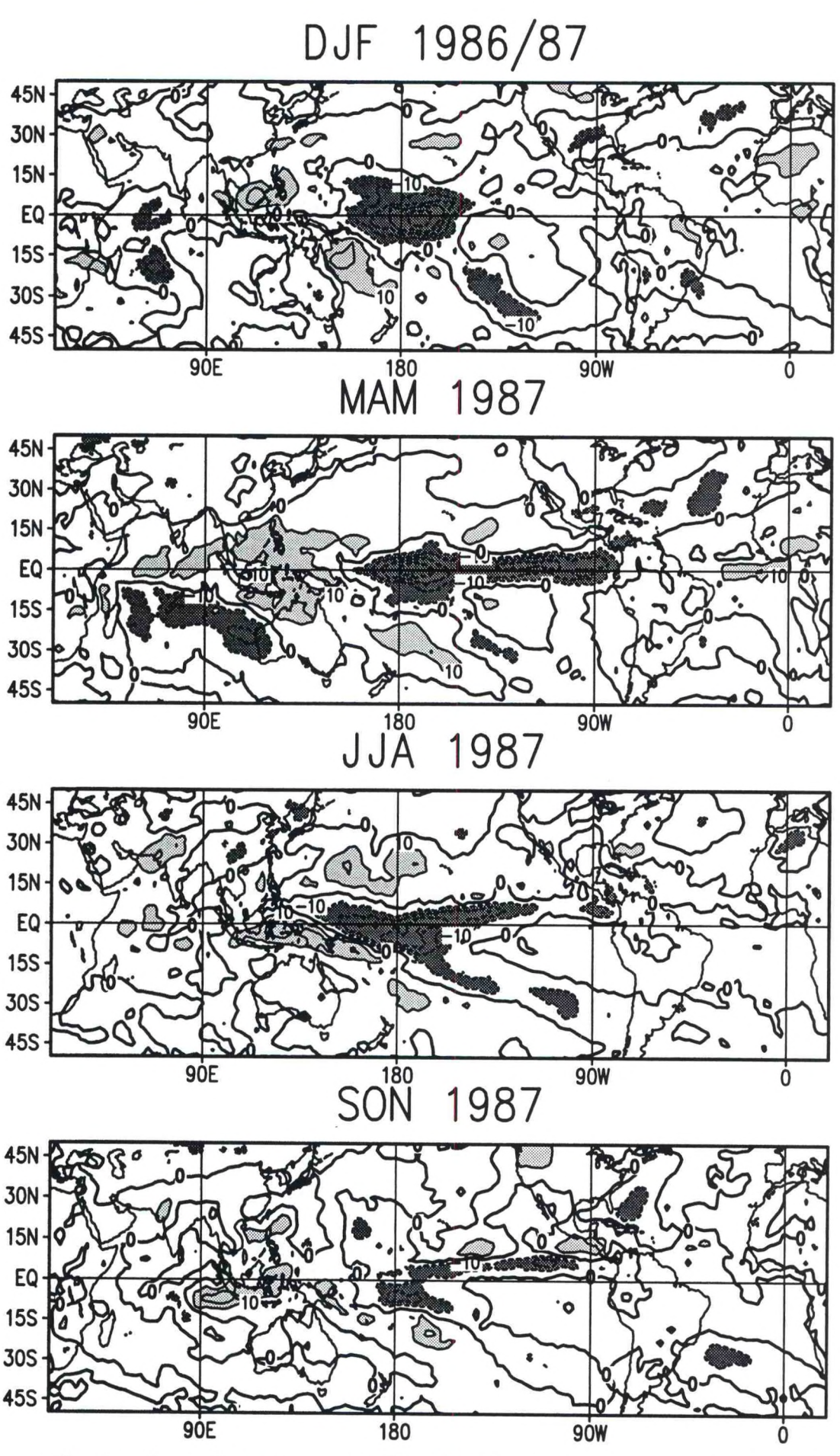

Outgoing Longwave Radiation Anomaly (W m^{-2})

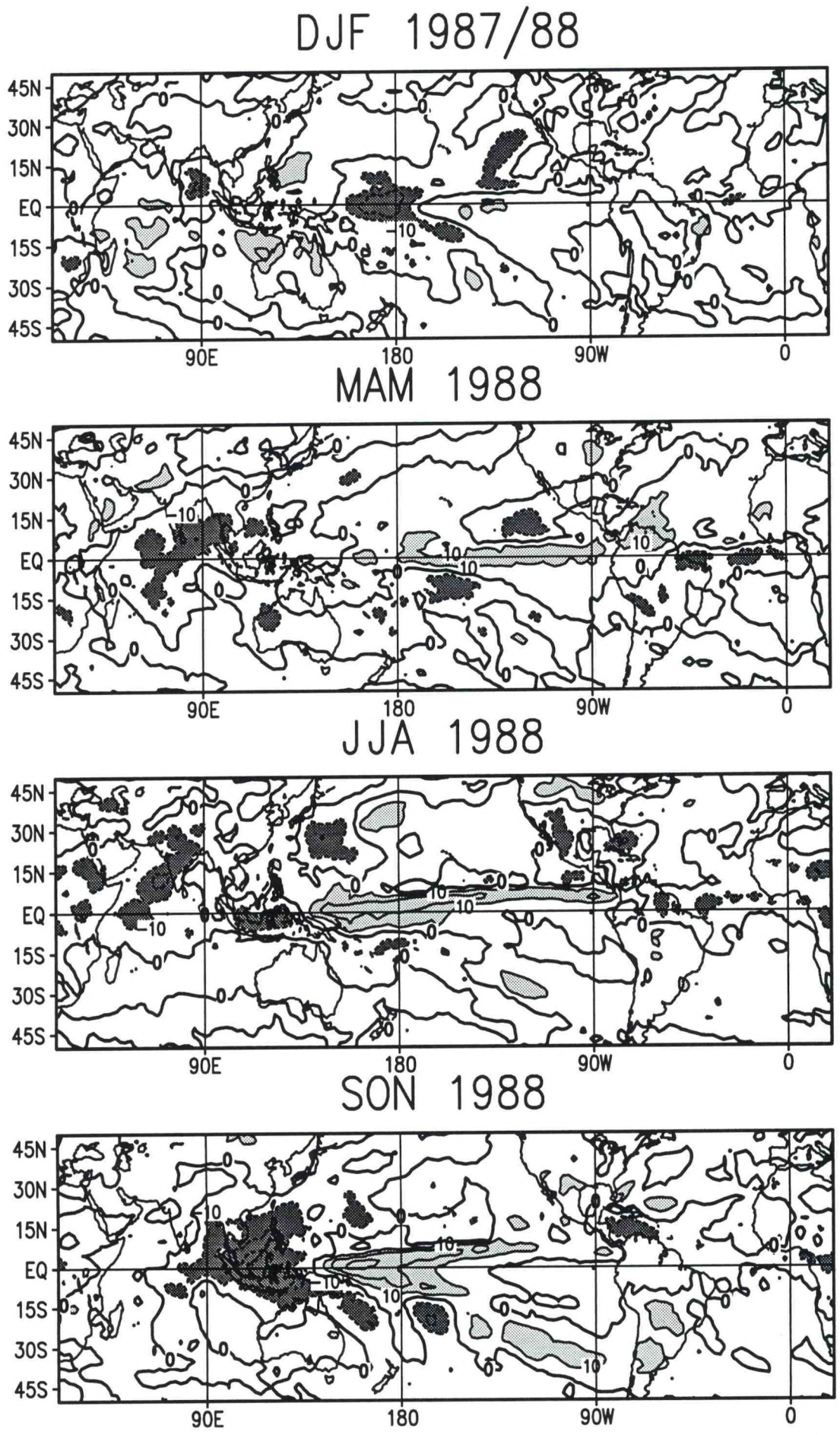

Outgoing Longwave Radiation Anomaly (W m^{-2})

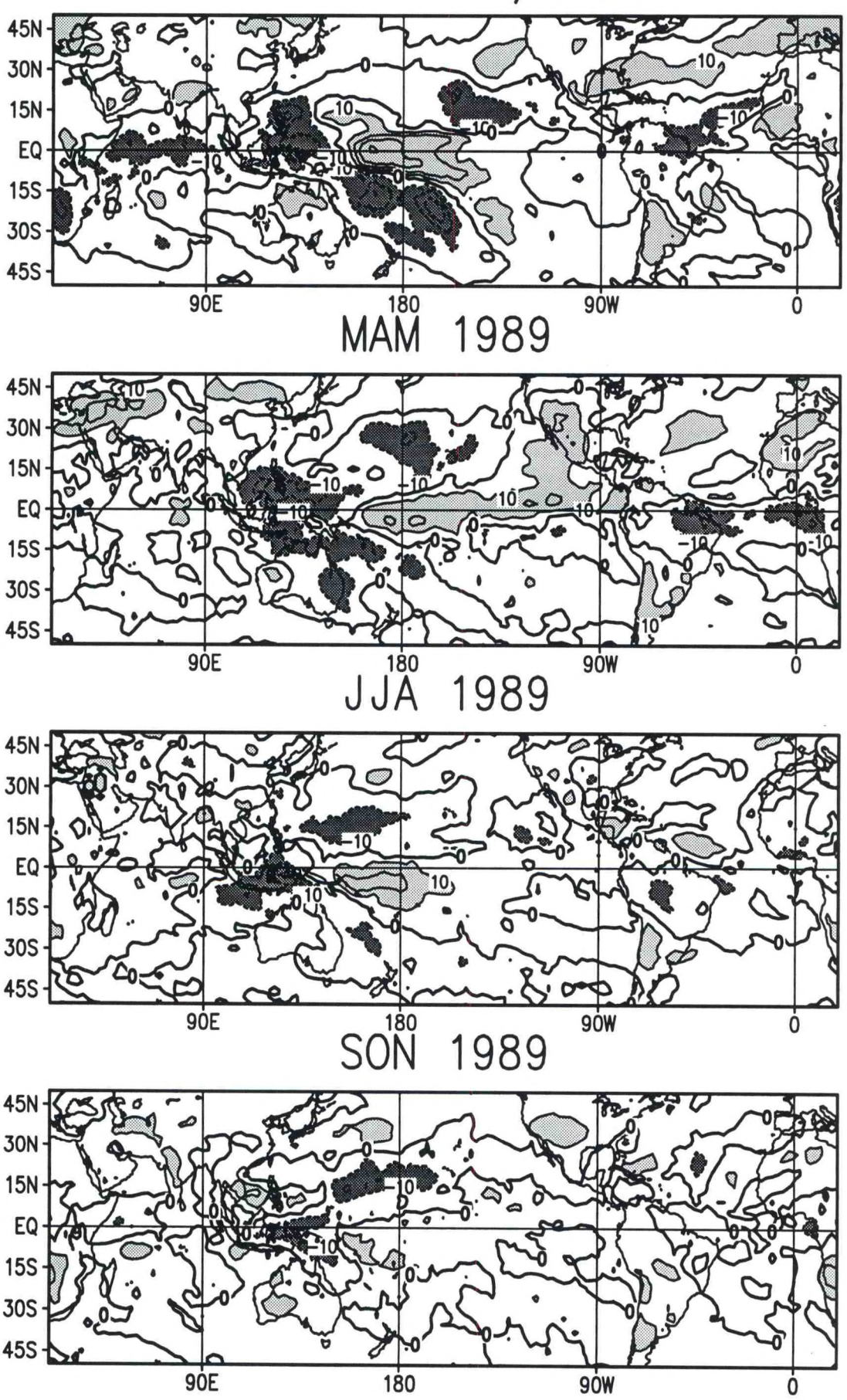

Outgoing Longwave Radiation Anomaly (W m^{-2})

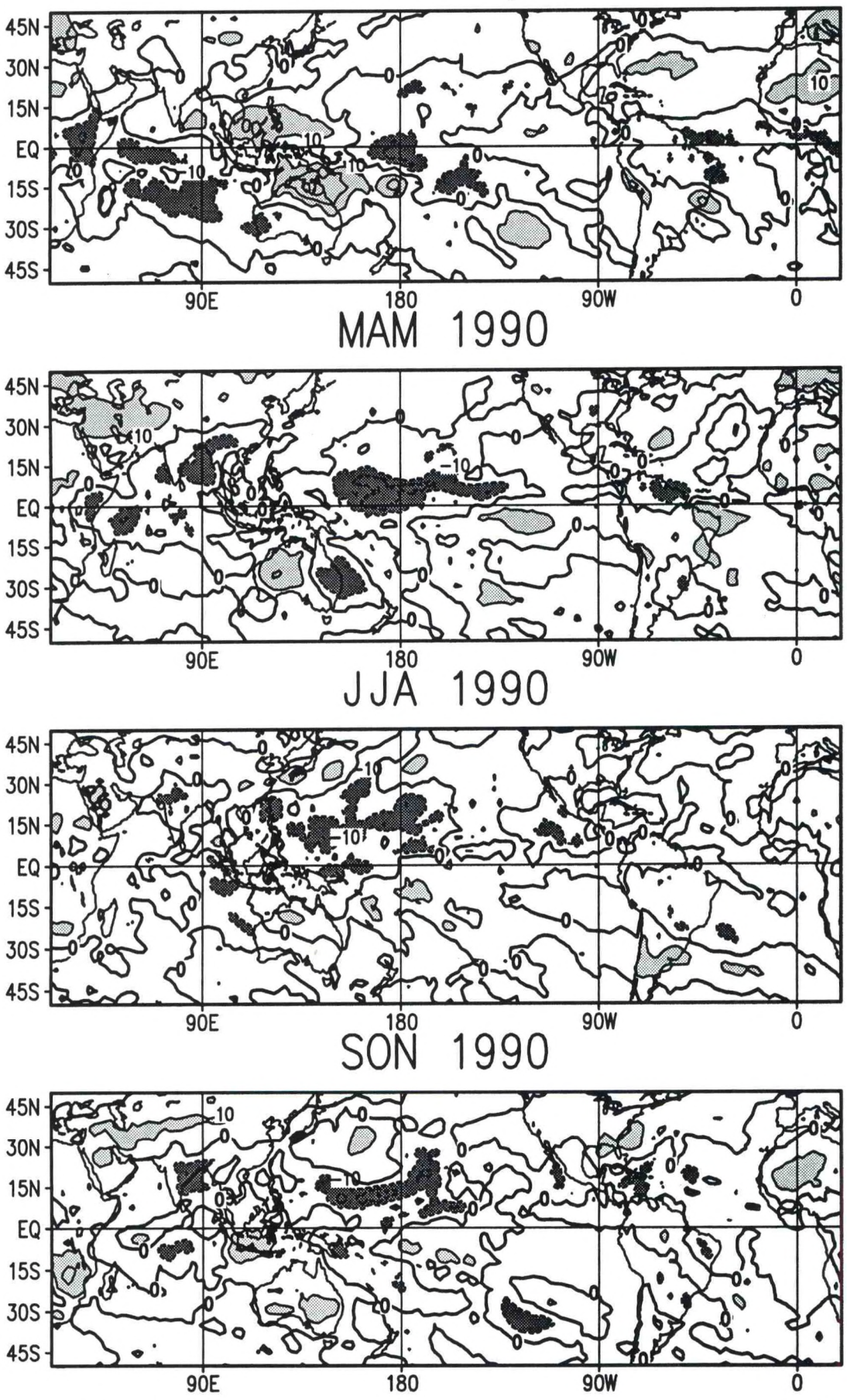

Outgoing Longwave Radiation Anomaly (W m^{-2})

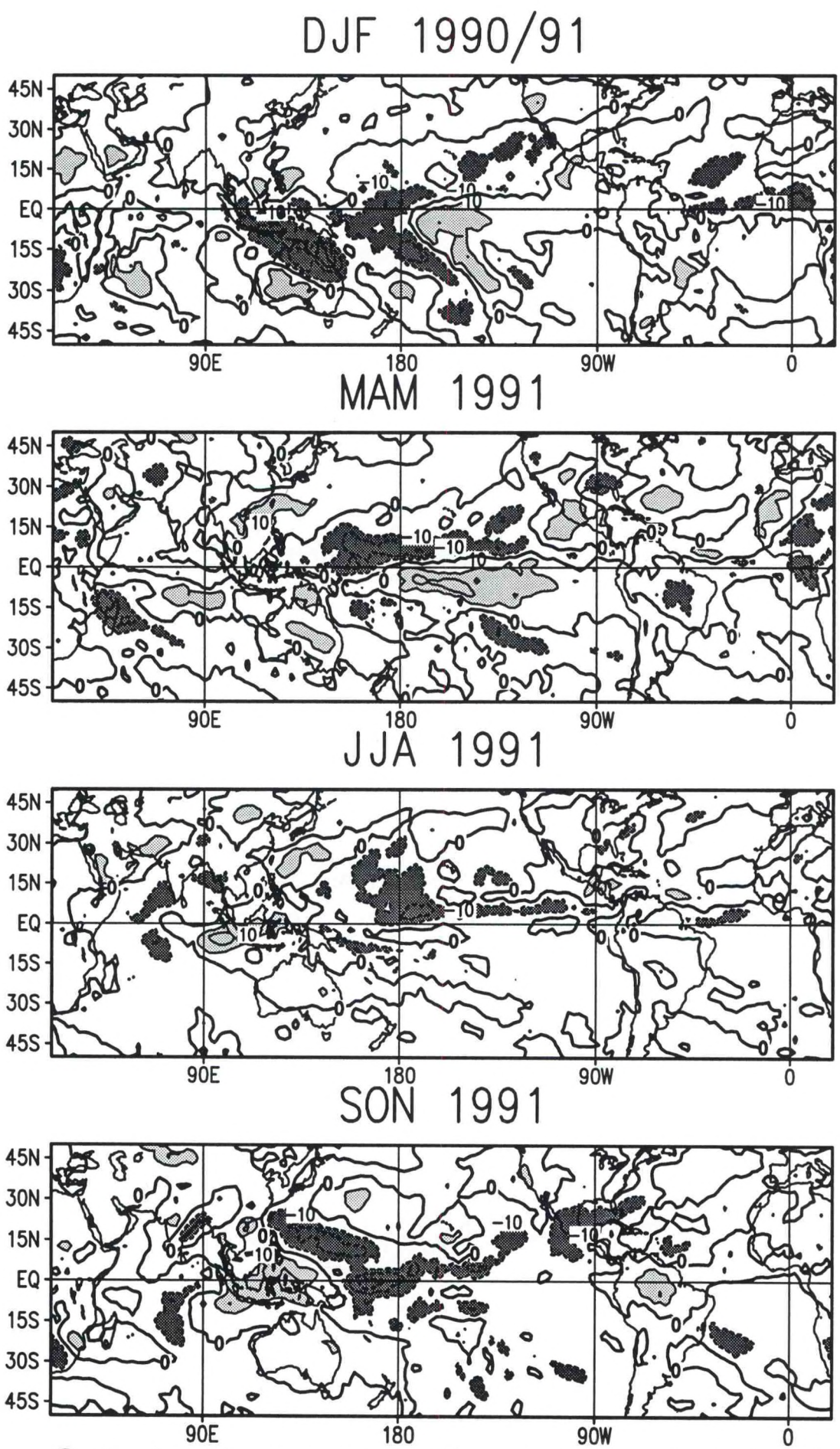

Outgoing Longwave Radiation Anomaly (W m^{-2})

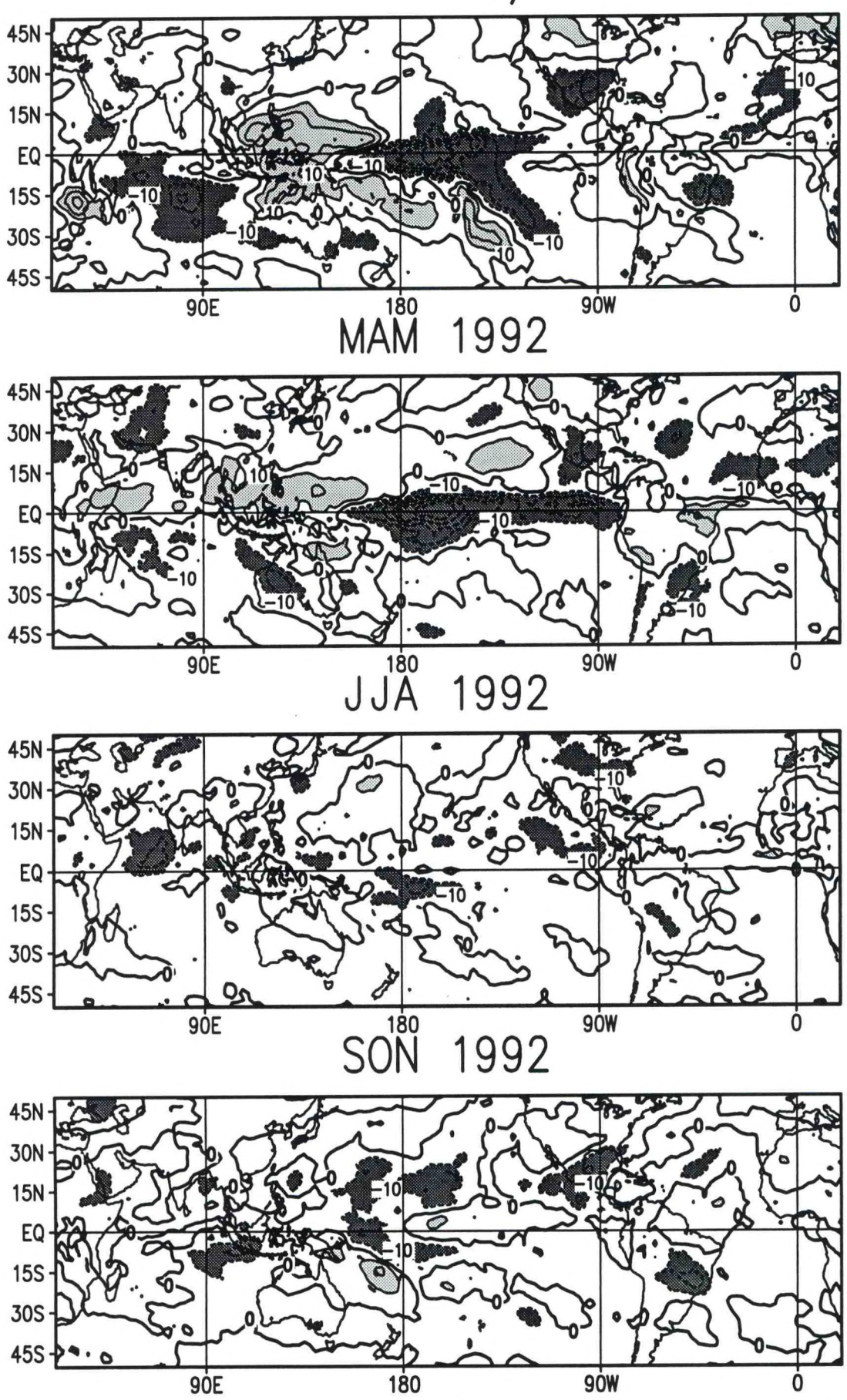

Outgoing Longwave Radiation Anomaly (W m^{-2})

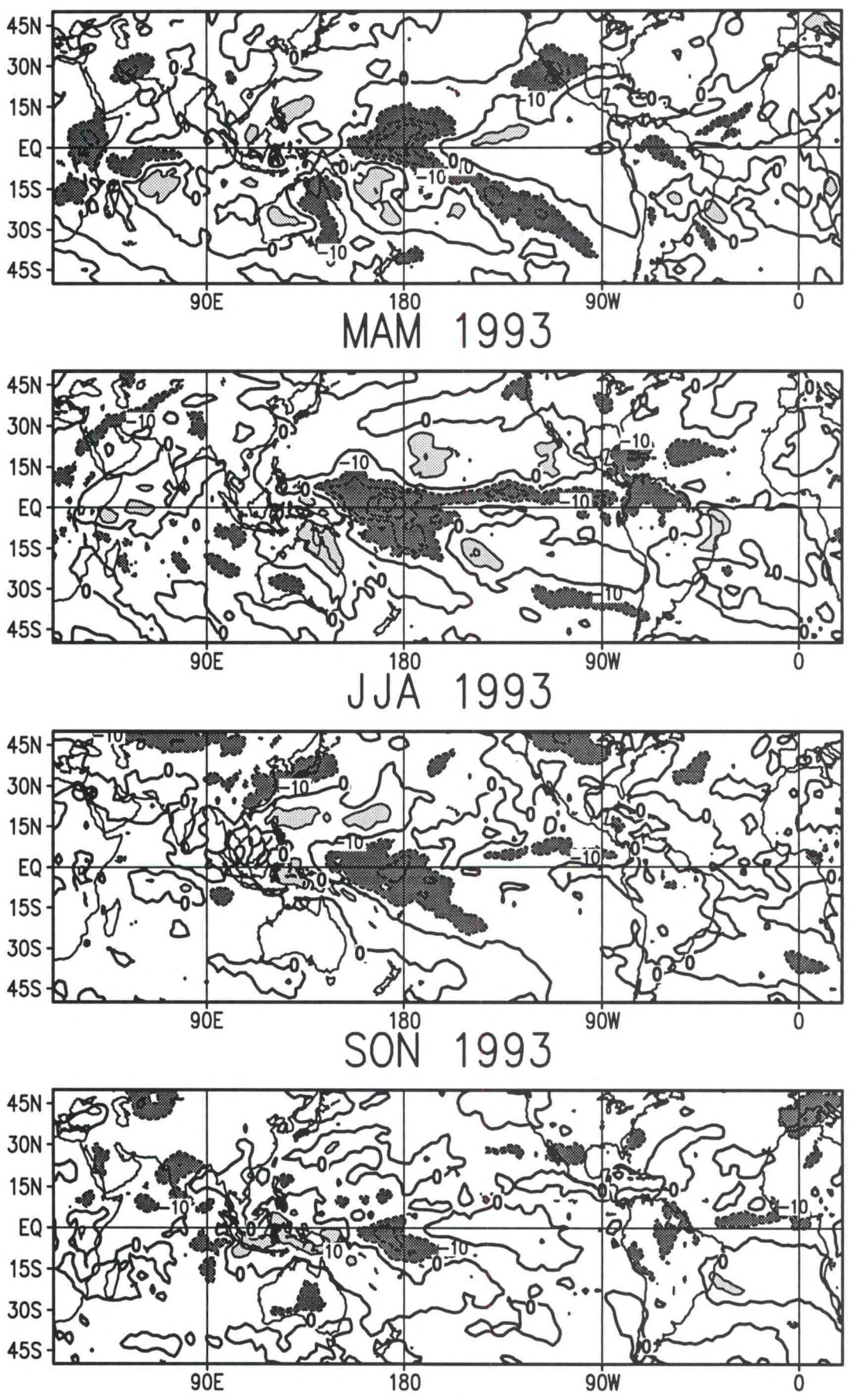

Outgoing Longwave Radiation Anomaly (W m^{-2})

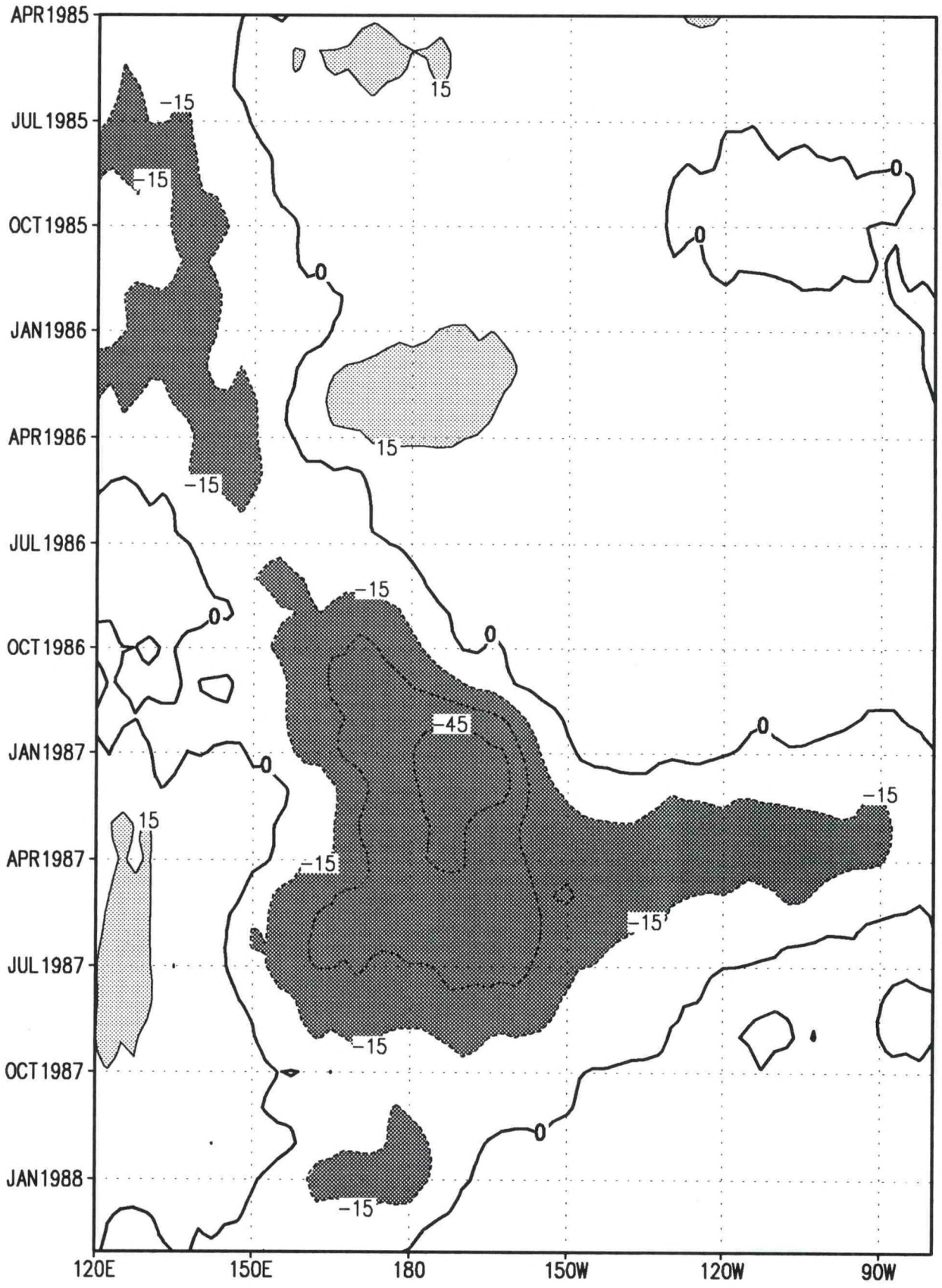

Outgoing Longwave Radiation Anomaly (W m^{-2})

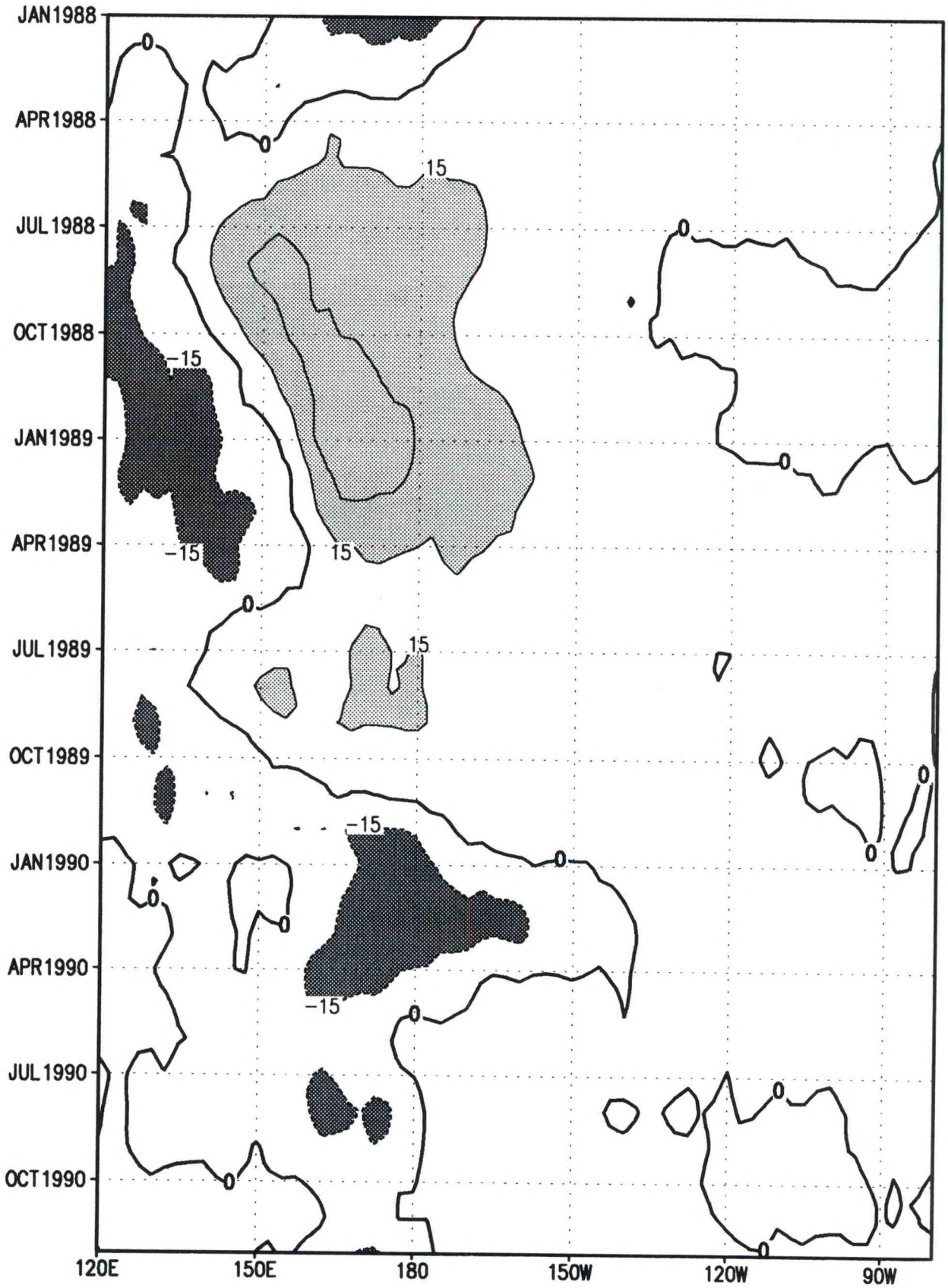

Outgoing Longwave Radiation Anomaly (W m^{-2})

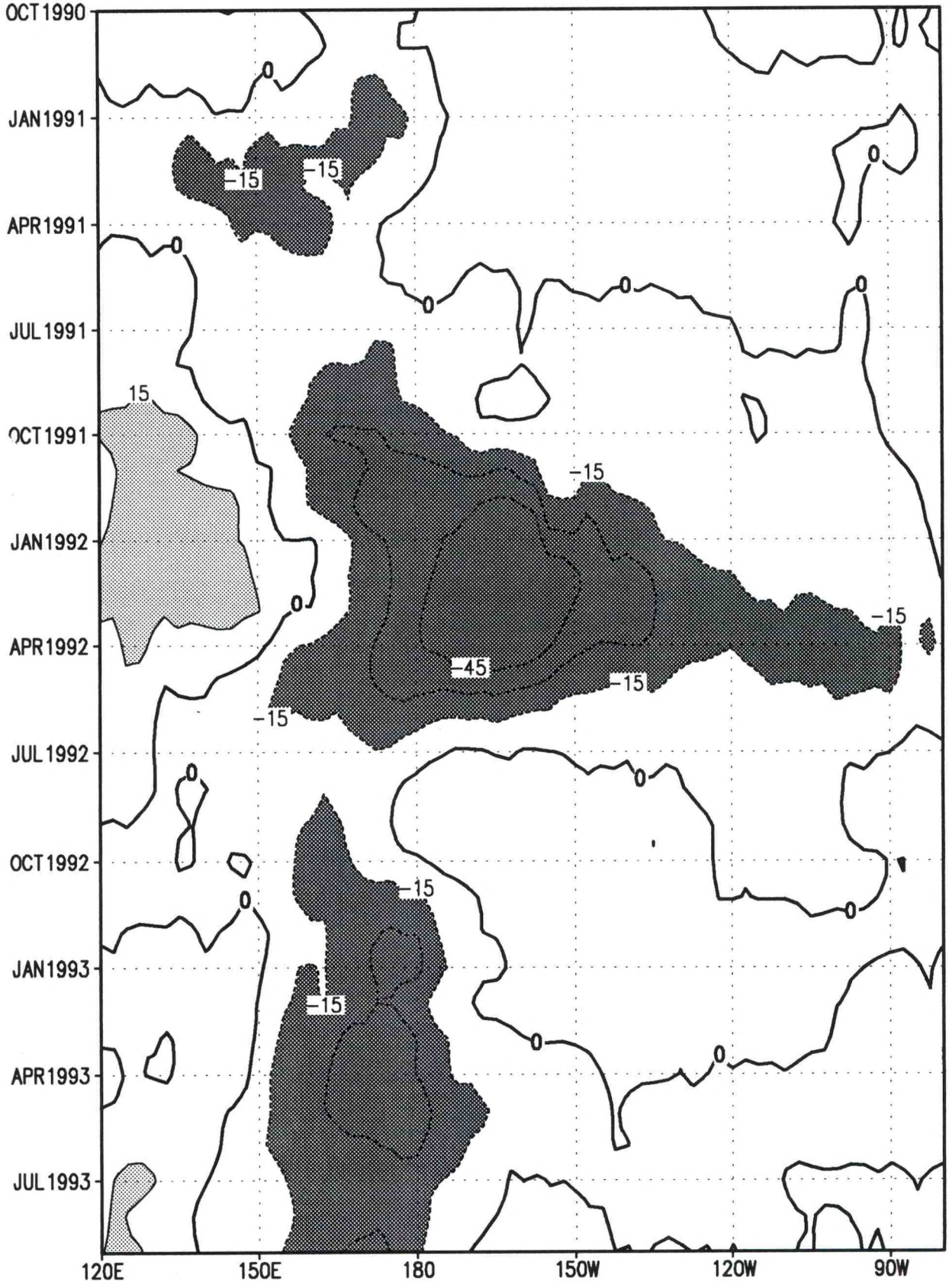

Outgoing Longwave Radiation Anomaly (W m^{-2})

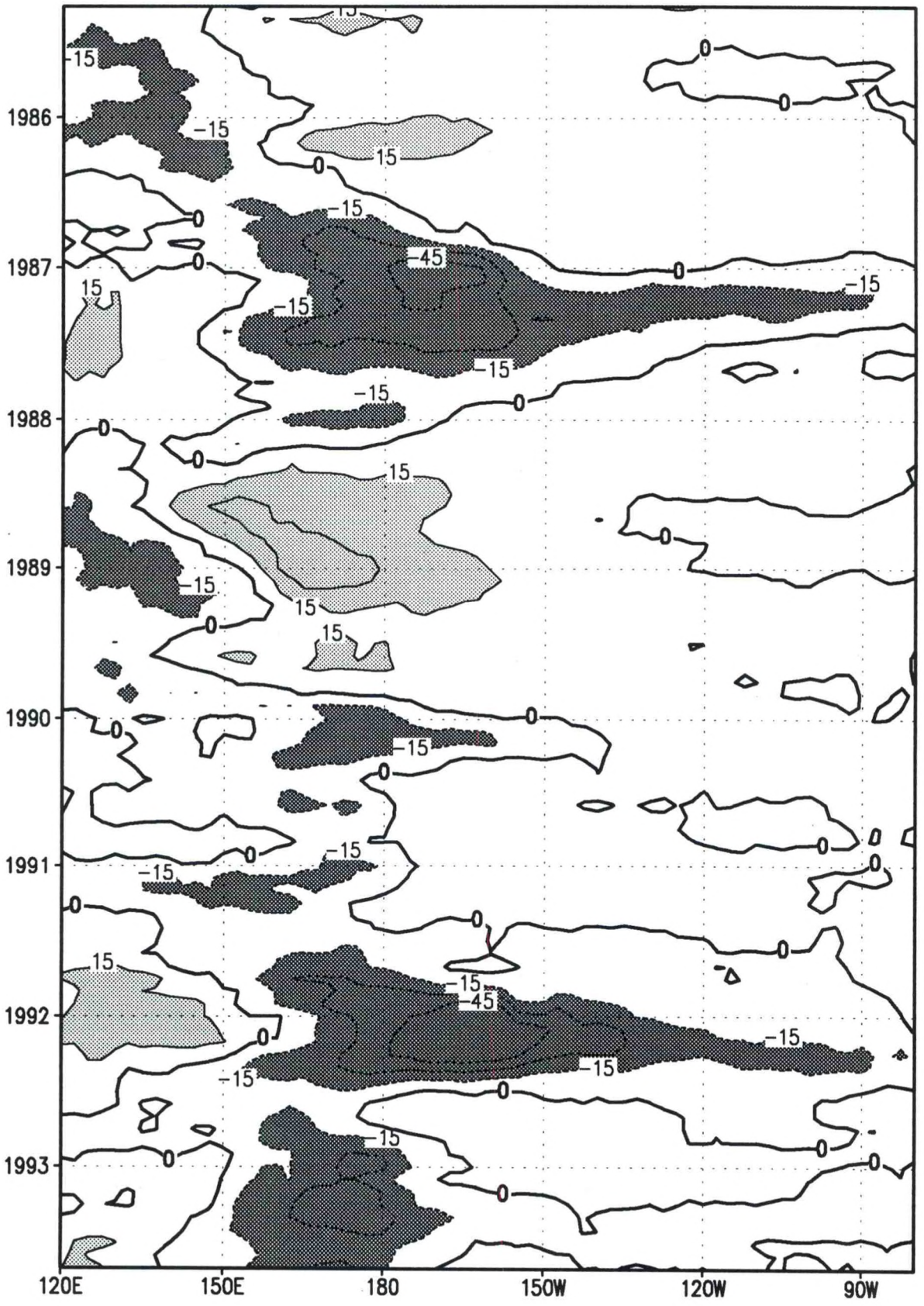

Outgoing Longwave Radiation Anomaly (W m^{-2})

200 mb WIND ANOMALY

Seasonal Maps (pp. 81-88): Seasonal-mean 200 mb vector wind anomaly (ms^{-1}) for all longitudes from 50°N to 50°S. Wind speed anomalies greater than 10 ms^{-1} are contoured, and contour interval is 5 ms^{-1}. Positive (negative) OLR anomalies exceeding ± 10 W m^{-2} are shaded light (dark), indicating suppressed (enhanced) convection in the tropics and subtropics. Zero contour is shown thick solid.

Time-Longitude Section (pp. 89-92): Monthly-mean 200 mb zonal wind anomaly (ms^{-1}) along the equator over the Pacific Ocean between 120°E and 80°W. Westerly (easterly) anomalies are shown by positive (negative) values. Contour interval is 2.5 ms^{-1}, with negative values dashed. Values exceeding ± 2.5 ms^{-1} are shaded, with positive (negative) values shown dark (light). Zero contour is shown thick solid.

Time-Longitude Section (pp. 93-96): Monthly-mean 200 mb zonal wind anomaly (ms^{-1}) along the equator for all longitudes. Westerly (easterly) anomalies are shown by positive (negative) values. Contour interval is 2.5 ms^{-1}, with negative values dashed. Values exceeding ± 2.5 ms^{-1} are shaded, with positive (negative) values shown dark (light). Zero contour is shown thick solid.

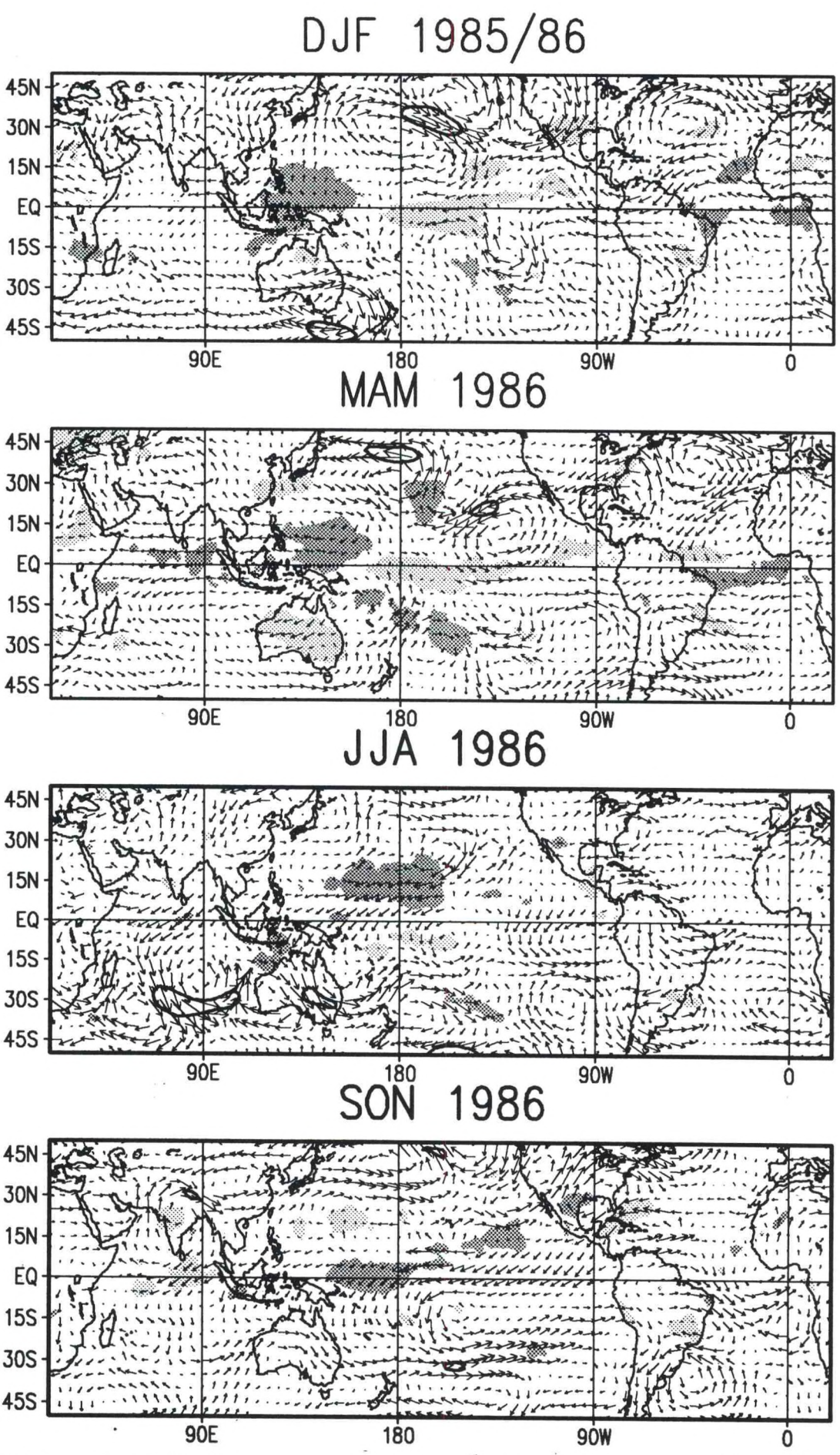

200 mb Wind Anomaly (m s^{-1}), OLR Anomaly (W m^{-2})

DJF 1986/87

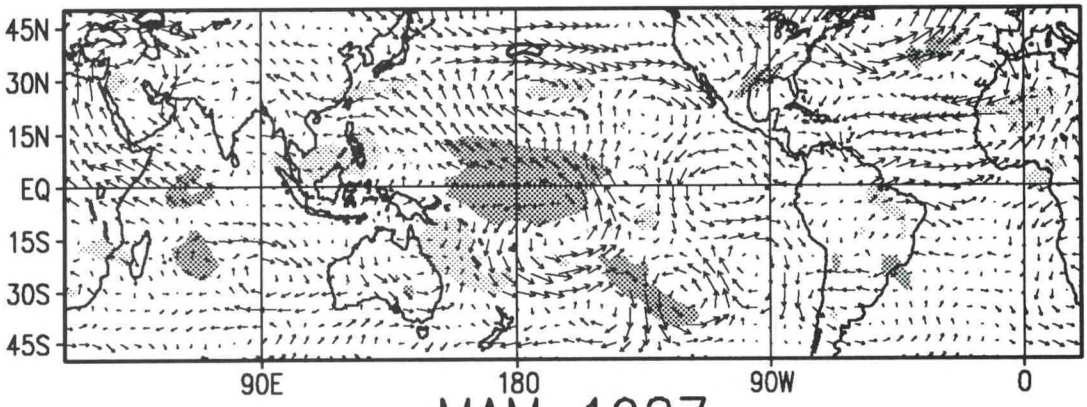

MAM 1987

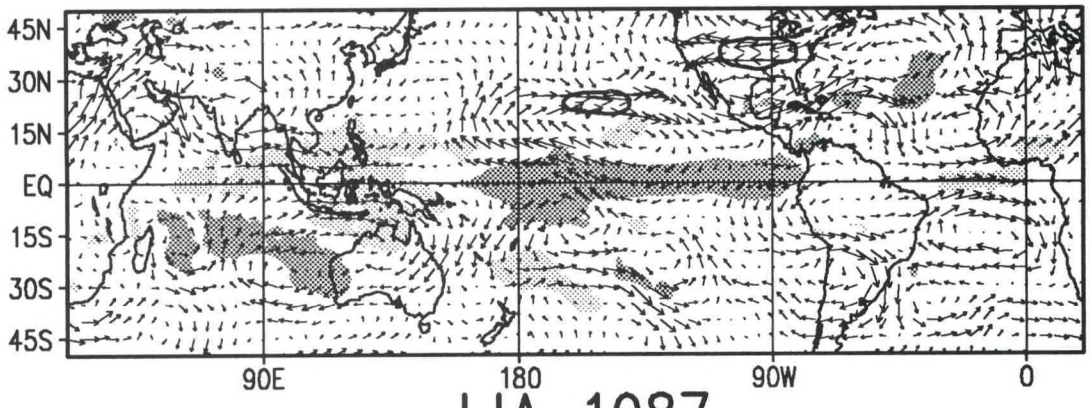

JJA 1987

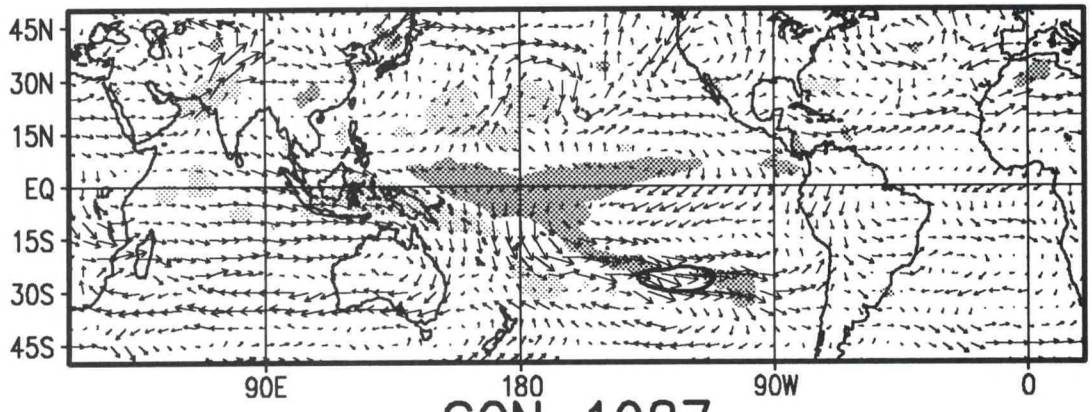

SON 1987

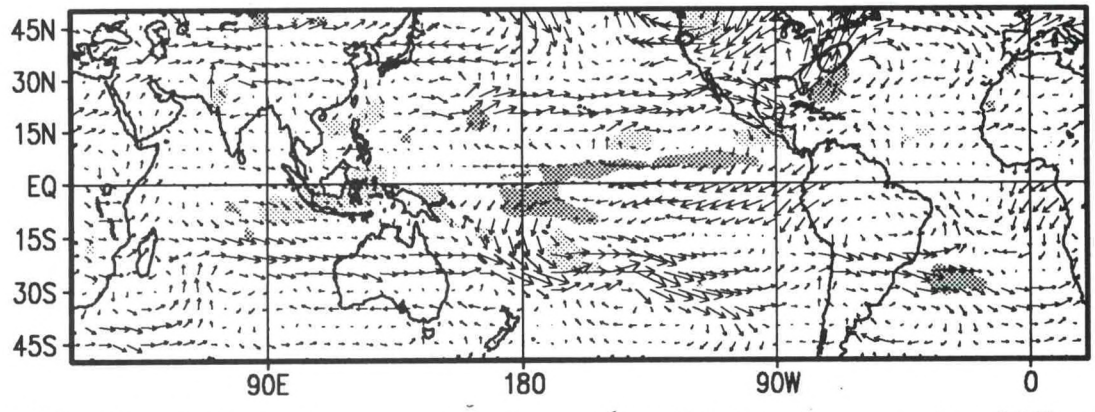

200 mb Wind Anomaly (m s^{-1}), OLR Anomaly (W m^{-2})

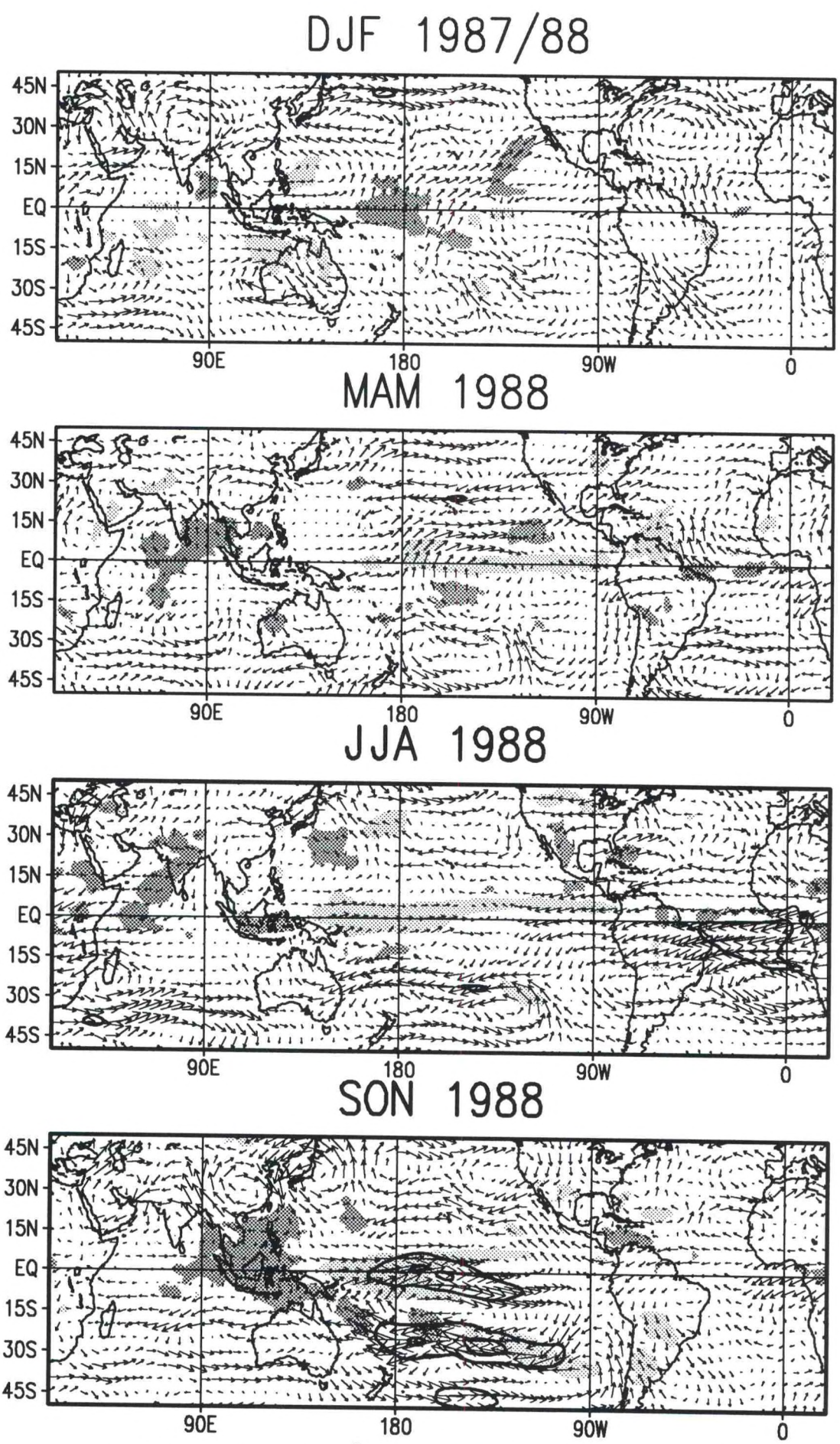

200 mb Wind Anomaly (m s^{-1}), OLR Anomaly (W m^{-2})

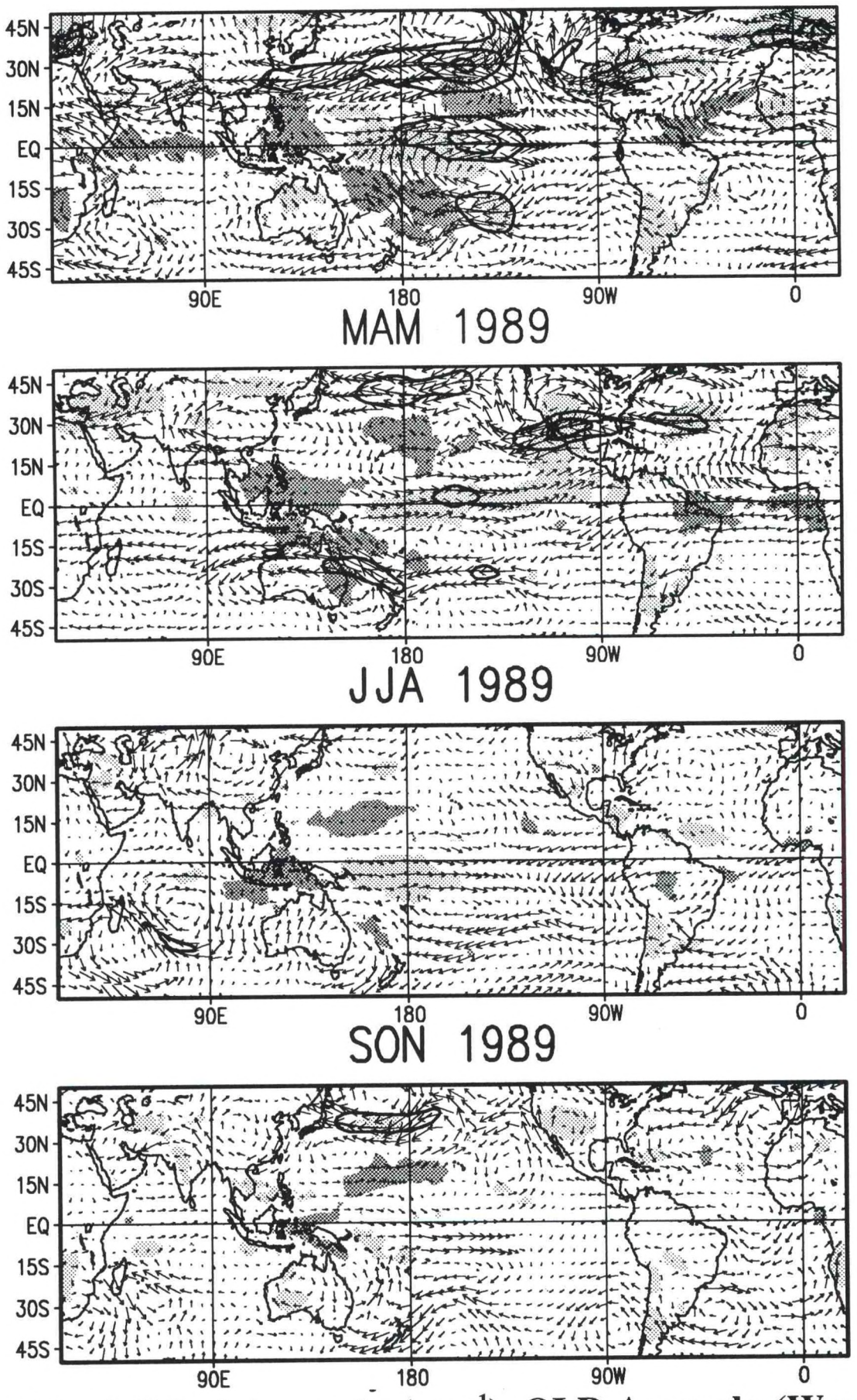

200 mb Wind Anomaly (m s^{-1}), OLR Anomaly (W m^{-2})

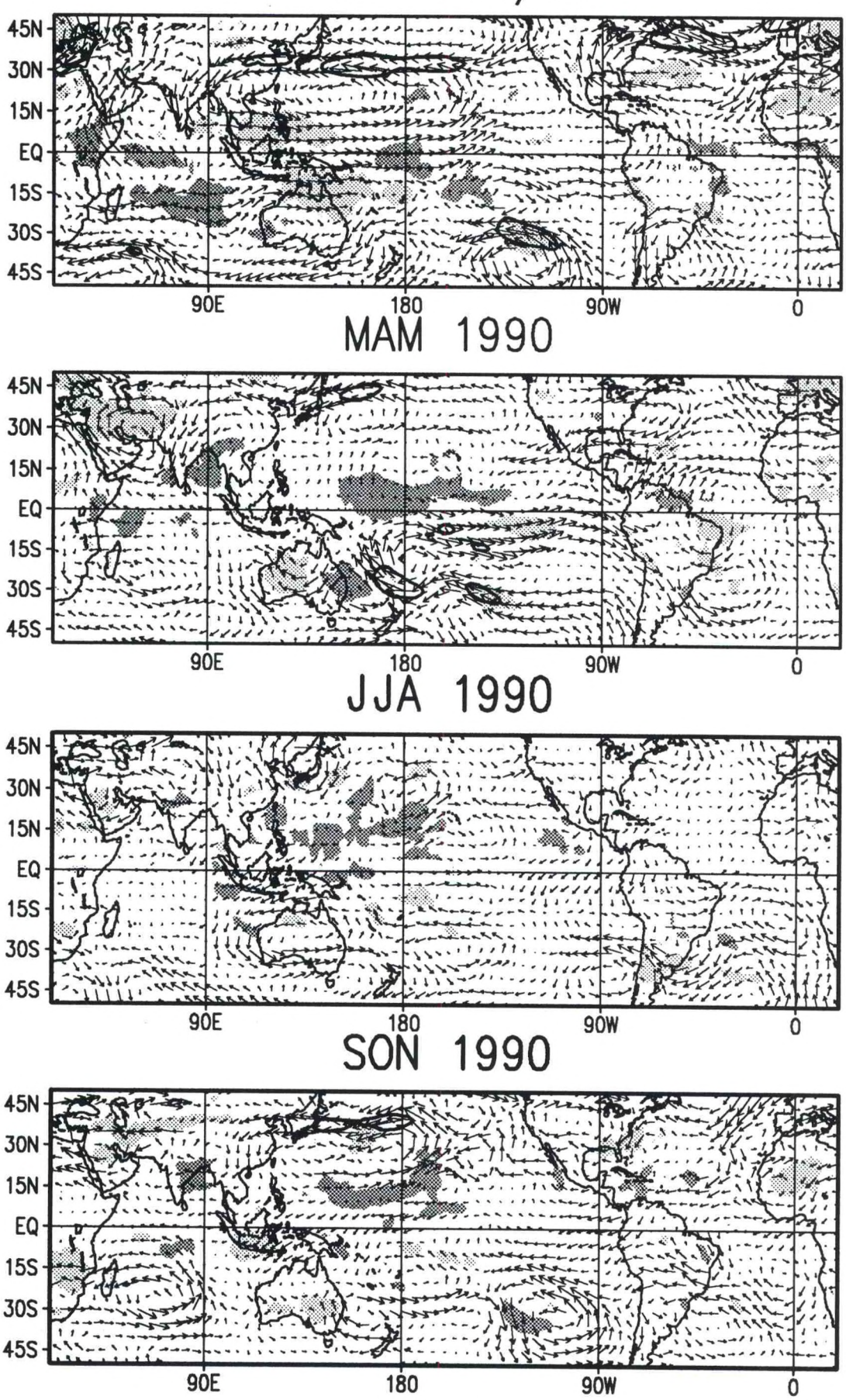

200 mb Wind Anomaly (m s^{-1}), OLR Anomaly (W m^{-2})

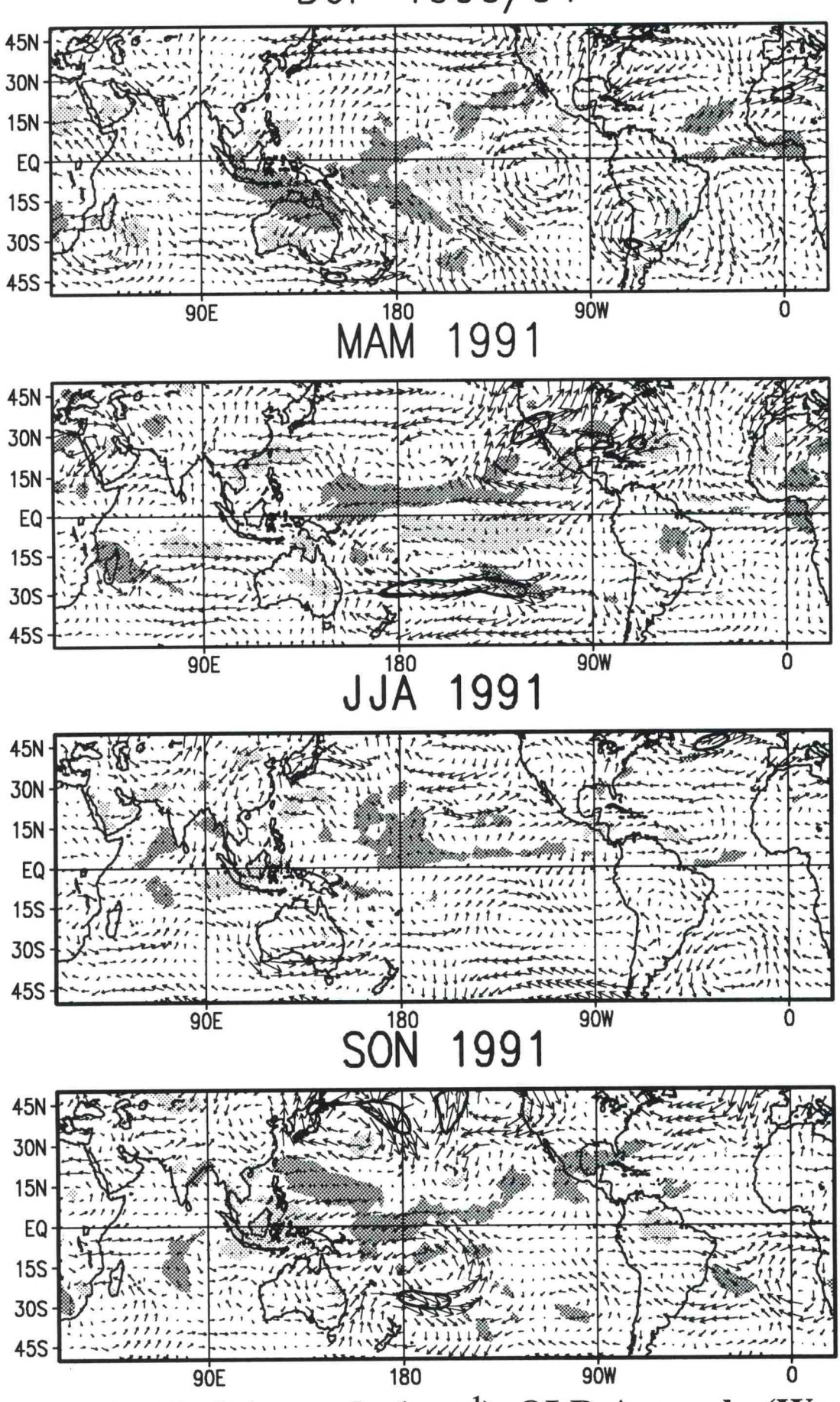

200 mb Wind Anomaly (m s^{-1}), OLR Anomaly (W m^{-2})

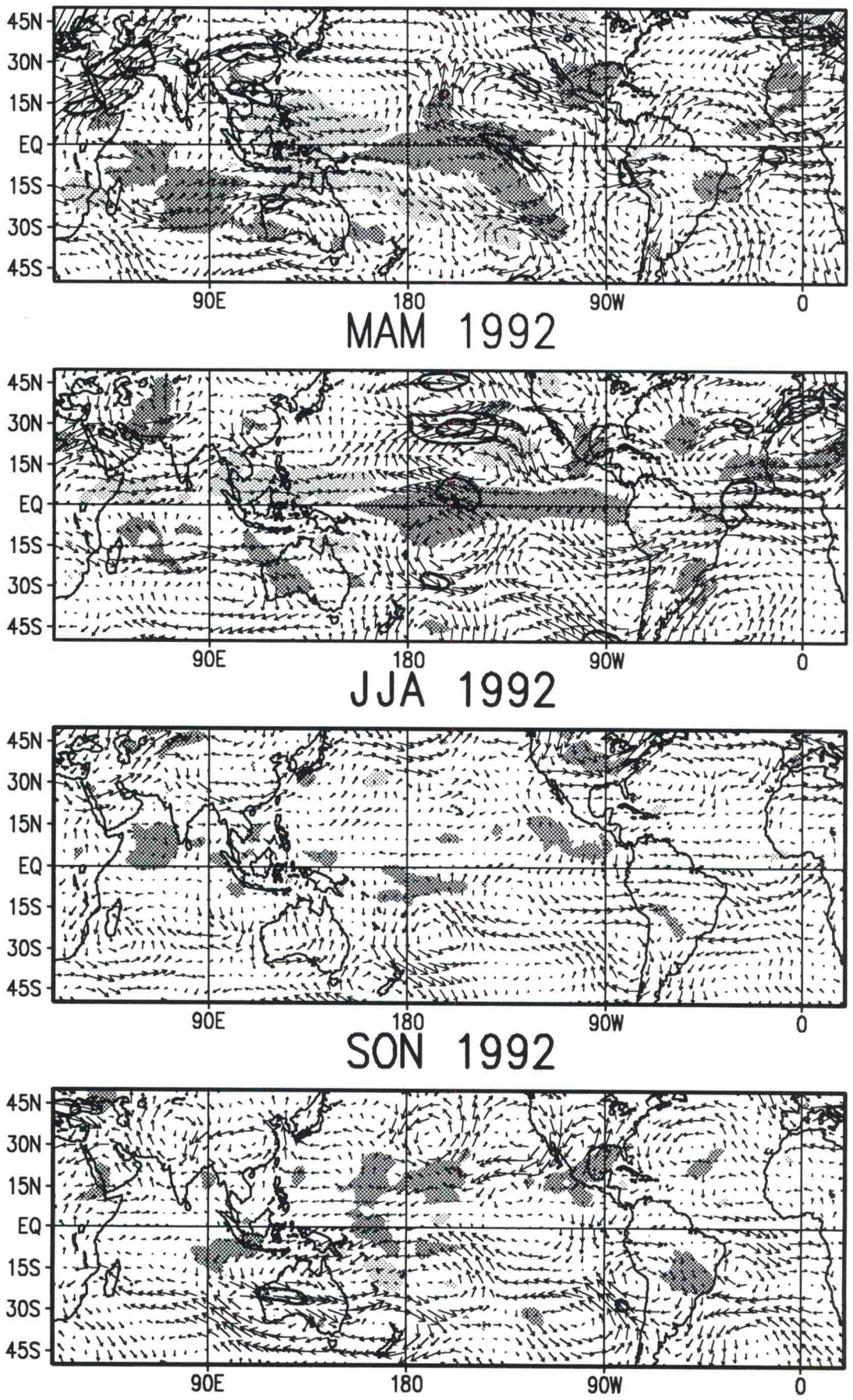

200 mb Wind Anomaly (m s^{-1}), OLR Anomaly (W m^{-2})

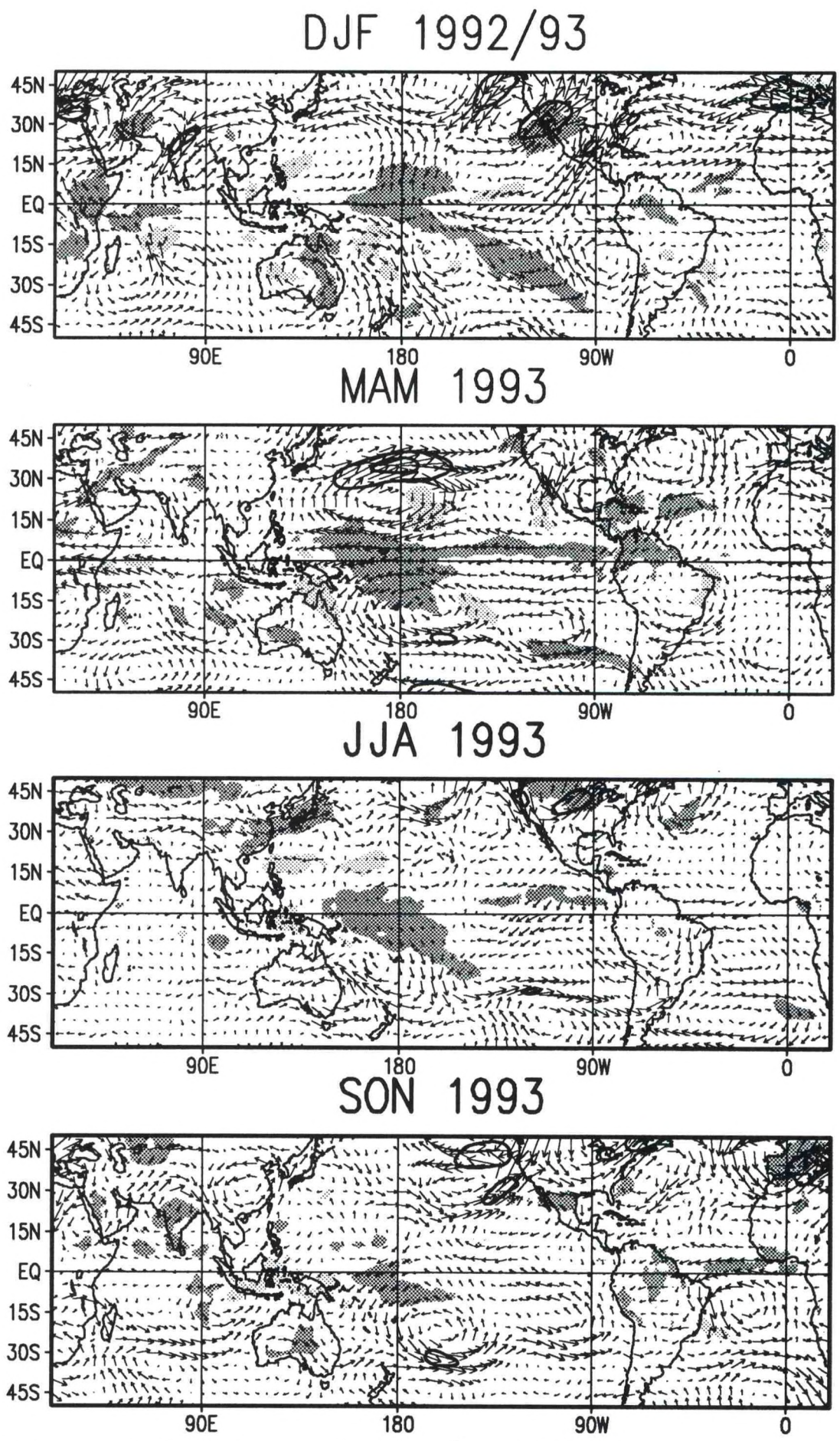

200 mb Wind Anomaly (m s^{-1}), OLR Anomaly (W m^{-2})

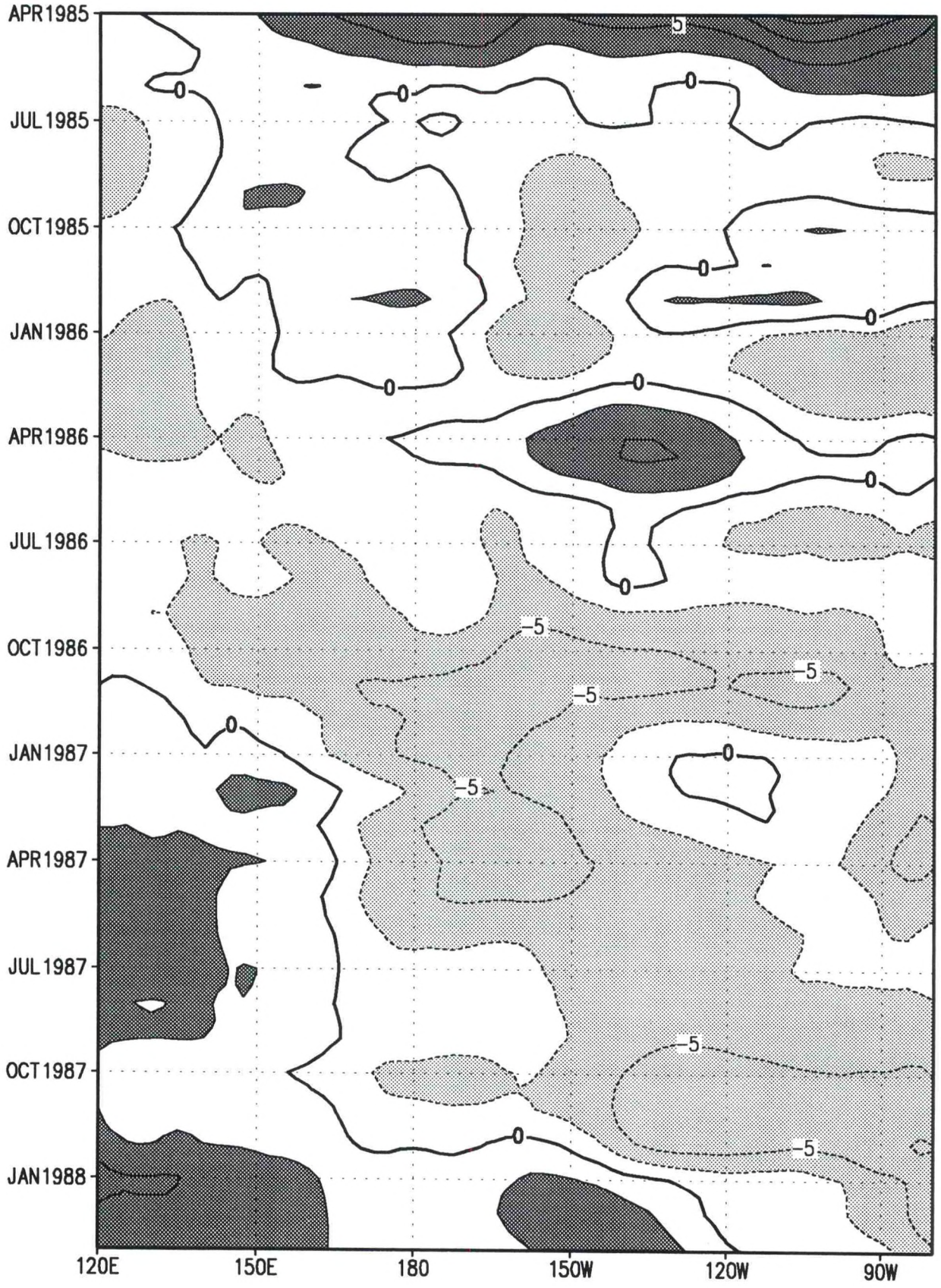

200 mb Zonal Wind Anomaly (ms^{-1})

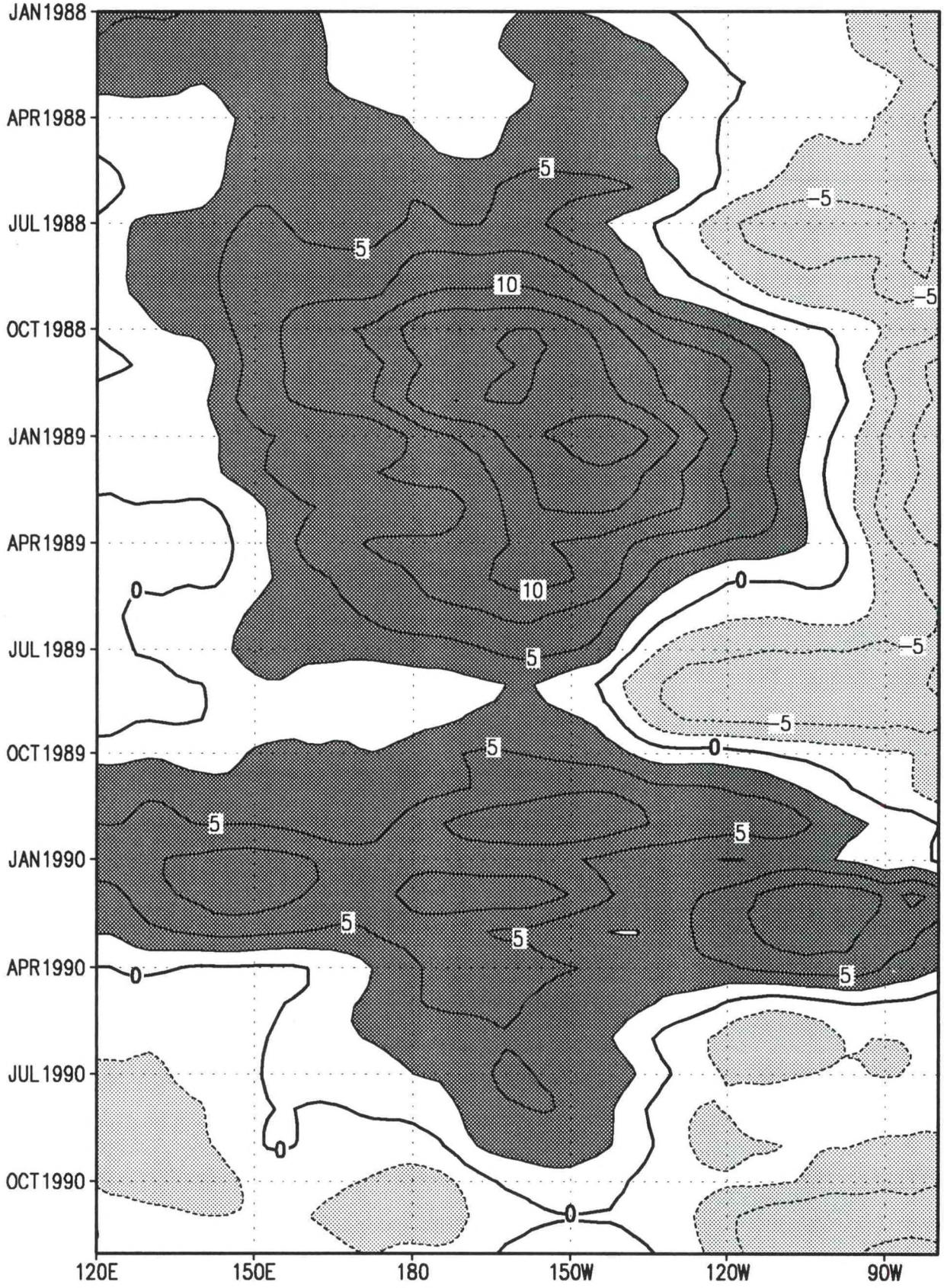

200 mb Zonal Wind Anomaly (ms^{-1})

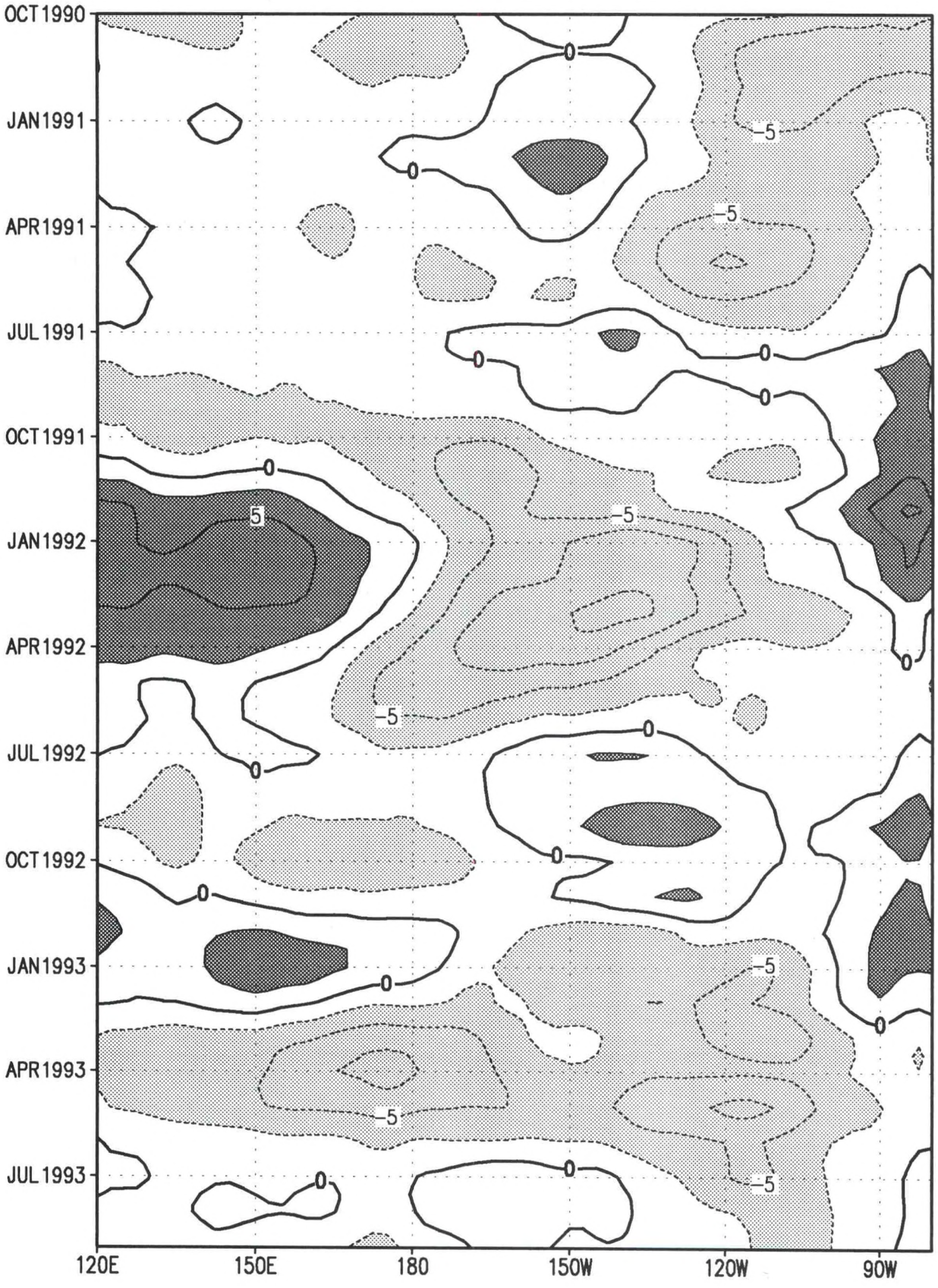

200 mb Zonal Wind Anomaly (ms^{-1})

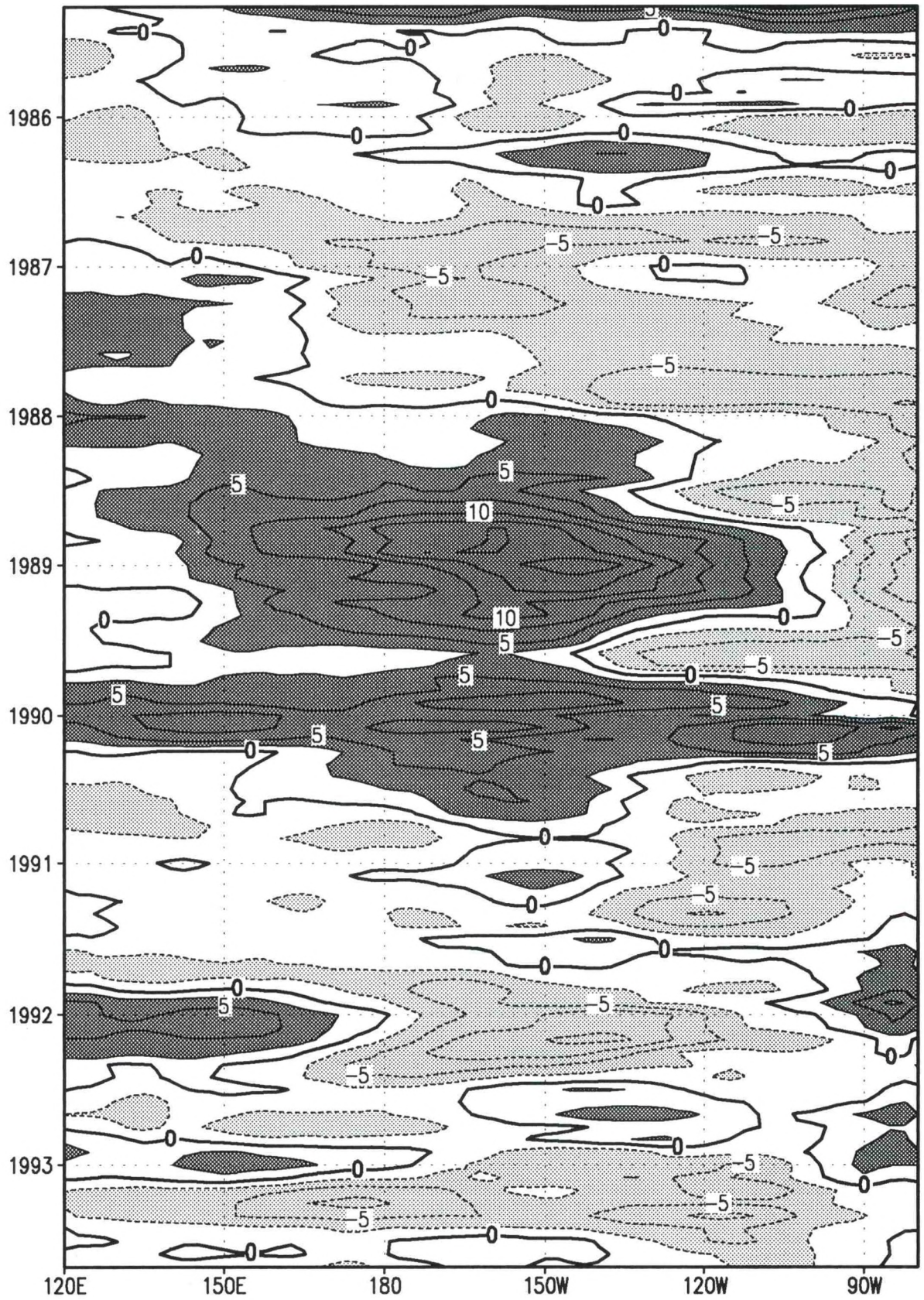

200 mb Zonal Wind Anomaly (ms^{-1})

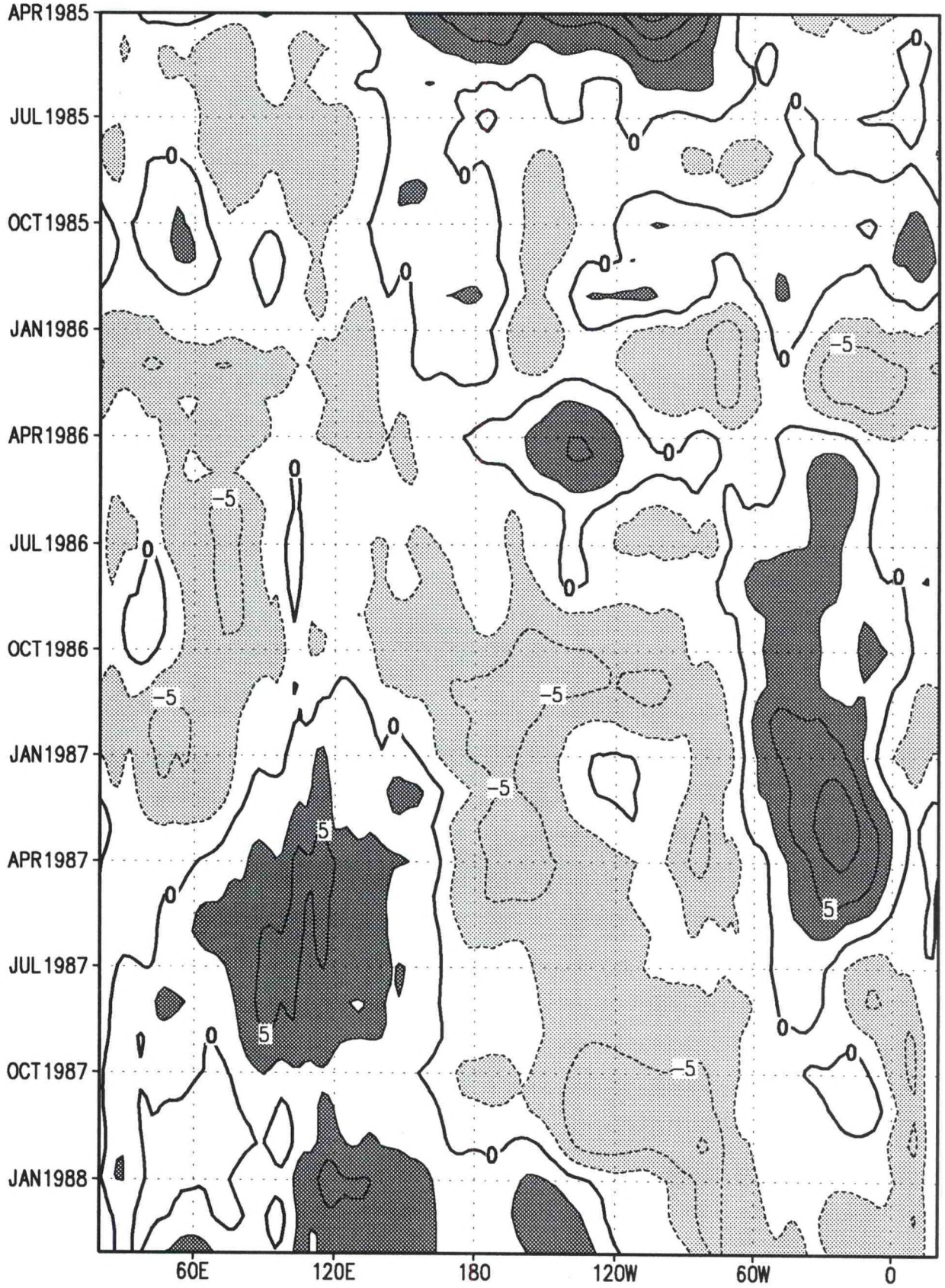

200 mb Zonal Wind Anomaly (ms^{-1})

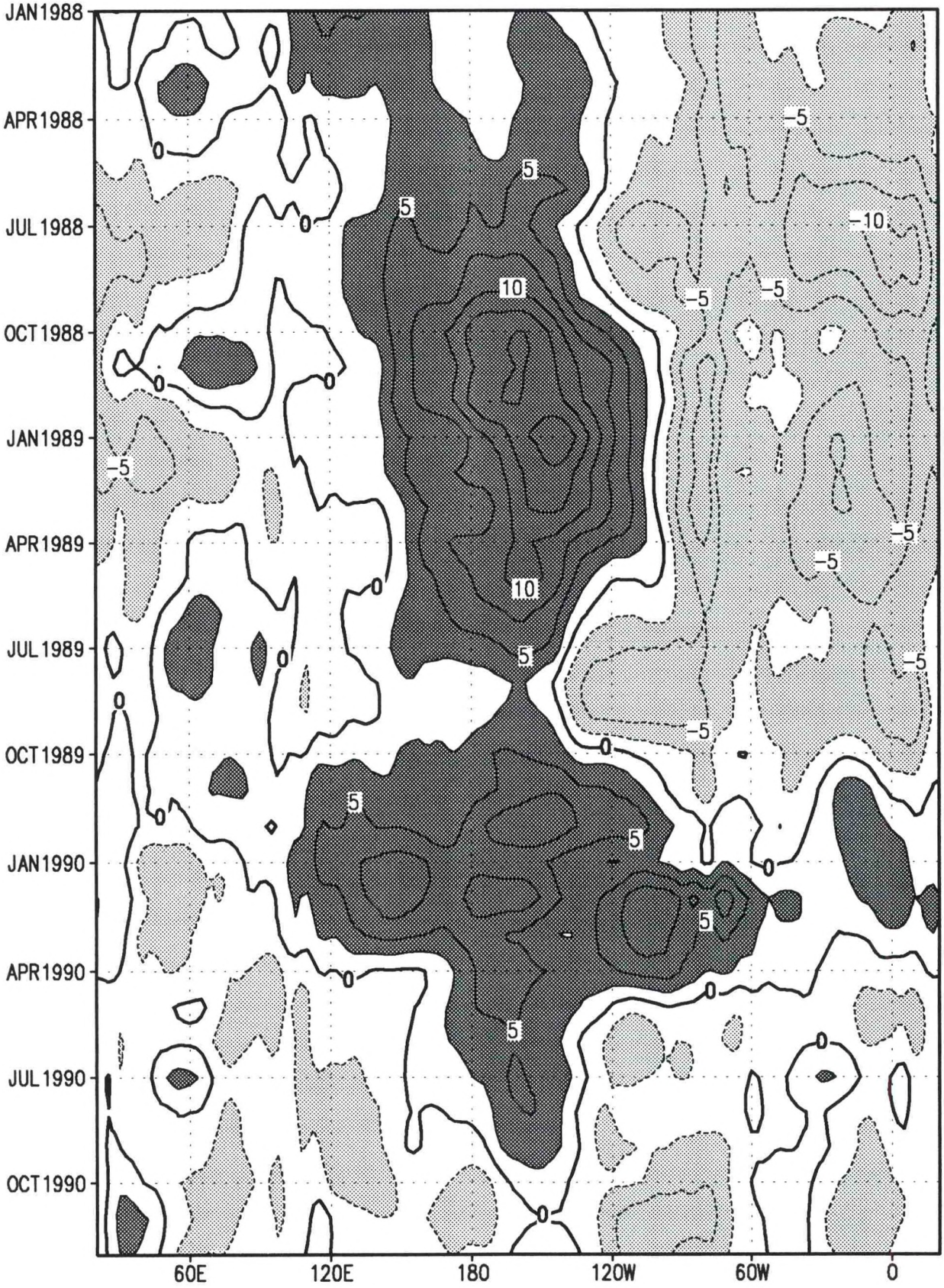

200 mb Zonal Wind Anomaly (ms^{-1})

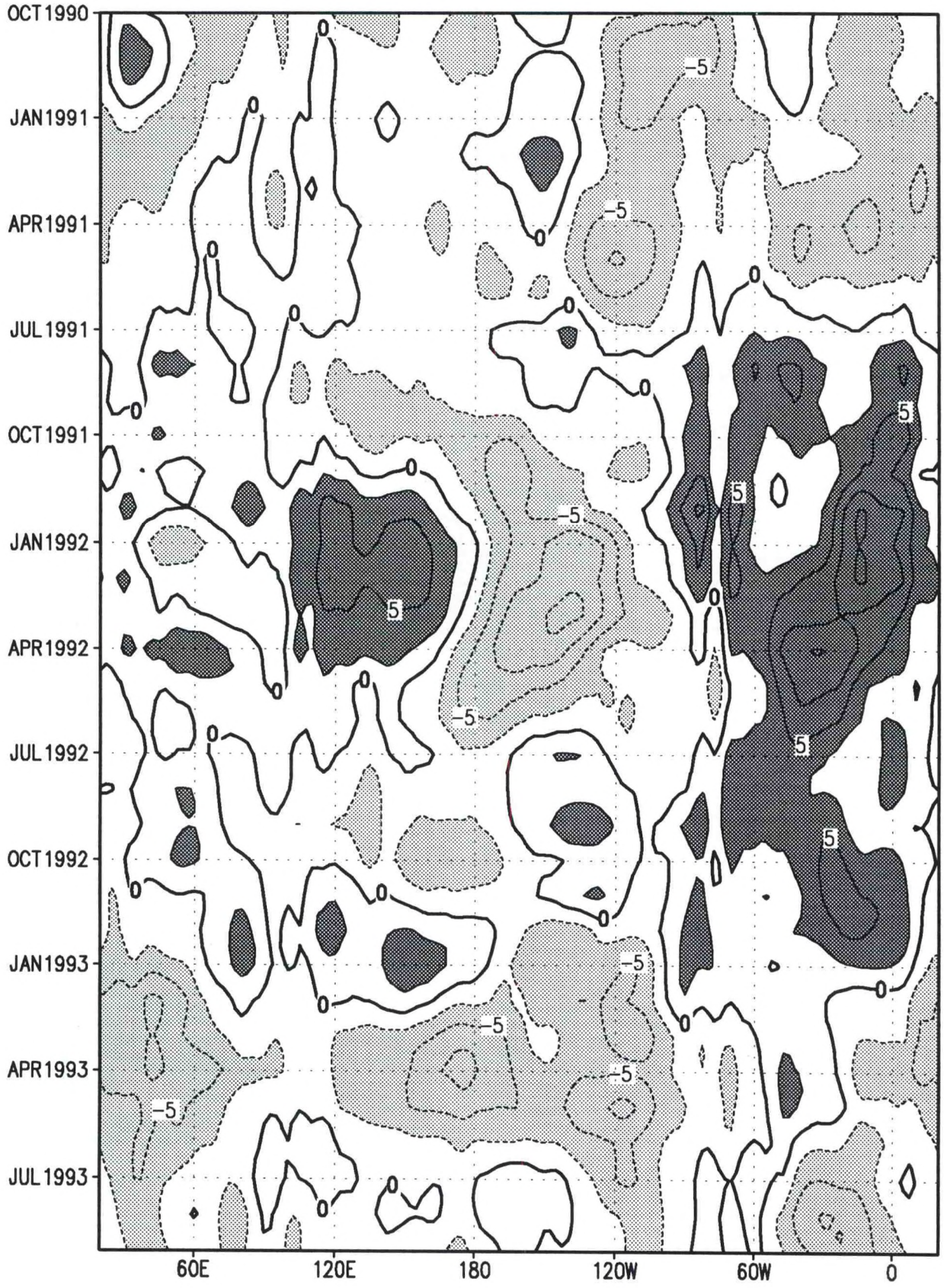

200 mb Zonal Wind Anomaly (ms^{-1})

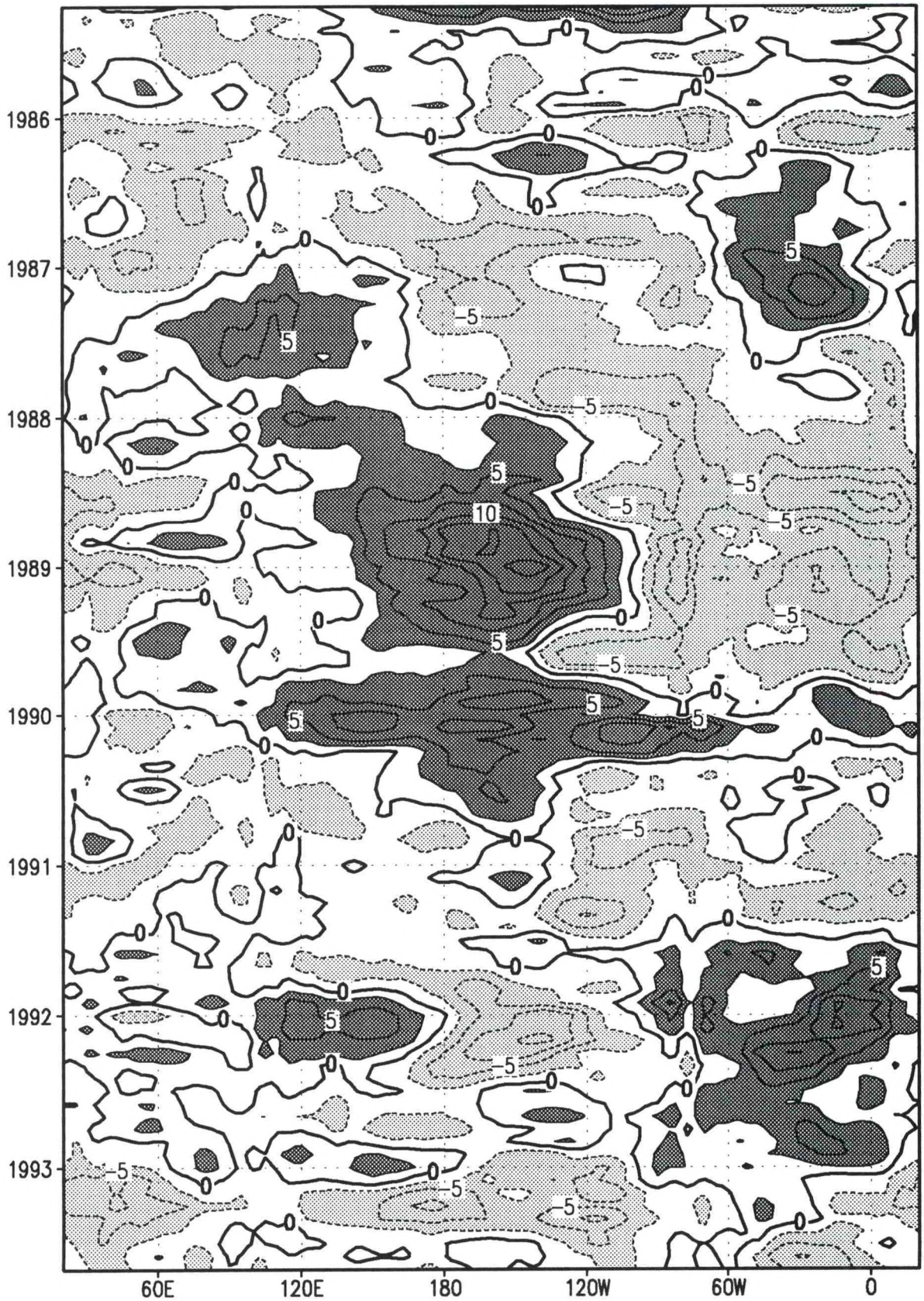

200 mb Zonal Wind Anomaly (ms^{-1})

850 mb WIND ANOMALY

Seasonal Maps (pp. 98-105): Seasonal-mean 850 mb vector wind anomaly (ms^{-1}) for all longitudes from 50°N to 50°S. Wind speed anomalies greater than 3 ms^{-1} are contoured, and contour interval is 2 ms^{-1}. Positive (negative) OLR anomalies exceeding ± 10 W m^{-2} are shaded light (dark), indicating suppressed (enhanced) convection in the tropics and subtropics. Zero contour is shown thick solid.

Time-Longitude Section (pp. 106-109): Monthly-mean 850 mb zonal wind anomaly (ms^{-1}) along the equator over the Pacific Ocean between 120°E and 80°W. Westerly (easterly) anomalies are shown by positive (negative) values. Contour interval is 2.0 ms^{-1}, with negative values dashed. Values exceeding ± 1.0 ms^{-1} are shaded, with positive (negative) values shown dark (light). Zero contour is shown thick solid.

Time-Longitude Section (pp. 110-113): Monthly-mean 850 mb zonal wind anomaly (ms^{-1}) along the equator for all longitudes. Westerly (easterly) anomalies are shown by positive (negative) values. Contour interval is 2.0 ms^{-1}, with negative values dashed. Values exceeding ± 1.0 ms^{-1} are shaded, with positive (negative) values shown dark (light). Zero contour is shown thick solid.

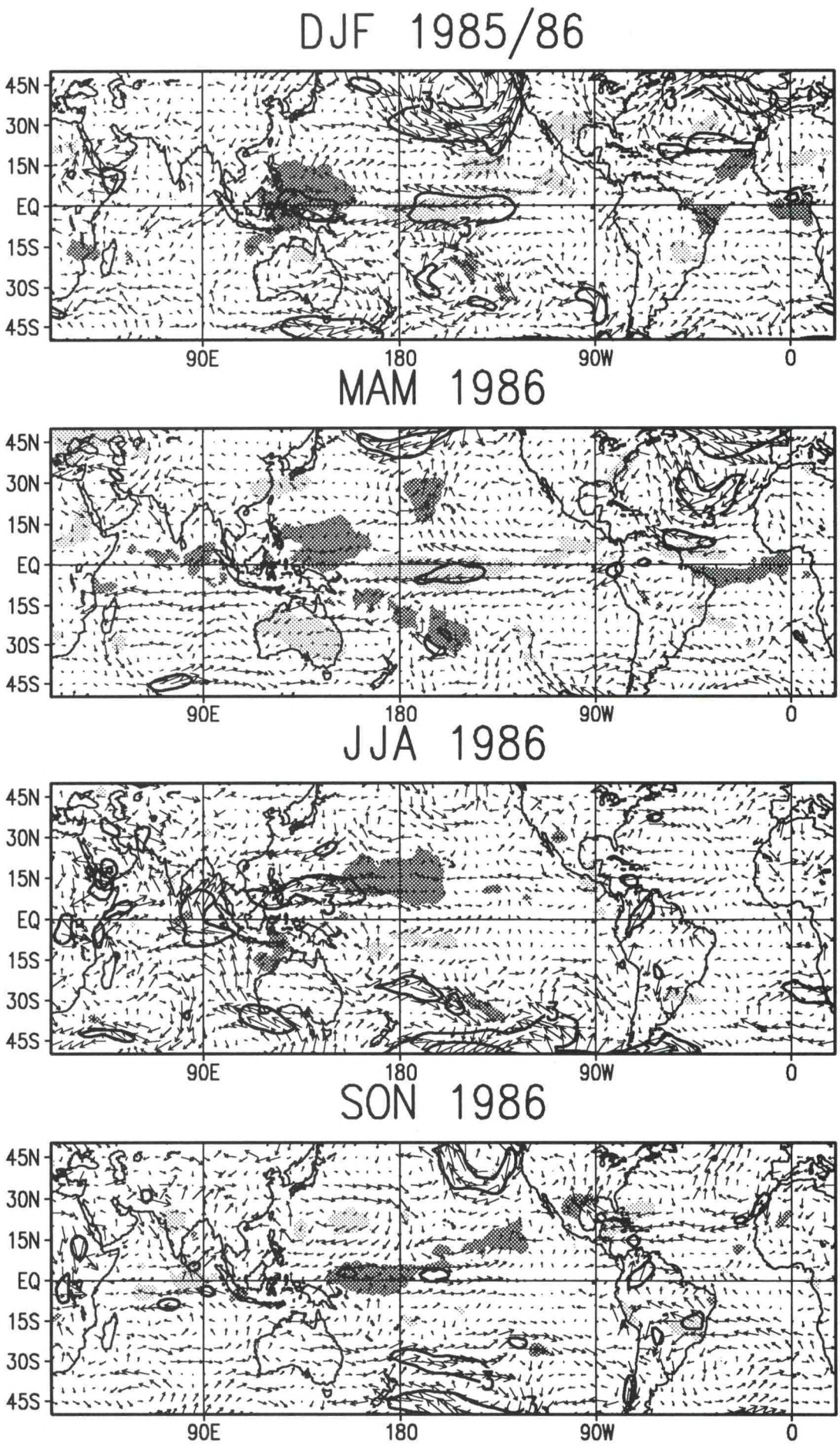

850 mb Wind Anomaly (m s^{-1}), OLR Anomaly (W m^{-2})

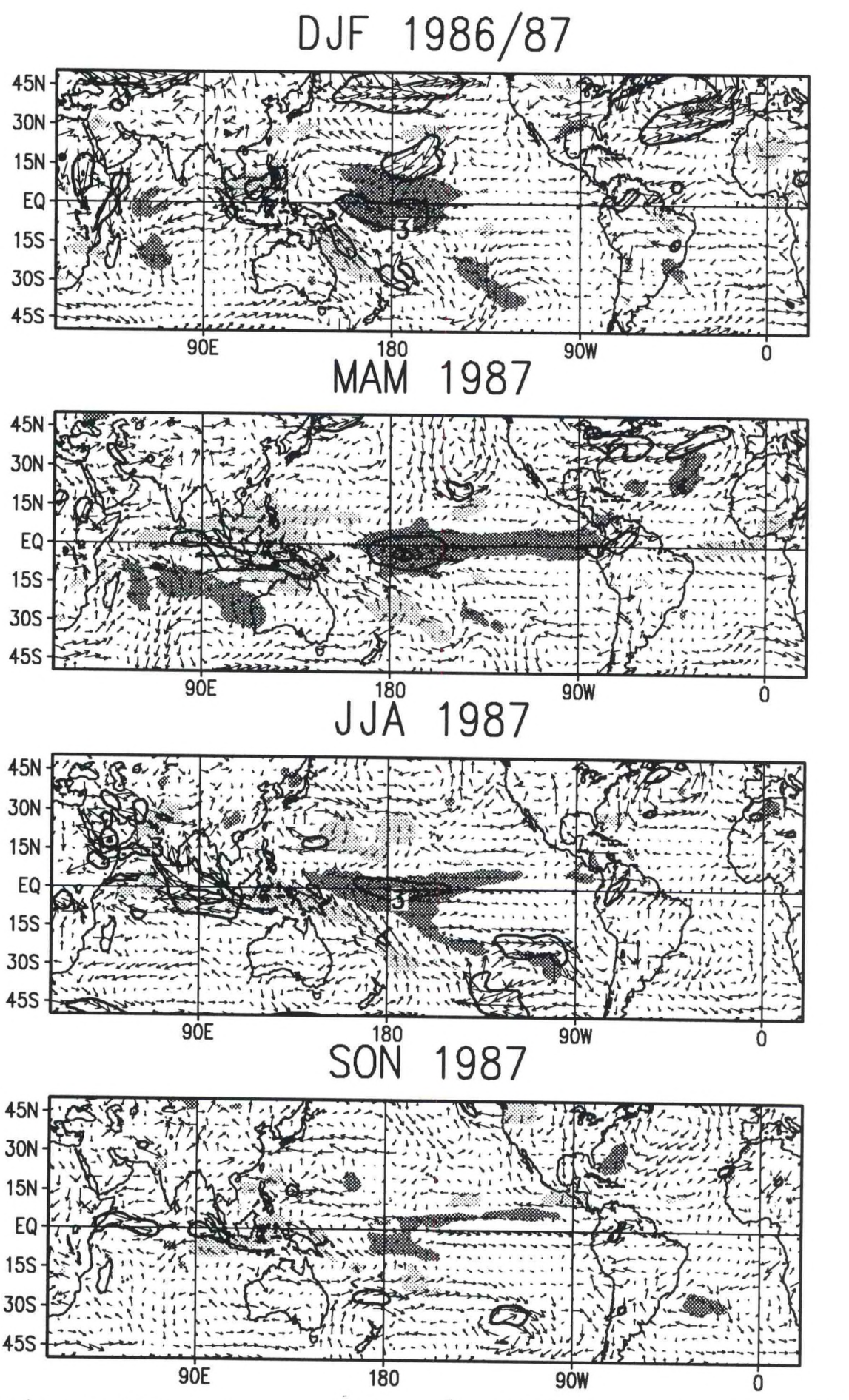

850 mb Wind Anomaly (m s^{-1}), OLR Anomaly (W m^{-2})

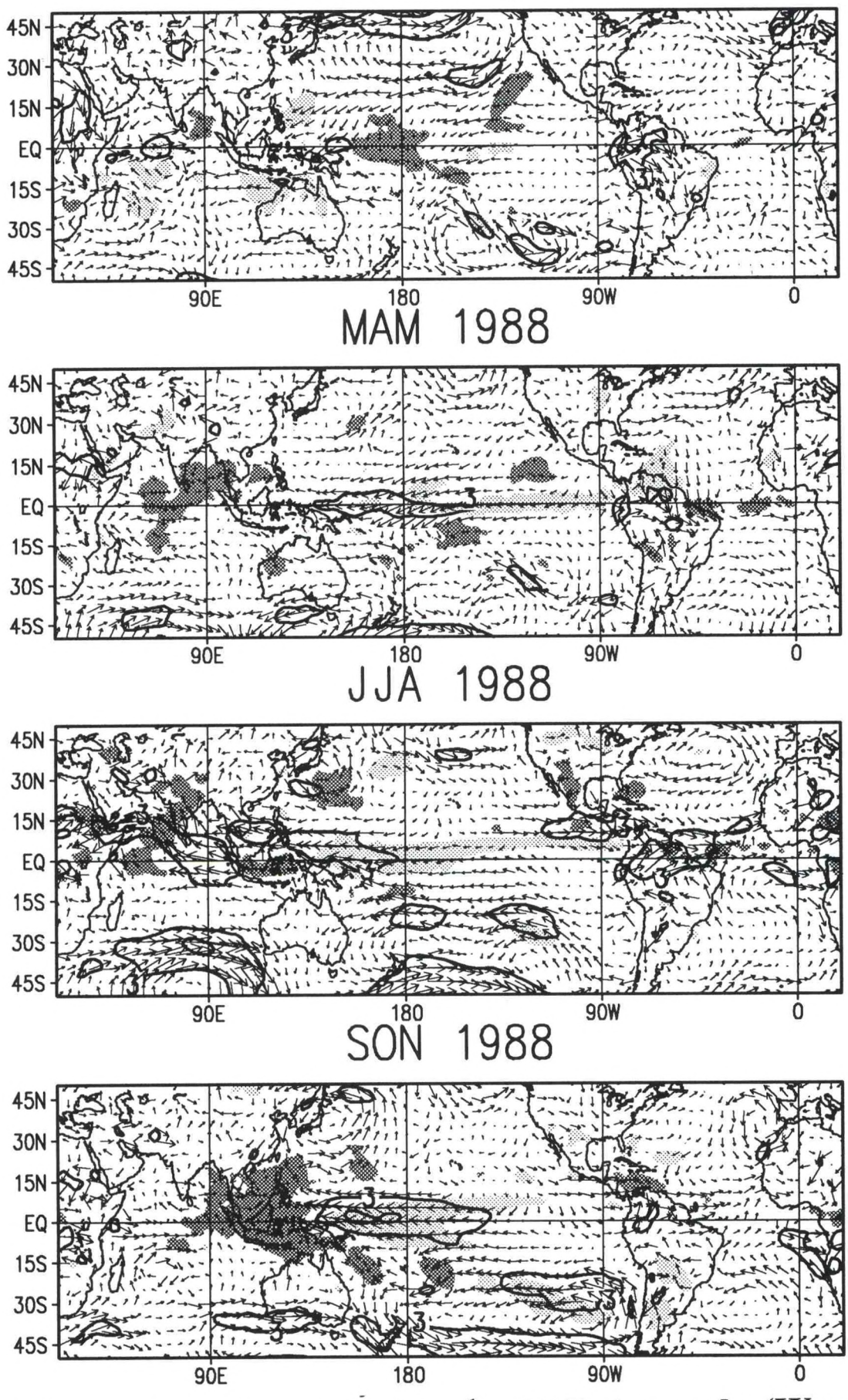

850 mb Wind Anomaly (m s^{-1}), OLR Anomaly (W m^{-2})

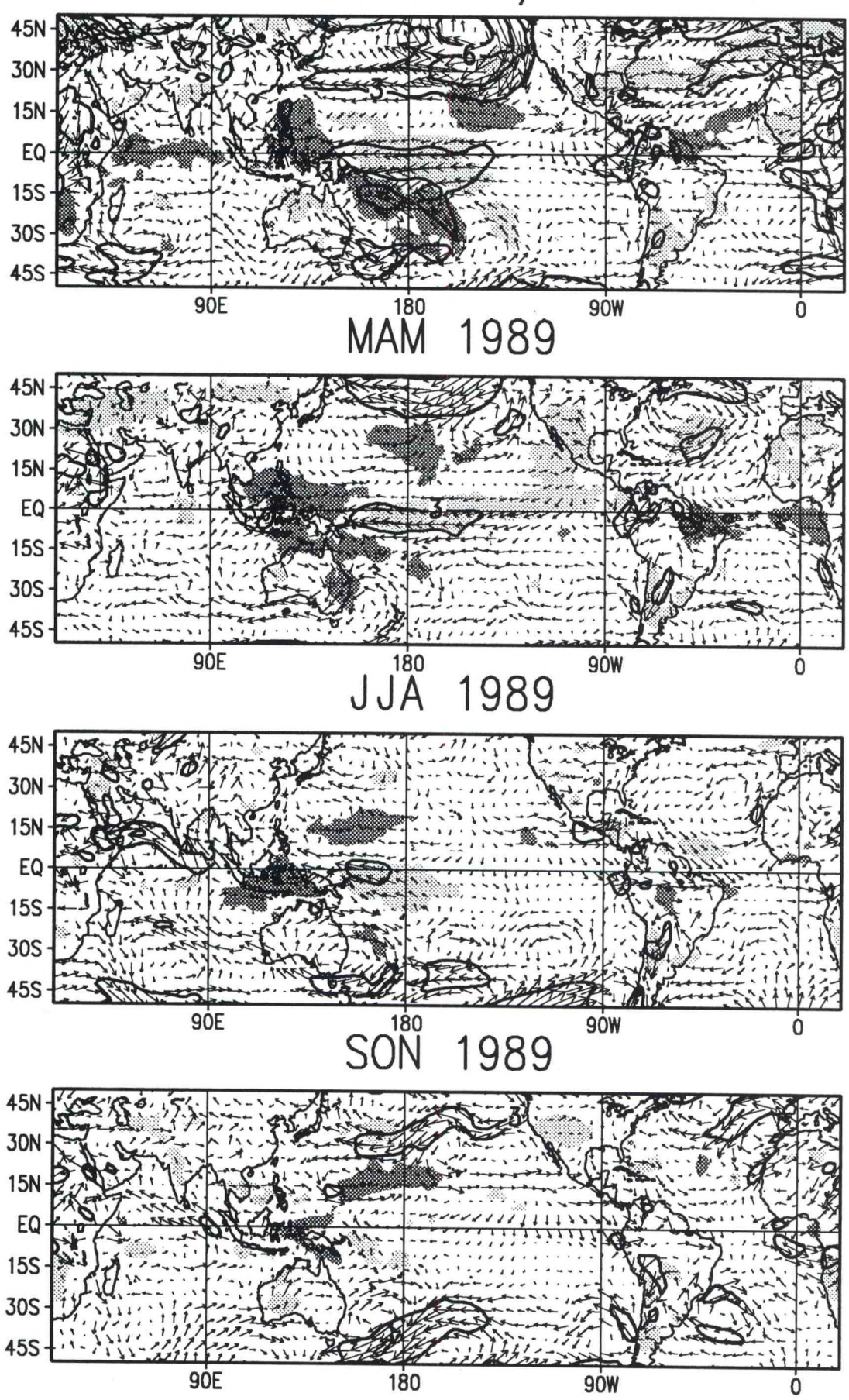

850 mb Wind Anomaly (m s^{-1}), OLR Anomaly (W m^{-2})

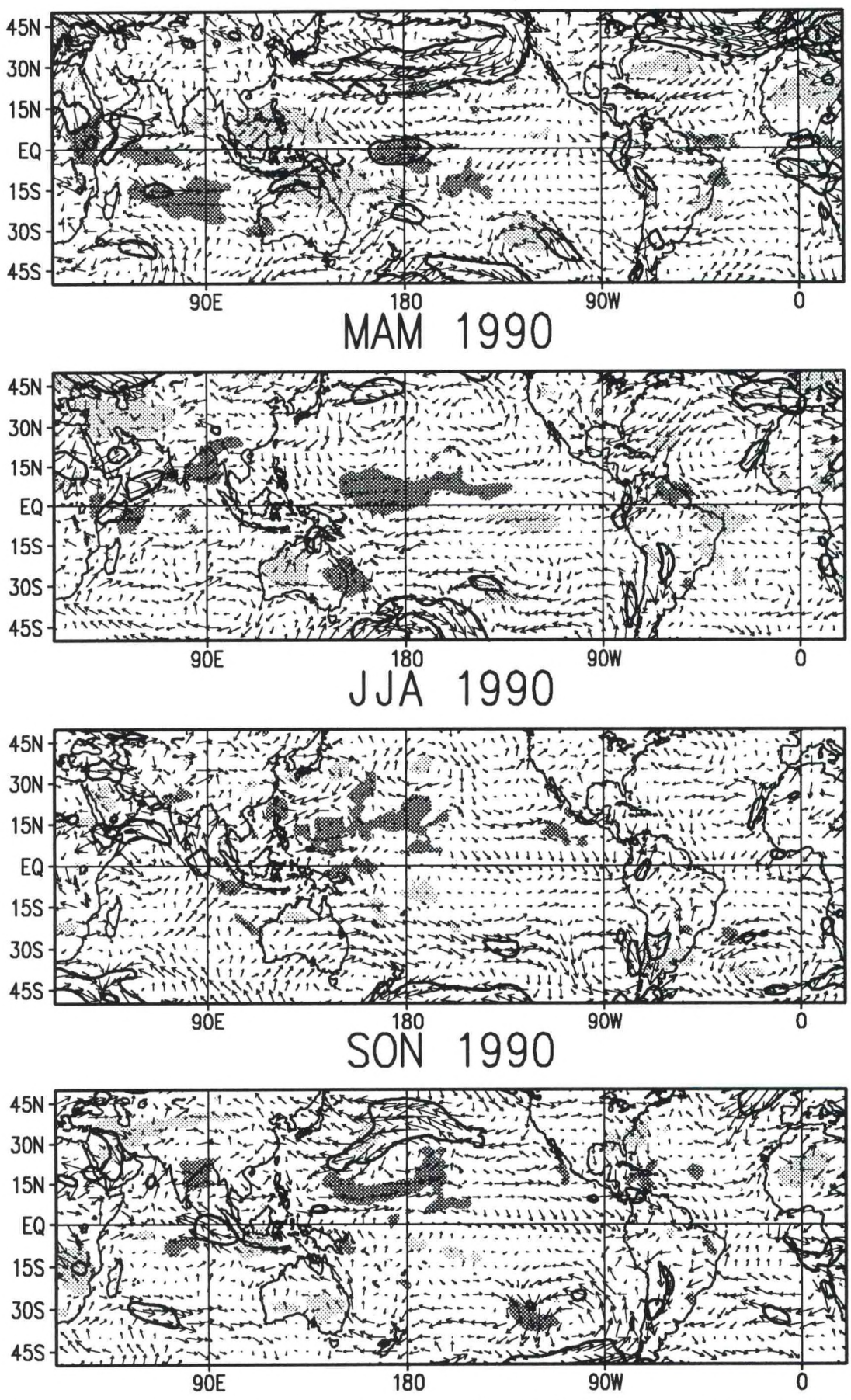

850 mb Wind Anomaly (m s^{-1}), OLR Anomaly (W m^{-2})

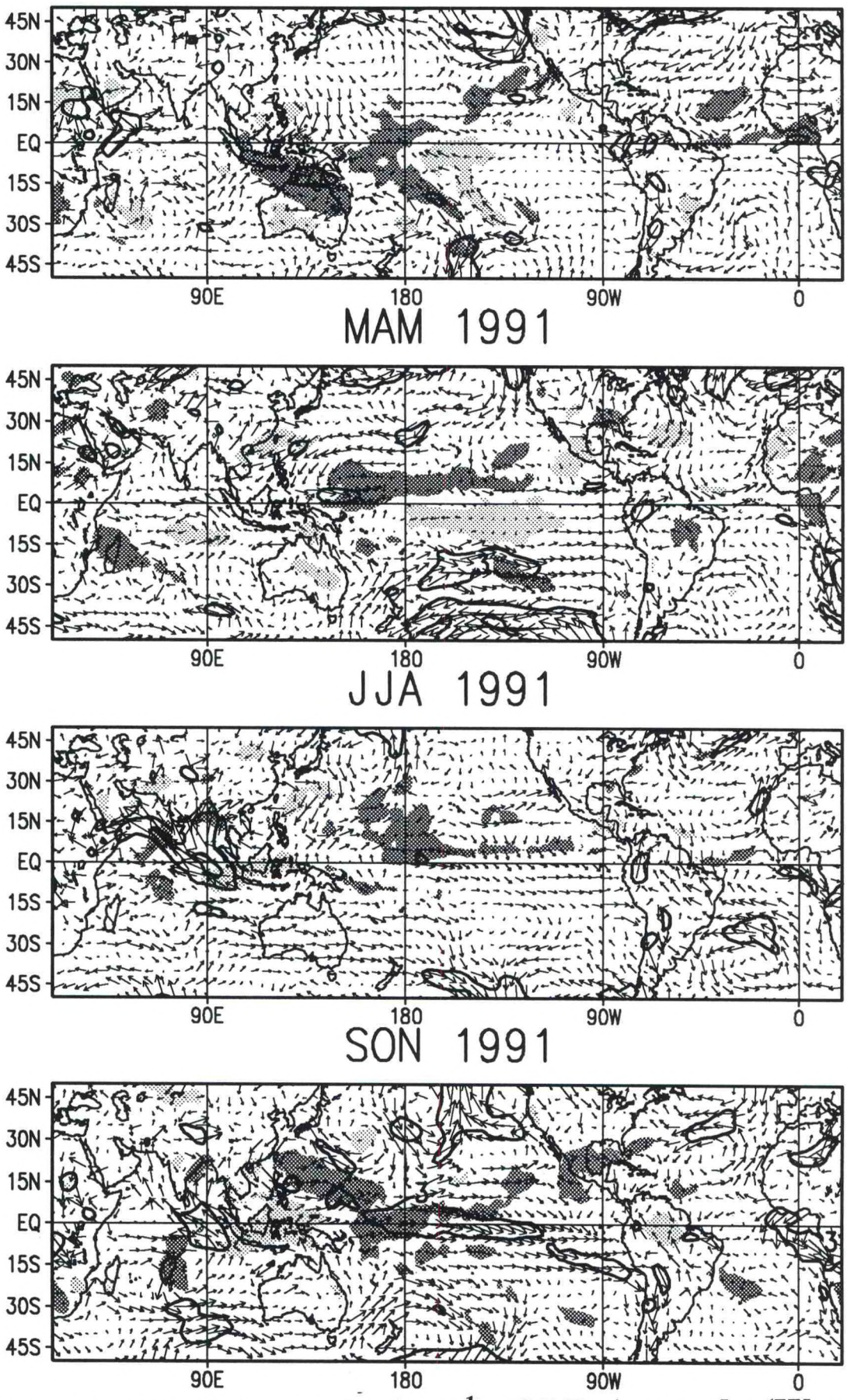

850 mb Wind Anomaly (m s^{-1}), OLR Anomaly (W m^{-2})

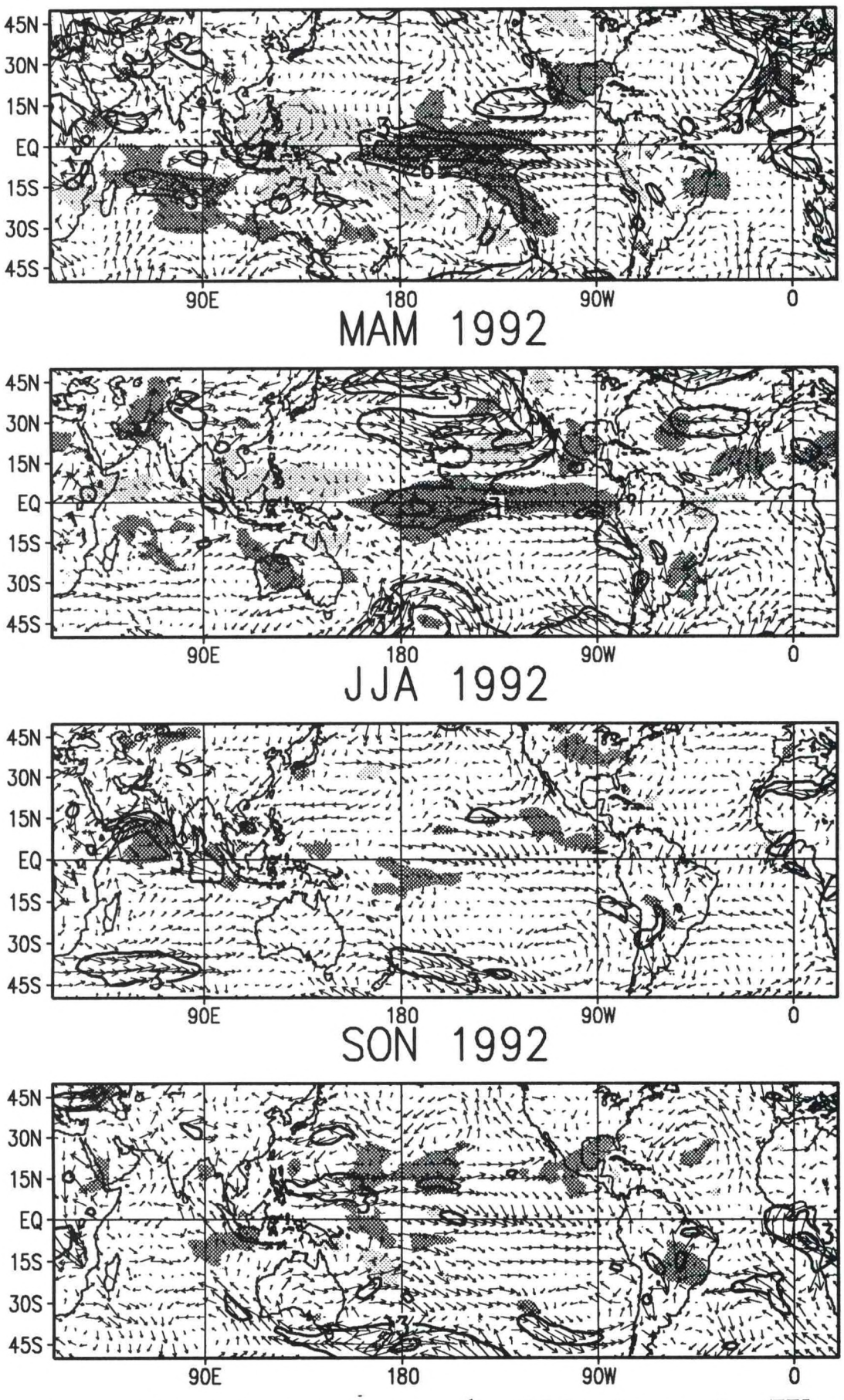

850 mb Wind Anomaly (m s^{-1}), OLR Anomaly (W m^{-2})

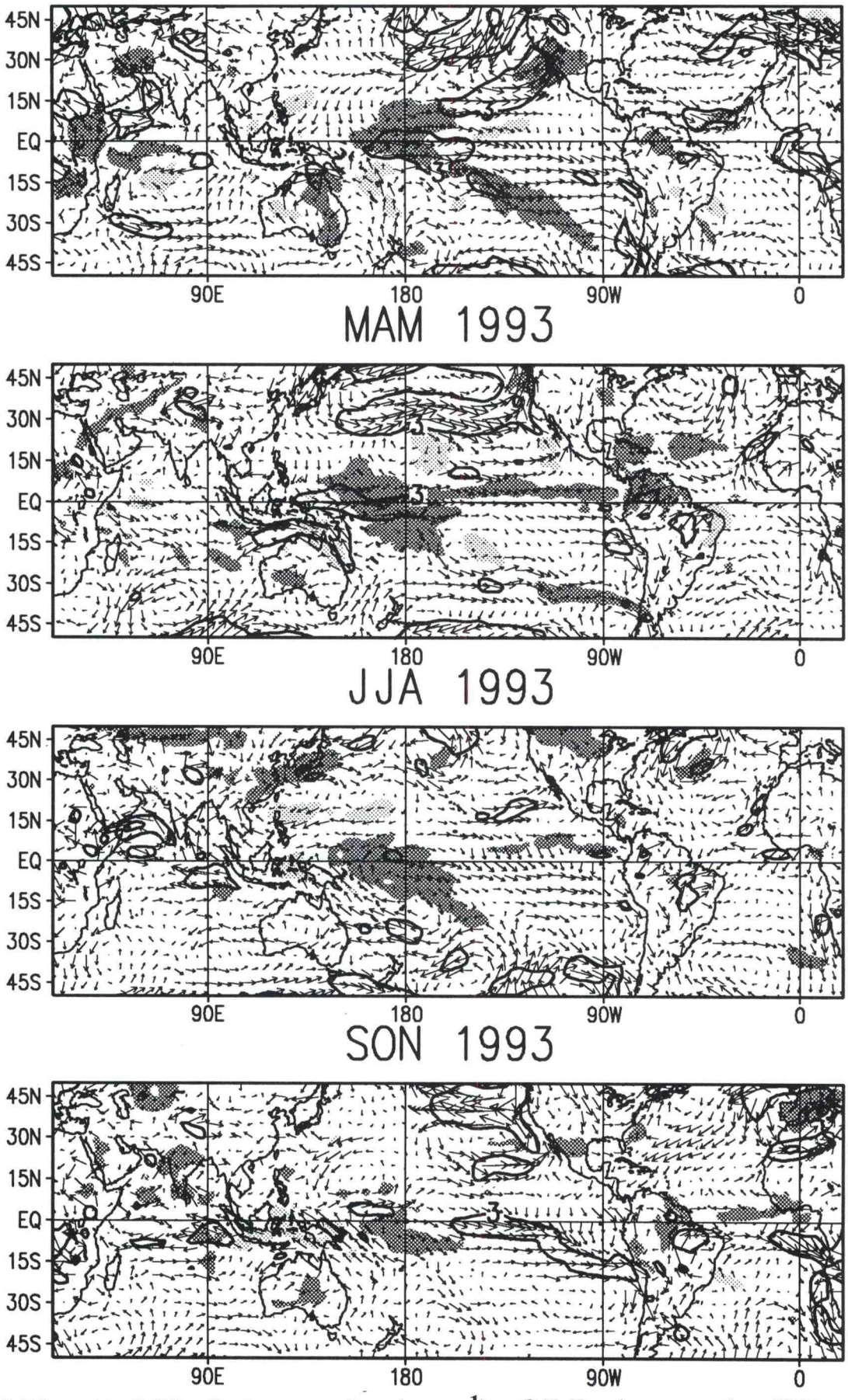

850 mb Wind Anomaly (m s^{-1}), OLR Anomaly (W m^{-2})

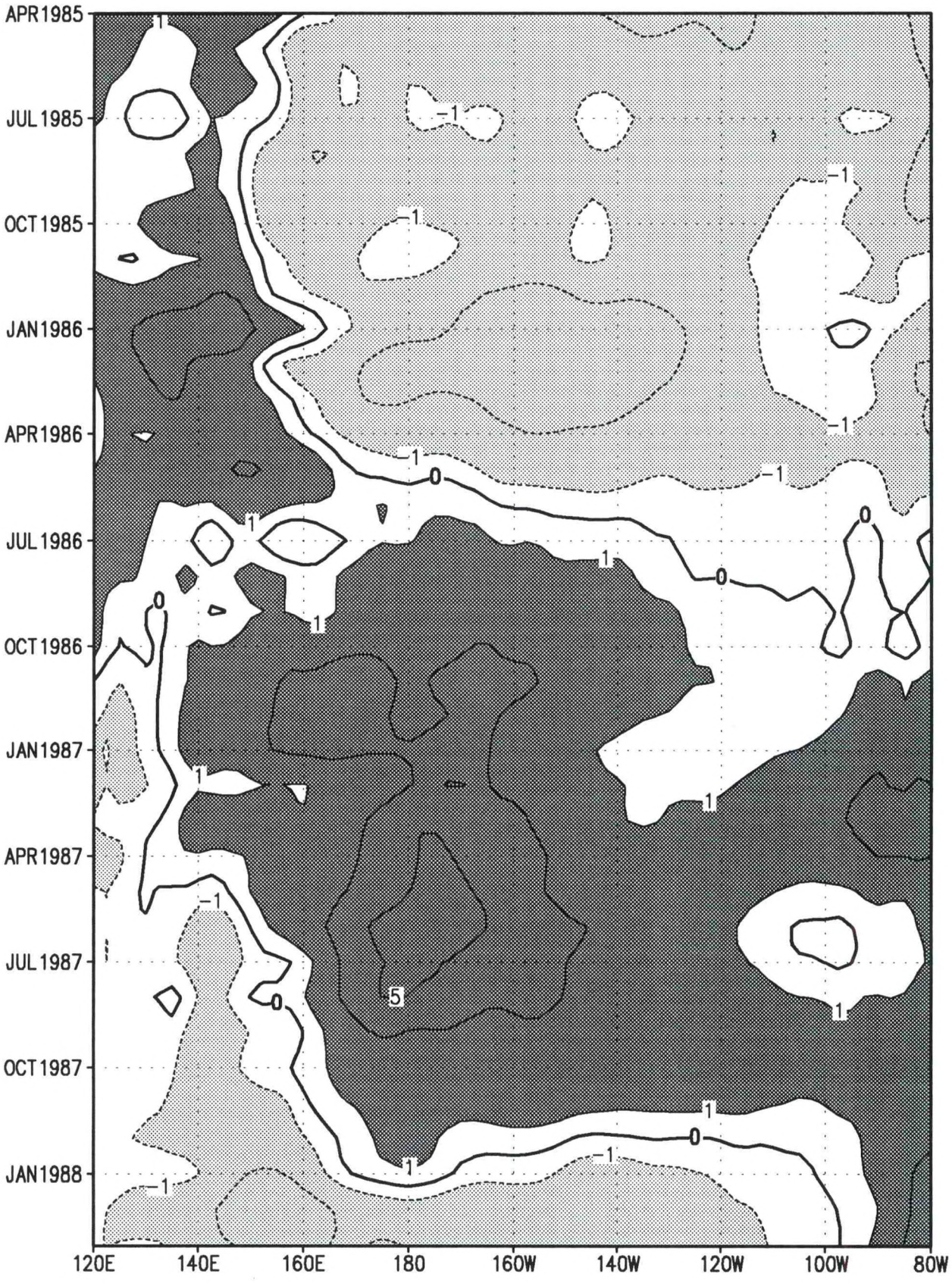

850 mb Zonal Wind Anomaly (ms^{-1})

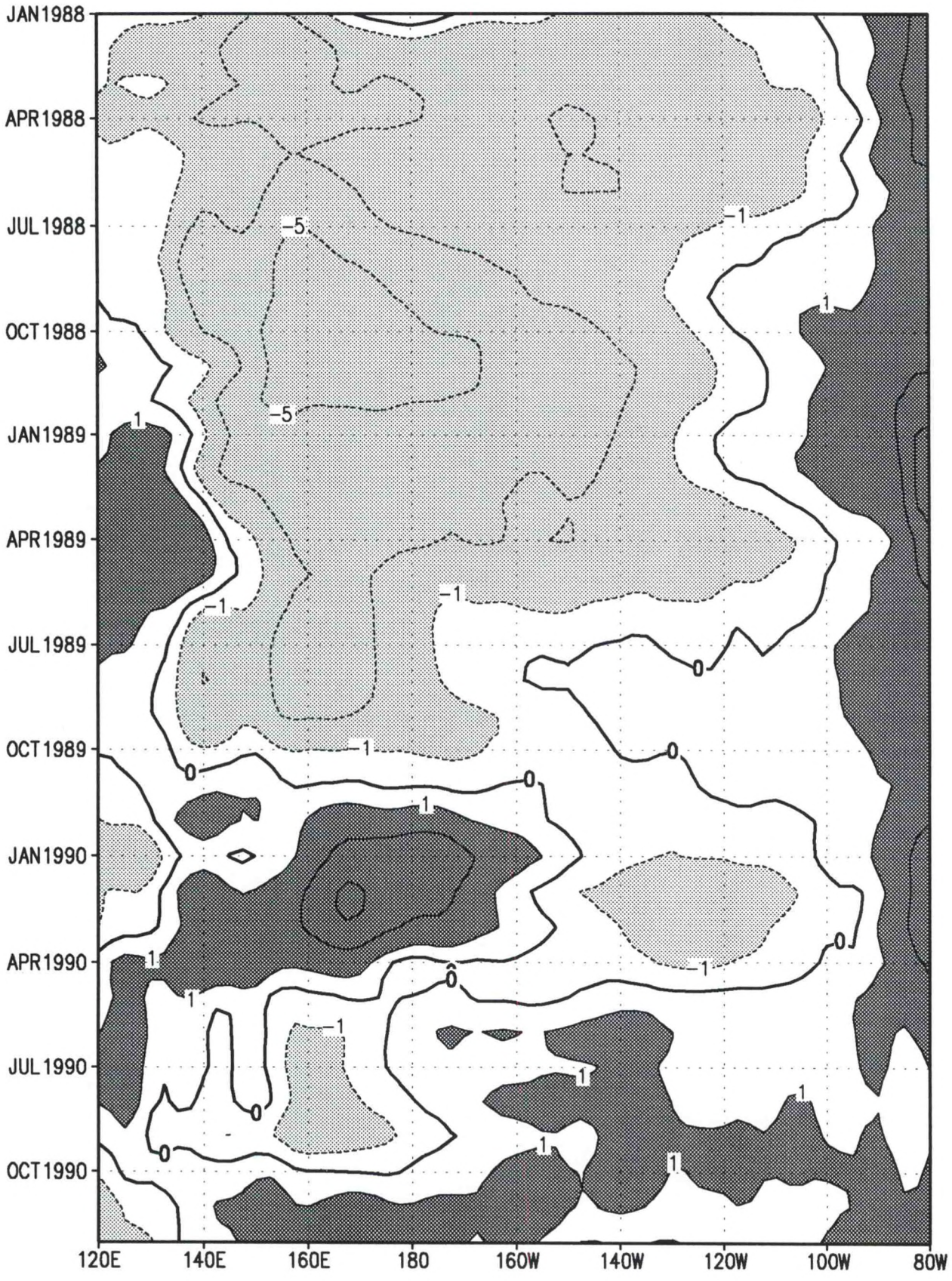

850 mb Zonal Wind Anomaly (ms^{-1})

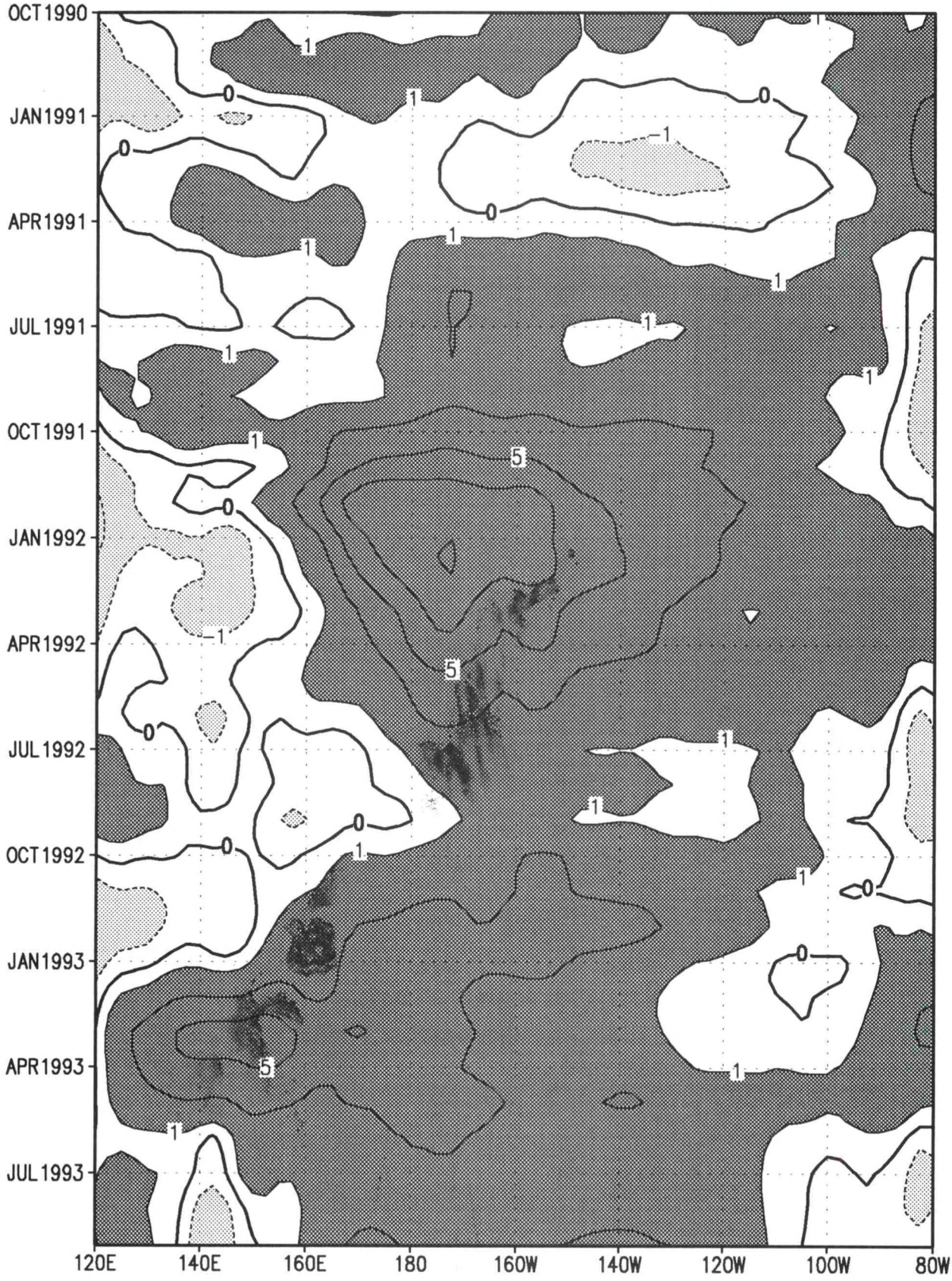

850 mb Zonal Wind Anomaly (ms^{-1})

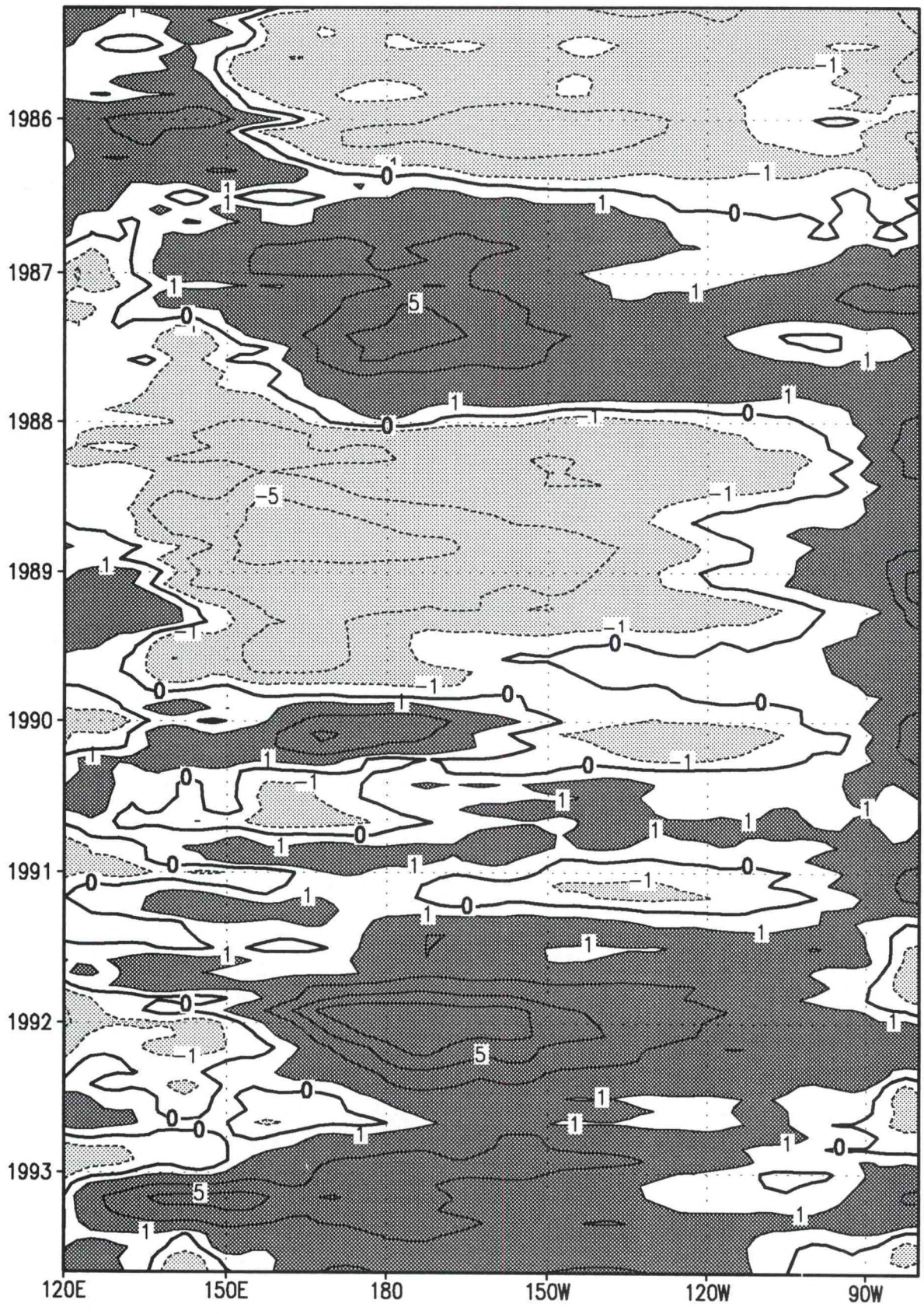

850 mb Zonal Wind Anomaly (ms^{-1})

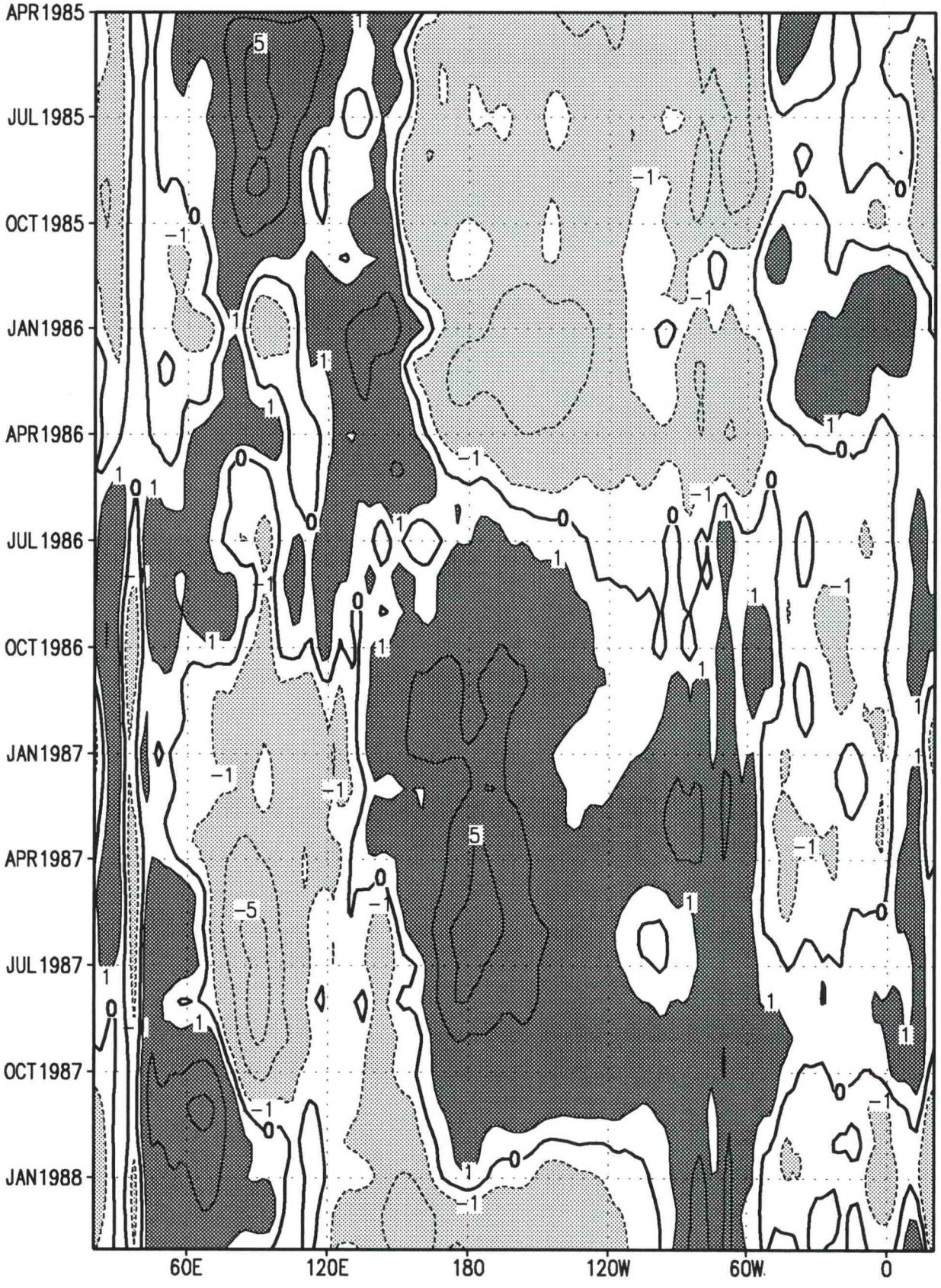

850 mb Zonal Wind Anomaly (ms^{-1})

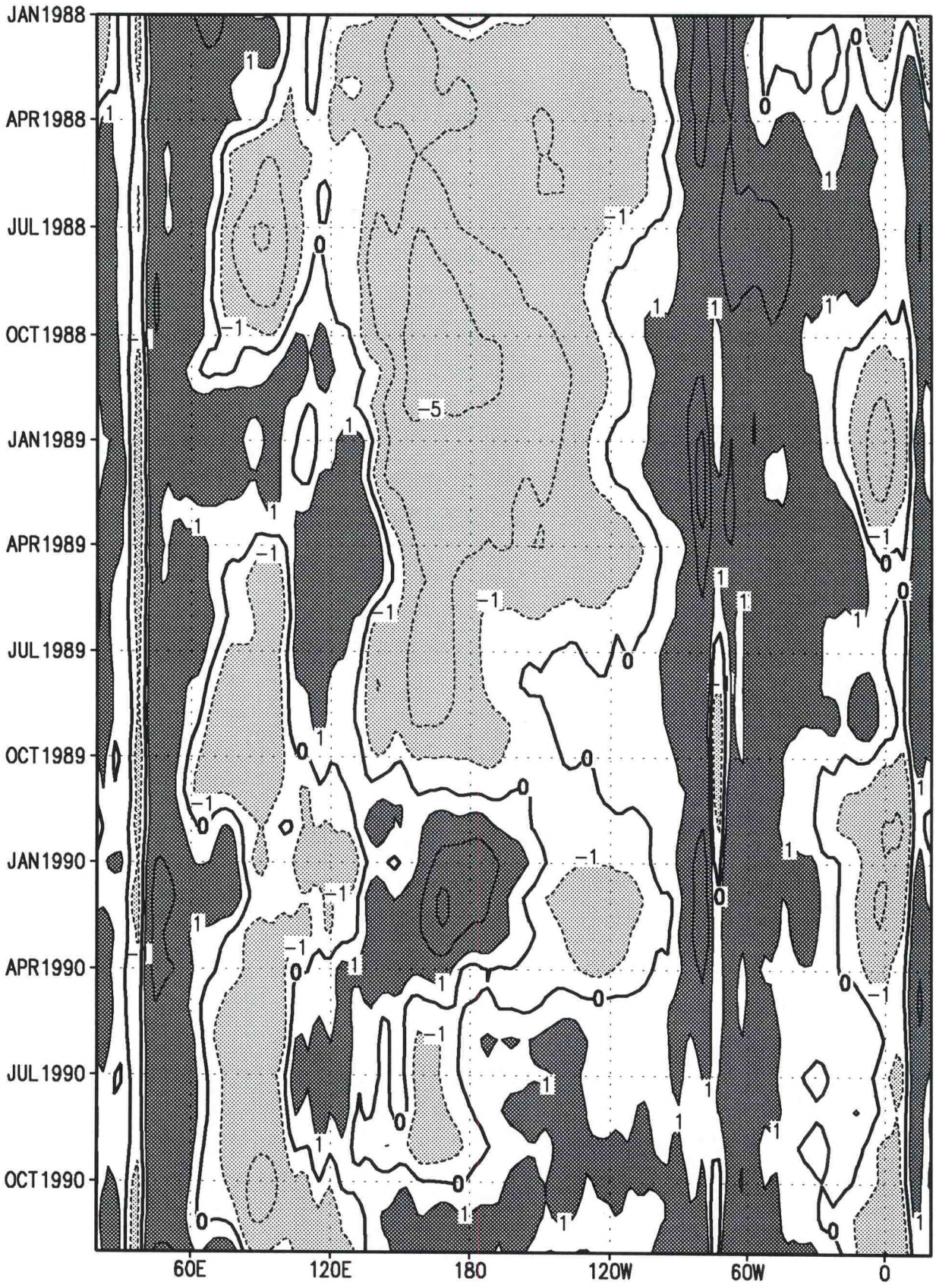

850 mb Zonal Wind Anomaly (ms^{-1})

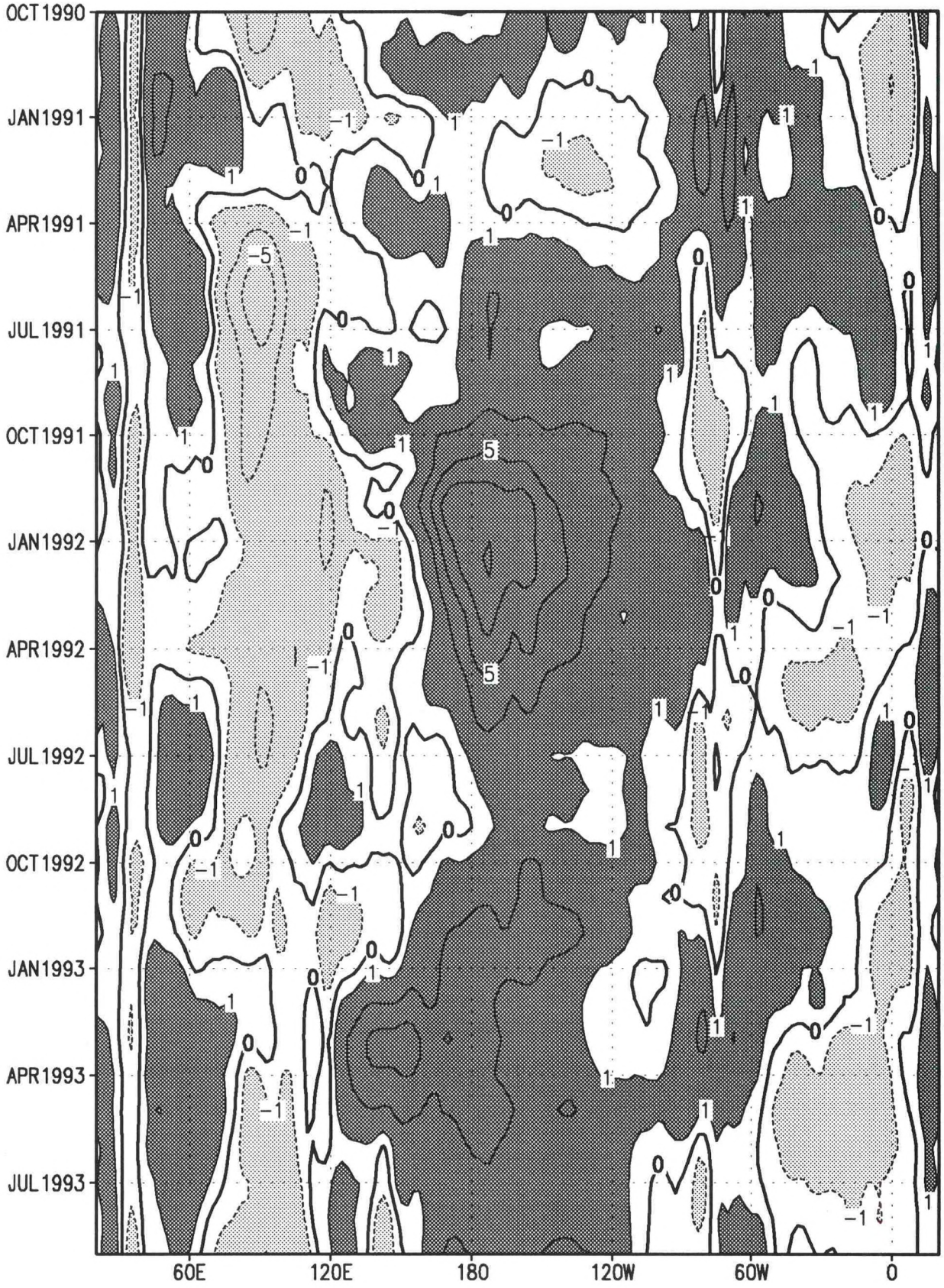

850 mb Zonal Wind Anomaly (ms^{-1})

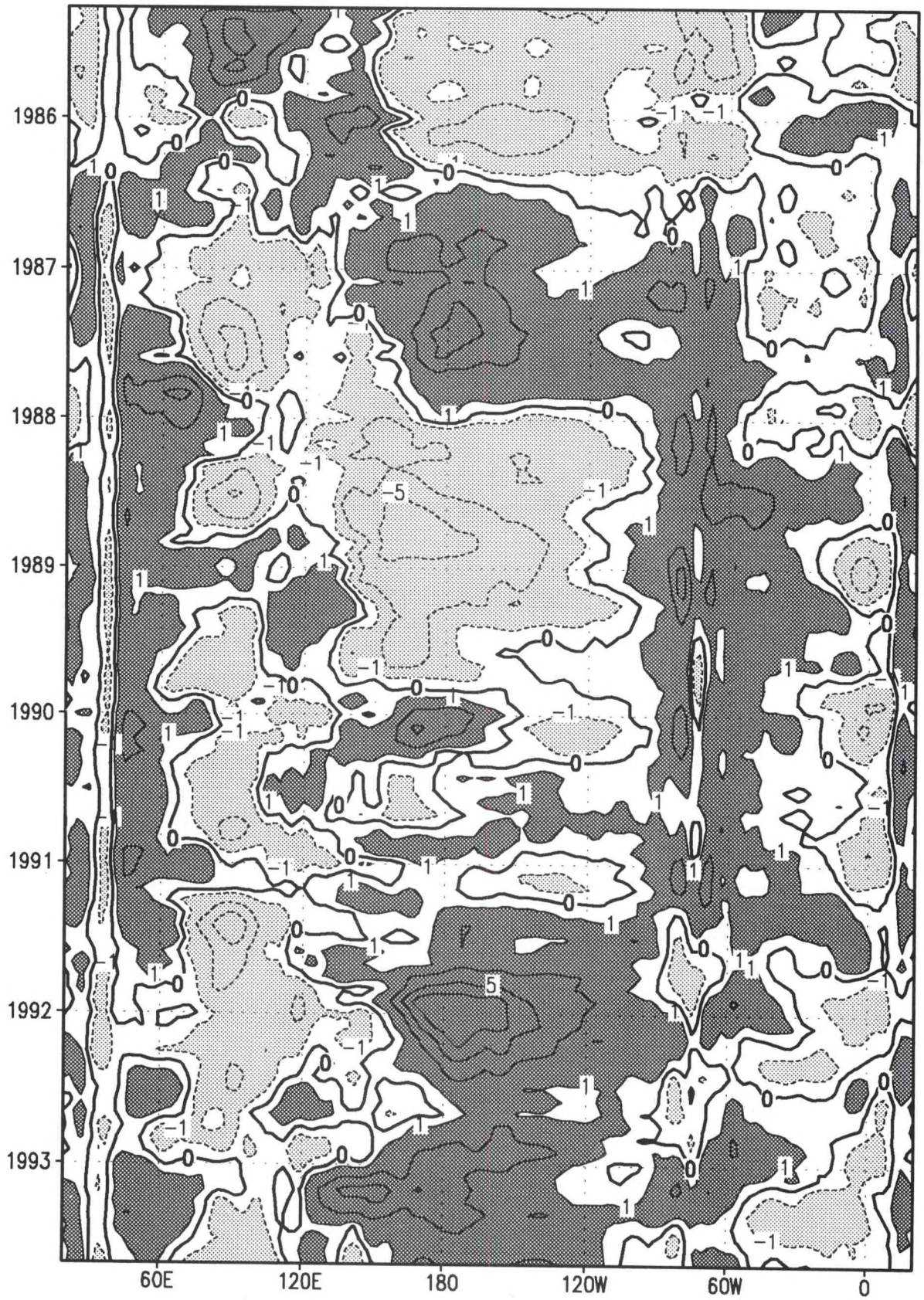

850 mb Zonal Wind Anomaly (ms^{-1})

EQUATORIAL ZONAL WIND ANOMALY CROSS-SECTION

Height-Longitude Section (pp. 115-122): Seasonal-mean zonal wind anomalies (ms^{-1}) along the equator for all longitudes. Positive (westerly) anomalies greater than 1 ms^{-1} are shaded dark with solid contours. Negative (easterly) anomalies less than -1 ms^{-1} are shaded light with dashed contours. Contour interval is 2 ms^{-1}, with contours starting at ± 1 ms^{-1}. Zero contour is shown thick solid. Vertical axis is atmospheric pressure (mb) and horizontal axis is longitude.

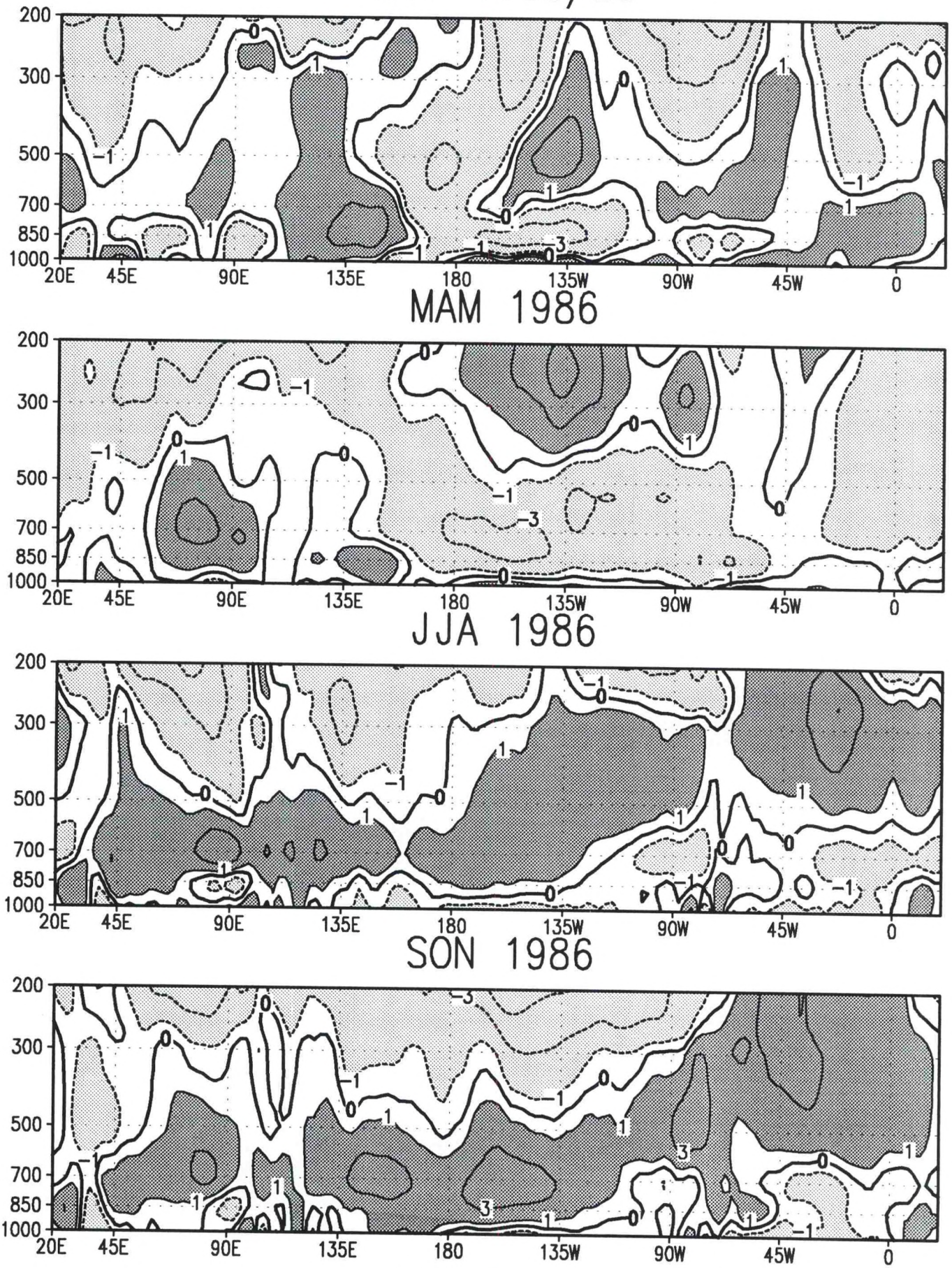

Zonal Wind Anomaly (ms^{-1})

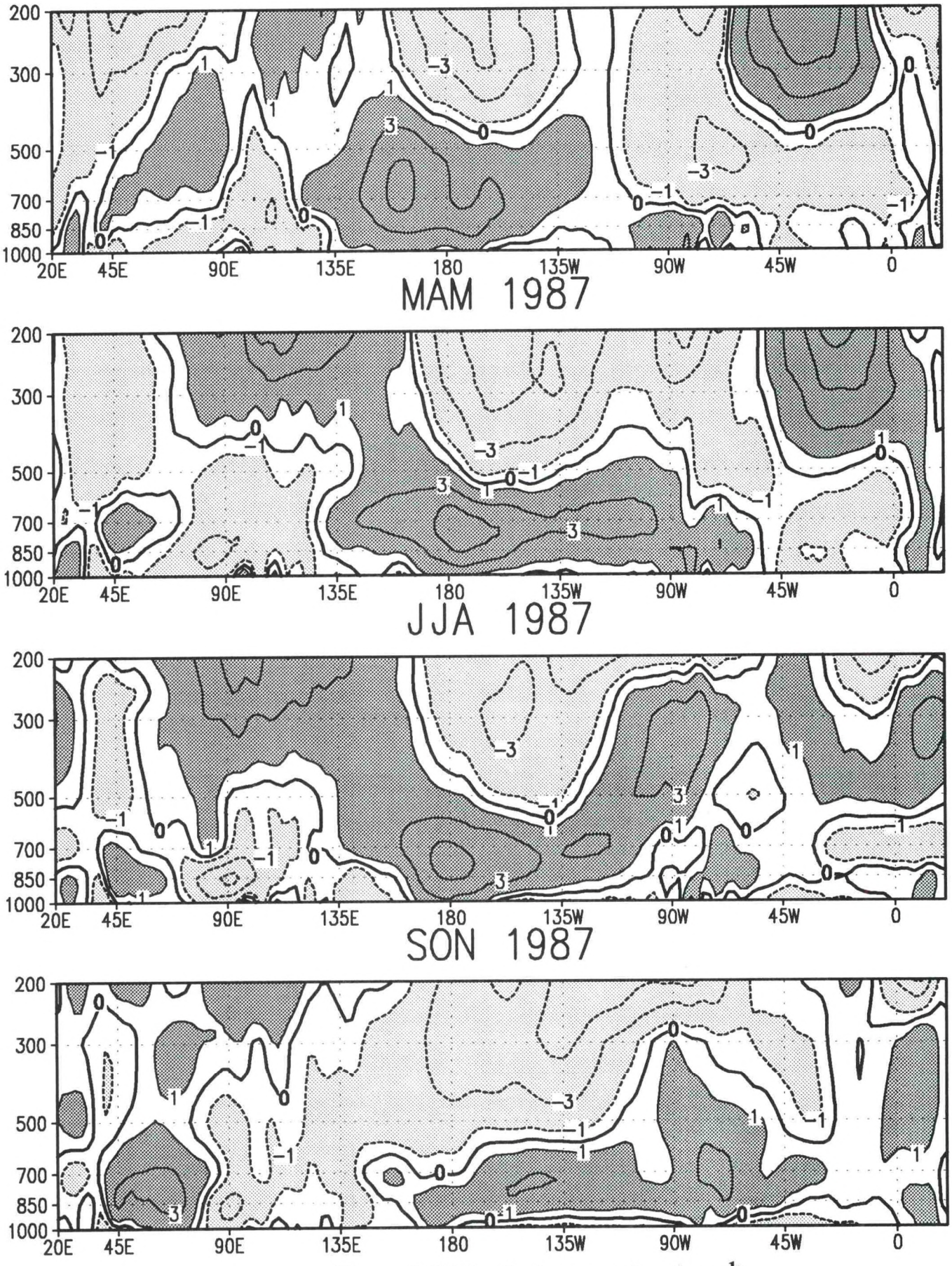

Zonal Wind Anomaly (ms^{-1})

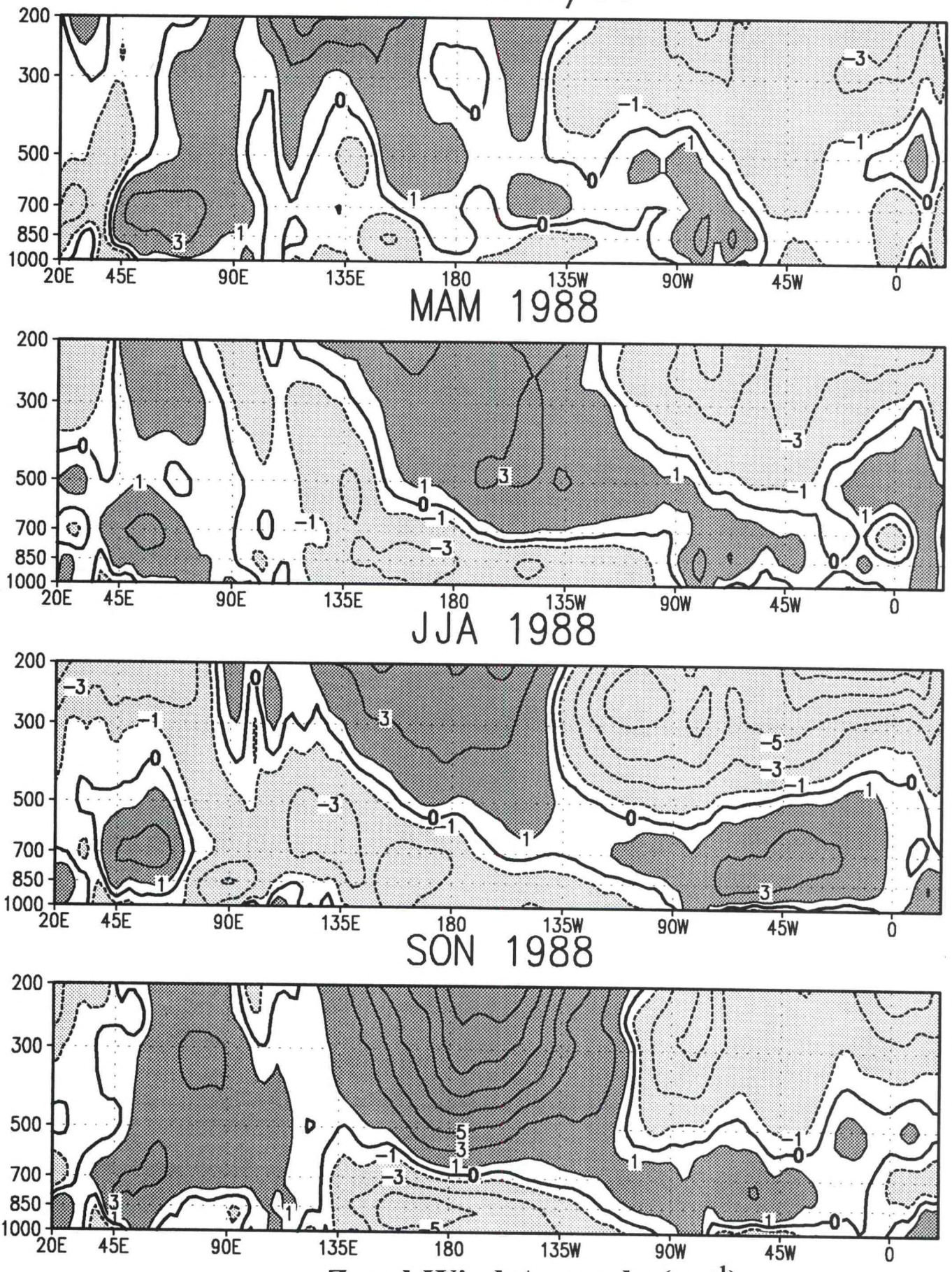

Zonal Wind Anomaly (ms^{-1})

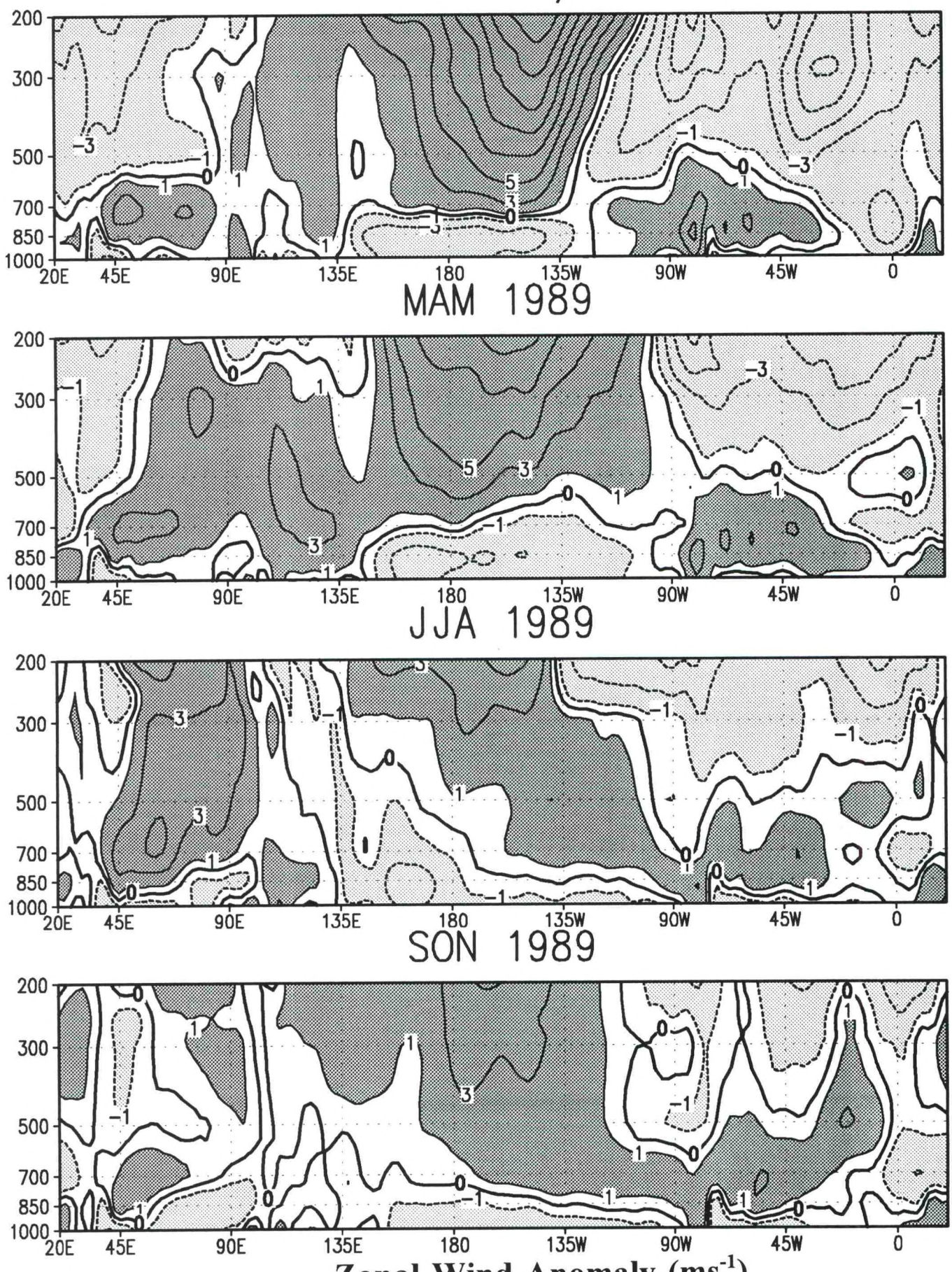
DJF 1988/89
MAM 1989
JJA 1989
SON 1989
200
300
500
700
850
1000
20E
45E
90E
135E
180
135W
90W
45W
0
Zonal Wind Anomaly (ms-1)

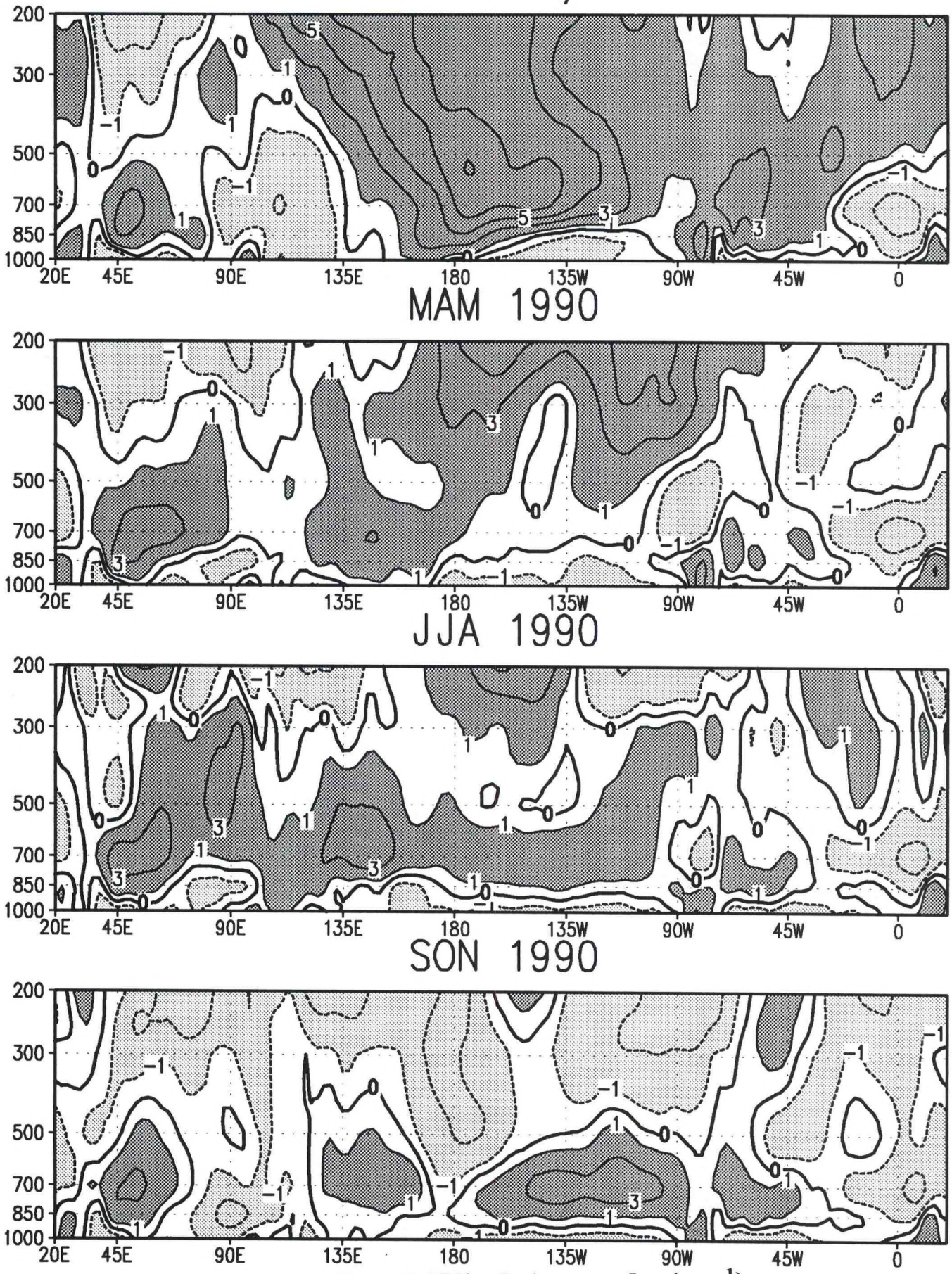

Zonal Wind Anomaly (ms^{-1})

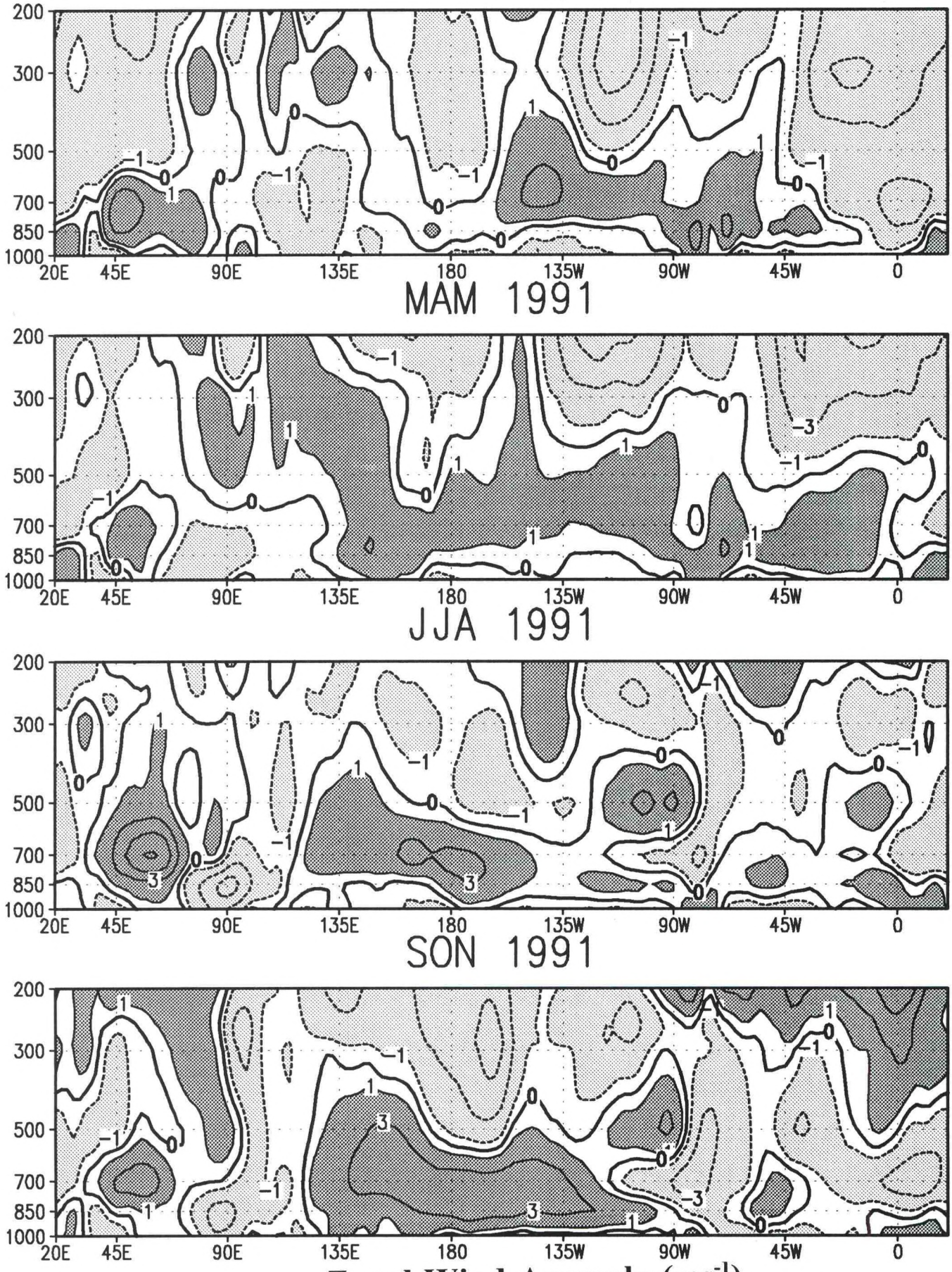
DJF 1990/91
MAM 1991
JJA 1991
SON 1991
200
300
500
700
850
1000
20E
45E
90E
135E
180
135W
90W
45W
0
Zonal Wind Anomaly (ms-1)

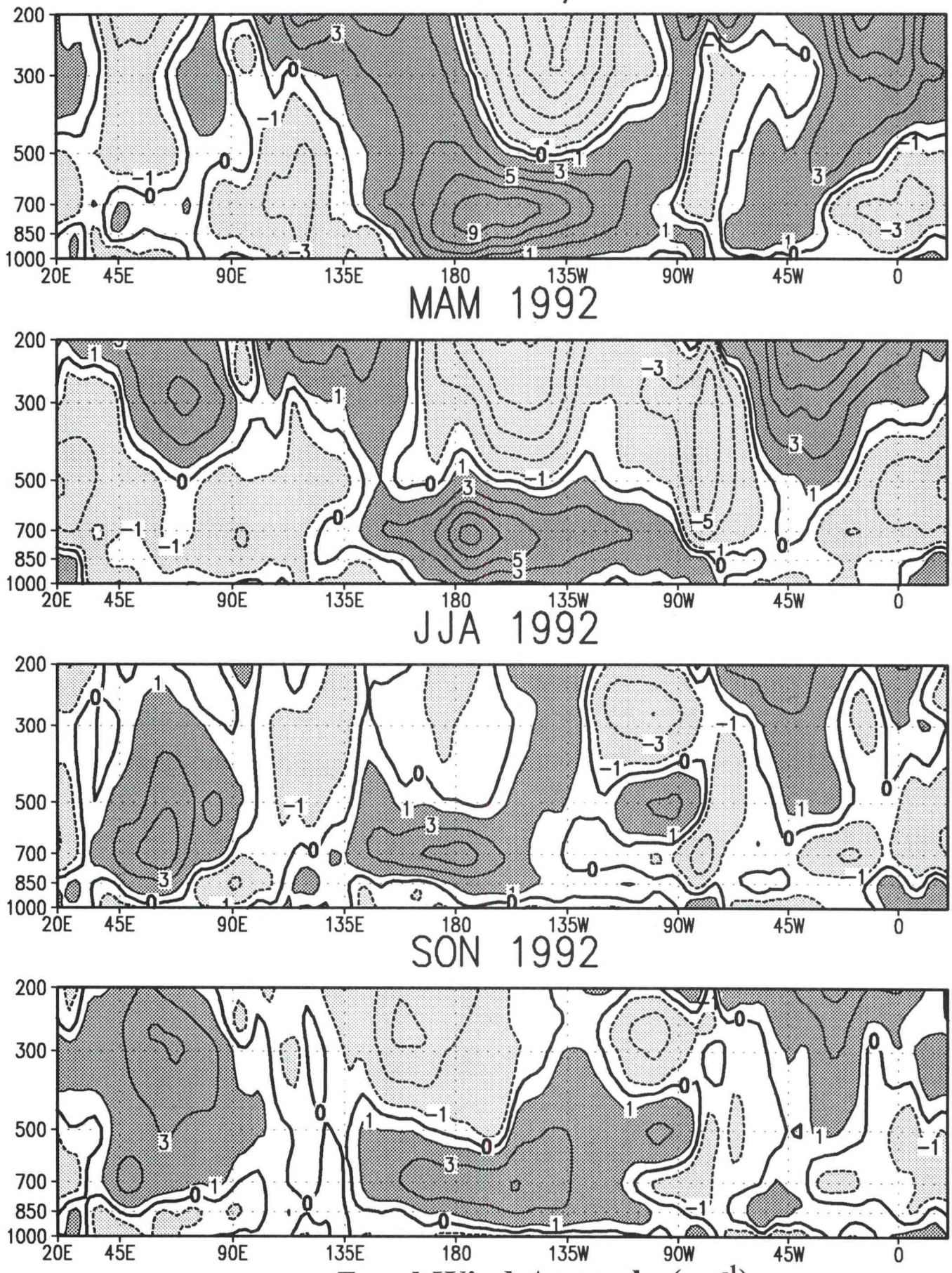
DJF 1991/92
MAM 1992
JJA 1992
SON 1992
200
300
500
700
850
1000
20E
45E
90E
135E
180
135W
90W
45W
0
Zonal Wind Anomaly (ms-1)

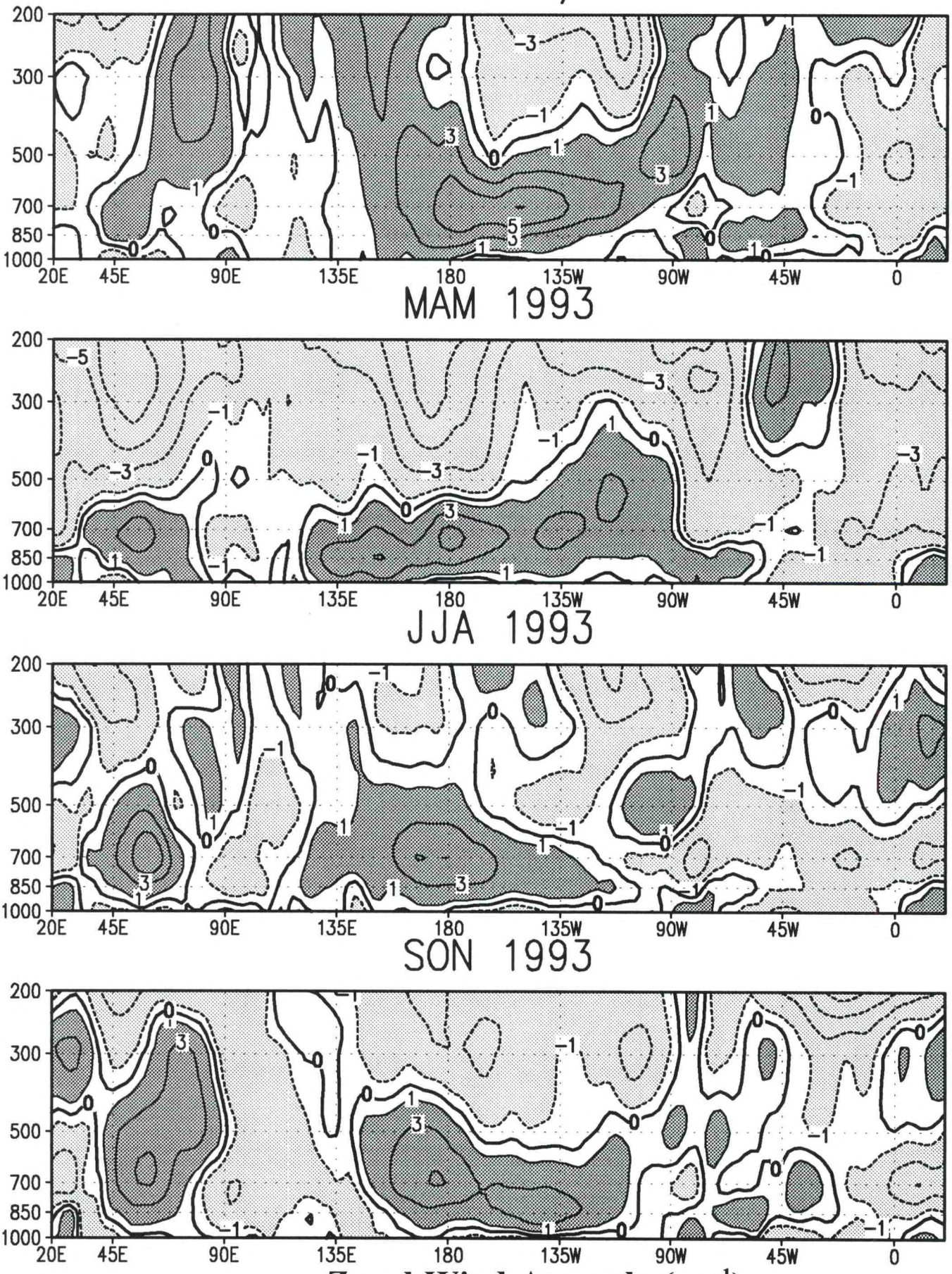
DJF 1992/93
MAM 1993
JJA 1993
SON 1993
200
300
500
700
850
1000
20E
45E
90E
135E
180
135W
90W
45W
0
Zonal Wind Anomaly (ms-1)

200 mb GEOPOTENTIAL HEIGHT ANOMALY

Time-Longitude Section (pp. 124-127): Monthly-mean 200-mb geopotential height anomalies (m) along the equator over the Pacific Ocean between 120°E and 80°W. Contour interval is 20 m. Positive anomalies greater than 20 m are shaded dark with solid contours. Negative anomalies below -20 m are shaded light with dashed contours. Zero contour is shown thick solid.

Time-longitude Section (pp. 128-131): Monthly-mean 200-mb geopotential height anomalies (m) along the equator for all longitudes. Contour interval is 20 m. Positive anomalies greater than 20 m are shaded dark with solid contours. Negative anomalies below -20 m are shaded light with dashed contours. Zero contour is shown thick solid.

Time-Latitude Section (pp. 132-135): Monthly-mean 200-mb geopotential height anomalies (m), averaged at each latitude over the Pacific sector (120°E to 90°W), for latitudes between 75°S and 75°N. Contour interval is 15 m, and contours start at ±10 m. Positive anomalies greater than 10 m are shaded dark with solid contours. Negative anomalies below -10 m are shaded light with dashed contours. Zero contour is shown thick solid.

Cautionary Note:

A revision of the objective analysis scheme of the NMC global spectral Medium Range Forecast Model (MRF) was implemented on 25 June 1991. The new objective analysis is still based on optimal interpolation equations, but is solved globally directly in the model's coordinate system (spectral space in the horizontal and sigma coordinates in the vertical). This system is referred to as Spectral Statistical Interpolation (SSI).

In this new system, small-scale noise is removed, and smoother fields are evident, particularly in the tropics. The result is a "bias" in the height fields compared to the 1979-1988 climatological mean fields because the new system diagnoses heights from analyzed temperature rather than directly analyzing heights. Thus, height anomaly fields in the tropics after June 1991 should be interpreted with caution.

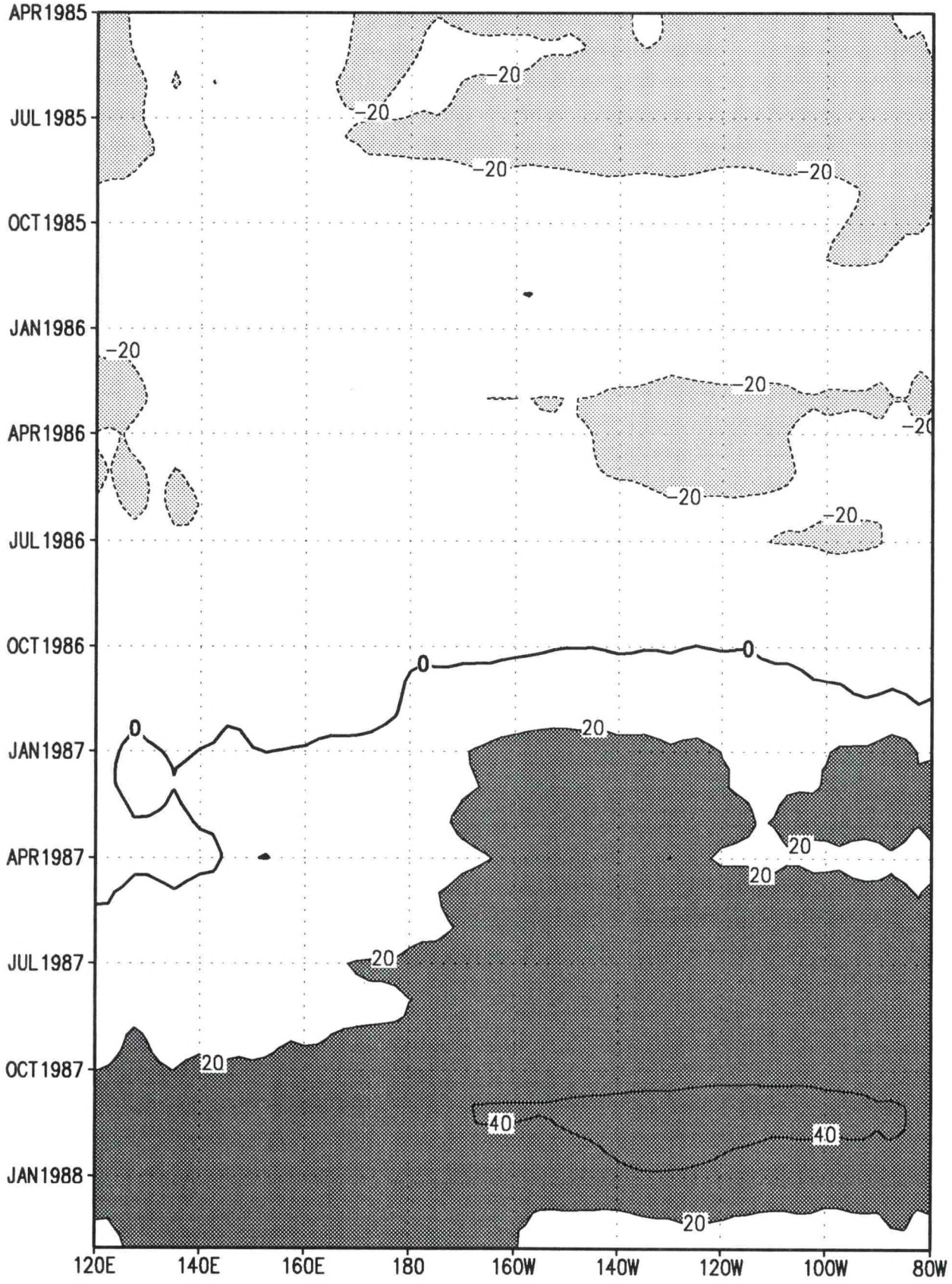

200 mb Height Anomaly (m)

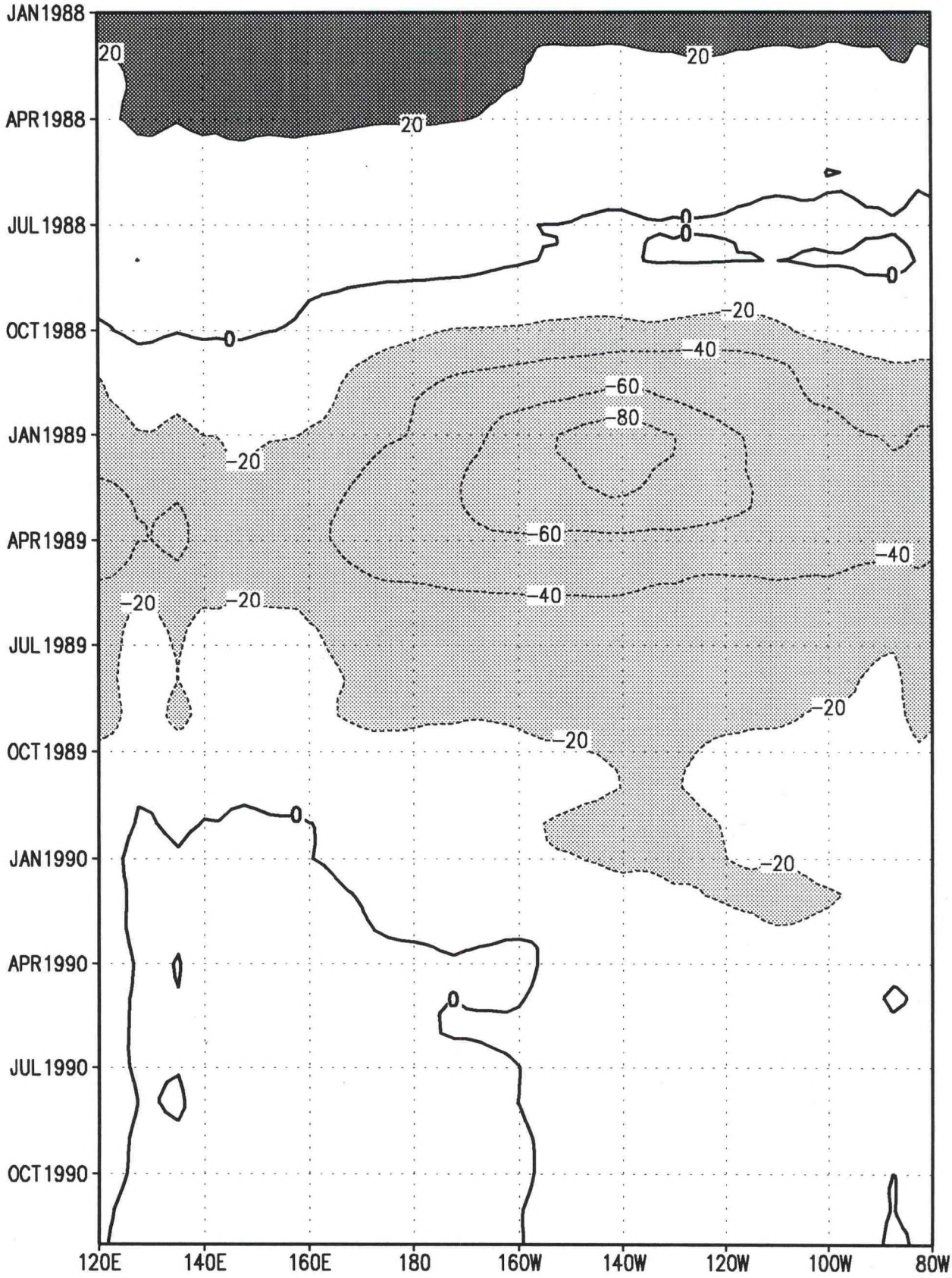

200 mb Height Anomaly (m)

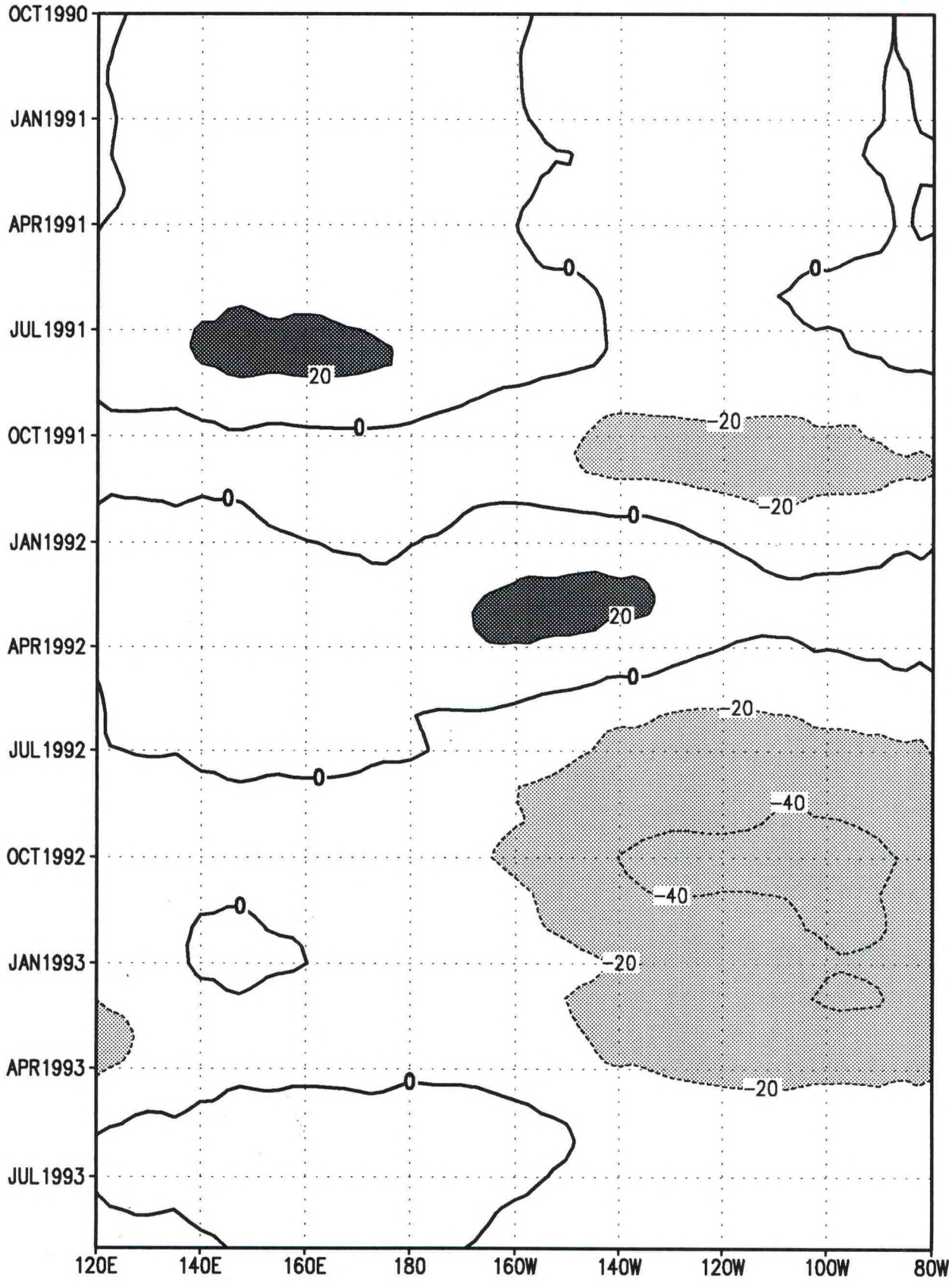

200 mb Height Anomaly (m)

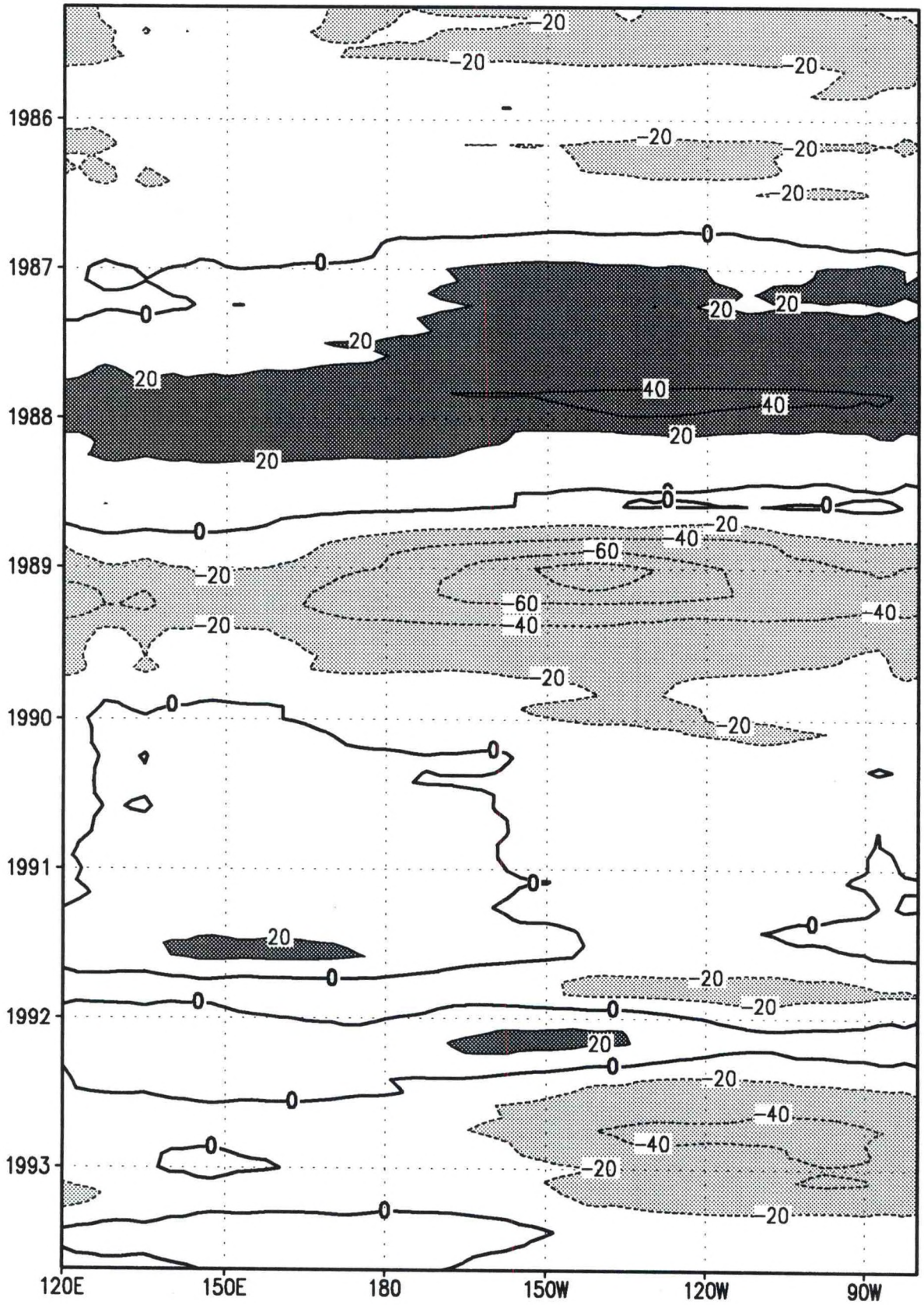

200 mb Height Anomaly (m)

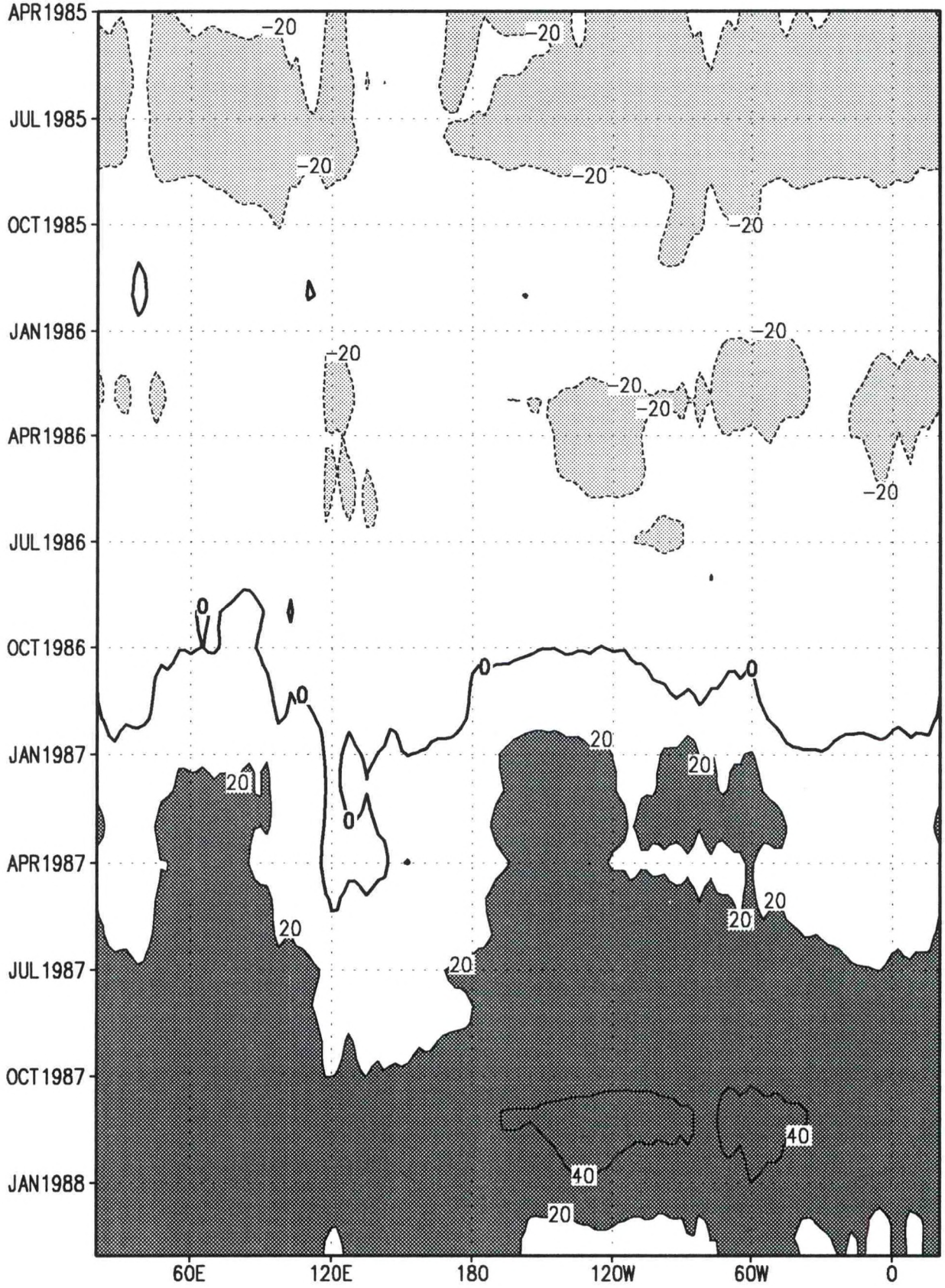

200 mb Height Anomaly (m)

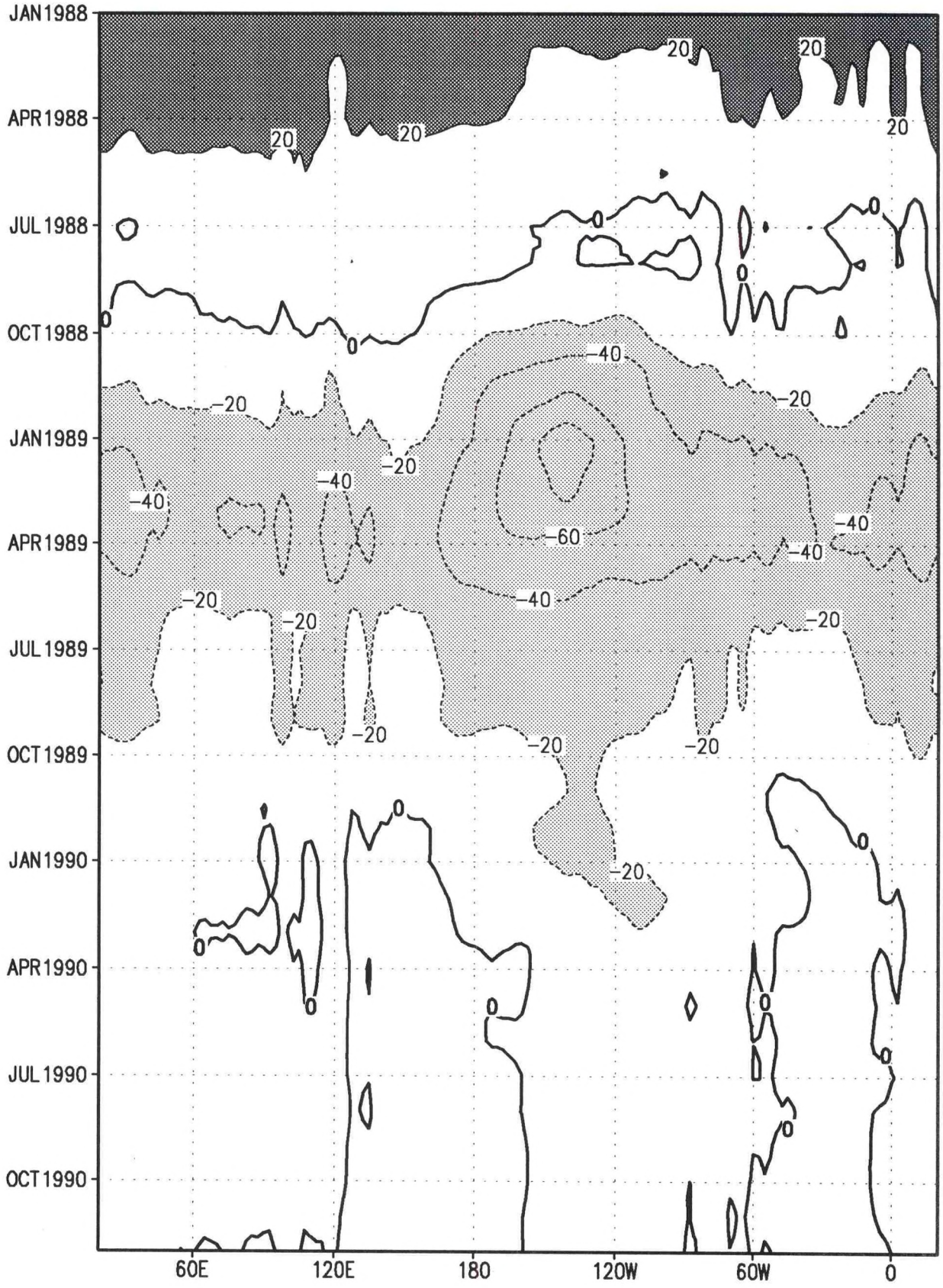

200 mb Height Anomaly (m)

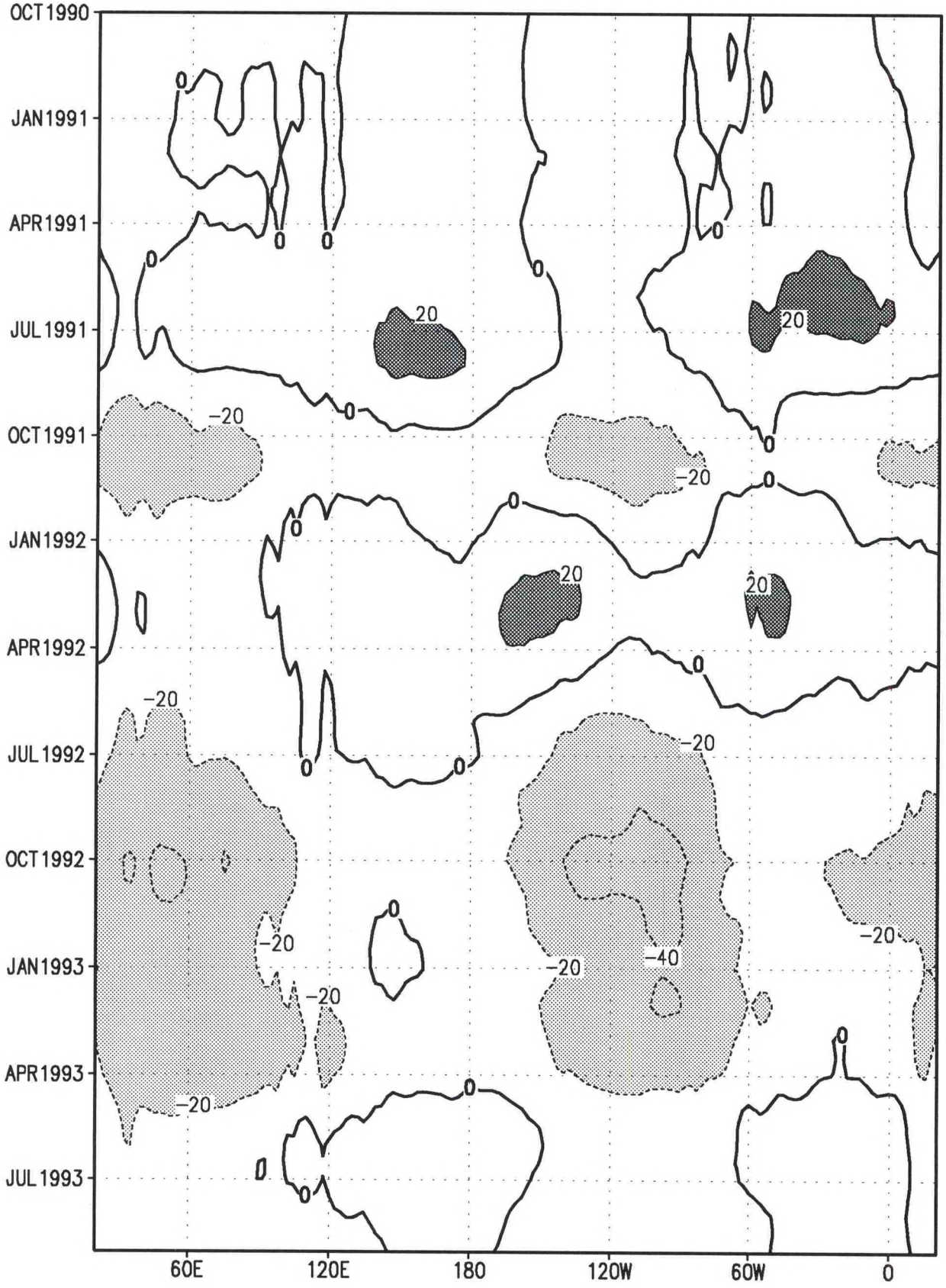

200 mb Height Anomaly (m)

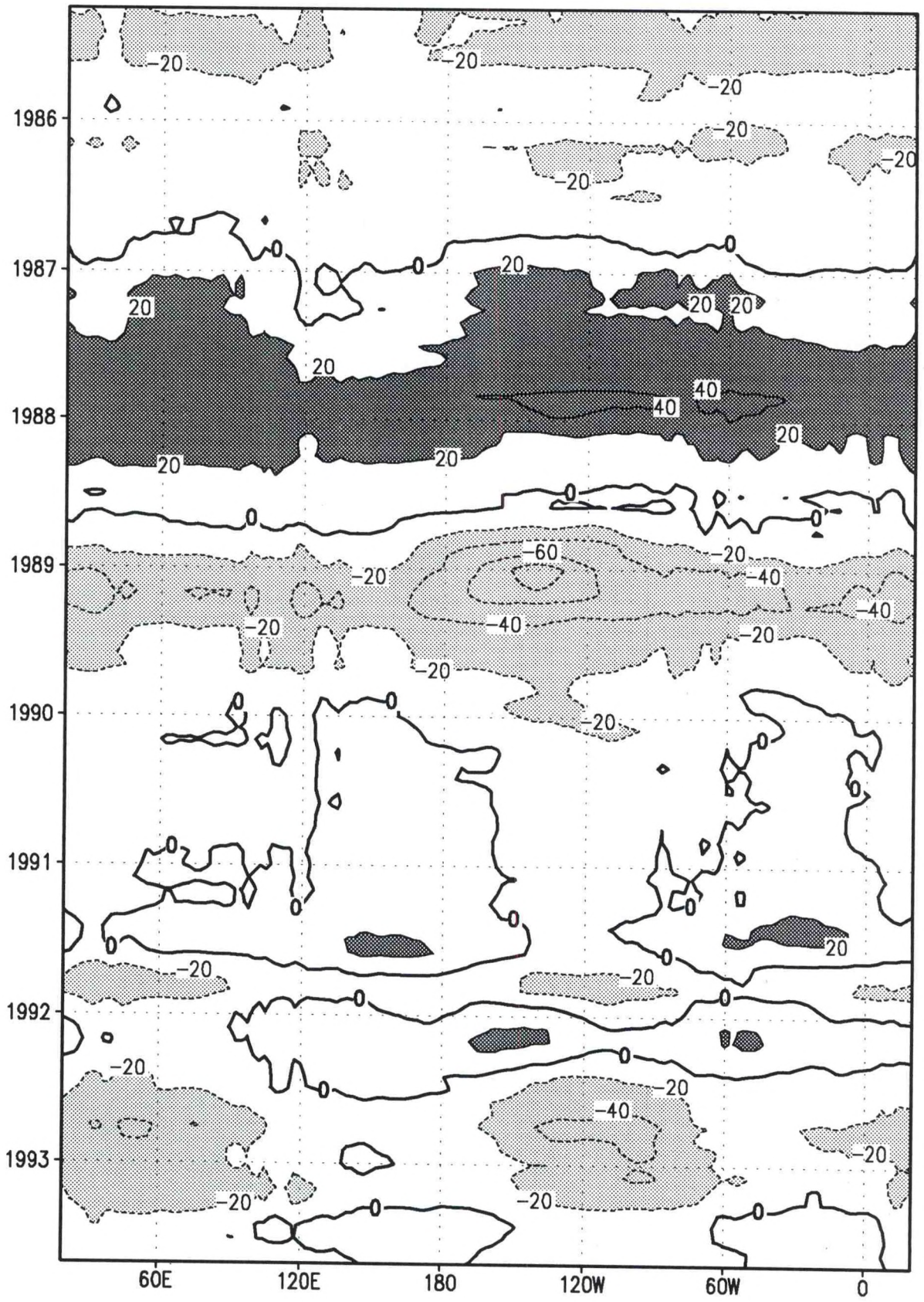

200 mb Height Anomaly (m)

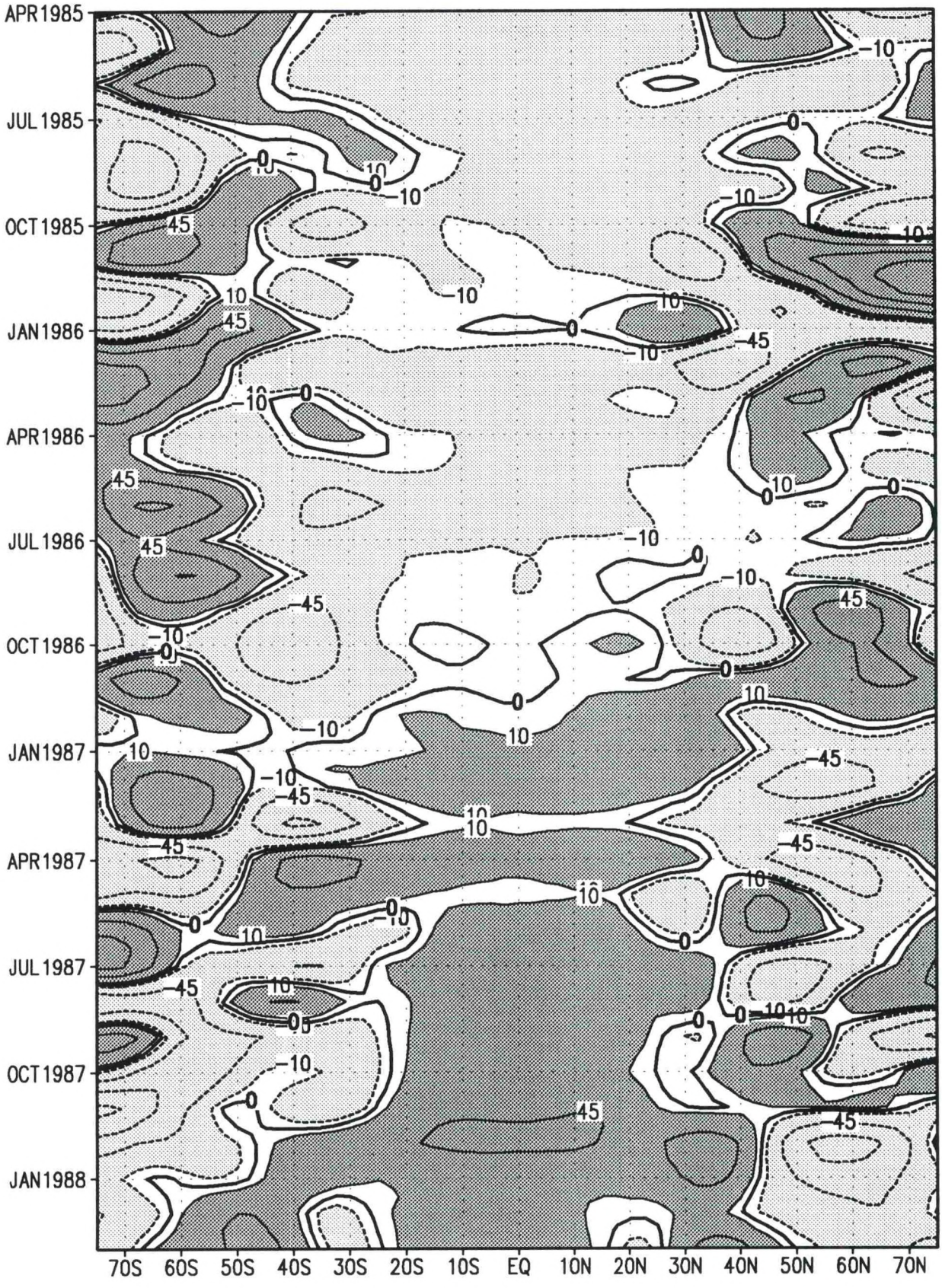

200 mb Height Anomaly (m)

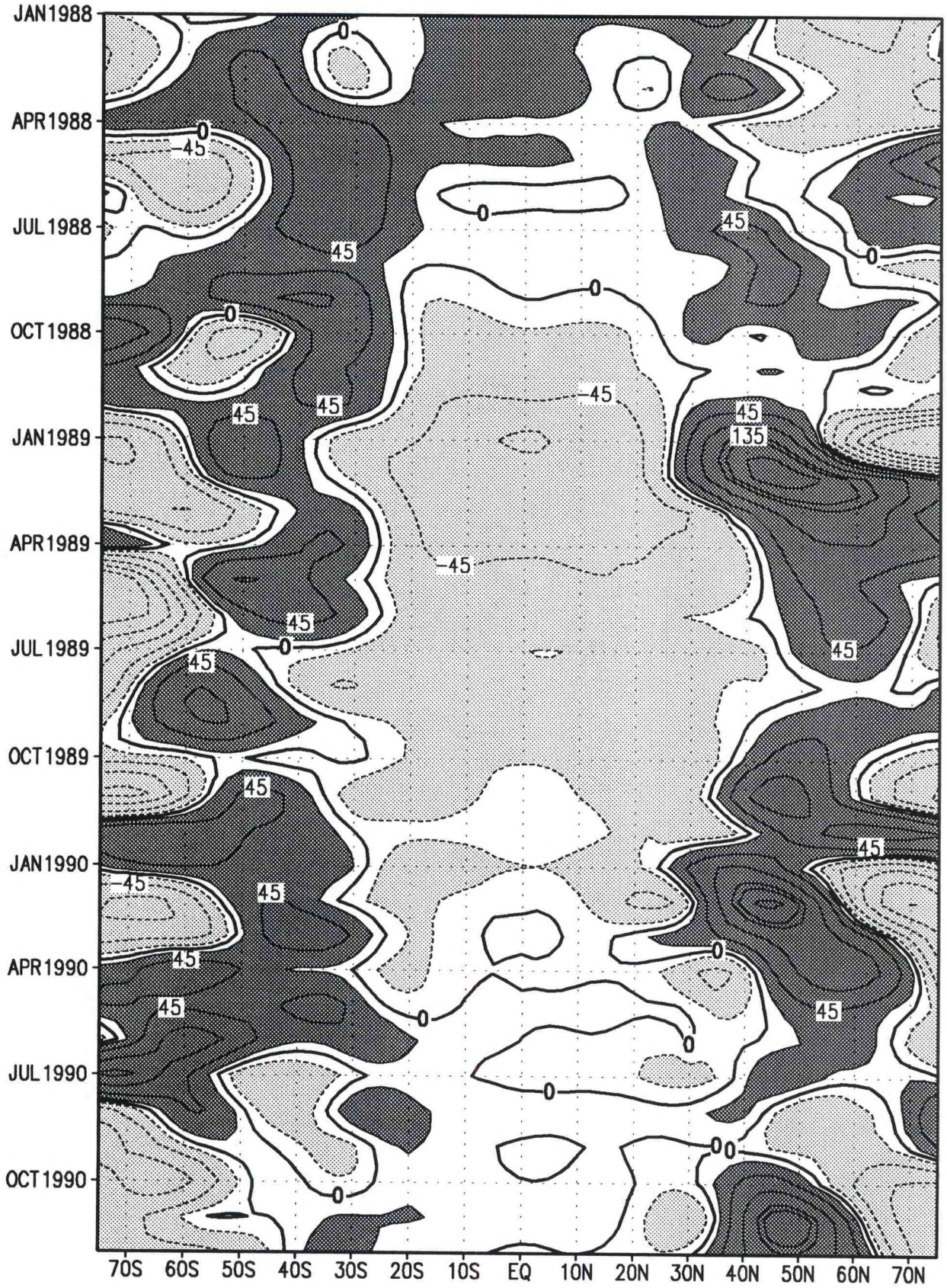

200 mb Height Anomaly (m)

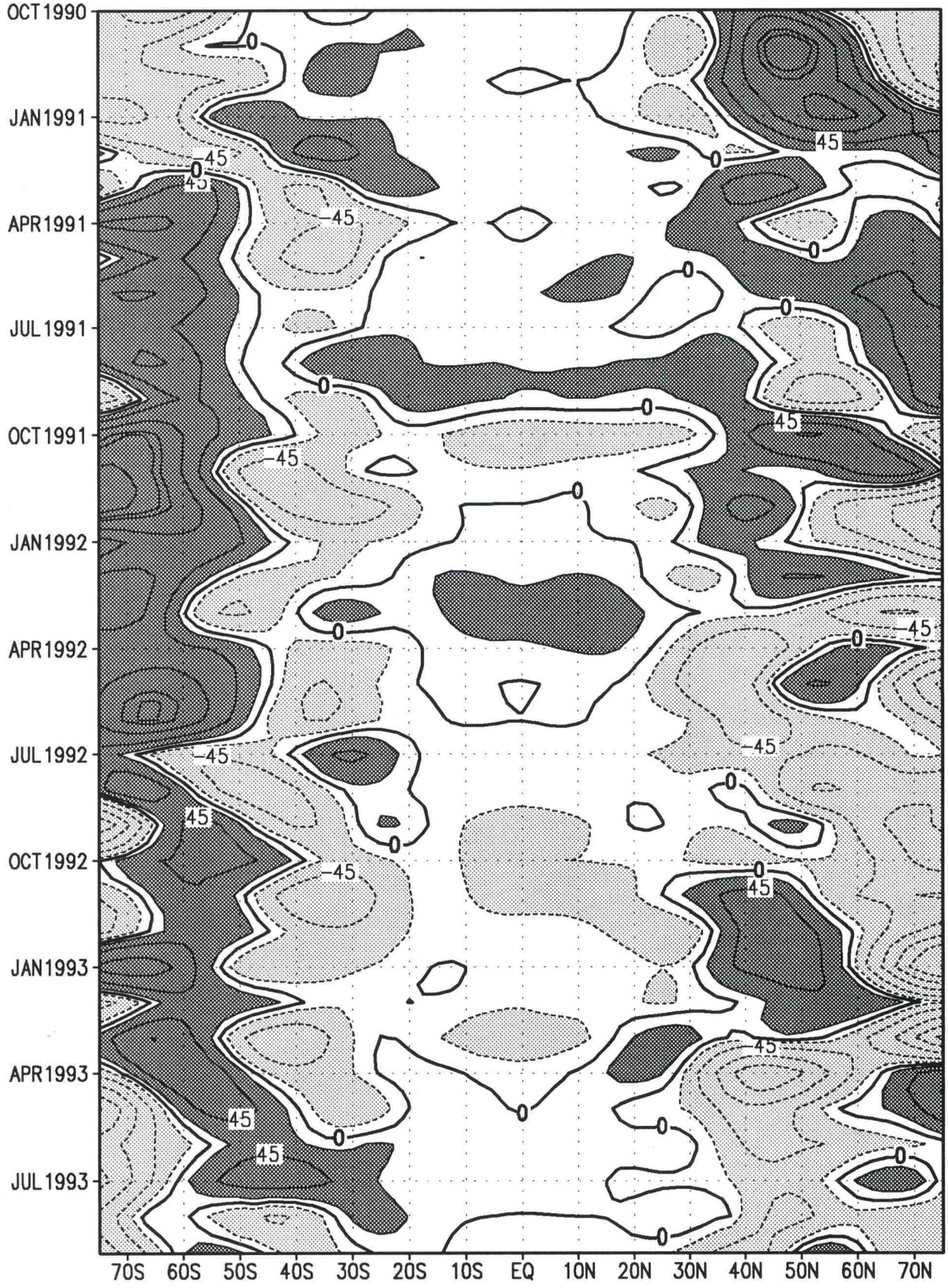

200 mb Height Anomaly (m)

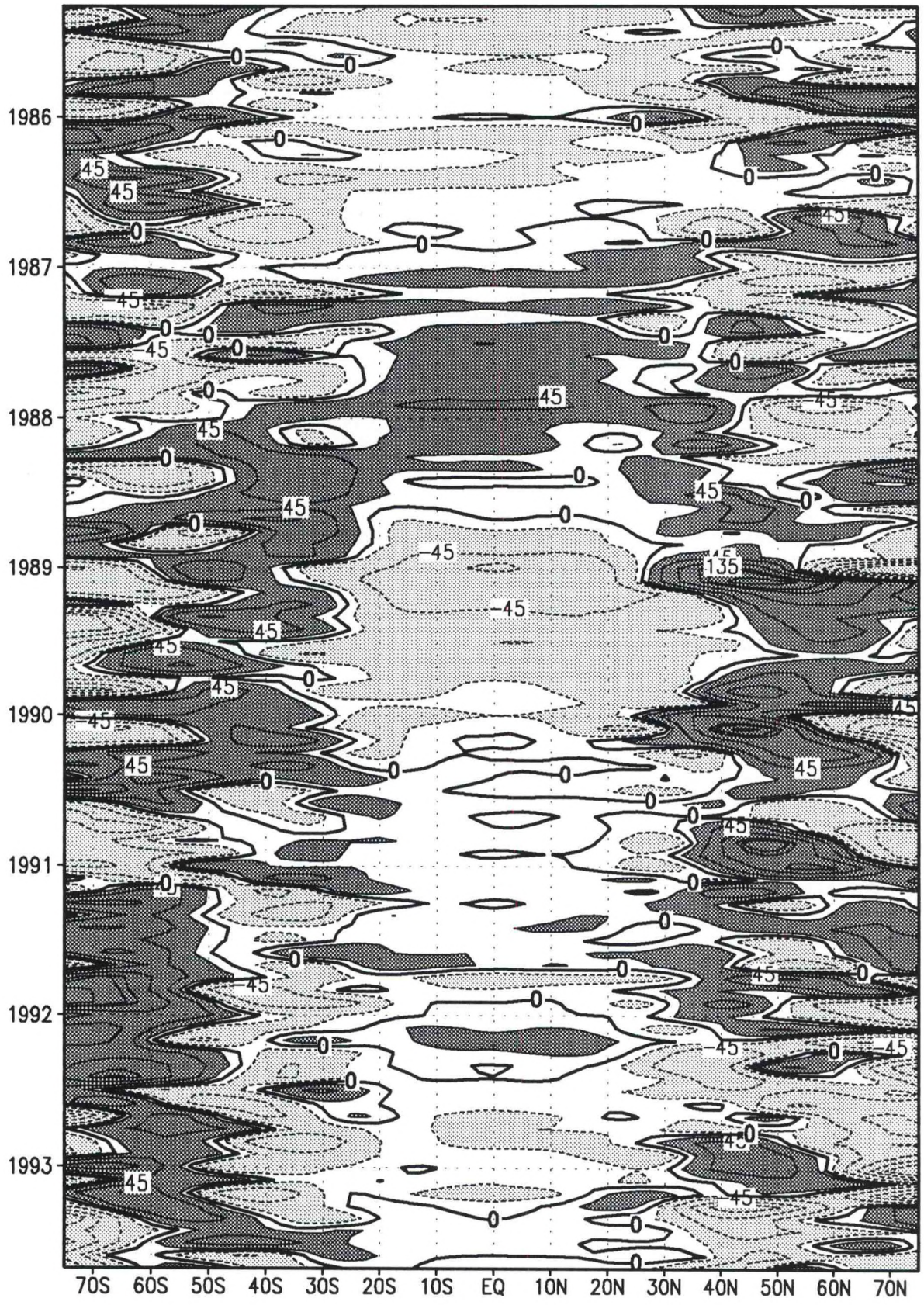

200 mb Height Anomaly (m)

EQUATORIAL GEOPOTENTIAL HEIGHT CROSS-SECTION

Height-Longitude Section (pp. 137-144): Seasonal-mean geopotential height anomalies (m) along the equator over all longitudes. Contour interval is 10 m, with negative values dashed and shaded light, and positive values solid and shaded dark. Zero contour is shown thick solid. Vertical axis is atmospheric pressure (mb) and horizontal axis is longitude.

Cautionary Note:

A revision of the objective analysis scheme of the NMC global spectral Medium Range Forecast Model (MRF) was implemented on 25 June 1991. The new objective analysis is still based on optimal interpolation equations, but is solved globally directly in the model's coordinate system (spectral space in the horizontal and sigma coordinates in the vertical). This system is referred to as Spectral Statistical Interpolation (SSI).

In this new system, small-scale noise is removed, and smoother fields are evident, particularly in the tropics. The result is a "bias" in the height fields compared to the 1979-1988 climatological mean fields because the new system diagnoses heights from analyzed temperature rather than directly analyzing heights. Thus, height anomaly fields in the tropics after June 1991 should be interpreted with caution.

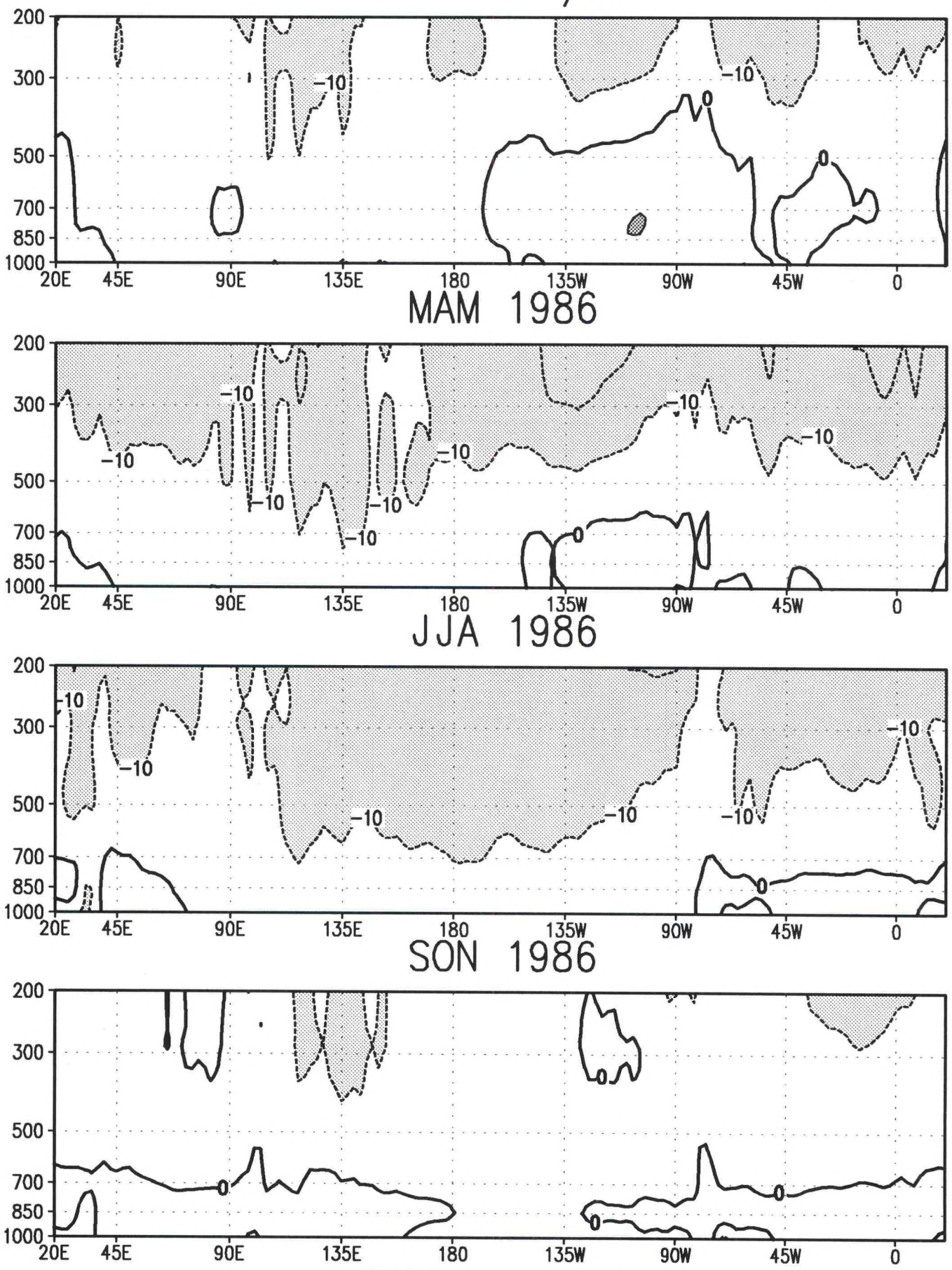

Height Anomaly (m)

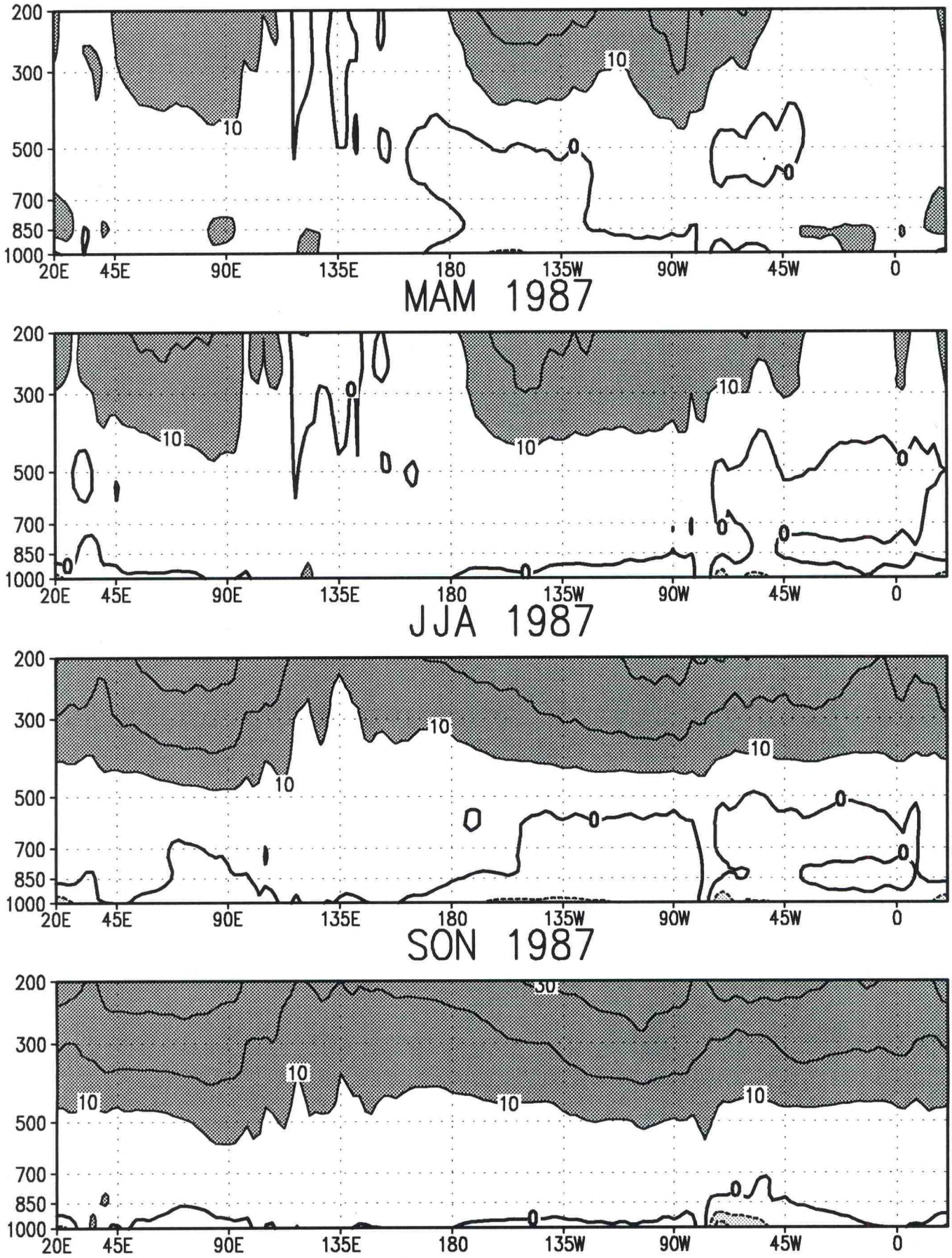

Height Anomaly (m)

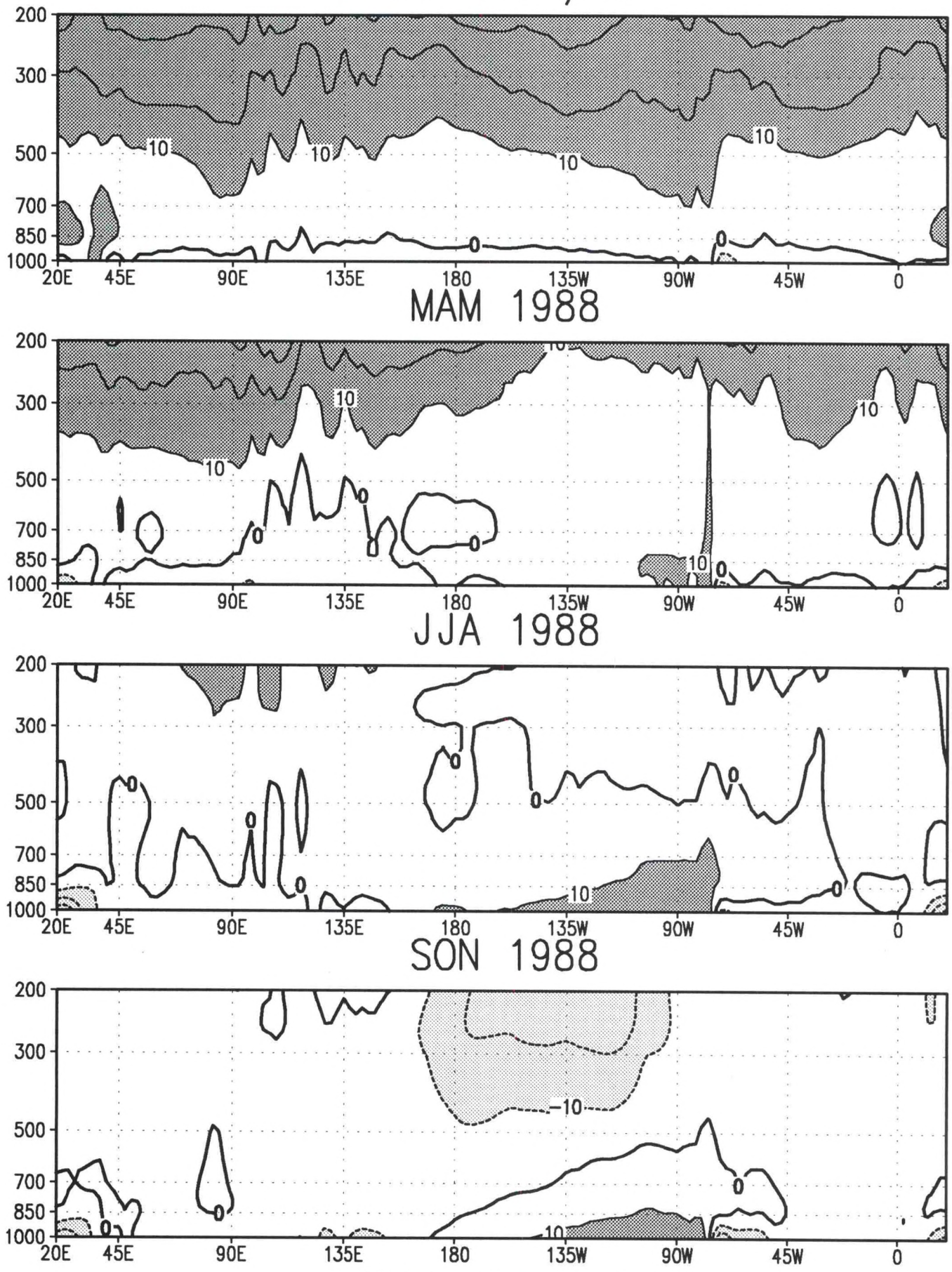

Height Anomaly (m)

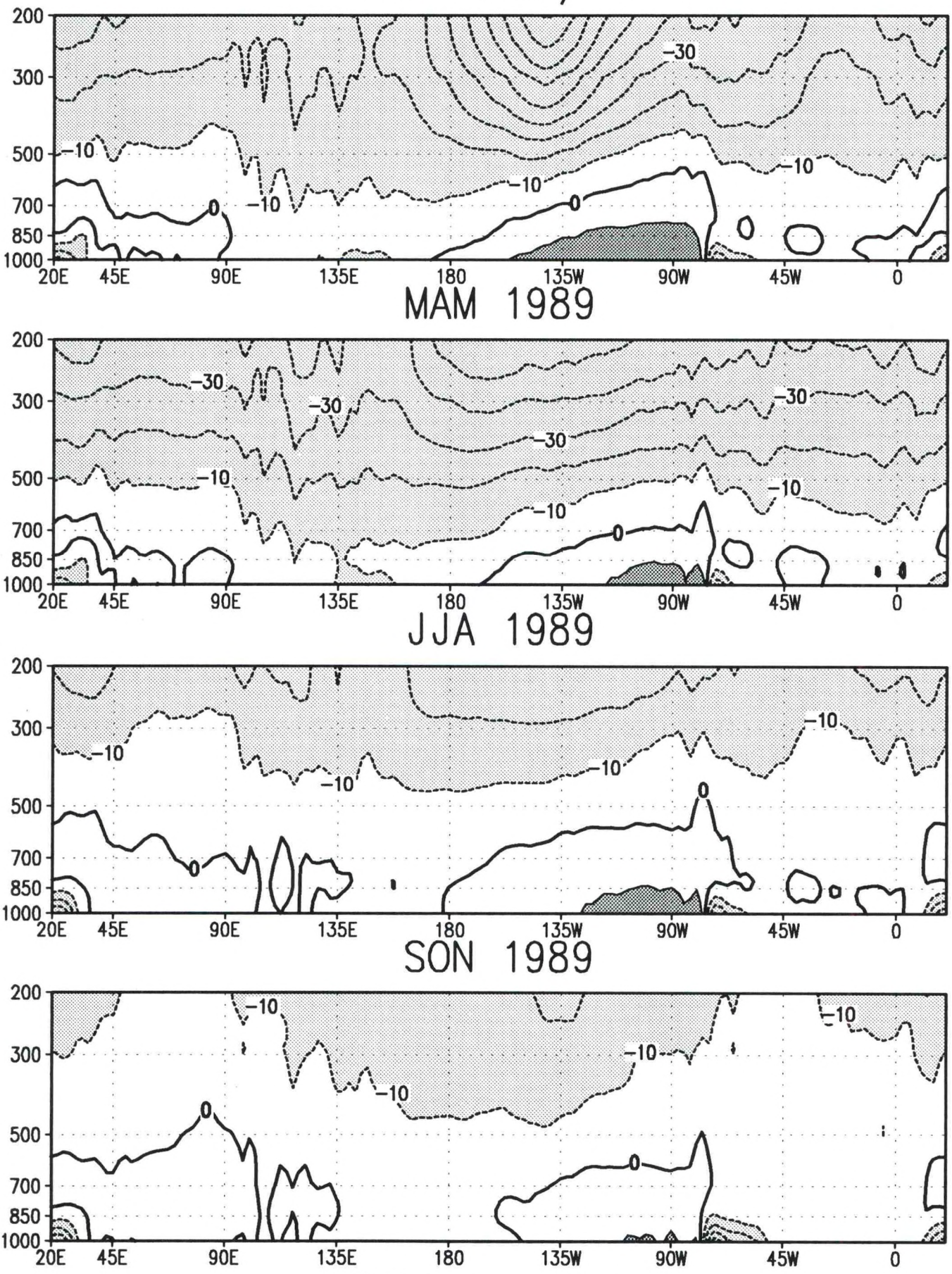

Height Anomaly (m)

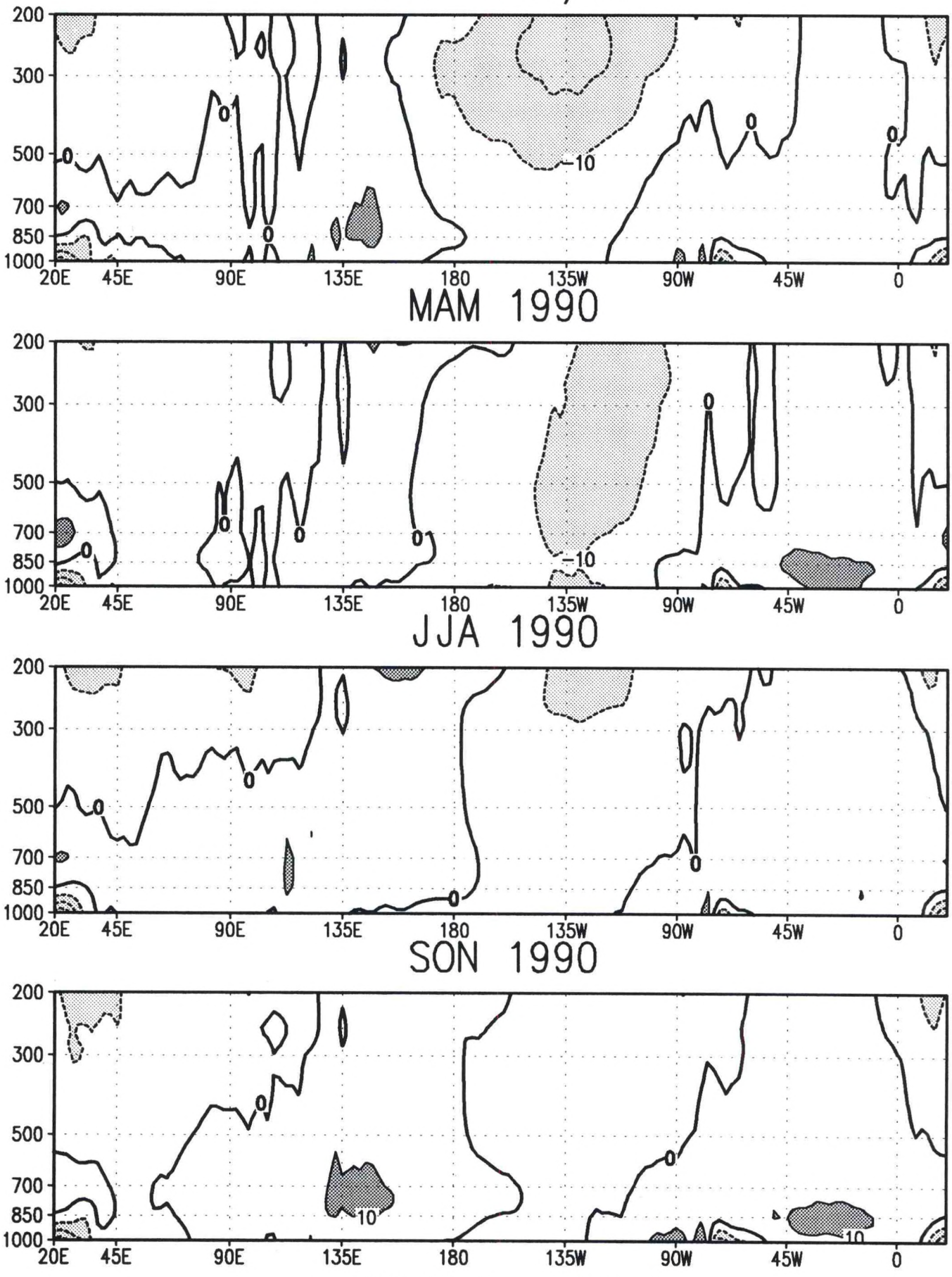

Height Anomaly (m)

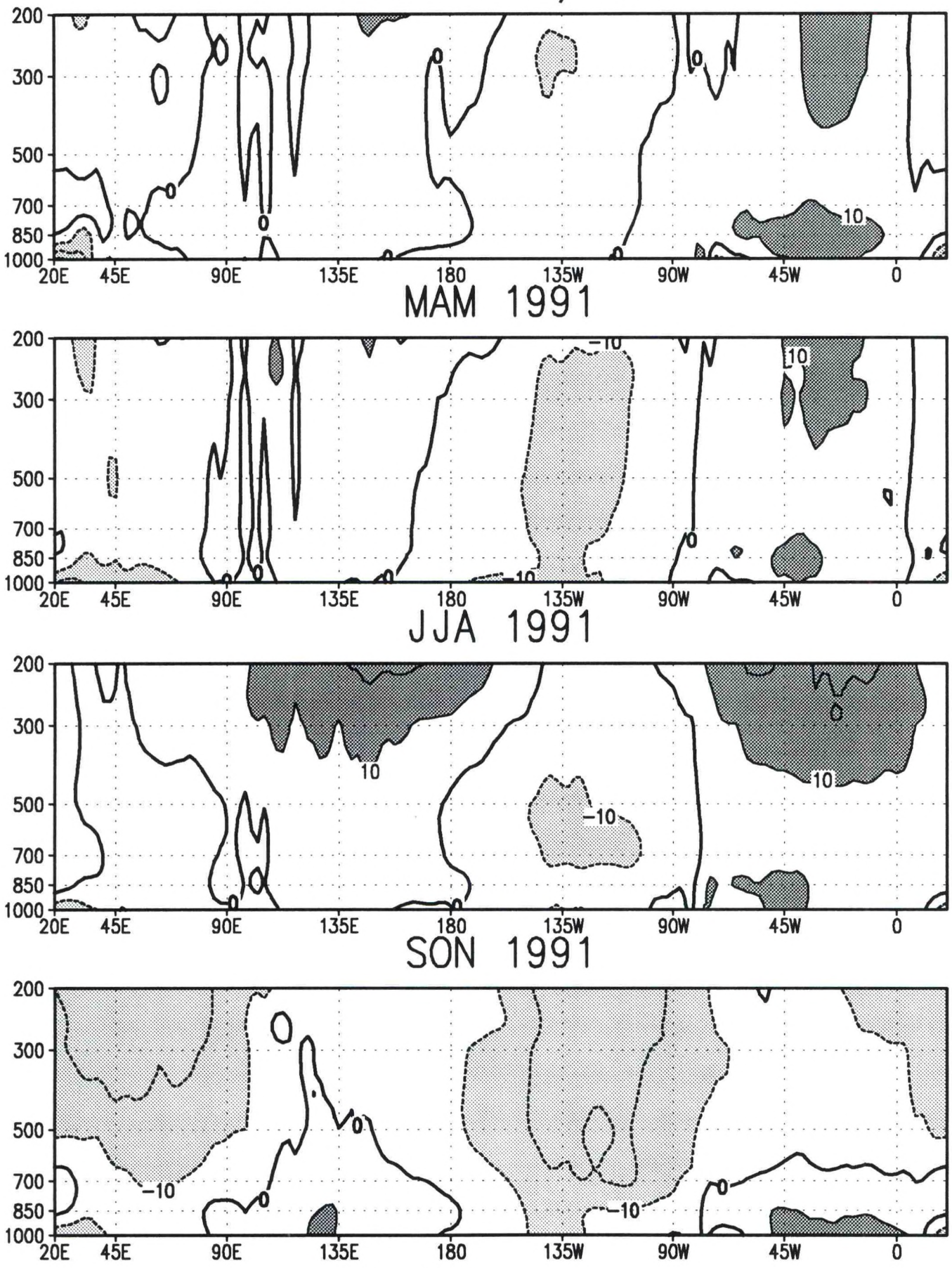

Height Anomaly (m)

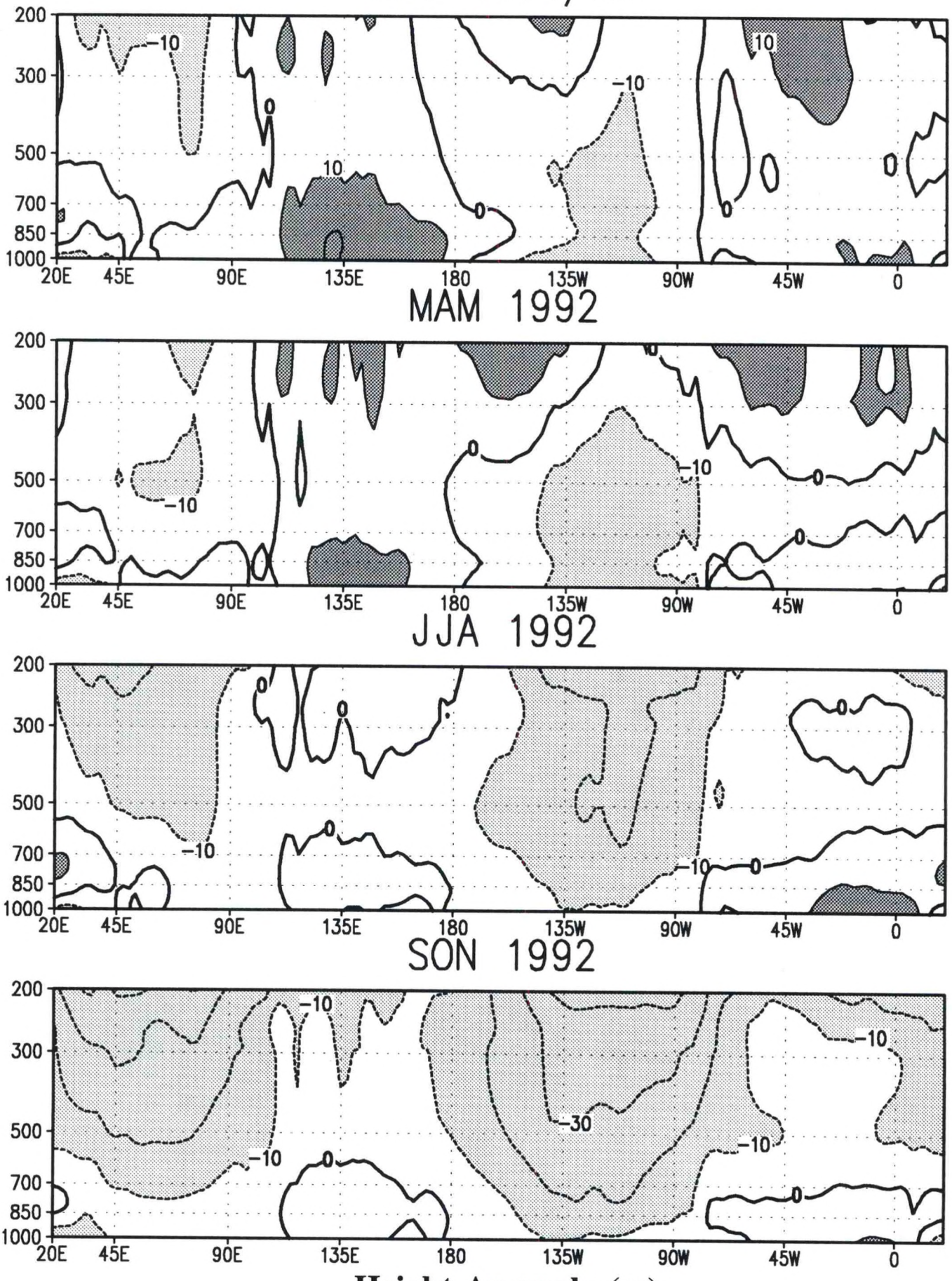

Height Anomaly (m)

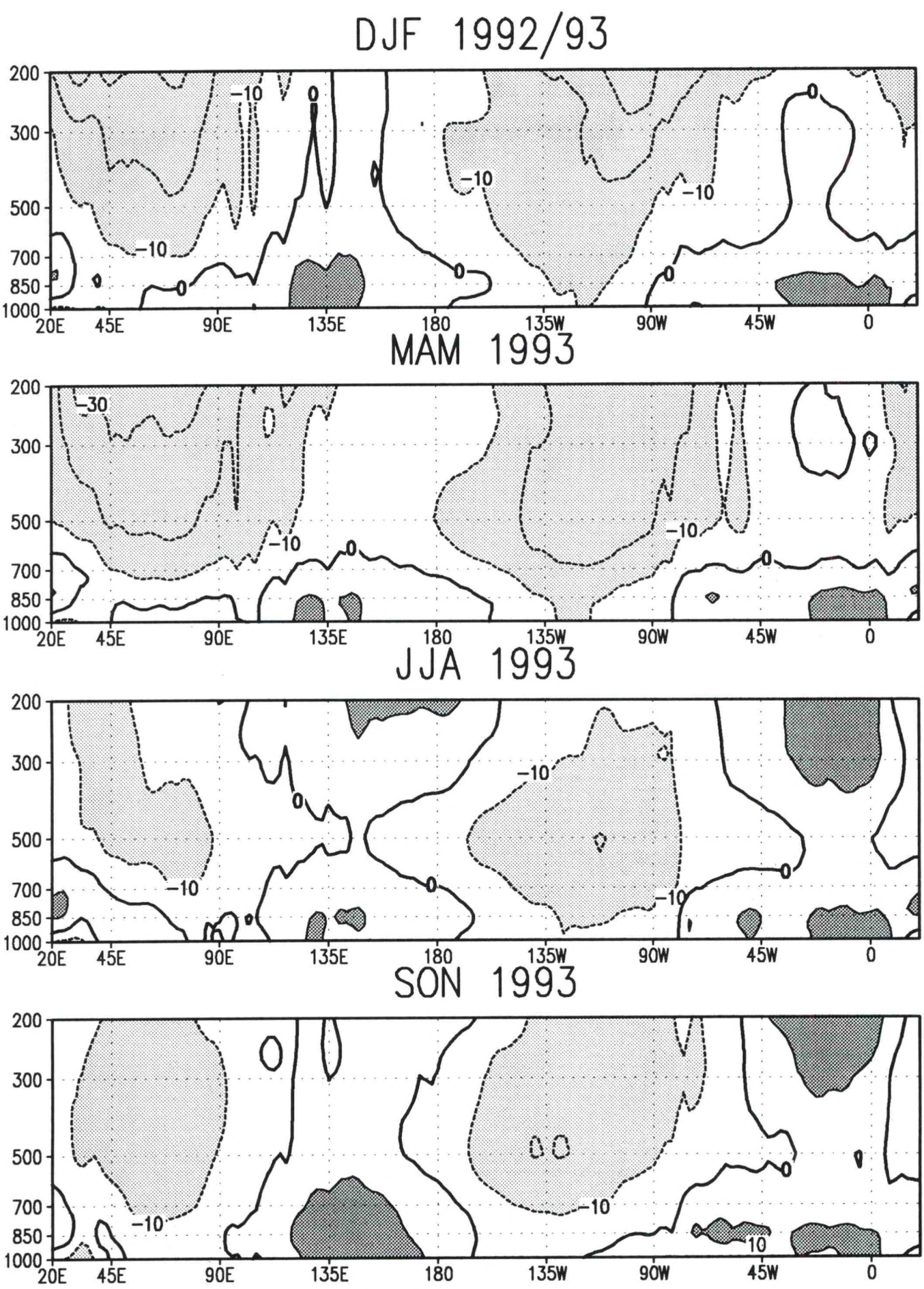

Height Anomaly (m)

SEA-LEVEL PRESSURE (SLP) ANOMALY

Seasonal Maps (pp. 146-153): Seasonal-mean SLP anomalies (mb) for all longitudes from 50°N to 50°S. Contour interval is 1 mb, with negative values dashed. Zero contour is shown thick solid.

Time-Longitude Section (pp. 154-157): Monthly-mean SLP anomalies (mb) along the equator over the Pacific Ocean between 120°E and 80°W. Contour interval is 1 mb. Positive anomalies greater than 1 mb are shaded dark with solid contours. Negative anomalies below -1 mb are shaded light with dashed contours. Zero contour is shown thick solid.

Time-Longitude Section (pp. 158-161): Monthly-mean SLP anomalies (mb) along the equator for all longitudes. Contour interval is 1 mb. Positive anomalies greater than 1 mb are shaded dark with solid contours. Negative anomalies below -1 mb are shaded light with dashed contours. Zero contour is shown thick solid.

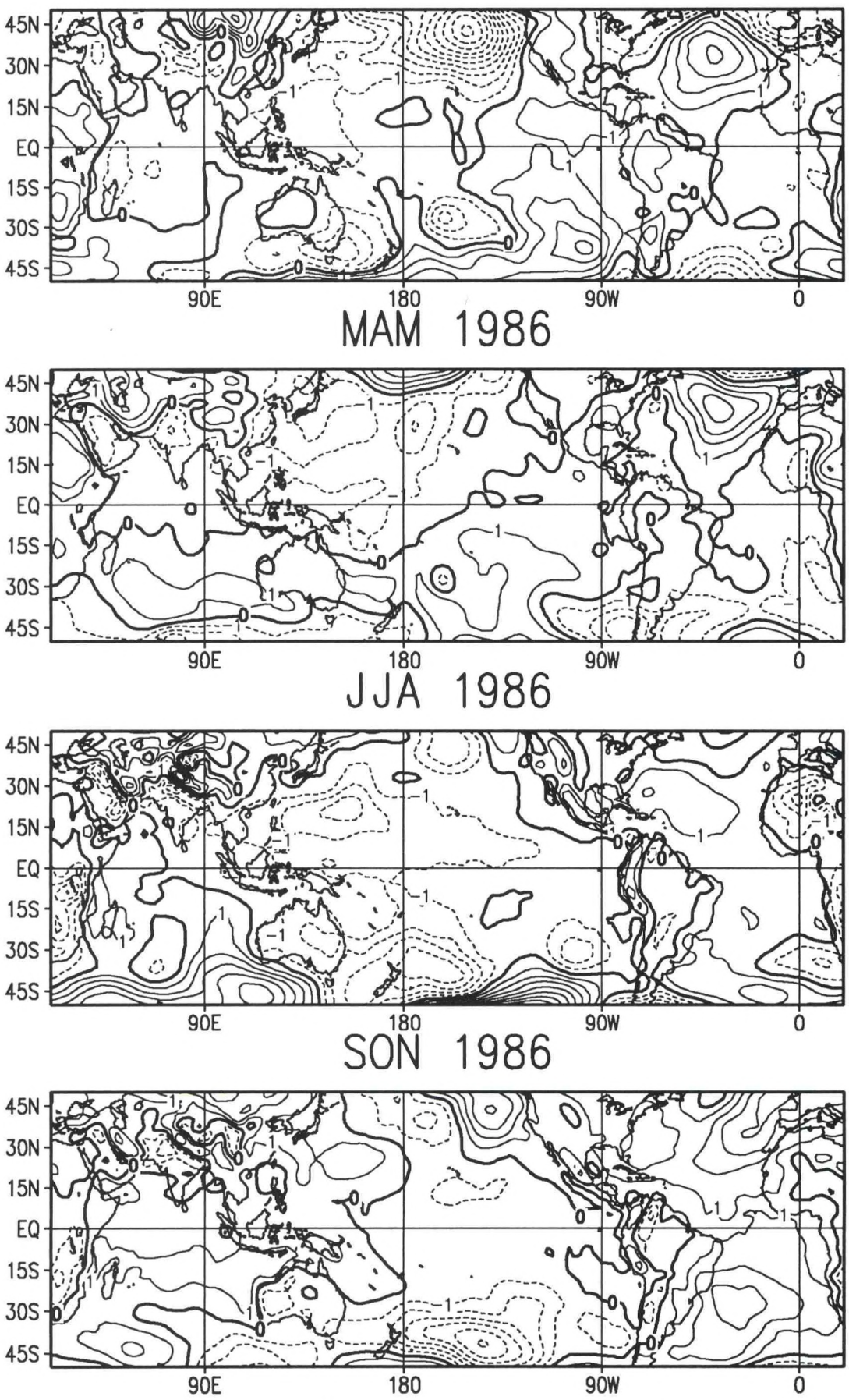

Sea-Level Pressure Anomaly (mb)

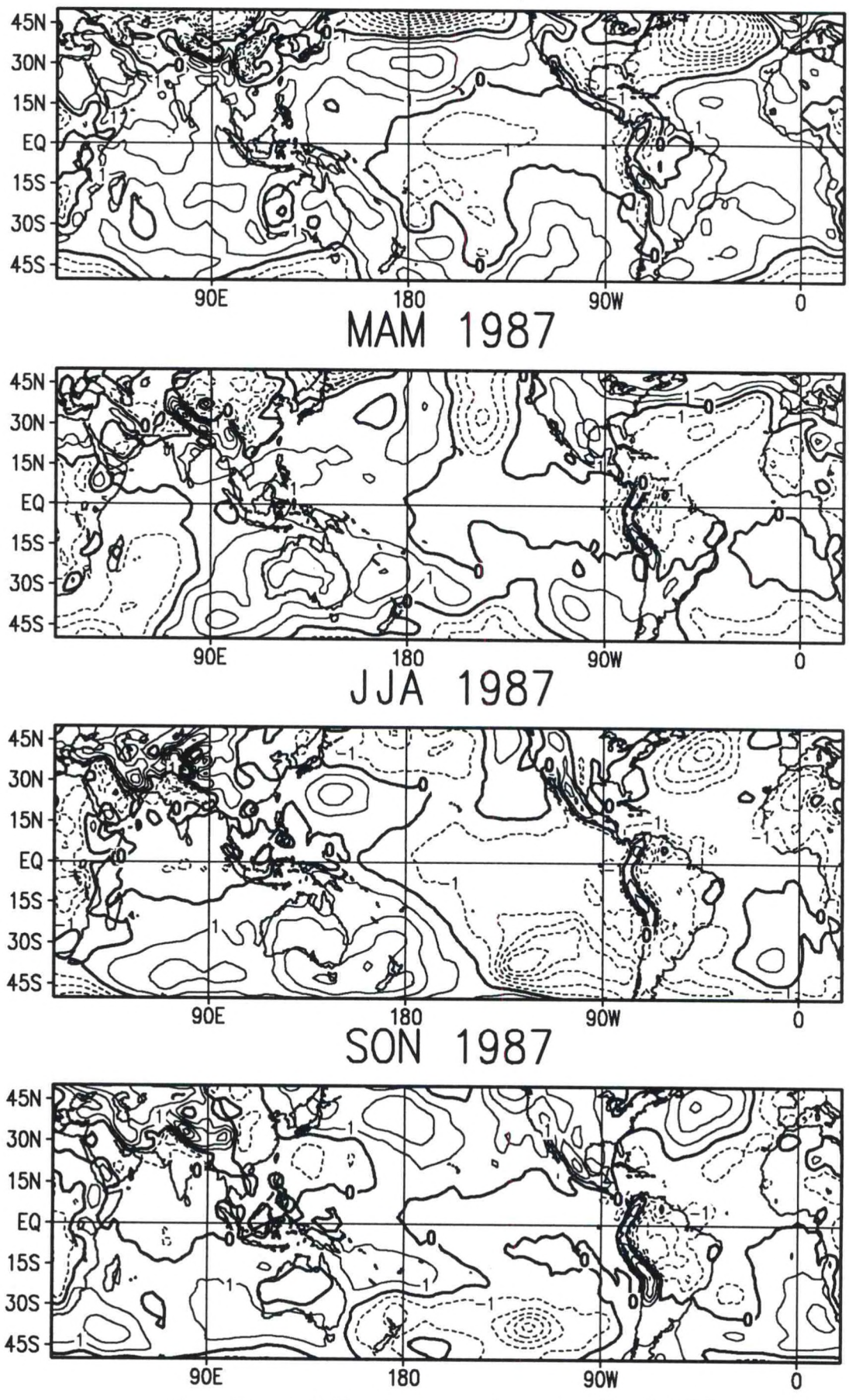

Sea-Level Pressure Anomaly (mb)

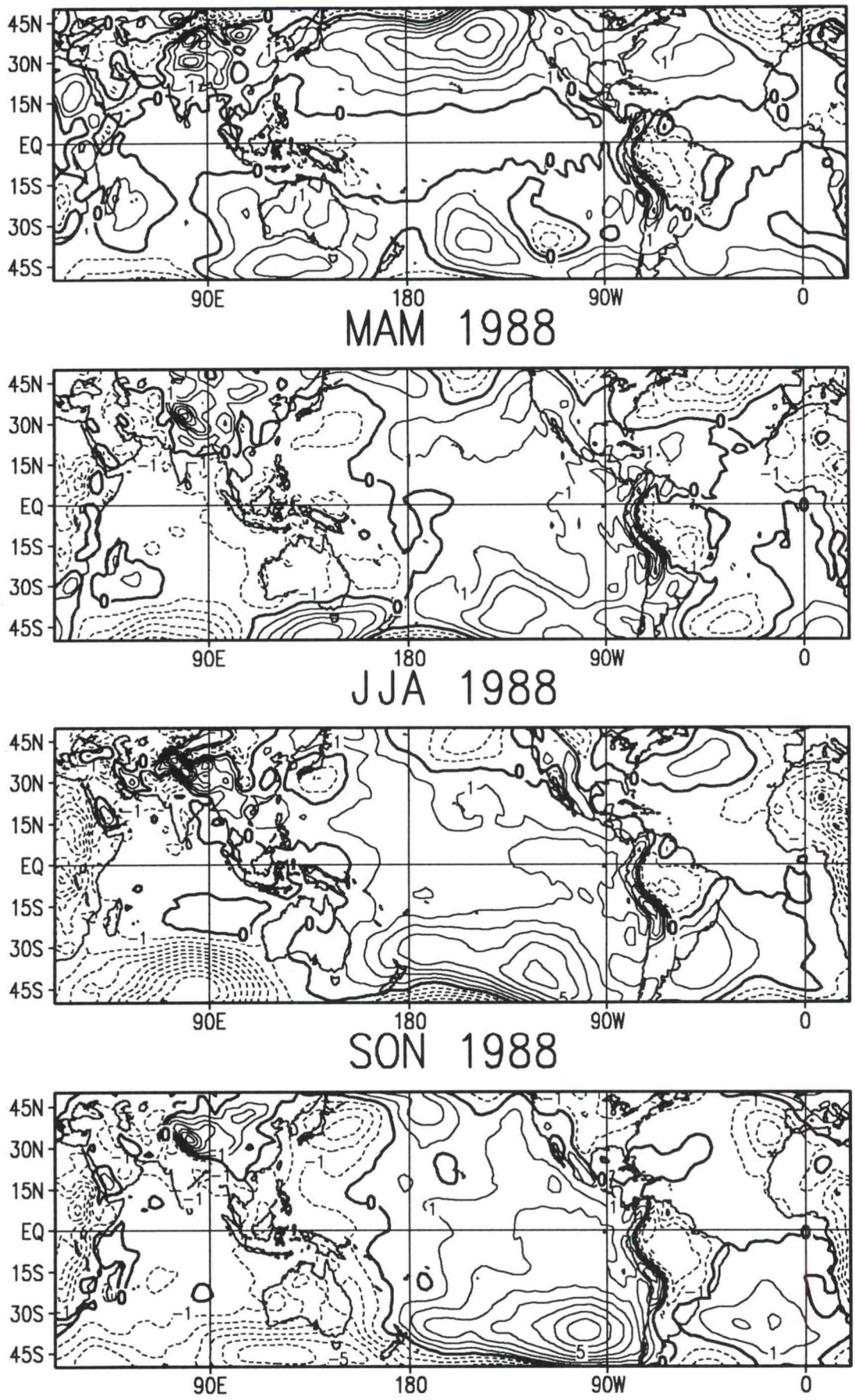

Sea-Level Pressure Anomaly (mb)

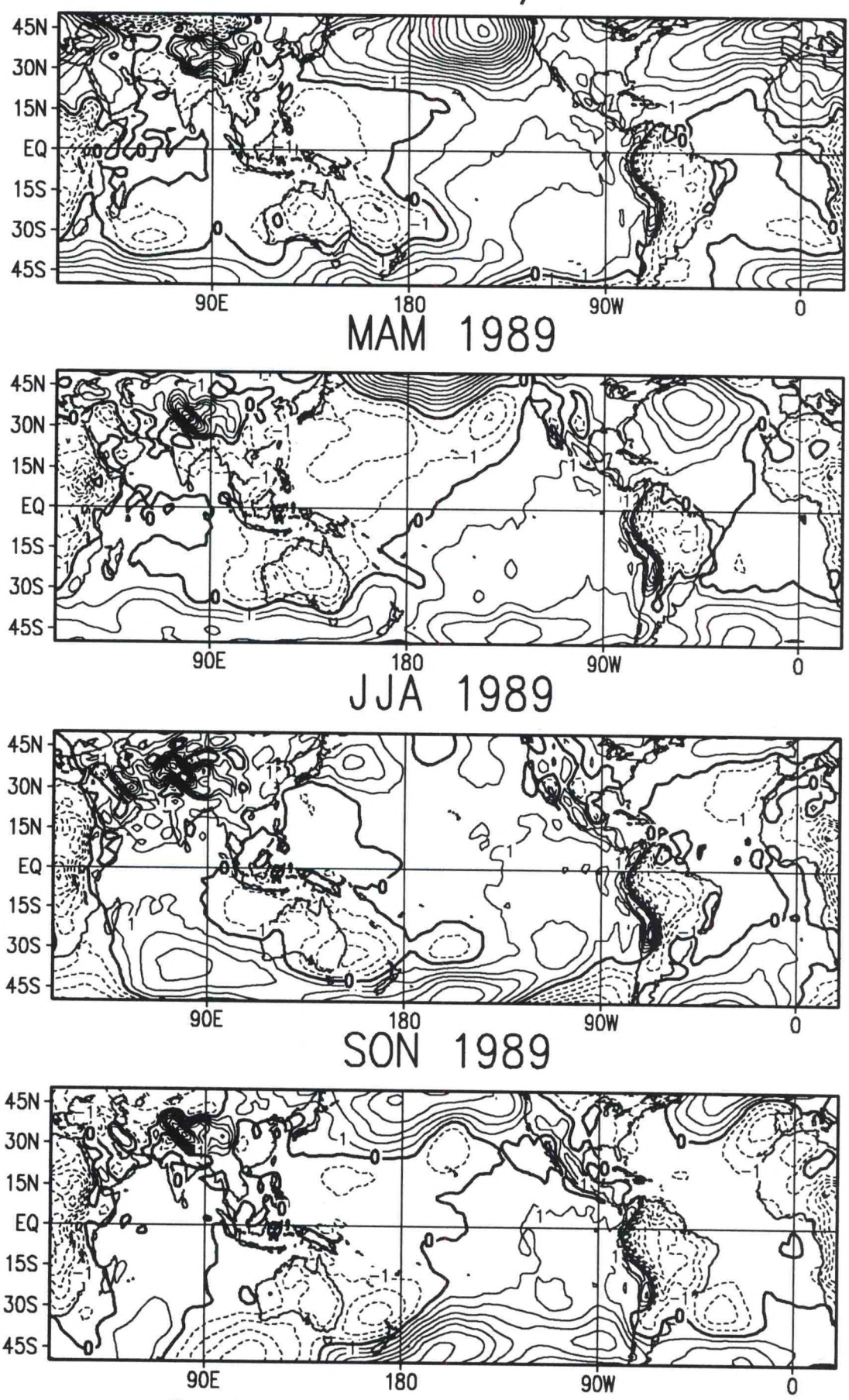

Sea-Level Pressure Anomaly (mb)

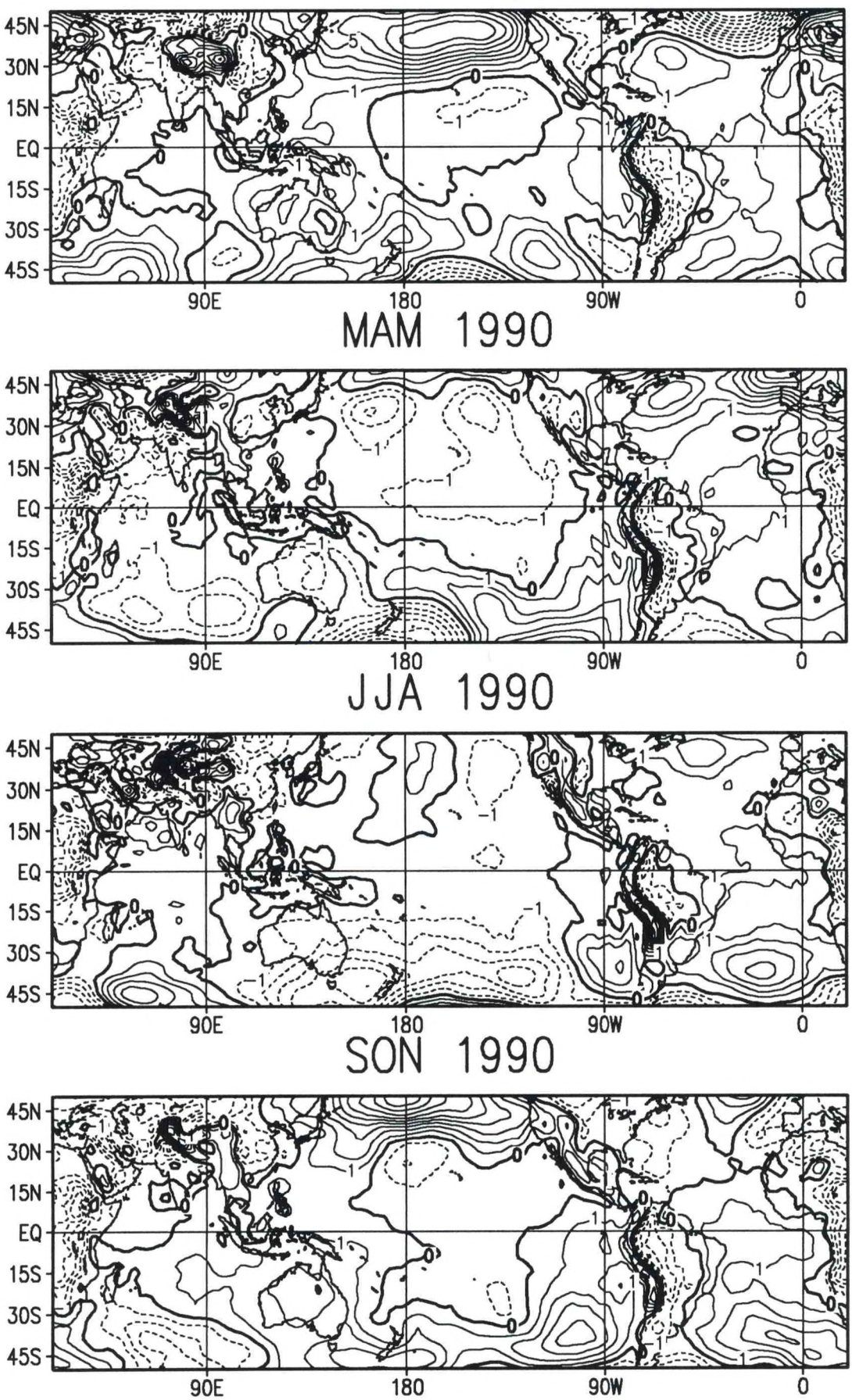

Sea-Level Pressure Anomaly (mb)

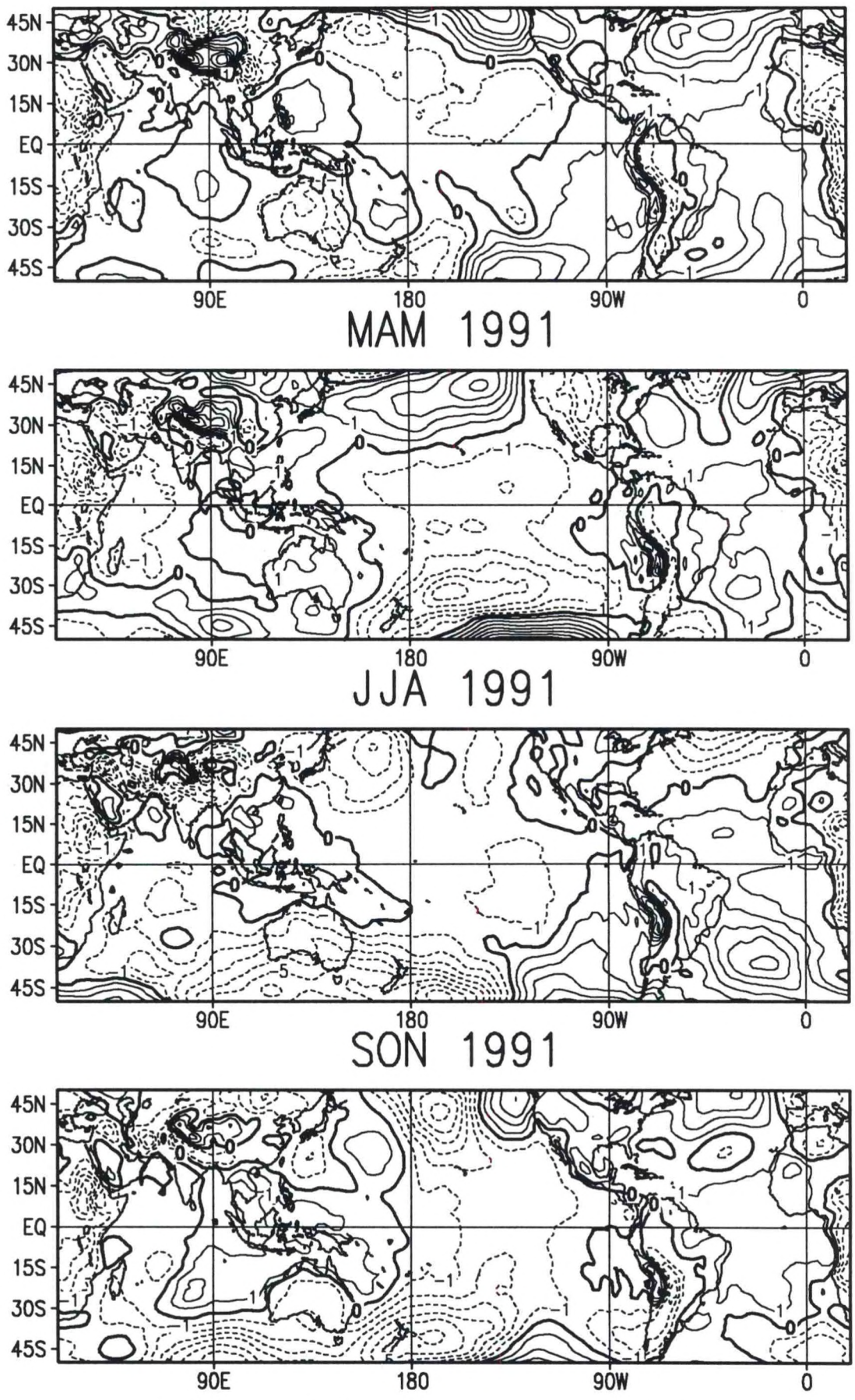

Sea-Level Pressure Anomaly (mb)

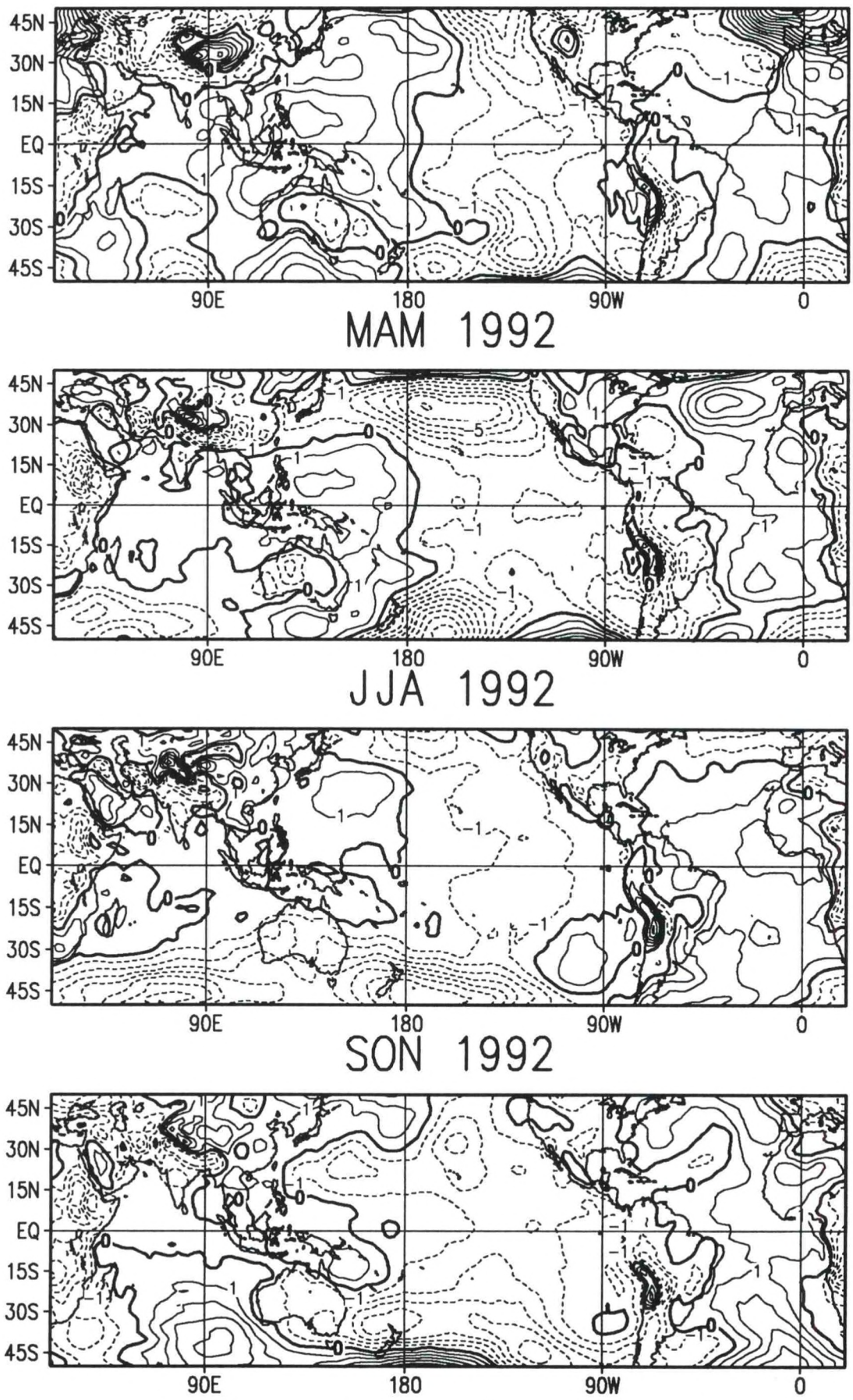

Sea-Level Pressure Anomaly (mb)

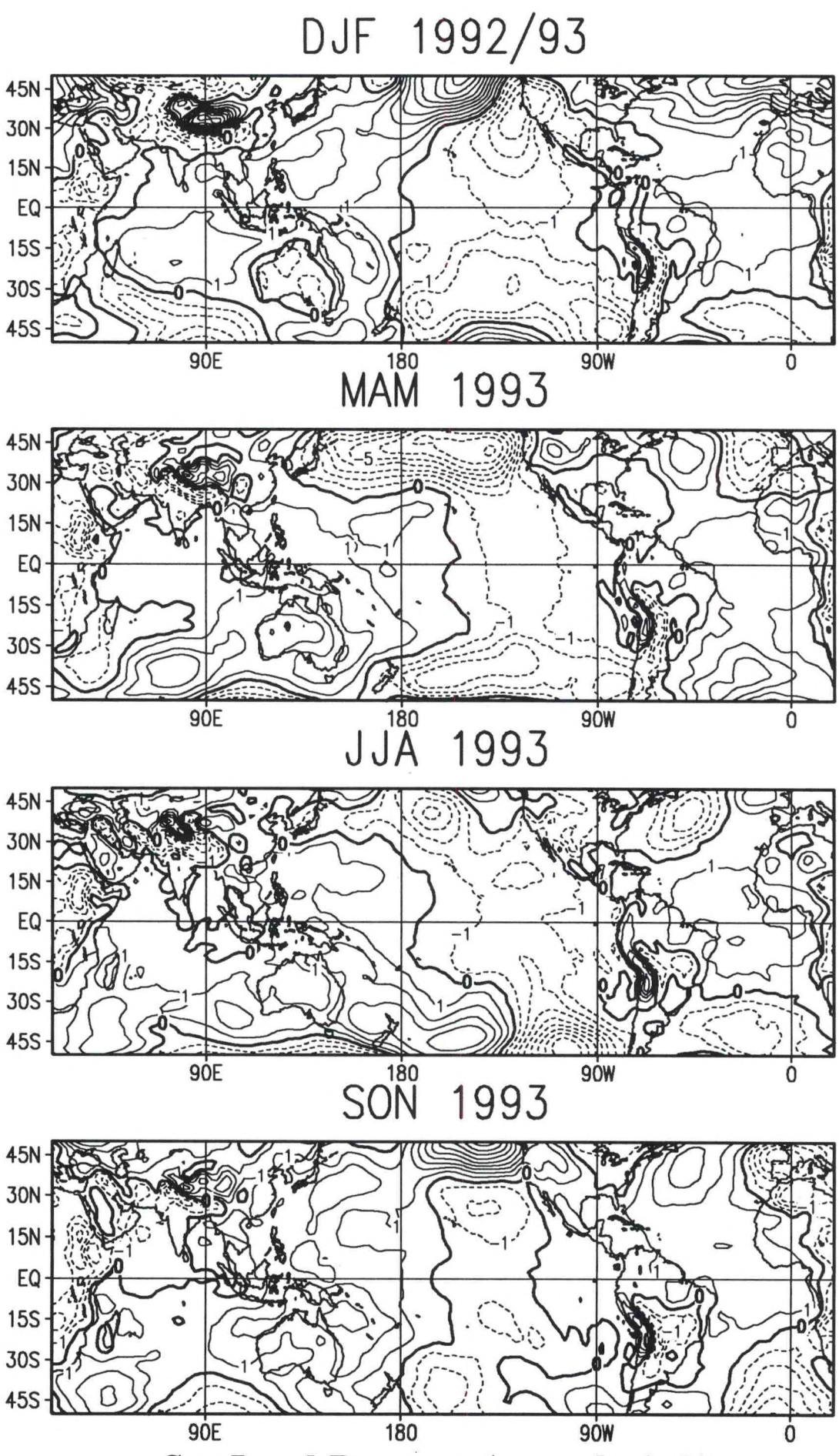

Sea-Level Pressure Anomaly (mb)

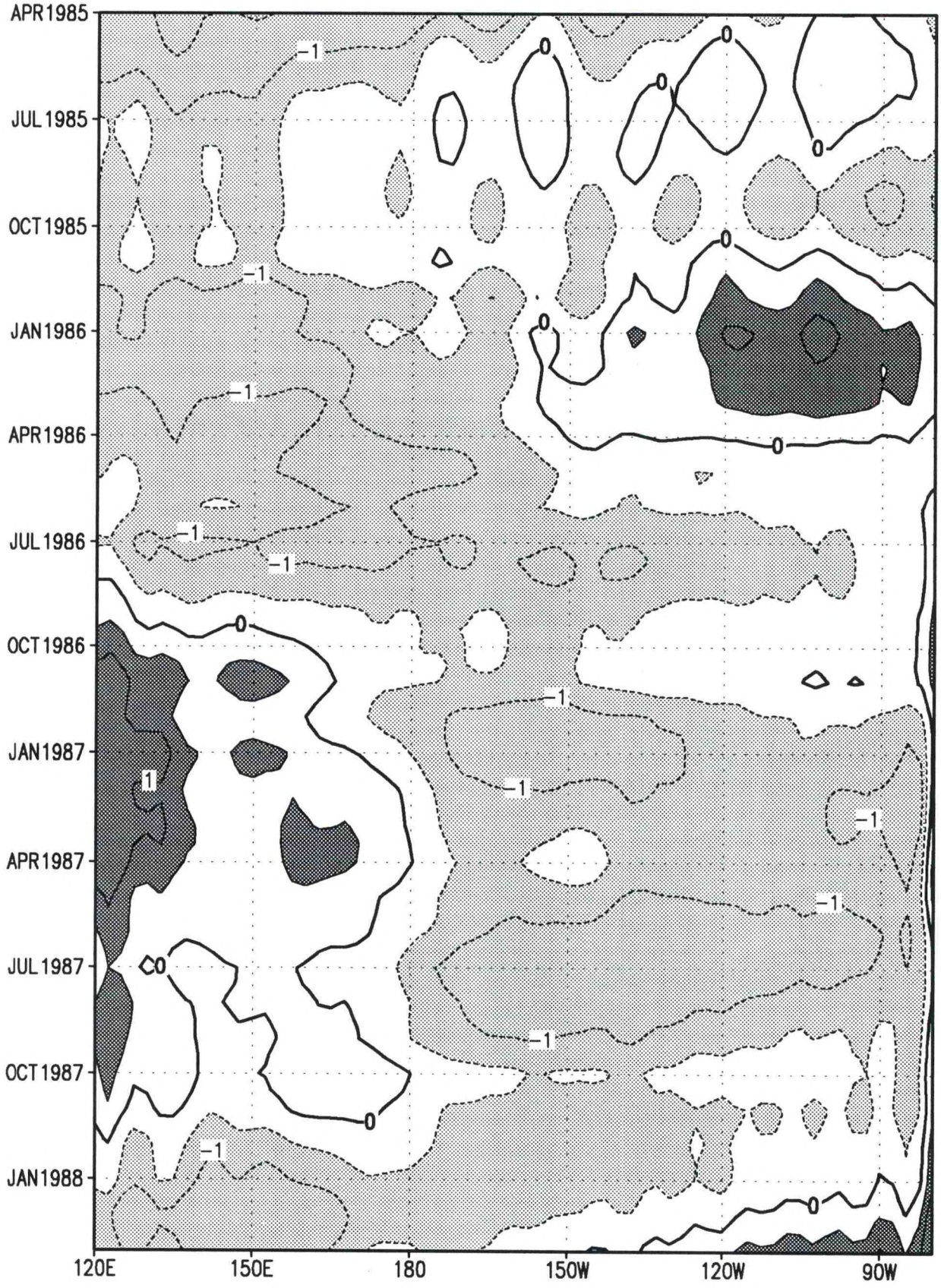

Sea-Level Pressure Anomaly (mb)

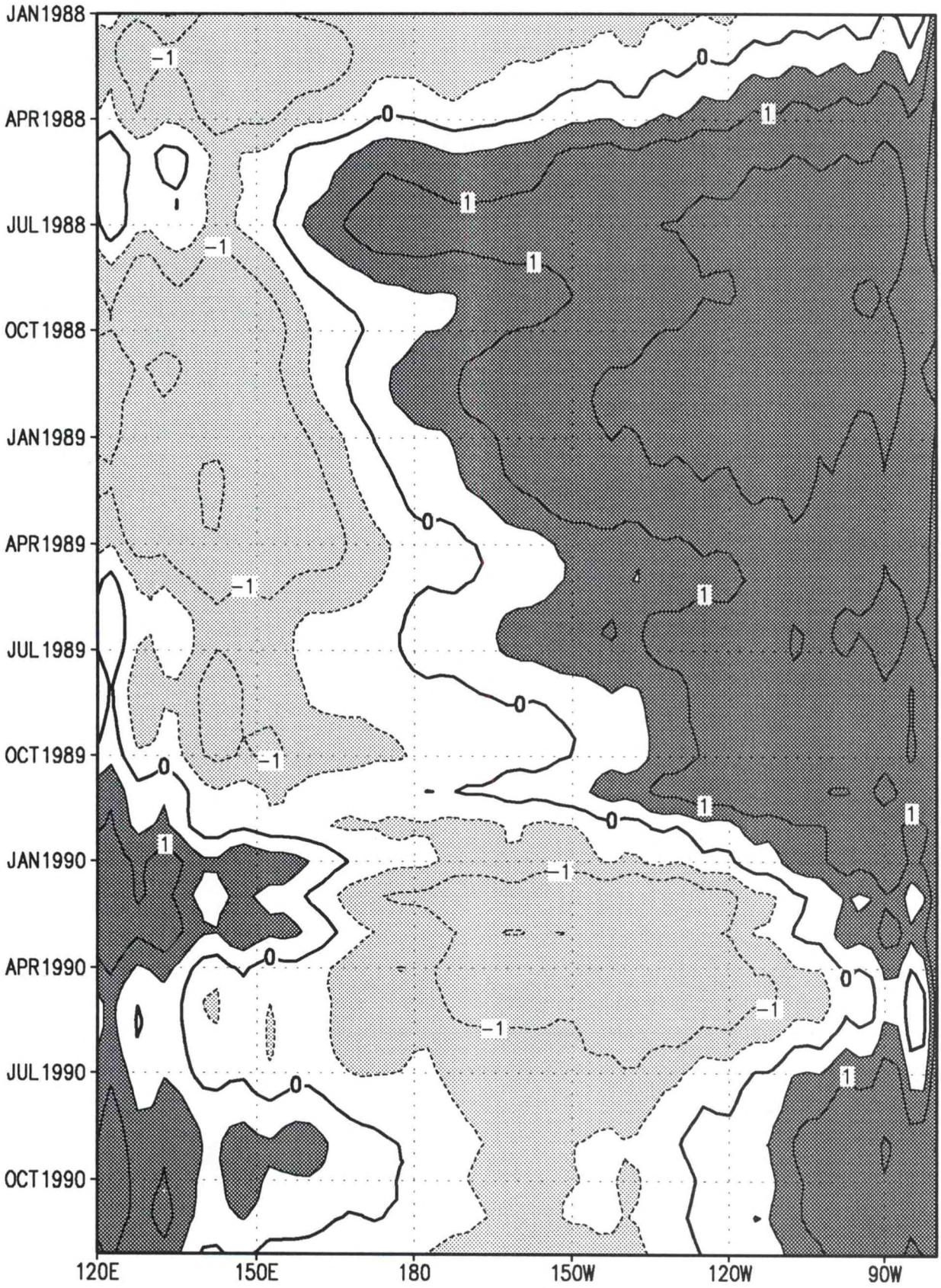

Sea-Level Pressure Anomaly (mb)

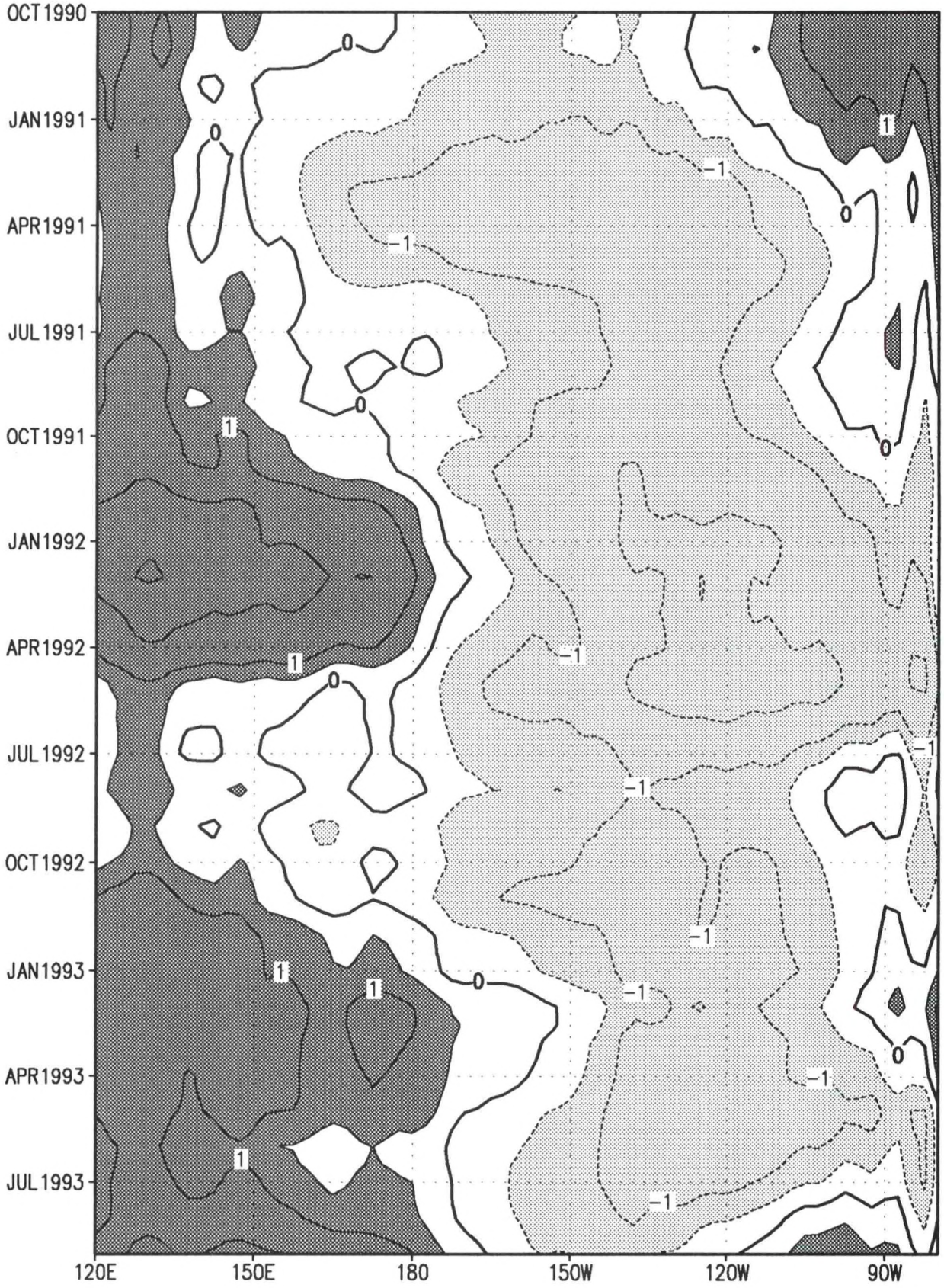

Sea-Level Pressure Anomaly (mb)

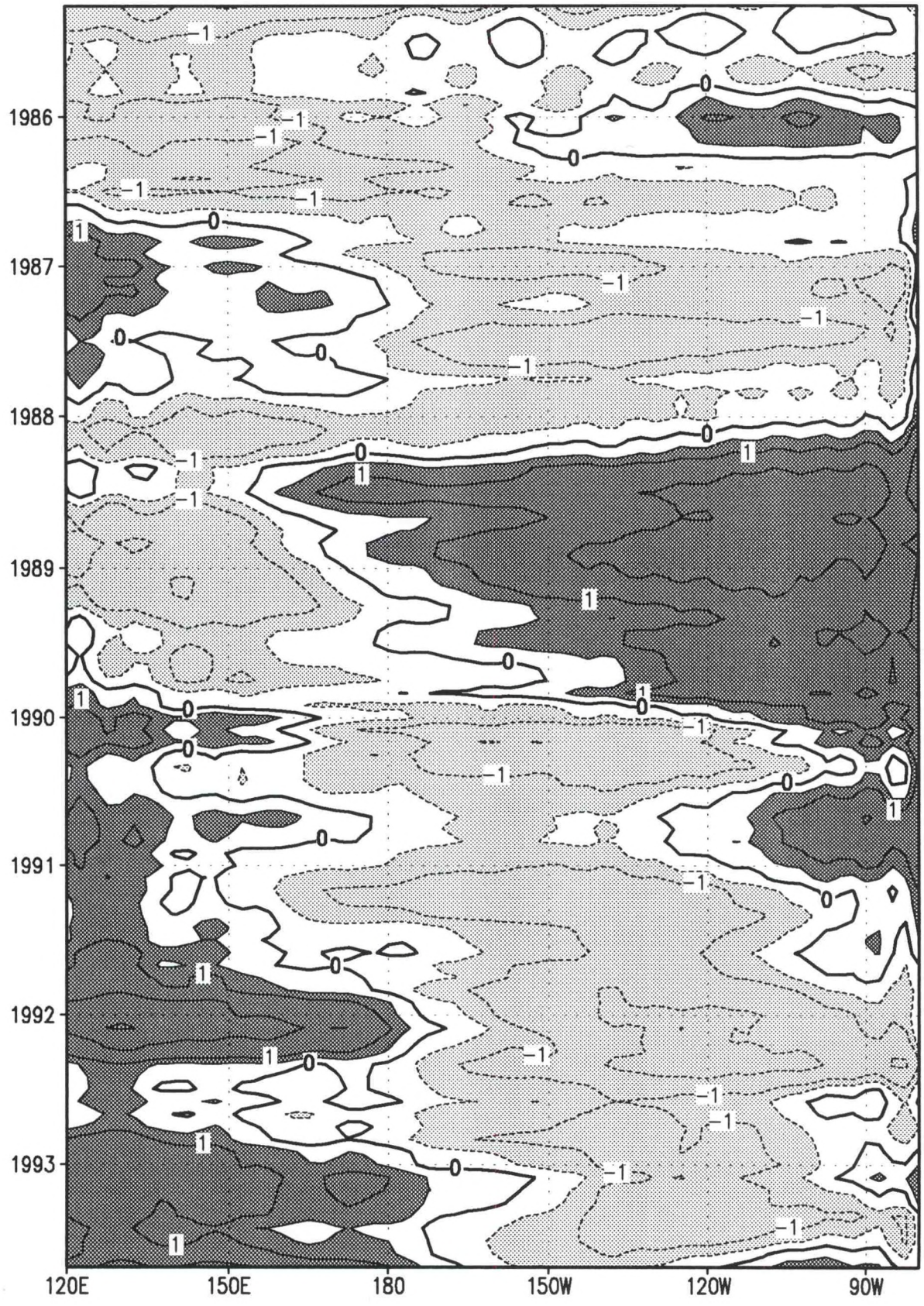

Sea-Level Pressure Anomaly (mb)

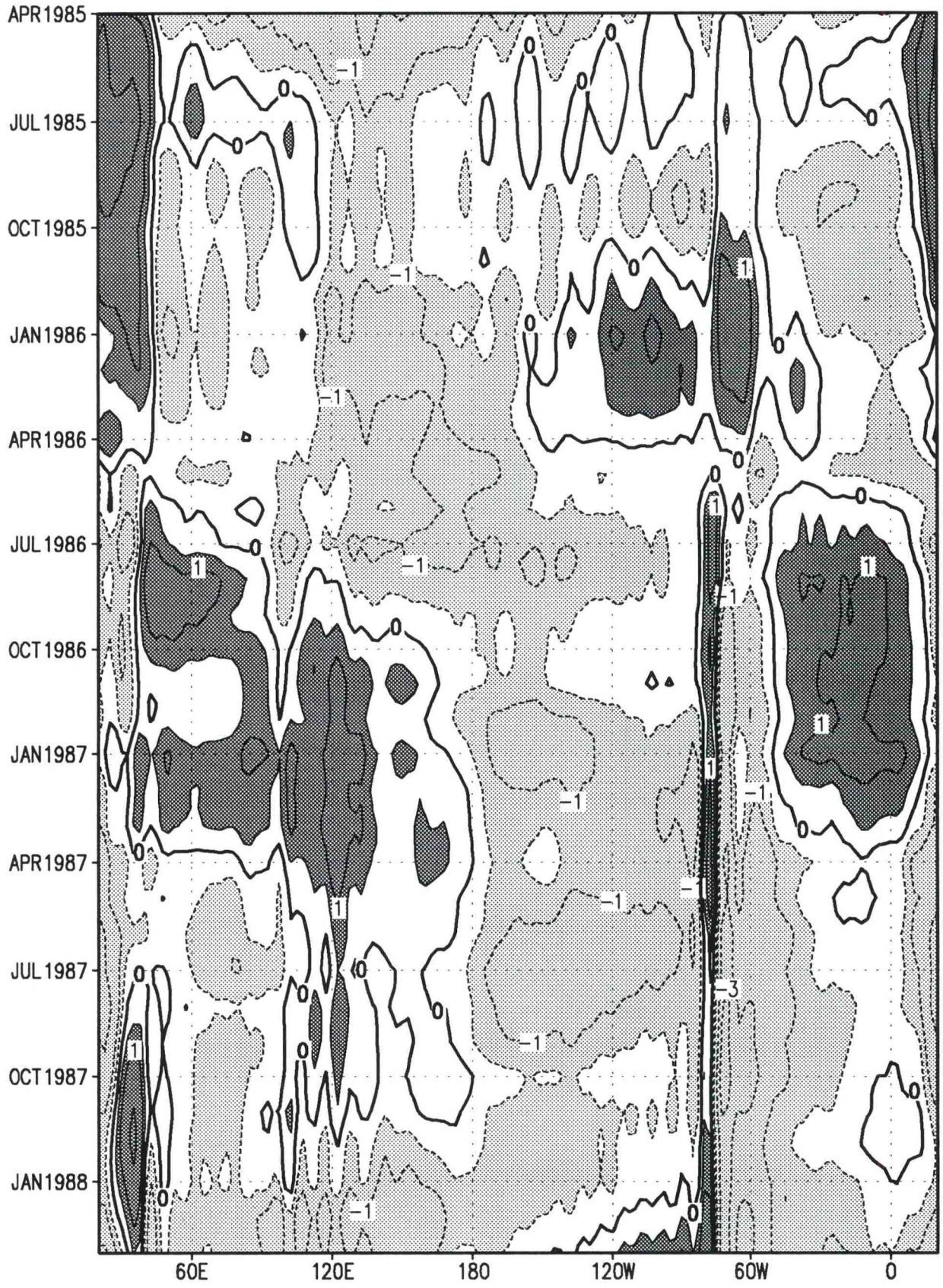

Sea-Level Pressure Anomaly (mb)

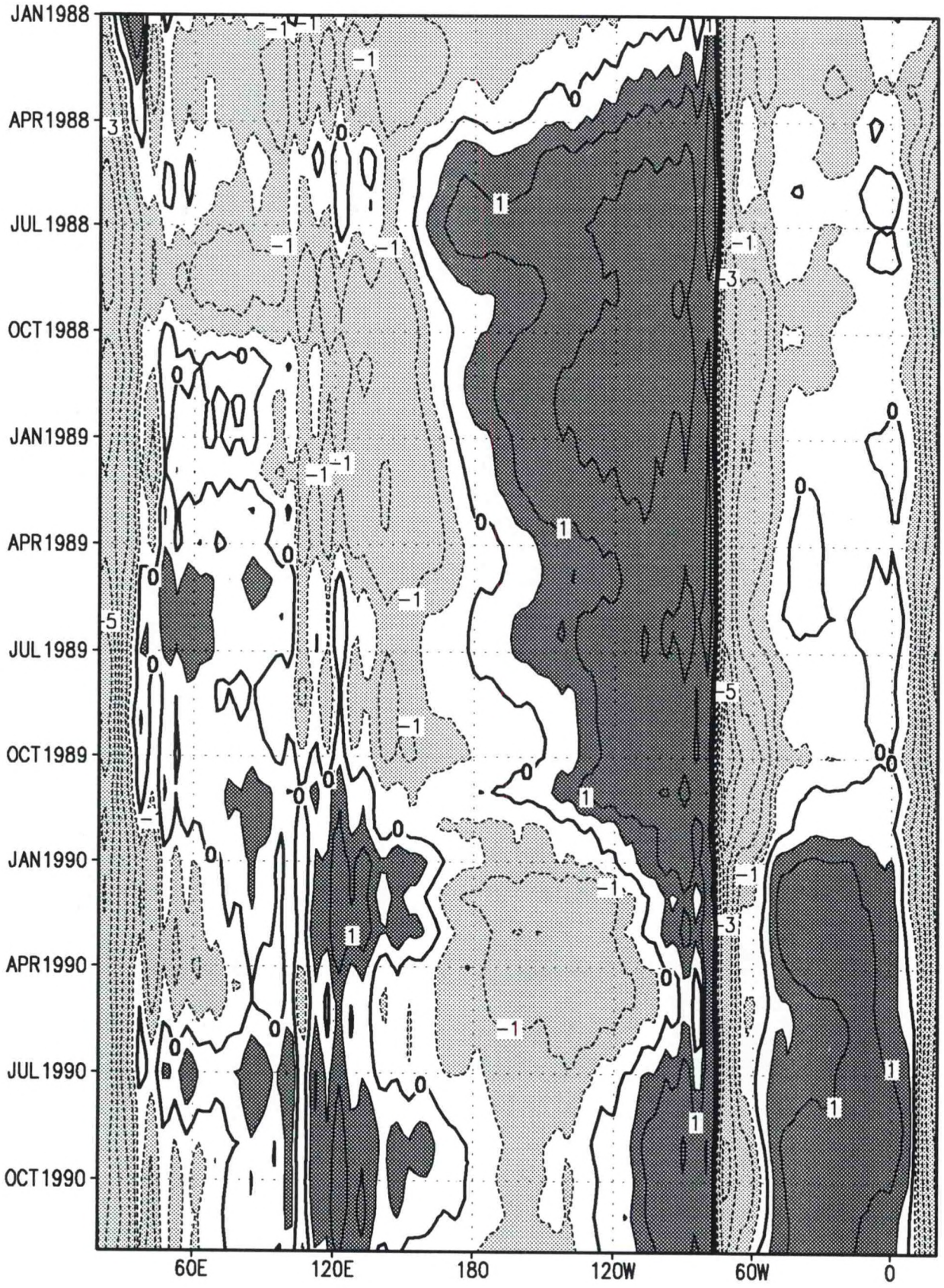

Sea-Level Pressure Anomaly (mb)

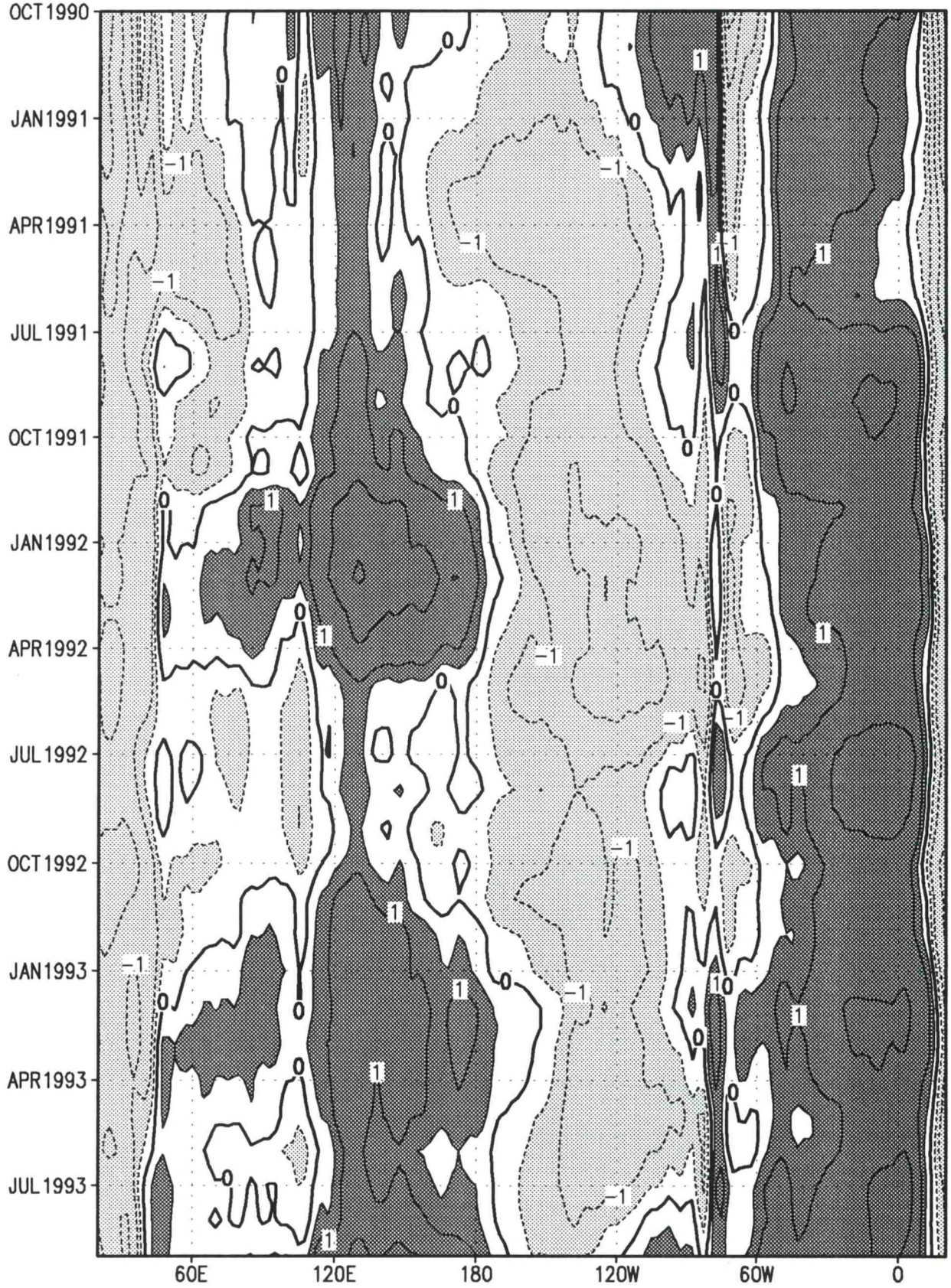

Sea-Level Pressure Anomaly (mb)

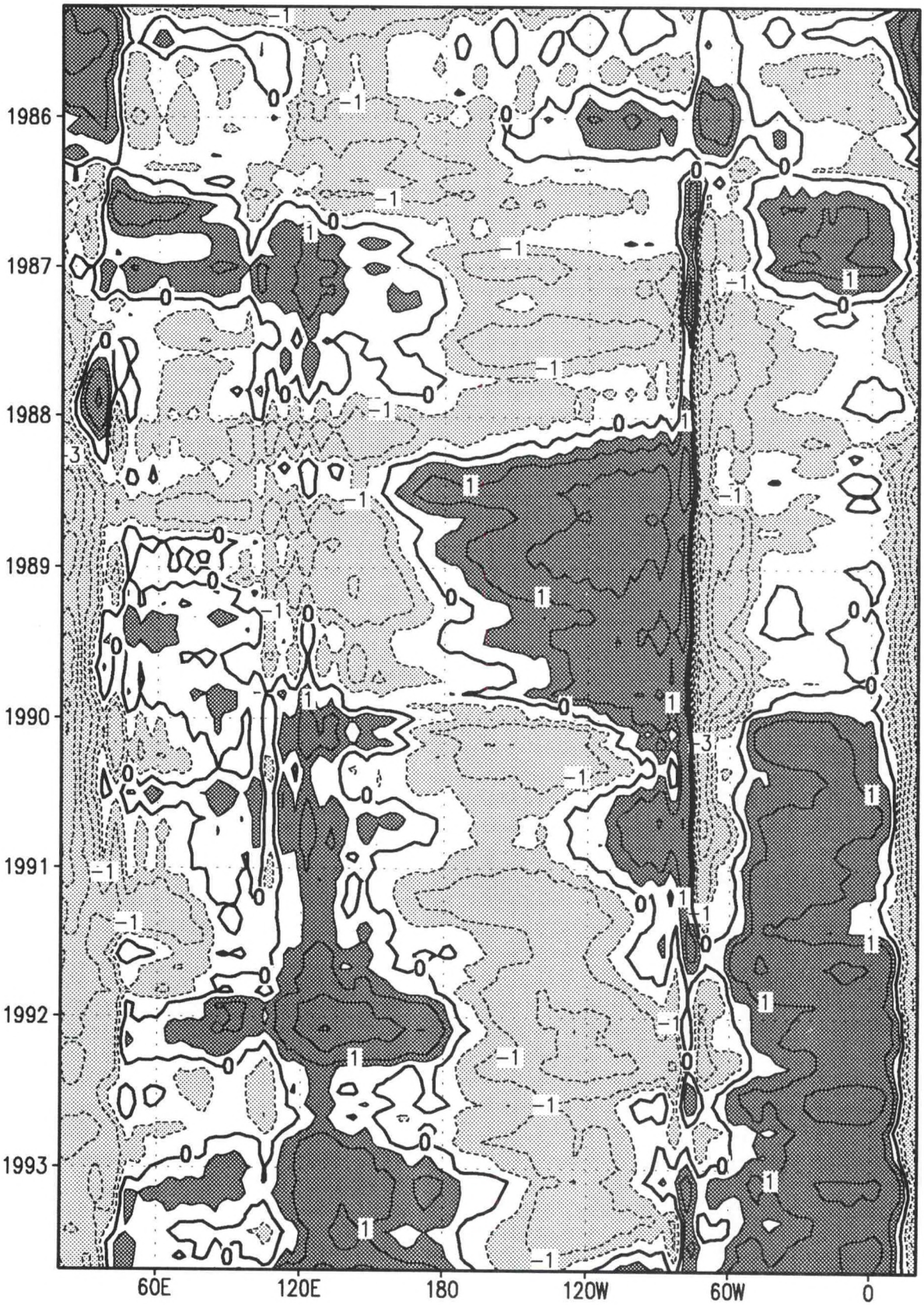

Sea-Level Pressure Anomaly (mb)

500 mb TEMPERATURE ANOMALY

Time-Longitude Section (pp. 163-166): Monthly-mean 500-mb temperature anomaly (°C) along the equator over the Pacific Ocean between 120°E and 80°W. Contour interval is 1°C. Positive anomalies greater than 1°C are shaded dark with solid contours. Negative anomalies below 1°C are shaded light with dashed contours. Zero contour is shown thick solid.

Time-Longitude Section (pp. 167-170): Monthly-mean 500-mb temperature anomaly (°C) along the equator for all longitudes. Contour interval is 1°C. Positive anomalies greater than 1°C are shaded dark with solid contours. Negative anomalies below 1°C are shaded light with dashed contours. Zero contour is shown thick solid.

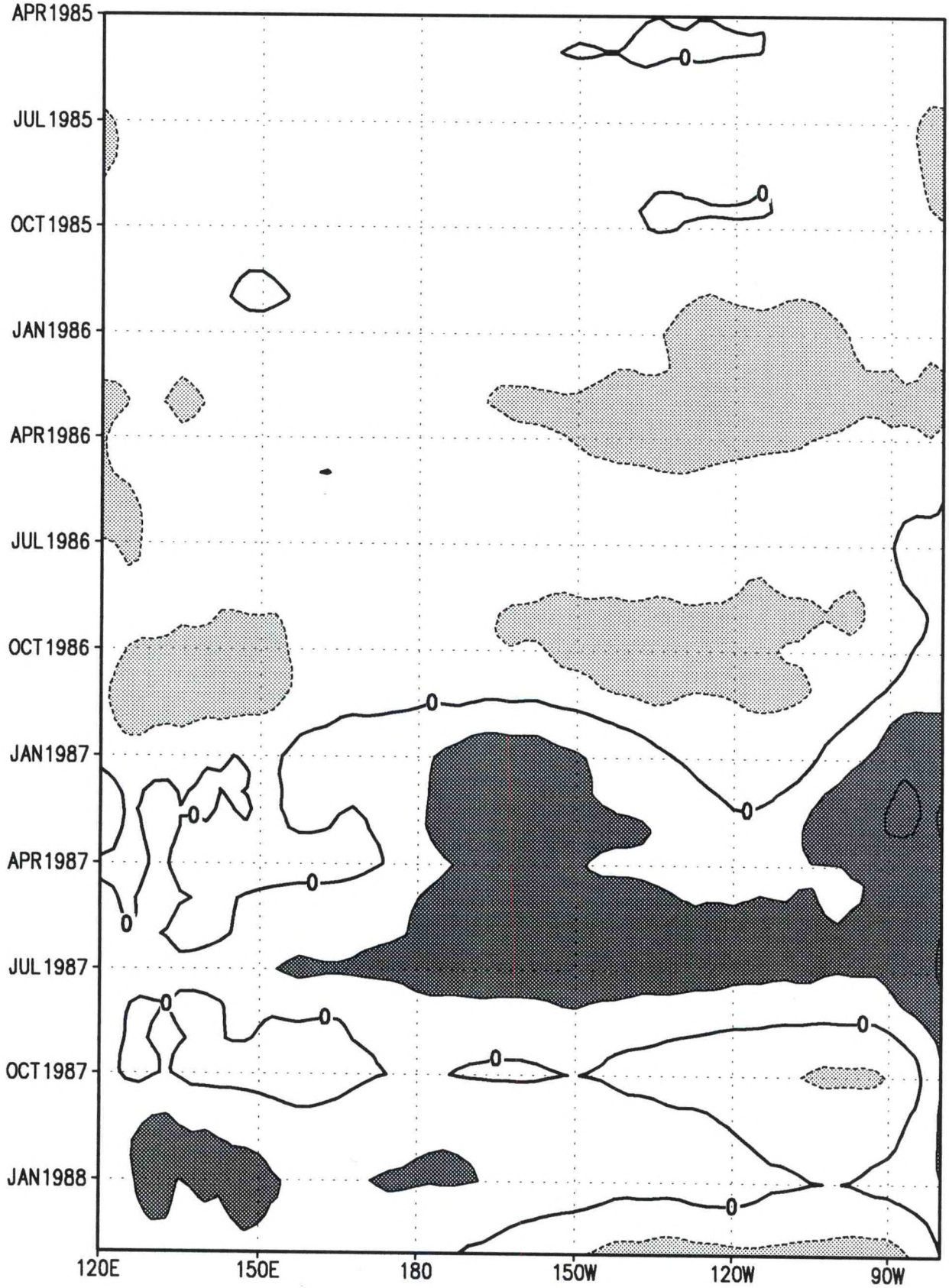

500 mb Temperature Anomaly (°C)

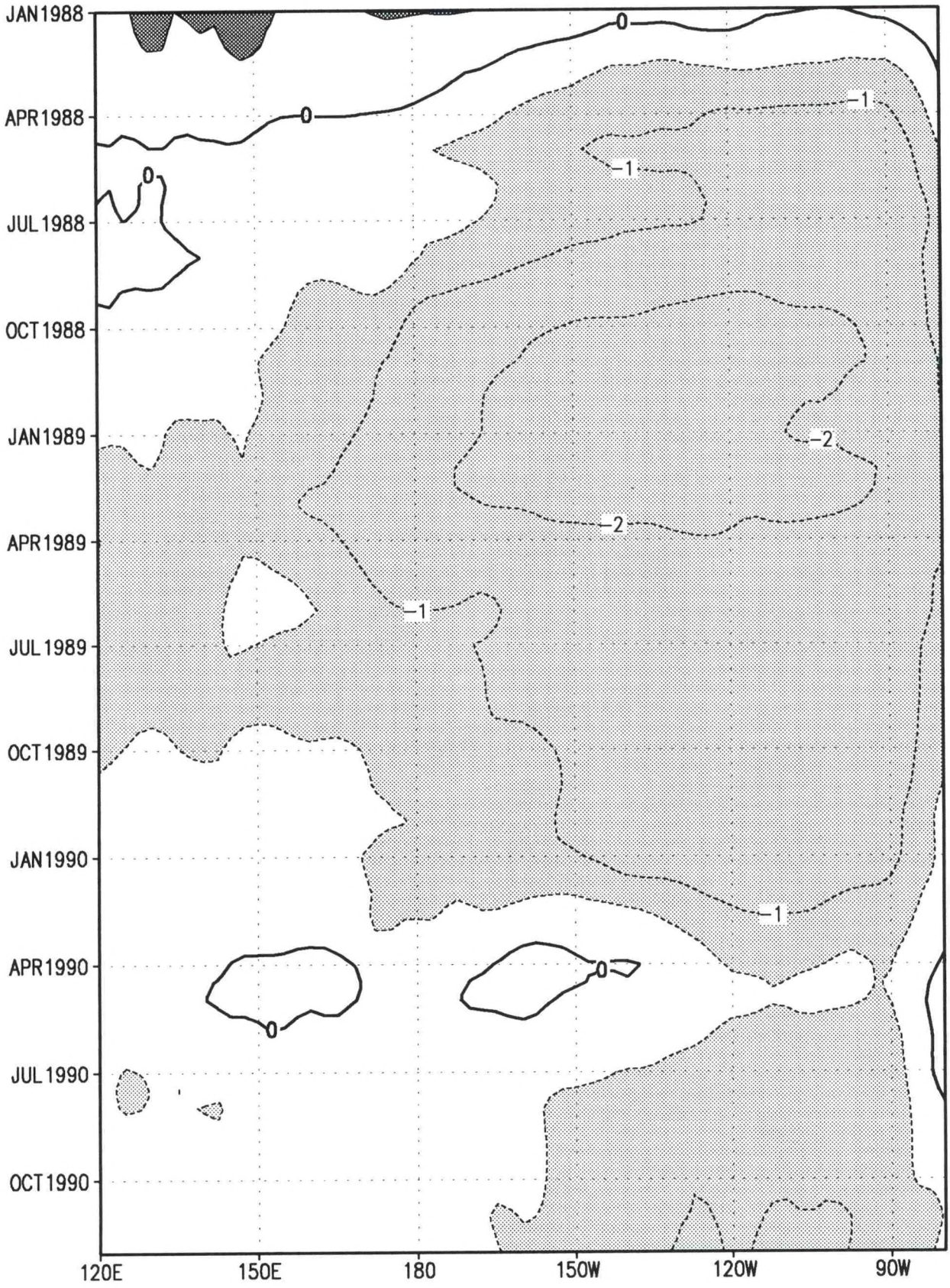

500 mb Temperature Anomaly (°C)

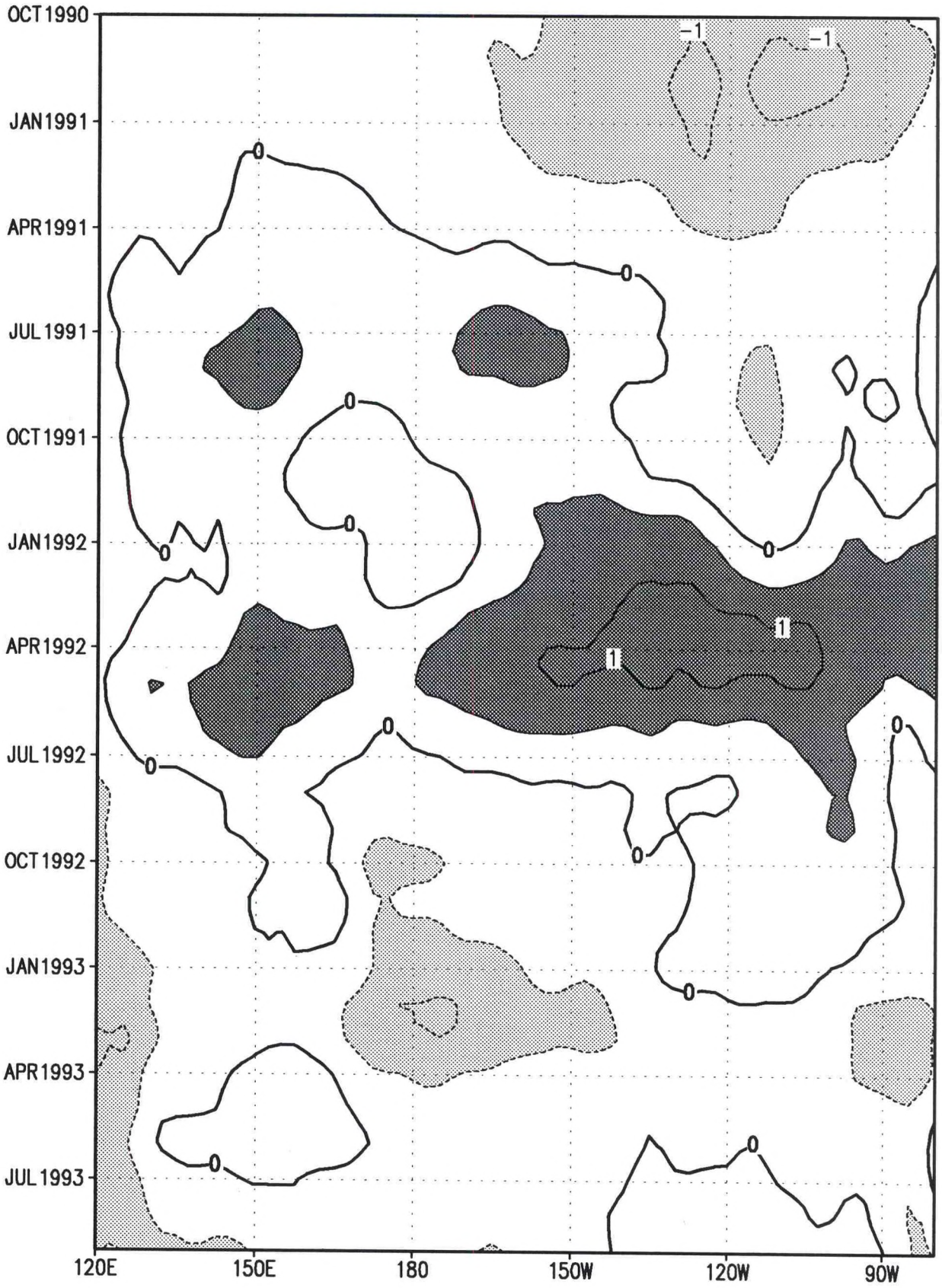

500 mb Temperature Anomaly (°C)

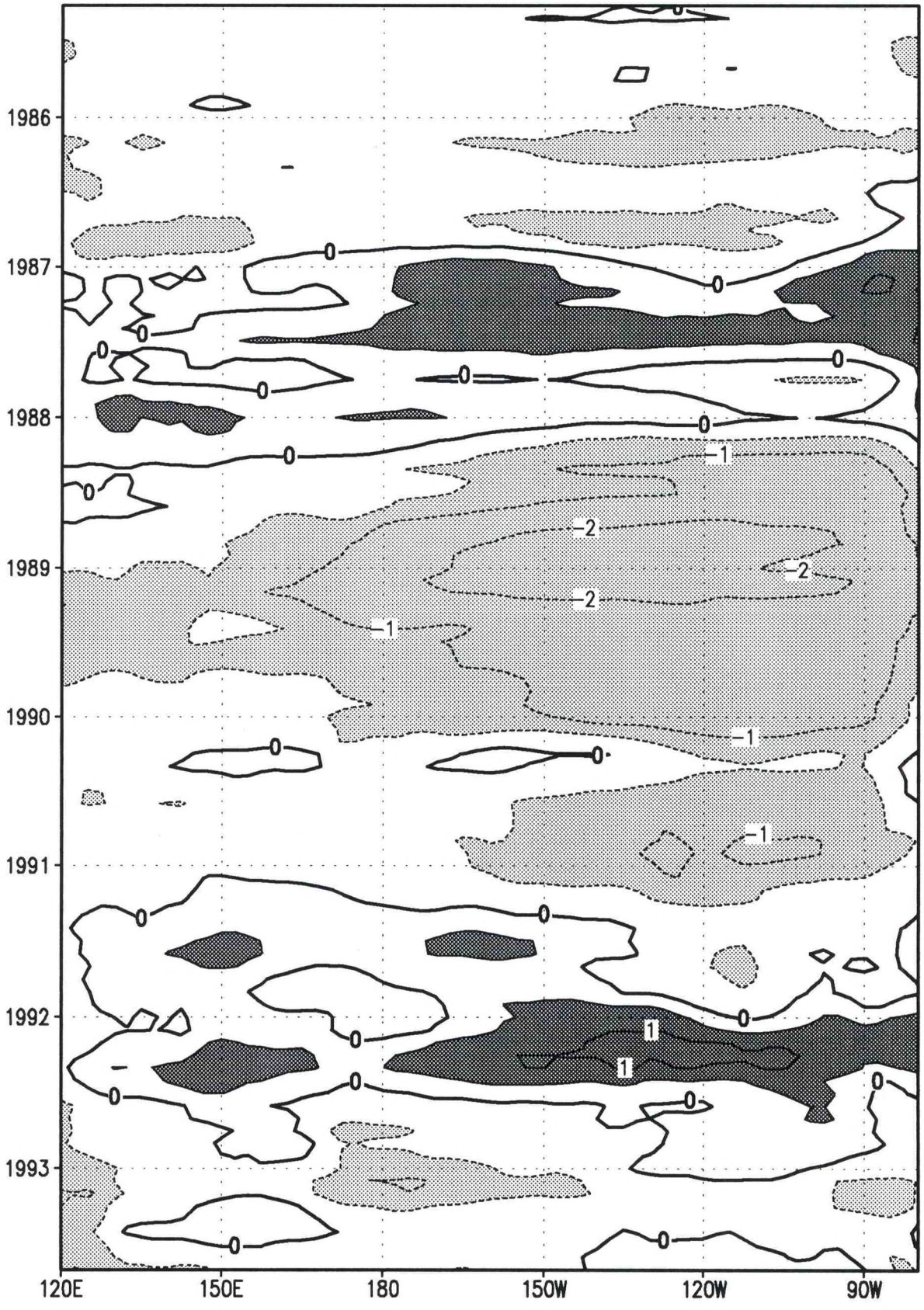

500 mb Temperature Anomaly (°C)

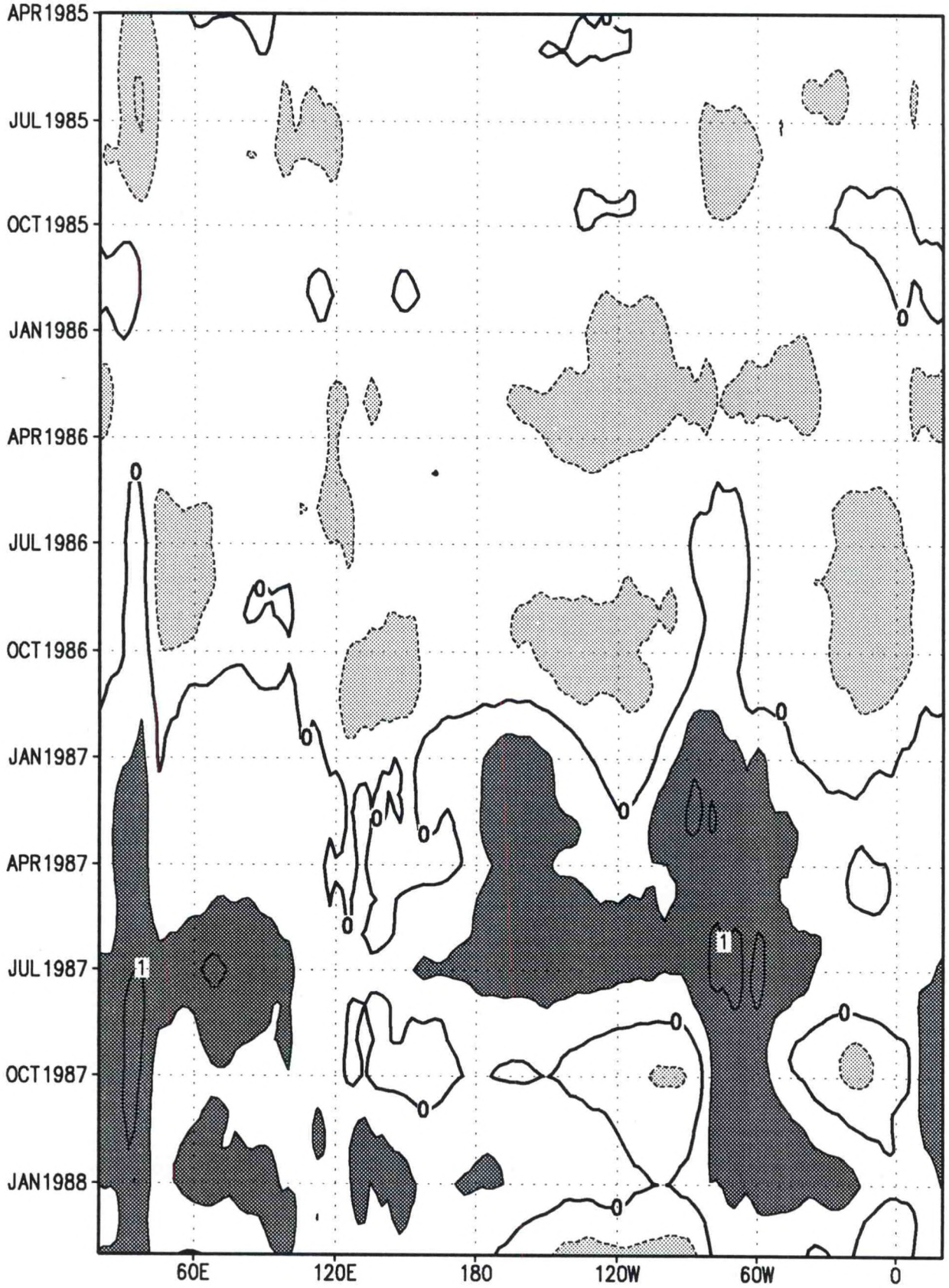

500 mb Temperature Anomaly (°C)

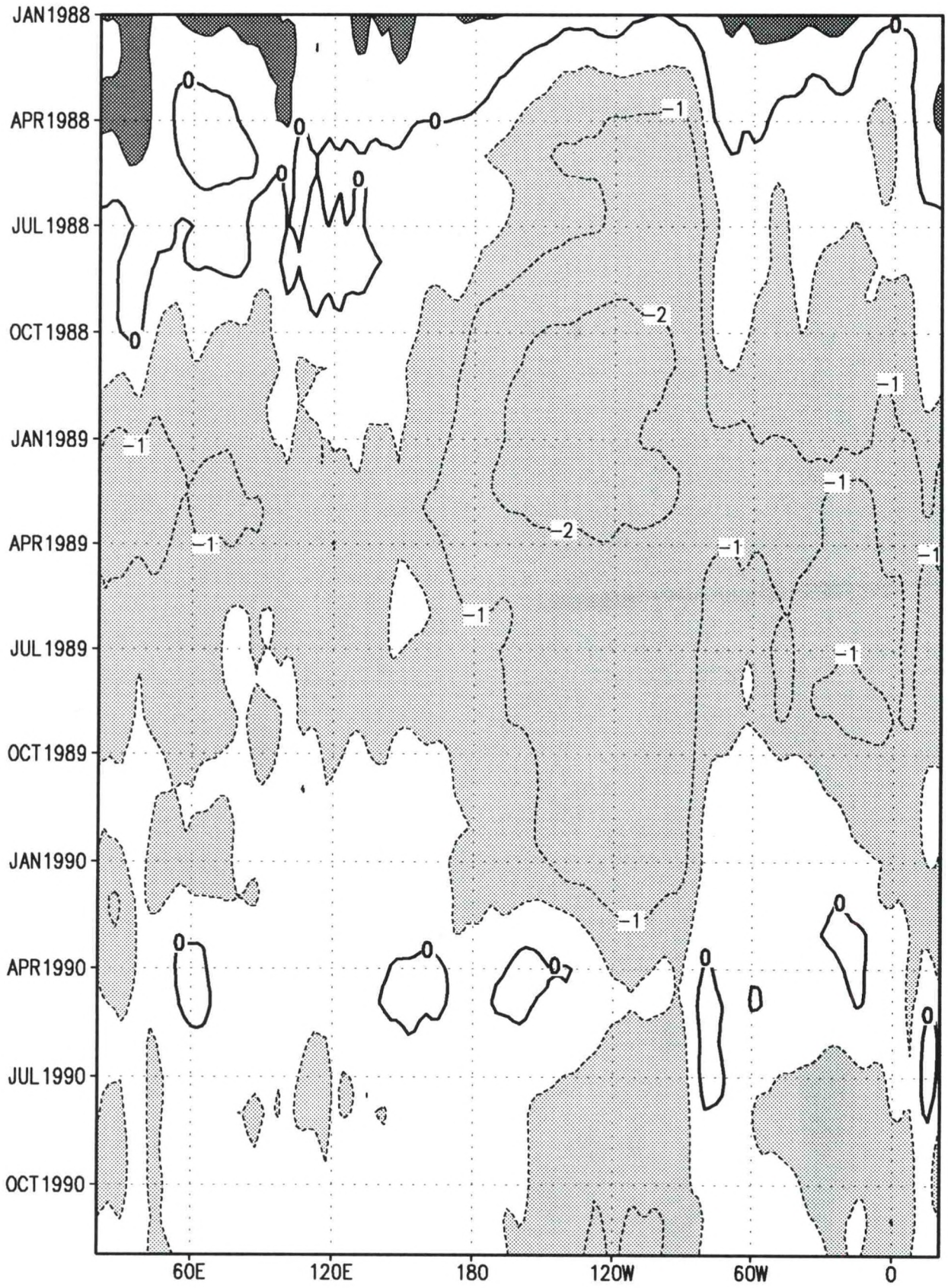

500 mb Temperature Anomaly (°C)

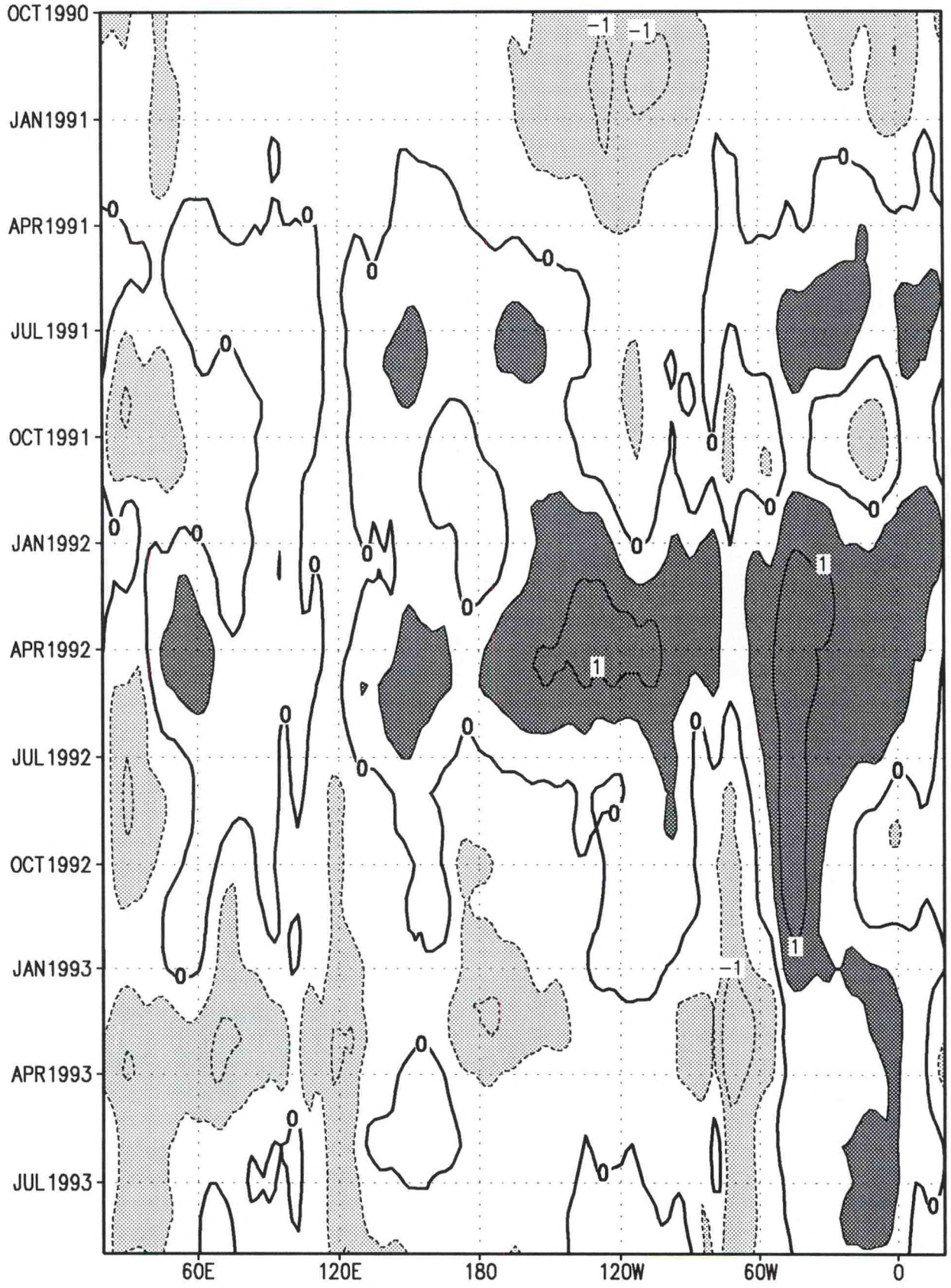

500 mb Temperature Anomaly (°C)

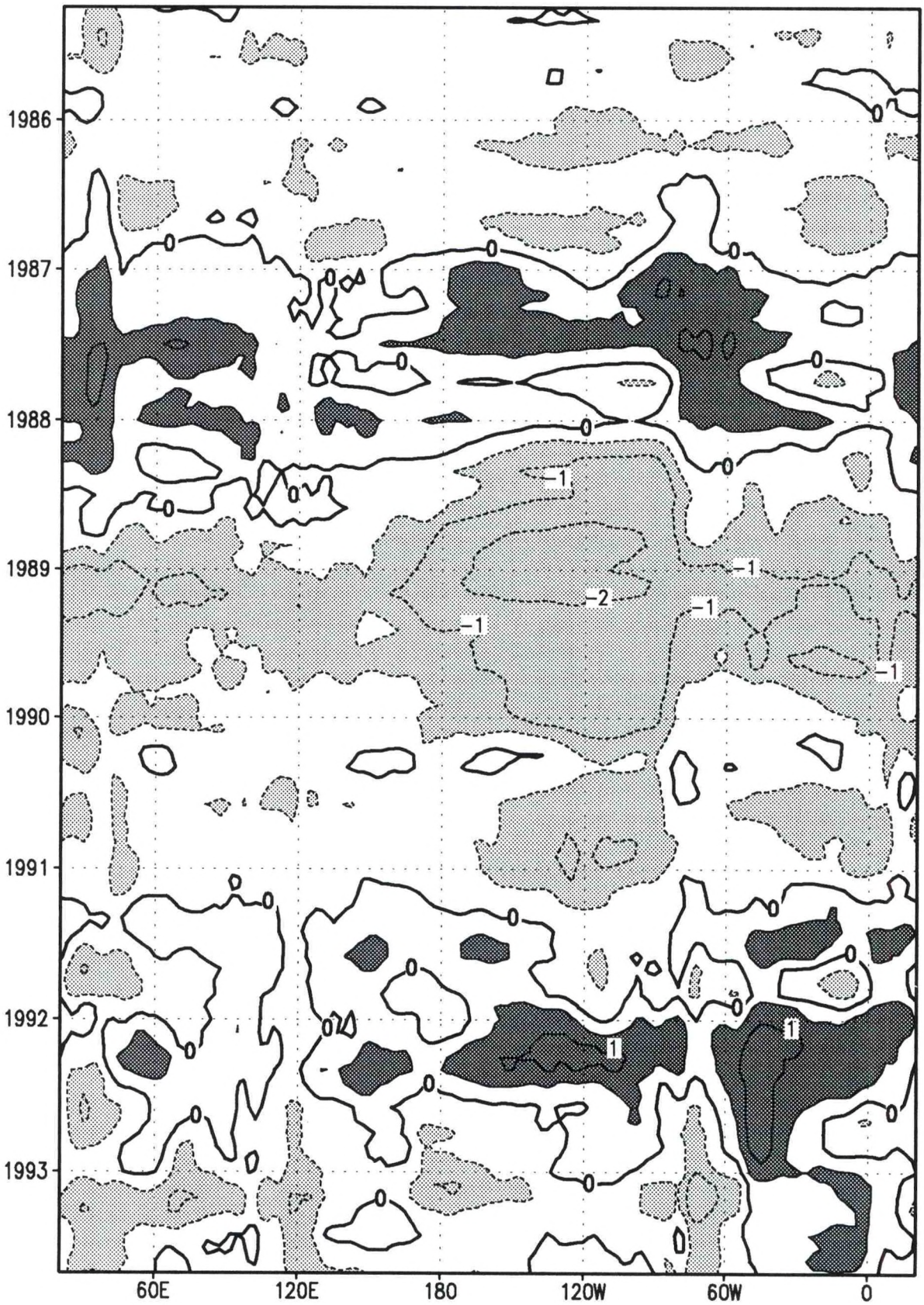

500 mb Temperature Anomaly (°C)

500 mb GEOPOTENTIAL HEIGHT and ANOMALY

Northern Hemisphere Seasonal Maps (pp. 172-179): 500-mb geopotential height and anomalies. Heights (m) are contoured thick every 120 m. Anomalies (m) are contoured thin every 30 m. Negative anomalies are dashed and shaded light; positive anomalies are solid and shaded dark.

Southern Hemisphere Seasonal Maps (pp. 180-187): 500-mb geopotential height and anomalies. Heights (m) are contoured thick every 120 m. Anomalies (m) are contoured thin every 30 m. Negative anomalies are dashed and shaded light; positive anomalies are solid and shaded dark.

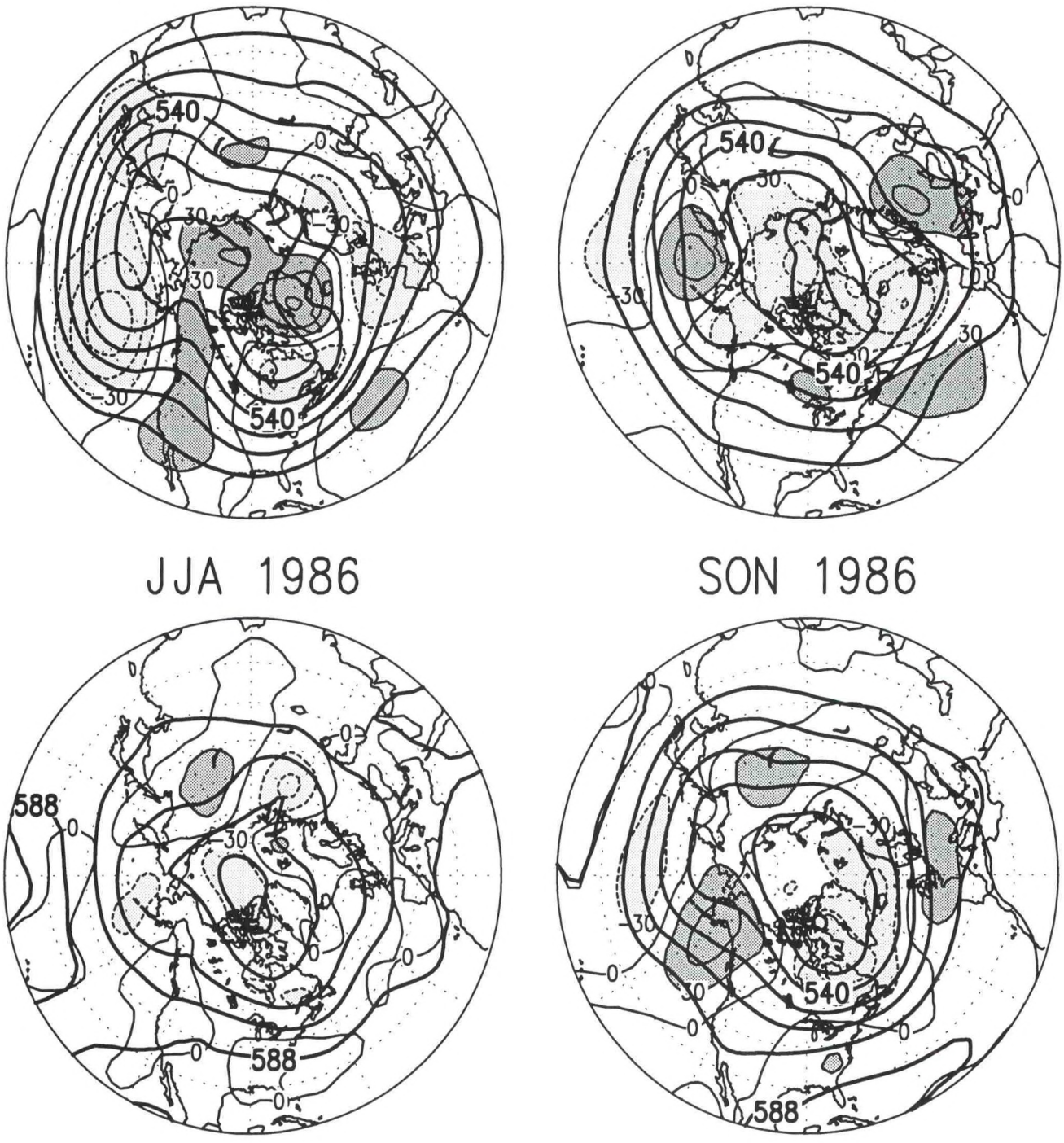

500 mb Heights and Anomalies (m)

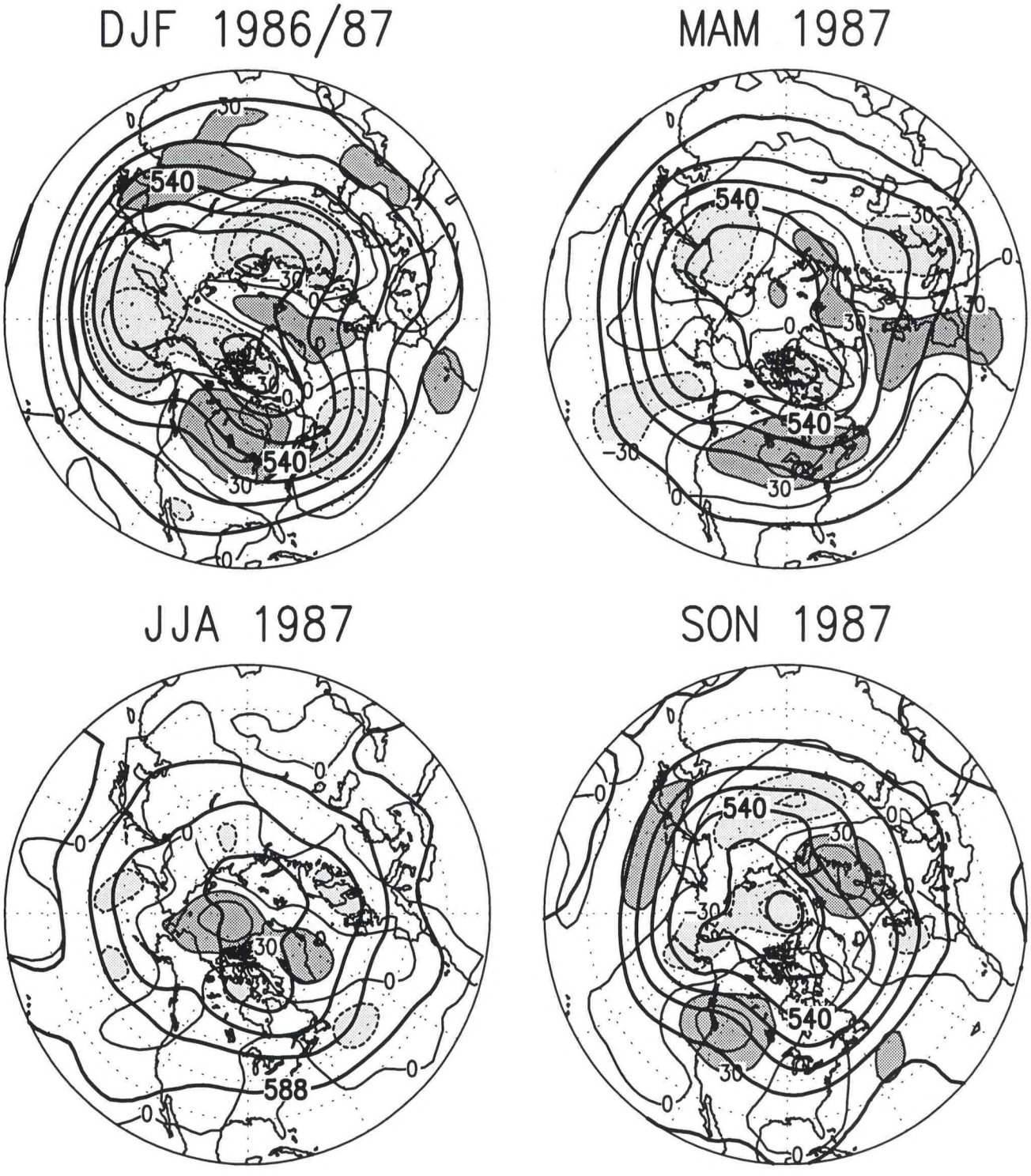

500 mb Heights and Anomalies (m)

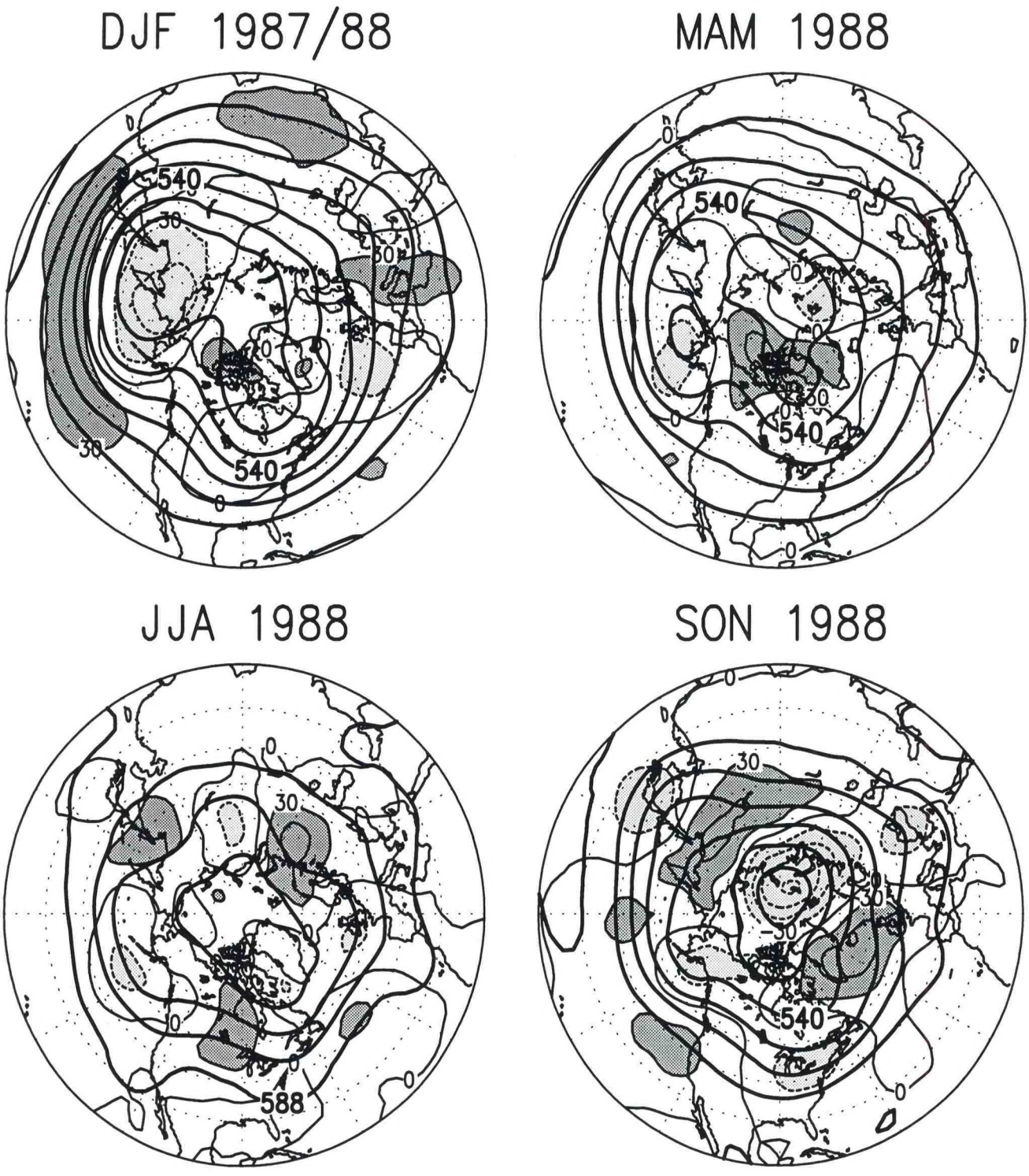

500 mb Heights and Anomalies (m)

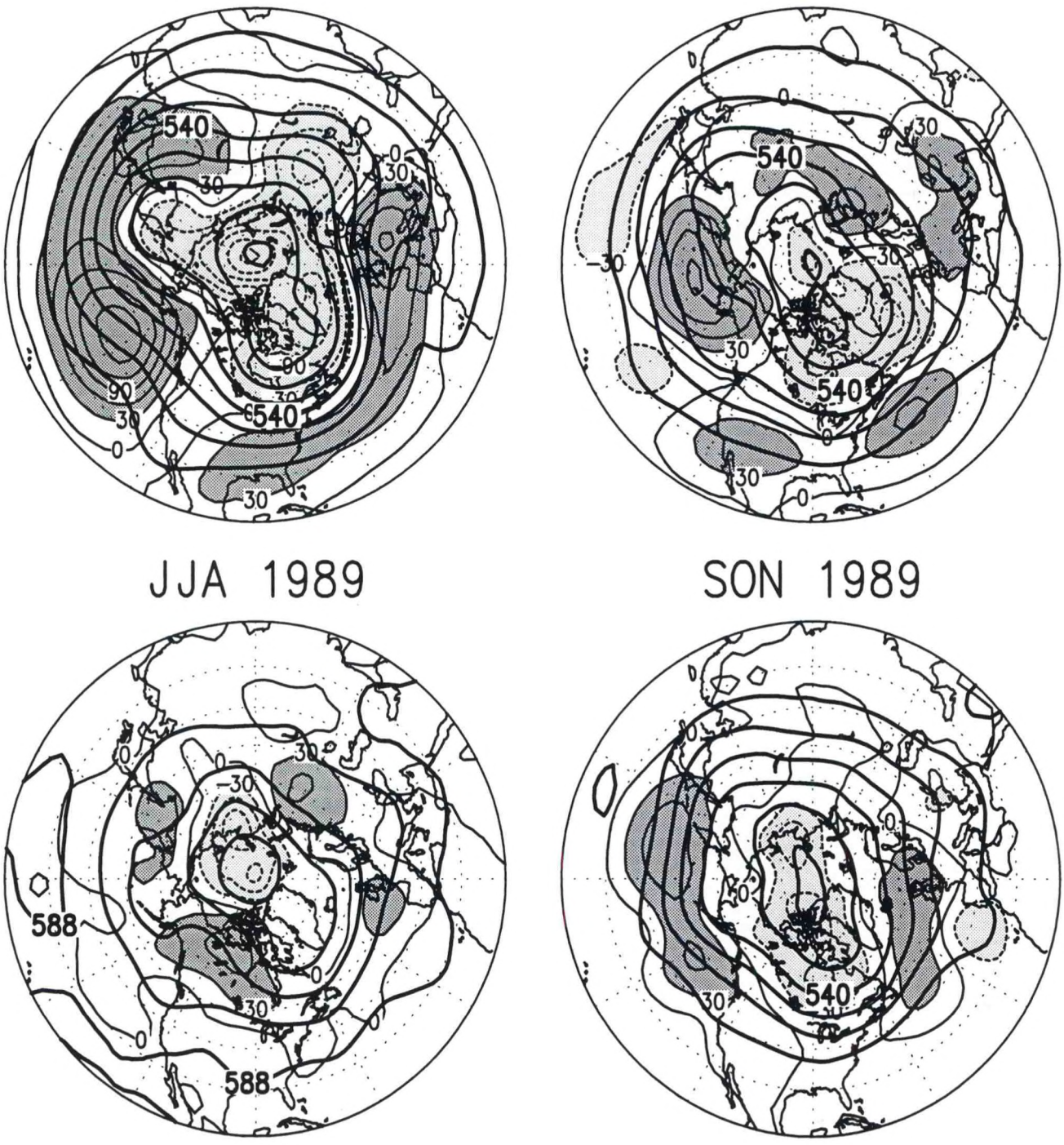

500 mb Heights and Anomalies (m)

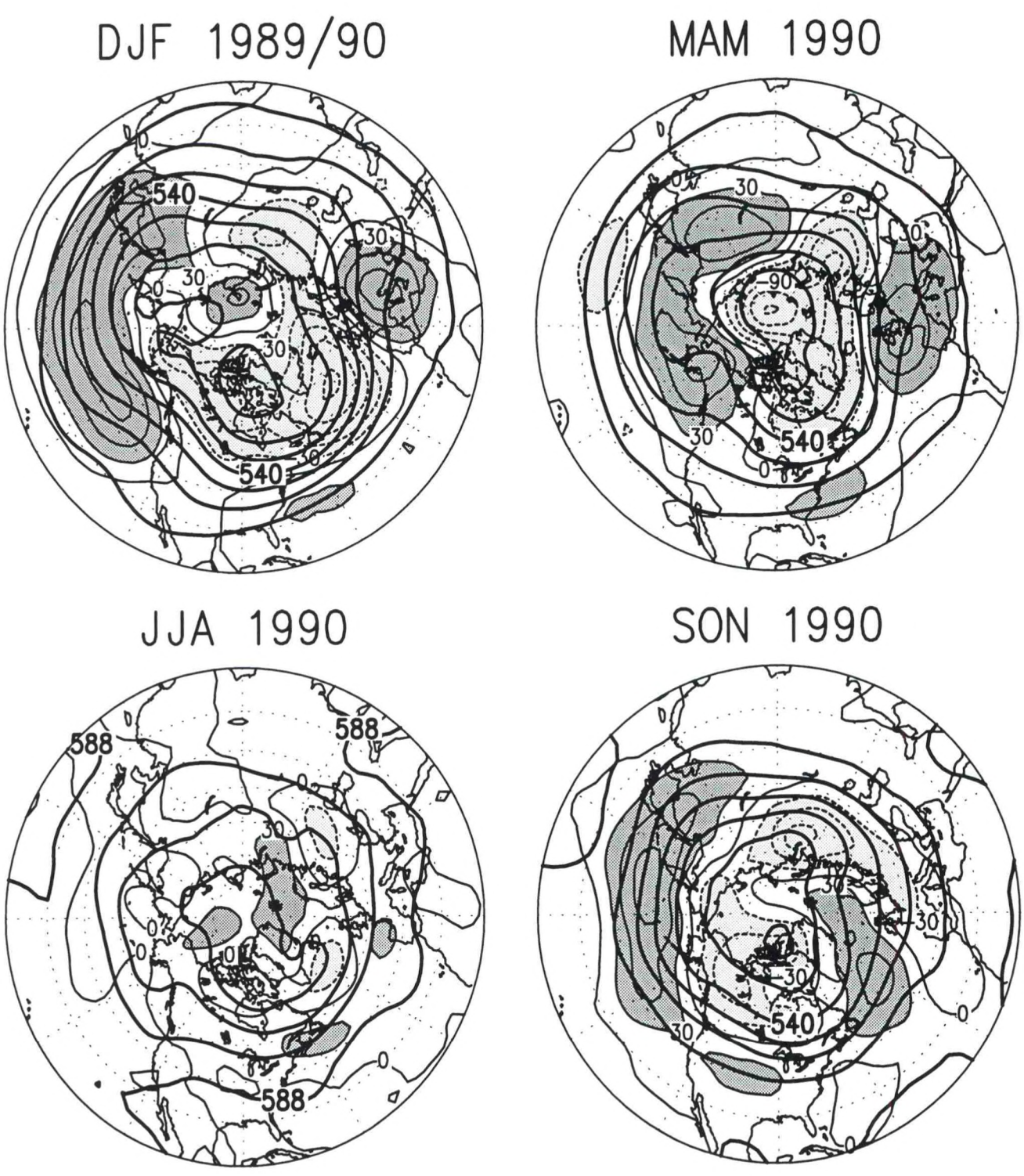

500 mb Heights and Anomalies (m)

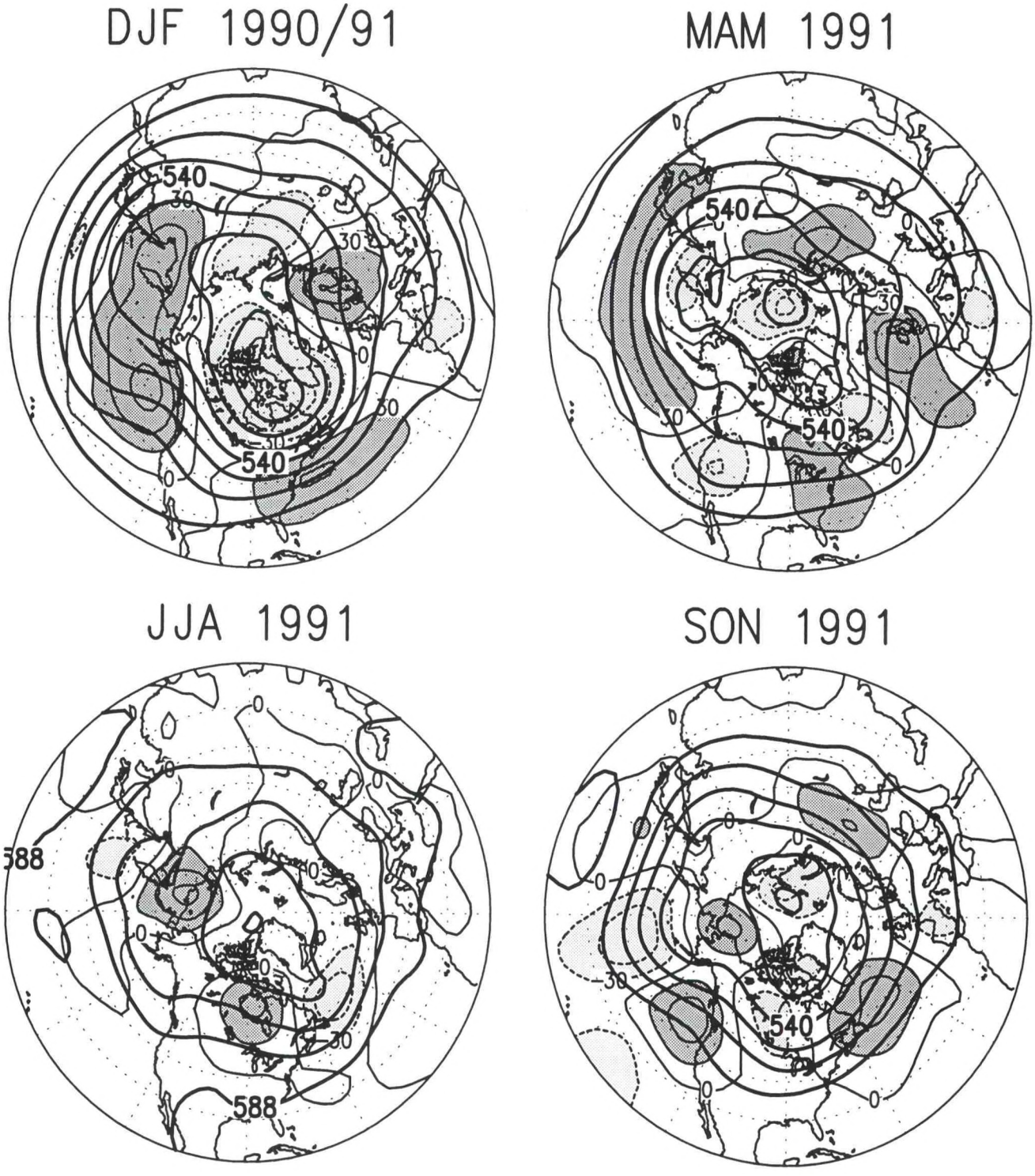

500 mb Heights and Anomalies (m)

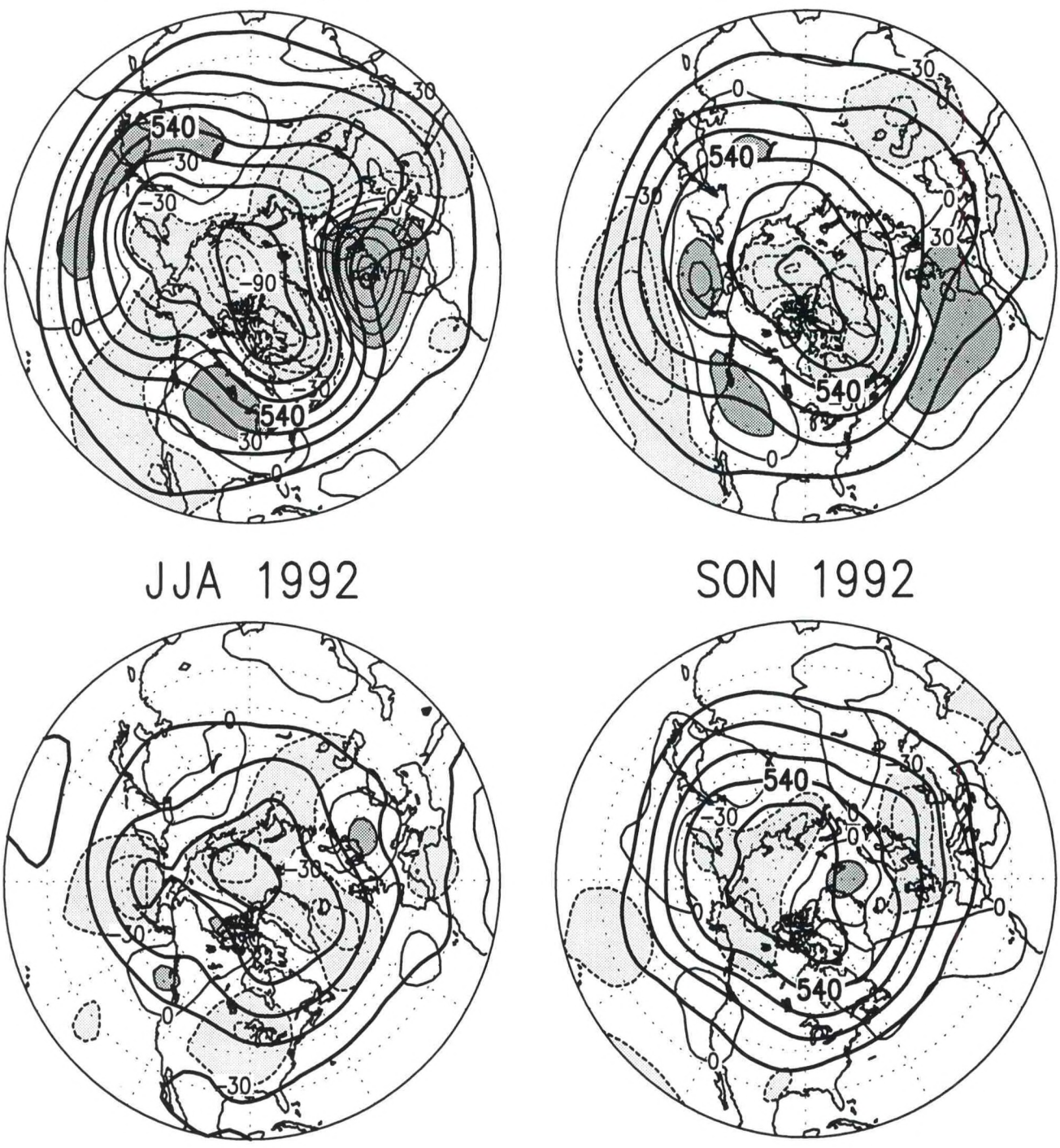

500 mb Heights and Anomalies (m)

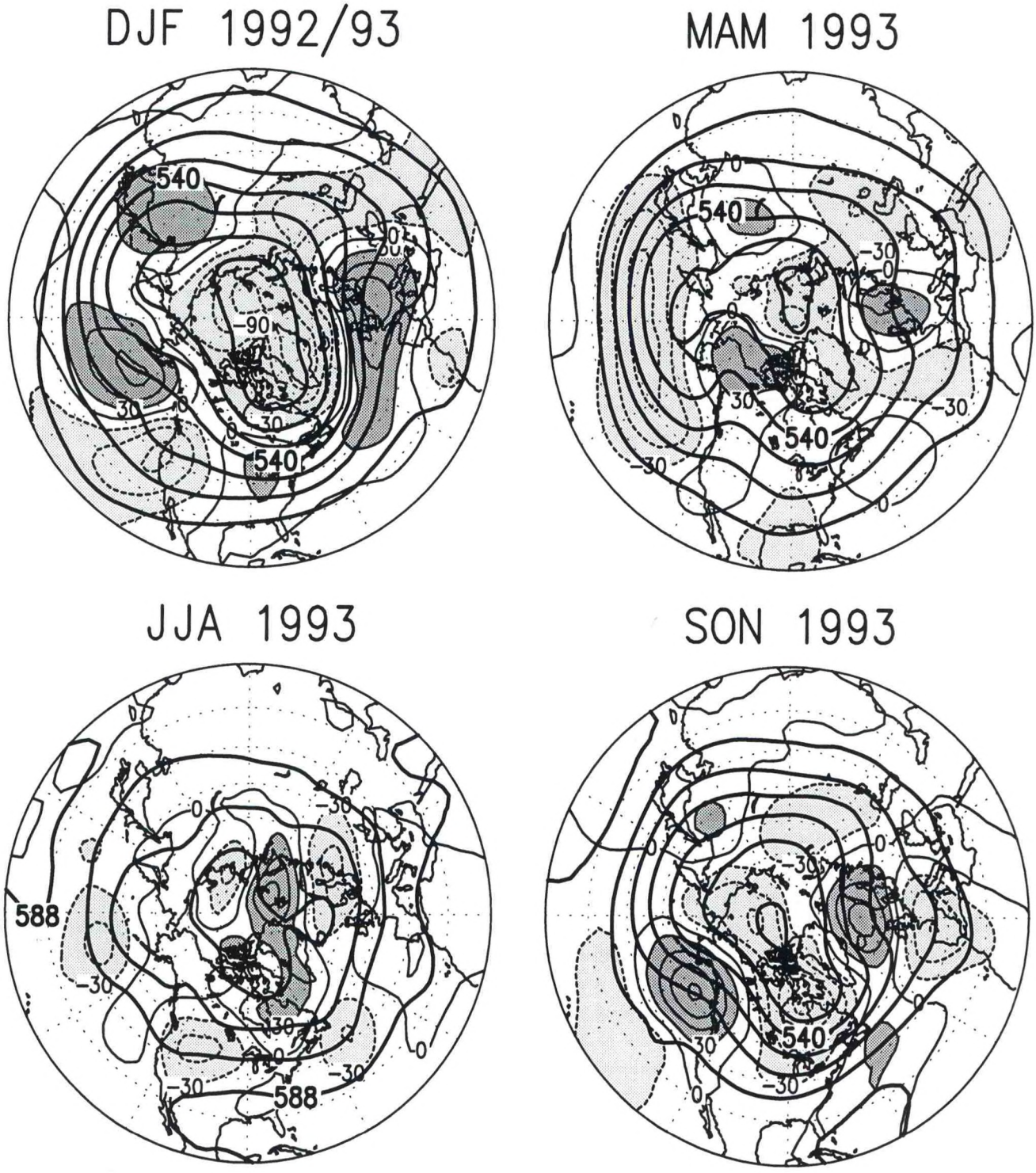

500 mb Heights and Anomalies (m)

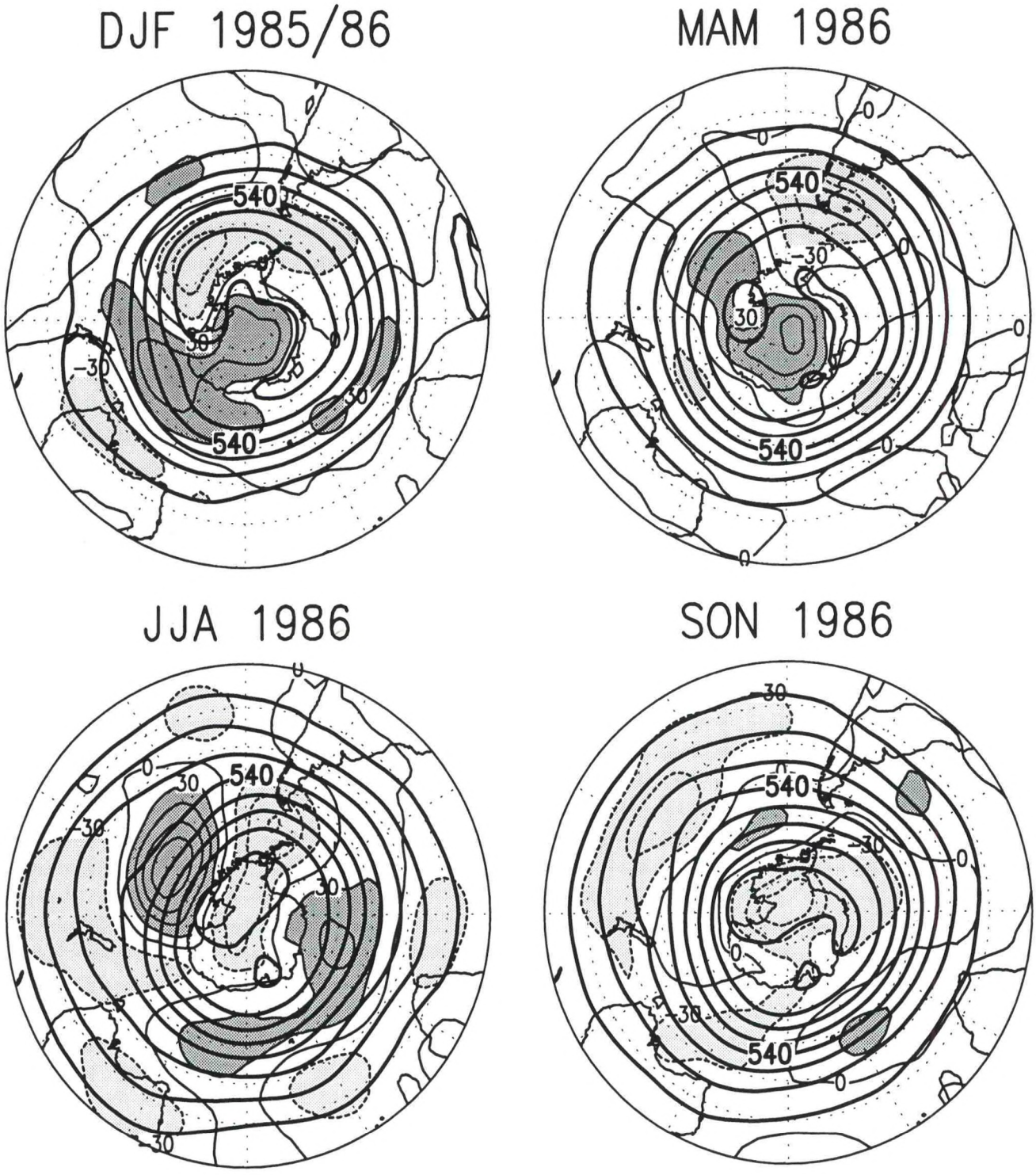

500 mb Heights and Anomalies (m)

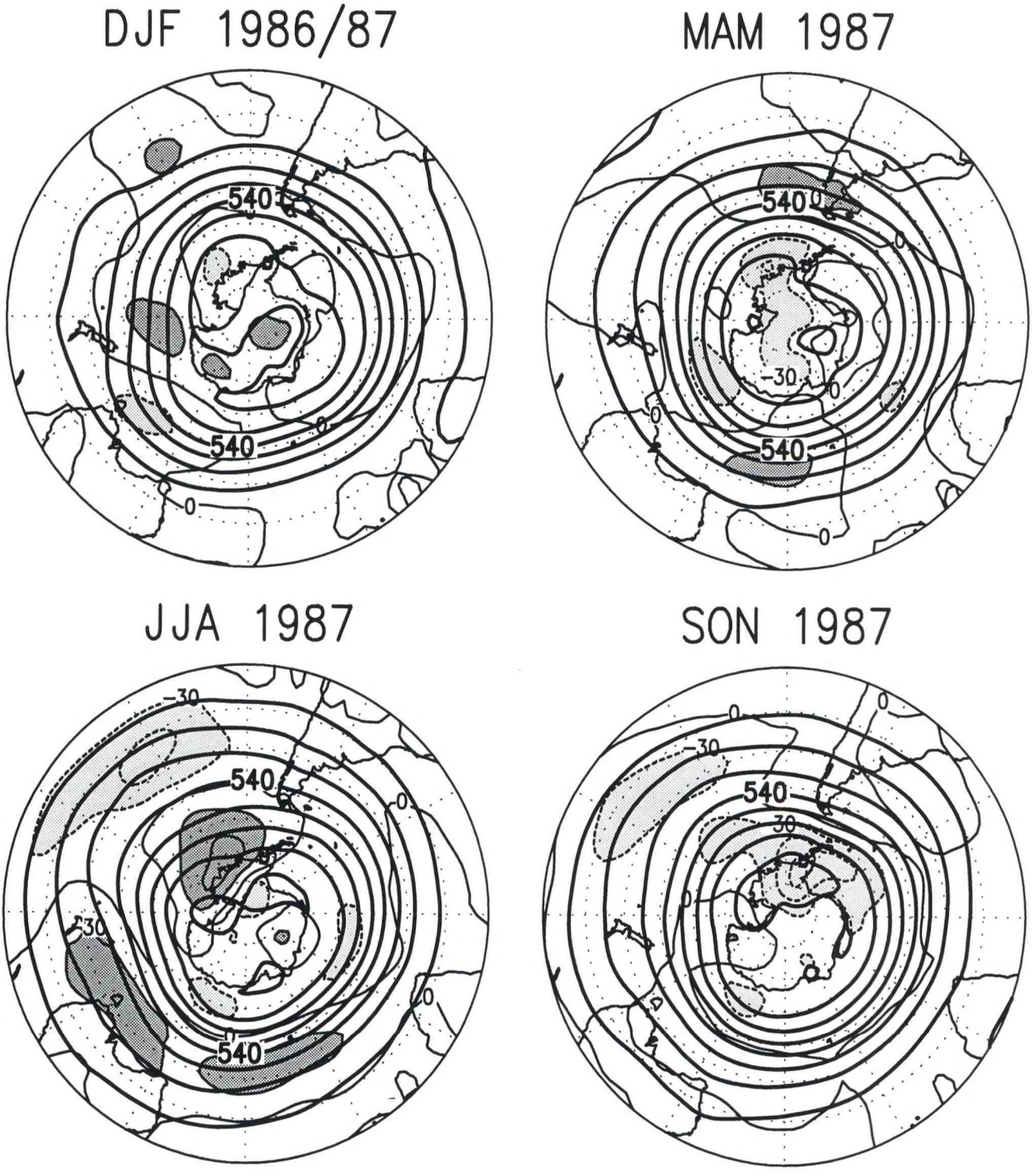

500 mb Heights and Anomalies (m)

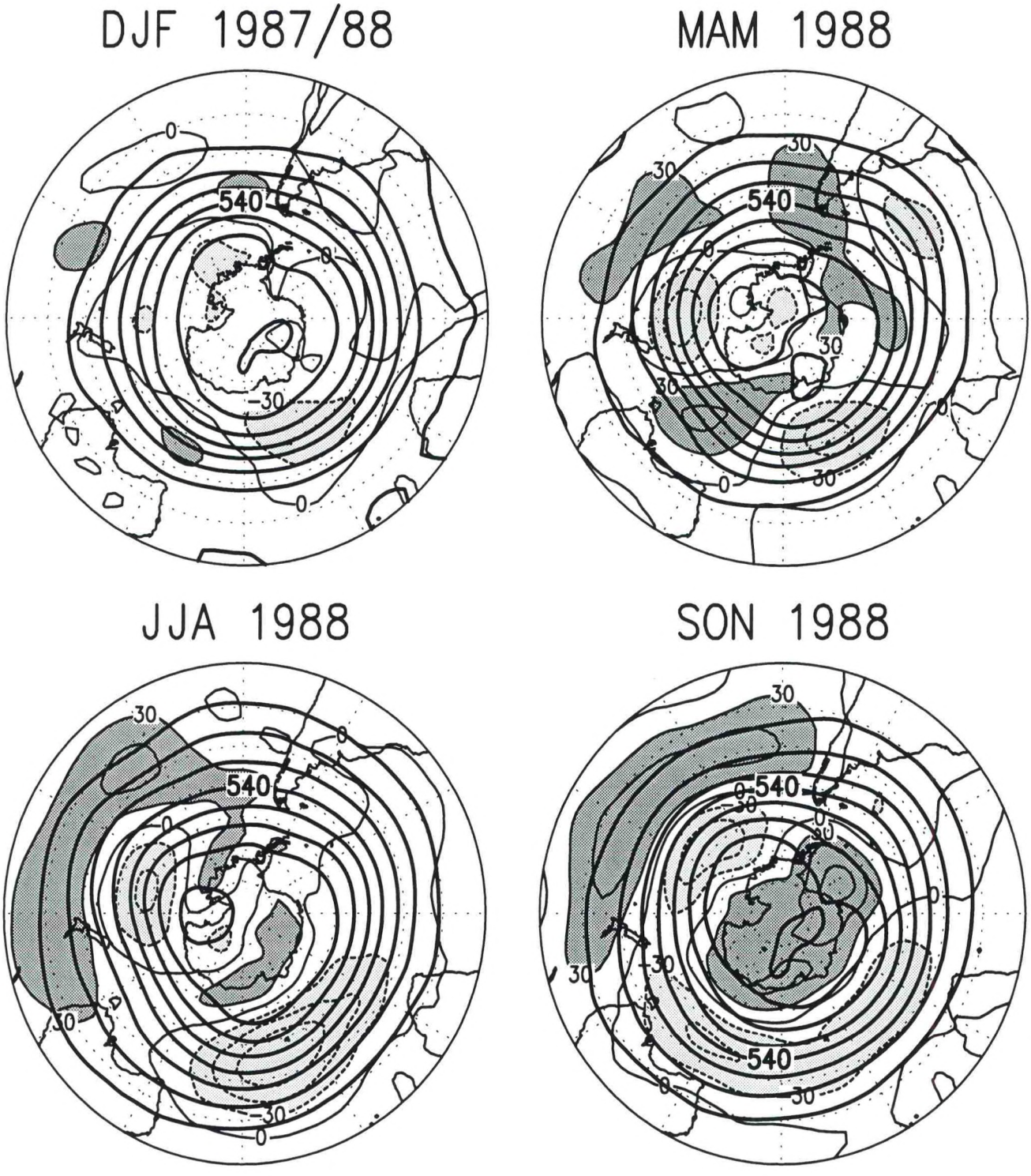

500 mb Heights and Anomalies (m)

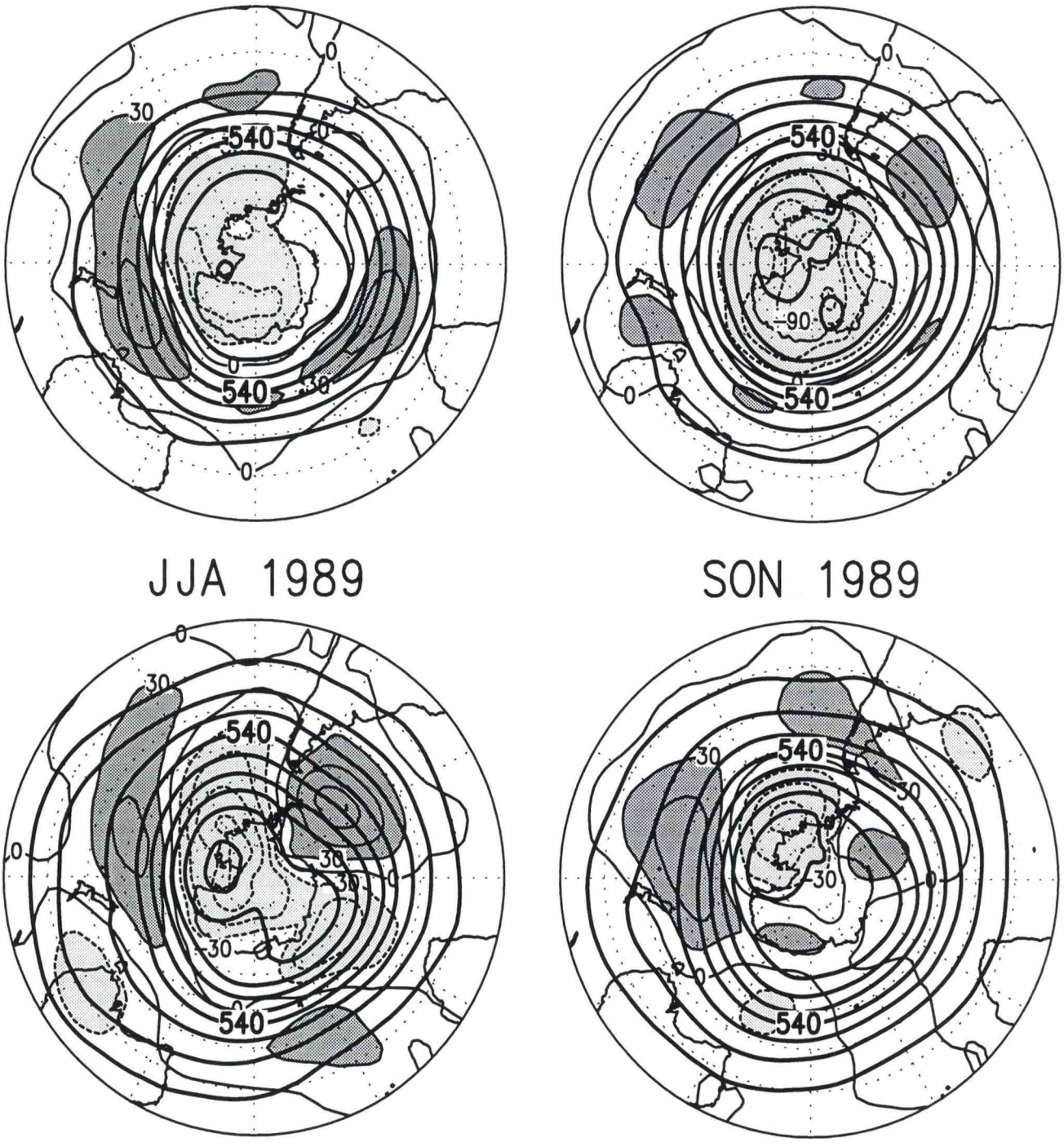

500 mb Heights and Anomalies (m)

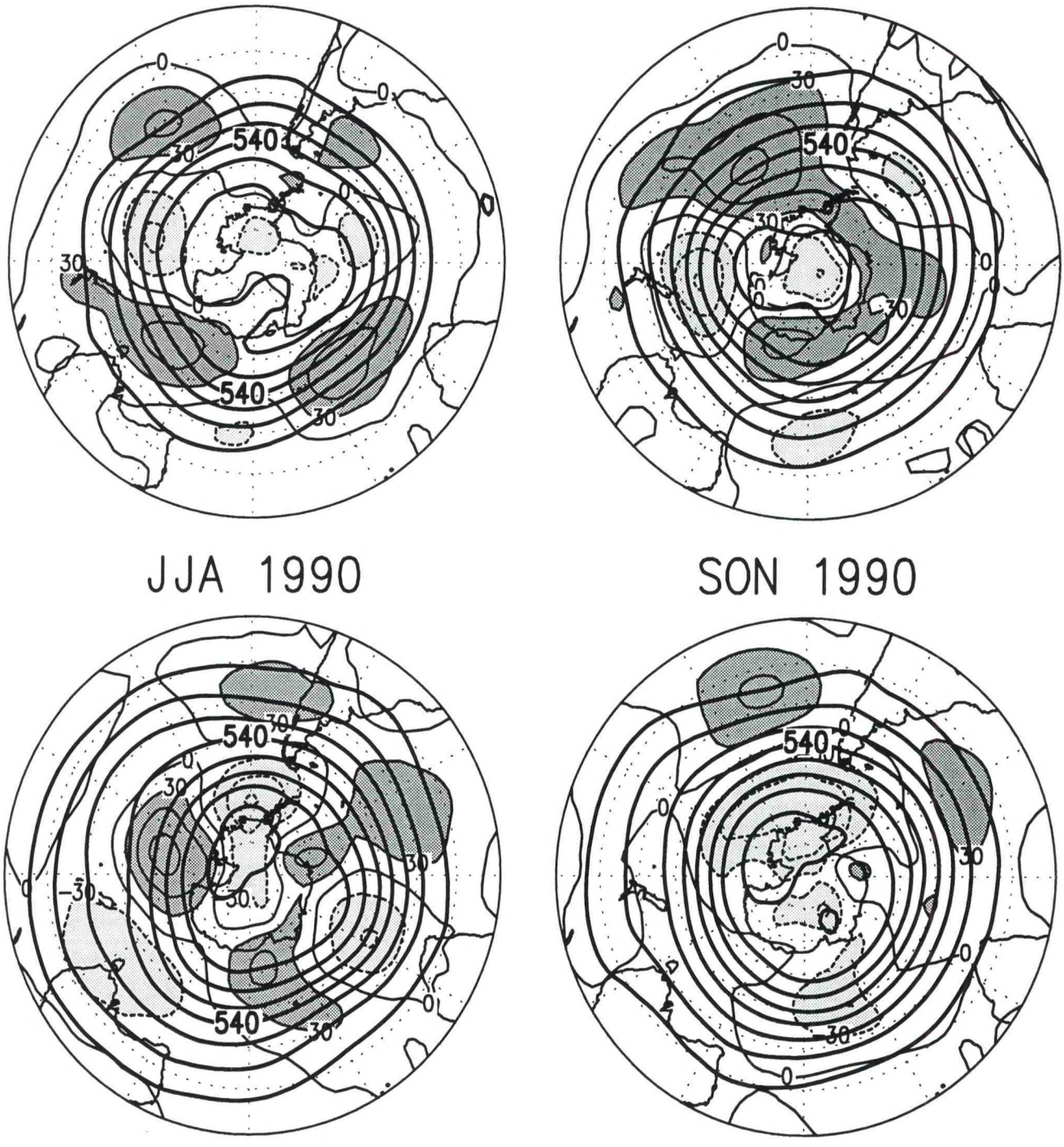

500 mb Heights and Anomalies (m)

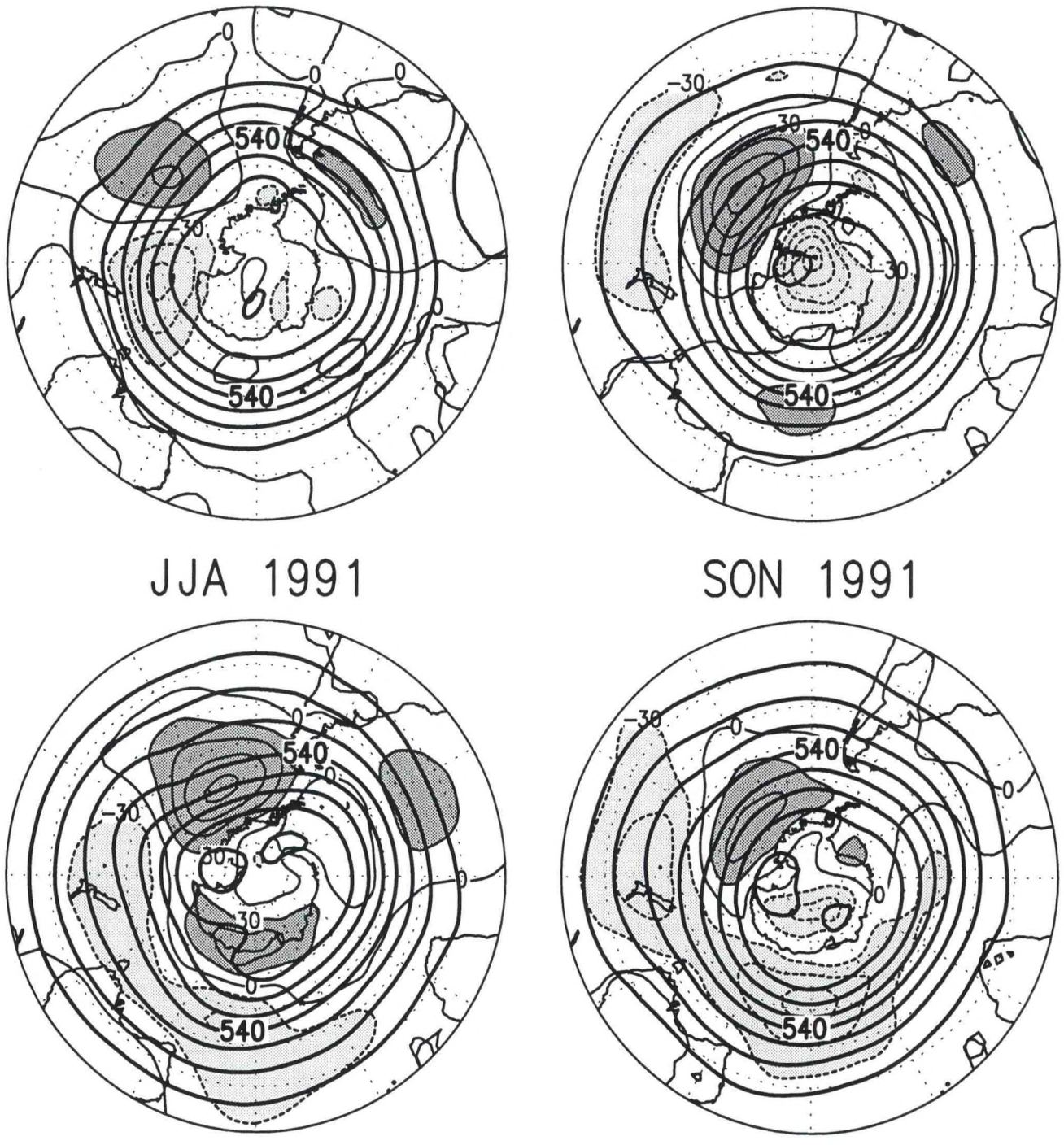

500 mb Heights and Anomalies (m)

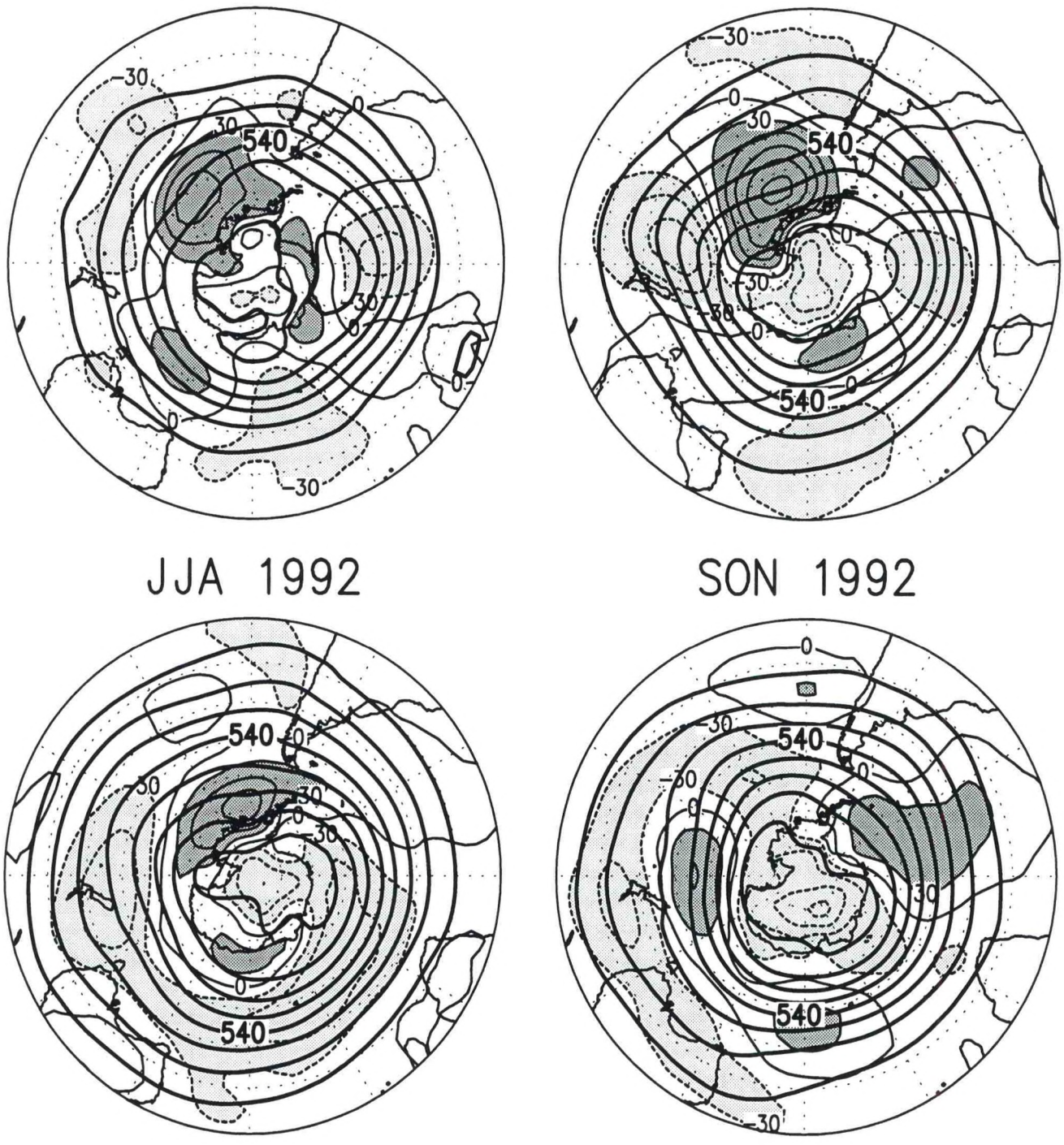

500 mb Heights and Anomalies (m)

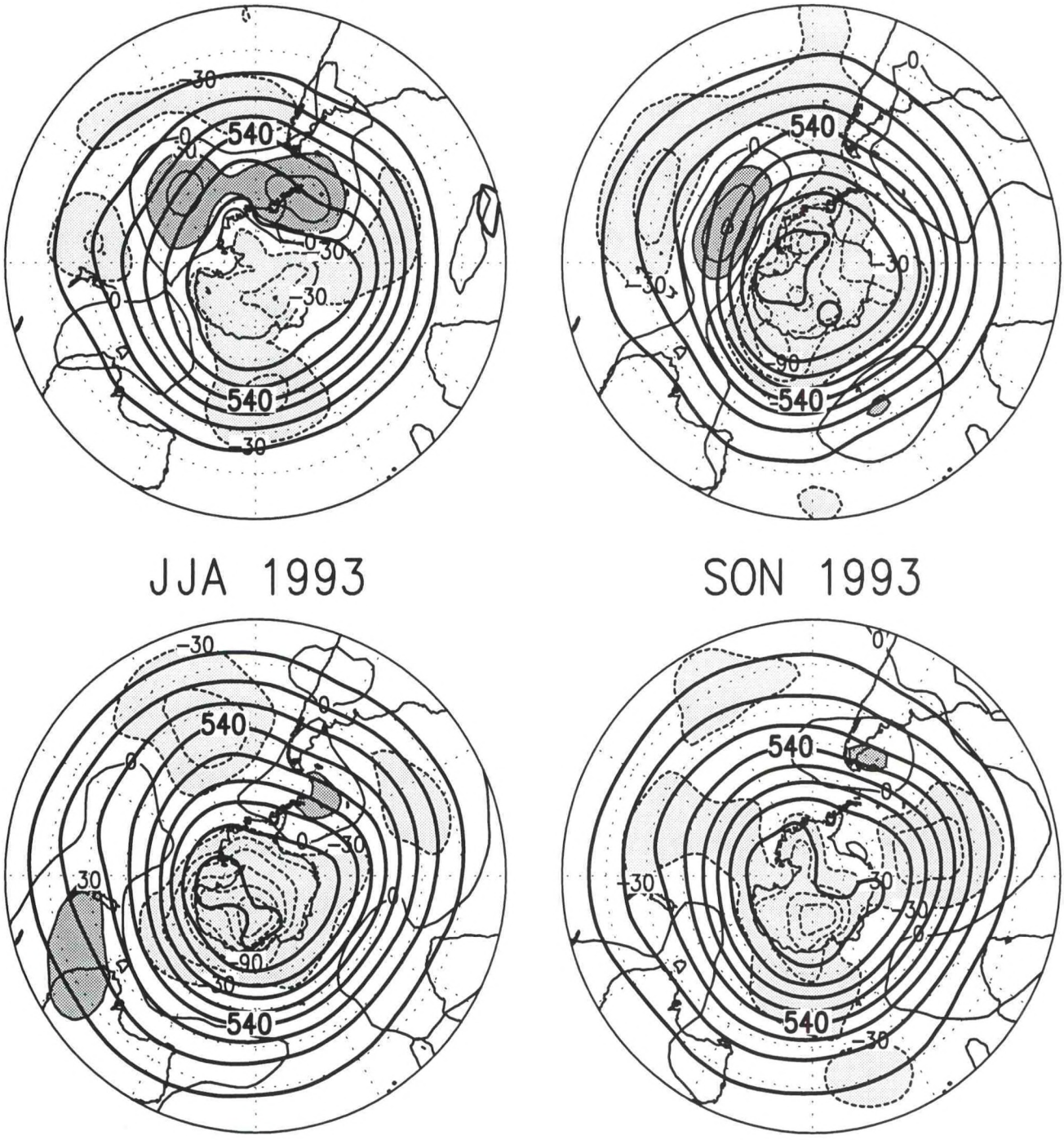

500 mb Heights and Anomalies (m)

700 mb ANOMALOUS STORM TRACK INTENSITY

Northern Hemisphere Seasonal Maps (pp. 189-196): 700-mb geopotential heights overlayed with anomalous variance of high-pass filtered (periods < 10 days) heights. Heights (m) are contoured thick every 60 m. Anomalous variance is normalized by the standard deviation of the high-pass filtered variance calculated over the 1964-1993 base period. Contour interval (thin contours) for anomalous variance is 0.5 standard deviations (σ). Thin solid contours and shading (dashed contours) indicate above- (below-) normal high frequency variability. Values exceeding 0.5σ are shaded dark and values less than -0.5σ are shaded light.

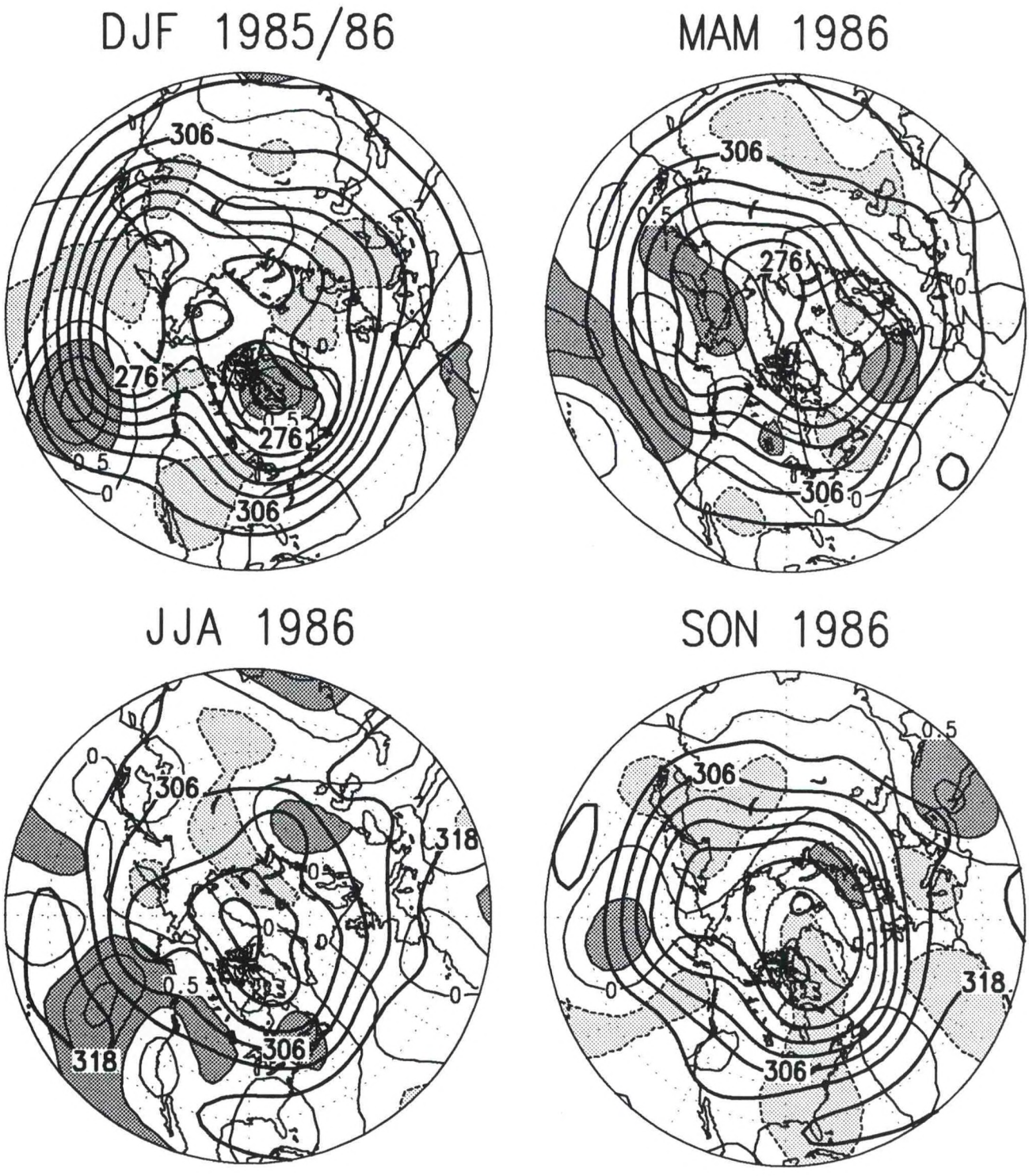

700 mb Heights and Anomalous HF Variability

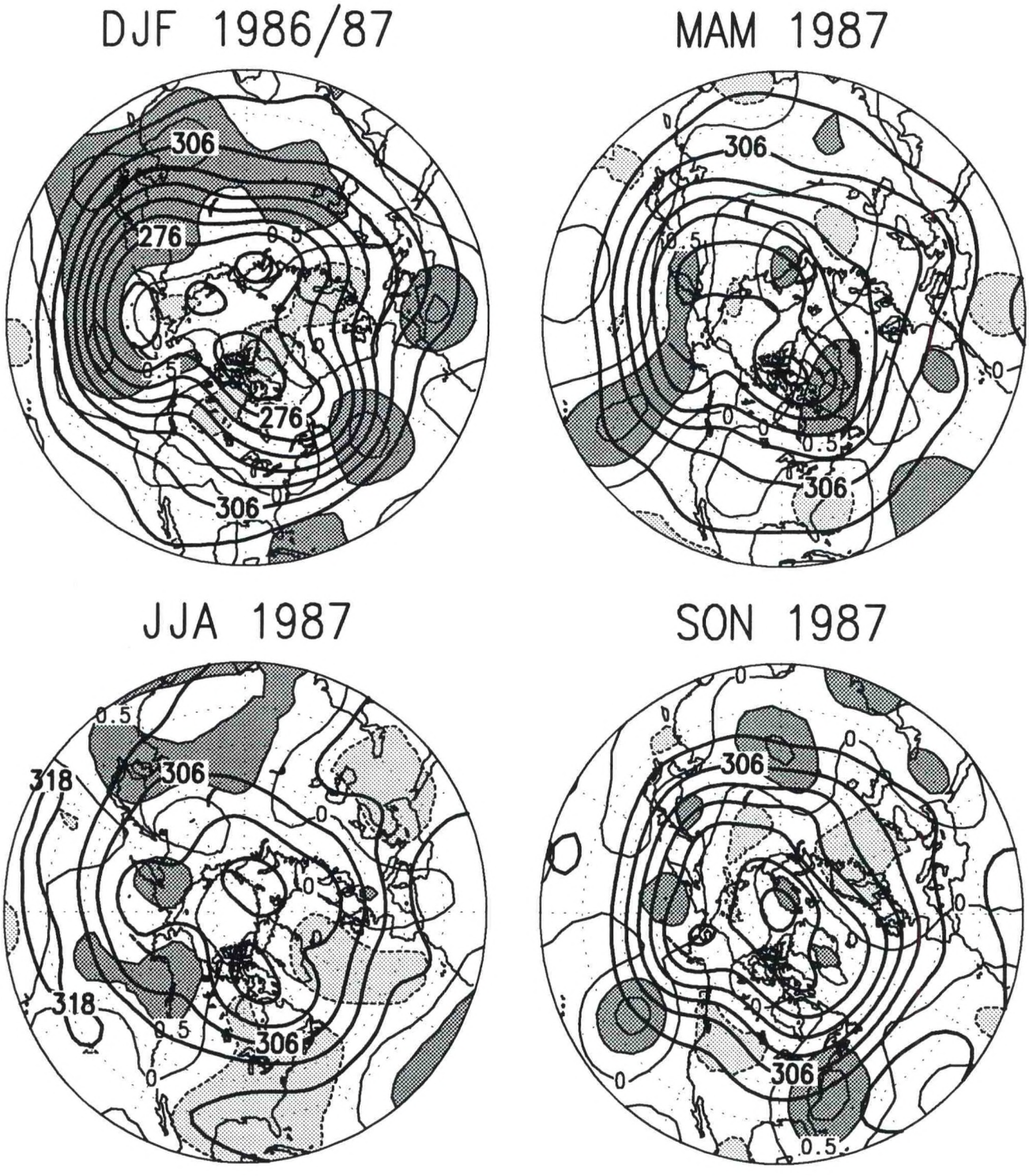

700 mb Heights and Anomalous HF Variability

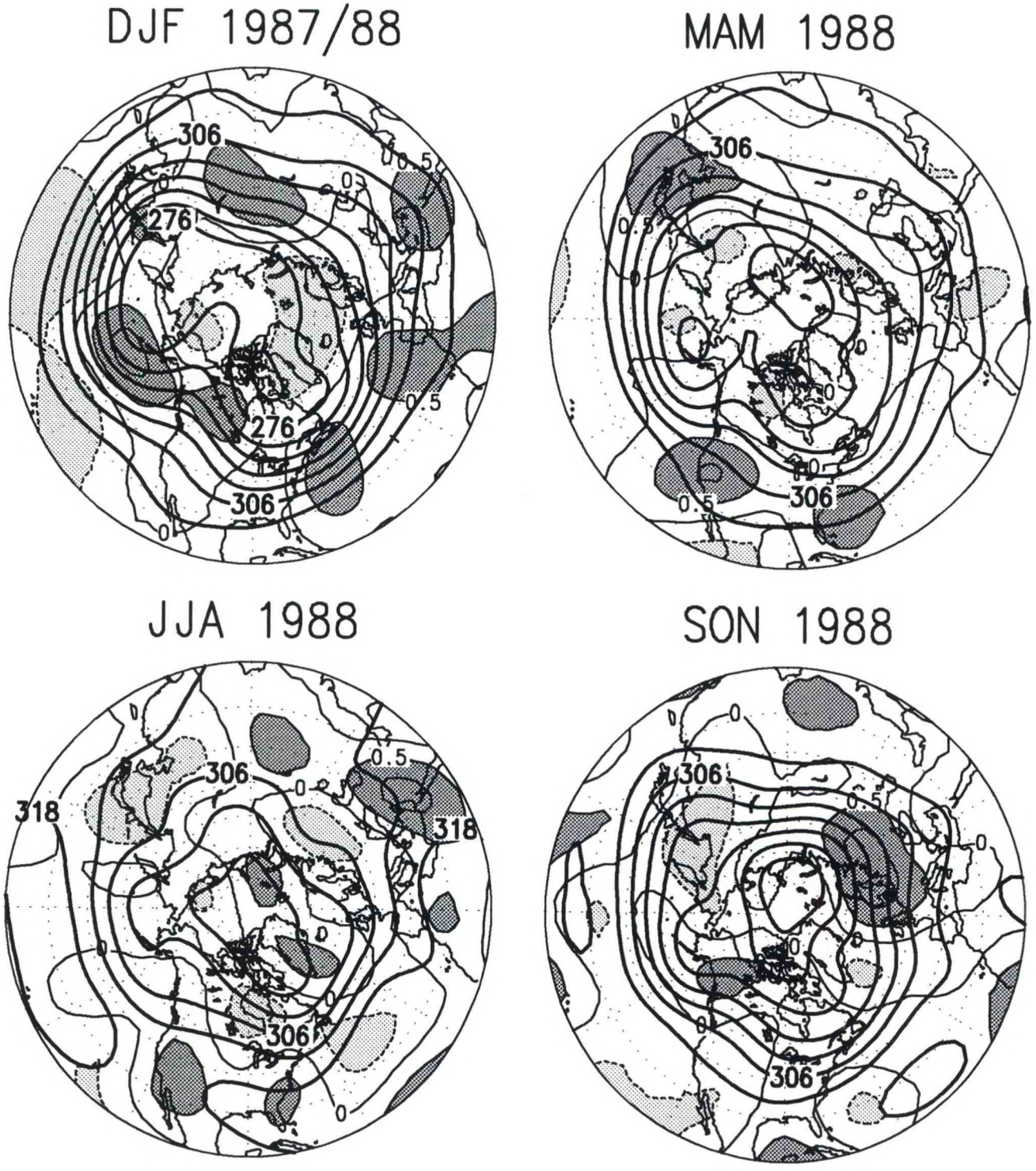

700 mb Heights and Anomalous HF Variability

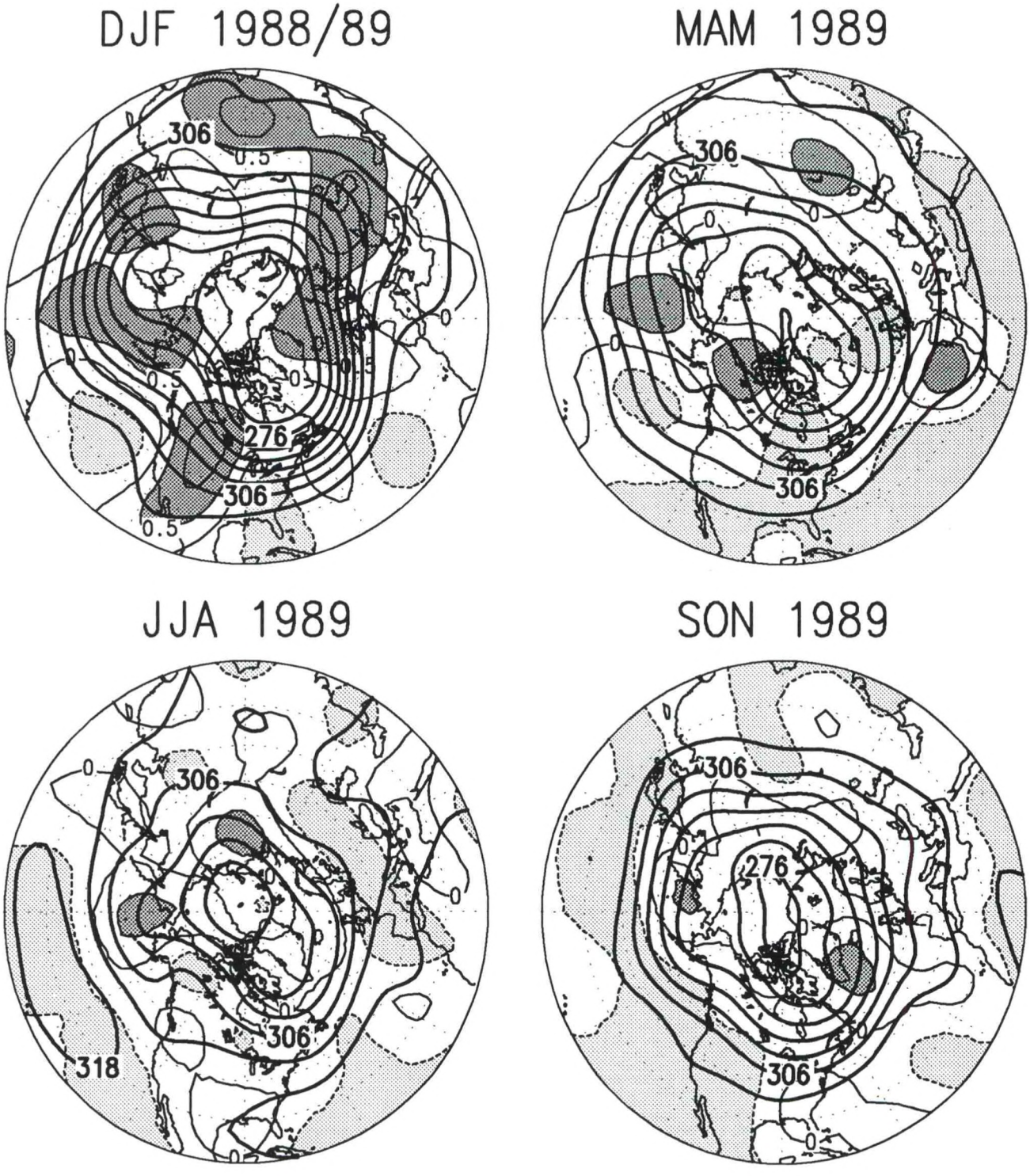

700 mb Heights and Anomalous HF Variability

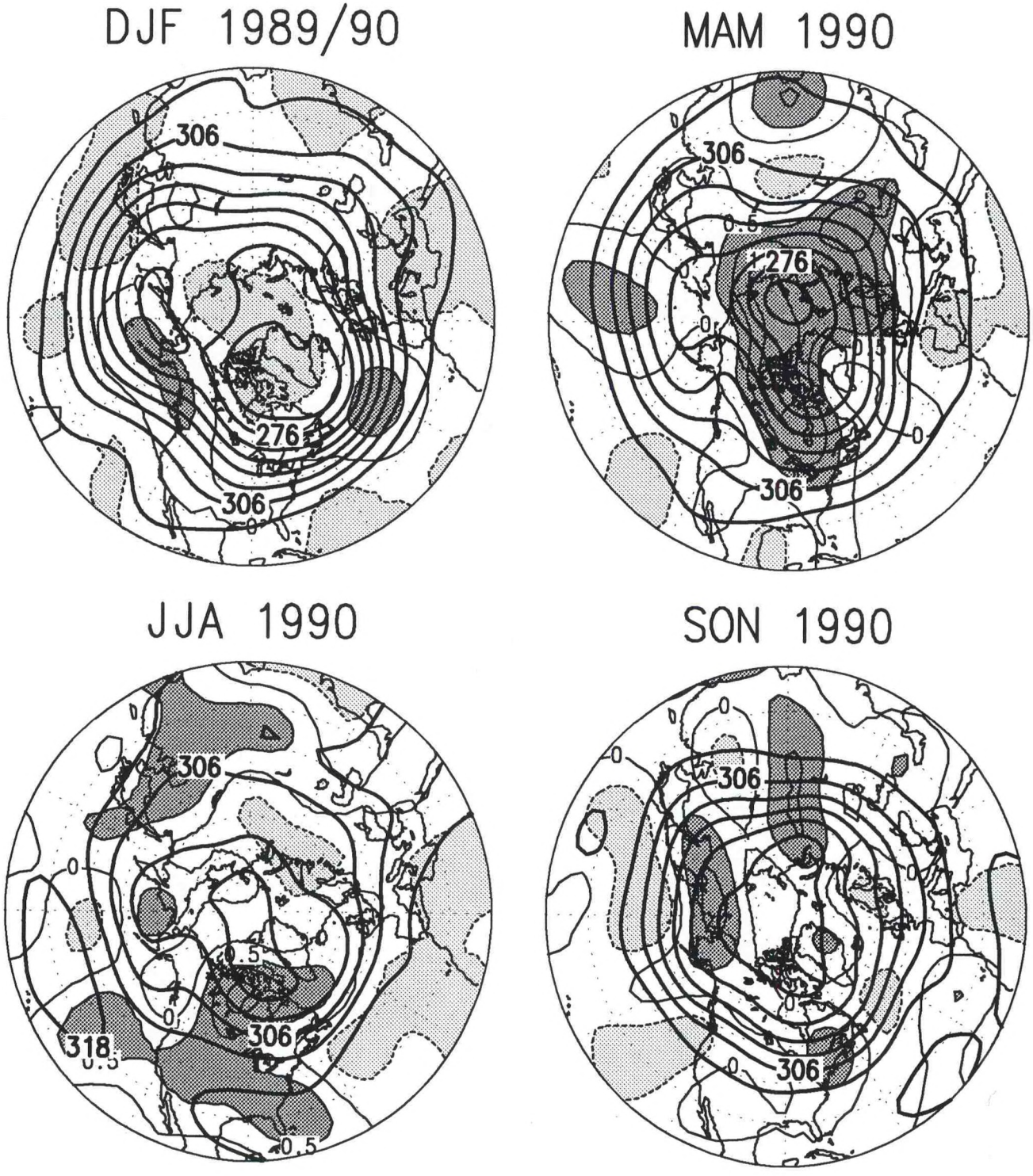

700 mb Heights and Anomalous HF Variability

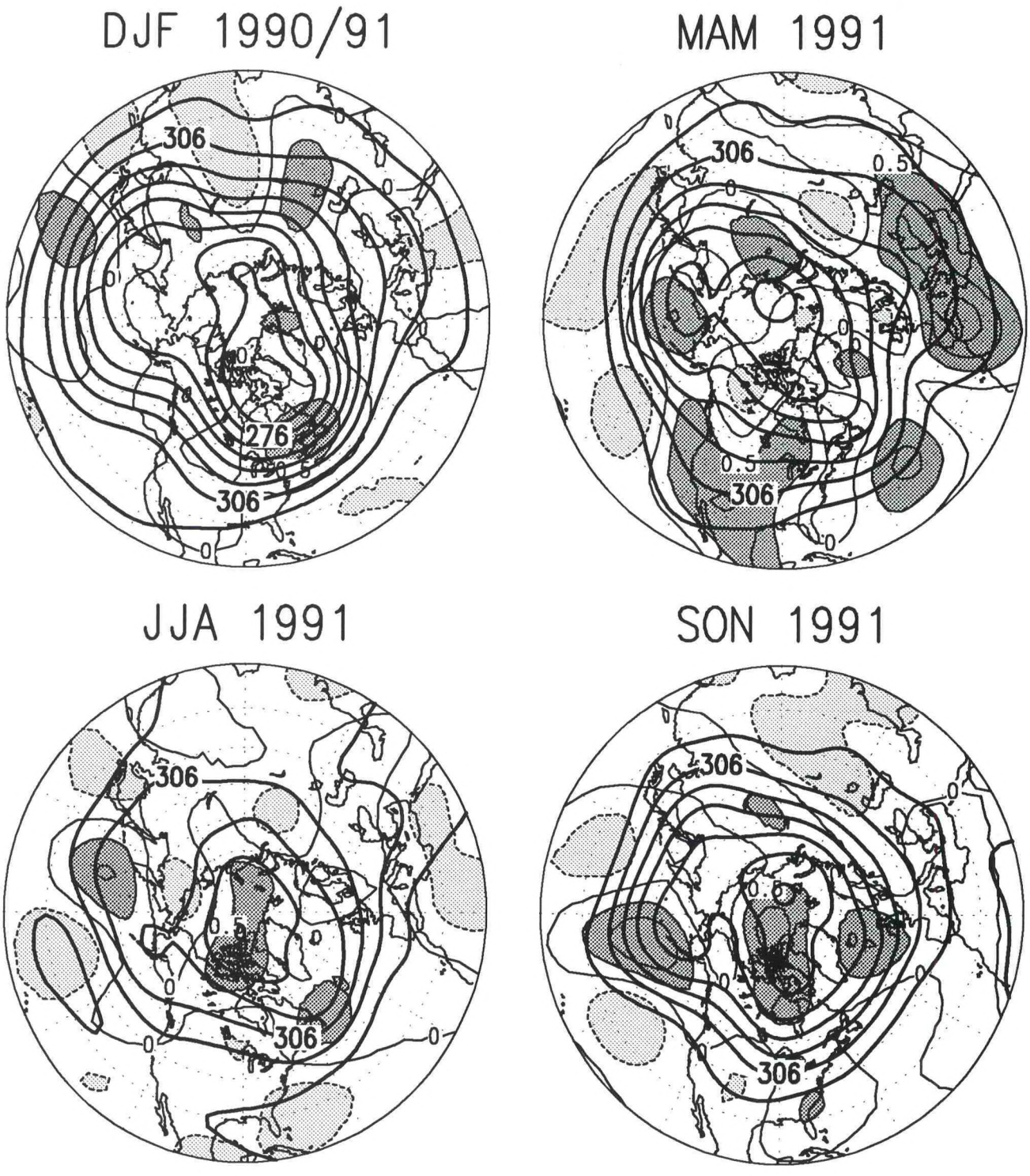

700 mb Heights and Anomalous HF Variability

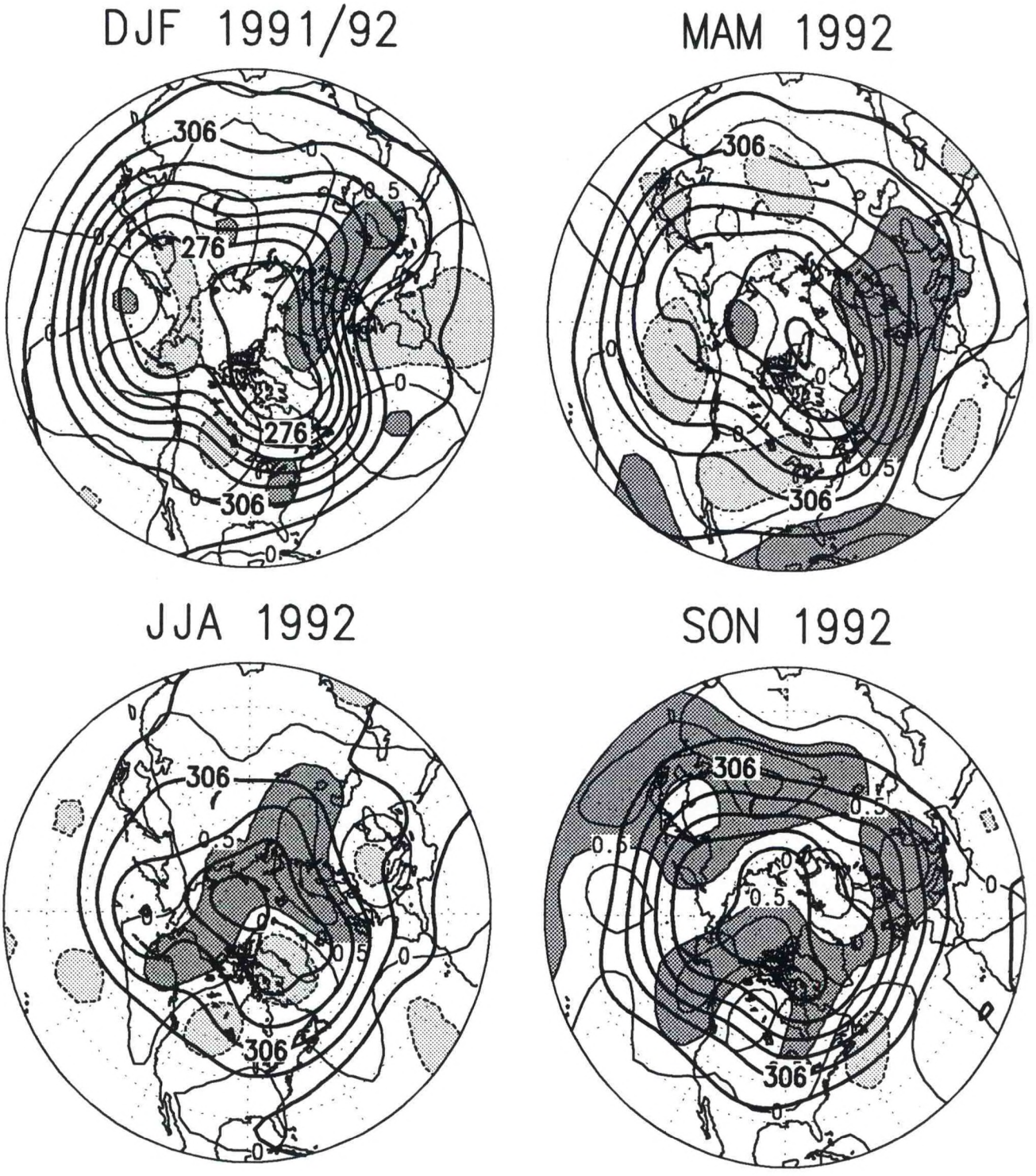

700 mb Heights and Anomalous HF Variability

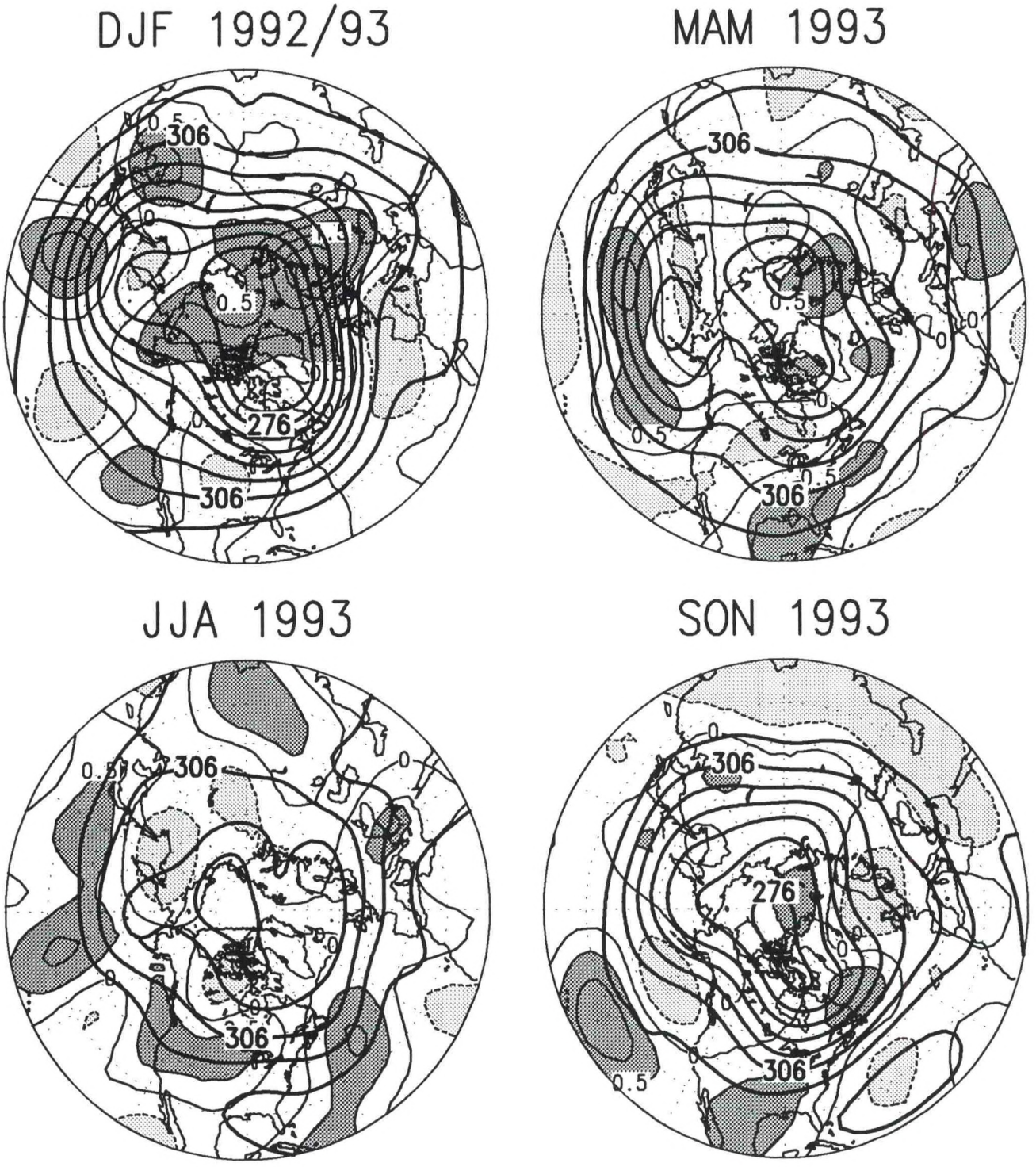

700 mb Heights and Anomalous HF Variability

SURFACE AIR TEMPERATURE ANOMALY

Northern Hemisphere Seasonal Maps (pp. 198-205): Surface air temperature anomaly (°C). Solid contours and dark shading indicate anomalies greater than 1°C. Dashed contours and light shading indicate anomalies below -1°C. Contour interval is 1°C, and the zero contour is shown thick solid. The contoured values are defined using a modified Cressman (1959) analysis. The analysis is suppressed in regions where no data is available. Anomalies are computed with respect to the 1961-1990 base period.

Southern Hemisphere Seasonal Maps (pp. 206-213): Surface air temperature anomaly (°C). Solid contours and dark shading indicate anomalies greater than 1°C. Dashed contours and light shading indicate anomalies below -1°C. Contour interval is 1°C, and the zero contour is shown thick solid. The contoured values are defined using a modified Cressman (1959) analysis. The analysis is suppressed in regions where no data is available. Anomalies are computed with respect to the 1961-1990 base period.

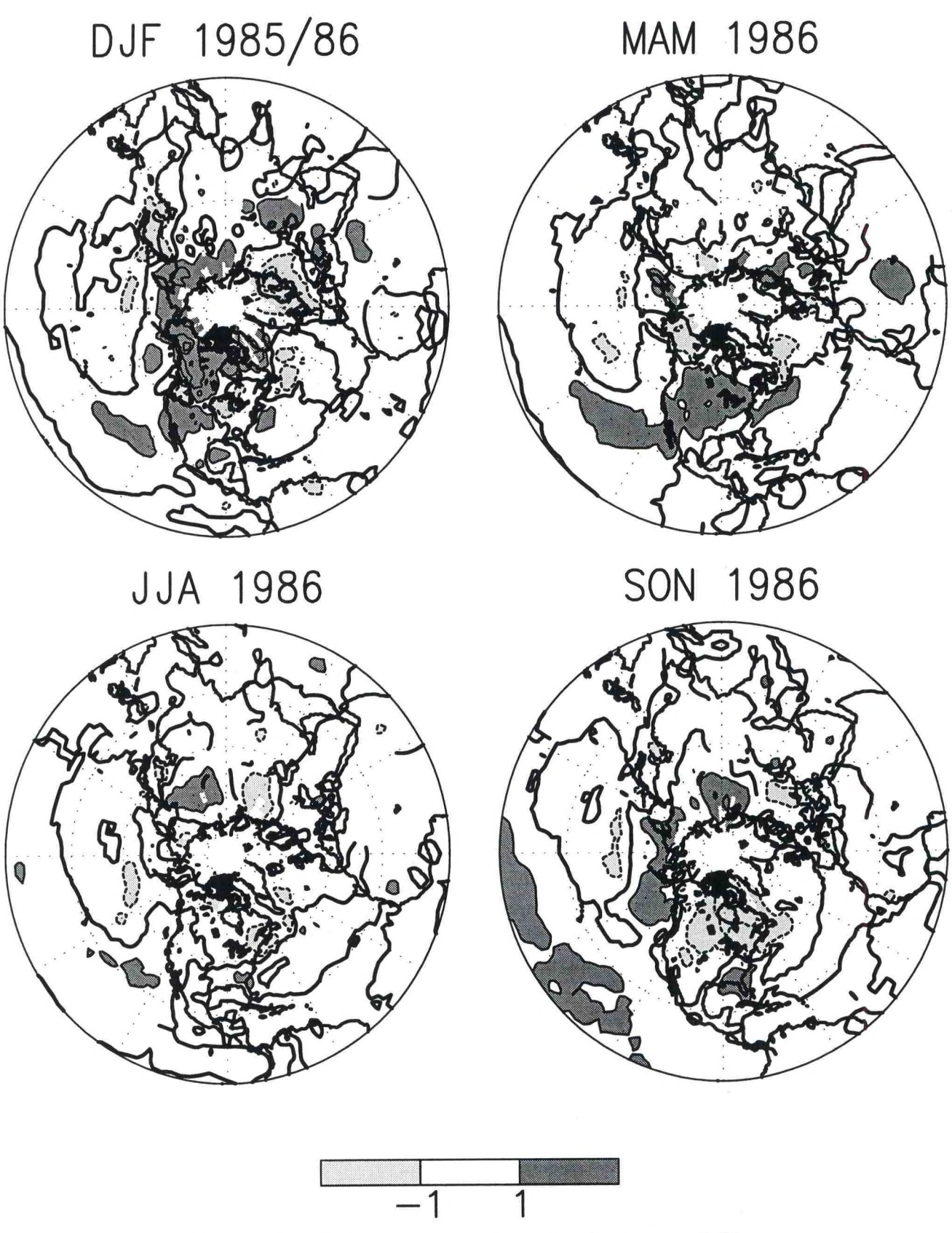

Surface Temperature Anomaly (°C)

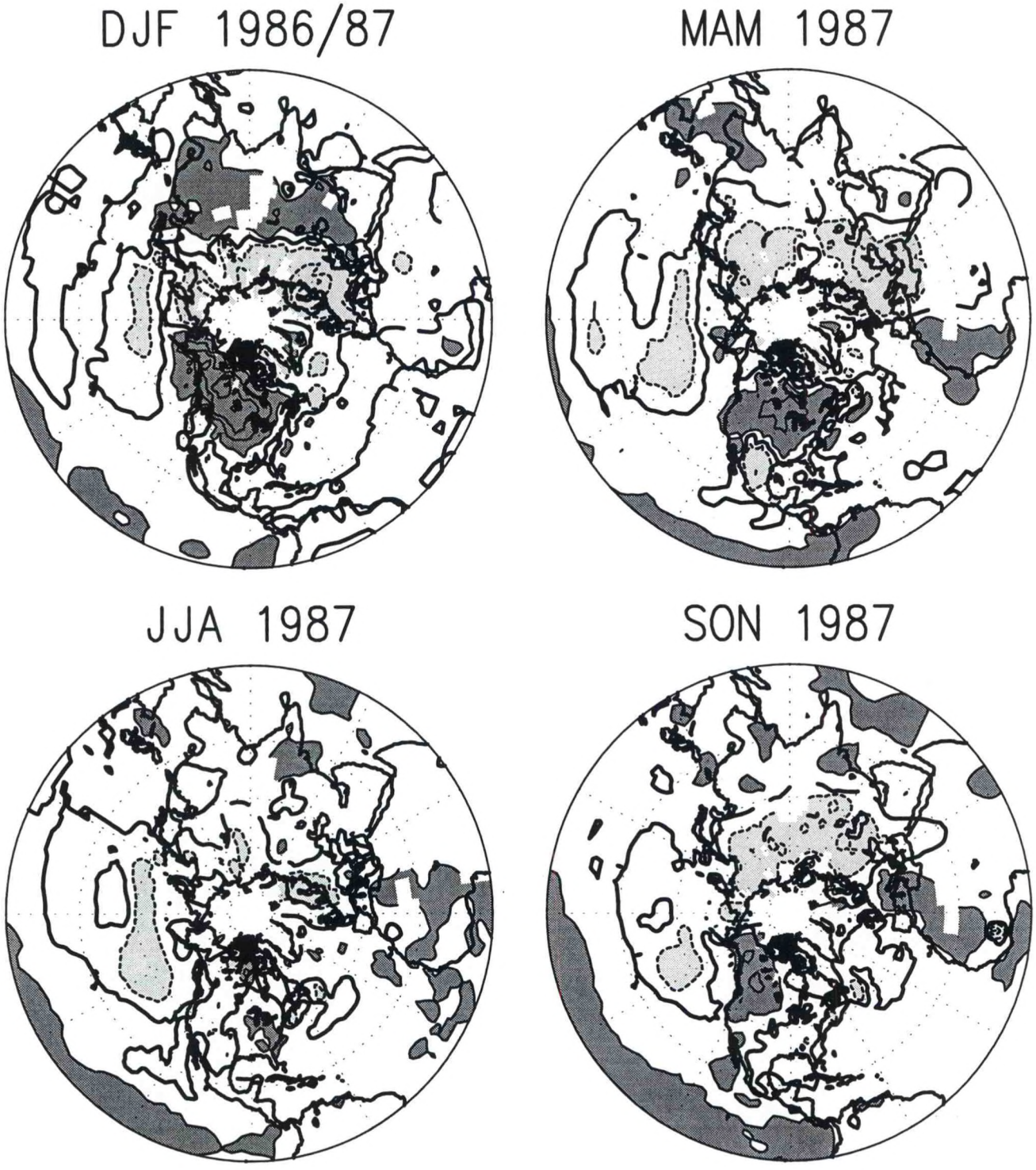

Surface Temperature Anomaly (°C)

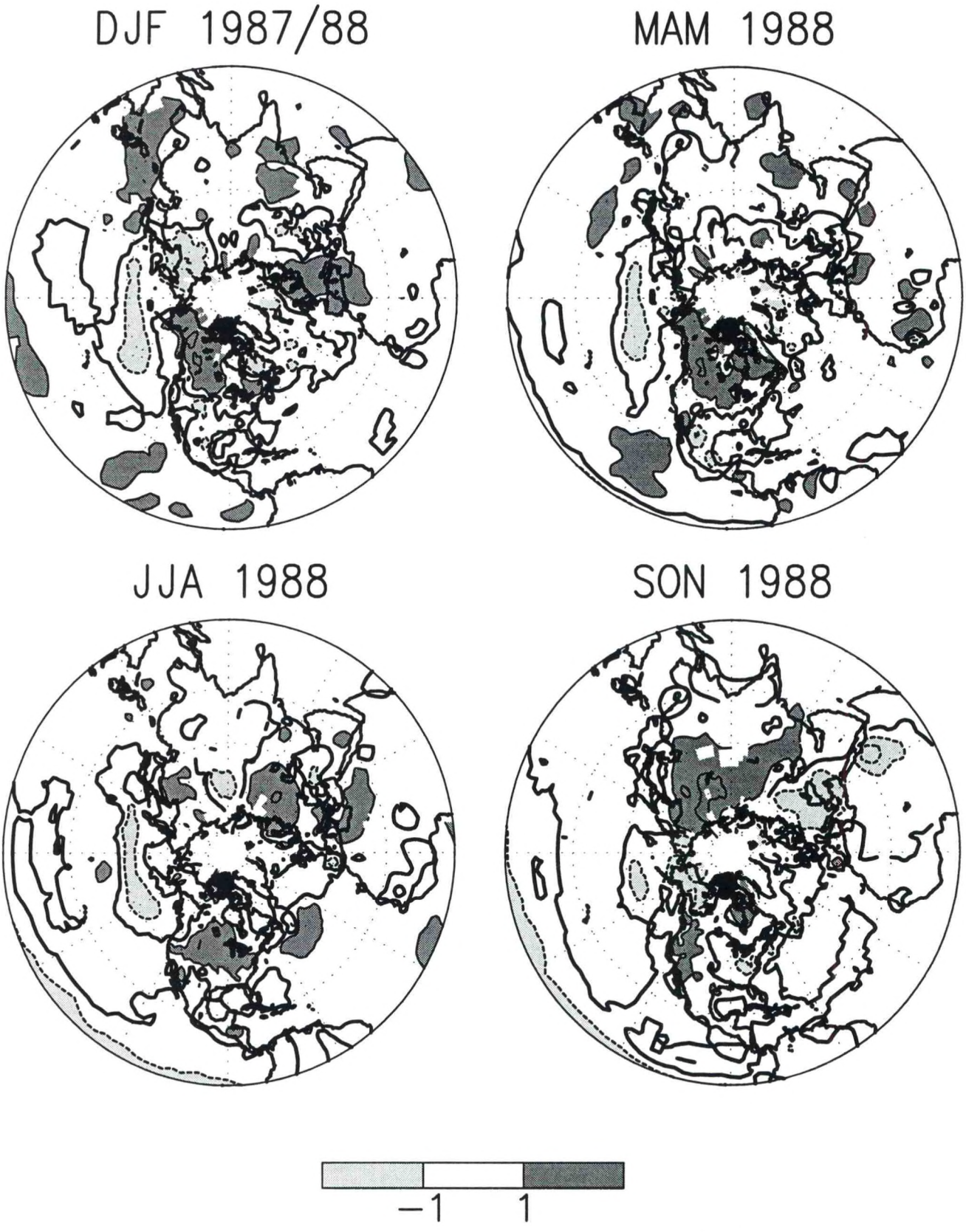

Surface Temperature Anomaly (°C)

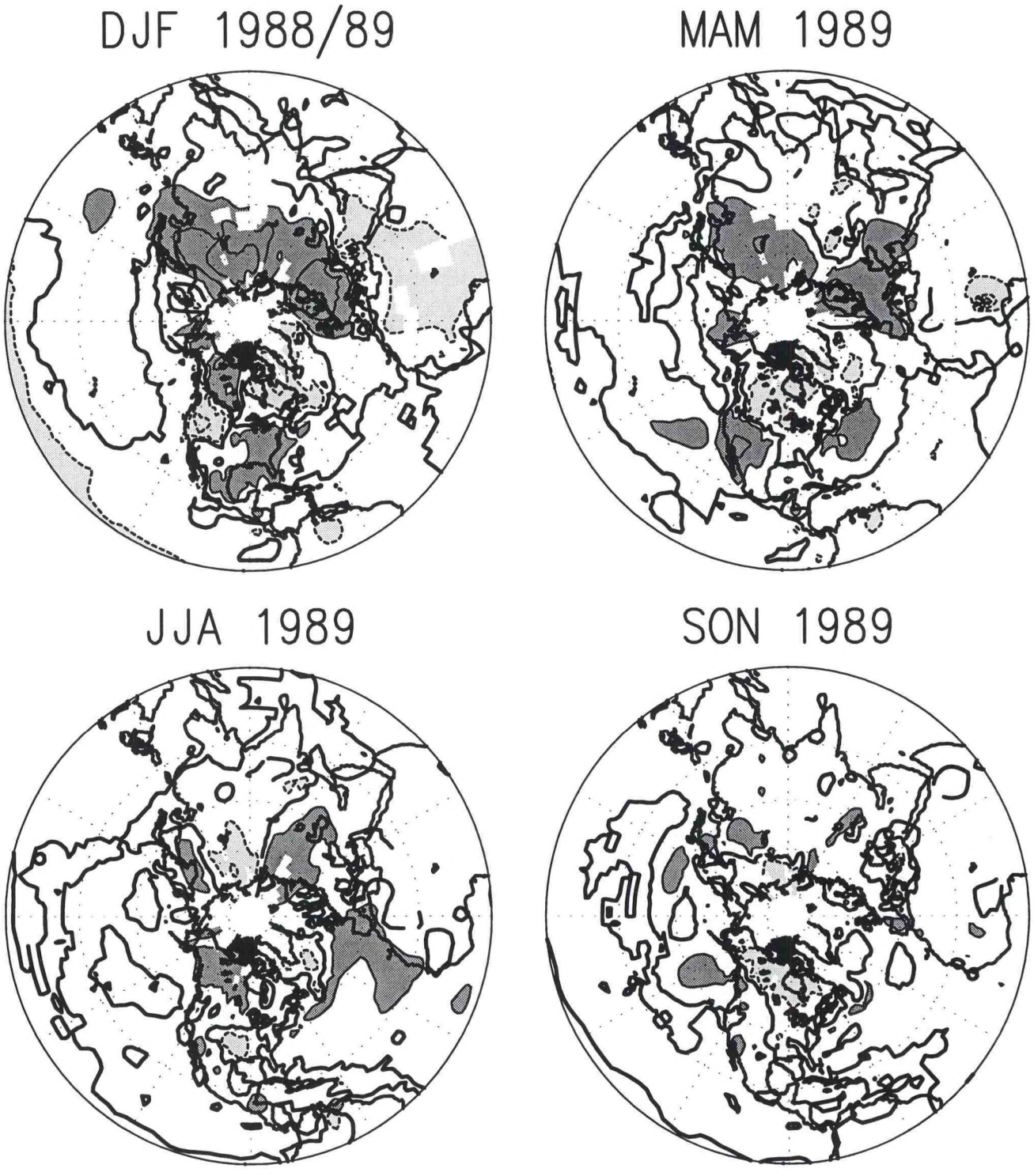

Surface Temperature Anomaly (°C)

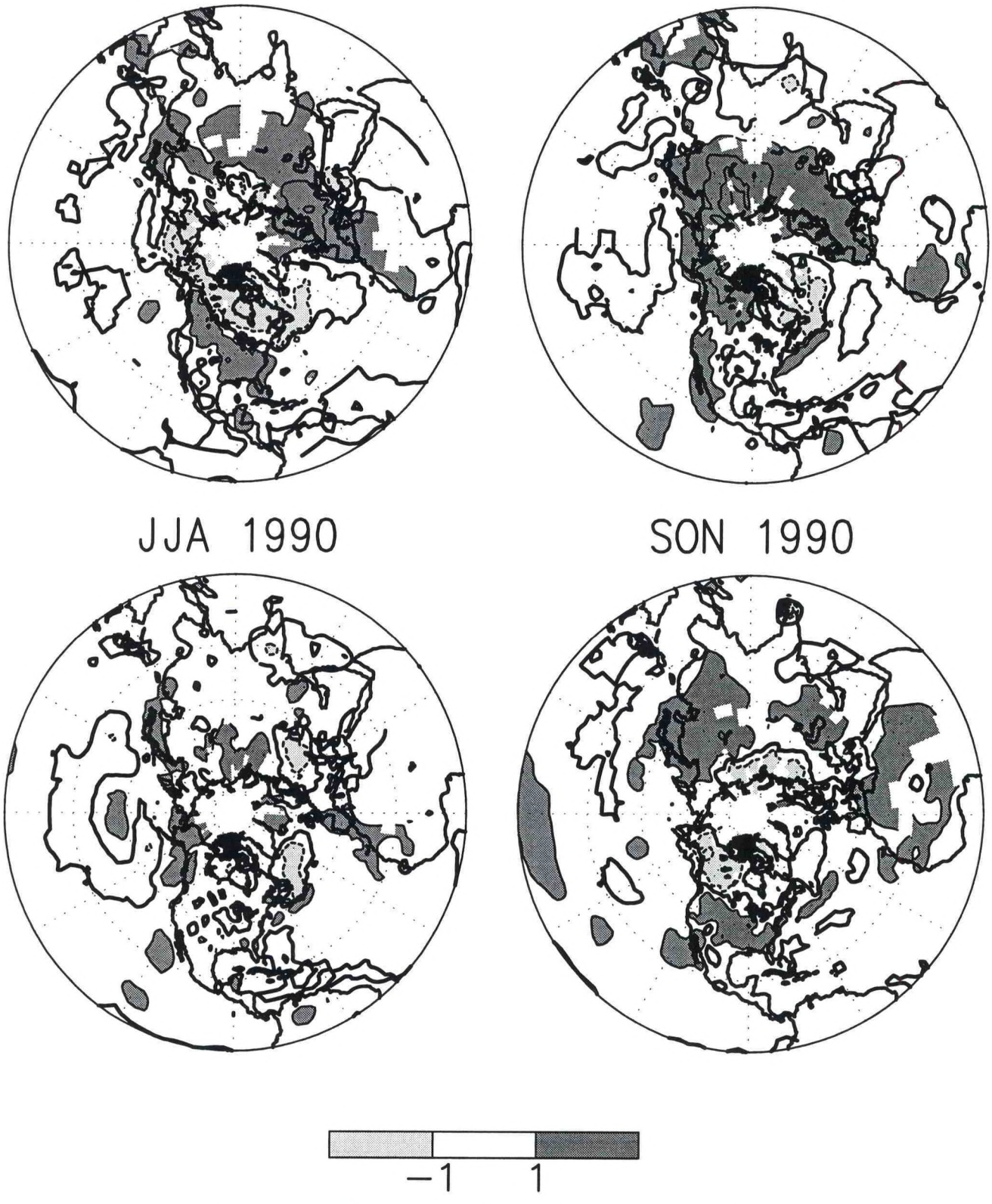

Surface Temperature Anomaly (°C)

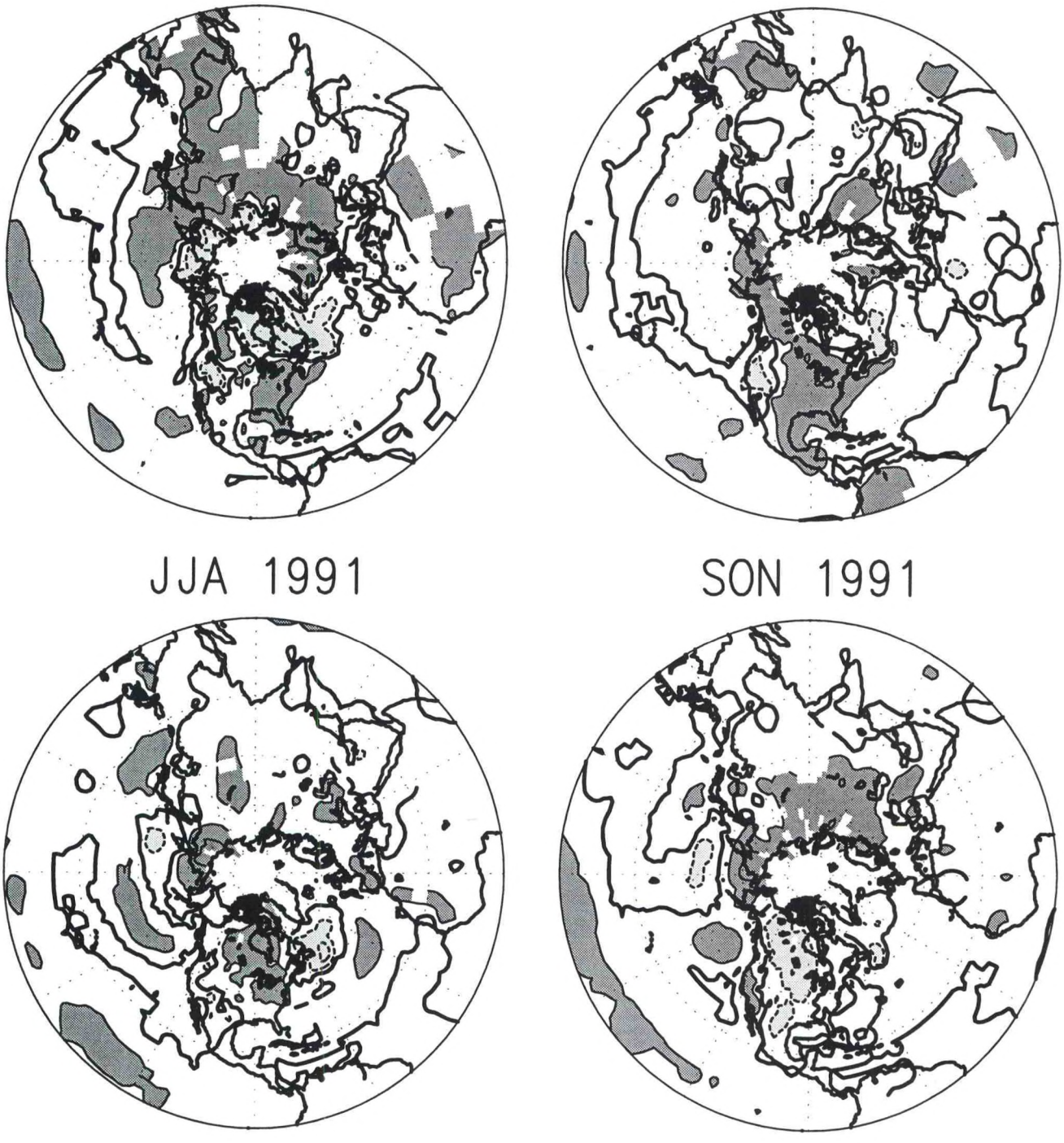

Surface Temperature Anomaly (°C)

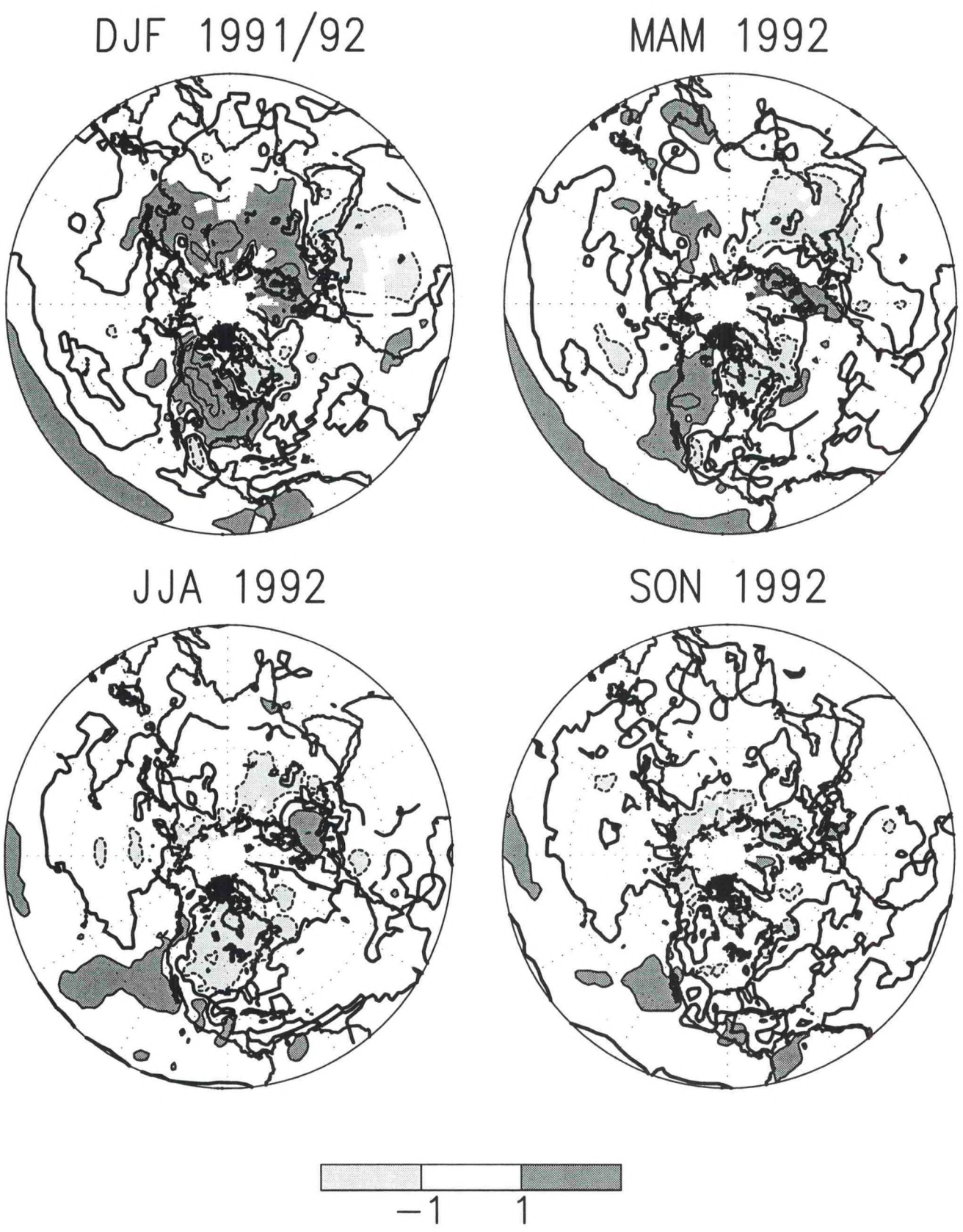

Surface Temperature Anomaly (°C)

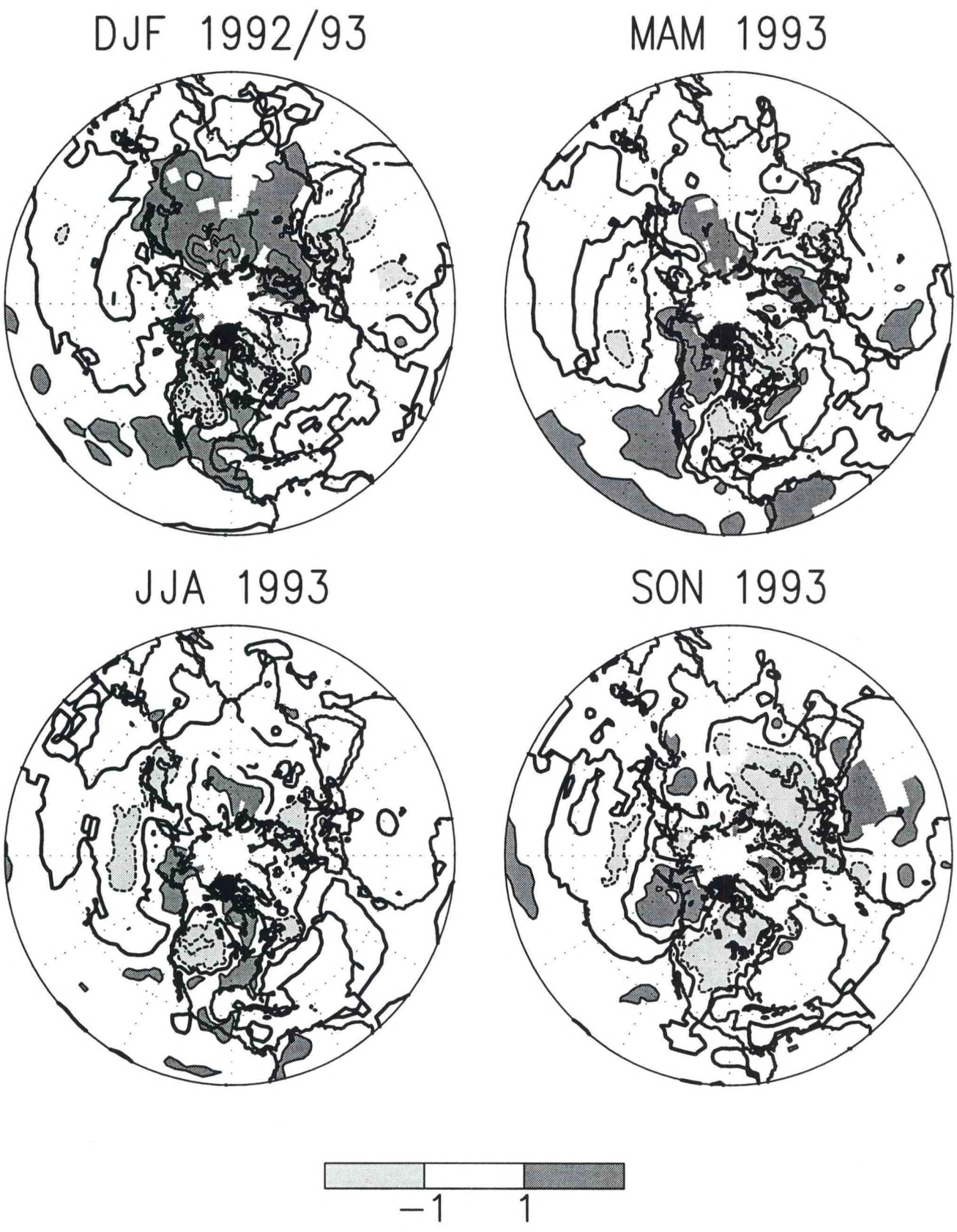

Surface Temperature Anomaly (°C)

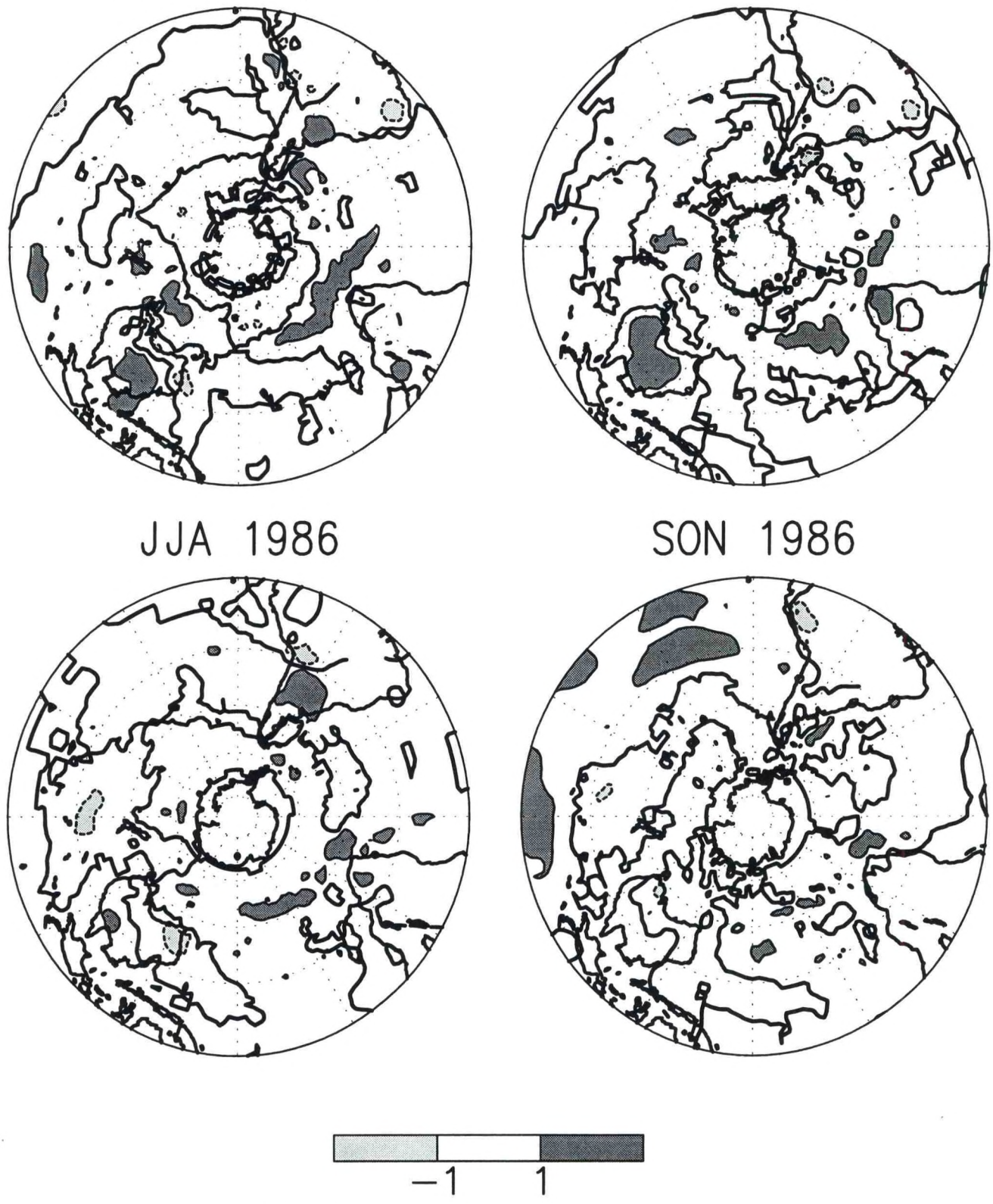

Surface Temperature Anomaly (°C)

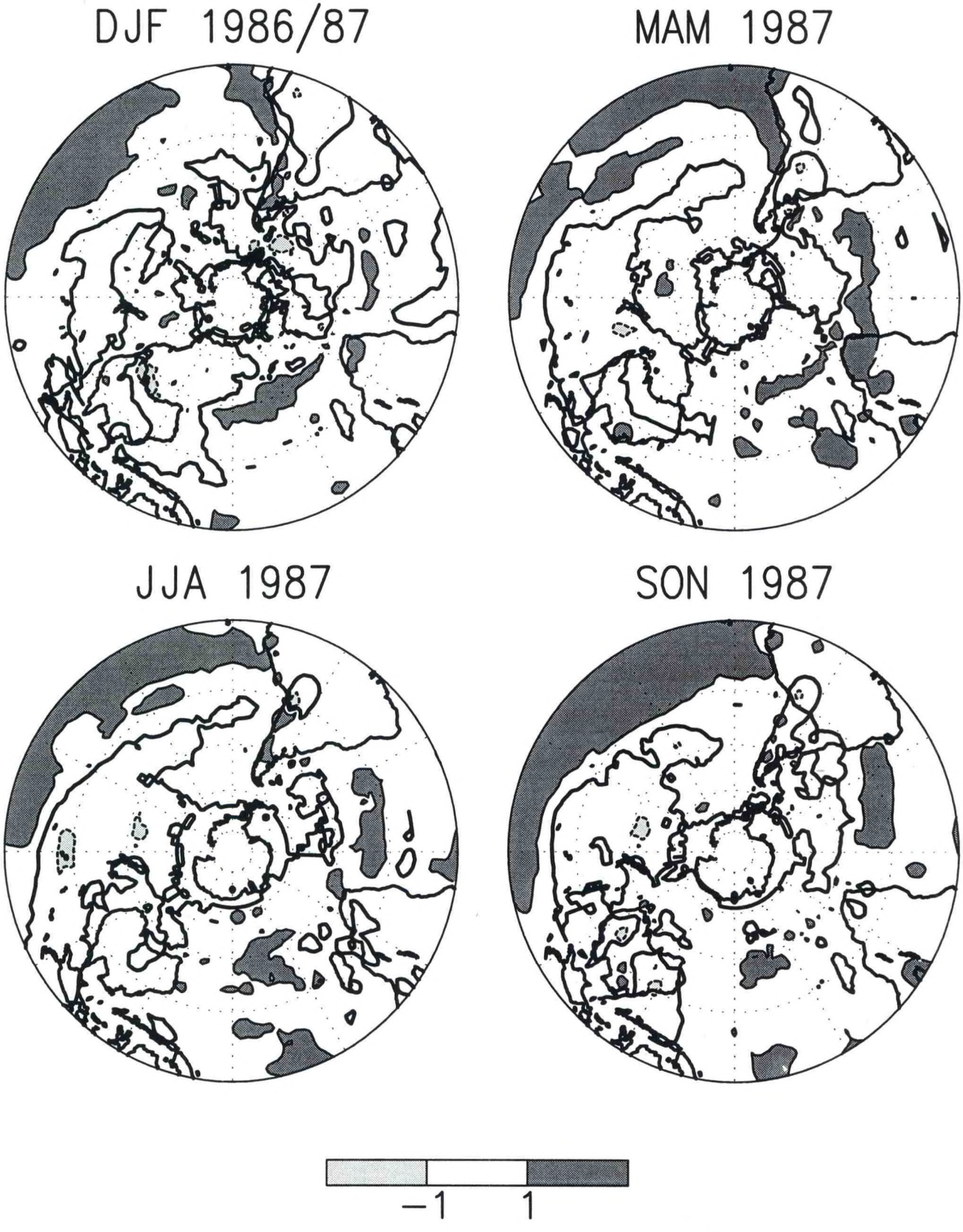

Surface Temperature Anomaly (°C)

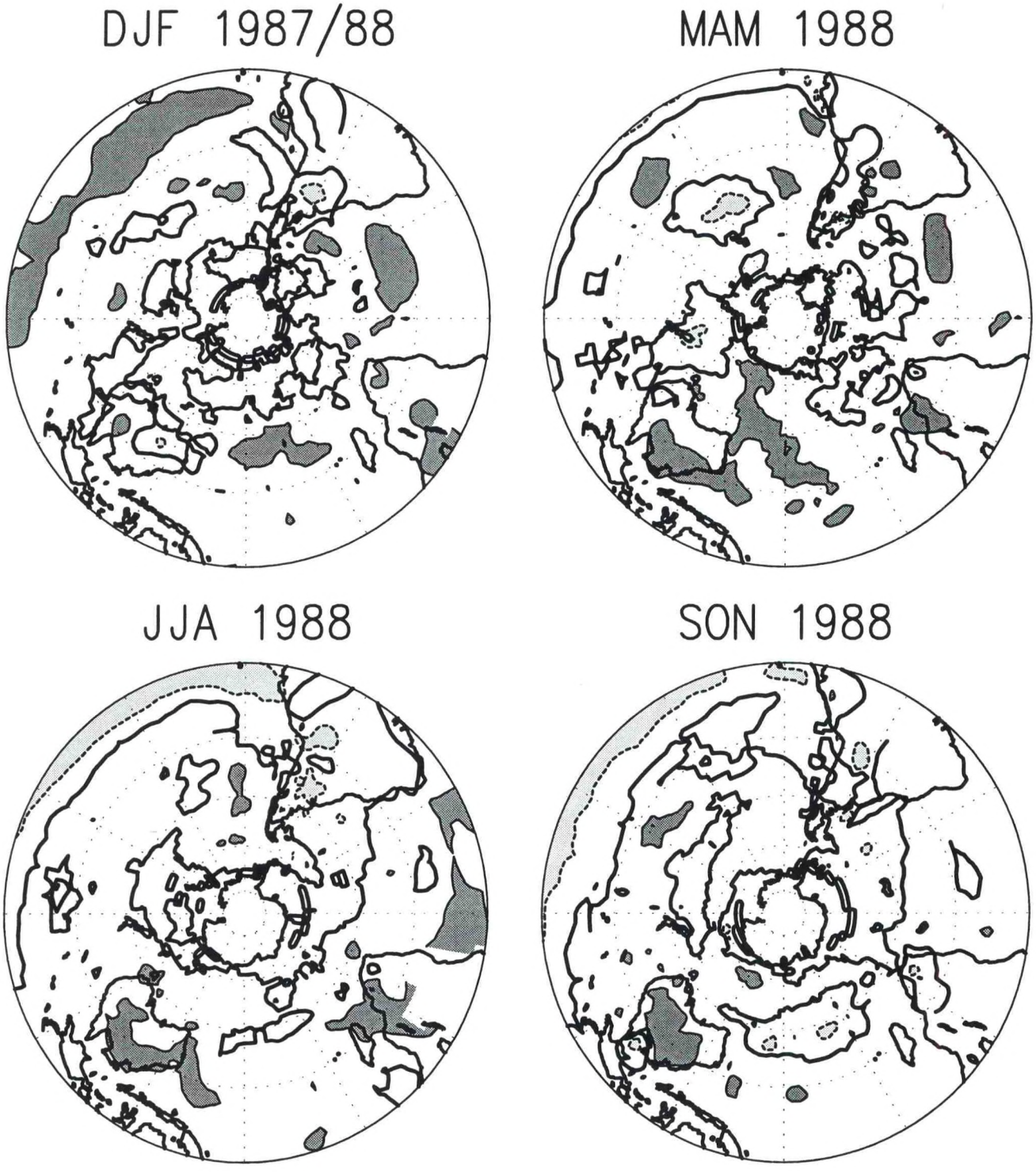

Surface Temperature Anomaly (°C)

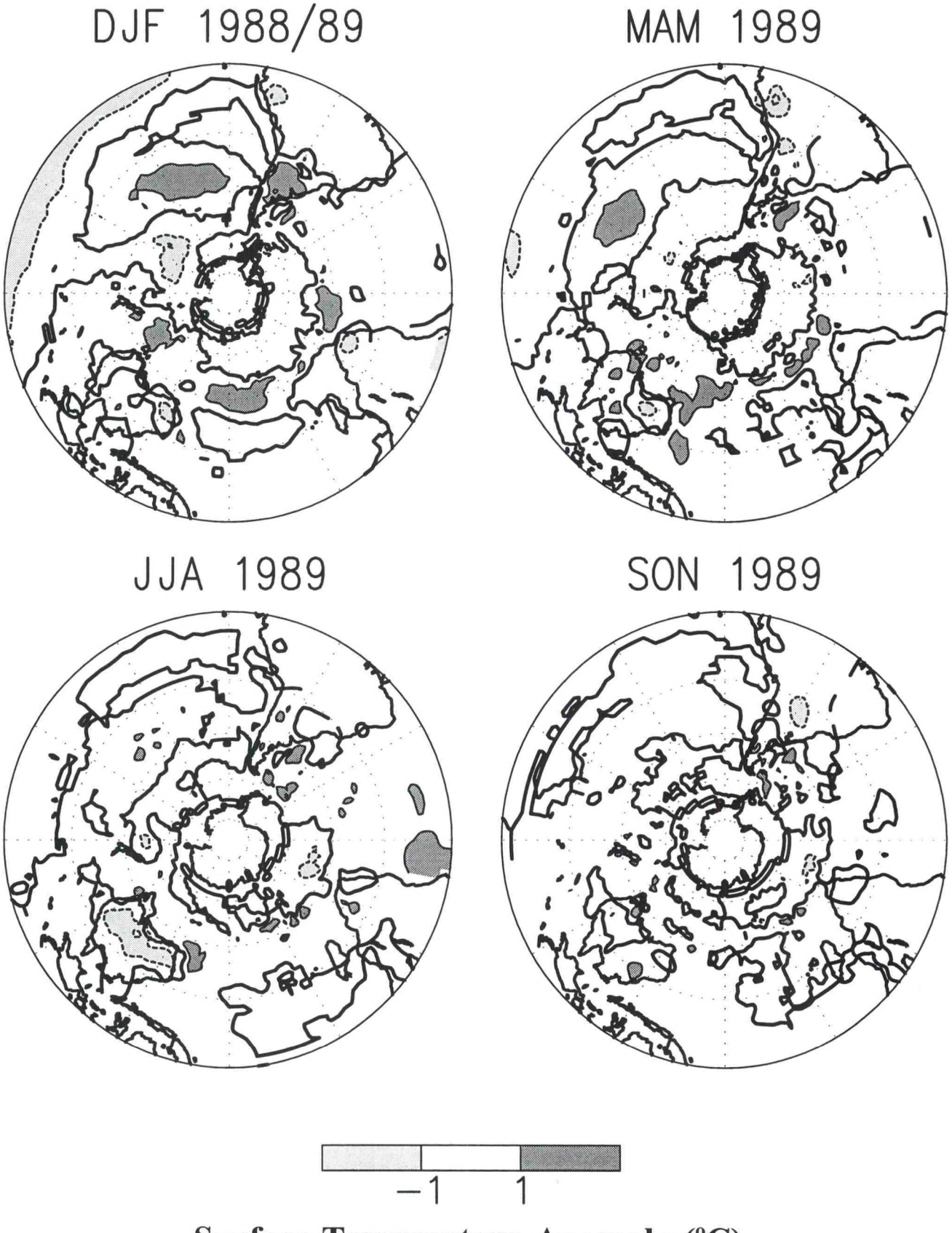

Surface Temperature Anomaly (°C)

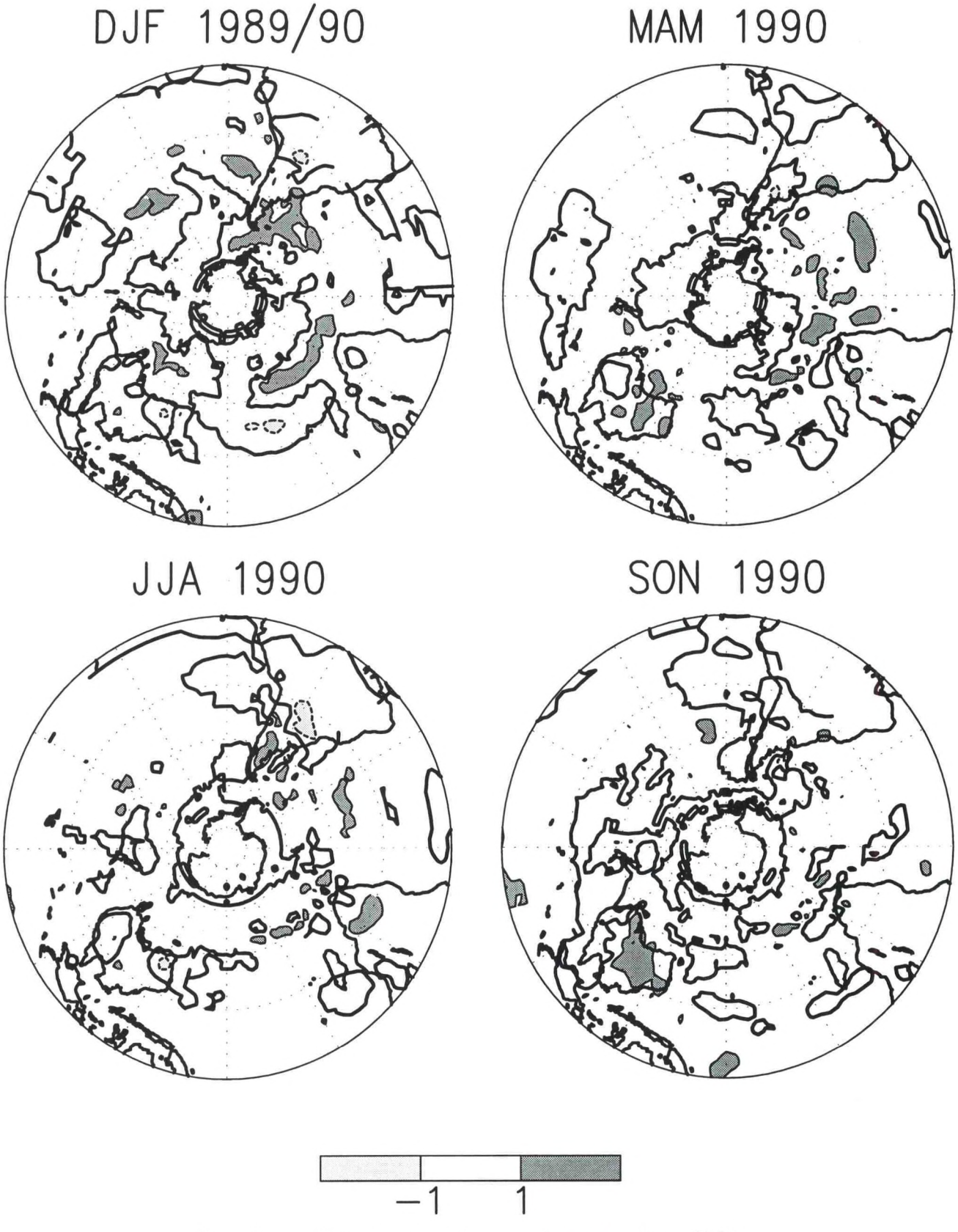
DJF 1989/90
MAM 1990
JJA 1990
SON 1990
−1
1
Surface Temperature Anomaly (°C)

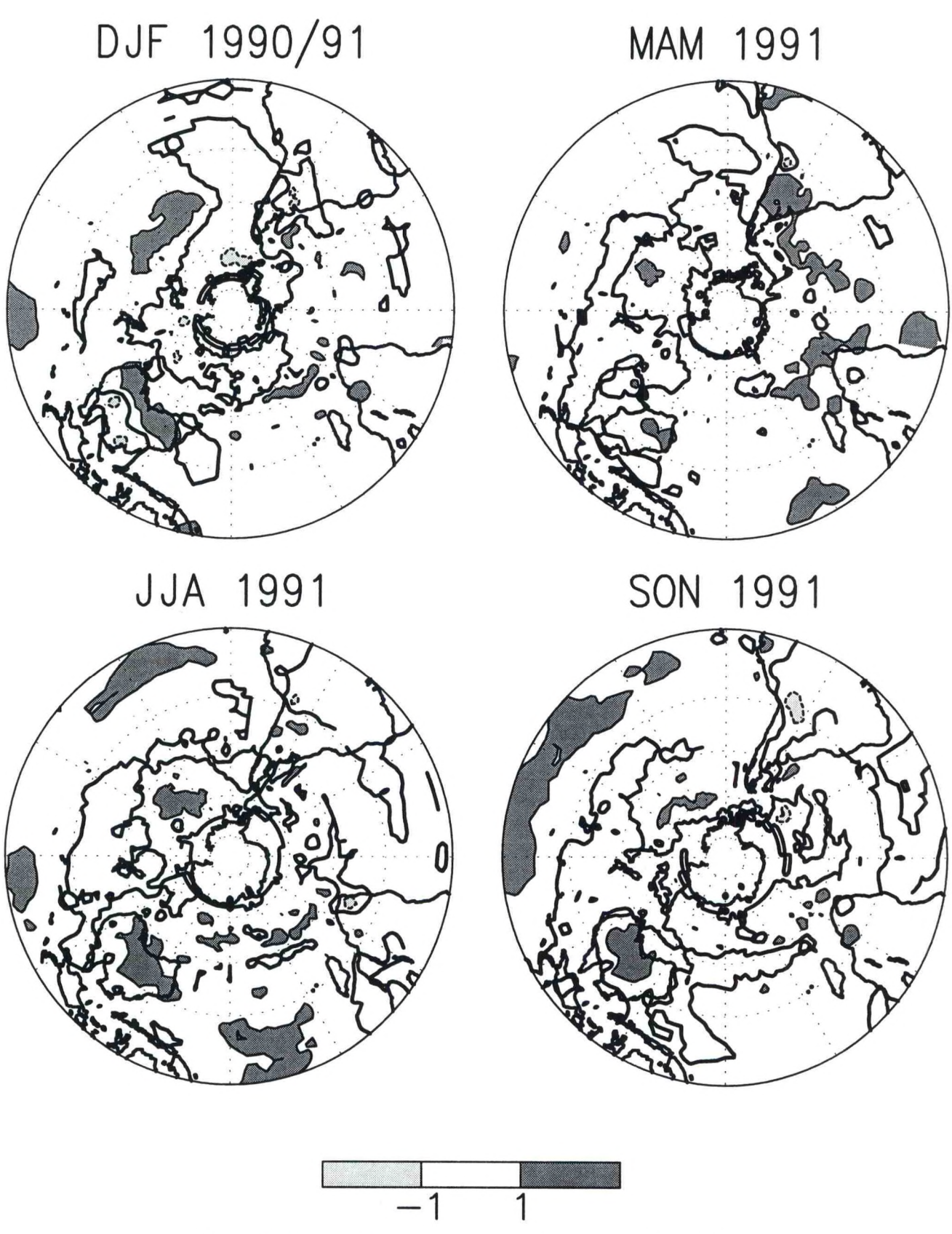

Surface Temperature Anomaly (°C)

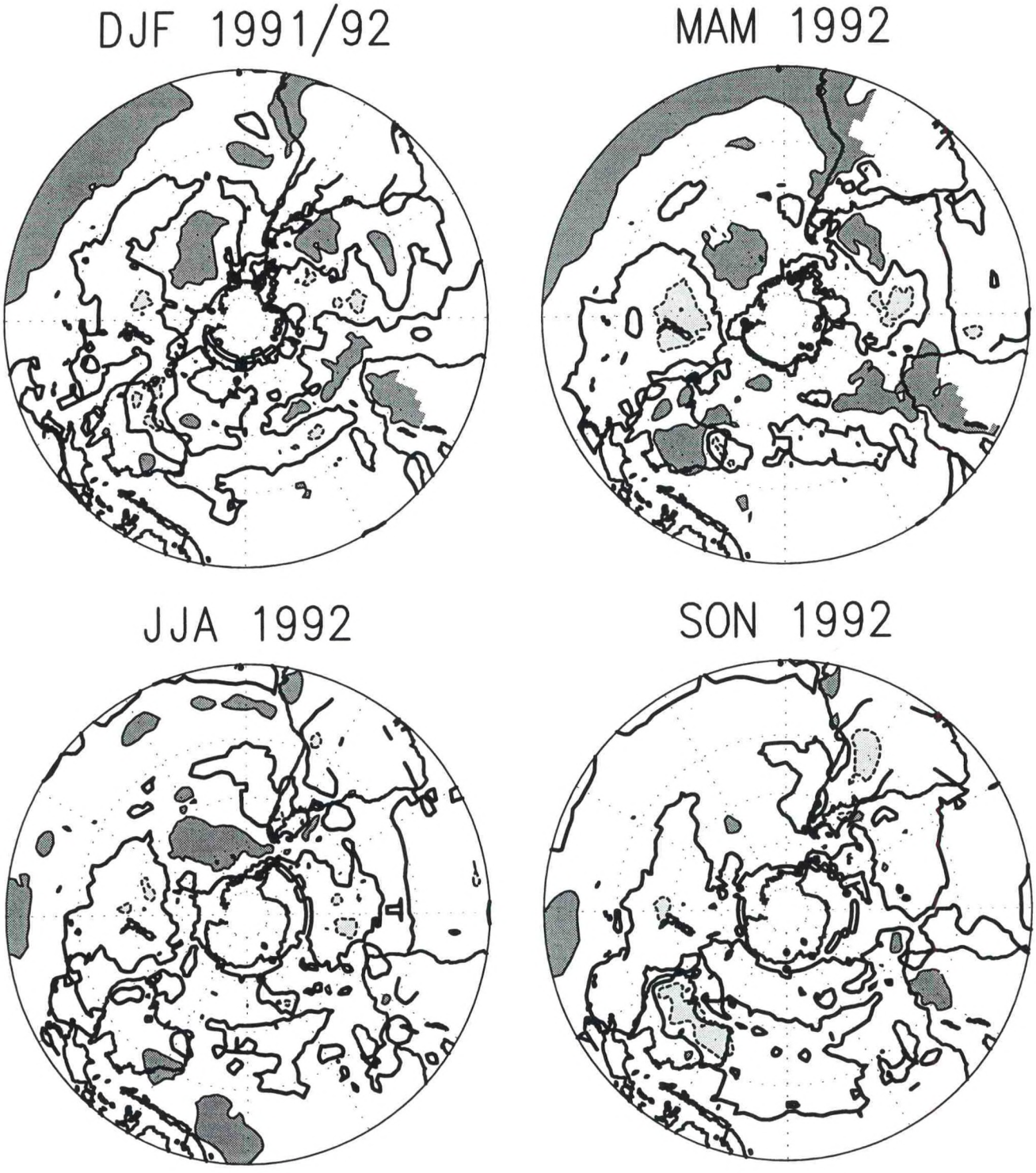

Surface Temperature Anomaly (°C)

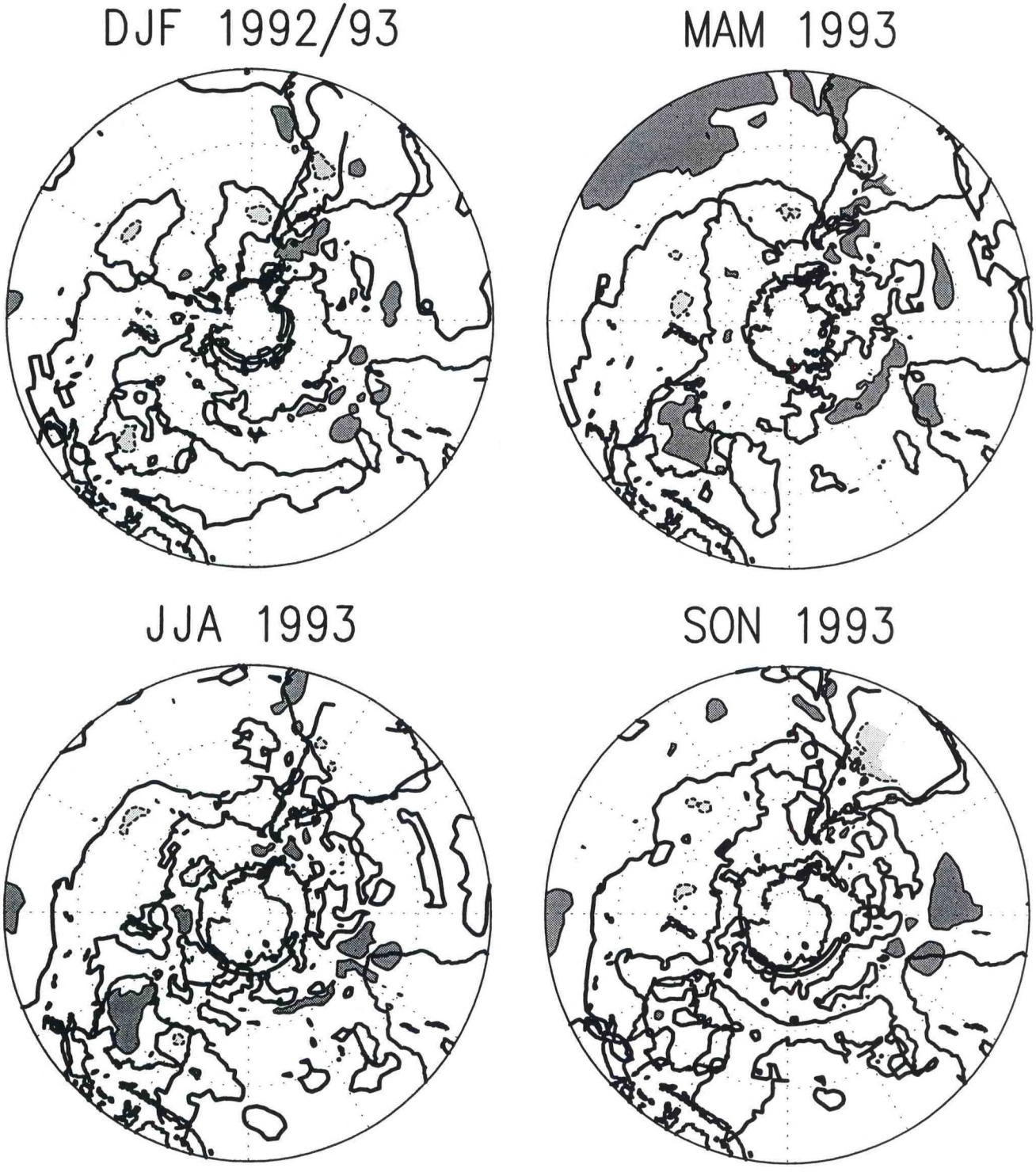
DJF 1992/93
MAM 1993
JJA 1993
SON 1993
−1
1
Surface Temperature Anomaly (°C)

PRECIPITATION ANOMALY

Northern Hemisphere Seasonal Maps (pp. 215-222): Precipitation anomaly, expressed as percentiles of the Gamma distribution (Ropelewski et al. 1985), e.g., the "30 percentile" implies that the precipitation total was in the lowest thirtieth percent of the historical record under the assumption that the probability distribution of precipitation is described by a Gamma distribution function. Solid contours and dark shading indicate the 70th percentile, while dashed contours and light shading indicate the 30th percentile. The contoured values are defined using a modified Cressman (1959) analysis. The analysis is suppressed in regions where no data is available. Anomalies are computed with respect to the 1961-1990 base period.

Southern Hemisphere Seasonal Maps (pp. 223-230): Precipitation anomaly, expressed as percentiles of the Gamma distribution (Ropelewski et al. 1985), e.g., the "30 percentile" implies that the precipitation total was in the lowest thirtieth percent of the historical record under the assumption that the probability distribution of precipitation is described by a Gamma distribution function. Solid contours and dark shading indicate the 70th percentile, while dashed contours and light shading indicate the 30th percentile. The contoured values are defined using a modified Cressman (1959) analysis. The analysis is suppressed in areas with insufficient data. Anomalies are computed with respect to the 1961-1990 base period.

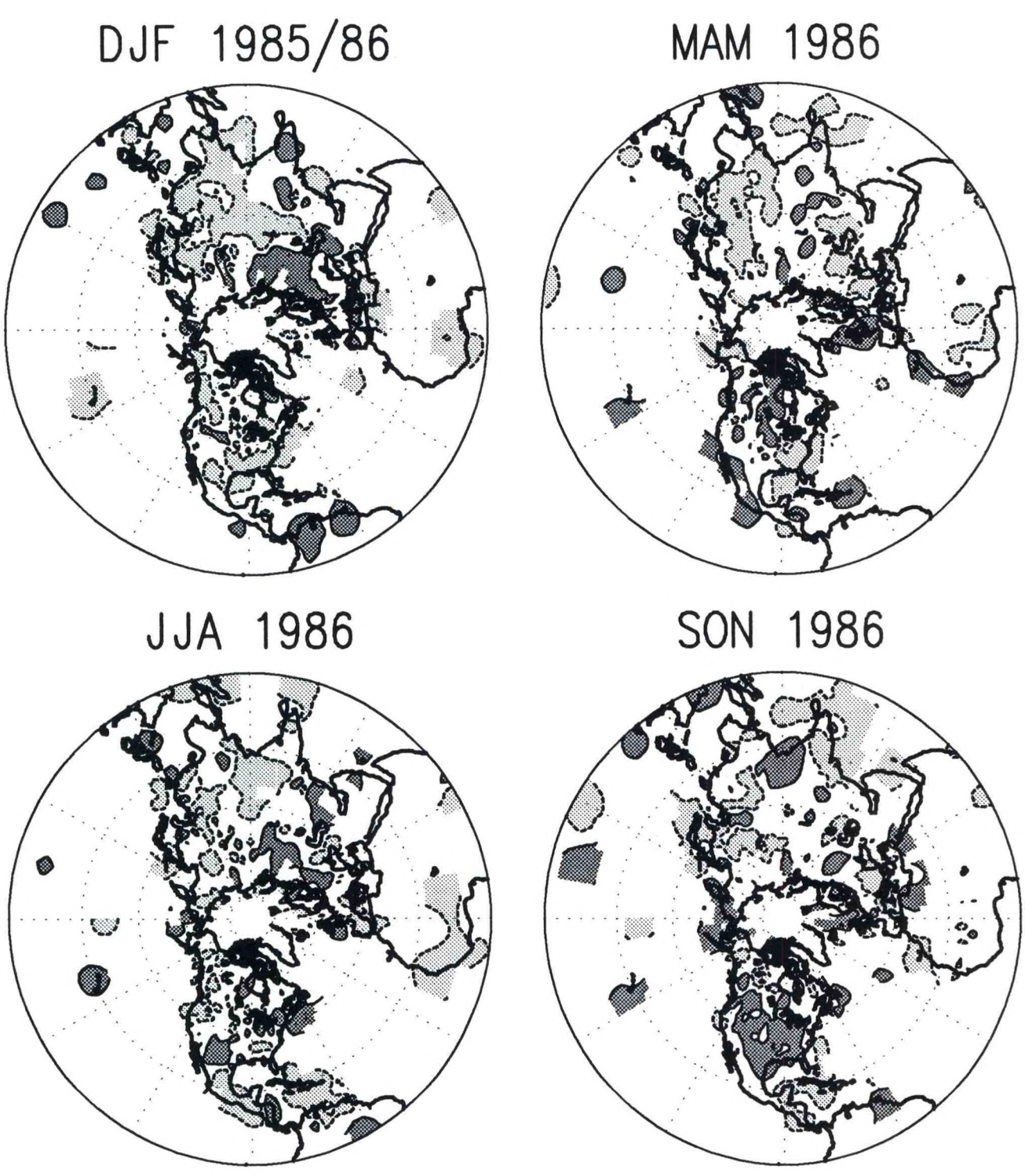
DJF 1985/86
MAM 1986
JJA 1986
SON 1986
30
70
Precipitation Percentile

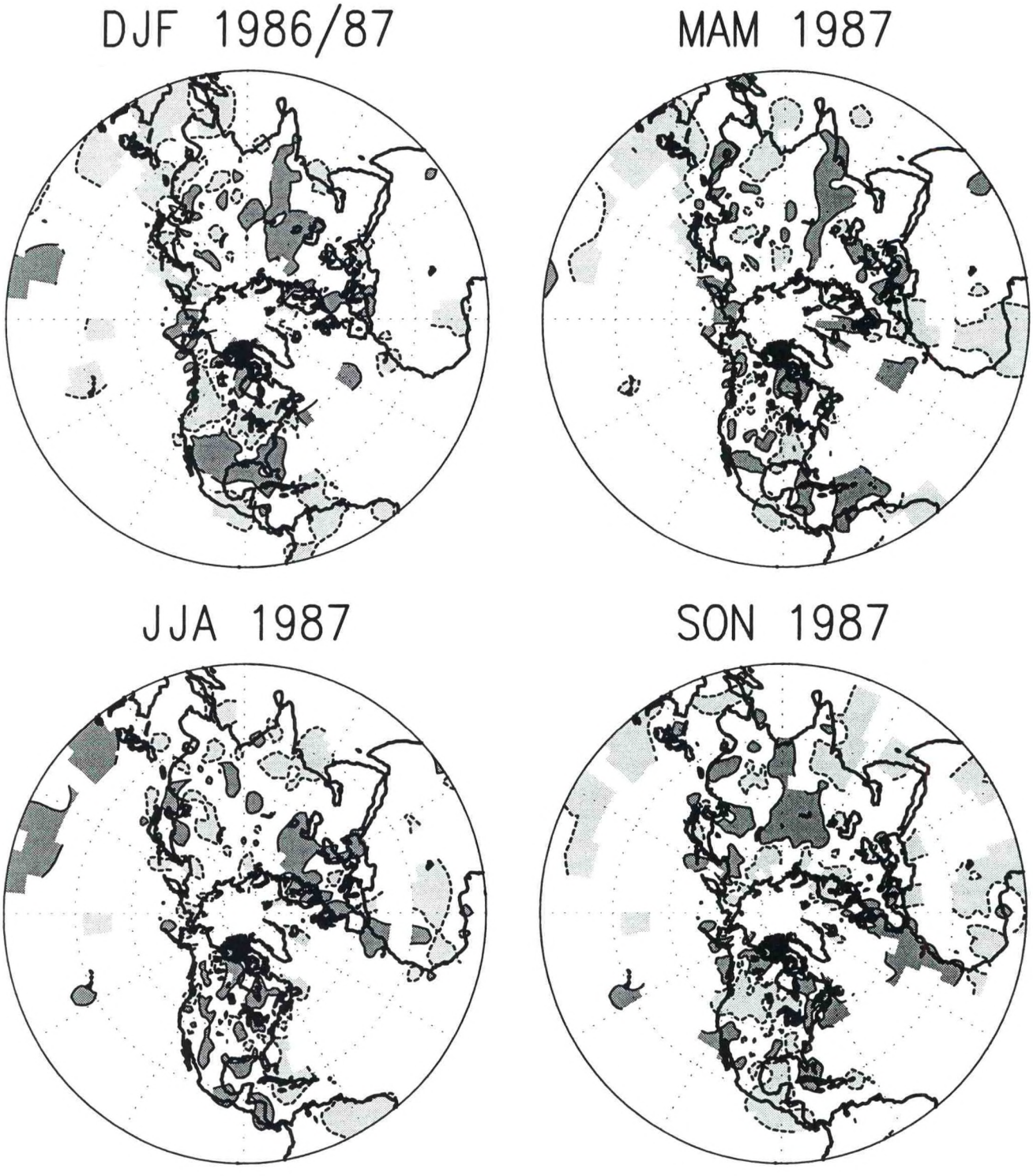
DJF 1986/87
MAM 1987
JJA 1987
SON 1987
30
70
Precipitation Percentile

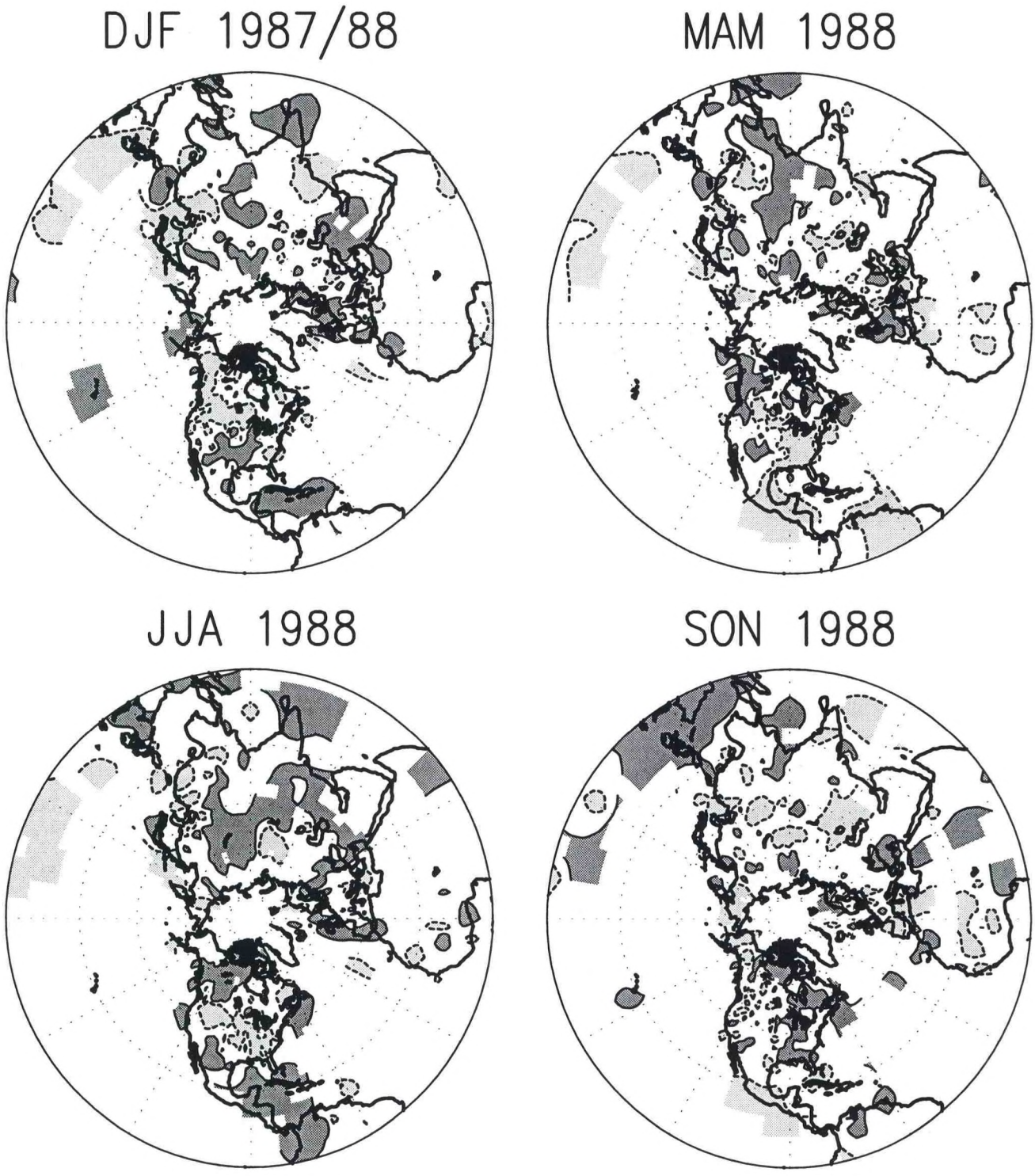
DJF 1987/88
MAM 1988
JJA 1988
SON 1988
30
70
Precipitation Percentile

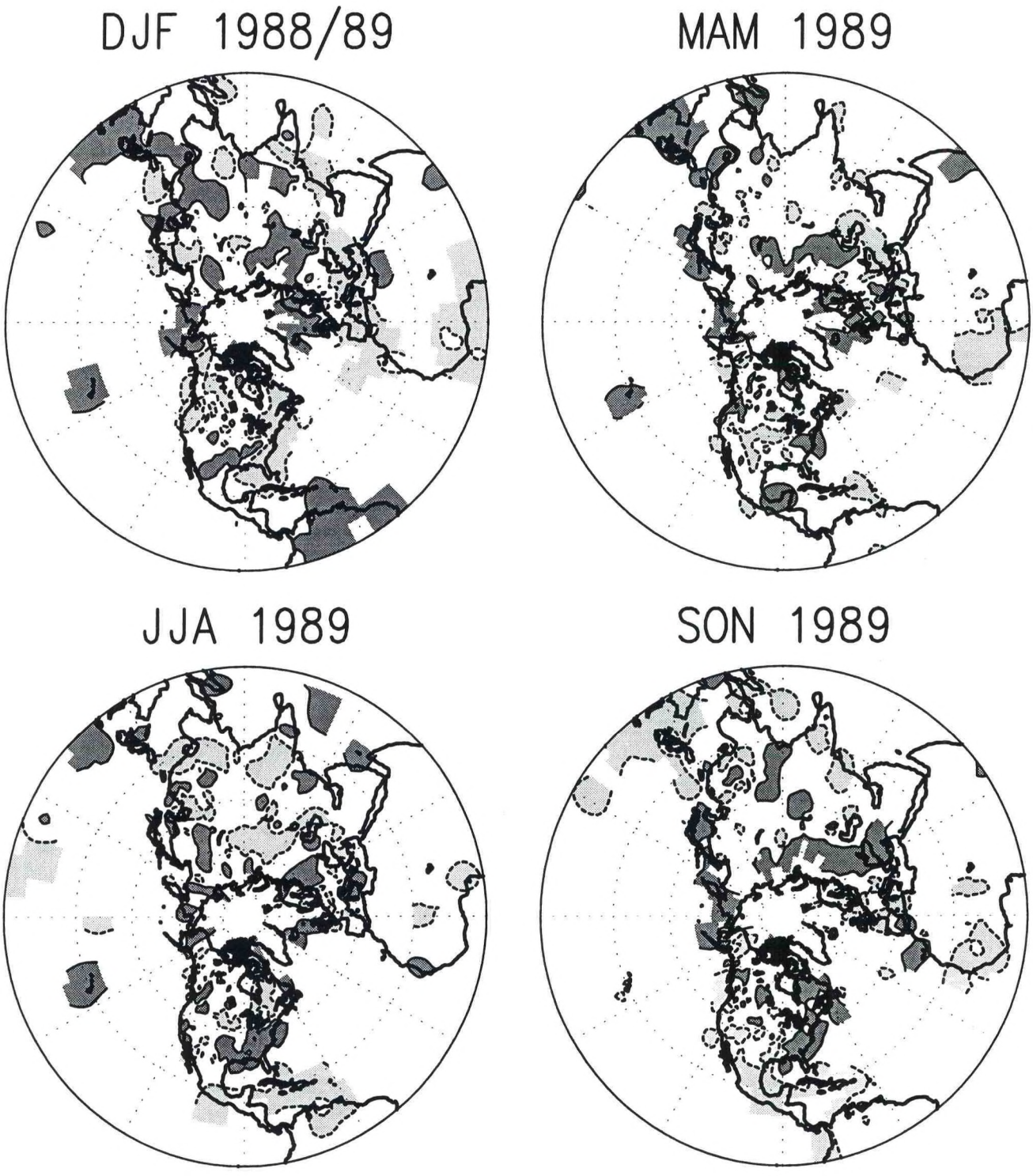
DJF 1988/89
MAM 1989
JJA 1989
SON 1989
30
70
Precipitation Percentile

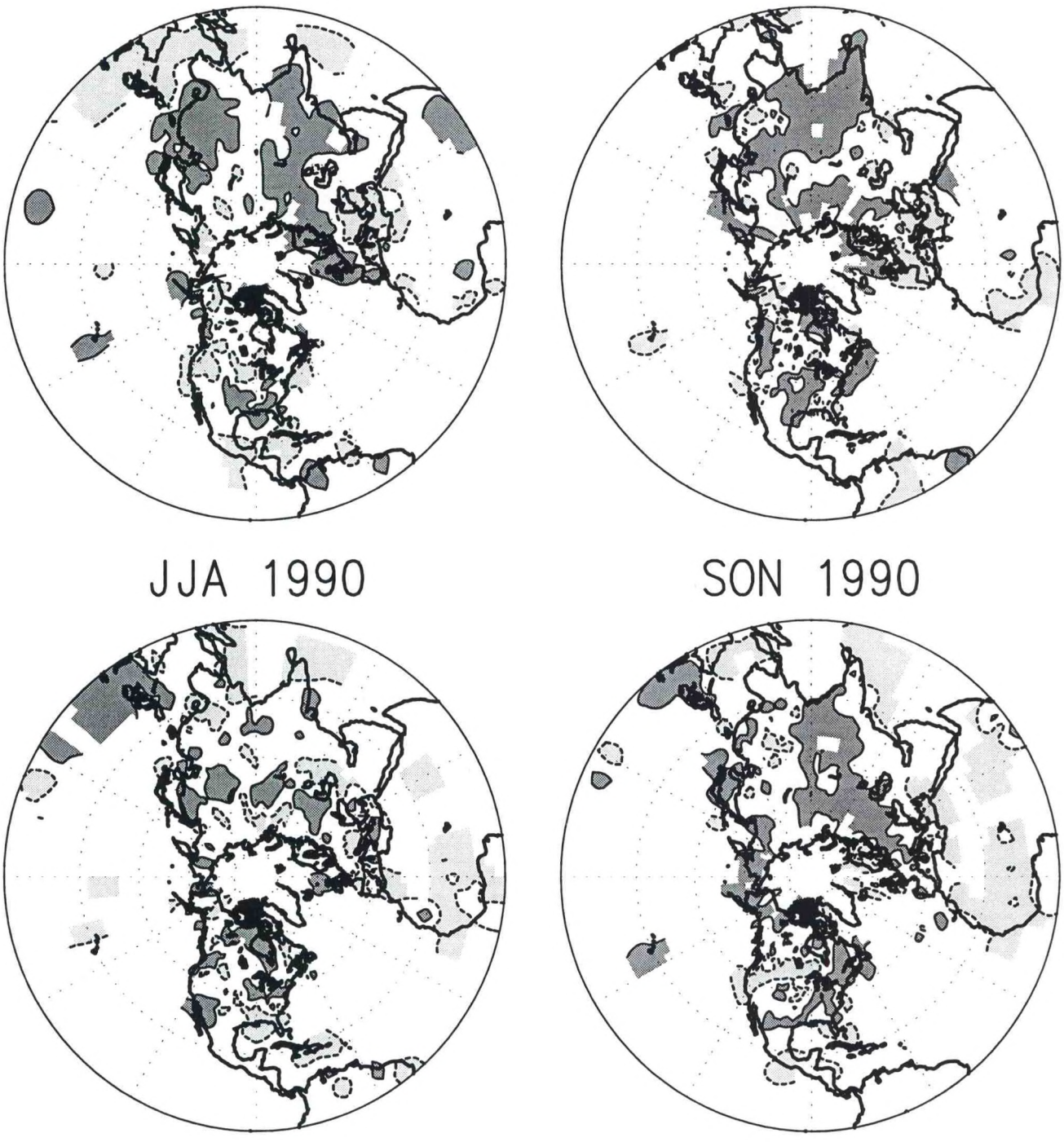
DJF 1989/90
MAM 1990
JJA 1990
SON 1990
30
70
Precipitation Percentile

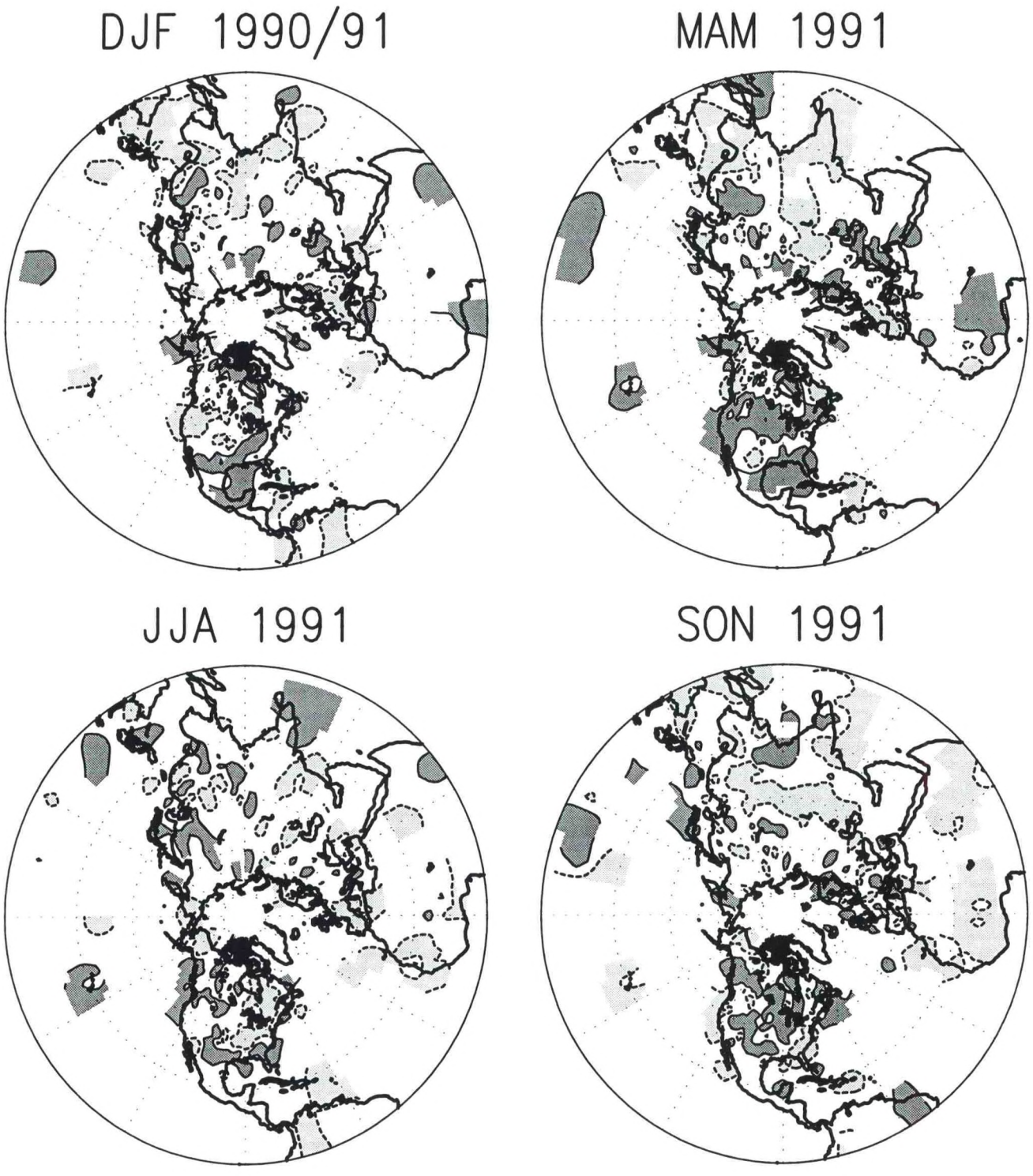
DJF 1990/91
MAM 1991
JJA 1991
SON 1991
30
70
Precipitation Percentile

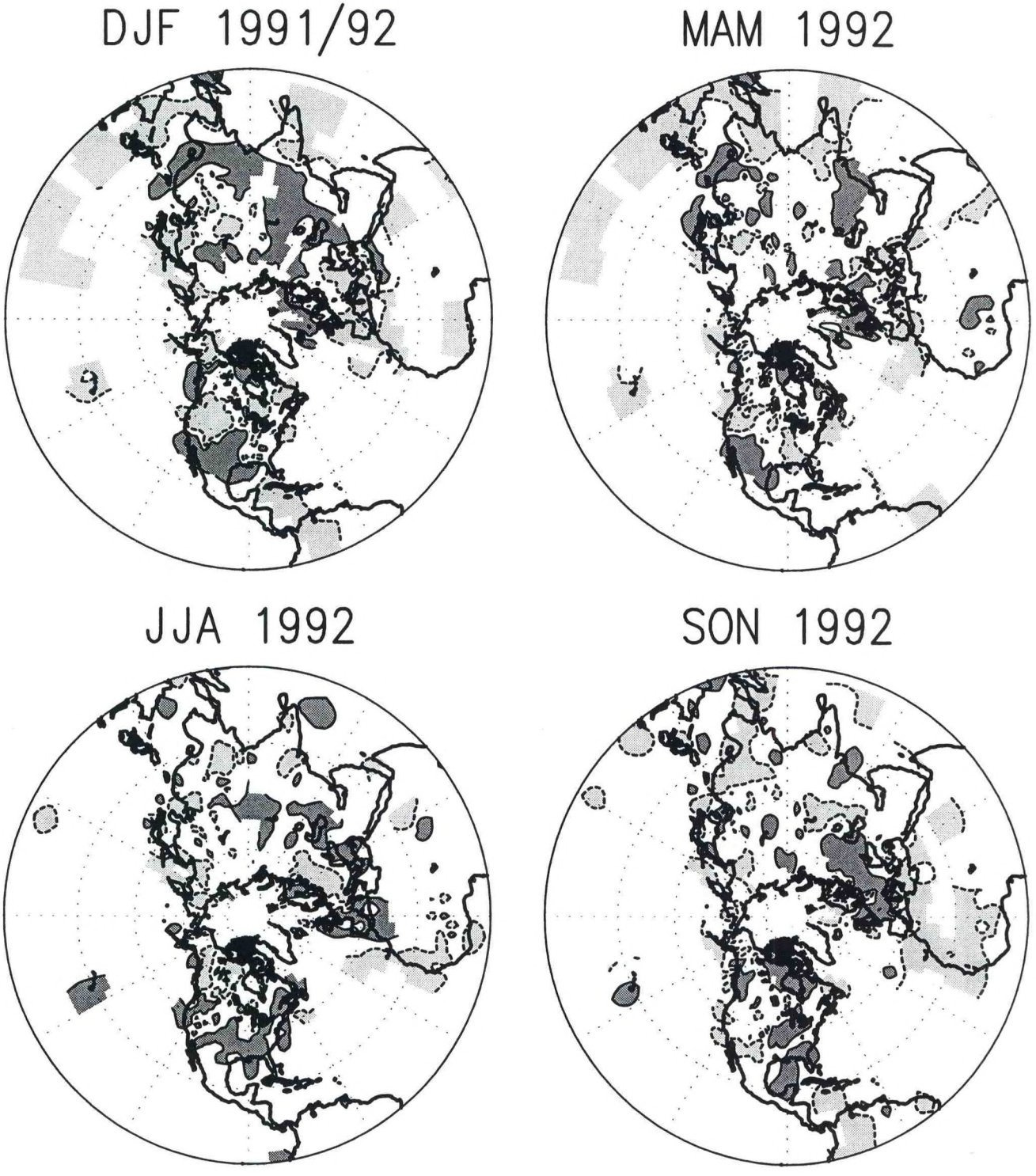
DJF 1991/92
MAM 1992
JJA 1992
SON 1992
30
70
Precipitation Percentile

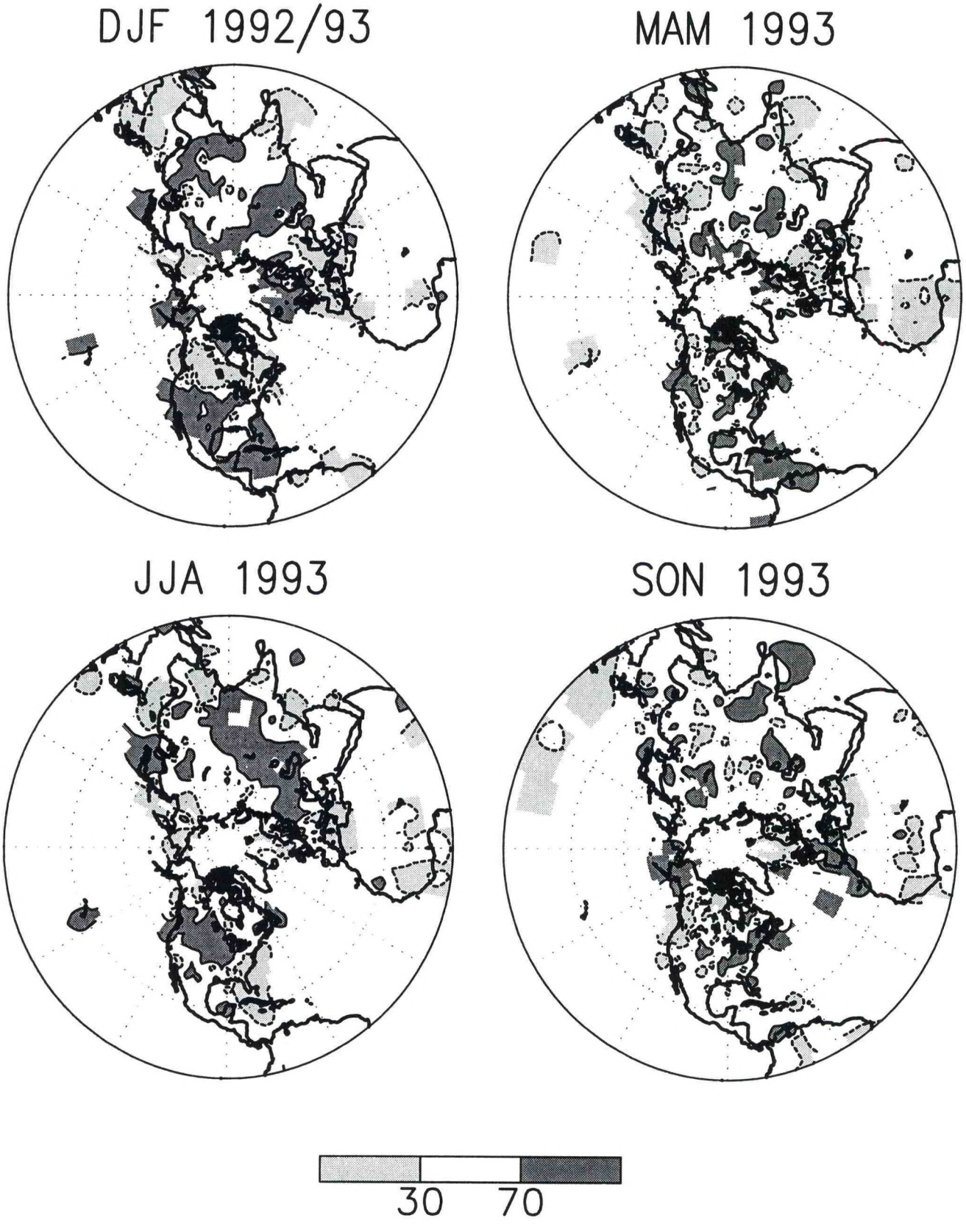

Precipitation Percentile

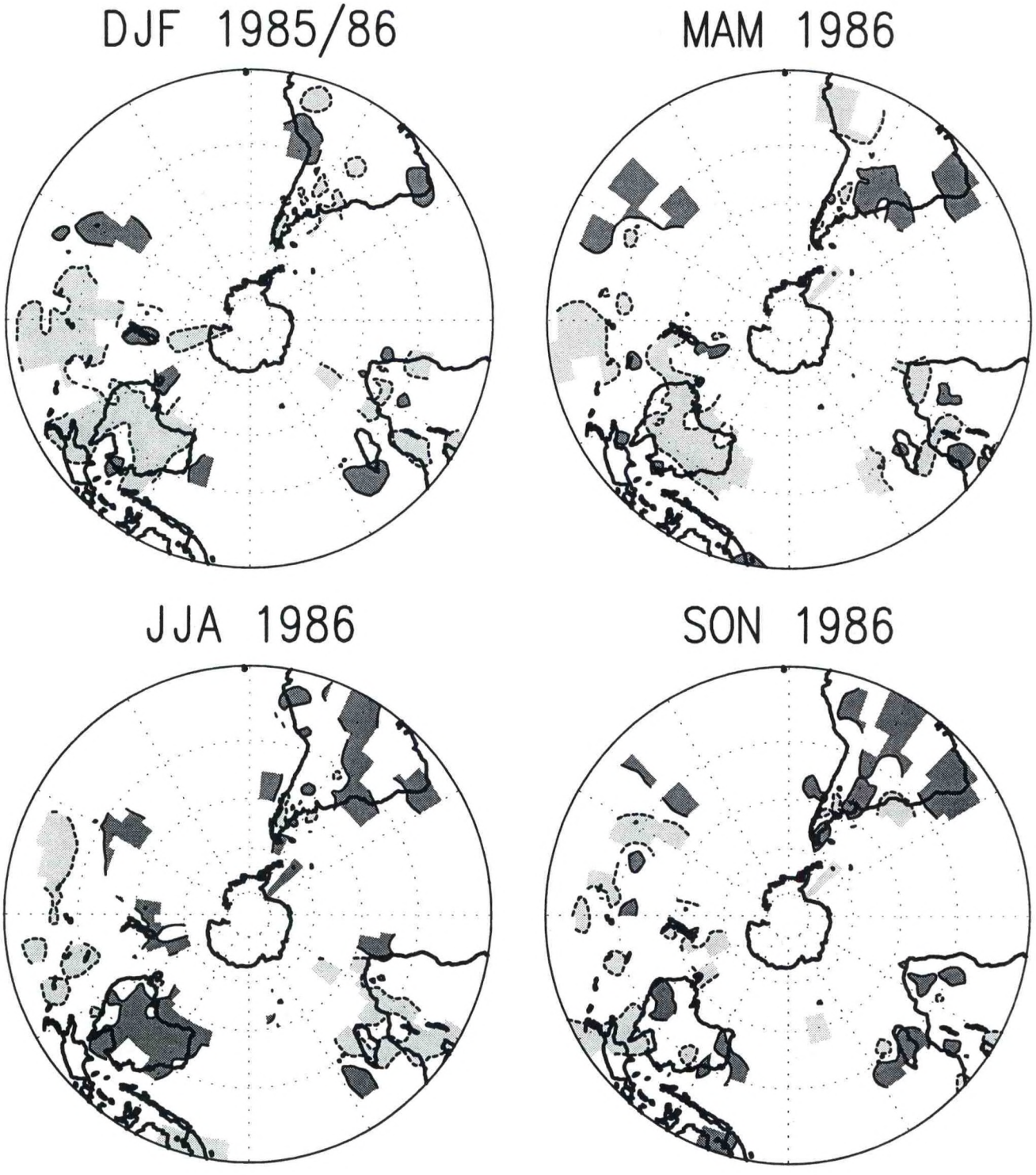
DJF 1985/86
MAM 1986
JJA 1986
SON 1986
30
70
Precipitation Percentile

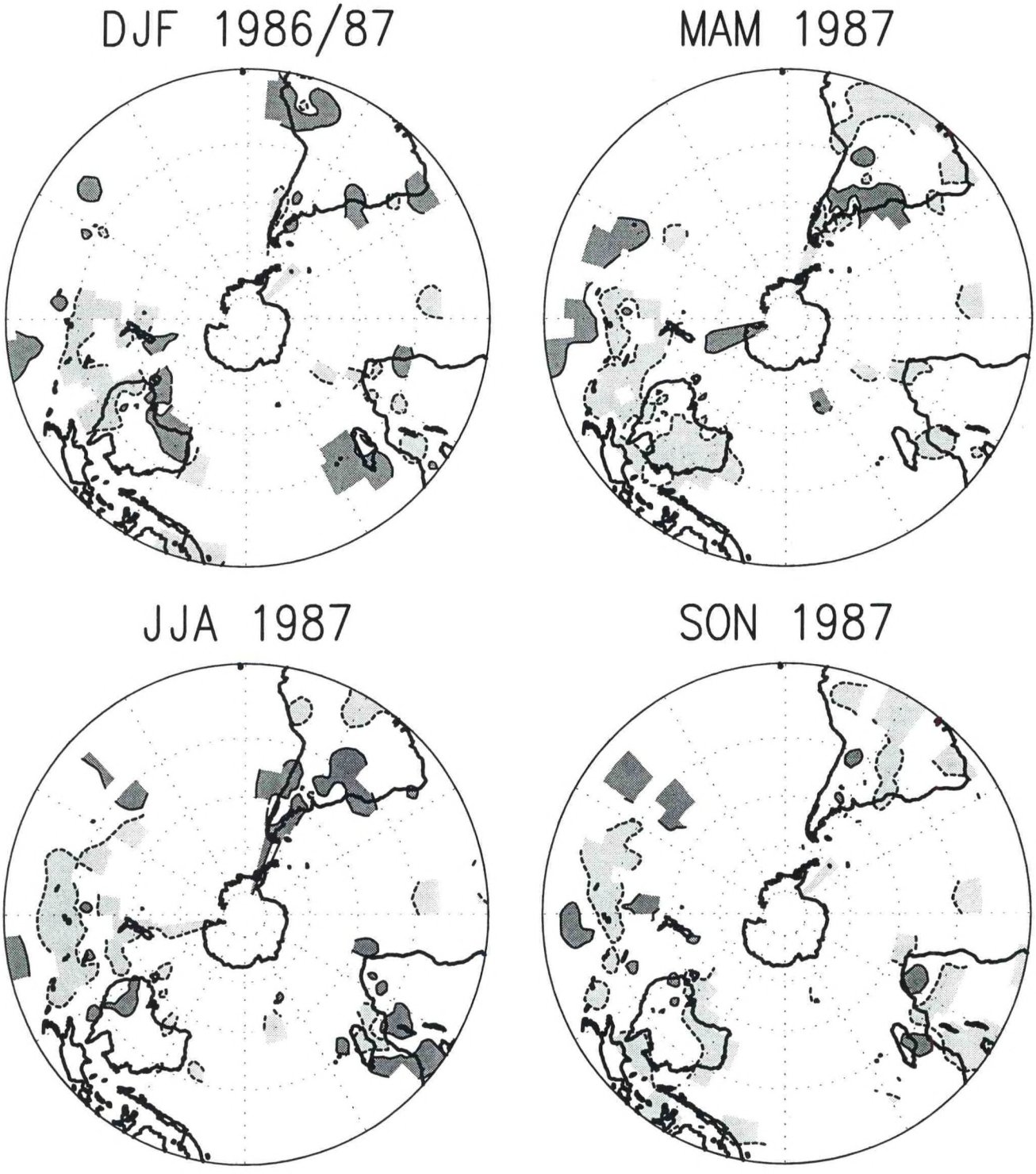
DJF 1986/87
MAM 1987
JJA 1987
SON 1987
30
70
Precipitation Percentile

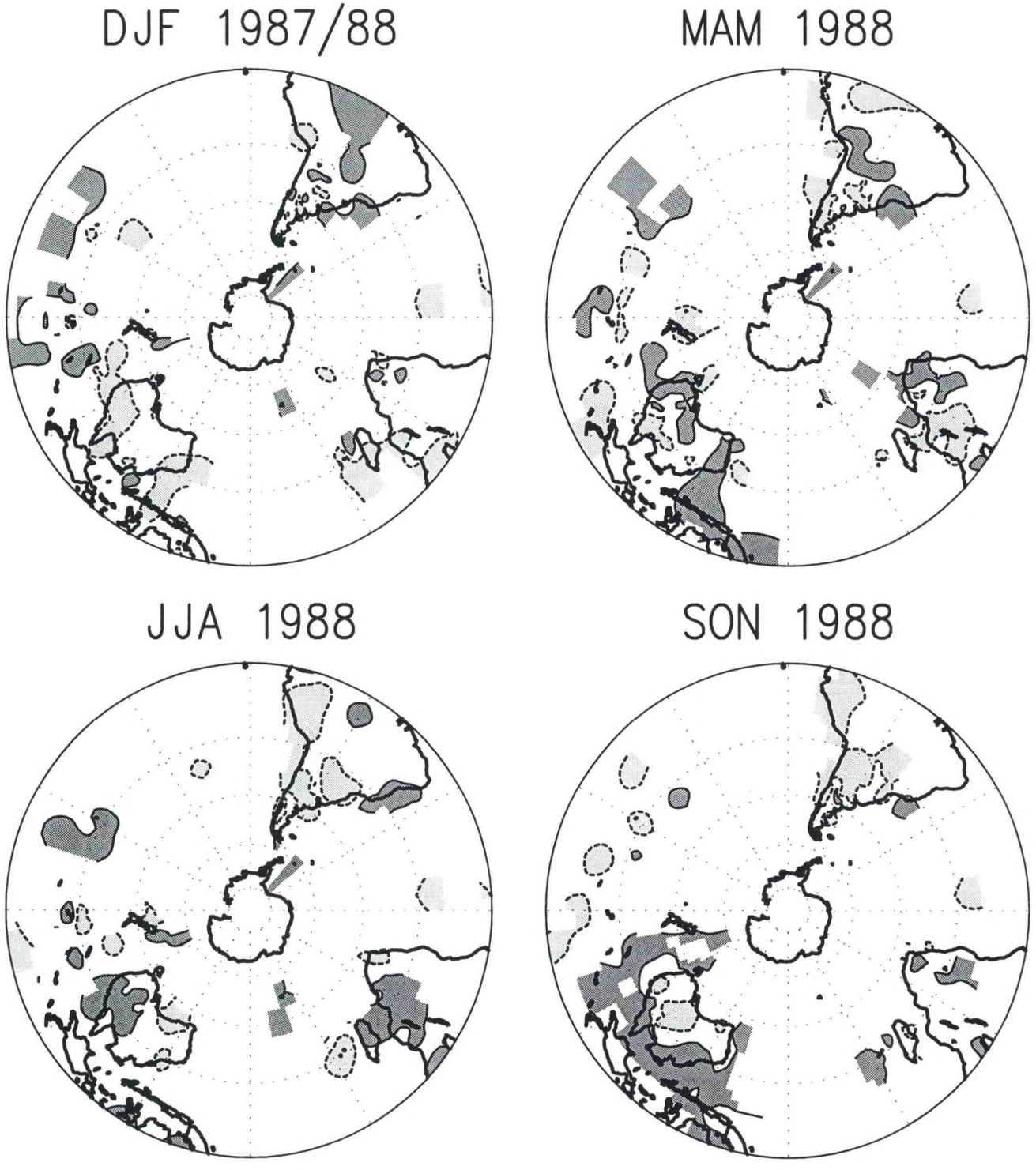
DJF 1987/88
MAM 1988
JJA 1988
SON 1988
30
70
Precipitation Percentile

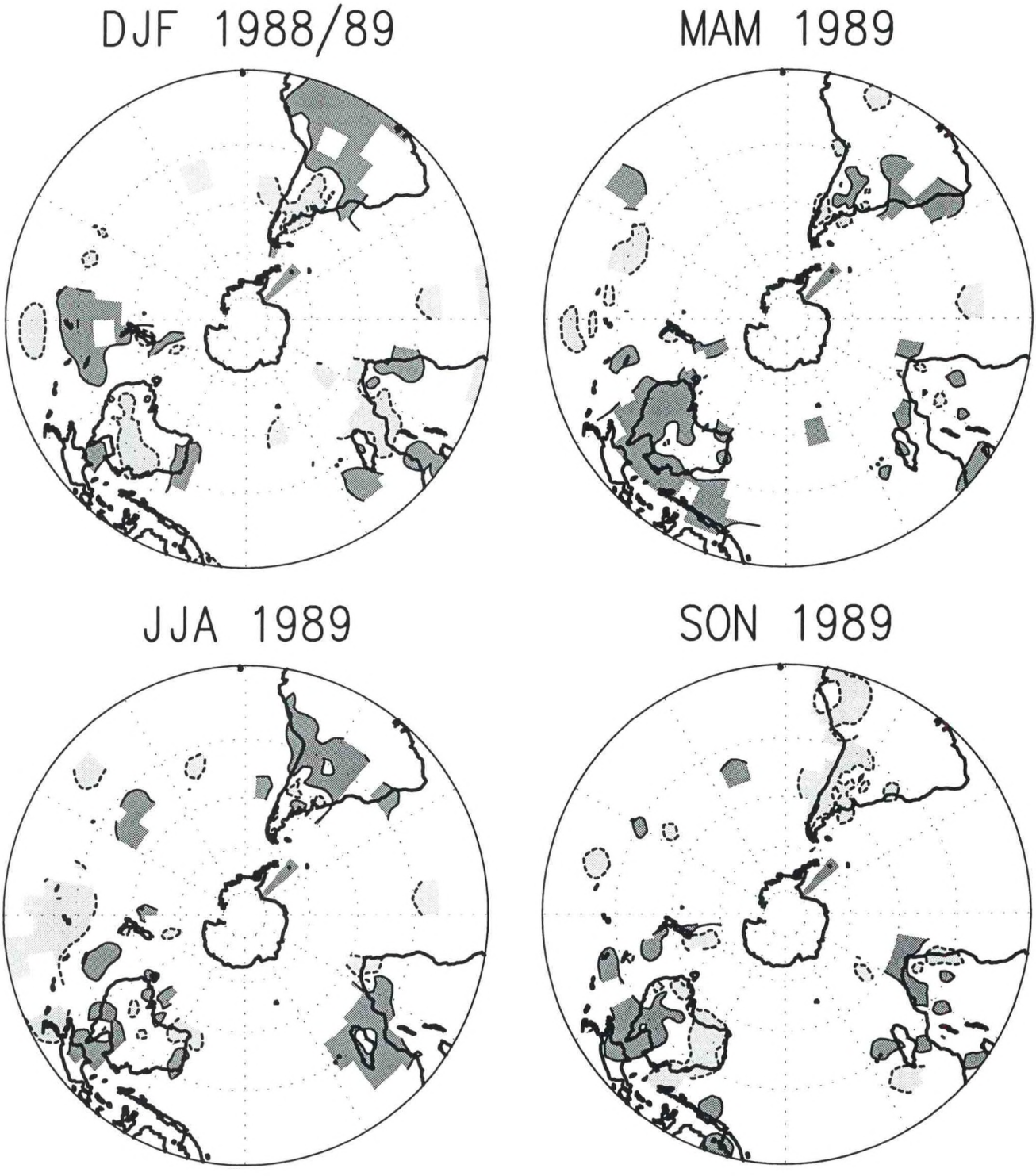
DJF 1988/89
MAM 1989
JJA 1989
SON 1989
30
70
Precipitation Percentile

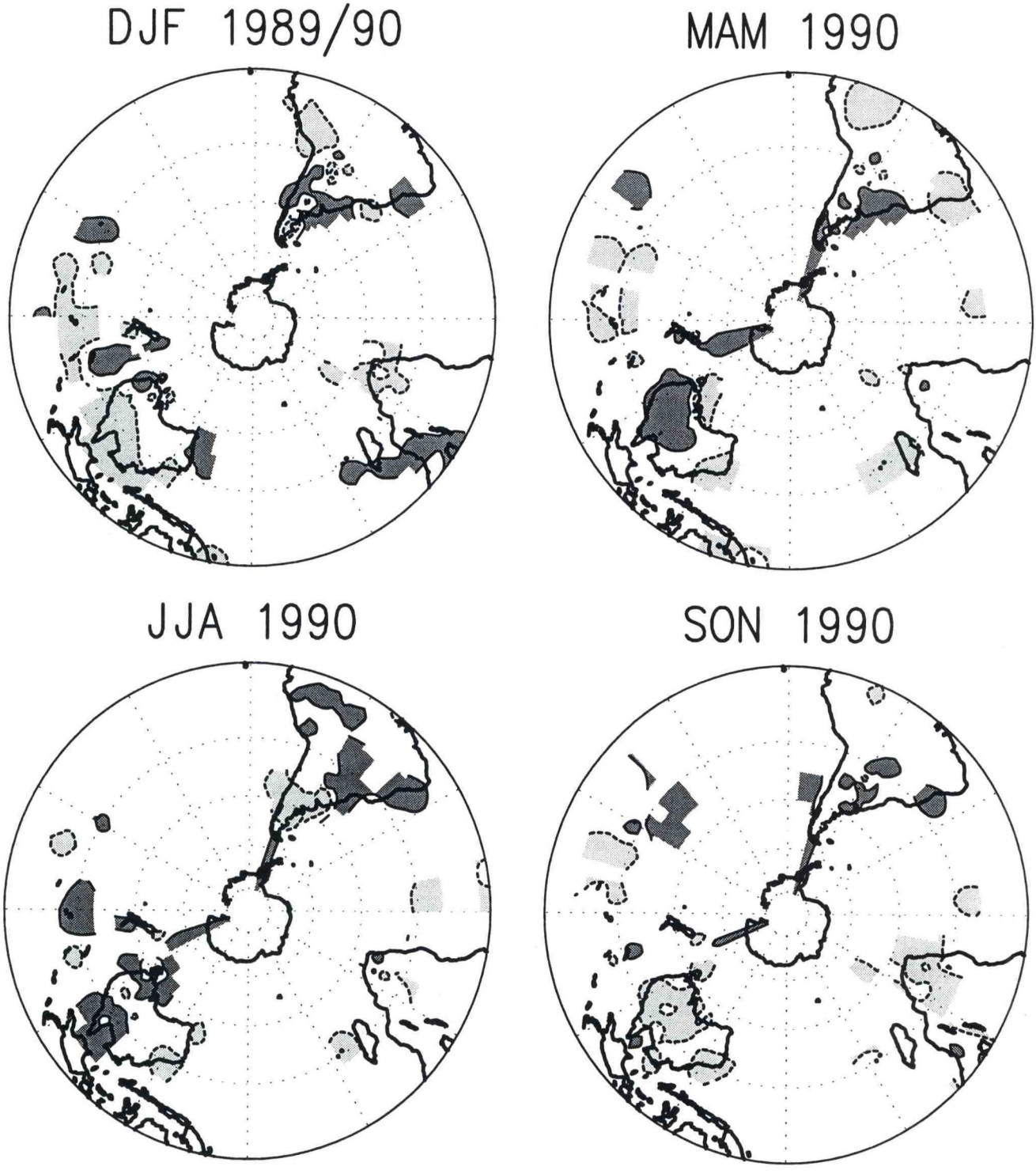
DJF 1989/90
MAM 1990
JJA 1990
SON 1990
30
70
Precipitation Percentile

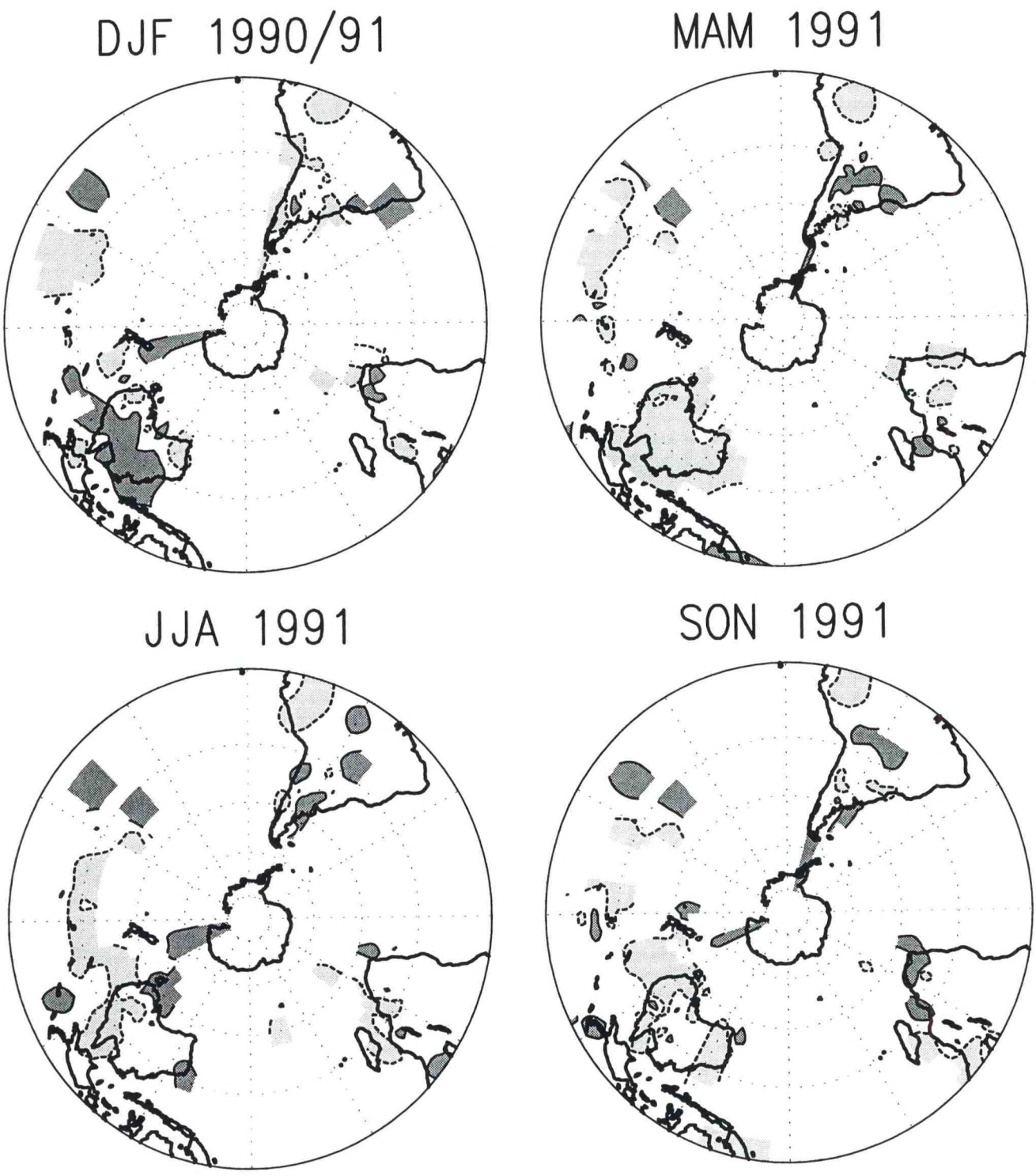
DJF 1990/91
MAM 1991
JJA 1991
SON 1991
30
70
Precipitation Percentile

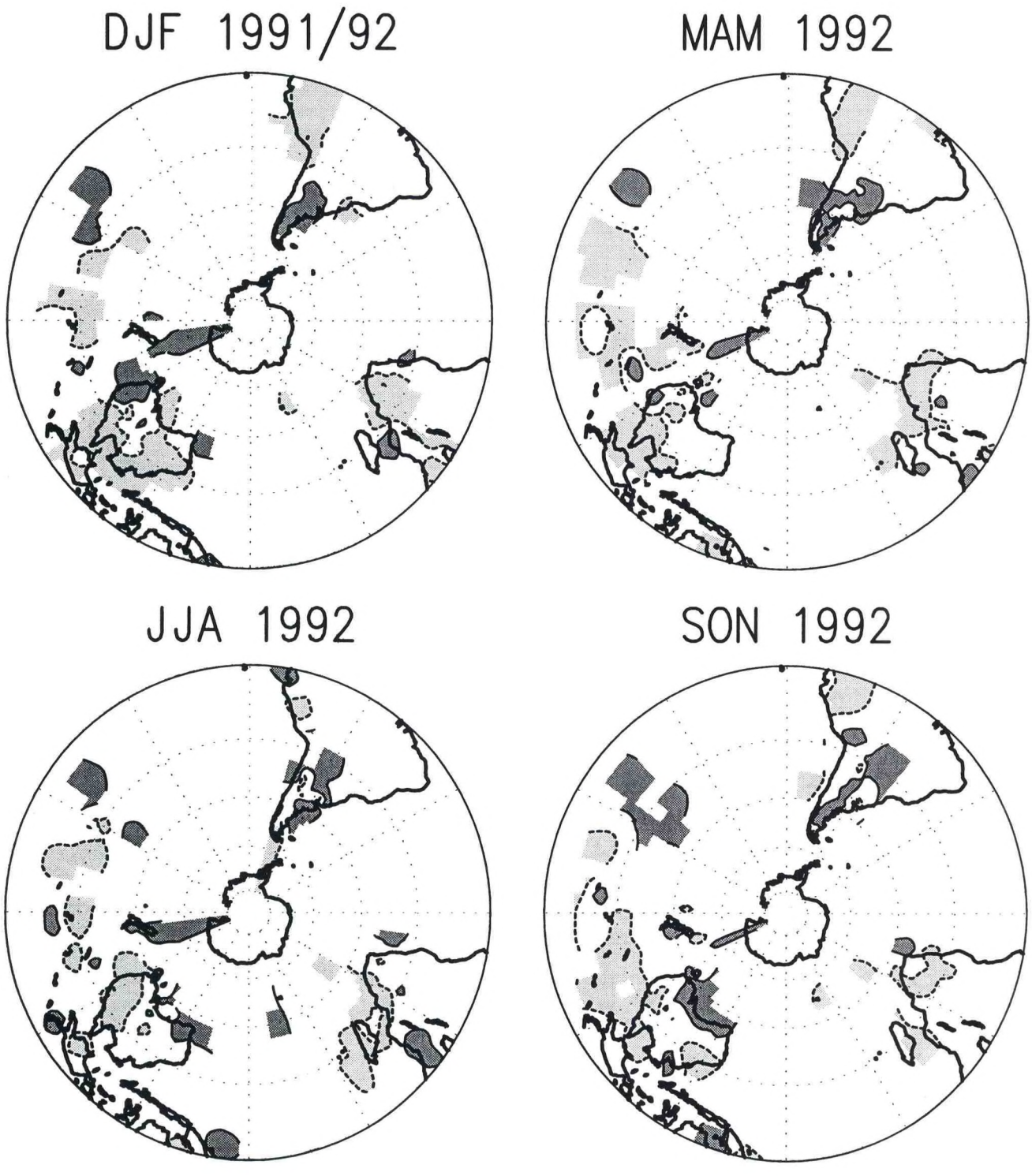
DJF 1991/92
MAM 1992
JJA 1992
SON 1992
30
70
Precipitation Percentile

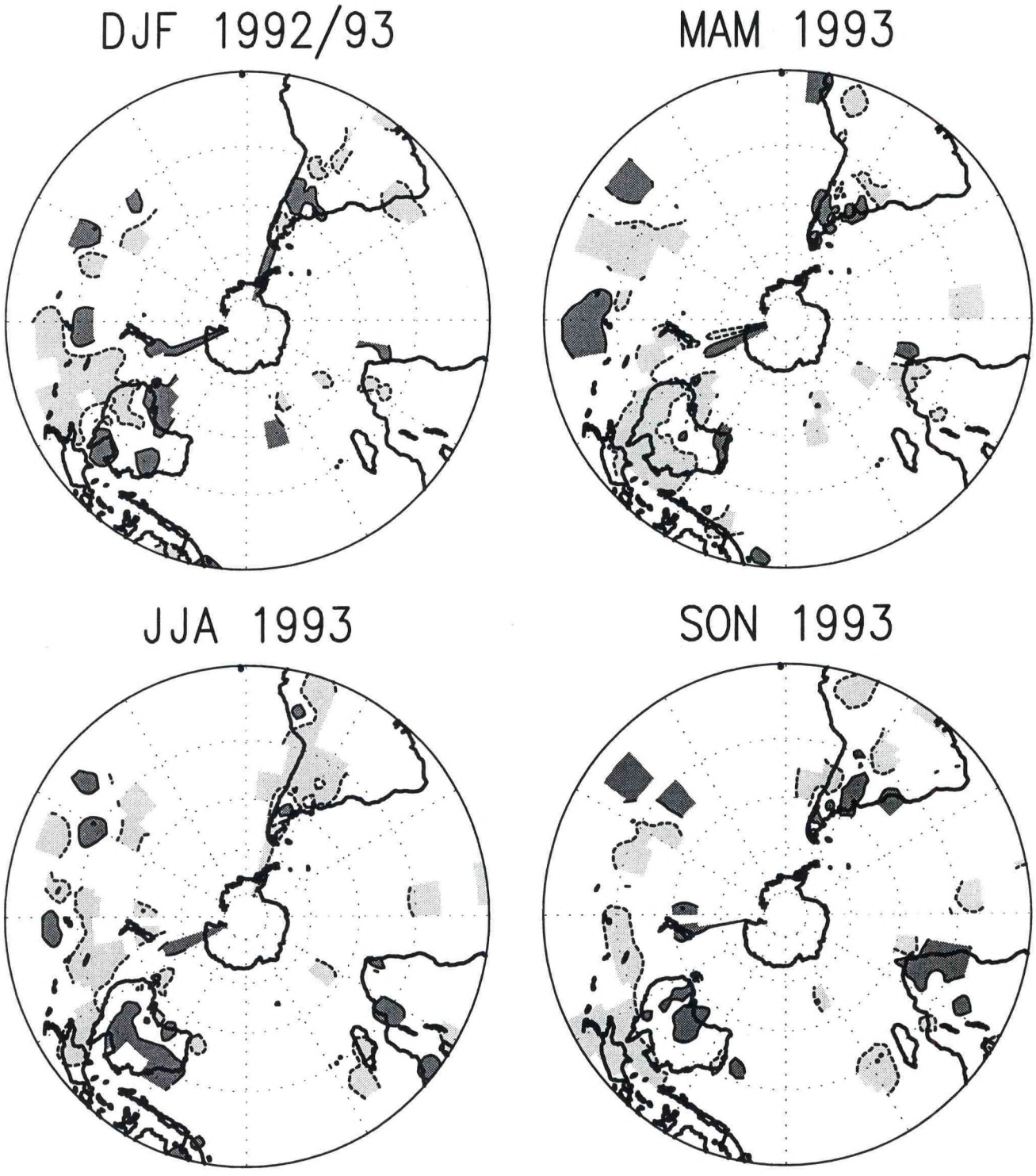
DJF 1992/93
MAM 1993
JJA 1993
SON 1993
30
70
Precipitation Percentile

NORTHERN HEMISPHERE TELECONNECTIONS

Summary Table (p. 232): Calendar months in which each teleconnection patterns appears as a leading rotated mode, along with the numerical value of the mode for each month. See caption at bottom of Table.

Teleconnection Patterns (pp. 233-256): Patterns (or eigenvectors) showing the primary modes of low frequency variability of the Northern Hemisphere extratropical atmospheric circulation (termed teleconnection patterns) for selected calendar months. The positive phase of the pattern is shown in all panels, and a negative phase can be obtained by reversing the signs of the anomalies. Negative anomalies are contoured dashed and shaded, while positive anomalies are contoured solid. The contour interval is 0.25. No map is shown when the pattern is not one of the leading 10 modes for that season.

Patterns are calculated using Rotated Principal Component Analysis (RPCA- 10 varimax spatial rotations) applied to monthly mean 700-mb height anomalies between January 1964- July 1994. Separate patterns are calculated for each calendar month by using all of the height anomaly fields for the three-month period centered on that month: [i.e., The July loading patterns are calculated based on the June through August anomaly fields].

Time Series (pp. 233-256): Standardized time series for the above teleconnection patterns, shown for two periods: the entire record from January 1964-January 1994 (top panel), and the period covered by this atlas from January 1986-February 1994 (bottom panel). No value is plotted for months in which the pattern does not appear as a leading mode.

The time series' are constructed as follows: For each month in the data record, the observed amplitudes of the ten teleconnection patterns corresponding to that calendar month are first calculated using a Least-Squares regression analysis. In this analysis, the amplitudes are determined simultaneously such that the combined sum of their products with the corresponding pattern eigenvectors explains the maximum spatial structure of the observed height anomaly field during the month. For each pattern, the amplitudes are then assembled into a continuous time series, and standardized (mean equal to zero and variance equal to 1.0) for each calendar month independently.

NORTHERN HEMISPHERE TELECONNECTION PATTERNS

PATTERN	DEC	JAN	FEB	MAR	APR	MAY	JUN	JUL	AUG	SEP	OCT	NOV
NAO	2	2	3	1	1	2	3	2	2	5	1	1
EA	6	6	7	6	10	---	---	---	---	8	7	5
EA-JET	---	---	---	---	6	9	7	3	7	---	---	---
WP	4	3	4	3	4	4	6	7	8	10	4	6
EP	9	10	9	10	8	3	1	1	---	---	6	9
NP	---	---	---	2	2	1	2	6	---	---	---	---
PNA	3	1	2	5	5	10	---	---	6	6	5	2
EATL/ WRUS	7	8	10	7	9	7	---	---	---	7	3	4
SCAND	5	9	8	8	3	5	---	---	10	1	2	3
POLAR-EURASIA	1	4	1	---	---	---	---	---	---	---	---	---
TNH	8	7	---	---	---	---	---	---	---	---	---	8
PT	---	---	---	---	---	8	4	4	4	---	---	---
ASIAN SUMMER	---	---	---	---	---	---	5	5	5	---	---	---

Table showing the calendar months in which a particular teleconnection pattern appears as a leading rotated mode. Tabulated values indicate the mode number of the pattern for that calendar month (i.e., a 1 indicates that the pattern appears as the leading rotated mode during the month, etc...). No value is plotted when a pattern does not appear as a leading rotated mode in a given calendar month.

The teleconnection patterns and mode numbers are determined from a Rotated Principal Component Analysis (RPCA- 10 varimax rotations) applied to monthly mean 700-mb height anomalies between January 1964-July 1994. Separate patterns are calculated independently for each calendar month by using all of the height anomaly fields for the three-month period centered on that month: [i.e., The July patterns are calculated based on the June through August anomaly fields].

Pattern names and abbreviations are: North Atlantic Oscillation (NAO); East Atlantic pattern (EA); East Atlantic Jet pattern (EA- JET); West Pacific pattern (WP); East Pacific pattern (EP); North Pacific pattern (NP); Pacific/ North American pattern (PNA); East Atlantic/ Western Russia pattern (EATL/ WRUS- called Eurasia-2 pattern by Barnston and Livezey, 1987, *Mon. Wea. Rev.*, **115**, 1083-1126); Scandinavia pattern (SCAND- called Eurasia-1 pattern by Barnston and Livezey 1987); Polar- Eurasia pattern (no abreviation); Tropical/ Northern Hemisphere pattern (TNH); Pacific Transition pattern (PT); and Asian Summer pattern (no abbreviation).

NORTH ATLANTIC OSCILLATION (NAO)

JAN

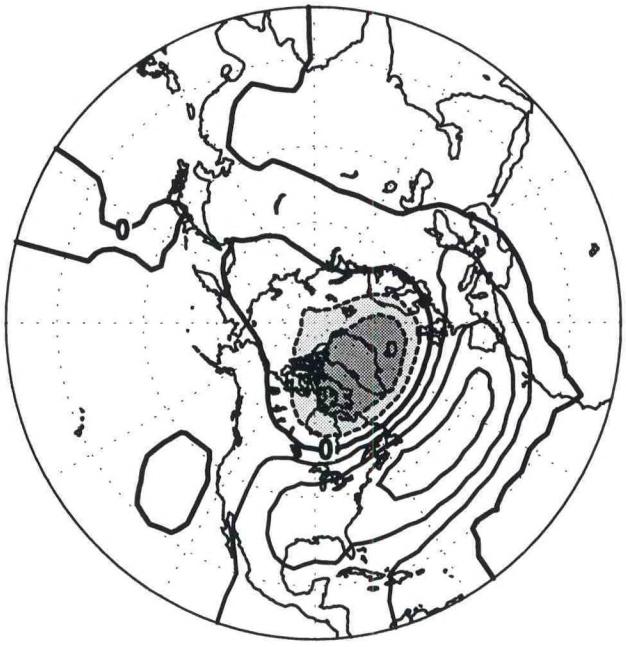

APR

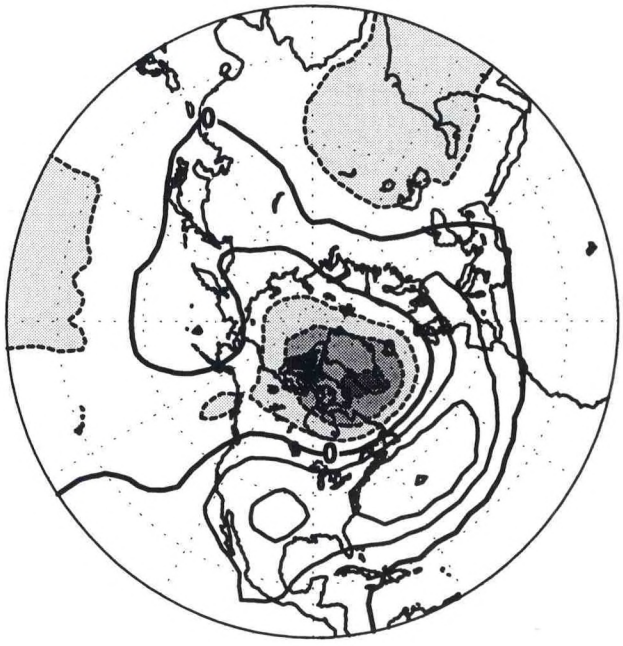

JUL

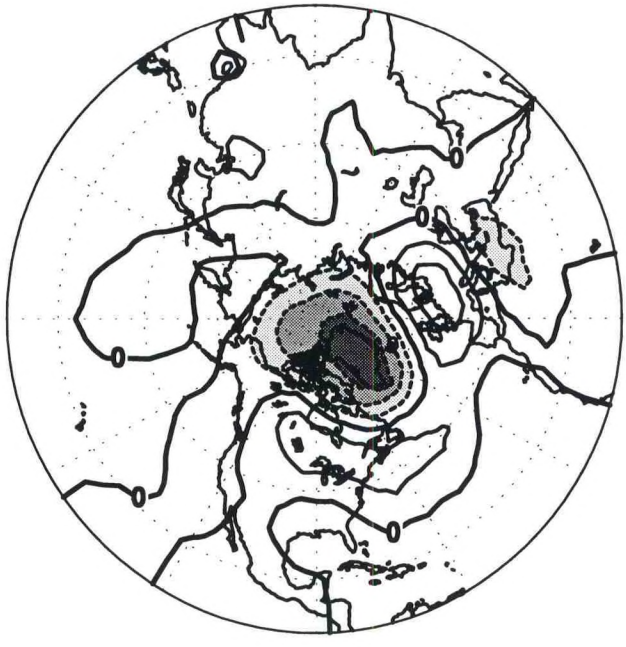

OCT

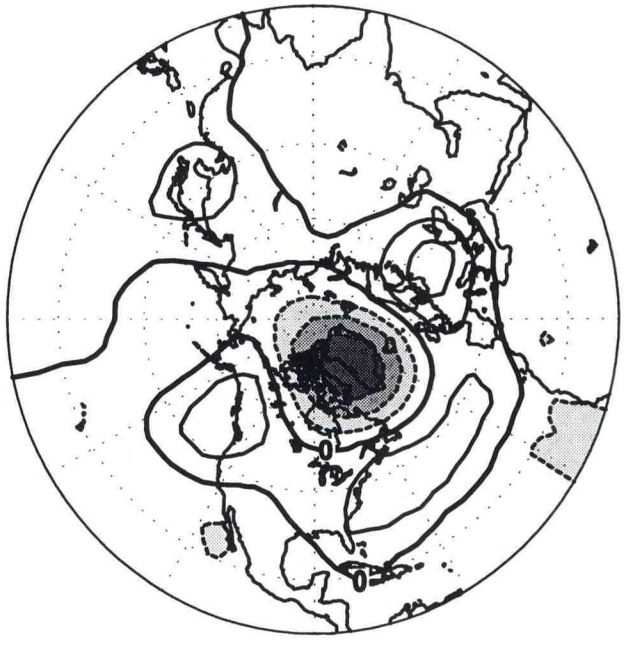

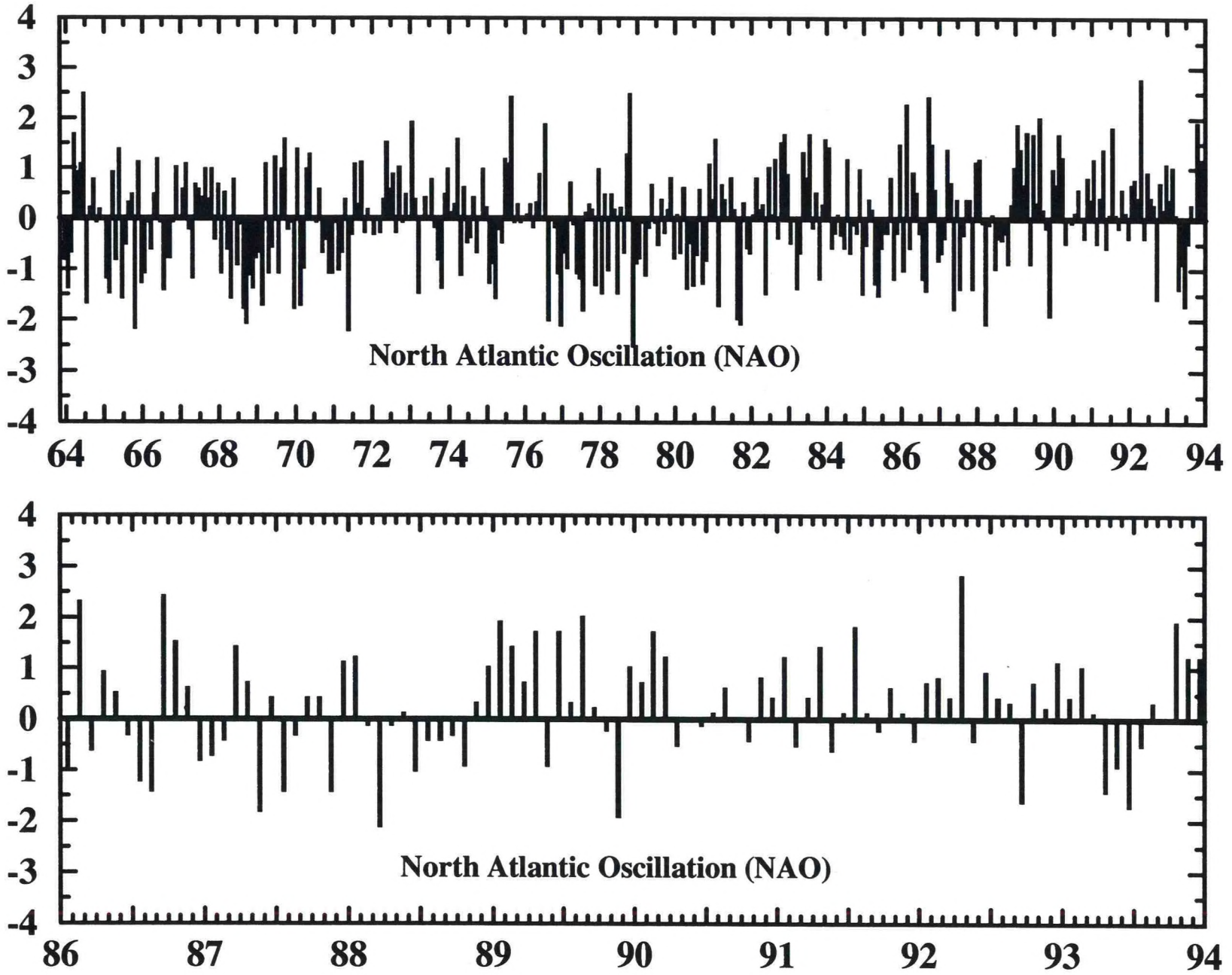
4
3
2
1
0
-1
-2
-3
-4
North Atlantic Oscillation (NAO)
64 66 68 70 72 74 76 78 80 82 84 86 88 90 92 94
4
3
2
1
0
-1
-2
-3
-4
North Atlantic Oscillation (NAO)
86 87 88 89 90 91 92 93 94

EAST ATLANTIC (EA)

JAN

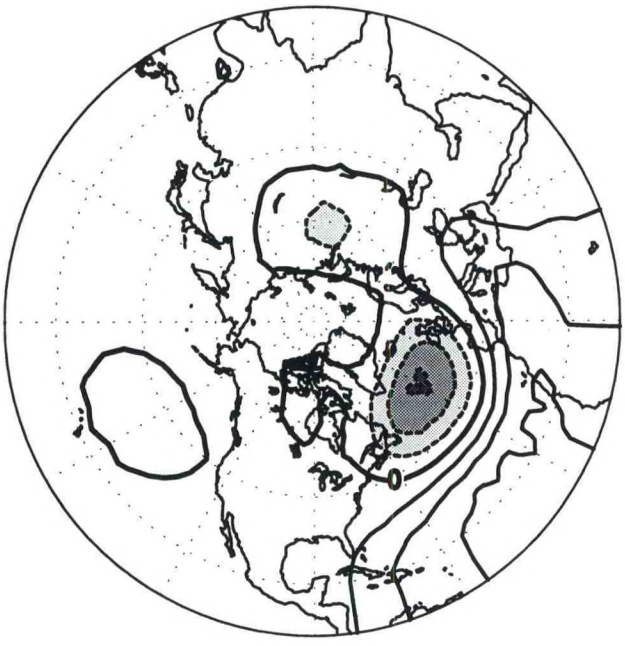

APR

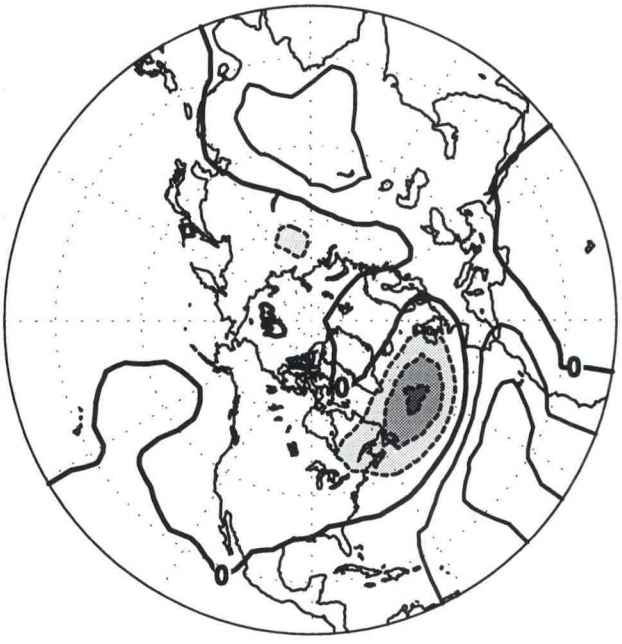

OCT

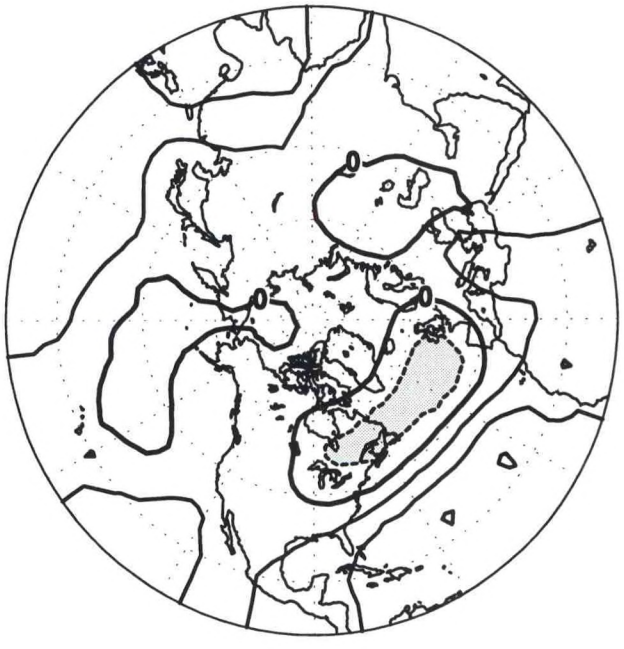

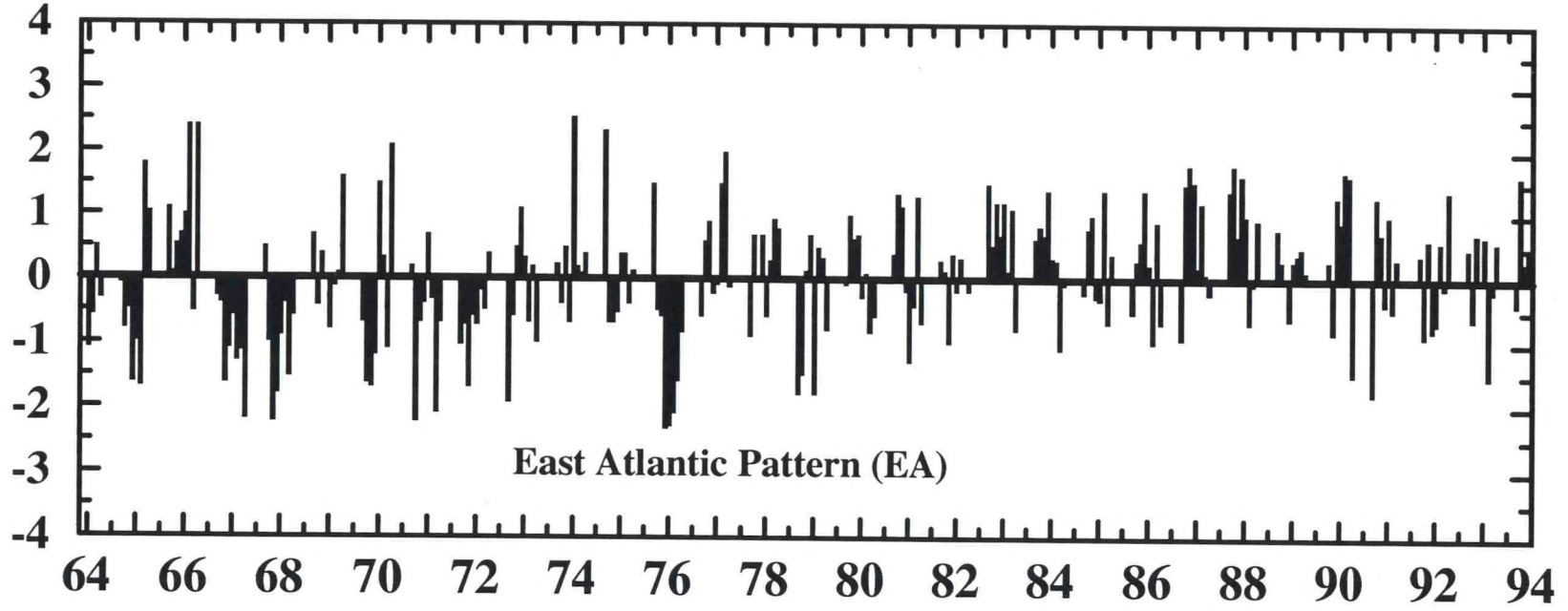
4
3
2
1
0
-1
-2
-3
-4
East Atlantic Pattern (EA)
64 66 68 70 72 74 76 78 80 82 84 86 88 90 92 94

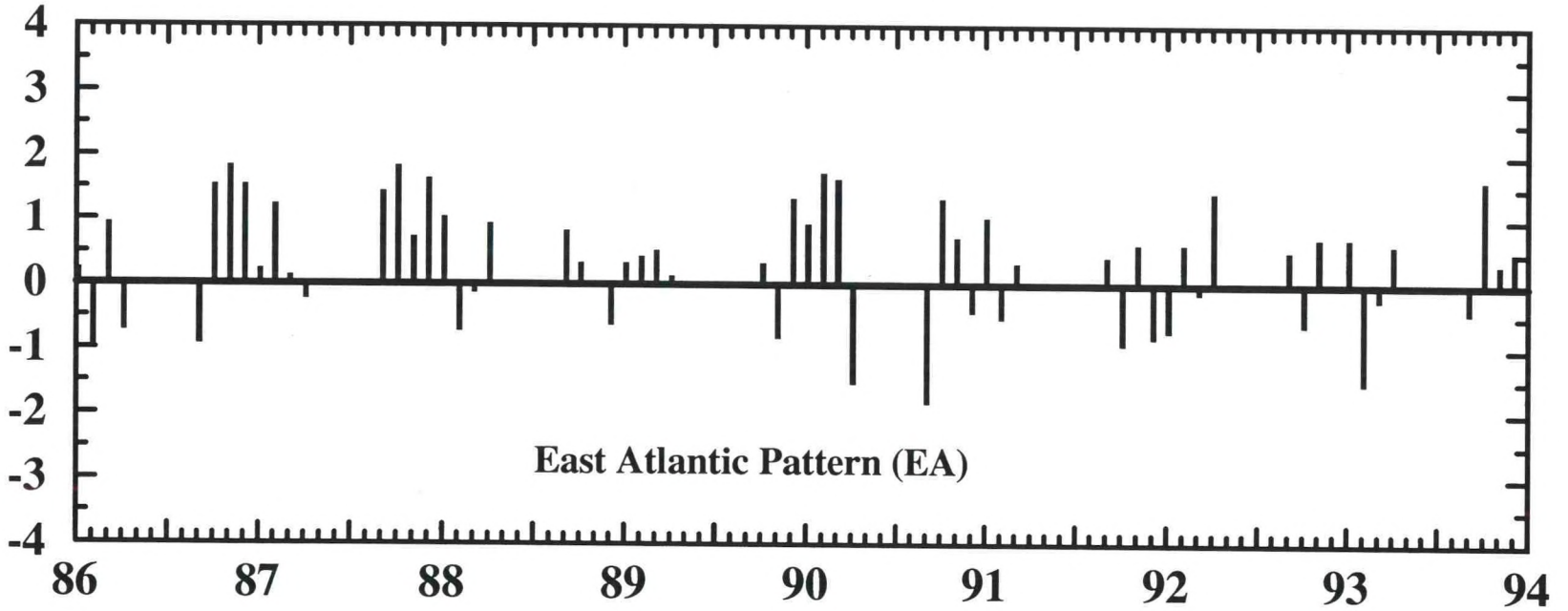
4
3
2
1
0
-1
-2
-3
-4
East Atlantic Pattern (EA)
86 87 88 89 90 91 92 93 94

EAST ATLANTIC JET (EA-JET)

APR

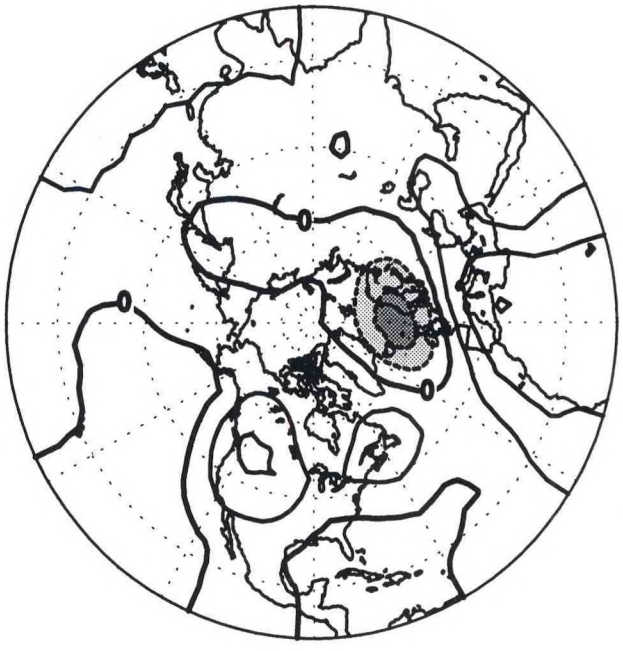

JUL

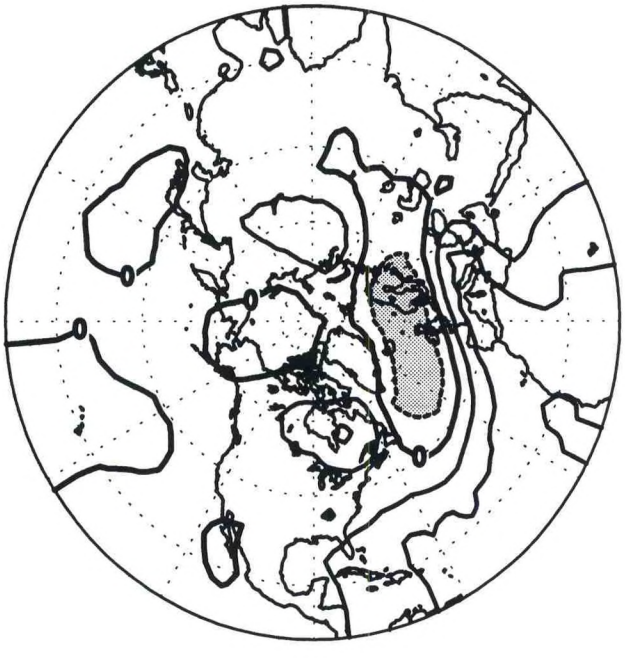

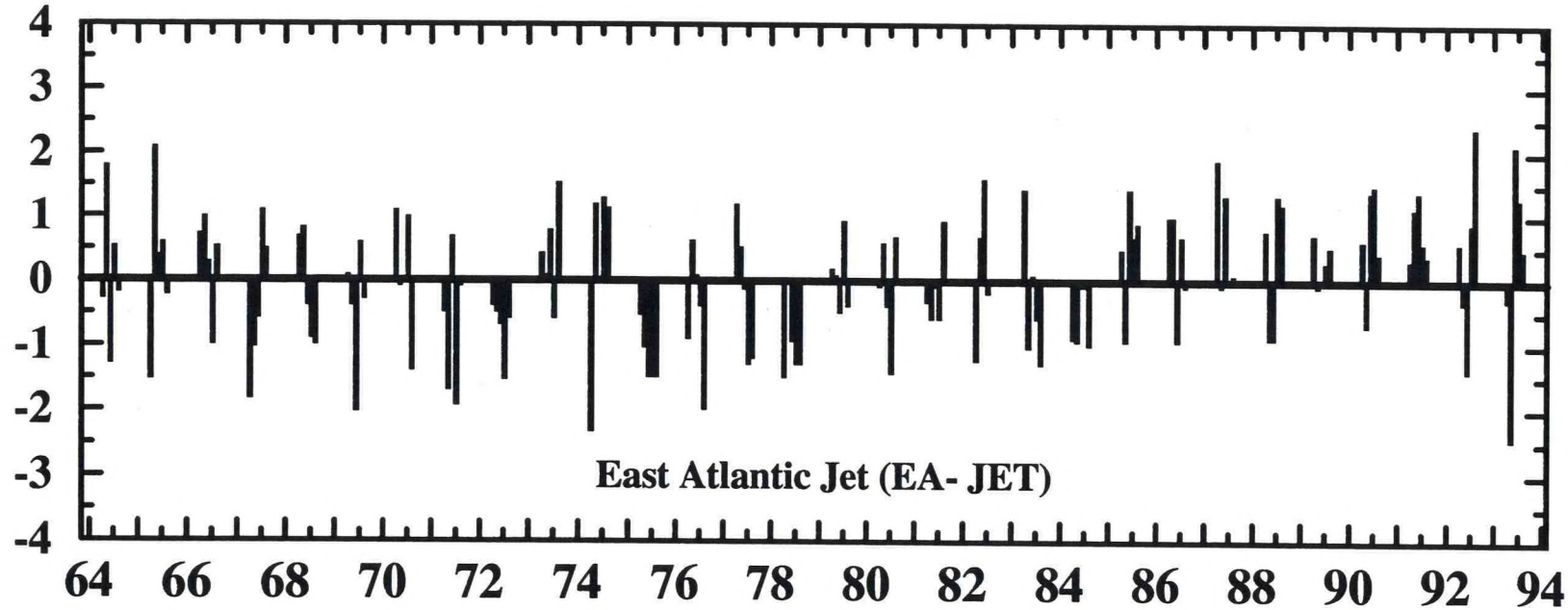
4
3
2
1
0
-1
-2
-3
-4
East Atlantic Jet (EA- JET)
64 66 68 70 72 74 76 78 80 82 84 86 88 90 92 94

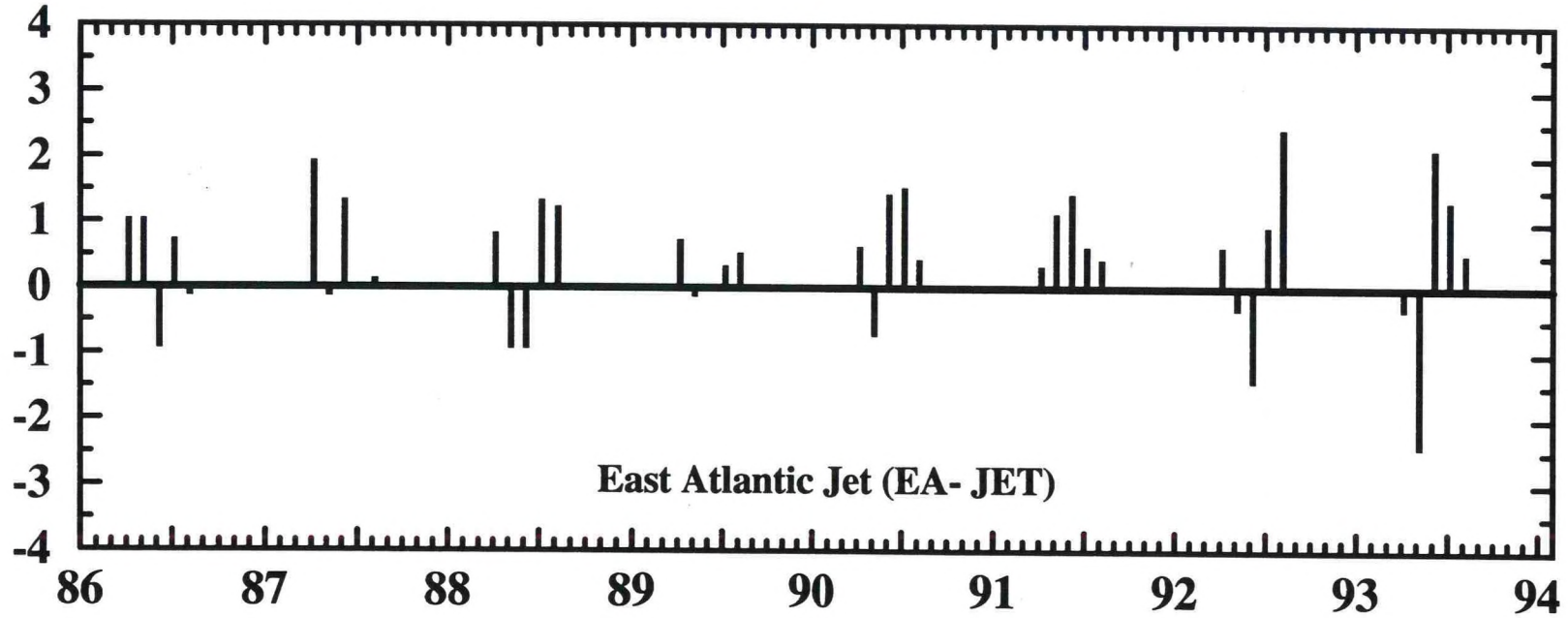
4
3
2
1
0
-1
-2
-3
-4
East Atlantic Jet (EA- JET)
86 87 88 89 90 91 92 93 94

WEST PACIFIC PATTERN (WP)

JAN

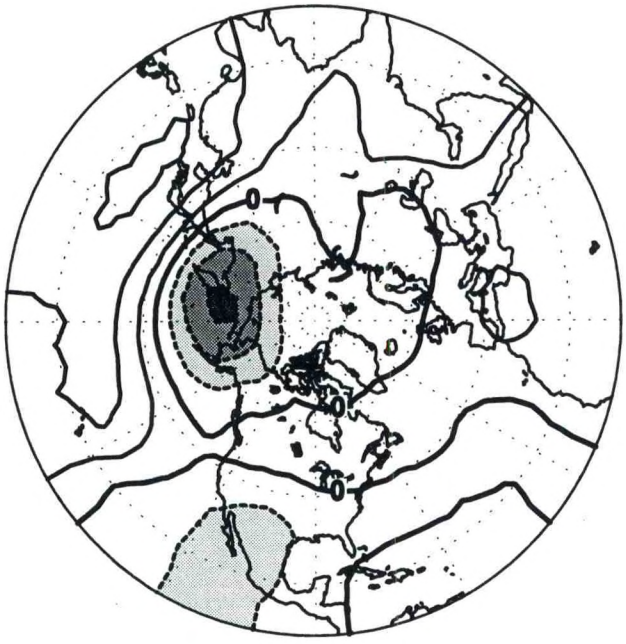

APR

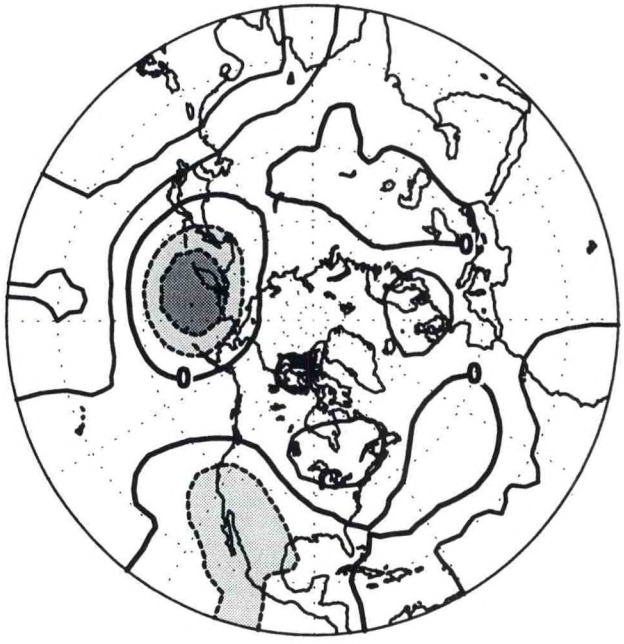

JUL

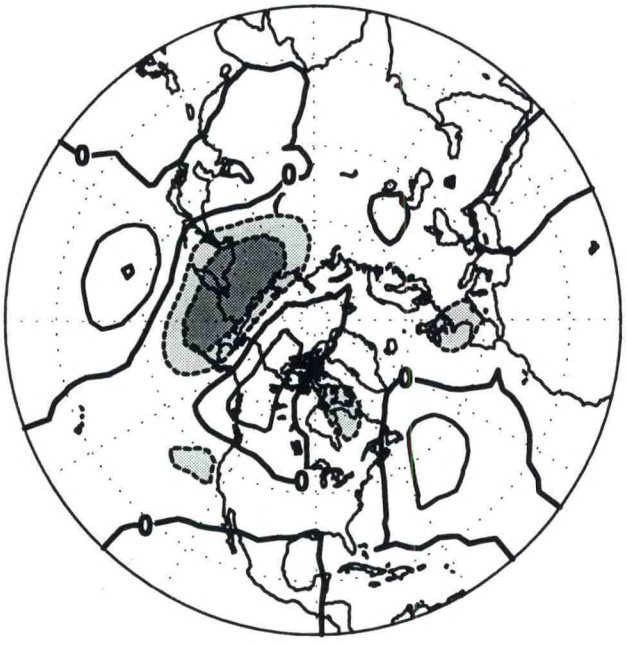

OCT

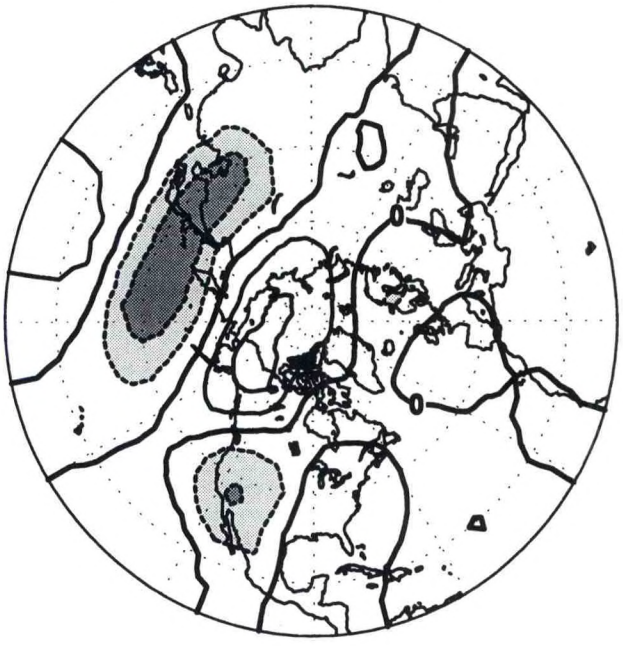

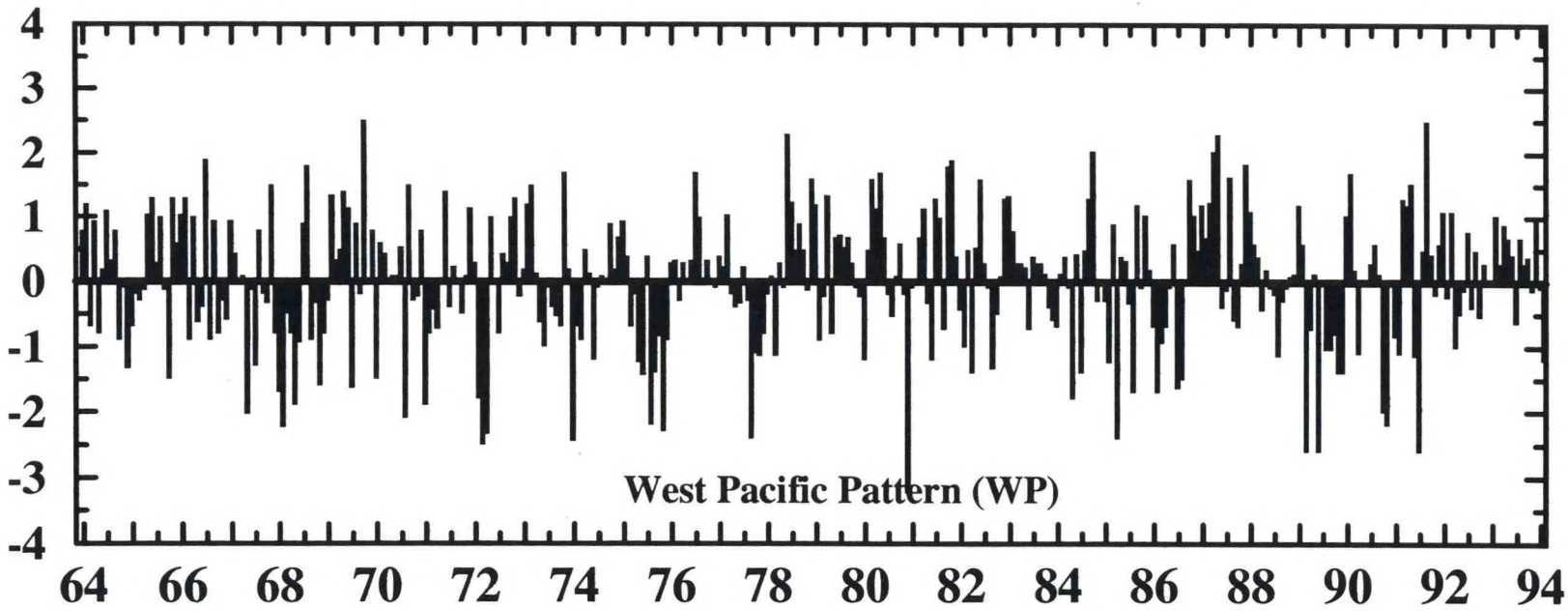
4
3
2
1
0
-1
-2
-3
-4
West Pacific Pattern (WP)
64 66 68 70 72 74 76 78 80 82 84 86 88 90 92 94

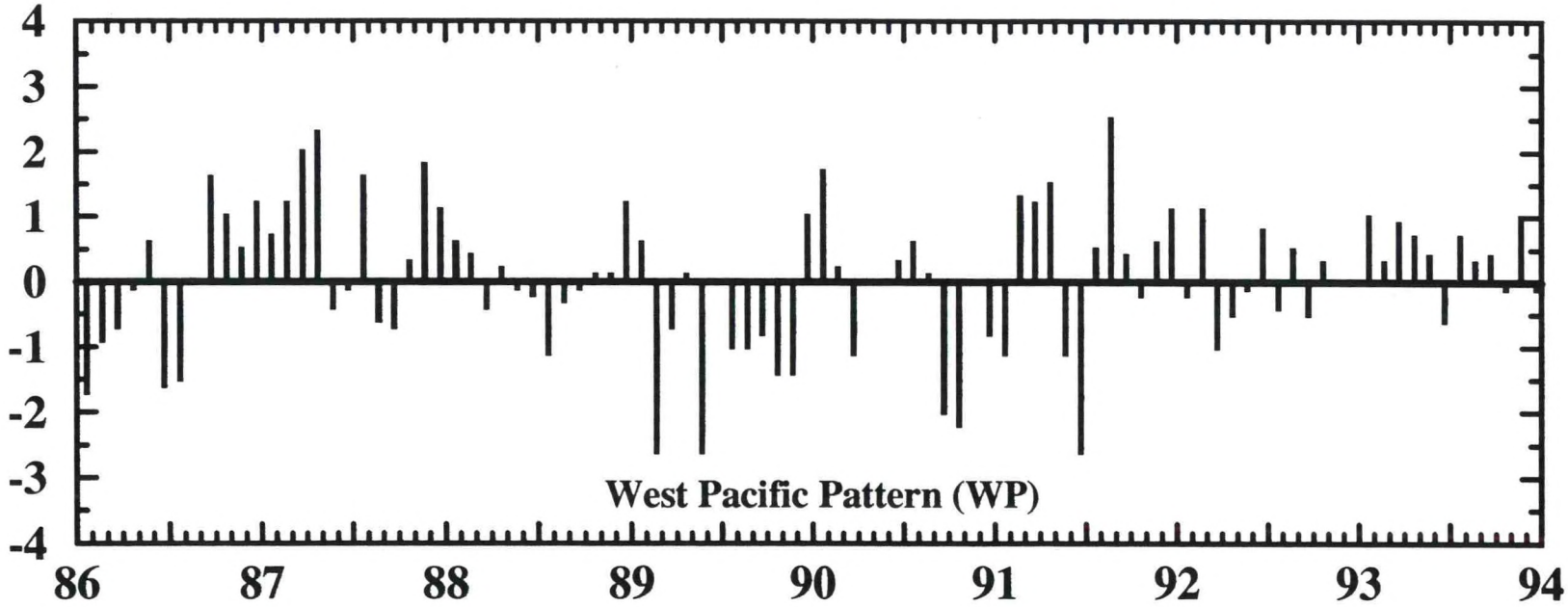
4
3
2
1
0
-1
-2
-3
-4
West Pacific Pattern (WP)
86 87 88 89 90 91 92 93 94

EAST PACIFIC (EP)

JAN

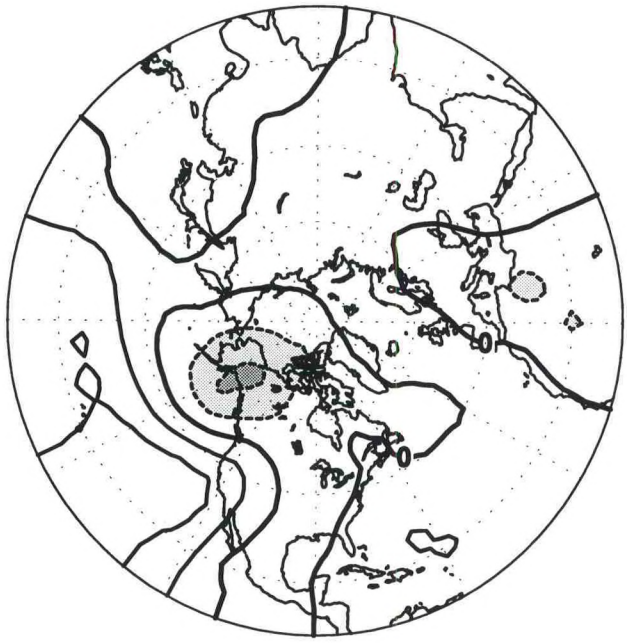

MAR

JUL

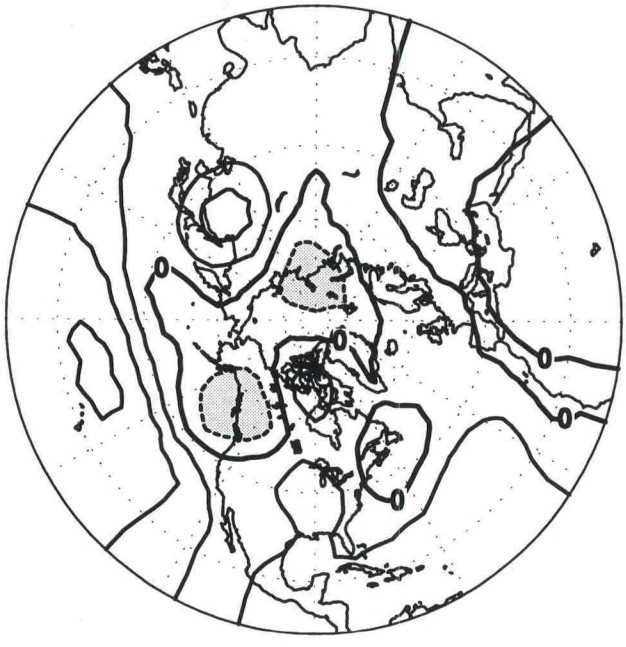

OCT

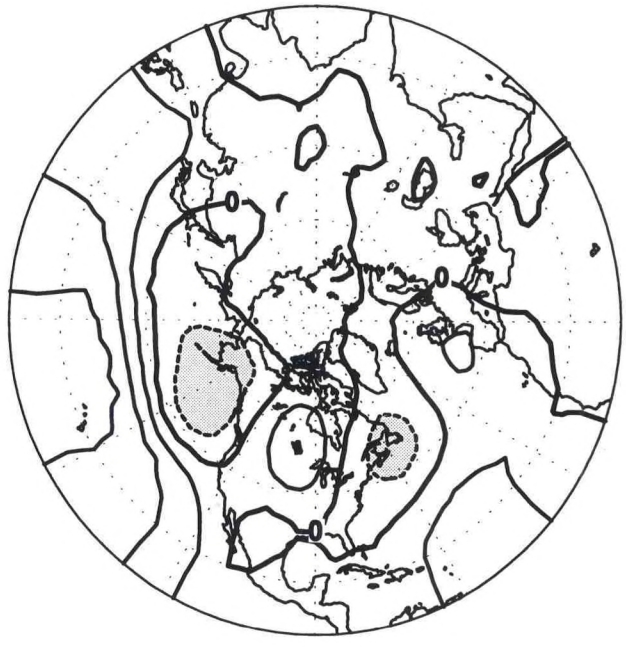

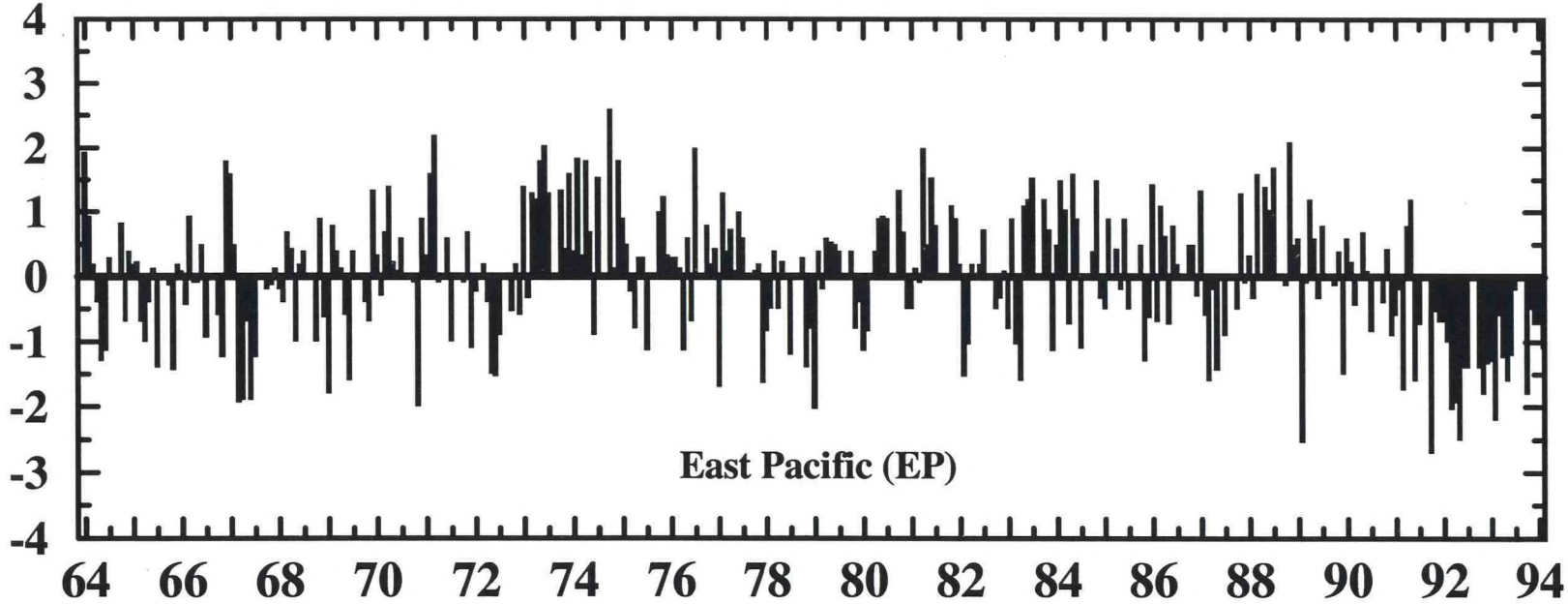
4
3
2
1
0
-1
-2
-3
-4
East Pacific (EP)
64 66 68 70 72 74 76 78 80 82 84 86 88 90 92 94

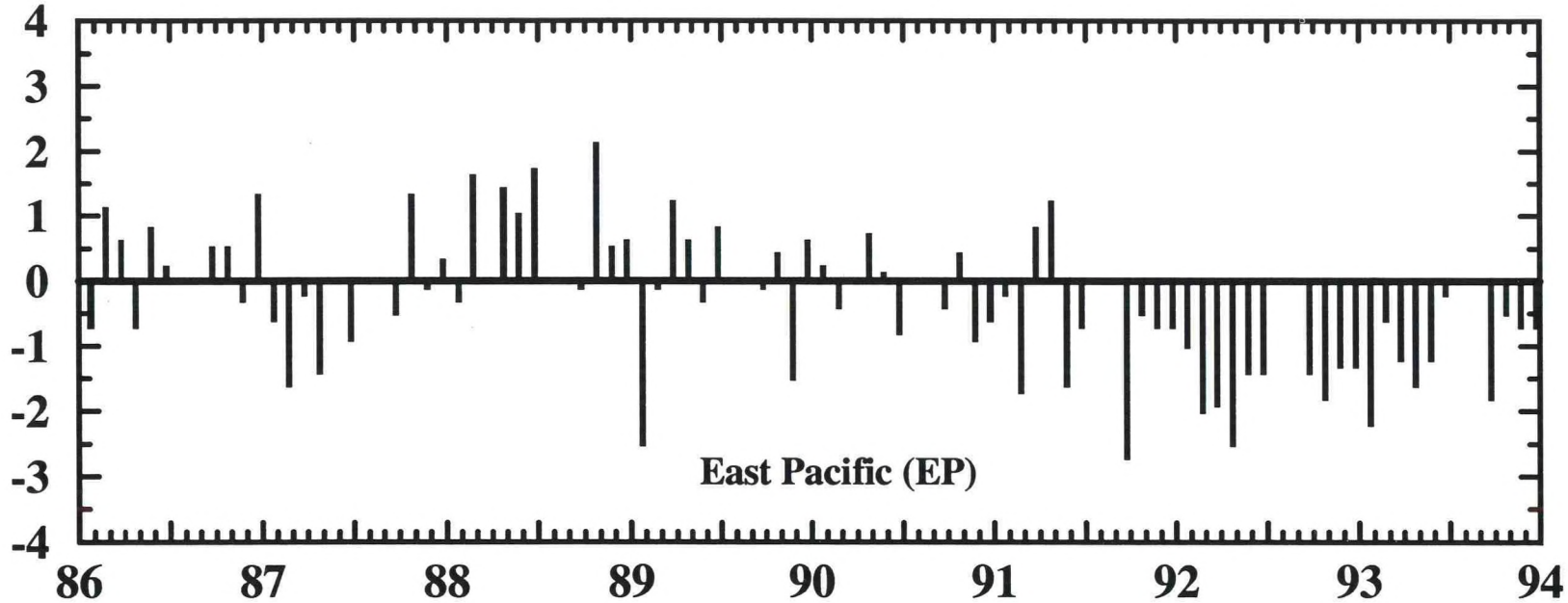
4
3
2
1
0
-1
-2
-3
-4
East Pacific (EP)
86 87 88 89 90 91 92 93 94

NORTH PACIFIC PATTERN (NP)

APR

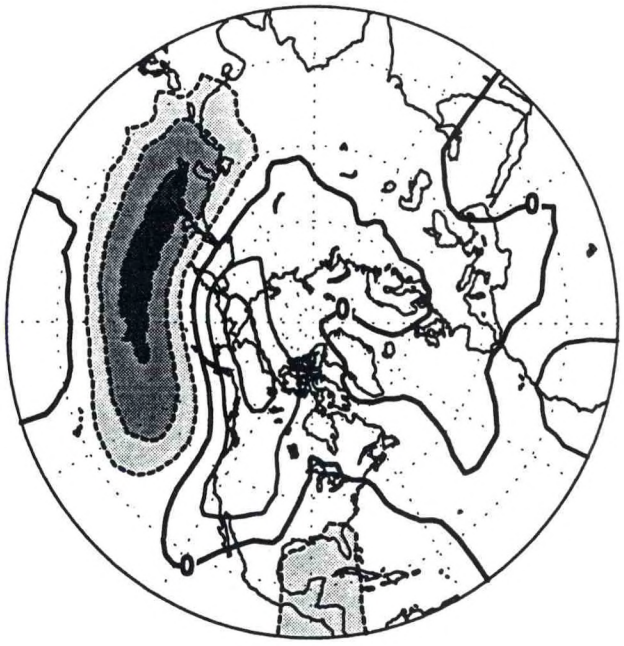

JUL

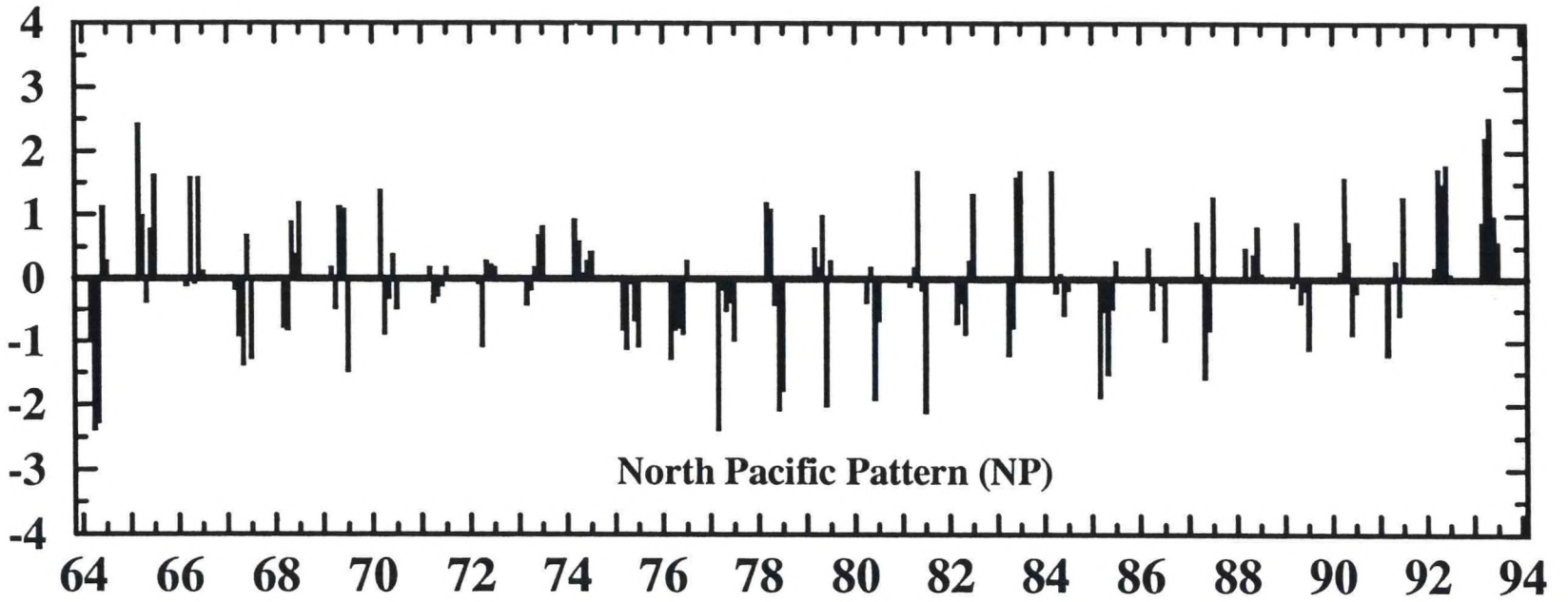
4
3
2
1
0
-1
-2
-3
-4
North Pacific Pattern (NP)
64 66 68 70 72 74 76 78 80 82 84 86 88 90 92 94

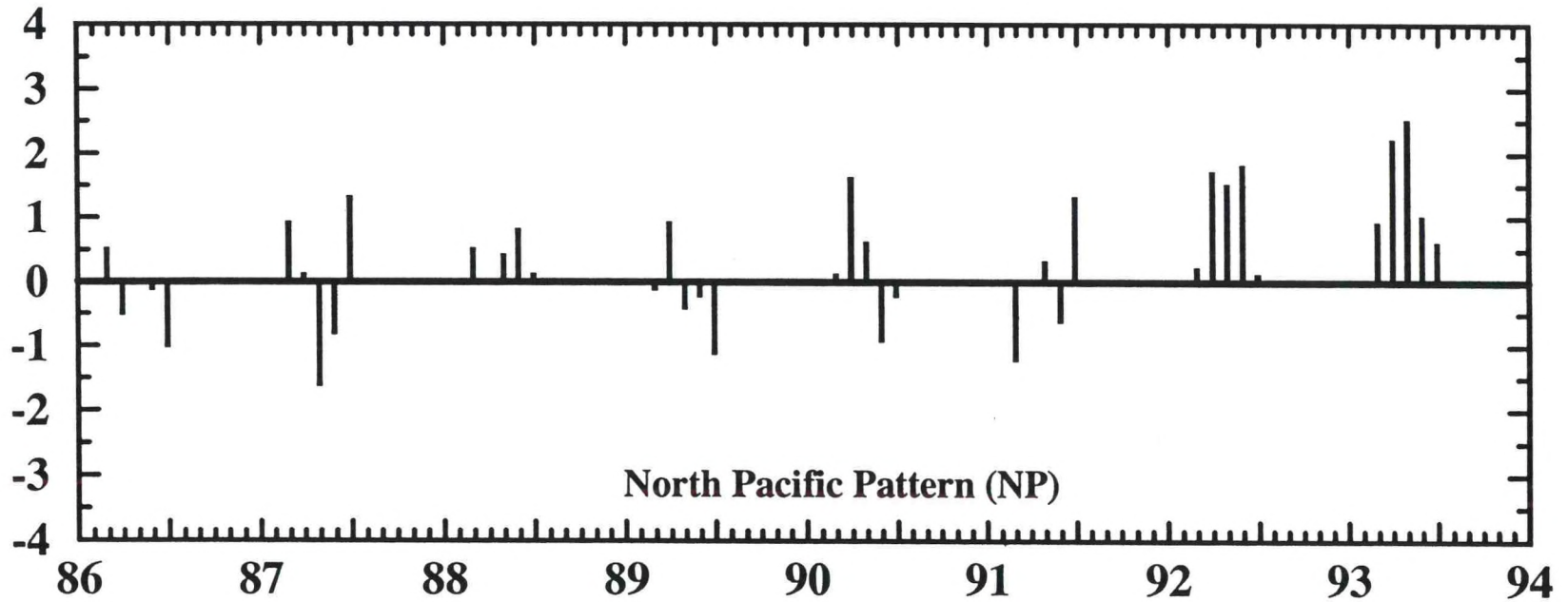
4
3
2
1
0
-1
-2
-3
-4
North Pacific Pattern (NP)
86 87 88 89 90 91 92 93 94

PACIFIC/NORTH AMERICAN PATTERN (PNA)

JAN

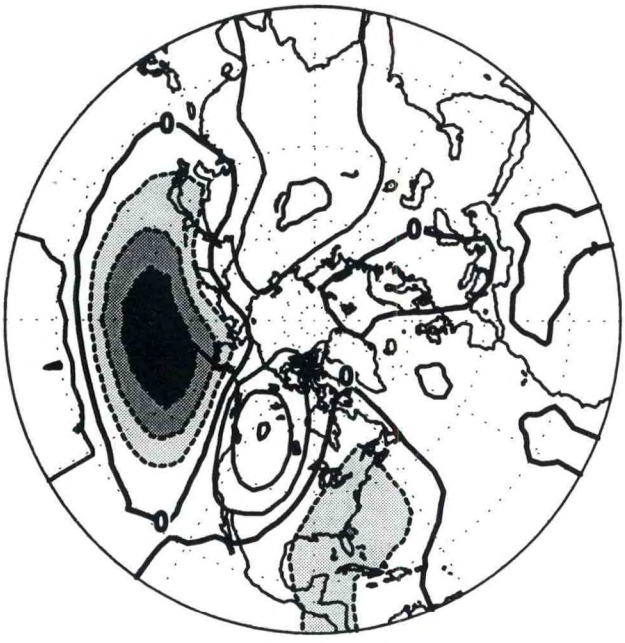

APR

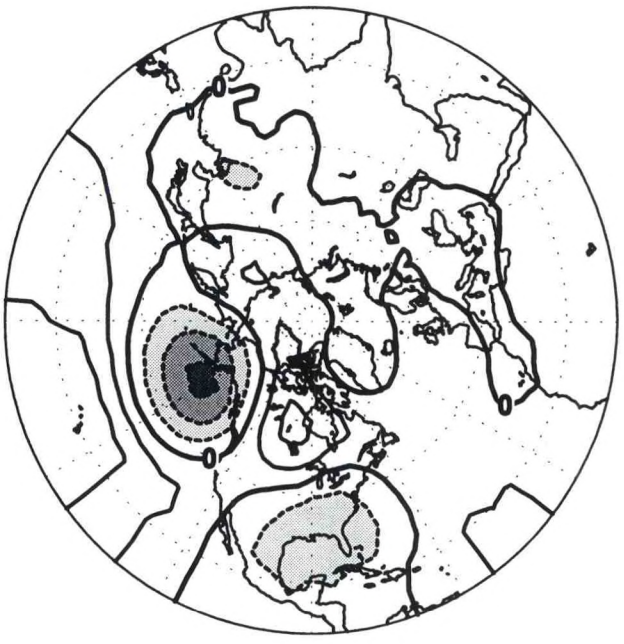

OCT

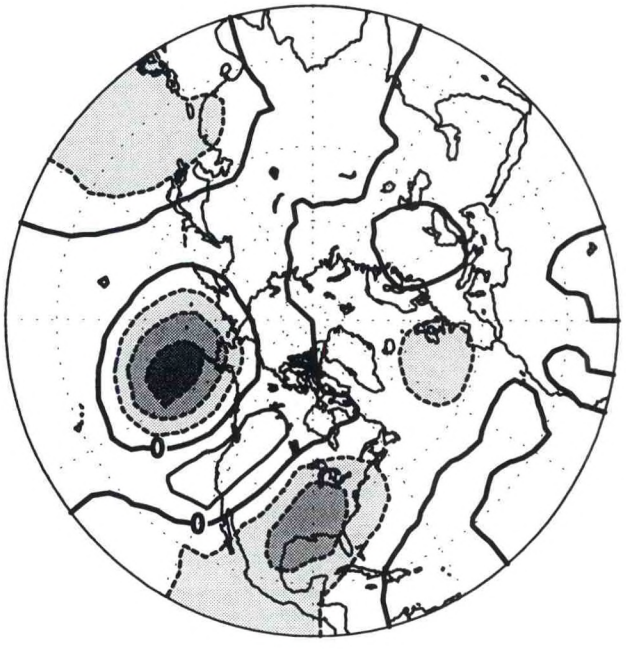

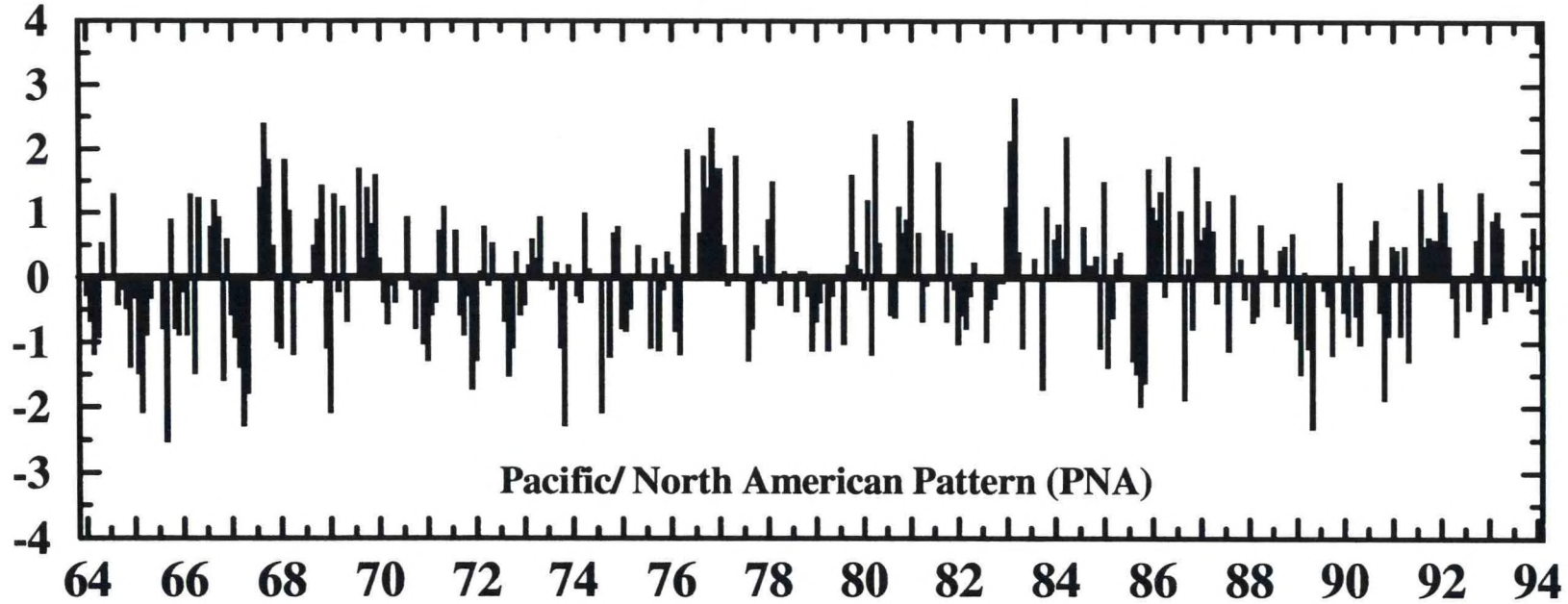
4
3
2
1
0
-1
-2
-3
-4
Pacific/ North American Pattern (PNA)
64 66 68 70 72 74 76 78 80 82 84 86 88 90 92 94

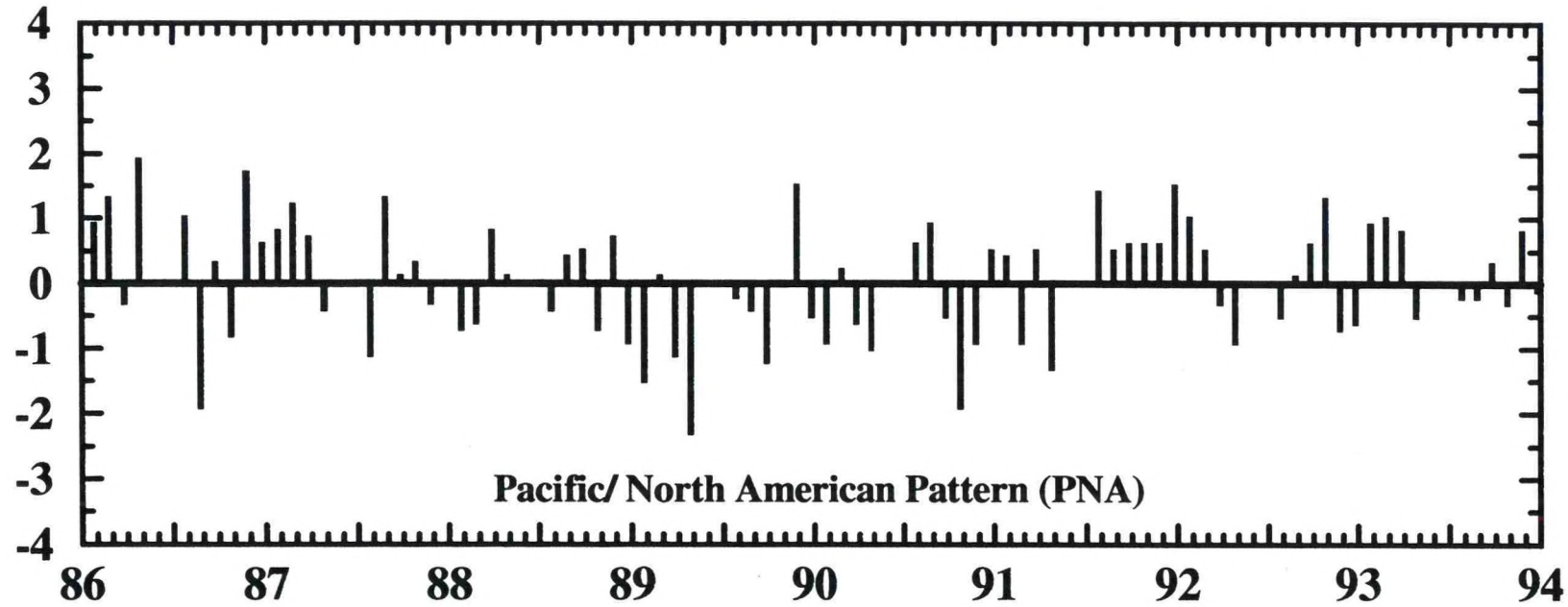
4
3
2
1
0
-1
-2
-3
-4
Pacific/ North American Pattern (PNA)
86 87 88 89 90 91 92 93 94

EAST ATLANTIC/ WEST RUSSIA (EATL/WRUS)

JAN

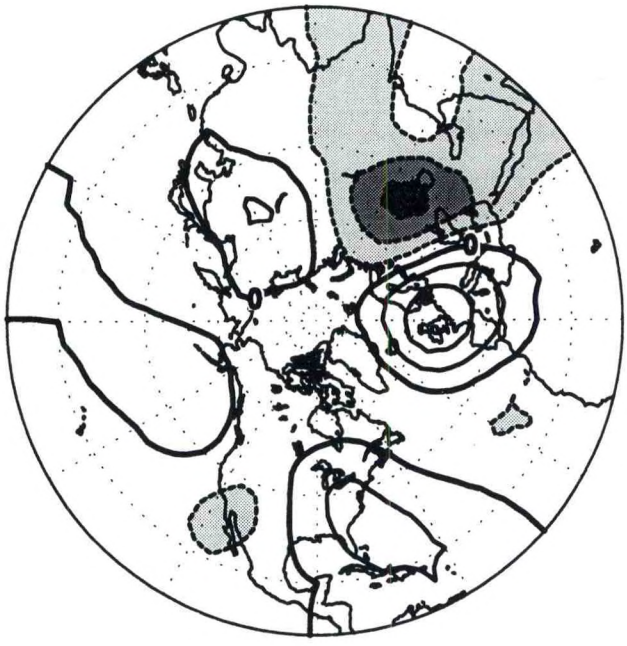

APR

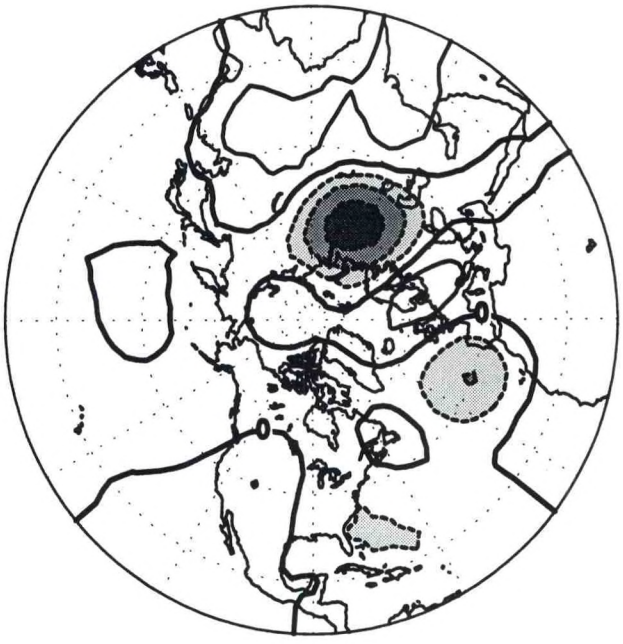

OCT

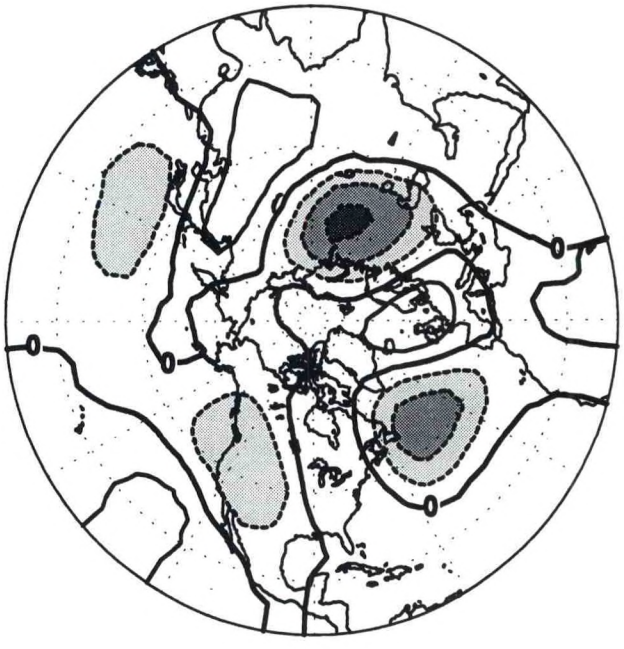

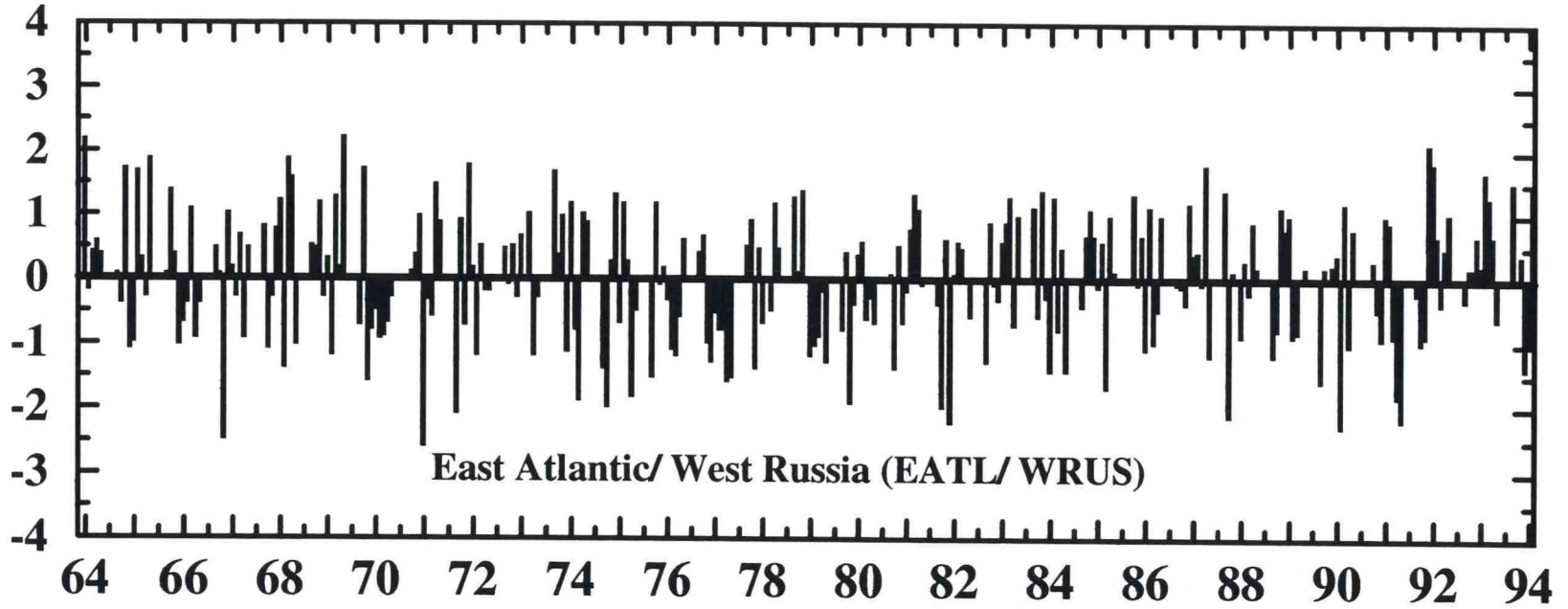
4
3
2
1
0
-1
-2
-3
-4
East Atlantic/ West Russia (EATL/ WRUS)
64 66 68 70 72 74 76 78 80 82 84 86 88 90 92 94

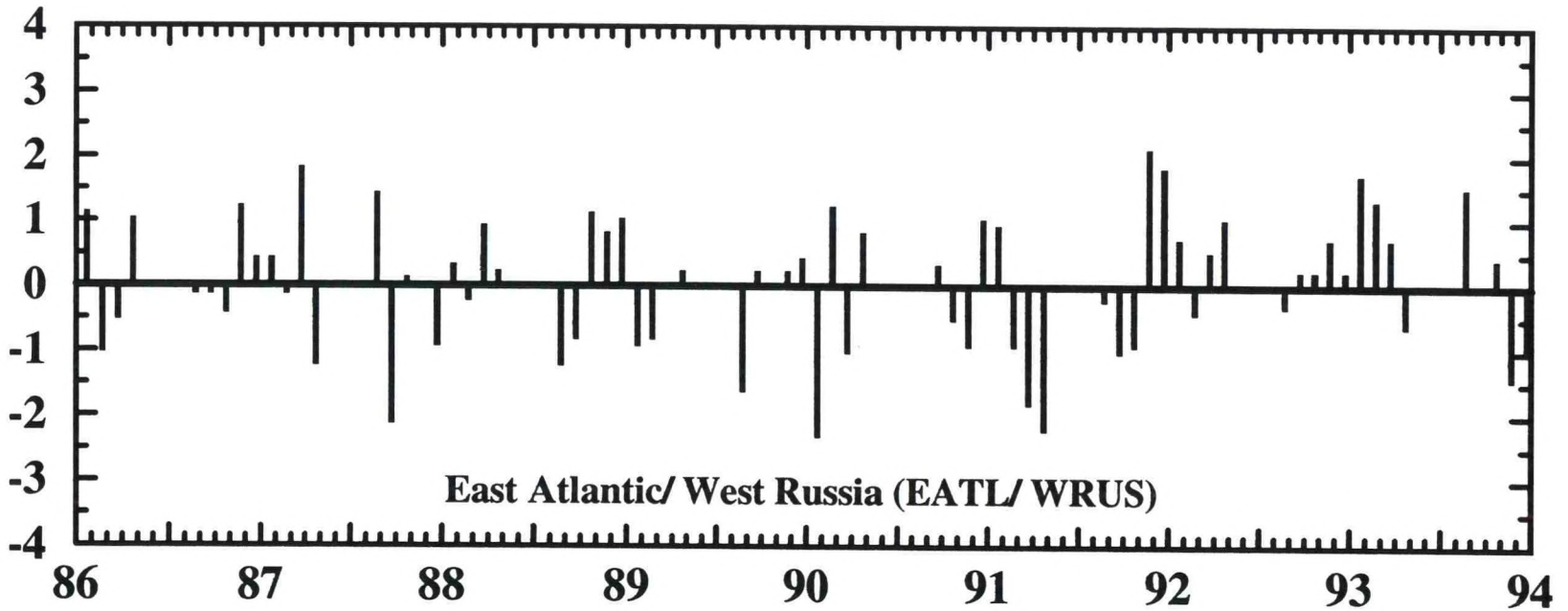
4
3
2
1
0
-1
-2
-3
-4
East Atlantic/ West Russia (EATL/ WRUS)
86 87 88 89 90 91 92 93 94

SCANDINAVIA (SCAND)

JAN

APR

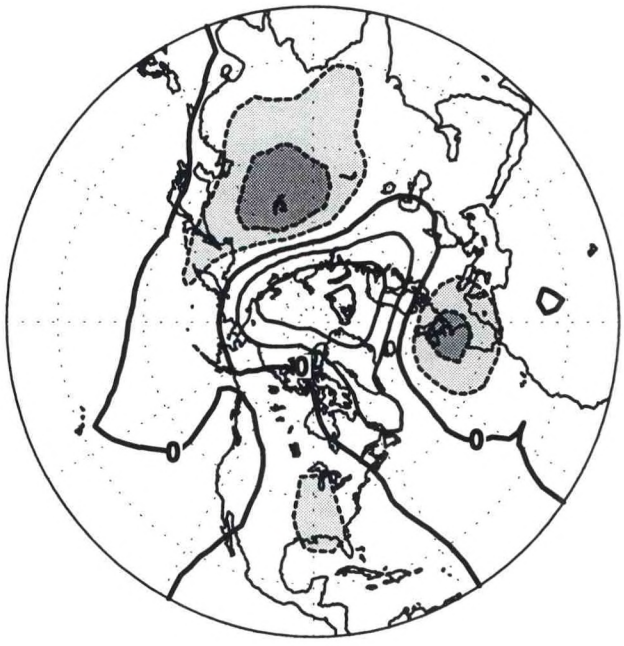

OCT

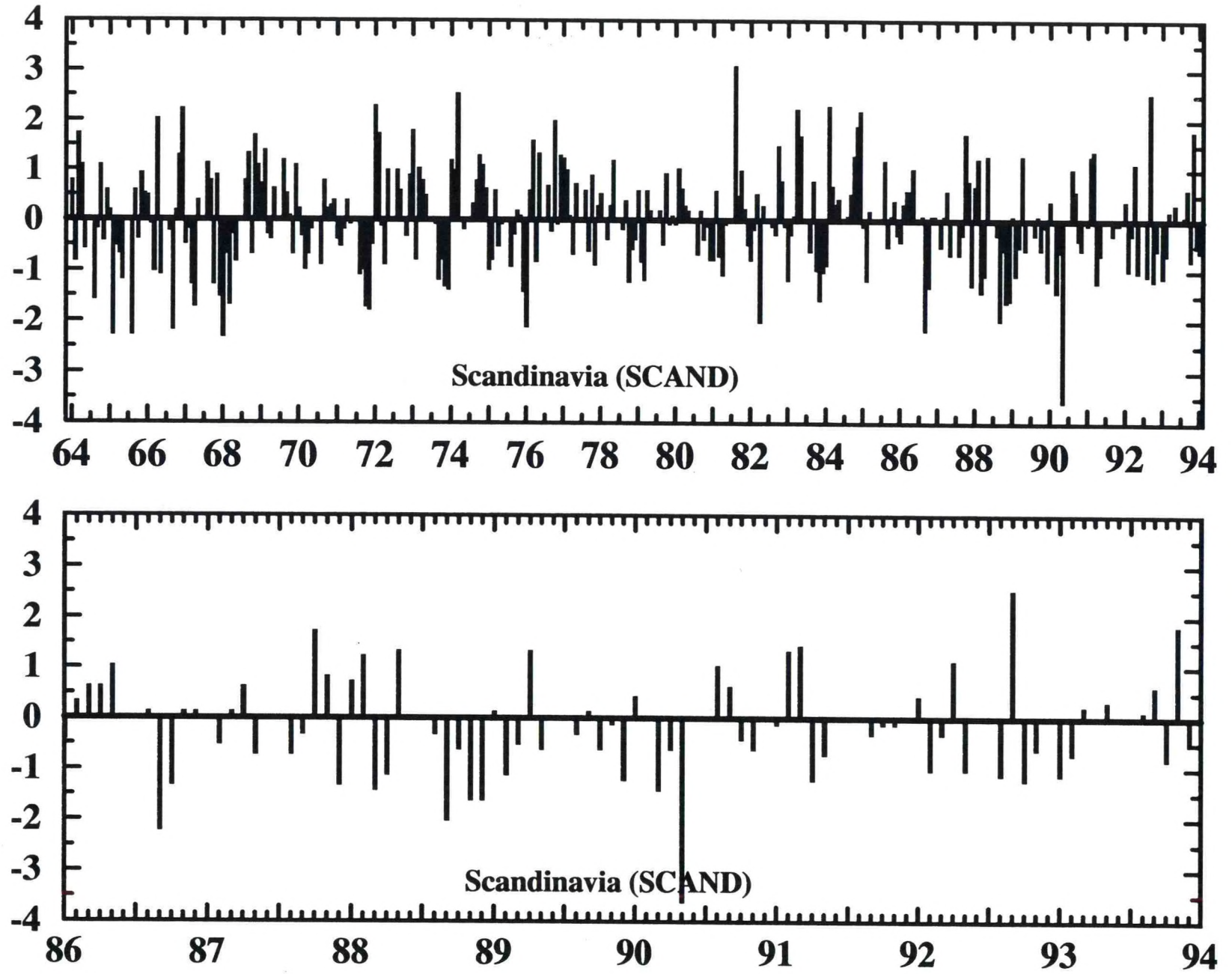
4
3
2
1
0
-1
-2
-3
-4
Scandinavia (SCAND)
64 66 68 70 72 74 76 78 80 82 84 86 88 90 92 94
4
3
2
1
0
-1
-2
-3
-4
Scandinavia (SCAND)
86 87 88 89 90 91 92 93 94

WINTER PATTERNS

POLAR/ EURASIAN

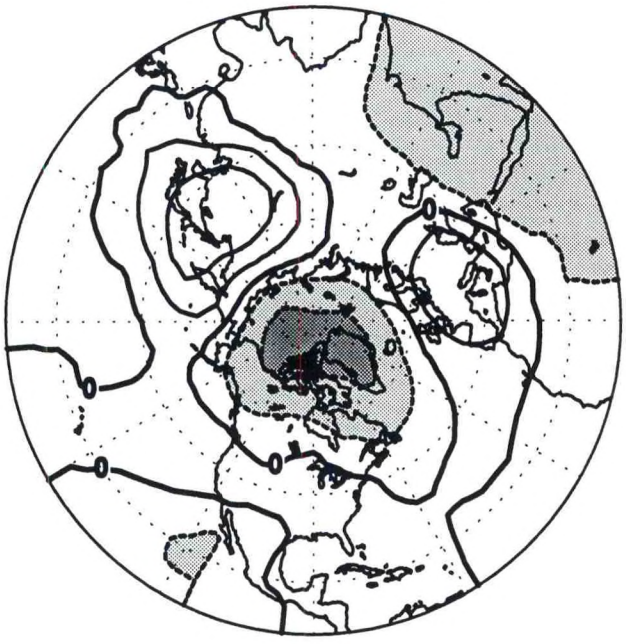

TROPICAL/ NORTHERN HEMISPHERE

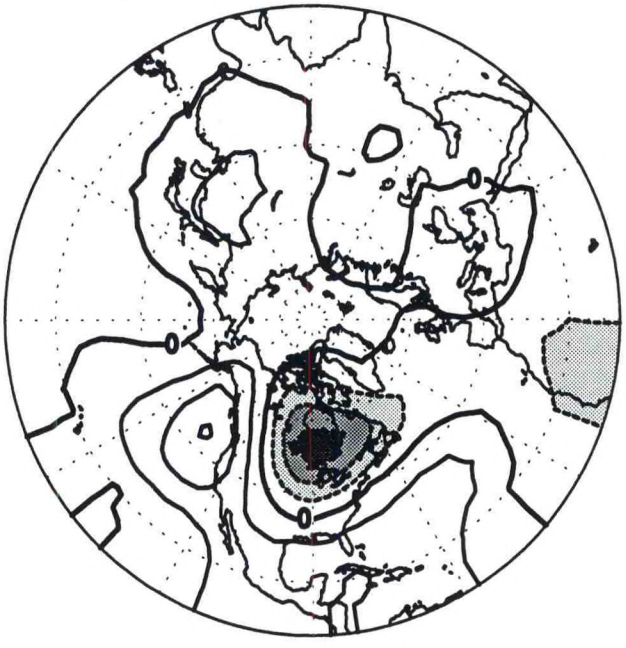

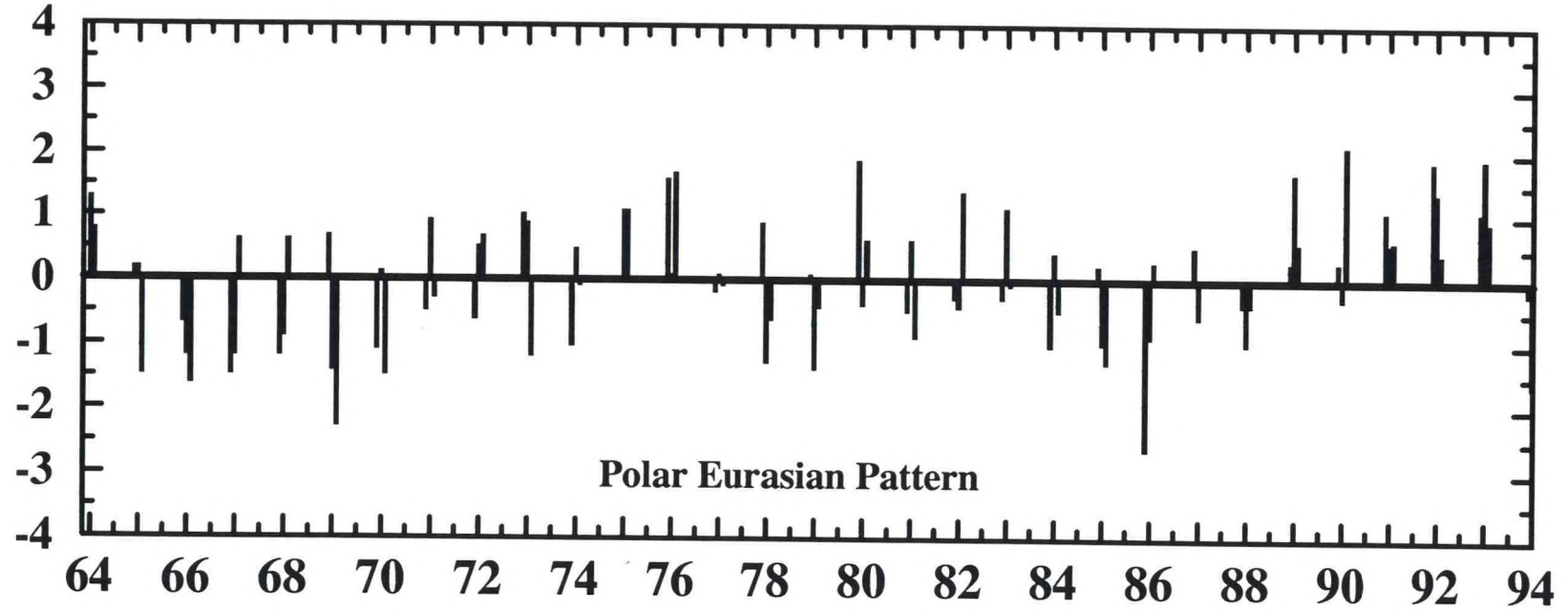
4
3
2
1
0
-1
-2
-3
-4
Polar Eurasian Pattern
64 66 68 70 72 74 76 78 80 82 84 86 88 90 92 94

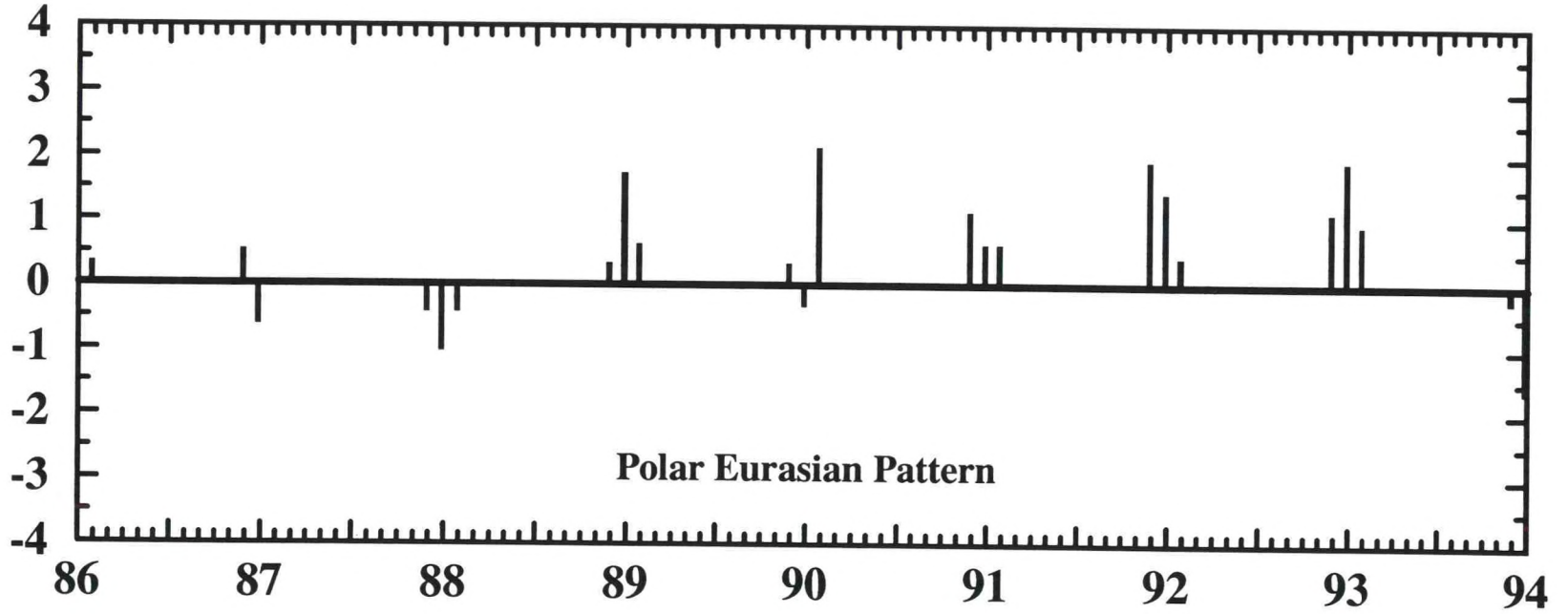
4
3
2
1
0
-1
-2
-3
-4
Polar Eurasian Pattern
86 87 88 89 90 91 92 93 94

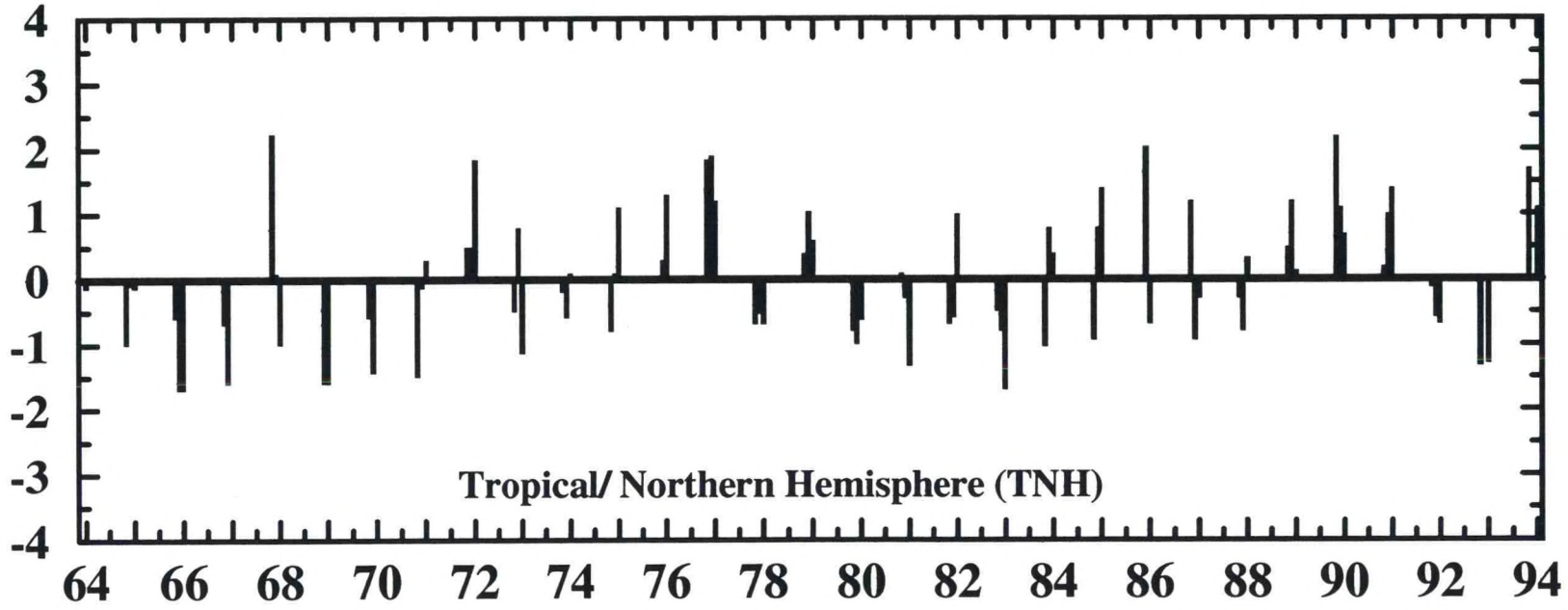
4
3
2
1
0
-1
-2
-3
-4
Tropical/ Northern Hemisphere (TNH)
64 66 68 70 72 74 76 78 80 82 84 86 88 90 92 94

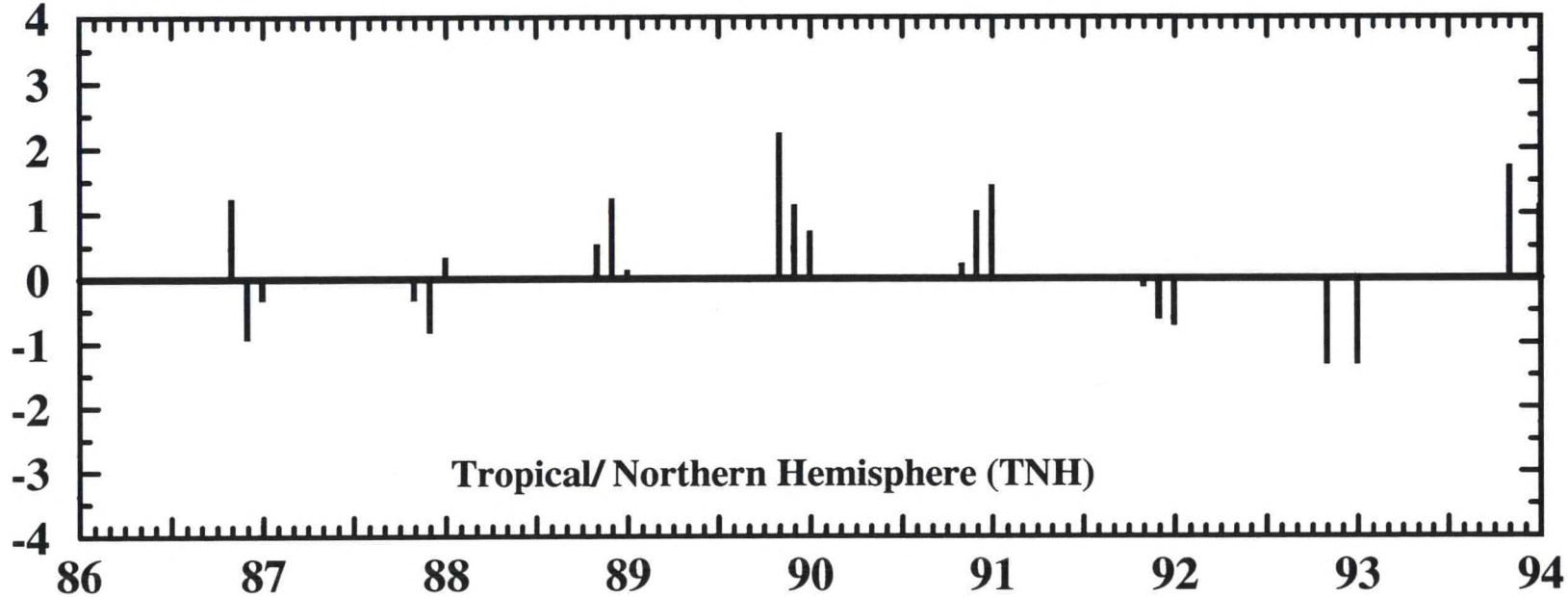
4
3
2
1
0
-1
-2
-3
-4
Tropical/ Northern Hemisphere (TNH)
86 87 88 89 90 91 92 93 94

SUMMER PATTERNS

ASIAN SUMMER

PACIFIC TRANSITION

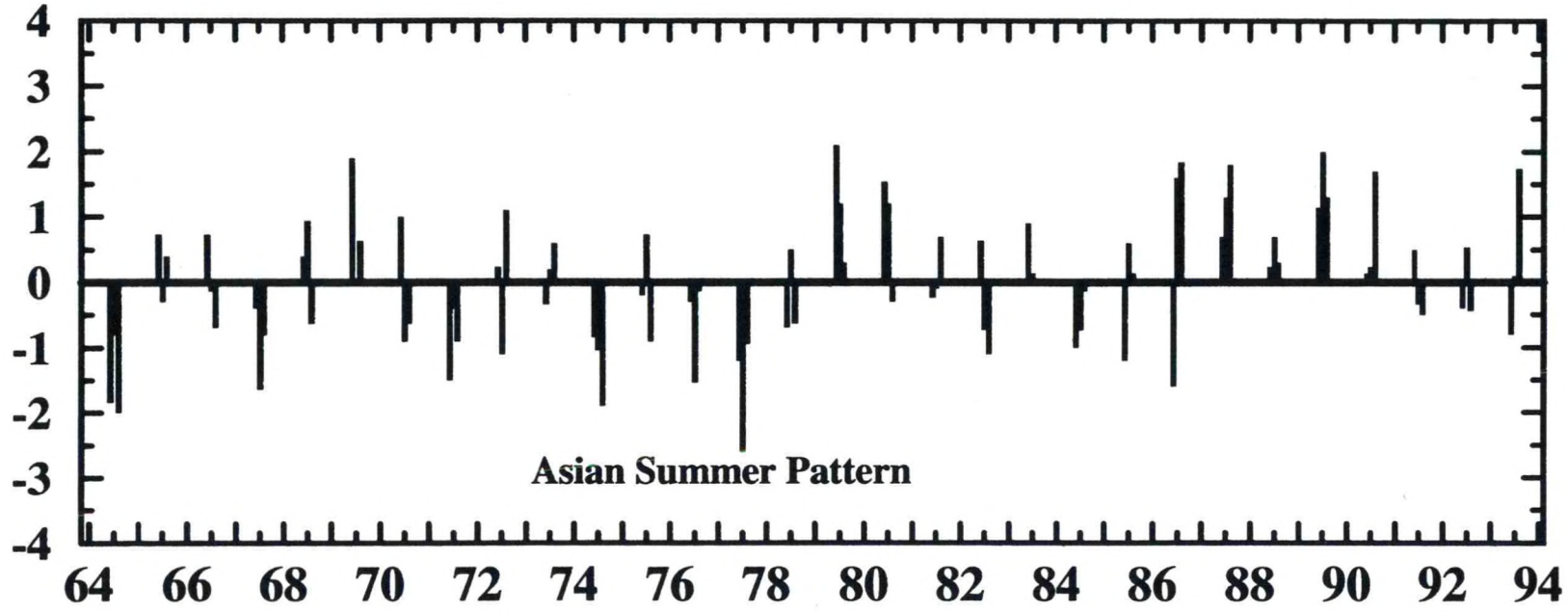
4
3
2
1
0
-1
-2
-3
-4
Asian Summer Pattern
64 66 68 70 72 74 76 78 80 82 84 86 88 90 92 94

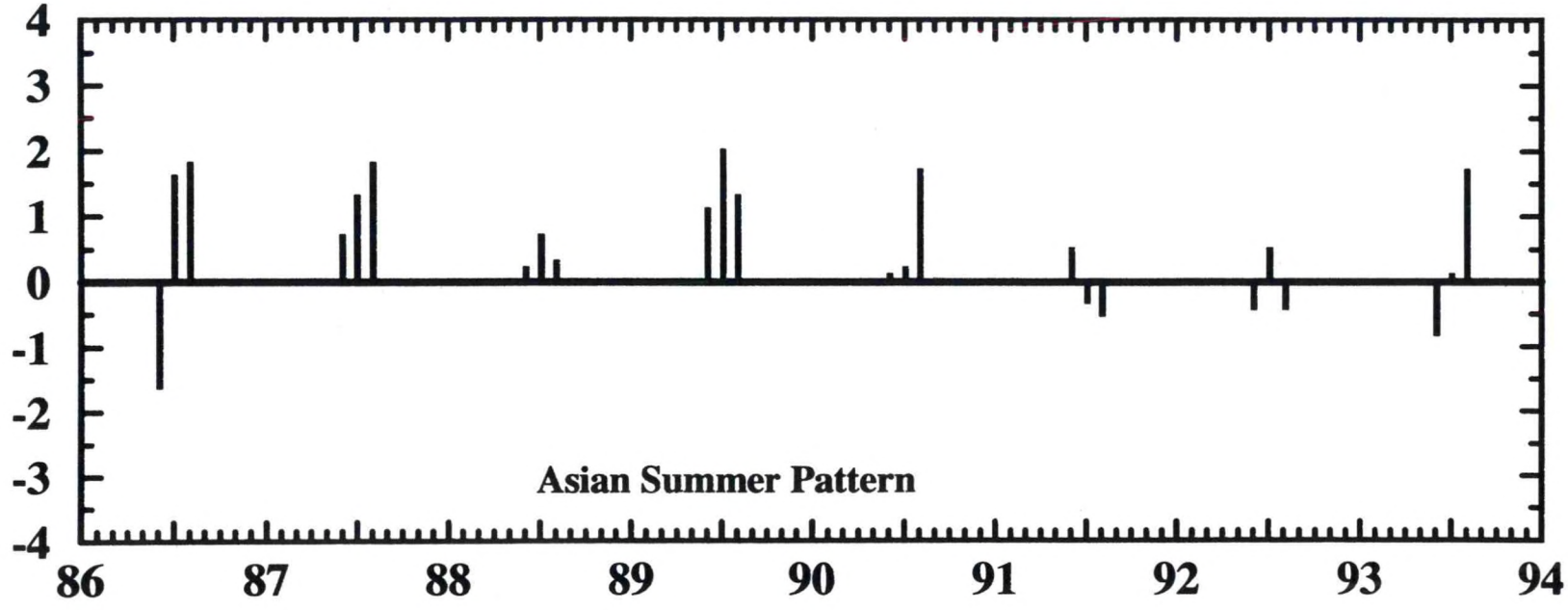
4
3
2
1
0
-1
-2
-3
-4
Asian Summer Pattern
86 87 88 89 90 91 92 93 94

☆ U.S. GOVERNMENT PRINTING OFFICE: 1995 — 386-626/37952